A study, by inelastic neutron scattering, of adsorbed benzene, of metal -Arene complexes and of hydrogen attached to metal clusters

D. Graham

A STUDY, BY INELASTIC NEUTRON SCATTERING, OF ADSORBED BENZENE, OF METAL π-ARENE COMPLEXES AND OF HYDROGEN ATTACHED TO METAL CLUSTERS

By

D. Graham B.Sc.

A thesis submitted in partial fulfilment of the requirements for the Degree of Doctor of Philosophy in the University of Durham.

"He either fears his fate too much
Or his deserts are small
That dares not put it to the touch
To win or lose it all"

James Graham
Marquis of Montrose (1612-50)

To Marilyn

ACKNOWLEDGEMENTS

I should like to thank Professor T.C. Waddington and Dr. J. Howard, under whose supervision this work was tackled, for encouragement and advice.

The experimental work was undertaken at Durham, A.E.R.E. Harwell and at the I.L.L. Genoble. I have received much help and particulary want to thank the technical staff at Durham for aid. At Harwell, I acknowledge the assistance of the University support section especially Mr. D.H.C. Harris, Mr. G. Haines and Mr. N. Hance. At Grenoble, my thanks go to Dr. J. Tomkinson, whose friendly encouragement and useful discussion must be noted.

A special thanks go to my fellow neutron scatterers and other friends at Durham for their moral, as well as technical support in the past three years and for making it as enjoyable as it was.

My profound thanks finally go to my wife, Marilyn, who typed the thesis in her usual organized manner. Further, she steadfastly reassured me and endured my many absences from home whilst I was neutron scattering.

D. Graham, B.Sc.

Title: "A Study, by Inelastic Neutron Scattering of Adsorbed Benzene, of Metal π -Arene Complexes and of Hydrogen Attached to Metal Clusters"

ABSTRACT

Studies of transition metal hydridocarbonyls show that the hydrogen vibrations are decoupled from the metal-carbonyl skeleton. The hydrogen modes of (μ_2-H) species ($HW_2(CO)_9NO$, $HRe_3(CO)_{14}$, $H_3Mn_3(CO)_{12}$, $H_3Re_3(CO)_{12}$, $H_2FeRu_3(CO)_{13}$ and $H_4Ru_4(CO)_{12}$), (μ_3-H) species ($H_4Re_4(CO)_{12}$, $HFeCo_3(CO)_{12}$ and $H_2Ru_6(CO)_{18}$), (μ_6-H) species ($CsHCo_6(CO)_{15}$) and $(\mu_2\text{-H})_2$ species ($H_2Os_3(CO)_{10}$) can be described in terms of C_{2v}, C_{3v}, O_h and D_{2h} 'local' symmetry respectively. The (μ_2-H) spectra are complex and a description that involves framework metal-carbonyl deformations with associated hydrogen motion is postulated. The vibrational data has assisted in the analysis of previous spectra of hydrogen adsorbed on transition metal surfaces. Evidence is overwhelmingly in favour of (μ_3-H) species on Ni while (μ_2-H) and (μ_3-H) species are found on Pt. It is suggested the hydrogen site(s) cannot be described confidently for the H/W system with present data. A study of C_6H_6 and, to a lesser extent, C_7H_7, π -complexes was carried out to assist in adsorbed benzene studies. Adsorbed benzene on both NaI3X and AgI3X zeolites resembled that found in weak C_6H_6 complexes. The only major difference between the two M^+-C_6H_6 interactions was that a higher torsional frequency existed in AgI3X. A stronger complexing of benzene took place on Pt black. This was deduced from the high frequency skeletal vibrations, the large increase in υ_{11} and the large torsional effective force constant. The benzene lies in a position, above single Pt atoms, of at least C_{2v} symmetry. Only one surface structure was indicated at $\leqslant 1$ monolayer coverage whereas at ~ 2 monolayers the IINS spectra resembled that of solid and clathrated benzene.

CONTENTS

CHAPTER 1

INTRODUCTION

Introduction

This study was undertaken to facilitate the unique properties of the neutron to analyse and understand some chemical systems that were proven to be difficult by other spectroscopic techniques, such as infra-red and Raman spectroscopy.

These unique properties of the neutron scattering technique allow one to observe the vibrational motion that involve the hydrogen atom in particular, since the incoherent scattering cross-section, a property that describes the scattering efficiency from a specific nucleus type (i.e. the isotope) and which depends on the spin orientations of the sample, is so much greater for hydrogen than for any other isotope type, including deuterium. Hydrogen has an anomalously large incoherent cross-section because of the random distribution of spin states, which is not isotopic in origin. The majority of elements have small incoherent cross-sections whereas those with only one isotope and no spin will therefore have no incoherent cross-section (e.g. C and O). This then can be used to great effect in that the molecular vibrations that involve hydrogen motion can be separated from the others since they have much greater intensity in the neutron spectrum. The technique thus lends itself very well to deuteration experiments since the cross-section of deuterium is very much lower than hydrogen. Such isotopic substitution experiments can take the form of total substitution, which leads to deuteration shifts, and of selective deuteration, which allows one to 'remove' certain modes from IINS spectra

by reducing their intensity and shifting the frequency. Further, the inelastic neutron scattering technique (IINS) is not subject to electromagnetic selection rules and so all the modes are formally 'active' (though only those involving hydrogen motion are, to a first approximation, found in the neutron spectrum).

Except in the quasi-elastic region, the resolution of the IINS instruments is, as yet, rather poor, when compared with infra-red and Raman spectrometers. This is particularly disadvantageous when vibrational modes occur close together. However, there are many cases when optical spectral assignments are difficult or impossible. It must be noted though that it is very difficult to carry out a full molecular vibrational analysis from just IINS data alone and assignments are usually carried out using a combination of IINS and other spectroscopic data, when available, though this is not always the case. Since the neutron has very different properties from electromagnetic radiation, IINS data is a function of the scattering vector, amplitude of vibration and normal mode frequency, it is expected that the data obtained is complimentary to that obtained by other techniques.

This thesis decribes vibrational studies carried out in four particular areas that have proven difficult using only infra-red and Raman techniques. They are:

(i) Transition metal hydridocarbonyls
(ii) C_nH_n organometallic species
(iii) Benzene adsorbed onto platinum black
(iv) Benzene adsorbed into the supercages of Na and Ag13X zeolites.

The study of hydrogen attached to metal clusters, in the form of transition metal carbonyls, is an exciting and important field that particularly lends itself to neutron scattering. A review of this area is given in Chapter 4. Vibrational studies of proton vibrations in transition metal hydridocarbonyls has proven difficult in the past, using infra-red and Raman spectroscopy, especially when the hydrogen has been in a bridging position. Often the vibrations involve small or negligible transition dipole moment or polarizability changes. Sample decomposition, band broadening and the highly coloured nature of compounds also are prejudicial to these techniques. However, the IINS method is non-destructive, whether a compound is highly coloured or not makes no difference and band broadening is not a problem, if the band has sufficient IINS intensity. The vibrations may involve small changes in polarizability or dipole moment but may still have a large scale hydrogen atom vibrational amplitude which creates the IINS intensity.

This latter property is especially pertinent in the study of C_nH_n organometallic complexes. The dynamics of this group of compounds is especially interesting, not only in their own right scientifically, but also since the metal-hydrocarbon interaction is of specific interest with regards hydrocarbon-metal/zeolite behaviour and hence both heterogeneous and homogeneous catalysis. This study involves benzene and tropyllium organometallics. The latter are, within this thesis, only of spectral interest, but the former are of major importance in the catalytic

field and of special import to this present field of enquiry since a vibrational analysis is carried out of benzene adsorbed on platinum black and in type X zeolite supercages. Use is made of data from the organometallics, and of benzene alone, in the analysis of the neutron spectra of the adsorbed species.

The metal - (π-arene) vibrations are usually weakly, if not formally inactive, in the infra-red and Raman and the metal-(arene) torsion and deformation modes are in this class. These bands are usually associated with intense IINS features. In the infra-red and Raman the frequency, in which these skeletal framework vibrations fall, is usually quite complex with low frequency intra- and inter-molecular vibrations generally making it difficult to differentiate any active skeletal bond.

Problems exist in the study of absorbed species by infra-red spectroscopy. Often the surface adsorbs, very strongly, any infra-red radiation particularly in the low frequency region of interest. The material, upon which the adsorbate is being adsorbed, must also be translucent, if reflection techniques are not being facilitated. This is not always possible, and, usually involves the use of a transparent support. Thus, infra-red studies have usually involved zeolite or silica/alumina type adsorbents. The Raman techniques is similar but also suffers from fluorescence of the sample, which then entails either cooling of the sample, wavelength changes of the elastic line, heating in oxygen, calcination etc. Electron energy loss spectroscopy has been successful recently in such

studies but can suffer from poor resolution, experimental difficulties and selection rule problems, though the latter is not always a problem and can be an advantage. Further, the methods cannot be used below 250cm^{-1} at present.

The neutron scattering techniques does not suffer from many of these disadvantages discussed above, but it does have poor resolution in the regions of interest. One particular disadvantage is the necessity to place sufficient hydrogeneous material in the beam of neutrons so that enough neutron scattering events can be recorded since the sensitivity of the method is so low. A neutron scattering experiment can allow such since the technique is not a surface probe, in reality. Large surface area samples must be used to ensure the necessary quantity of adsorbed material can be achieved. The scattering that takes place from the background material, i.e. the sample before adsorption, is not negligible but can be taken into account, since the ratio of the signal due to the scattering from the adsorbed species alone to the the scattering from the background material is usually high.

CHAPTER 2

GENERAL THEORY

2.1. Introduction

The neutron was discovered in 1932 and in 1936 it was found that it could be diffracted. However, neutron sources were feable and it was not until the advent of nuclear reactors that neutrons first were used as a tool. Since the 1940's the intensity of neutron fluxes has increased up to 10^4 times and the use of the neutron has paralleled this increase.

The neutron is an uncharged elementary particle, of spin $\frac{1}{2}$, with a rest mass 1.675×10^{-27}kg (1836 times that of the electron) and a magnetic dipole of -1.9125 nuclear Bohr magnetons. Further, it produces no detectable primary ionization in its passage through matter but interacts with matter predominantly by nuclear collisions and, to a lesser extent, with unpaired electrons.

2.2. Neutron Properties

2.2.1. Neutron properties and spectroscopy

The utility of neutrons in the study of materials whether they are solids, liquids or gases, arises from the following basic properties:

(a) The neutron, on its passage through matter, is likely to either pass through entirely, be scattered or be adsorbed by forming a compound excited nucleus and decaying along specific lines. The neutron, because of its uncharged nature, can penetrate very deeply into the atom and interact with the nucleus because there are no coulombic forces to overcome. The scattering is finally produced by a neutron/nuclear force field interaction.

(b) The wavelength of thermal neutrons, 0.5 - 20Å, is of the same order as interatomic spacings in matter and thus interference effects can occur which can yield information on the structure of the target system. (Wavelengths up to 100Å can be used on an ultra cold source at the Institute Laue Langevin).

(c) The energy of thermal neutrons is of the order of magnitude of vibrational energy levels in matter. Thus one may get a measureable change in the incident neutron energy on scattering due to either neutron energy loss or in neutron energy gain.

(d) The neutron has a magnetic moment and can thus interact with unpaired electrons in magnetic atoms resulting in information on magnetic structure and dynamics. Further, magnetic interactions are possible with atomic magnetic moments, nuclei magnetic moments and nuclei electric fields though these can be neglected in comparison to the contributions from neutron/unpaired electron magnetic interactions.

2.2.2. Neutron properties and vibrational spectroscopy

The usefulness of neutrons to the study of molecular vibrations, in particular, is further enhanced by the following points:

(a) There are no electromagnetic selection rules to be obeyed, in principle, and thus all normal modes of vibration should be active. However, in the linear X-H-X system the symmetric stretch will be a normal mode but if σ_{incoh} of the X atoms is zero then the mode will be inactive, since for activity at least one of the scattering atoms

involved in the normal mode should have $\sigma_{incoh} \neq 0$.

(b) Neutrons can probe a molecular target on a time scale between 10^{-7} and 10^{-12} seconds. Thus both vibrational and diffusive motions, of the order of 10^{12} cycles per second, can be observed.

(c) The neutron, because of its large mass compared to other scatter radiations, can produce momentum transfers of the right order of magnitude for various scattering studies. One can study the angular dependancy of spectral features.

(d) The neutron/nucleus interaction can vary from one atom type to another and thus an "effective selection rule" can be formed because of preferential scattering of neutrons by one type over another. Such scattering is characterised by the scattering length, b, a function of the interaction potential between neutron and nucleus. This is a very short range potential of the order of 10^{-4} Å and is negligible compared to a thermal neutron wavelength, which is of the order of an Å. Thus, for such a fixed nucleus, the distribution of scattered waves is spherically symmetrical ie. the scattering is isotropic. The scattering length varies from nucleus to nucleus in an apparent random way determined by nuclear structure. The presence of an isotopic mixture in a scattering system or of spin dependent interactions gives rise to a process known as incoherent scattering whereas coherent scattering, analogous to scattering of electromagnetic radiation, can be seen from a system of identical nuclei having zero spin or within a system where the spins are all aligned e.g. using a magnetic field and

a polarised neutron beam. For a system with identical nuclei with non-zero spin the neutron/nucleus interaction depends on the relative orientations of the neutron and nuclear spins and therefore gives rise to incoherence. Each nucleus scatters independently and no interference effects are observed. For nuclei with zero spin, incoherence can still arise if the scattering length can fluctuate from nucleus to nucleus, because of isotopic effects, and is due to the random distribution of the deviations of the scattering lengths from their mean value, whereas the coherent scattering is the scattering the same system would give, if all the scattering lengths were equal to the average scattering length, $\bar{b}$. Thus coherence and incoherence can occur together or coherence occurs alone. These terms will be discussed later.

The incoherent scattering component of hydrogen is 40 times as large as its coherent contribution and the incoherent scattering cross section of hydrogen is greater than an order of magnitude larger than the incoherent scattering cross-sections of other nuclei. This will result in an incoherent vibrational neutron spectrum of a sample containing hydrogen being dominated by the scattering from protons and so those normal vibrations involving proton motion will be very intense compared to any other. This also results in an "effective selection rule"; that is, those bands involving hydrogen motion will dominate an incoherent neutron spectrum. Table 2.1 shows the coherent and incoherent cross sections of the more important atoms found in this study (1). Due to the variation from isotope to isotope, of the incoherent scattering, one can apply

isotopic substitution techniques to neutron scattering for hydrogen and deuterium. Substitution of deuterium for hydrogen brings about changes in the spectrum due to frequency position and band intensity. This offers a guide to analysis. The anomalously large incoherent scattering cross section of hydrogen arises from its non-zero nuclear spin which produces an average (weighted) close to zero.

Element	σ_{coh} $(10^{-28}m^2)$	σ_{incoh} $(10^{-28}m^2)$
H	1.8	79.7
D	5.6	2.0
C	5.6	0.0
N	11.1	0.3
O	4.24	0.0
Na	1.65	1.7
Al	1.5	0.0
Si	2.16	0.0
Cl	11.5	3.5
Mn	1.9	0.4
Br	5.79	0.3
Ru	6.7	0.1
Pd	4.5	0.3
Ag	4.48	1.8
W	2.86	2.8
Re	10.6	-
Os	14.4	0.5
Pt	11.3	0.7

Table 2.1

Cross Sections of the Majority of Elements Used in This Study

Neutron scattering processes

There are several types of experiment possible arising from the general properties of the neutron and the target system.

(a) Neutron diffraction

The intensity of the elastic scattering, that which sees no energy transfer, can be measured as a function of momentum transfer. Though in gases there is no such elastic peak in the spectrum because the atom is free to recoil. There is also, perhaps, no true elastic peak in liquids though diffraction studies have been carried out on liquids.

A diffraction pattern from a sample is gathered by collecting neutrons at different values of the scattering angle.

(b) Quasi-elastic scattering

If the scattering nuclei undergo some diffusive process then as a result of this the sharp elastic line becomes broadened. This quasi-elastic broadening is a feature of random rather than oscillatory motions and can yield information on the rate and geometry of such motions. The quasi-elastic peak, whose position is independent of momentum transfer, increases in width as the liquid-like characteristics of the sample increase.

(c) Inelastic neutron scattering

The total scattering intensity is both a function of momentum and energy transfer between neutron and sample. The inelastic part contains information about the rotational and vibrational motions in the system. This can be gained

from the energy transfer positions, frequencies, in the inelastic spectrum whether it be neutron energy gain or loss.

(d) Magnetic scattering

If the atoms contain unpaired electron spins additional information can be gained on the magnetic structure (the spin ordering pattern) and the interactions taking place between the spins.

Table 2.1 summarizes the information available from neutron scattering experiments.

	Elastic Scattering	Inelastic Scattering
Coherent Scattering	Crystal and Magnetic Structures	Dispersion Relations
Incoherent Scattering	Diffusion coefficients and the frequency distribution functions relationship with temperature	Frequency Distribution Function

Table 2.2

2.2.3. Neutron Scattering and other Techniques

Table 2.3 shows the range of energy and momentum transfers which can be studied with neutron scattering and they are compared with other scattering techniques.

Scattering Radiation	Wavelength Å	Momentum Å	Energy (mev)	Transfer range (mev)
Neutron	1-100	0.6-6	1-600	1-600
Electron	~0.1	~60	$\sim 5 \times 10^7$	wide range
X-Ray	~1	~1	$\sim 1 \times 10^7$	wide range
Light	>1000	~0.001	$\sim 1 \times 10^4$	100

Table 2.3

It is apparent that neutron scattering is the only technique that offers both energy and momentum transfers in the right order of magnitude for the study of thermal motions and structure. The neutron wavelength is akin to interatomic distances and the energy resolution available is of the order of energy level spacings. With X-rays and electrons the energy transfer is too high and for Raman scattering the momentum transfer is too small between radiation and sample.

Molecular spectroscopy, till the recent advent of other techniques, had been solely the ground of infrared spectroscopy, and to a lesser extent, Raman spectroscopy. However, certain systems can not be fully analyzed by each method alone or by combination because of optical selection rules, very small dipoles or very small polarisability changes. Due to certain disadvantages of the neutron scattering technique, it has become apparent that optical

methods and neutron scattering can be complimentary and that combinations of data from them both are powerful tools in analysing molecular systems. Neutron scattering is also complimentary to X-ray scattering studies though neutrons are virtually a unique tool for structural studies of hydrogeneous compounds since the hydrogen electron cloud is of such low density that X-rays cannot, with any accuracy, establish the proton position.

As with other techniques, neutron spectroscopy suffers a few disadvantages. At present neutron spectra mirror the relatively poor resolution that can be attained by neutron spectrometers. It can also take up to two days to gather enough scattering information to complete a spectrum. Neutron spectrometers are not readily available and time must be arranged well in advance.

However, now more intense neutron sources and better spectrometers are being designed and tested that will allow more experiments to be carried out in less time and with better energy and momentum resolution.

2.2.4. Neutron Scattering Cross-Sections

Figure 2.1 schematically shows a typical neutron scattering event.

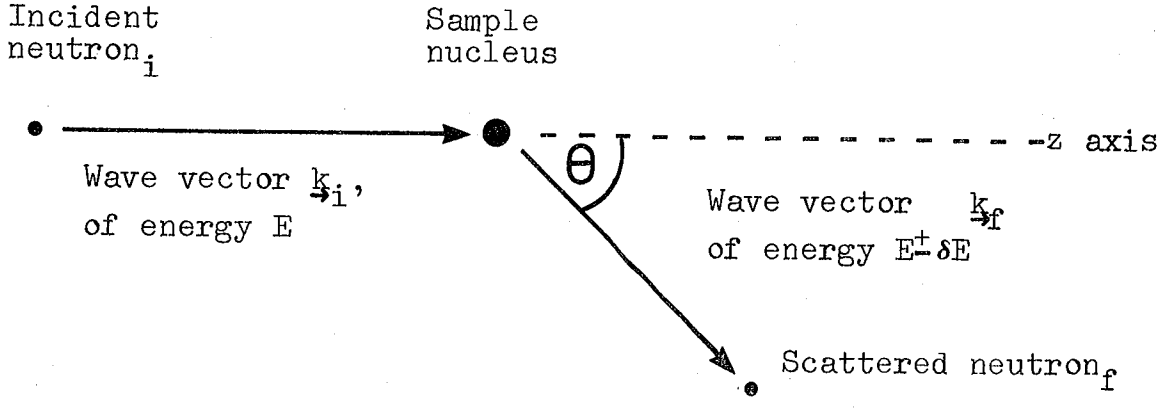

Figure 2.1

The results of such an event are expressed in terms of the cross-section (measured in units of m^2)

One can measure the number of neutrons, per unit time, so scattered in terms of the incident and final energy of the neutron and the direction of scatter into a specific small solid angle of space. Such a cross-section is defined as shown in equation 2.1 where

$$\left(\frac{\delta^2\sigma}{\delta\Omega\,\delta E}\right) = \frac{\left(\begin{array}{l}\text{Number of neutrons of incident energy E}\\ \text{scattered per second into a small solid}\\ \text{angle},\delta\Omega\text{, in a direction }(\theta,\phi)\text{, with final}\\ \text{energy between E' and E'+dE'}\end{array}\right)}{\left(\begin{array}{l}\text{(Incident neutron flux},\Phi)\text{x(small solid}\\ \text{angle},\delta\Omega)\text{x(energy transfer, }\delta E'\text{)}\end{array}\right)} \qquad 2.1$$

σ = cross section. This is known as the partial differential cross-section. Other cross-sections can be defined and they correspond to situations where a) the energy is not analyzed but the neutrons are counted. This is the differential cross-section. b) All directions of scatter are taken into account, not just $\delta\Omega$. This is known as the total scattering cross-section.

From such measured cross-sections, various theoretical expressions can be derived that allow one to analyze the scattering data. These will be discussed in detail in section 2.3

The scattering cross-section of any particular fixed nucleus can be derived from the wave functions of the incident neutron, Figure 2.1, and that of the scattered neutron at point r. This relation involves the constant b, known as the scattering length. As the scattering is spherically symmetric, the wave function of the scattered neutrons at point r is written in the form shown in

equation 2.2. (The scattering length, $\underrightarrow{b}$, can be related

$$\Psi_{scat.} = -\frac{\underrightarrow{b}}{r} \exp(i\underrightarrow{k}r) \qquad 2.2.$$

to the scattering amplitude f by $-\underrightarrow{b}=f$). From 2.2. the total cross section σ_{tot} can be expressed in terms of b as in equation 2.3.

$$\sigma_{tot} = 4\pi\underrightarrow{b}^2 \qquad 2.3.$$

For a free nucleus equation 2.4. is derived where M = mass of and m is the neutron mass. With a solid,

$$\sigma_{tot} = \frac{4\pi\underrightarrow{b}^2}{1+\frac{M}{m}^2} \qquad 2.4.$$

the total cross-section would lie somewhere between these values since each nucleus is neither free nor strictly rigidly bound. The values of $\sigma_{tot.}$ for incoherent and coherent scattering for a selection of nuclei are given in Table 2.1.

2.3. Neutron Scattering Theory

2.3.1. Introduction

The theory of neutron scattering has been very well documented (1-12). The purpose of this chapter is to very briefly develop the theoretical concepts discussed in much greater depth in the above references. The usefulness of the neutron as a spectroscopic tool and its particular use in molecular vibrational studies of systems containing hydrogen is demonstrated. The equations and functions used in later data analysis are derived with respect to molecular vibrations.

2.3.2. Derivation of the partial differential cross-section term, $\frac{\delta^2\sigma}{\delta\Omega\delta E}$

The partial differential scattering cross-section is measured in many neutron scattering experiments and this can be derived from basic principles.

For a neutron/nucleus interaction the neutron wave-vector is $\underset{\rightarrow}{k}_i$ incident on a nucleus which has an initial state symbolised by λ_i. After interaction the states of the neutron and nucleus are $\underset{\rightarrow}{k}_f$ and λ_f respectively. The differential scattering cross-section can be defined as in equation 2.5.

$$\left(\frac{d\sigma}{d\Omega}\right)_{\lambda_i \longrightarrow \lambda_f} = \frac{1}{\Phi} \cdot \frac{1}{d\Omega} \cdot \sum W_{\underset{\rightarrow}{k}_i \lambda_i \longrightarrow \underset{\rightarrow}{k}_f \lambda_f} \qquad 2.5.$$

(Φ is the neutron flux and W is the number of transitions per second taking place from the initial to the final state). This transition term can be further stated to be a function of the neutron/nucleus interaction, V, using Fermi's Golden Rule, equation 2.6. where $\rho_{\underset{\rightarrow}{k}_i}$ is the number of momentum states in $d\Omega$ per unit energy range for neutrons in their initial state.

$$\sum W_{\underset{\rightarrow}{k}_i \lambda_i \longrightarrow \underset{\rightarrow}{k}_f \lambda_f} = \frac{2\pi}{\hbar} \cdot \rho_{\underset{\rightarrow}{k}_i} \left| \langle f \left| V \right| i \rangle \right|^2 \qquad 2.6.$$

$\left| \langle f \left| V \right| i \rangle \right|$, from first order perturbation theory, is the transition probability per unit time from the initial to the final state. The brackets $\langle \text{-----} \rangle$ indicate the equilibrium ensemble average. Substitution of values for the flux, solid angle and $\rho_{\underset{\rightarrow}{k}_i}$ in equation 2.6. leads to

equation 2.7.

$$\left(\frac{d\sigma}{d\Omega}\right)_{\lambda_i \rightarrow \lambda_f} = \frac{\vec{k}_f}{\vec{k}_i} \left(\frac{m}{2\pi\hbar}\right)^2 |\langle f | V | i \rangle| \qquad 2.7.$$

If E_i and E_f are the initial and final energies of the neutron and E_{λ_i} and E_{λ_f} are the initial and final energies of the scattering system then equation 2.8. can be derived.

$$E_i + E_{\lambda_i} = E_f + E_{\lambda_f} \qquad 2.8.$$

Therefore, the energy distribution of the scattered neutrons can be expressed as a δ function and the partial differential scattering cross-section can thus be derived as shown in equation 2.9.

$$\left(\frac{d^2\sigma}{d\Omega dE}\right) = \frac{\vec{k}_f}{\vec{k}_i} \left(\frac{m}{2\pi\hbar^2}\right)^2 |\langle f | V | i \rangle|^2 \delta (E_{\lambda_i} - E_{\lambda_f} + E_i - E_f) \qquad 2.9.$$

The interaction potential is not known exactly but neutron/nuclei interactions are known to be very short range and thus will give isotopic scattering from a single point nucleus. $|\langle f | V | i \rangle|^2$ is the transition probability per unit time from the initial to the final state and the matrix element $\langle f | V | i \rangle$ can be evaluated by integrating with respect to the neutron co-ordinate $\underset{\rightarrow}{r}$. The potential of the neutron due to the j^{th} nucleus has been shown to have the form $V_j(\underset{\rightarrow}{r}-\underset{\rightarrow}{R}_j)$ where $\underset{\rightarrow}{r}$ and $\underset{\rightarrow}{R}_j$ are the position vectors or co-ordinates of the neutron and the j^{th} nucleus respectively (8). The total potential of the system can be expressed as $\sum_j V_j(\underset{\rightarrow}{r}-\underset{\rightarrow}{R}_j)$.

Now when j = 1 and the specific nucleus involved in the neutron/nucleus interaction is placed at the origin,

ie. $\underset{\rightarrow}{R}_j = \underset{\rightarrow}{R}_1 = 0$, then the interaction potential can be expressed as $V(\underset{\rightarrow}{r})$. Fermi (13) has shown that for an array of bound mono-isotopic nuclei the interaction potential can be expressed as a delta function, using the Born approximation as in equation 2.10.

$$V(\underset{\rightarrow}{r}) = \left(\frac{2\pi\hbar^2}{m}\right) \underset{\rightarrow}{b}\,\delta(\underset{\rightarrow}{r}) \qquad 2.10$$

This potential is known as the Fermi pseudopotential. The magnitude and sign of the scattering length, b, is determined by the shape, depth and range of $V(\underset{\rightarrow}{r})$. $\delta(\underset{\rightarrow}{r})$ is a three dimensional Dirac delta function which ensures the conservation of energy in the neutron/nucleus system and treats the very short range interaction and replaces it with a point source. For the general scattering system the pseudopotential takes the form of equation 2.11.

$$V(\underset{\rightarrow}{r}) = \left(\frac{2\pi\hbar^2}{m}\right)\sum_j \underset{\rightarrow}{b}_j\,\delta(\underset{\rightarrow}{r}-\underset{\rightarrow}{R}_j) \qquad 2.11$$

Thus the partial differential scattering cross-section in equation 2.10 can further expressed as follows, using the potential function in equation 2.12.

$$\left(\frac{d^2\sigma}{d\Omega dE}\right)_{\lambda_i\rightarrow\lambda_f} = \frac{\underset{\rightarrow}{k}_f}{\underset{\rightarrow}{k}_i}\left|\sum \underset{\rightarrow}{b}_j\langle\lambda_f\left|\exp(i\underset{\rightarrow}{Q}.\underset{\rightarrow}{R}_j)\right|\lambda_i\rangle\right|^2 \delta(E_{\lambda_i}-E_{\lambda_f}+E_i-E_f) \qquad 2.12$$

The $\exp(i\underset{\rightarrow}{Q}.\underset{\rightarrow}{R}_j)$ is the wave function of the scattering system and $\underset{\rightarrow}{Q}$ is the scattering vector, having a value $(\underset{\rightarrow}{k}_i-\underset{\rightarrow}{k}_f)$.

However, in an actual experiment one does not measure the cross-section for a process in which the scattering system goes from $\lambda_i \rightarrow \lambda_f$. To obtain the quantity

$(d^2\sigma/d\Omega dE)$ defined on page (18) one must sum the cross-section, stated in equation 2.12, over all the final scattering states λ_f, keeping λ_i constant, and then averaging overall λ_i. The new expression is written in equation 2.13 in terms of the time dependent Heisenberg operator $\underset{\rightarrow}{R}_j(t)$ where $\hbar\omega = E_i - E_f$.

$$\left(\frac{d^2\sigma}{d\Omega dE}\right) = \frac{\underset{\rightarrow}{k}_f}{\underset{\rightarrow}{k}_i}\left(\frac{1}{2\pi\hbar}\right)\sum b'_j b''_j \int_{-\infty}^{\infty} \langle \exp(-i\underset{\rightarrow}{Q}.\underset{\rightarrow}{R}_{j_f}(0))\exp(i\underset{\rightarrow}{Q}.\underset{\rightarrow}{R}_{j_i}(t))\rangle \text{-----}\exp(-i\omega.t)dt \qquad 2.13$$

Hence the δ-function for energy can be expressed as an integral with respect to time in equation 2.14

$$\delta(E_{\lambda_i} - E_{\lambda_f} + E_i - E_f) = \left(\frac{1}{2\pi\hbar}\right)\int_{-\infty}^{\infty} \exp\left\{ i(E_{\lambda_f} - E_{\lambda_i})t/\hbar \right\}\exp(-i\omega t)dt \qquad 2.14$$

The Heisenberg operators $\underset{\rightarrow}{R}_{j_f}(0)$ and $\underset{\rightarrow}{R}_{j_i}(t)$ are related to the position vectors $\underset{\rightarrow}{R}_j$ of the j^{th} nucleus by equation 2.15 where H is the Hamiltonian of the target system ie. it reflects the properties of the scattering system.

$$\exp(i\underset{\rightarrow}{Q}.\underset{\rightarrow}{R}_j(t)) = \exp\left(\frac{iHt}{\hbar}\right)\exp(i\underset{\rightarrow}{Q}.\underset{\rightarrow}{R}_j)\exp\left(\frac{-iHt}{\hbar}\right) \qquad 2.15$$

$\langle \exp(-\underset{\rightarrow}{Q}.\underset{\rightarrow}{R}_{j_f}(0))\exp(i\underset{\rightarrow}{Q}.\underset{\rightarrow}{R}_{j_i}(t))\rangle$ is the thermal average of the expectation value of the time dependent operators within the brackets

2.3.3. Incoherent and Coherent Scattering of Neutrons

The scattering from an assembly of nuclei can be split into two parts. The scattering lengths vary in an apparently random way from nucleus to nucleus and are a function

of the relative orientation and nuclear spins. (The state of the neutron is, in fact, specified entirely by momentum in the form of the wave vector, $\underset{\rightarrow}{k}_i$, and the neutron spin is ignored in this discussion). Coherent scattering arises from the average scattering length, $\overline{\underset{\rightarrow}{b}}$, and incoherent from the root mean square deviation of the scattering lengths, $(\overline{\underset{\rightarrow}{b}^2} - \overline{\underset{\rightarrow}{b}}^2)^{\frac{1}{2}}$.

The coherent scattering depends on the correlation between the positions of the same nucleus at different times and the correlation between positions of different nuclei at different times. It therefore allows for interference effects because coherent scattering is that which some system would give if all the scattering lengths were equal to $\overline{\underset{\rightarrow}{b}}$. The incoherent scattering depends only on the correlation between the position of the same nucleus at different times. Thus incoherent scattering arises from the random distribution of the deviations of the scattering lengths from the mean value and no interference effects are allowed.

In equation 2.13 there is a $(\underset{\rightarrow}{b}'_j \underset{\rightarrow}{b}''_j)$ term. Thus equation 2.13 can be split into two parts because

if $j' = j''$ then $\overline{\underset{\rightarrow}{b}_j \underset{\rightarrow}{b}_{j''}} = \overline{\underset{\rightarrow}{b}}^2$

if $j' \neq j''$ then $\overline{\underset{\rightarrow}{b}_j \underset{\rightarrow}{b}_{j''}} = \overline{\underset{\rightarrow}{b}}^2$

Thus the deviations $= (\overline{\underset{\rightarrow}{b}^2} - \overline{\underset{\rightarrow}{b}}^2) = \overline{(\underset{\rightarrow}{b} - \overline{\underset{\rightarrow}{b}})^2}$

$$\left(\frac{d^2\sigma}{d\Omega dE}\right) = \left(\frac{d^2\sigma}{d\Omega dE}\right)_{inc.} + \left(\frac{d^2\sigma}{d\Omega dE}\right)_{coh.} \qquad 2.16.$$

Further, equation 2.13 can be written as equation 2.17 where $S(\underset{\rightarrow}{Q},\omega)$ is known as the scattering law or scattering function.

$$\left(\frac{d^2\sigma}{d\Omega dE}\right) = \frac{k_f}{k_i} \left(\frac{1}{2\pi\hbar}\right) \overline{b}^2 . S(\underset{\rightarrow}{Q},\omega) \qquad 2.17.$$

This space-time correlation function represents the basic dynamic properties of the scattering system which is independent of the scattered neutron. Equation 2.17 can be expressed in the two following forms where $\sigma_{coh} = 4\pi\overline{b}^2$ and $\sigma_{inc} = 4\pi(\overline{b^2} - \overline{b}^2)$.

$$\left(\frac{d^2\sigma}{d\Omega dE}\right)_{coh} = \frac{k_f}{k_i} \cdot S_{coh}(\underset{\rightarrow}{Q},\omega) \cdot \frac{\sigma_{coh}}{4\pi} \cdot \frac{1}{2\pi\hbar} \qquad 2.18.$$

$$\left(\frac{d^2\sigma}{d\Omega dE}\right)_{inc} = \frac{k_f}{k_i} \cdot S_{inc}(\underset{\rightarrow}{Q},\omega) \cdot \frac{\sigma_{inc}}{4\pi} \cdot \frac{1}{2\pi\hbar} \qquad 2.19.$$

The $S_{inc}(\underset{\rightarrow}{Q},\omega)$ term is used in this neutron scattering study.

2.3.4. Correlation Functions

Equation 2.19 was developed for the scattering of neutrons from an array of nuclei, however, in this form it does not show clearly the relationship between properties of the array and the real experimental spectrum. Van Hove developed more useful relationships (14).

The cross-sections can be related to the thermal averages of operators belonging to the system and the new functions can be used to calculate various real properties of the scattering system. $S(\underset{\rightarrow}{Q},\omega)$ is the double Fourier transform, over space and time, of a function, named as $G(\underset{\rightarrow}{r},t)$. This is the Van Hove space-time correlation function or the time dependent pair correlation function. $G(\underset{\rightarrow}{r},t)$ is the probability of finding any particle at the

origin $\underset{\rightarrow}{r}=0$ at time t=0 then, finding any particle at $\underset{\rightarrow}{r}=\underset{\rightarrow}{r}$ and time t=t. This only applies to a classical system with all the nuclei equivalent.

They are related by an intermediate function $I(\underset{\rightarrow}{Q},t)$. $S(\underset{\rightarrow}{Q},\omega)$ is the Fourier transform of $I(\underset{\rightarrow}{Q},t)$ in time which is the Fourier transform of $G(\underset{\rightarrow}{r},t)$ in space.

Finally $S(\underset{\rightarrow}{Q},\omega)$ is related to $G(\underset{\rightarrow}{r},t)$ in equation 2.20 where the minus sign is arbitrary and indicates that $E_f > E_i$.

$$S(\underset{\rightarrow}{Q},\omega) = \left(\frac{1}{2\pi\hbar N}\right)\iint \exp(i(\underset{\rightarrow}{Q}\cdot\underset{\rightarrow}{r}-\omega t))G(\underset{\rightarrow}{r},t)d\underset{\rightarrow}{r}dt \qquad 2.20$$

For $S_{inc}(\underset{\rightarrow}{Q},\omega)$ one can derive the self time dependent pair correlation function $G_{self}(\underset{\rightarrow}{r},t)$. This is done again in equation 2.21 and 2.22 by using the intermediate function $I_{self}(\underset{\rightarrow}{Q},t)$ where $S_{inc}(\underset{\rightarrow}{Q},\omega)$ is the incoherent scattering function.

$$G_{self}(\underset{\rightarrow}{r},t)=\left(\frac{1}{(2\pi)^3}\right)\int \frac{1}{N}\sum_j \langle\exp(-i\underset{\rightarrow}{Q}\cdot\underset{\rightarrow}{R}_j(0))\exp(i\underset{\rightarrow}{Q}\cdot\underset{\rightarrow}{R}_j(t))\rangle \text{ ------ } \exp(-i\underset{\rightarrow}{Q}\cdot\underset{\rightarrow}{r})d\underset{\rightarrow}{Q}. \qquad 2.21$$

$$S_{inc}(\underset{\rightarrow}{Q},\omega)=\left(\frac{1}{2\pi\hbar}\right)\int \frac{1}{N}\sum \langle\exp(-i\underset{\rightarrow}{Q}\cdot\underset{\rightarrow}{R}_j(0))\exp(i\underset{\rightarrow}{Q}\cdot\underset{\rightarrow}{R}_j(t))\rangle \text{ ------ } \exp(i\omega\cdot t)dt \qquad 2.22$$

For a classical system $G_s(\underset{\rightarrow}{r},t)$ is the probability density of finding any given particle at the origin $\underset{\rightarrow}{r}=0$ at time, t=0 and then finding the same particle at $\underset{\rightarrow}{r}=\underset{\rightarrow}{r}$ and at time t=t. (Note that $G_{total}(\underset{\rightarrow}{r},t) = G_{self}(\underset{\rightarrow}{r},t) + G_{other}(\underset{\rightarrow}{r},t)$ and $G_{other}(\underset{\rightarrow}{r},t)$ refers to any particle at $\underset{\rightarrow}{r}=0$ and t=0 and another particle at $\underset{\rightarrow}{r}=\underset{\rightarrow}{r}$ and t=t.) $S_{inc}(\underset{\rightarrow}{Q},\omega)$ is the double Fourier transform of $G_{self}(\underset{\rightarrow}{r},t)$.

$S_{inc}(\underset{\rightarrow}{Q},\omega)$ can be related to the partial differential scattering cross-section using by the following equation 2.23.

$$\left(\frac{d^2\sigma}{d\Omega dE}\right)_{inc} = \frac{\sigma_{inc}}{4\pi} \cdot \frac{k_f}{k_i} \cdot N \cdot S_{inc}(\underset{\rightarrow}{Q},\omega). \qquad 2.23$$

2.3.5. Principle of Detailed Balance

Equation 2.24 can be proven

$$S(-\underset{\rightarrow}{Q},-\omega) = \exp(-\hbar\omega\beta).S(\underset{\rightarrow}{Q},\omega) \qquad 2.24$$

This is known as the principle of detailed balance (2) where $\beta = \frac{c\hbar\nu}{KT}$. For the transition step that contributes to $S(\underset{\rightarrow}{Q},\omega)$, a neutron would loose energy in the process equal to the transition energy, $\hbar\omega$, and the scattering system would gain energy, $\hbar\omega$, everytime the scattering system moved from a low energy level, λ'_i, to a higher energy, λ''_f. The reverse obviously can happen where the system looses energy with every transition, equal to $\hbar\omega$, and changes from a higher energy level λ''_i, to a lower energy level λ'_f. The second process has a function $S(-\underset{\rightarrow}{Q},-\omega)$ and the probabilities that a neutron will bring about a transition are the same for both directions. The probability that the system is in a lower energy level is higher, initially, by the factor $1/\exp(-\hbar\omega\beta)$. This would apply in a neutron energy loss situation.

A further function $\widetilde{S}(\underset{\rightarrow}{Q},\omega)$ from Schofield (15) can be derived which is even in ω. So that $\widetilde{S}(\underset{\rightarrow}{Q},\omega)$ can replace $S(-\underset{\rightarrow}{Q},-\omega)$ in equation 2.24. Equation 2.25 can be used to compare computed and experimentally determined scattering functions.

$$\widetilde{S}(\underset{\rightarrow}{Q},\omega) = \widetilde{S}(\underset{\rightarrow}{Q},-\omega) = \exp(-\tfrac{1}{2}\hbar\omega\beta).S(\underset{\rightarrow}{Q},\omega) \qquad 2.25$$

$G(\underset{\rightarrow}{r},t)$ can also be defined in this way. Egelstaff (16) has further defined $S(\alpha,\beta)$, in equation 2.26 where α and β are dimensionless variables $\alpha = \frac{\hbar Q^2}{2MT}$ and $\beta = \frac{\hbar\omega}{T}$.

$$S(\alpha,\beta) = KT\ \widetilde{S}\ (\underset{\rightarrow}{Q},\omega) \qquad 2.26$$

β is chosen as positive if the neutron gains energy. This function expresses the energy and the momentum of the atoms in the system as an average and concentrates attention on the atomic motion rather than the atomic structure. The S_{self} term can be calculated from $S(\alpha,\beta)$ by removing a correction factor due to the atomic structure.

2.3.6. The Incoherent Scattering Function and Molecular Vibrations

In this section the functions utilised in presenting the incoherent inelastic neutron scattering (IINS) data are set out. The standard assumption is that the rotational, translational and vibrational motions of the system can be treated as if dynamically independent. This implies the total wave function of that system is the product of the three independent wave functions. (Ψ spin is neglected and the Ψ rot./ Ψ vib. interaction is taken as negligible). The total scattering function can then be expressed in terms of the convoluted independent scattering functions, in equation 2.27 though only the $S_{vib.}(\underset{\rightarrow}{Q},\omega)$ is the term of interest.

$$S(\underset{\rightarrow}{Q},\omega) = \int S_{trans.}(\underset{\rightarrow}{Q},\omega) \bigstar S_{rot.}(\underset{\rightarrow}{Q},\omega) \bigstar S_{vib.}(\underset{\rightarrow}{Q},\omega) \qquad 2.27$$

★ expresses a convolution of the form (11) shown in equation 2.28.

$$S(\underset{\rightarrow}{Q},\omega) = S_{trans.}(\underset{\rightarrow}{Q},\omega-\omega')\, S_{rot.}(\underset{\rightarrow}{Q},\omega')d\omega' \qquad 2.28$$

This convolution leads to a broadening of the inelastic spectral features though studies of broadening are usually limited to the quasi-elastic region.

The scattering function has been discussed by Zermach and Glauber (17) for molecular vibrations and they have shown, in equation 2.29 that for an oriented assembly of harmonic oscillators in the form of a single crystal.

$$\left(\frac{d^2\sigma}{d\Omega dE}\right)_{inc.} = \frac{\underset{\rightarrow}{k_f}}{\underset{\rightarrow}{k_i}}\left(\frac{1}{2\pi\hbar}\right)\sum b^2 \prod \left\{ \exp\left[-(\underset{\rightarrow}{Q}.\underset{\rightarrow}{C_L^\lambda})^2\left(\frac{\hbar}{2\nu_\lambda\, cm_L}\right) - - - - \right.\right.$$

$$- - - \coth\left(\frac{ch\nu_\lambda}{2KT}\right)\Bigg]\left(\exp\left(-\frac{n_\lambda ch\nu_\lambda}{2KT}\right)\right) I_{n_\lambda} - - - -$$

$$\left. - - - \left(\frac{\hbar(\underset{\rightarrow}{Q}.\underset{\rightarrow}{C_L^\lambda})}{2m_L c\nu_\lambda \sinh\left(\frac{ch\nu_\lambda}{2KT}\right)}\right)\delta\left(\hbar\nu_\lambda - \hbar\sum |n_\lambda|\,\nu_\lambda\right)\right\} \qquad 2.29.$$

where:-

n = no. of quanta of energy $ch\nu_\lambda$ involved in the transition. (where $n>0$ neutron energy gain and $n<0$ neutron energy loss.

λ = normal mode transition.

ν_λ = frequency of transition (ie of n quanta).

m = mass of L^{th} nucleus.

k = Boltzman constant.

C_L^λ = Normalised polarisation (or amplitude) vector for each atom of type L in the normal mode λ determined by the system dynamics.

I_{n_λ} = Modified Bessel function.

Since the system is dominated by the hydrogen scattering in the samples used in this study then the summation over all the atoms is not required. Further, the $S_{inc}(\underset{\rightarrow}{Q},\omega)$ is a more desirable function. Further, the modified Bessel function may be written as a series shown in equation 2.30.

$$I_{n_a}(x) = \left(\frac{x}{2}\right)^{|n|_a} \sum_{k=0}^{\infty} \frac{\left[y/2\right]^{2k}}{k!\left(|n|_a + k\right)!} \qquad 2.30.$$

In some cases, it may be replaced by the first term of its power expansion when the argument is small (<0.01) ie. $I_n(x) = \left(\frac{x}{2}\right)^{|n|} \cdot \left[|n|!\right]^{-1}$. This term arises because of the three dimensional space co-ordinate system used to describe the molecular vibration. Equation 2.31 may be derived from the expression arrived at in equation 2.29.

$$S^{\lambda}_{inc}(\underset{\rightarrow}{Q},\omega) = \prod_{\lambda}\left\{ \exp\left[-(\underset{\rightarrow}{Q}\cdot\underset{\rightarrow}{C}^{\lambda}_{L})^2 \cdot \frac{\hbar}{2m_L c\nu_\lambda} \cdot \coth\left(\frac{\beta}{2}\right)\right] \cdot \exp\left(-n_\lambda \frac{\beta}{2}\right) - - - \frac{1}{|n_\lambda|!} \left(\frac{\hbar(\underset{\rightarrow}{Q}\cdot\underset{\rightarrow}{C}^{\lambda}_{L})^2}{4mc\nu_\lambda \sinh\left(\frac{\beta}{2}\right)}\right)^{|n|_\lambda} \delta\left(\hbar\nu - \hbar\sum |n_\lambda|\nu_\lambda\right)\right\} \qquad 2.31$$

This is the scattering function for the transfer of n_λ quanta, each of energy $ch\nu_\lambda$, to the normal mode λ. Scattering due to overtones and combinations would involve simultaneous transfer of quanta to different or the same λ so the intensity would involve products of the first term of the Bessel function. This is usually a small term and only when the scattering vector and/or β are large does such scattering, due to overtones and combinations, become large.

2.3.7. Elastic and Inelastic Neutron Scattering

Equation 2.31 can be utilised to find the incoherent scattering functions in elastic and inelastic scattering. The elastic and inelastic contributions can be found by varying n_λ. With elastic scattering $n_\lambda = 0$ because there is no energy transfer but in inelastic scattering $n_\lambda = \pm n$ where n=1 for a specific fundamental and 2 for an overtone etc. and n=0 for all other fundamentals. (+n found in neutron energy gain and -n in neutron energy loss situations). Combination bands can also occur involving simultaneous transfer of quanta to different normal modes. Thus this involves products of, say, $(n^a \times n^b)$.

Thus the scattering functions can be defined as shown in equations 2.32. and 2.33.

Elastic scattering

$$S^{0}_{inc}(\underset{\rightarrow}{Q},\omega) = \exp\left\{ - (\underset{\rightarrow}{Q}.\underset{\rightarrow}{C}^{\lambda})^2 \cdot \frac{\hbar}{2mc\nu_\lambda} \cdot \coth\left(\frac{\beta}{2}\right)\right\} \qquad 2.32$$

Inelastic scattering (n=+1)

$$S^{+1}_{inc}(\underset{\rightarrow}{Q},\omega) = \sum \exp\left[-(\underset{\rightarrow}{Q}.\underset{\rightarrow}{C}^{\lambda})^2 . \frac{\hbar}{2m_L c\nu_\lambda} \cdot \coth\left(\frac{\beta}{2}\right)\right] \exp\left(-\frac{\beta}{2}\right) - -$$

$$- - \left(\frac{\hbar\left[\underset{\rightarrow}{Q}.\underset{\rightarrow}{C}^{\lambda}\right]^2}{4mc\nu_\lambda \sinh\left[\frac{\beta}{2}\right]}\right) \cdot \delta\left(\hbar\nu - \hbar\nu_\lambda\right) \qquad 2.33$$

Now the mean amplitude of vibration of the L^{th} nucleus, in this case hydrogen, in the normal mode λ, can be denoted by $|\underset{\rightarrow}{u}^{\lambda}|$ and shown to be of the form in equation 2.34.

$$|\underset{\rightarrow}{u}^{\lambda}| = \left(\frac{\hbar}{2mc\nu_\lambda} \cdot \left(\coth \frac{ch\nu_\lambda}{2KT}\right) \cdot \underset{\rightarrow}{C}^{\lambda}\right) \qquad 2.34$$

Further the Debye Waller factor, W_L, can be expressed as shown in equation 2.35.

$$W_L = \frac{\hbar}{4mc} \sum_{\lambda} \frac{1}{\nu_\lambda} \cdot (\underset{\rightarrow}{Q}.\underset{\rightarrow}{C}^{\lambda})^2 . \coth\left(\frac{\beta}{2}\right) \qquad 2.35.$$

Both elastic and inelastic contributions are attenuated by the Debye - Waller factor, which arises because interference effects between atoms and different sites are smoothed out by thermal vibrations. At equilibrium, each atom in the sytem generates a thermal cloud, ellipsoidal in shape, due to its vibratory motions, and the extent of the cloud is temperature dependent. For elastic scattering equations 2.32, 2.34, 2.35 can be combined to form equation 2.36.

$$S^{0}_{inc}(\underset{\rightarrow}{Q},\omega) = \exp(-2W_L) \qquad 2.36.$$

The elastic scattering from a simple harmonic oscillator has been shown not to be isotropic when the incident neutron energy is small so that the scattering has a very small angular dependence. If the incident energy is large then there can be substantial angular dependence, ie. in $\underset{\rightarrow}{Q}$.

For inelastic scattering equation 2.33, 2.34, 2.35 can be combined to form equation 2.37.

$$S^{+1}_{inc}(\underset{\rightarrow}{Q},\omega) = \frac{1}{2}\sum_{\lambda} (\underset{\rightarrow}{Q}.\underset{\rightarrow}{u})^{\lambda 2} . \exp(-2W) . \exp\left(-\frac{\beta}{2}\right) . \delta(\hbar\nu - \hbar\nu_\lambda) \qquad 2.37.$$

In equation 2.37, it is apparent why the scattering intensity from hydrogen is so high: a) the scattering intensity will be high for atoms with large σ_{inc} values. Hydrogen has such a high σ_{inc} value, b) the scattering

will be most intense for atoms with high mean amplitudes of vibration. Hydrogen with its small mass is such an atom. Now spectra look different in energy gain and energy loss, using $S(\underset{\rightarrow}{Q},\omega)$, so the symmetrical scattering function $\widetilde{S}(\underset{\rightarrow}{Q},\omega)$, is more relevant to real situations and these look the same ie. $\widetilde{S}(\underset{\rightarrow}{Q},\omega) = \widetilde{S}(\underset{\rightarrow}{Q},-\omega)$. The following formula in equation 2.38, can be used.

$$\widetilde{S}_{inc}(\underset{\rightarrow}{Q},\omega) = \sum\left(\frac{\hbar\,(\underset{\rightarrow}{Q}.\underset{\rightarrow}{C}^{\lambda})^2}{4mc\upsilon_{\lambda}\sinh\left(\frac{\beta}{2}\right)}\right).\exp(-2W).\delta\,(\hbar\upsilon-\hbar\upsilon_{\lambda}) \qquad 2.38$$

2.3.8. Functions Used With Powdered Samples

Up to now the equations have been developed for single crystals. However, large samples are required in IINS, especially where a small quantity of hydrogen is present per molecule as in transition metal hydrido-carbonyls. Thus, powdered samples have to be employed which, of course, contain many small single crystals randomly oriented. This leads to a large loss of information since it would be necessary to detect neutrons at all possible scattering orientations in order to calculate $\widetilde{S}_{inc}(\underset{\rightarrow}{Q},\omega)$ in equation 2.38.

The scattering function for a powdered sample is found by averaging over all possible orientations as in equation 2.39.

$$S_{inc}(\underset{\rightarrow}{Q},\omega) = \left(\frac{\hbar Q^2}{4mc\upsilon_{\lambda}\sinh\left[\frac{\beta}{2}\right]}\right)\exp(-2W(\upsilon_{\lambda}))\sum|\underset{\rightarrow}{C}^{\lambda}|^2\,\delta(\hbar\upsilon-\hbar\upsilon_{\lambda}) \qquad 2.39$$

The amplitude weighted density of states, $g(\upsilon)$, is found here as the term $\sum|\underset{\rightarrow}{C}^{\lambda}|^2.\delta(\hbar\upsilon-\hbar\upsilon_{\lambda})$. The Debye-Waller

factor is now expressed as an energy dependent quantity, as proven by Reynolds et al (17). $g(\nu)$ can thus be expressed as shown in equation 2.40.

$$g(\nu) = 4mc\nu_\lambda \sinh\left[\frac{\beta}{2}\right] \cdot \left[\frac{\tilde{S}_{inc}(\vec{Q},\omega)}{\vec{Q}^2}\right] \exp(2W(\nu_\lambda)) \qquad 2.40.$$

The Debye-Waller factor is very difficult to calculate and is usually set to one. Thus $g(\nu)$ can be processed from experimental data but, once again, other functions are preferred. $\rho(\nu)$ is the amplitude weighted density of states at zero Q and is expressed as in equation 2.41.

$$\rho(\nu) = 4mc\nu_\lambda \cdot \sinh\left[\frac{\beta}{2}\right] \cdot \lim_{\vec{Q}\to 0} \left[\frac{\tilde{S}_{inc}(\vec{Q},\omega)}{\vec{Q}^2}\right] \cdot \exp(2W(\nu_\lambda)) \qquad 2.41.$$

$\rho(\nu)$ can be related to $P(\alpha,\beta)$ by extrapolating $P(\alpha,\beta)$ to zero α. $P(\alpha,\beta)$ can be related to $S(\alpha,\beta)$, as shown in equation 2.42.

$$P(\alpha,\beta) = \frac{KT}{\hbar} g(\nu) = 2\beta\sinh\left[\frac{\beta}{2}\right] \exp(2W(\nu_\lambda)) \frac{S(\alpha,\beta)}{\alpha} \qquad 2.42.$$

Most time-of-flight data is expressed as $P(\alpha,\beta)$ in a plot of $\sum^{t} P(\alpha,\beta)$ against where t = number of scattering angles.

2.3.9. Temperature and Momentum Dependence of IINS Bands

The intensity of bands in IINS spectra are very much dependent on momentum and temperature as shown in the following.

2.3.9.1. Momentum Dependence

Now equation 2.31 can be put into a suitable form to make it relevant for polycrystalline samples and equation 2.43 is arrived at.

$$S^{n_\lambda}_{inc}(\underset{\rightarrow}{Q},\omega) = \sum \frac{1}{|n_\lambda|!} \left(\frac{\hbar(\underset{\rightarrow}{Q}.\underset{\rightarrow}{e}^\lambda_L)^2}{4mc\nu_\lambda \sinh\left(\frac{\beta}{2}\right)} \right)^{|n_\lambda|} . \exp(-n_\lambda \tfrac{\beta}{2}) . - - -$$

$$- - \exp(-2W(\nu_\lambda)) \, \delta(\hbar\nu - \hbar\sum |n_\lambda| \nu_\lambda) \qquad 2.43.$$

One can study different momentum transfers by taking different scattering angles for the same energy transfer when dealing with the energy transfer $c\hbar\nu_\lambda$ for the normal mode λ , as in equation 4.44.

$$S^n_{inc}(\underset{\rightarrow}{Q},\omega_\lambda) \propto (\underset{\rightarrow}{Q}^2)^n . \exp(-2W(\nu_\lambda)) \qquad 2.44.$$

When $\underset{\rightarrow}{Q}$ is large the total overtone contribution manifests itself as an increase in the general background scattering and not as discrete bands and at any point in the spectrum the scattering can be due to a fundamental and an overtone(s). Such scattering is a function of the scattering angle and, of course, the incident energy. This complicates the experiment and an approximation, due to Placzek (19) is taken where all the scattering is treated as though it is incoherent since interference from different sites is not likely to be important.

2.3.9.2. Temperature Dependence

The scattering function contains many terms which involve temperature and thus the temperature dependence of an IINS spectrum can be complex. The situation is clarified by taking three different areas of temperature.

(i) Very low temperature (eg. 4K)

With a very low temperaure, the β value $\left[\frac{ch\nu}{KT}\right]$ becomes large and $\sinh\left[\frac{\beta}{2}\right]^{-1} \approx \exp\left(-\frac{\beta}{2}\right)$. Also $\coth\frac{\beta}{2}$ would tend to one. Thus equation 2.45 can be derived.

$$S_{inc}^{n_\lambda}(\vec{Q},\omega) = \frac{1}{n}\sum_{\lambda}\left(\frac{c\hbar Q^2}{4m\nu_\lambda}\right)^n \cdot |\vec{C}^{\lambda}|^2 \cdot \exp\left(-\frac{\beta}{2}(n+n_\lambda)\right) - - -$$

$$- - \exp\left(-2W(\nu_\lambda)\right)\delta(\hbar\nu - |n_\lambda|\hbar\nu_\lambda) \qquad 2.45.$$

In the system, the excited states will be very poorly populated at 4K and thus in a neutron energy gain situation where $n_a=n$, there will be very few neutrons which will gain energy because equation 2.45 contains the very small $\exp(-\beta n)$ term.

For such a reason, neutron energy gain experiments are rarely run at very low temperature. In a neutron energy loss situation, $n_a=-n$, the $\exp\left(-\frac{\beta}{2}(n-n_\lambda)\right)$ term disappears. Thus $S_{inc}^{n}(\vec{Q},\omega)$ becomes independent of temperature and thus a high scattering intensity could be achieved.

(ii) Very high temperatures

The Debye-Waller factor at high temperatures varies linearly with temperature since the temperature dependent term $\coth\left[\frac{\beta}{2}\right] \approx \left[\frac{\beta}{2}\right]^{-1}$. Equation 2.46 has been derived (9).

$$S_{inc}^{n_\lambda}(\vec{Q},\omega) = \sum \exp\left(-2W(\nu_\lambda)\right)\left(\frac{Q^2|\vec{C}^{\lambda}|^2 KT}{m\nu_\lambda^2}\right)\delta(\hbar\nu - \hbar n_\lambda\nu_\lambda) \qquad 2.46$$

However, the derived equation is not much use because most chemical systems and compounds are not likely to be stable at the high temperature at which this equation is valid.

(iii) Intermediate values of temperature

Coth $(\frac{\beta}{2})$ is again approximated to $(\frac{\beta}{2})^{-1}$ and the following equation 2.47 has been derived where $P^n(\alpha,\beta)$ is the n^{th} transition contribution to $P(\alpha,\beta)$.

$$P^n(\alpha,\beta) \propto T^n \exp(-W(\upsilon_\lambda)) \qquad 2.47$$

This relationship has been used to good approximation in the low frequency region but becomes more complex in the higher frequency region. Overtones are known to increase in intensity quicker than fundamentals, as to be expected, and thus it is apparent that the intensity of overtones would have to be reduced with respect to fundametals to achieve a cleaner spectrum in the intermediate temperature range. This is attained by using low values of $\underset{\rightarrow}{Q}$ and thus small scattering angles, though the possibility of contamination of the scattered beam by the non-scattered beam would be large. One can also reduce the intensity due to overtones by increasing the incident neutron energy and thus increasing $\underset{\rightarrow}{k_i}$ and, obviously, $\underset{\rightarrow}{k_f}$ and reducing $\underset{\rightarrow}{Q}$, compared to $\underset{\rightarrow}{k_i}$ and $\underset{\rightarrow}{k_f}$.

The width of IINS bands is also temperature dependent as shown by Grant (20) in equation 2.48.

$$\text{Full width at half height (FWHH)} = \underset{\rightarrow}{k}\left[\frac{T}{m}\right]^{\frac{1}{2}}.\underset{\rightarrow}{Q}. \text{ cm}^{-1} \qquad 2.48$$

IINS bands have a specific width due to the recoil of the nucleus in the scattering event. To reduce the FWHH, one can reduce the temperature, T, and use a small $\underset{\rightarrow}{Q}$ value.

2.4. Torsional Barrier Calculations

In the study of the C_nH_n complexes and of C_6H_6 adsorbed on platinum black and in zeolite supercages it is possible to assign the torsional frequency(s) in

molecules/systems containing rotor(s). The mean square amplitude of vibration is inversely proportional to the product of the reduced mass and the torsional vibration frequency. If the rotor has a small reduced mass and the frequency of the torsion is low, the resultant vibrational amplitude is large. The torsional vibrations in the above studies are low ($<200cm^{-1}$) though the reduced masses of the C_6H_6/C_7H_7 rings are quite large.

For a rotor with N-fold symmetry, the potential function, which describes the motion, has an N-fold periodicity which can be expressed as a single Fourier series, equation 2.49, when the barrier is repeated N times in a full vibration.

$$V(\gamma) = \sum \frac{V_{kN}}{2} (1 - \cos kN\gamma) \qquad 2.49.$$

γ is the angle defining the rotation of the rotor with respect to the rest of the system framework. Values of N in C_6H_6 and C_7H_7 systems could be 6 and 7 respectively though site symmetry may increase these values by 2 or more times.

Usually the higher terms of the series are small such that $V_N \gg V_{2N} > V_{3N}$. Thus equation 2.50. can be derived where V_N is the torsional barrier height.

$$V(\gamma) = \frac{V_N}{2} (1-\cos N\gamma) \qquad 2.50.$$

Introducing the higher terms into equation 2.50. only changes the shape of the potential well rather than the height. As the perturbation due to the higher terms increases asymmetry, metastable wells and inflexions may occur in the potential (21).

The situation is more difficult to evaluate if unsymmetric rotors are taken with non-equivalent barriers e.g. in C_6H_5Cl.

The equations of motion can then be solved using the resulting Schröedinger equation which in its simplest form is shown in equation 2.51 where I_r is the reduced moment of inertia for the motion.

$$\frac{1}{I_r} \cdot \frac{d^2\psi(\gamma)}{d\gamma^2} + \frac{8\pi^2}{\hbar^2}\left[E - \frac{V_N}{2}(1-\cos N\gamma)\right]\psi(\gamma) = 0 \qquad 2.51.$$

This is directly related to Mathieu's equation 2.52

$$\frac{d^2y}{dx^2} + (b - s\cos^2 x)\, y = 0 \qquad 2.52.$$

where **s** is dimensionless and $= \frac{4V_N}{FN^2}$ (where $F = \frac{\hbar^2}{8\pi^2 I_r}$)

b is an eigenvalue and $= \frac{4E_{v\sigma}}{FN^2}$ (where $E_V = (E - \frac{V_N}{2})_{v\sigma}$)

v is the principal torsion quantum number

σ is the sublevel designation.

Mathieu's equation has different sets of solutions for different angular periods but the solution is laborious. However, the two extremes of the model (ie high and low torsional barrier heights) can help the solution to be obtained more easily.

(i) Low barrier approximation

If V_N approaches zero then $b_{v\sigma}$ is much larger than s. Thus equation 2.52 becomes equation 2.53.

$$\frac{d^2y}{dx^2} + b_{v\sigma}y = 0 \qquad 2.53.$$

The solutions are $y = e^{\pm ikx}$ where k = 0, 1,2,3···but

the condition $\psi(\gamma) = \psi(\gamma + \frac{2\pi}{N})$ requires k = 0,2,4,6... Therefore $b_v = k^2$ and equation 2.54 can be derived which is similar to the expression of a free rotor.

$$E_k - \frac{V_N}{2} = \left[\frac{N^2h^2k^2}{32\pi^2I_r}\right] \qquad 2.54.$$

(ii) High barrier approximation

The term cosNγ can be expanded as a series in equation 2.55.

$$\cos N\gamma = 1 - \frac{N^2\gamma^2}{2!} + \frac{N^4\gamma^4}{4!} - \frac{N^6\gamma^6}{6!} \ldots\ldots \qquad 2.55.$$

Thus, if V_N is high then the rotor will oscillate at the bottom of the well. The variation in γ will be small and the terms higher than γ^4 can be ignored. In Schrödingers equation 2.48 the term $\left[E - \frac{V_N}{2}(1-\cos N\gamma)\right]$ becomes $\left[E_q - \frac{V_N N^2}{4} \cdot \gamma^2\right]$ and produces the equation of a simple harmonic oscillator with the eigenvalues shown in equation 2.56. where q is the quantum number.

$$E_q = (q + \tfrac{1}{2}) \left[\frac{N^2h^2V_N}{8\pi^2I_r}\right] \qquad 2.56$$

Considering the 0→1 transition, equation 2.57 can be formed where V_N is the barrier height (cm^{-1}) and $\bar{\nu}$ is the torsional frequency (cm^{-1}). This equation gives a useful estimate if the height is greater than 10kJ mol^{-1}(22).

$$\overline{V_N} = \left[\frac{8\pi^2c.I_r}{N^2h}\right] . \bar{\nu}^2 \qquad 2.57$$

(iii) Das approximations

Das (23) developed a method for obtaining approximate solutions to the Mathieu equation which proves to be reasonable for determining high and intermediate barrier heights. The accuracy of which is dependent on the number

of terms included in the calculation.

For the first three terms equations 2.58, 2.59 and 2.60 are derived where $K = \left[\frac{N^2 h}{8\pi^2 c I_r}\right]$

$$\text{i)} \quad \overline{V_N} = \overline{\nu}^2/K \qquad 2.58.$$

$$\text{ii)} \quad \overline{V_N} = (\overline{\nu} + K/4)^2/K \qquad 2.59$$

$$\text{iii)} \quad \overline{V_N^2} = (\overline{\nu}^2 + 3K^2/16 + \overline{\nu}K/2)V_N/K + (K/16)^2 = 0 \qquad 2.60$$

In practice using 3 terms, the Das approximation can be in good agreement with those calculations using Mathieu's equation without approximations.

Where the torsional motion interacts with the overall motions of the species containing the rotating top, the full reduced moment of inertia for the internal rotation should include terms concerning the principal moments of inertia of the whole molecule as derived in equation 2.61.

$$I_r = I_A \left[1 - I_A \sum_g \lambda_g^2 / I_g \right] \qquad 2.61$$

where I_A = moment of inertia of a rotor about its axis

λ_g = cosine of angle between the axis of the rotor and the g^{th} principal axis of the whole molecule.

I_g = g^{th} principal moment of inertia.

I_r = reduced moment of inertia.

Multiple top rotors occur when more than one rotor group is attached to the same atom. This only occurs in this study in the complexes $(C_7H_7)_2TaCl_3$, $(C_6H_6PdAlCl_4)_2$ and $(C_6H_6PdAl_2Cl_7)_2$ (though the latter pair are a more complex multiple top). These systems will contain interacting rotors. In order to determine the modes of

vibration, the potential energy of each rotor is written as the sum of (a) the interaction with the framework in absence of other rotors and (b) involving the potential energy as a result of the interaction with the other rotors. (ie. the external and internal field respectively).

The number of torsional modes derived from the results of Ratcliffe and Waddington (20) expected in various conditions of the internal and external fields are:-

Internal field	External field	No. of torsional modes
Non-zero	Non-zero	Two
Non-zero	Zero	One
Zero	Non-zero	One

2.4 References

1. B.T.M. Willis (Ed.) "Chemical Applications of Thermal Neutron Scattering" Oxford Univ. Press (1973)
2. W. Marshall, S.W. Lovesey "Theory of Thermal Neutron Scattering" Oxford Univ. Press (1971)
3. P.A. Egelstaff (Ed.) "Thermal Neutron Scattering" Academic Press (1965)
4. V.F. Turchin "Slow Neutrons" Israel Prog. for Scientific Trans. (Jerus.) (1965)
5. I.I. Gurevich, L.V. Tarasov "Low Energy Neutron Physics" North Holland Pub. Co. Amsterdam (1968)
6. H. Boutin, S. Yip "Molecular Spectroscopy with Neutrons" The M.I.T. Press (Cambr. Mass.) (1968)
7. S.W. Lovesey, T. Springer "Dynamics of Solids and Liquids by Neutron Scattering" Springer-Verlag (1977)
8. G.L. Squires "Introduction to the Theory of Thermal Neutron Scattering" Cambridge Univ. Press (1978)
9. J. Howard, T.C. Waddington Adv. Infra-red, Raman Spec. 7 (1980) 86
10. G.E. Bacon "Neutron Scattering in Chemistry" Butterworths (London) (1977)
11. G. Allen, J.S. Higgins Rept. Progr. Phys. 36 1073 (1973)
12. T. Springer "Quasi-elastic Neutron Scattering for the Study of Diff. Mot. in Sols. and Liqs." Springer-Verlag (1976)
13. E. Fermi Ric. Sci. 7 (1936) 13
14. L. Van Hove Phys. Rev. 95 (1954) 249
15. P. Schofield Phys. Rev. Letts. 32 (1960) 52
16. P.A. Egelstaff "Inelast. Scatt. Neut. Sol. Liqs." Proc. Symp. Vienna (1960)
17. A.C. Zemach, R.J. Glauber Phys. Rev. 101 (1956) 118
18. P.A. Reynolds, J.K. Kjems, J.W. White J. Chem Phys. 56 (1972) 2928

19. G. Placzek Phys. Rev. 86 (1952) 377

20. K.A. Grant, P.J. Pugmire, R.C. Livingston. J. Chem. Phys. 52 (1970) 4424

21. C.I. Ratcliffe Ph.D. Thesis Durham (1975)

22. J.R. Durig, S.M. Craven, W.C. Harris Vibrational Spectra and Structure 1 (1972)

23. T.P. Das J. Chem. Phys. 25 (1956) 896

CHAPTER 3

EXPERIMENTAL DETAILS AND INSTRUMENTATION

3.1. Introduction

This chapter deals with the preparation and packing of model compounds and the surface samples of zeolites and platinum powders. It then goes on to describe the vacuum line manipulations necessary to produce active and chemisorbed surface systems. Details are given of the types of spectrometers used in the vibrational studies of the above systems, the sample cooling requirements and data processing. Finally, the principles used in the neutron spectrometer instrumentation are briefly discussed.

3.2. Sample Preparations

3.2.1. Organometallic compounds

The tropyllium and benzene compounds have their preparations described in the relevant chapters. The majority of the samples were not air stable and were thus sealed in thin-walled silica cells using a picene coated brass stopper. These cells came in two forms depending on the quantity of material being studied. 5 cm diameter round cells were used with sample thicknesses of 2-3 mm and, where larger quantities were necessary, square 5 cm x 5 cm cells with sample thicknesses of 3-5 mm were employed. Silica plates were used, of 1 mm thickness, instead of ordinary borosilicate glass because they did not contain the neutron adsorber B^{10}, a boron isotope. Silica glass does scatter slightly, giving rise to weak bands at 432,806,1076 and 1185 cm^{-1}. The spectrum also shows a steadily rising background after 700cm^{-1} on BFDDIDO, which is of instrumental origin. The silica

spectra are shown in Chapter 5 .

3.2.2. Hydridocarbonyls

Again details of particular preparations are given in the relevant sections. Special precautions and control of reaction conditions were employed in the production of the transition metal hydridocarbonyls because large quantities of the compounds were required for successful neutron scattering studies. Table 3.1 indicates the quantities handled in each case. In many of the original papers, preparations were described for small quantities of the pure compound, so scaling up procedures had to be adopted or, in most cases, the reactions were carried out a number of times due to the quantities of solvent being utilised.

Special precautions were taken that all reagents and solvents were purified. Experimental procedure was followed to the letter due to the importance of concentration, temperature, order of addition of reagents, dryness of nitrogen atmosphere etc. Any variance in these could have altered the nature of the final product in many cases.

All the transition metal hydridocarbonyls were packed in 5 x 5 cm square silica cells sealed with picene. In the case of $HRe_3(CO)_{14}$, $HFeCo_3(CO)_{12}$ and $CsHCo_6(CO)_{15}$ two cells were needed to accommodate such large quantities of material. These were placed back to back. Two cells were used because a single cell, in these cases, would have had an internal gap of > 0.8 cm and cells this big were difficult to test for leaks on a vacuum line because -

of the risk of implosion.

Transition metal hydridocarbonyl	Mass needed for 10% H scatterer (g)	Mass prepared (g)	Approx. % hydrogen scatterer used
$HRe_3(CO)_{14}$	32.49	22.75	7.0
$H_3Re_3(CO)_{12}$	10.58	10.65	9.4
$H_4Re_4(CO)_{12}$	9.23	3.38	3.3
$H_2FeRu_3(CO)_{13}$	12.82	11.57	9.3
$H_4Ru_4(CO)_{12}$	6.58	5.44	7.8
$H_2Ru_6(CO)_{18}$	19.70	20.75	10.0
$HFeCo_3(CO)_{12}$	20.15	32.48	12.5
$CsHCo_6(CO)_{15}$	32.10	53.26	15.0
$H_3Mn_3(CO)_{12}$	5.94	8.18	12.5
$HW_2(CO)_9NO$	23.00	17.95	7.5
$H_2Os_3(CO)_{10}$	15.06	16.23	10.1
Silica (2 mm)	-	-	3

Table 3.1

3.2.3. Zeolite preparation

Two zeolites were used in the study of the interaction of benzene with zeolites: Na13X, supplied by B.D.H. Ltd., and Ag13X, which was formed from Na13X by cation exchange. The preparation thus falls into two parts: the ion exchange and the general method of dehydration necessary to activate both zeolites.

(i) Ion exchange

The exchange of Na^+ with Ag^+ takes place readily and under appropriate conditions 100% Na^+ can be replaced (1)

A slurry was made of Nal3X in an aqueous silver nitrate solution and stirred for 5 days after which it was carefully filtered. This operation was repeated 3 times. Excess silver nitrate was removed by stirring the filtered Agl3X in deionised water until the dried product gave adequate analytical results for silver, sodium and aluminium.

(ii) Dehydration

Before the zeolites could be used, water had to be removed from the crystalline zeolite lattice. This was carried out on the vacuum line shown in Figure 3.1. This method, well developed by J. Howard (2), involved placing the necessary quantity of zeolite into the silica bulb A, which had a graded silica/pyrex seal allowing it to be sealed to the line which was evacuated and leak tested. After allowing the pressure to fall to 10^{-5} torr, the silica bulb was gently heated to 450°C in stages. The pressure was not allowed to rise above 10^{-4} torr. On reaching 450°C, the sample was pumped to 10^{-6} torr or for one hour, whichever was first, then allowed to cool to room temperature. The bulb/cell unit was sealed at B and removed from the vacuum line and the zeolite gently tapped from the bulb A to the aluminium cell C, which was then sealed at D and removed from the line This cell was run as a background spectrum before benzene adsorption.

Figure 3.2 shows typical cell types used to contain the zeolite. These were thin-walled aluminium cells which had aluminium/copperalloy friction welds, copperalloy/glass joints and glass breakseals. Larger cells, w.r.t. internal volume, were employed in deuterated

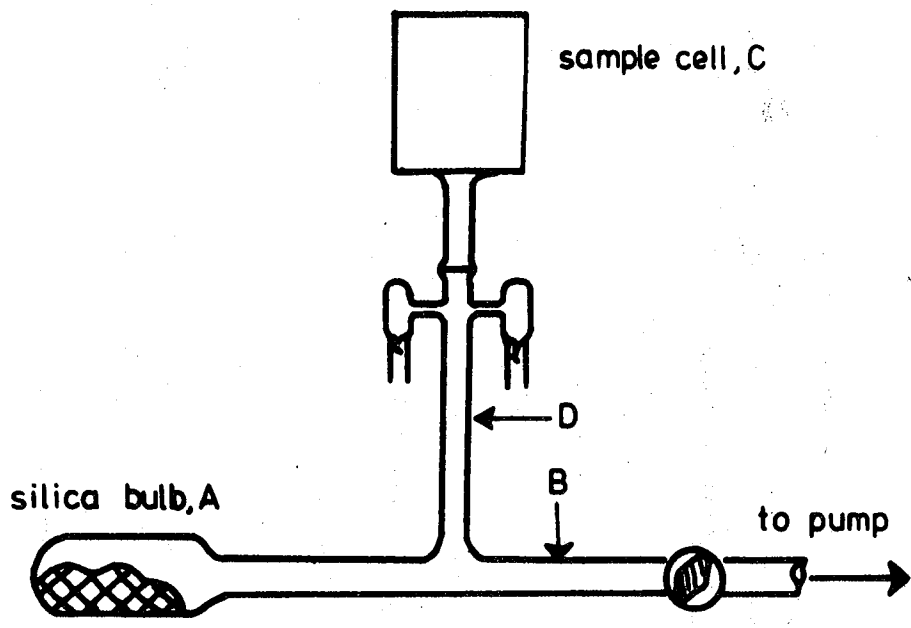

Figure (3-1) VACUUM LINE USED IN ZEOLITE DEHYDRATION

Figure (3-2) TYPICAL FLAT AND ROUND SAMPLE CELLS

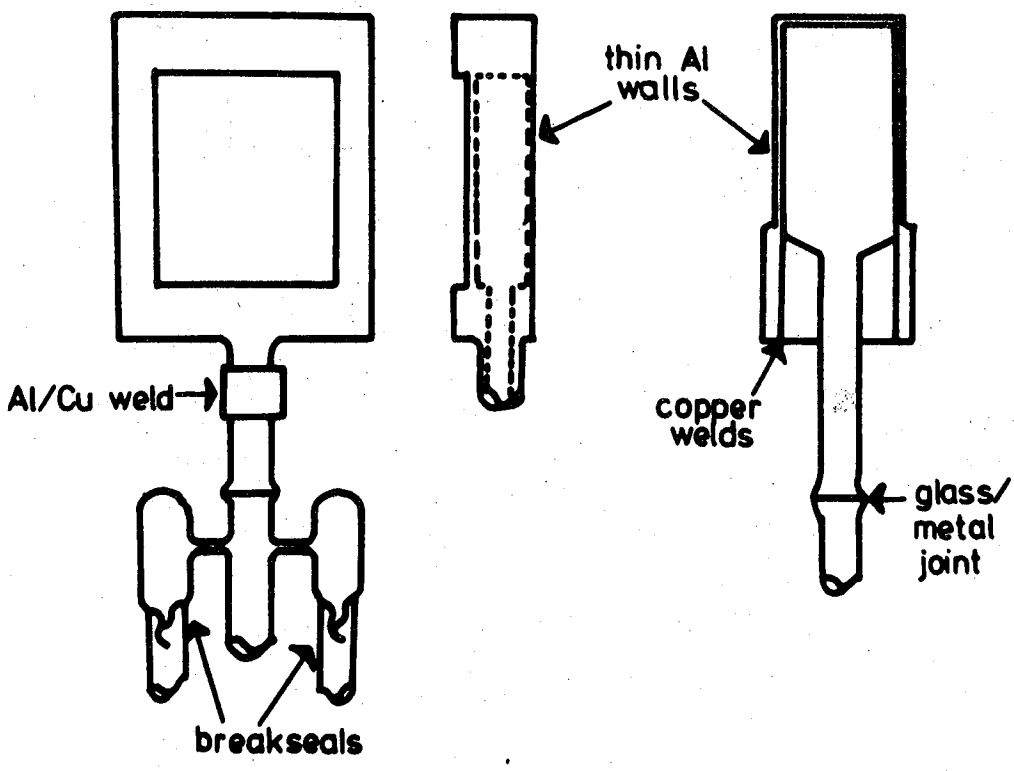

benzene/zeolite experiments due to the lower scattering cross-section of deuterium. Cells of cylindrical cross-section were used on Beryllium Filter detector spectrometers and flat cells on time-of-flight instruments.

3.2.4. Platinum preparation

Platinum powder (Platinum powder (Platinum black) No. 4) was supplied by Engelhard Sales Ltd., and, as described later, was found to have a surface area of 5 m^2/g (3). In carrying out a successful neutron scattering experiment about 80g were used and about 100g for deuterated work. The surface of the platinum had to be cleaned and this was achieved once again by using a well developed technique (2) involving an ultra-high vacuum system. Figure 3.3 shows the system units.

The platinum powder was placed in a thick-walled pyrex glass bulb A which had the sample cell C sealed to it. This unit was attached to the system at B and pumped, in various stages, to 10^{-8} torr. Hydrogen gas from a bulb D was allowed into the platinum system to approximately 10^{-3} torr. This reacted with surface oxygen producing water which was pumped off. This operation was repeated until the mass spectrometer indicated no further water was being produced. The platinum was then gently heated to 200°C until the pressure improved or for one hour, whichever was first, to reduce sintering. On cooling, the unit was removed at E after at least a pressure of 2×10^{-8} torr had been achieved. As with the zeolite sample, the powder was gently tipped into the sample cell and sealed at F.

Figure(3.3) SCHEMATIC U.H.V. SYSTEM

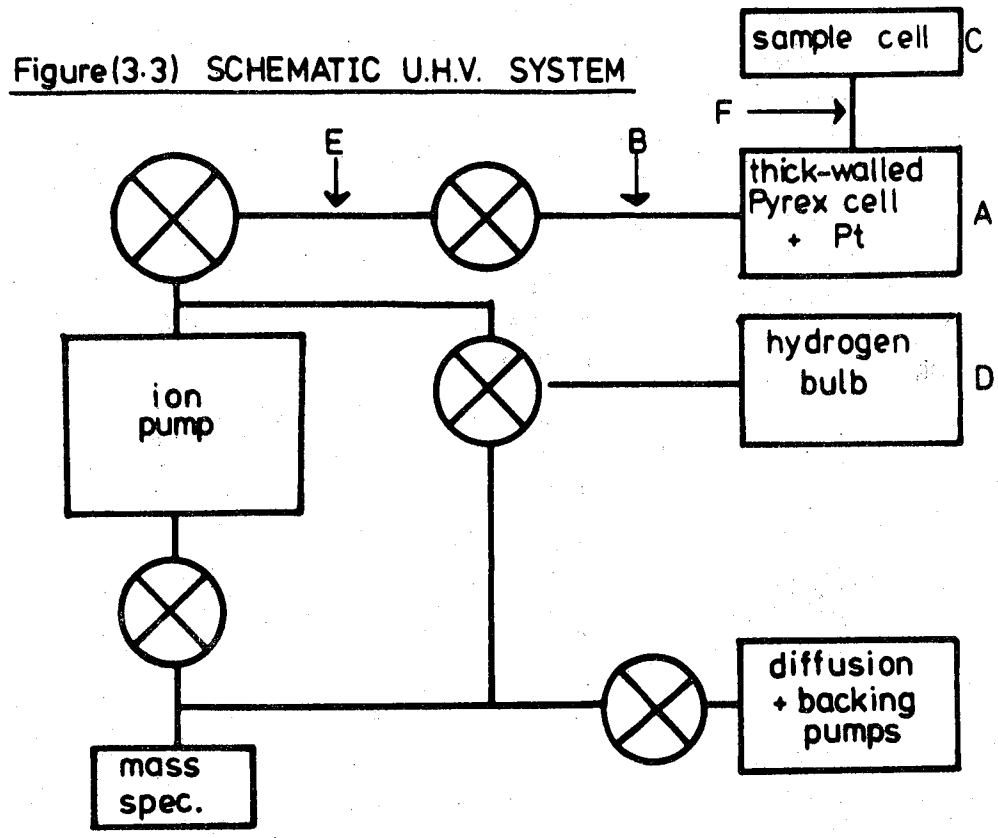

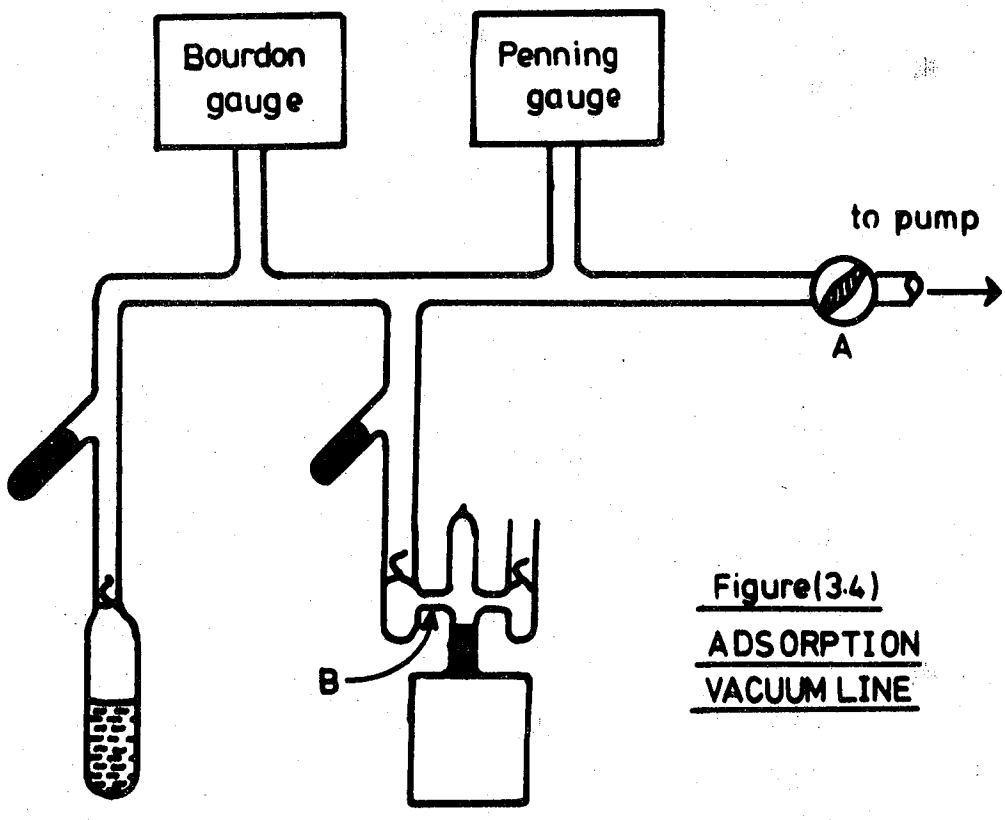

Figure(3.4)
ADSORPTION
VACUUM LINE

The scattering cells used for the platinum surface experiments were basically the same as those used for the zeolite work. The cells of cylindrical cross-section were increased in size to allow for the larger quantities of sample.

3.2.5. Benzene purification and packing

Benzene, C_6H_6, was supplied by Hopkin and Williams Ltd., and was of 'Analar' grade. It was initially dried using sodium wire for 2 weeks then distilled under a P_2O_5-dried nitrogen atmosphere from fresh sodium wire onto activated molecular sieve 3A. When required for use it was syringed under nitrogen. Benzene from this source was used in the benzene model compounds.

Hexadeutero-benzene, C_6D_6, was supplied by the Aldrich Chemical Company, Inc. and was 'Aldrich analyzed'. This was not purified but was kept under a nitrogen atmosphere and utilized immediately because of its hygroscopic nature.

The benzene used in the surface experiments was further purified by employing a freeze/thaw technique to remove dissolved air. This was carried out in glass phials with attendant break seals.

3.2.6. Technique of benzene adsorption

The adsorption isotherm for the benzene/NaI3X system was studied by Avgul, Kiselev et al (4). In the region 10-760 torr, at room temperature, saturation of the supercage was achieved ($\sim 5.4 C_6H_6$/supercage). Most studies of the C_6H_6/13X system used a reservoir of benzene of known weight and volume. For example, Freeman and Unland (5) in a Raman study adsorbed at 45 torr to achieve all

coverages at room temperature. Lechert et al (6) in a series of n.m.r. studies of benzene in 13X zeolites adsorbed at 100 torr from a known volume and found the exact quantity adsorbed by weight change. The use of the weight change technique was not applicable to the present study because of the glass blowing changes. However, the volume change was monitored and the benzene adsorbed was gauged to be within $\pm$ 0.1 ml.

The technique employed for both zeolite and platinum work was as follows. Figure 3.4 shows the vacuum line used with the sample and reservoir of benzene, which had been calibrated. After leak testing, the line was pumped to 10^{-6} torr using a trapped oil diffusion pump and Penning gauge. The line was sealed off from the pump at A and the Penning gauge was also sealed from the line because of the likely damage to it from benzene adsorption. Using ball bearings and a magnet, the breakseal above the benzene was broken and, using a Bourdon gauge and liquid nitrogen dewar (or liquid air), the necessary benzene pressure in the line could be achieved. The pressure was allowed to equilibriate, usually at 100 torr. The breakseal above the sample was broken and the adsorption allowed to take place. This was followed by the volume reduction in the benzene reservoir. After the necessary quantity of benzene had been adsorbed the sample was sealed from the vacuum line at B. If a second adsorption was necessary then the second breakseal above the sample would have been employed. (Usually more than one ball bearing was needed to break the seals because they would often be quite strong).

The benzene vapour in the line was then returned to the reservoir by use of the cold trap and then it was removed from the vacuum line and stoppered. The exact quantity of benzene which had left the reservoir could then be estimated once the benzene had liquidfied in the calibrated container. In the calculation of the benzene adsorbed on the sample, the surface area of the vacuum line had to be taken into account. This area was very small compared with the catalyst area. The pressure used in the adsorption was usually 100 torr but lower pressures were used to achieve greater control of the benzene removal from the reservoir so that fractions of a monolayer (on platinum) and fractions of the supercage would be filled (in the zeolites).

The adsorption isotherm for the benzene/Ag13X system had not been measured and the technique used for the Na13X system was quite reasonably extended to Ag13X.

The adsorption isotherm of benzene on platinum black and other metals had been measured by Babernics et al (7) but no diagram was given. Others carried out adsorptions at room temperature at a variety of constant pressures to achieve different coverages. For example Erkelens et al carried out the adsorptions at 15 torr (8) on silica supported platinum whereas Moyes et al (9) carried out experiments on films with only 0.5 mm Hg pressure at each coverage. Studies on single crystal faces were usually carried out at much lower pressures and measured in doses rather than in pressures. Since a large quantity of benzene had to be adsorbed, fairly high pressures were used in the method described above for the zeolites.

Adsorption was usually not as quickly carried out on the platinum black compared to the zeolites where initially the evaporation of the benzene sometimes was so quick that some freezing occurred on the surface so that heat had to be applied to keep the pressure constant.

3.3. Instrumentation

This section is split into 4 parts: a) a brief description of the spectrometers used at Durham, b) a description of the neutron sources employed, c) a sketch of the five neutron spectrometers utilised in the study and finally d) an indication of the principles involved in the spectrometers.

3.3.1. Optical spectrometers

The optical spectrometers used at Durham were:-

Near Infra-red:	Perkin Elmer 457 grating spectrometer
	Perkin Elmer 577 grating spectrometer
Far Infra-red:	Beckman-RIIC FS720 interferometer
Raman:	Cary 82 using Spectra-Physics He/Ne laser @ 15,802cm^{-1} and Ar/Kr laser @ 19436.3 cm^{-1}

The punched paper tape output from the FS720 was processed on the N.U.M.A.C. computer using programmes developed by Symon (10) and Jinks (11).

Low temperature spectra were obtained using cells of conventional design.

3.3.2. Neutron Sources

The neutron sources used in this study were:-

i) DIDO medium flux reactor at A.E.R.E. Harwell

ii) PLUTO medium flux reactor at A.E.R.E. Harwell

iii) I.L.L. high flux reactor at Grenoble, France.

The DIDO and PLUTO reactors are heavy water moderated and cooled and operate, at present, at 25.5 Mw (5). They are fuelled by enriched uranium/aluminium alloy aluminium-clad tubes. The neutron flux at the beam tubes is 1-2x 10^{14} neutrons $cm^{-2}s^{-1}$. DIDO reactor has a cold source which gives gains in longer wavelength neutrons which are utilised by 4H5 spectrometer.

The reactor at the Institut Laue-Langevin (I.L.L.) is a more intense neutron source with a flux at the beam holes of 1.5 x 10^{15} neutrons $cm^{-2}s^{-1}$. These fluxes are, in fact, measured near the reactor core and include neutrons travelling in all directions. The neutron flux at the sample is about 10^{10} times less after collimation and shielding etc. The I.L.L. has a 'hot' source, a 2000K graphite block, which increases the flux for neutron wavelengths less than 1Å.

3.3.3. Neutron spectrometers

Table 3.2 gives an indication of the energy ranges usually covered by the 5 spectrometers used in this study though others may have used them outside these ranges. A brief description follows of each spectrometer.

(i) DIDO Beryllium Filter Detector Spectrometer

Figure 3.5. shows a detailed drawing of HDDIDO which utilises neutrons from the 10H beam hole in DIDO reactor. The instrument is primarily used for measurements in chemical spectroscopy up to 2300cm^{-1}, however low count rates and unacceptably long count times above 1300cm^{-1} reduce its ability in a region better covered by IN1B. The aluminium monochromator is an aluminium crystal

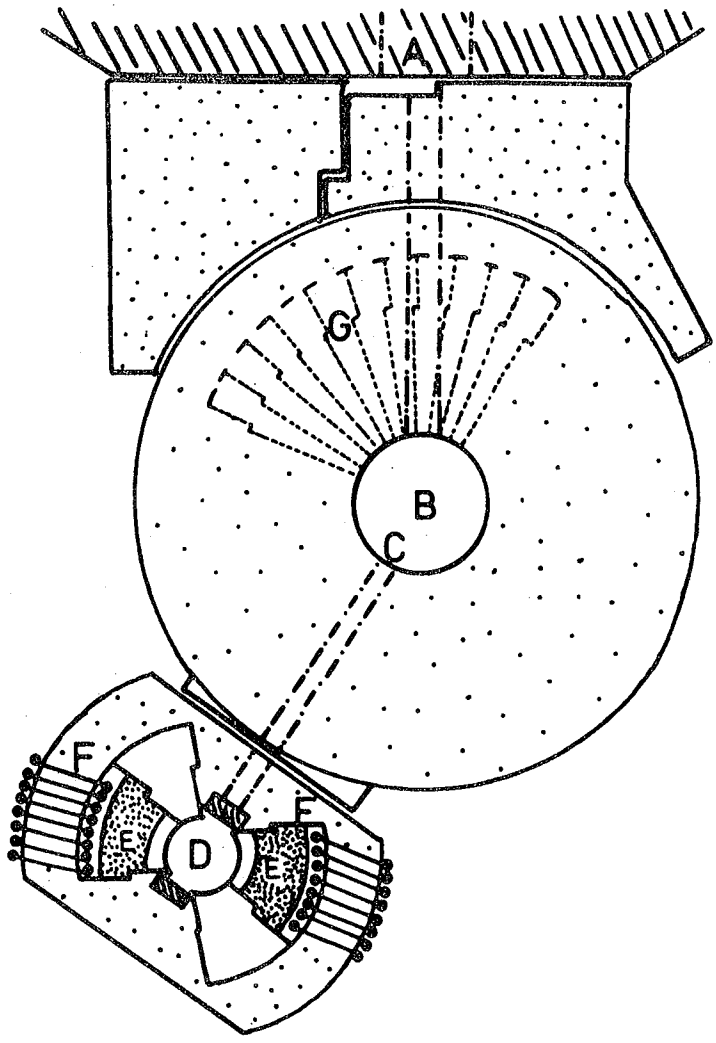

A In pile collimators
B Monochromator
C Beam shutter
D Sample position
E Be filter blocks (cooled)
F BF_3 detector arrays
G Shielding segments

Figure(3·5) BFDDIDO

Spectrometer	Abbreviated Name	Energy Range (cm^{-1})
DIDO Beryllium Filter detector	BFDDIDO	90-2300
PLUTO Beryllium Filter detector	BFDPLUTO	90-1000
DIDO Time-of-flight cold neutron twin rotor	4H5	0- 600
ILL Beryllium Filter detector (+ hot source)	IN1B	350-2500
ILL Time-of-flight rotating crystals	IN4	40- 300

Table 3.2.

which moves about an angle of ω about the incident beam. Selection of neutron energies incident at the sample, achieved by Bragg scattering from the monochromator crystal, is carried out by this motion and that of the movement of the large shielding drum, containing the sample and attentant filter assemblies, about an angle of 2θ with the monochromator. The beam size at the sample, after collimation, is (7 x 3)cm with the neutron flux at 1.1×10^4 neutrons cm^{-2} s^{-1} for an incident energy of $403cm^{-1}$. Scattered neutrons from the sample, with energy less than 5 mev, pass through the cooled (to 77K) 20 cm long beryllium blocks, which act as energy analyzers, and are detected by two banks of $8BF_3$ counters. (12)

(ii) ILL Beryllium Filter detector spectrometer

Figure 3.6 shows a detailed drawing of the spectrometer which utilises neutrons from H8 beam hole in the

Figure(3.6) IN1B

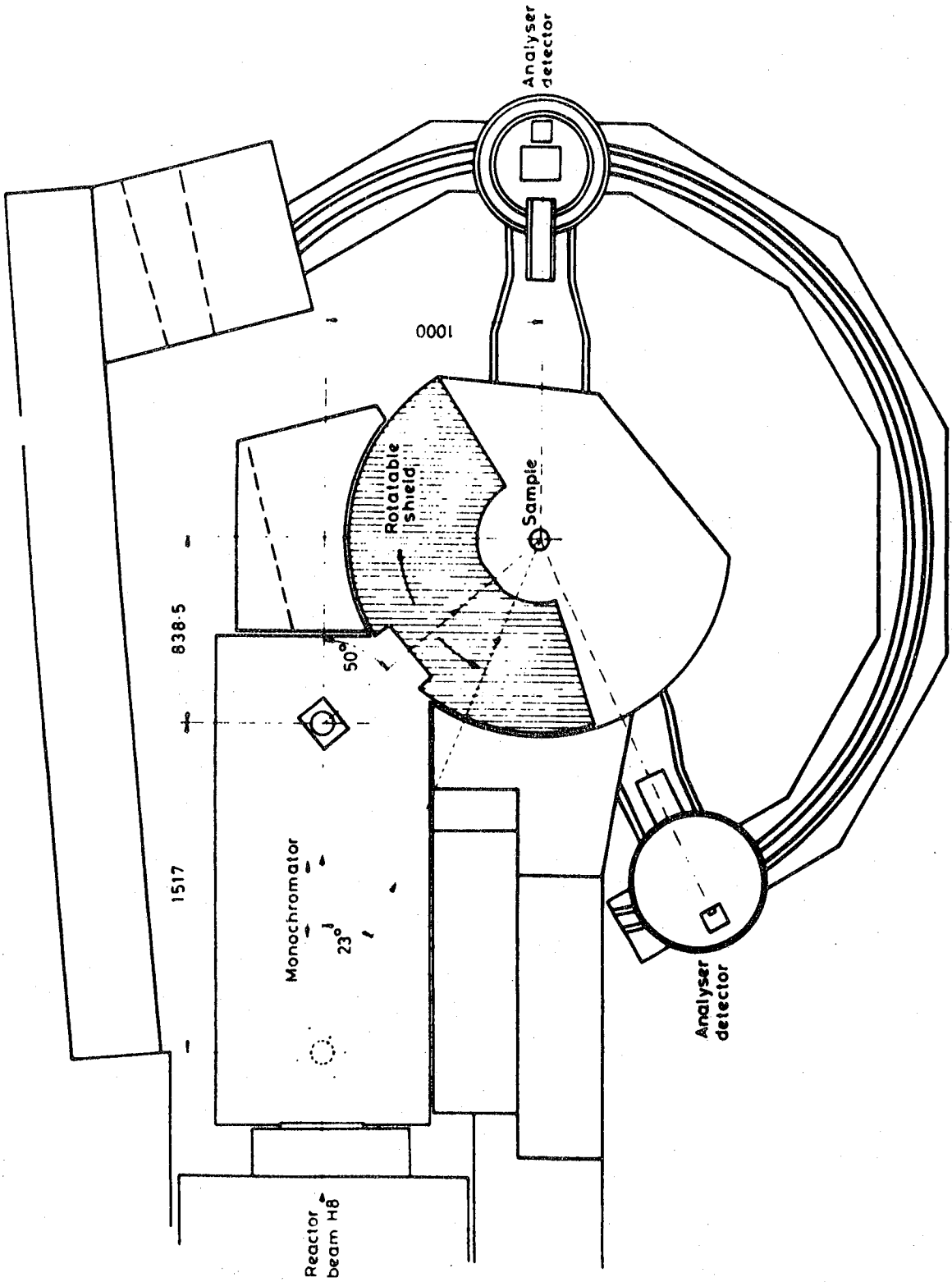

ILL Reactor. (13) The incident energy of the neutrons is varied by combined translations and rotations of the copper crystal on a monochromator table and the rotation of the monochromator shielding drum about the sample position. The incident energy ranges are 354-1128cm^{-1} for the Cu(200) plane, 726-2177cm^{-1} for Cu (220) plane and 1936-2420cm^{-1} for the Cu(331) plane. These ranges were used in the study of transition metal hydrido-carbonyls discussed later. The neutron flux at the sample, through the beam hole of 5.3 x 6.4 cm after collimation, is 3 x 10^7 neutrons $cm^{-2}s^{-1}$ @ 807cm^{-1} and 1.3 x 10^7 neutrons $cm^{-2}s^{-1}$ @ 1614cm^{-1}. After scattering, the neutrons pass through a cooled (to 77k) beryllium filter analyzer and are detected by $6He_3$ detectors. The whole beryllium filter assembly moves upon a steel rail.

The beryllium filter detector spectrometer in PLUTO functions much like IN1B except that the sample position also rotates about the monochromator. Both instruments can be used in a triple axis capacity where the analyzer and detector are split.

(iii) DIDO Time-of flight

Figure 3.7 shows a detailed drawing of the instrument which utilises neutron beam hole 4H in DIDO reactor. This instrument employs neutrons from a 'cold' source which gives gains in longer wavelength neutrons. Such longer wavelength neutrons are produced by using a moderator which removes neutron energy by recoil processes. Usually moderators have low molecular weights (eg H,D or C). The moderator material in the case of 4H5 takes the form

Figure(3.7) 4H5

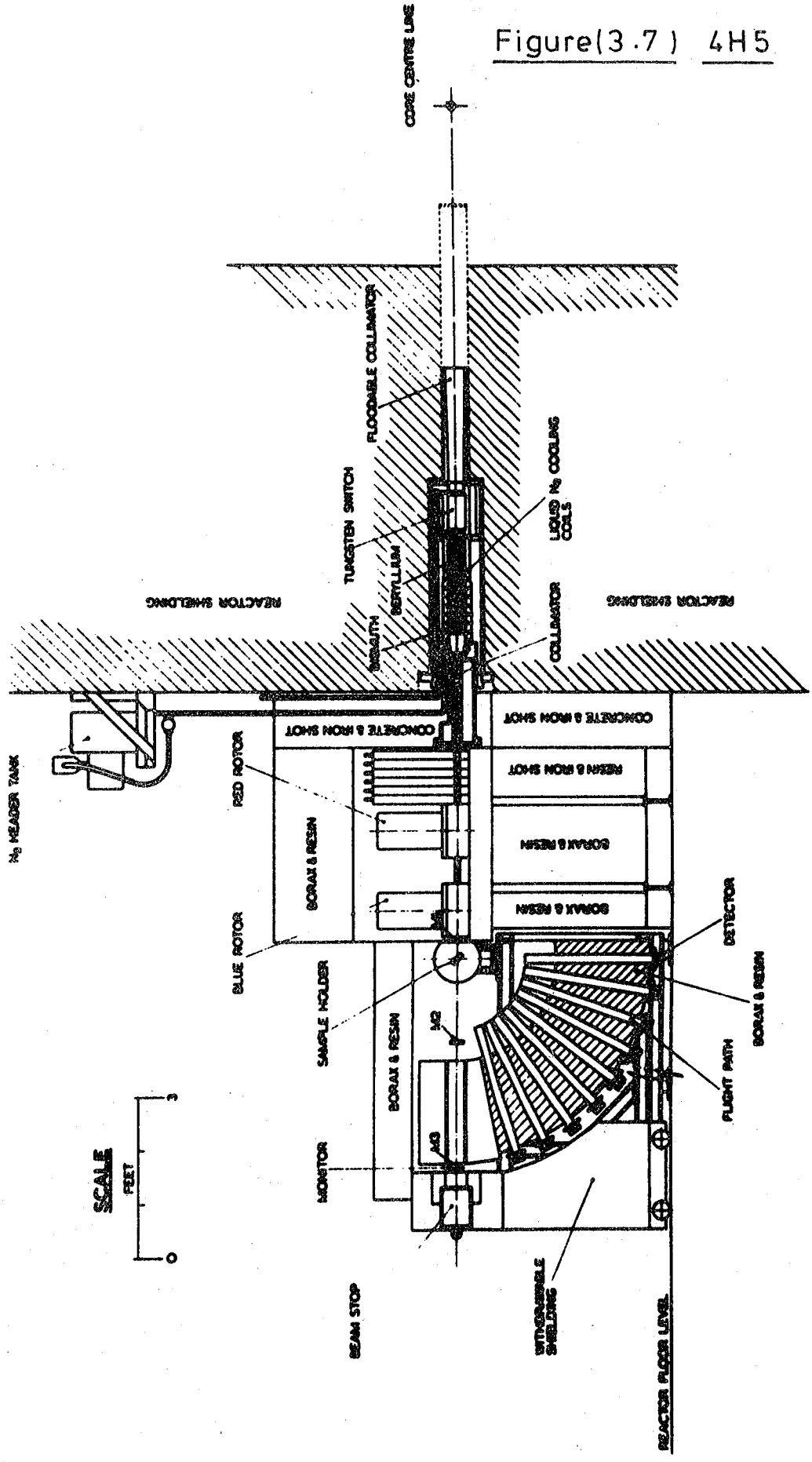

of a flask of liquid hydrogen. (A cooled source at the ILL is in the form of 25 litres of liquid deuterium cooled to 25K). The neutron beam is further cleaned up by using a beryllium/bismuth filter before wavelength selection. These low energy neutrons are then used to give neutron energy gain spectra whereas all the other spectrometers give neutron loss spectra. A pair of multi-slot rotors are used for obtaining the pulsed incident energy selection and monochromatisation. These turn on vertical axes and, depending on intensity and resolution considerations in any particular experiment, such parameters as rotor speed and slot number per rotor can be varied accordingly.

The maximum flux attained at the sample is 1×10^4 neutrons $cm^{-1}s^{-1}$ and the maximum beam size is 2.5 x 5 cm. The samples are contained in a sample changer which has positions available for sample, background and vanadium, a standard used to correct for different counter efficiencies. The sample changer, which can be cycled automatically, is pumped down to 10^{-4} torr to allow for cooling. The scattered neutrons are detected by an array of counters at 13 differing angles to the incident beam varying from 13^o to 90^o. The majority of the counters are He_3 and they lie at low and high scattering angles. Such factors as wavelength distribution in the incident beam, size of beam, sample to detector distance, whether energy gain or loss situations prevail are what influence the resolution of a time-of-flight spectrum from 4H5, and the following instrument, IN4. These factors have been discussed in Chapter 2. The technique of time-of-flight

is discussed later in the section dealing with energy selection.

(iv) ILL Time-of-flight

Figure 3.8. shows a drawing of this time-of-flight instrument. IN4 uses thermal neutrons from H12 beam hole at the ILL reactor and is used for a large range of energy and momentum transfers. The monochromator system usually consists of two single crystals such as graphite or copper and both can be rotated. The incident energy range selected by the graphite monochromator is 32-325cm^{-1}. This double monochromation reduces the background noise level and gives a peak/background ratio of 2400. The pulsed neutron flux at the sample, which is contained in a helium atmosphere below 1 torr, is about 3 x 10^4 neutrons $cm^{-2}s^{-1}$ for an incident energy of 102cm^{-1}. The beam size is usually 10 x 3 cm. The requirements of the experiment determine the positioning of the detectors in the argon-filled aluminium housing. These consist of 40 x 6 He_3 counters, which record simultaneously producing a large rate of detection, covering about two thirds of the scattering angle range of 150° which can be measured.

IN4 can be run in a neutron energy loss or neutron energy gain situation. With the samples being run at a low temperature (~4k) one can use the spectrometer in its neutron energy loss mode, which reduces collisional broadening and reduces widths of bands. The larger (x4) sample to detector length of ~4 metres also enables a better separation of scattered neutron velocities before detection than 4H5 in Dido, thus giving better

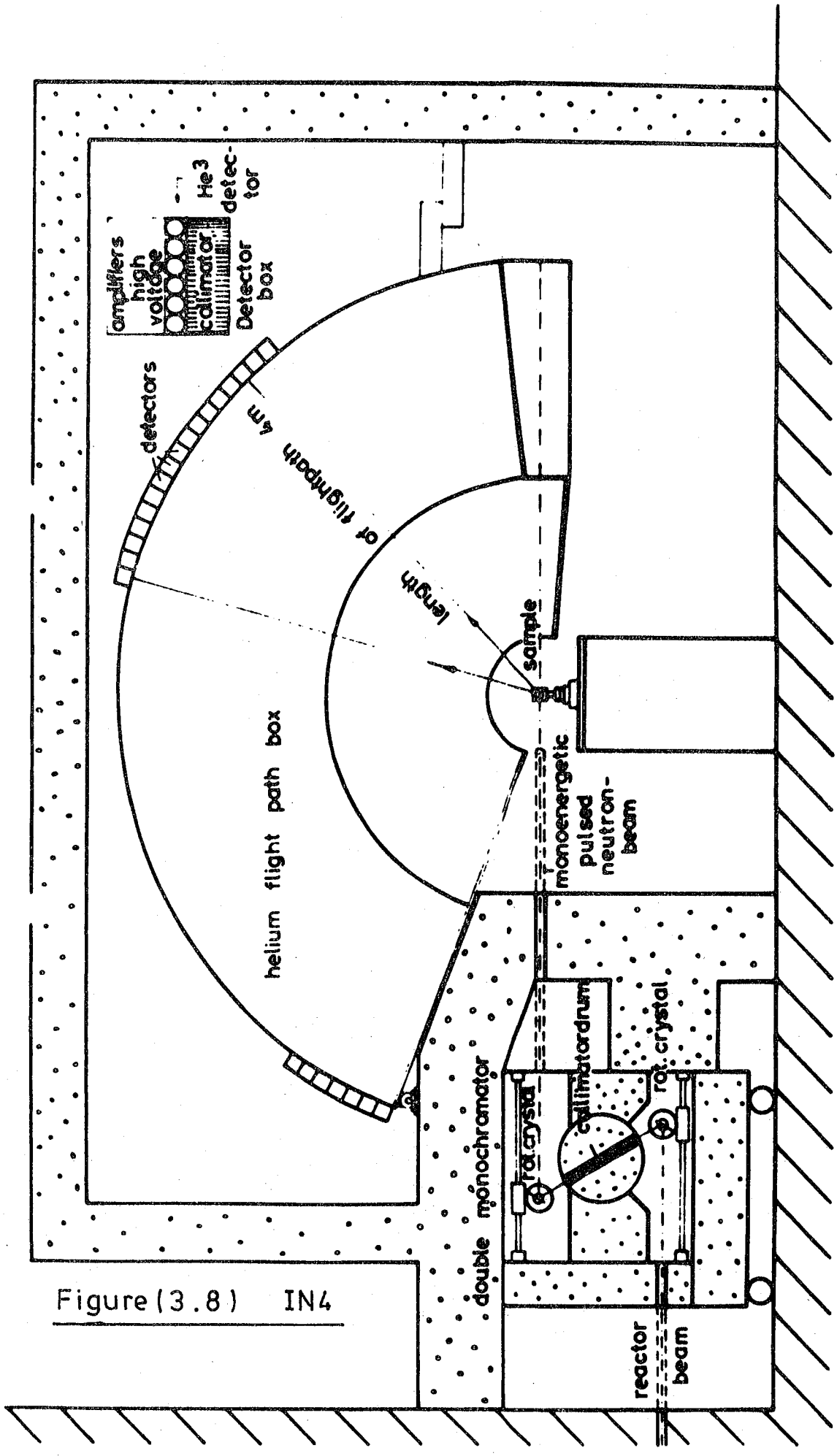

Figure (3.8) IN4

energy resolution.

3.3.4. Sample cooling requirements

All three beryllium filter spectrometers used cryostats to house the sample and were cooled by either liquid nitrogen or liquid helium. This, as shown previously, was to reduce multiple quantum scattering and, thus, reduce bandwidths due to a reduction in the Debye-Waller factor. With DIDO and PLUTO spectrometers the Durham cryostat, designed and used previously, was employed (2).

The 4H5 instrument employed a sample changer which could be set at a preselected temperature in the 100-300K range using a piped liquid nitrogen supply. Here nitrogen gas was blown through tubes which led into the base plate, which was in contact with the sample. The neutron energy loss situation of IN4 enabled the sample to be cooled to 4K using piped liquid helium to a helium cryostat.

3.3.5. Data control, collection and analysis

BFDDIDO is controlled by a distributed microprocessor system and entails use of paper tapes to position drum and monochromator. Data output, from a DECwriter, is in the form of paper tape and printed counts versus energy. BFDPLUTO is controlled by a PDP8 computer and data output is as above. IN1B is controlled by a CARINE computer with conventional BFDS programmes and data output is, again, as above.

The spectra from each of the above instruments is usually normalised by counting at each energy for the same number of monitor counts. The monitor, which lies

on the incident beam axis before the sample, is a detector which counts neutrons. Using a pre-scaling factor one can control the length of a scan at each incident energy by counting a specific number of neutrons detected at the monitor. On the DIDO beryllium filter detector spectrometer the contribution to the background counts is large from sources such as the reactor variability, the instrument itself and other instruments. This is time dependent. This situation is not so true on the IN1B instrument and, to a lesser extent, BFDPLUTO. The IN1B data is left in its monitor normalised state. The total number of counts detected at any specific energy per unit time consists of the scattered neutrons from incoherent inelastic events from the sample, the background arising from the sample and the external source background. The BFDDIDO data is time normalised because of the greater spread in count times for successive energies than in other BFD cases and this removes the time variability in the large external source background.

The processing proceeds for the BFD instruments with the subtraction of a 'correction factor'. The resolution and relationship between observed peak position and true mode frequency have been thoroughly discussed by Gamlen et al (14). For an ideal system, the monochromatic neutron beam would have a peak maximum occuring $42cm^{-1}$ after the threshold if a purely rectangular transmission function was found for the beryllium filter. Since a strictly monochromatic beam is not found, the time distribution of incident energies has to be convoluted with the instrument response function to yield the

observed spectrum. This energy distribution is caused by the physical characteristics of the monochromator crystal, the energy dependence of the detectors and the beryllium filter transmission function, and, to a lesser extent, by collimator parameters producing a spread in the beam. The distribution is taken as a guassian $f(E_i) = (2\pi\sigma^2)^{-\frac{1}{2}}\exp(-E_i^2/2\sigma^2)$ and as σ changes, the convoluted spectrum changes from the asymmetric cut off function in Figure 3.9, where the beryllium filter cut off is 96.5% @ 42cm^{-1} and 100% @ 52cm^{-1}, to the shown symmetric shape due to the instrumental effects. The peak maximum displacement moves from 42cm^{-1} to an asymtopic value of 24.5cm^{-1}.

The major contribution to σ is the finite width of the 'soller slits', $\delta\theta$, a collimator characteristic and from Braggs law $dE_i = 2E_i\cot\theta\, d\theta$. From this dE_i can be calculated and equated to the full width at half peak height of the guassian.

$$dE_i = 2\sigma\sqrt{2\log_e 2} = 2.35\sigma$$

Figures 10 a,b, show plots of the peak maximum above the theshold as a function of the energy of the observed peak position for the two aluminium crystal planes used in this study. Using Δ cm^{-1} correction values, the true band centres can be calculated as follows:-

Band centre - Δ = true transition frequency (15)

Time-of-flight data is much more complex and has to be stored and processed to transform out characteristics of the instrument involved and to reduce the raw data to a medium suitable for transport and further analysis.

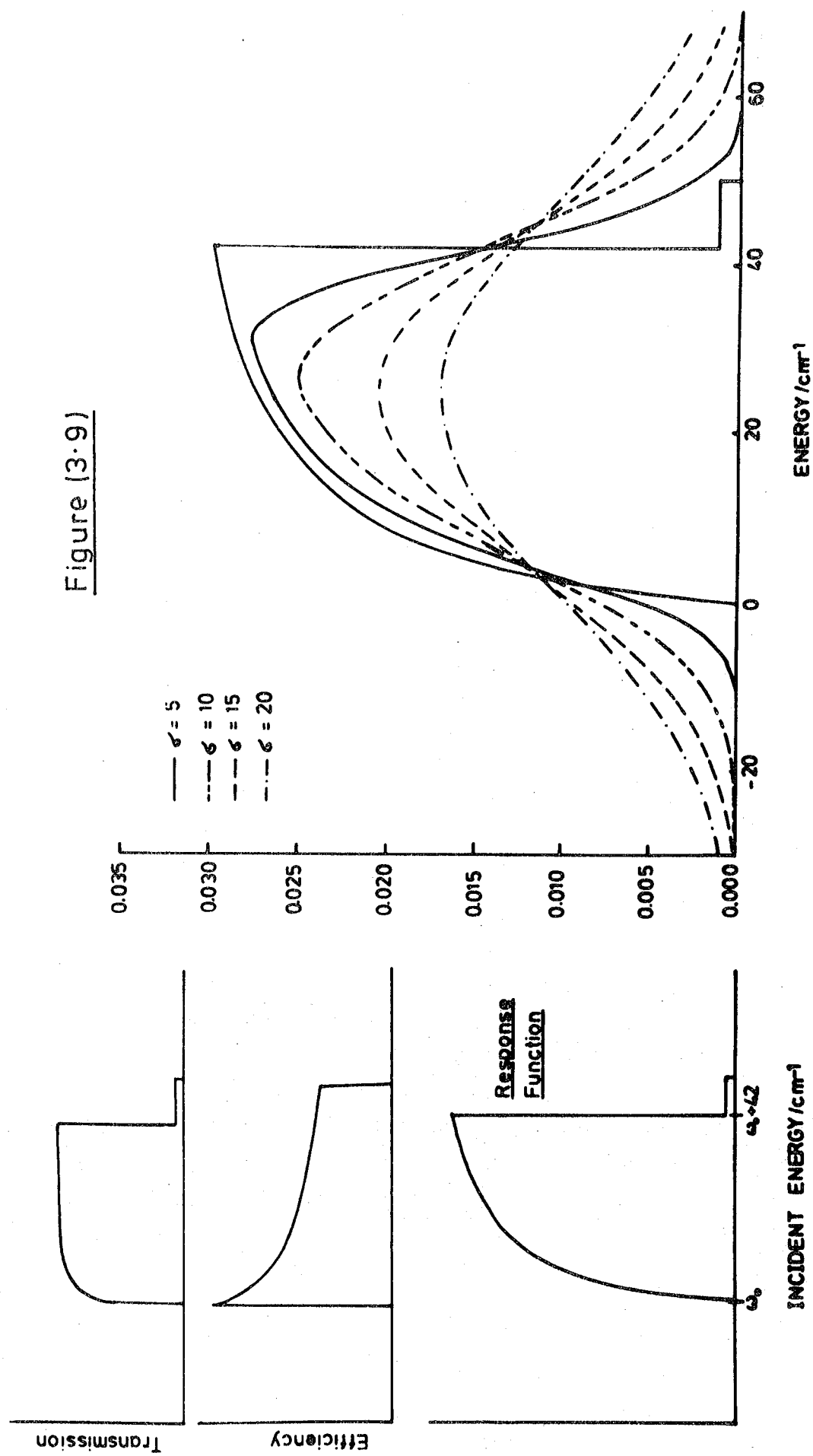
Figure (3·9)
Transmission
Efficiency
Response Function
INCIDENT ENERGY/cm⁻¹
ENERGY/cm⁻¹
σ = 5
σ = 10
σ = 15
σ = 20
0.035
0.030
0.025
0.020
0.015
0.010
0.005
0.000
-20
0
20
40
60

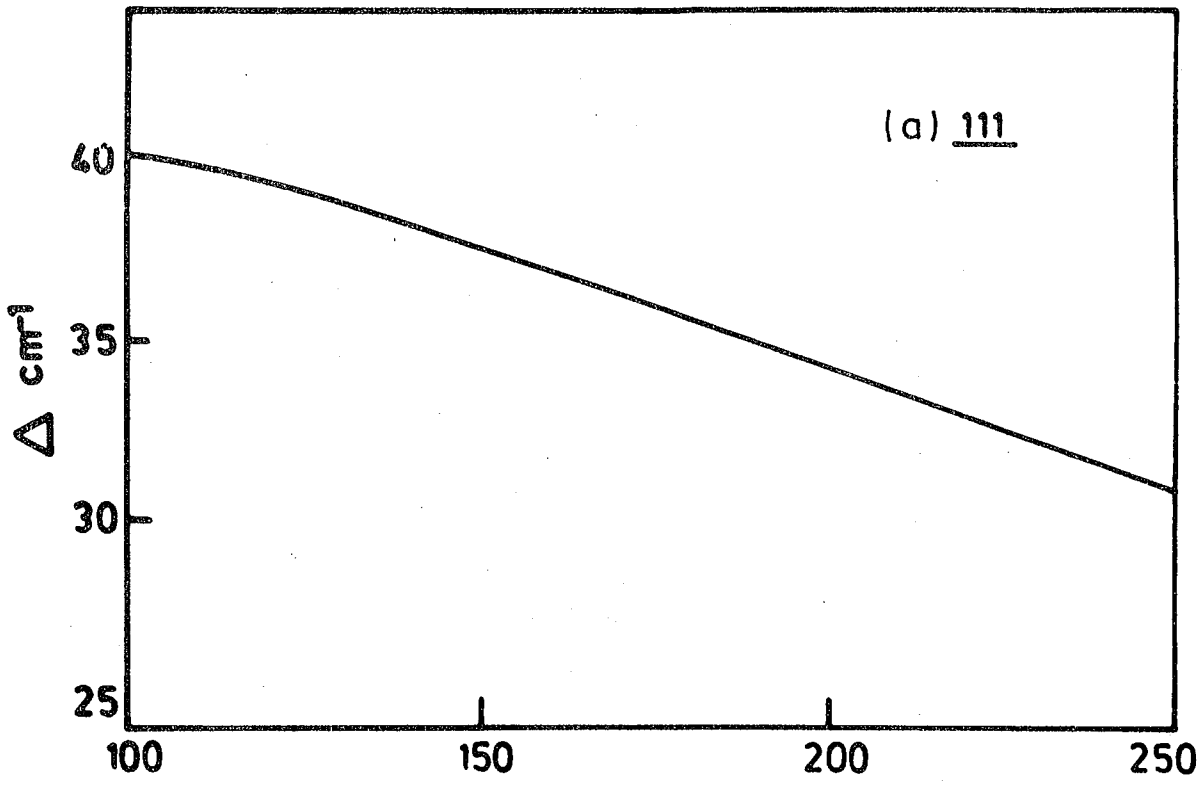
(a) 111
40
35
30
25
Δ cm⁻¹
100
150
200
250

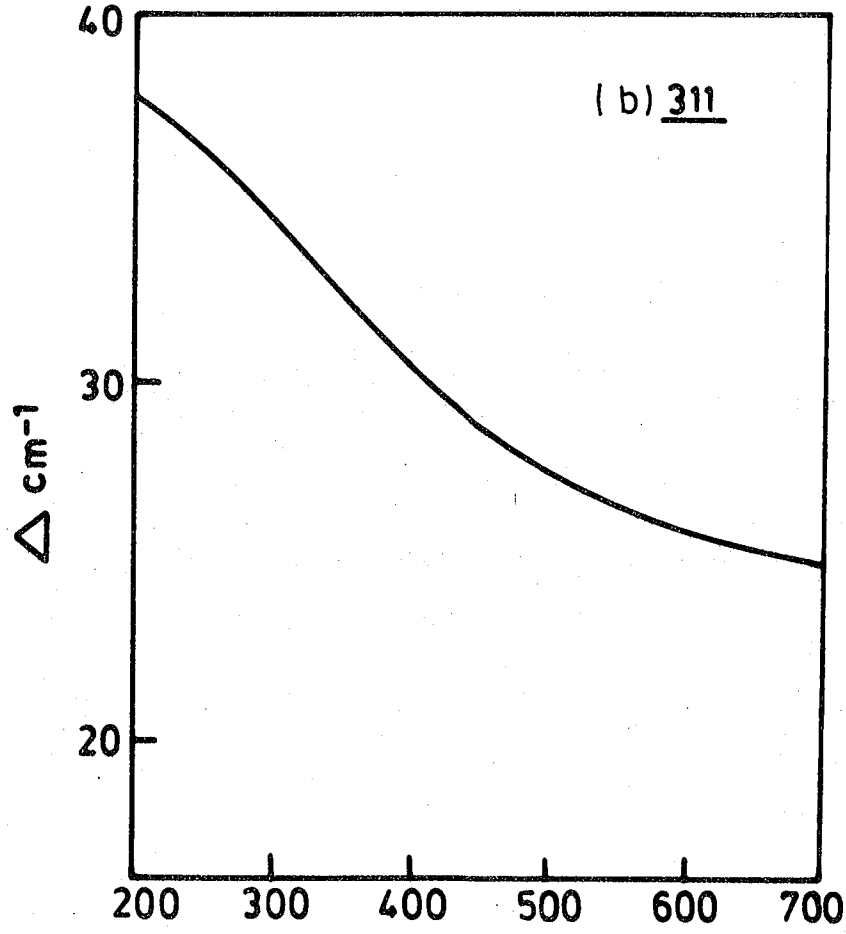
(b) 311
40
30
20
Δ cm⁻¹
200
300
400
500
600
700

Figure (3·10)

4H5 is controlled by a PDP8, named Cassandra, and subsequent processing of stored data from a DEC tape is carried out on a 370/165 computer at A.E.R.E. Harwell. The programme 'Clodop' (16) produces a line printer output of counts and the programme 'Prescat' analyses the vanadium and monitor counts. Data from 'Clodop' and and 'Prescat' is further reduced by 'Circa' which puts the data in a form which allows the user to choose the final form and to choose parameters needed for a graphical output. 'Circa' also gives a graphical output for every angle of intensity against time-of-flight. The Roundabout programmes are then employed. 'Dougal' smoothes a spectrum and locates peaks and shoulders, 'Dylan' allows measurements of the quasi-elastic peak, 'Florence' allows an evaluation of frequency distribution functions and, finally, 'Zebedy' which is a general plotting programme of various functions, discussed in Chapter 2. against energy (17).

IN4 is controlled by the data acquisition system 'Nicole' which obtains the time-of-flight distribution. After recording a spectrum, 'Prin4' is used in the initial data reduction where the user inserts information particular to the experiment, such as detector position, run temperature etc. 'Cross4', similar to 'Circa', is then utilised. At this stage, the user can make final adjustments to the data, such as carrying out background subtractions. Finally, the data can be plotted using an interrogative plotting programme.

3.3.6. Principles used in neutron instrumentation

(i) Monochromation

Peak flux in the beam tube may be about 10^{10} neutrons $cm^{-1}s^{-1}$ but, depending upon the solid angle subtended by the source area, the direction and energy of the neutrons will vary greatly. Monochromation of such a collimated beam reduces the useful flux by $\sim 10^5$. From a typical thermal neutron moderator, unlike a 'cold' or 'hot' source, the wavelength distribution will be Maxwellian and lie in the range $0 \leq \lambda \leq \infty$. Wavelength selection removes unwanted neutrons leaving a 'window' or band to strike the sample.

A variety of mechanical methods of velocity selection are available of which the simplest consists of two neutron-opaque rotating discs which rotate on an axis parallel to the incident beam. There are two slots on the discs which chop the neutron beam into pulses. The first chops the beam into pulseshaving the same velocity distribution as the incident beam and the second slot chops these pulses into further pulses having a specific velocity distribution dependent on the distance between the slots, the slot phasing and the available 'window' times. 4H5 uses rotors which are more complex in that the slot length is long and curved allowing velocity selection of slower neutrons. Diffraction techniques, as used on IN1B, BFDDIDO and IN4, are much in vogue. Neutrons of a particular wavelength can be selected by diffraction from a specific crystal plane. The wavelength can also be varied from a plane by varying the scattering angle. Higher

order scattering, when contamination of the incident beam by simultaneous reflection of neutrons with wavelengths of $\frac{\lambda}{2}$, $\frac{\lambda}{3}$ etc, can be removed by placing a suitable adsorber in the beam which transmits neutrons of wavelength, λ .IN4 improves the technique, by using two crystals which may also be both rotated, producing a clean monochromatic pulsed beam. The second crystal is mainly used to remove the higher order reflections from the first crystal.

Polycrystalline filters, such as beryllium, can be used to allow only neutrons of energy less than the threshold value for that material. Thus placing a cooled beryllium filter block before a chopper device would remove high energy neutrons and thus lessen contamination of the final beam-before-sample.

(ii) Analysis of the scattered neutron beam

The aim of the analysis is to compare the energy of the scattered neutrons with the incident beam energy and thus get an indication of the neutron energy and momentum gain and loss situation.

Time-of-flight techniques are used in 4H5 and IN4. The neutrons, after scattering, have a particular energy distribution with respect to the sample and conditions. This distribution can be energy analyzed by detectors placed at a measurable distance from the sample. The time-of-flight of the neutrons to travel the sample to detector distance can be measured, allowing a time-of-flight against neutron counts spectrum to be gathered for each angle. A good signal is achieved by accumulating the counts over a time interval, typically 6-20 μs. The

exact time interval, known as the time channel width, is chosen by matching the resolution of the channel width to other experimental requirements. Each pulse, after monochromation, is sorted into groups of arrival times, known as time channels. The resolution of these instruments has been discussed Harryman and Hayter (18).

(a) Rotor system

The monochromation achieved depends on the rotor speed, rotor type (eg. slot number) and rotor separation. Two sets of rotors are available for 4H5: having 6 and 12 slots respectively. The flux drops with the finer 12 slot rotors.

(b) Beam size at sample

Scans vertically and horizontally through the beam show an energy variation which can be reduced by decreasing the beam especially in the vertical dimension, though of course, the flux is decreased for particular incident energies.

(c) Angle of sample to beam

Resolution is increased by placing the sample at 90^{o} to the beam, in all rotor systems, rather than at, say, 45^{o} to the beam, though in such a configuration detectors placed at $>80^{o}$ to the beam are probably defunct

(d) Thickness and type of detectors

The basic efficiency of a particular type of detector increases the number of detected neutrons per unit time though, of course, this increases the background count as well. Improvement can be made by fitting less sensitive detectors. Polycrystalline filters and crystals can also

be used, as discussed previously. The former transmitting neutrons below a fixed value, and the latter, diffracting neutrons of a known wavelength using known crystal spacings and scatter angles.

(iii) Detectors

Neutron detectors are, in fact, detectors of secondary products arising from adsorption of neutrons by various nuclei since neutrons are non-ionising. The following reactions are used:-

$^{10}B(n,\alpha)^{7}Li$ (in BF_3 detectors)

$^{3}He(n,p)^{3}H$ (in ^{3}He detectors)

$^{6}Li(n,\alpha)^{3}H$ (in LiF/ZnS scintillators)

The secondary products are detected by a light flash in a scintillator or by ionization of a gas particle. On 4H5, at present, more efficient He_3 detectors are being installed, replacing the earlier BF_3 type. The attraction is that quite high pressures of helium (2~10 atm.) can be used with modest voltages on the electrode. Further, helium-3 has a somewhat higher cross section than boron.

3.4. References

1. H.J. Sherry J. Chem. Phys. 70 1158 (1966)
2. J. Howard Ph.D. Thesis (Durham) (1976)
3. Pt. black surface area measured by J. Howard/ D. Cunningham (Durham)
4. N.N. Avgul, A.V. Kiselev, A.A. Lopatkin, I.A. Lygina, M.V. Serdabov Kolloidn Zh. 25 (1963) 111
5. J.J. Freeman, L.L. Unland J. Catal. 54 (1978) 183
6. H. Lechert, K.P. Wittern Ber. Bunsenges. Phys. Chem. 82 (1978) 1054
7. L. Babernics, P. Tetenyi, L. Kertesz J. Catal. (1973) 237
8. J. Erkelens, S.H. Eggink-du-Burck J. Catal. 15 (1969) 62
9. R.B. Moyes, K. Baron, R.C. Squire J. Catal.22 (1971) 333
10. D.A. Symon Ph.D. Thesis (Durham) (1972)
11. M.J. Jinks Personal Communication to (2)
12. A.H. Baston, D.H.C. Harris A.E.R.E.-R9278 (1978)
13. 'Neutron beam facilities at the HFR available for Users' I.L.L. (1977)
14. P.H. Gamlen, N.F. Hall, A.D. Taylor A.E.R.E.-RRL74/693 (1974)
15. T.C. Waddington, J. Howard Advances Infra-red and Raman Spec. 7 (1980) 86
16. A.H. Baston A.E.R.E. M-2570 (1972)
17. R.E. Ghosh A.E.R.E. USS/P19 (Rev) (1974)
18. M.B.M. Harryman, J.B. Hayter A.E.R.E.-RRL73/25 (1972)

CHAPTER 4

BACKGROUND STUDY OF THE TRANSITION METAL HYDRIDOCARBONYLS

4.1 Introduction

The transition metal hydridocarbonyl clusters are a group of complexes which have a short history yet, within the past decade, has undergone a rapid development. This chapter is used as a vehicle to indicate, briefly, the types of clusters that have been synthesized, their characteristics and the particular aspects of the unique metal-hydrogen bonding which has made this group of compounds so important. The part the clusters play in the present controversy about the analogy between the bonding of small ligands, such as hydrogen, to clusters and to metal surfaces and its relevance to this work is discussed.

4.2. Characteristics of Transition Metal Hydridocarbonyls

Since the mid-1960's, a number of reviews have appeared in the literature of direct relevance to various aspects of transition metal hydridocarbonyl research (1-15). It is not the purpose of this section to reiterate such work in full but to briefly summarise the major areas of research which are relevant to this study and to indicate the state-of-the-art.

4.2.1. Structural Studies: Diffraction Techniques

The first transition metal hydridocarbonyls were reported by Heiber et al (16,17) and they were formulated as $HCo(CO)_4$ and $H_2Fe(CO)_4$. Questions were raised as to the types of bonding that existed in such complexes. Heiber originally proposed that the hydrogen lay buried in the electron orbitals near to the nucleus of the metal atom (18). Later proposals postulated it was bonded to

the terminal oxygen atoms forming -M-CO-H entities (19). This was later dismissed due to the lack of infra-red bands due to -OH stretching (20). With the onset of better spectral techniques and early diffraction experiments, an alternative proposal that the hydrogen was bonded to the metal atom and occupied a co-ordinate position about that atom was put forward. Such early diffraction data was unsuccessful in locating the hydrogen. Its position was inferred from the disposition of other ligands, as in the case of $HPtBr(PEt_3)_2$ (21) which has bromine and phosphorus atoms occupying 3 of the 4 corners of a distorted square about the platinum atom, the fourth site presumably occupied by the hydrogen. Thus the hydrogen was accepted as a 'stereochemically active ligand'.

X-ray diffraction has remained one of the workhorses in characterising such molecules and has in recent years, by the use of refining and image enhancing techniques, 'located' the approximate position of the hydrogen ligand. This has been achieved not only by using data from automated diffractometers, but also by enhancement of the hydrogen atom position in conventional difference Fourier maps. This was effected by eliminating the high angle reflections because the hydrogen scattering is confined to the small scattering angles. The deletion of successive high angle reflections dramatically improves the picture and removes noise peaks. Further, a symmetry averaging method can be used in the cases of symmetric structures by producing composite difference Fourier sections even when the individual sections are too noisy. Thus the information from the six mirror planes of $H_4Re_4(CO)_{12}$ were

added together (22). This removed the noisy peaks and left a clean composite section with the 'true' X-ray determined hydrogen position peaks.

However, to thoroughly understand the complex bonding situations taken up by the hydrogen atom, it became evident that it was necessary to determine, reliably and accurately, the hydrogen position. X-ray diffraction techniques are subject to large uncertainties and systematic errors, especially with compounds containing a number of heavy metals. Metal-hydrogen distances by such techniques are erroneous since the X-rays are diffracted by the hydrogen electron cloud around the nucleus, which is skewed somewhat, with bonding, towards the metal atom. Thus X-ray M-H distances are shorter than the accurate values derived from neutron diffraction data which involve scattering from the nucleus. The first neutron diffraction studies carried out on K_2ReH_9 (23) and $HMn(CO)_5$ (24) where the metal-hydrogen bond-lengths corresponded to normal covalent bonds. Even at present the method is not as common as X-ray diffraction, which remains the more used technique, though, of course this problem is not peculiar to just hydrogen in clusters.

By 1970, terminal M-H bonds were being well characterized. However, other types of M-H bonds were proposed in various polynuclear hydridocarbonyls. The hydrogen position in $(Et_4N)^+(HCr_2(CO)_{10})^-$ was studied and a Cr-H-Cr bridge was postulated (25). The disposition of the carbonyl groups in $H_4Re_4(CO)_{12}$ seemed to indicate the hydrogen was bridging the Re_3 faces forming an M_3H system (22). The direct location of the hydrogen in $H_3Mn_3(CO)_{12}$ was accomplished

by enhancing techniques and three M_2H bridging units were shown to exist (26). More bridged hydrogens have been found and a complex bonding picture is starting to unfold. The finer details are discussed later in this chapter.

4.2.2. Structural Studies: Magnetic Resonance

Nuclear magnetic resonance techniques have been used with success in differentiating between various types of hydrogen within hydridocarbonyls. It is only recently that there have been any exceptions to the following rules: a terminally bonded hydrogen usually gives a signal at τ = 10-26ppm (eg.19.85ppm in $H_2Os_3(CO)_{12}$) (27) and τ = 25-33ppm when the hydrogen is bridging (eg. at 26.25ppm in $HRe_3(CO)_{14}$ (28)). These signals are temperature sensitive, and where both are found, they can broaden and coalesce (29) indicating site exchange. This is discussed in detail by Evans (11). In some complexes hydrogen and carbonyl scrambling has been shown to exist at room temperature. Exceptions to the rule are usually due to unusual circumstances. $H_4Re_4(CO)_{12}$ is coordinatively unsaturated with four M_3H face bridging units and has a τ value of 15.08ppm (30). $H_2Os_3(CO)_{10}$, also unsaturated with an Os=Os double bond and two bridging hydrogens, has a τ value of 21.36ppm (31). More unusual τ values are found when hydrogen is hexacoordinated (i.e. lying in an interstitial six-coordinate hole) as in $HRu_6(CO)_{18}^-$ with a τ value of -6.41ppm and in $HCo_6(CO)_{15}^-$ with τ = -13.2ppm (13).

Proton N.M.R. has sometimes failed to distinguish any inequivalence in hydrogen positions and ^{13}C n.m.r. has been used in carbonyl studies to indirectly help in location. Sometimes a signal has not been found at all and an

explanation, which has been discussed, is that broadening to such an extent has been caused by a quadropolar interaction as with $HFeCo_3(CO)_{12}$ (32) or by paramagnetism, in $H_3Ni_4Cp_4$ with its three unpaired electrons (33).

4.2.3. Structural Studies: Vibrational Spectroscopy

Many problems were found when applying this spectroscopic technique to the characterisation of hydridocarbonyls and little work has been done until recently. Infra-red and Raman spectroscopy have been proven very useful tools in the analysis of hydrogen bonded systems but, in comparison, have not been as successful with metal hydrides.

The metal-hydrogen vibrational modes are frequently broad, weak and are sometimes not even seen, though recently low temperature infra-red or Raman spectroscopy have proved fruitful.

Terminal metal-hydrogen systems have been studied with relative ease with the M-H stretch readily identifiable in the infra-red spectrum. With the study of bridging hydrogens the situation has not been favourable with infra-red spectroscopy though Raman spectroscopy has been more useful in discerning vibrations too weak and broad to be seen by the former technique. However, in many cases, it appears that the transition dipole or polarisability changes are too small to produce a satisfactory infra-red absorption or Raman scattering respectively. There is also a paucity of data from the Raman technique in the study of these bridged species because some synthetic chemists have not used the method and, further, because many of the compounds are highly coloured and readily decompose in a laser beam. Various spinning devices, low temperatures and low powered

lasers are presently being used to rectify this situation.

The first vibrational studies were involved in characterising the metal-terminal hydrogen bond, whose stretch occurs in the 1900cm^{-1} region of the infra-red spectrum with a peak width at half height, $\Delta \upsilon_{\frac{1}{2}}$, of approximately 10-30cm^{-1}. The intensity of these bands are very sensitive to other ligands, especially trans to the hydride. In the Raman spectrum, the mode is usually of medium-strong intensity following the complimentary intensity relationships which are usually observed between the two spectroscopic methods, eg. $HMn(CO)_5$: υ_{MH}(1780cm^{-1}) is medium strong in the Raman (34) which can be contrasted with the difficulties experienced in observing the mode in the infra-red (35).

With bridging hydrogens, the problem is increased because the bands, which shift to lower frequencies, are considerably broadened. The stretching mode is at 1100$\pm$ 300cm^{-1} with $\Delta \upsilon_{\frac{1}{2}} \sim$ 100cm^{-1}.

Kirtley (36) discussed this broadening and felt that some of the explanations of similar broadening in hydrogen bonded species were not applicable to metal bridged systems because of the strong M-H bonding whereas in a hydrogen bonded system, YHY, the Y-Y interaction may be negligible. However, the possibility remained that the vibrations were interacting with lower frequency deformations and that combination of other fundamental vibrations, intensified by Fermi resonance, was taking place. Kirtley went on to indicate that the hydrogen vibrations were interacting with the carbonyl deformations in much the same way. This affect was greater for protonated hydridocarbonyls

than for deuterated forms due to the greater hydrogen vibrational amplitude.

Such broadening, if slight, will not necessarily be observed by inelastic neutron scattering (IINS) since the IINS bands in the 1000-2000cm^{-1} region will be quite broad, in any case, due to the poor instrument resolution compared with infra-red and Raman techniques. TheIINS bands may be even broader if the broad band takes the form of multiple maxima covering a region of $>100cm^{-1}$ as found in many low temperature infra-red or Raman spectra of hydridocarbonyls.

With $H_3Re_3(CO)_{12}$, with three MHM bridging hydrogens, very little is seen in the infra-red (70). A Raman study (38), however, found three shallow maxima at 1100, 1076 and 1000cm^{-1} which were observed at 792, 752 and 692cm^{-1} on deuteration. Such multiple maxima, which complicate the assignment, are found with many hydridocarbonyls. Claydon and Shephard (39) have attributed such maxima in strongly hydrogen bonded systems to Fermi resonance of the broad hydrogen modes with overtones of lower lying bands. Such features have been found by low temperature studies in the 900cm^{-1} region for the $(HM_2(CO)_{10})^-$ ions by Cooper et al (40). They postulated that Fermi resonance with M-C and M-C-O overtones might account for the observed structure. Later, Cooper et al (41) went on to test this hypothesis by studying $(HW_2(CO)_{10})^-$. They substituted ^{18}O for ^{16}O and expected a change not only in the M-C-O fundamentals but also in the M-H vibrations due to Fermi resonance. This did not happen and rules out the effect for the above ion type, if not for all hydridocarbonyls.

Other explanations of this such as multiple well minima and factor group coupling are discussed in Chapter 5.

Another complicating factor is that moderately strong bands can suddenly appear at low temperatures e.g. 1680cm^{-1} in $(Et_4N)^+(HW_2(CO)_{10})^-$ at 77K (42). These broaden and disappear at higher temperatures. The band centres do not appear to move on increasing the temperature. This behaviour has yet to be explained (40). It is known that these ions have a geometry dependent upon the type of counter ion and this variation would seem to indicate the ease with which the molecule can distort. $(HW_2(CO)_{10})^-$ may be deforming at low temperatures. The band is at a fairly high frequency and it could mean that the hydrogen has some terminal character and the MHM bond could be asymmetric.

Since it became apparent that the vibration frequencies involving hydrogen motion, vary with the MHM bond angle in bridged systems, there have been a number of studies seeking relationships between the variations in MHM bond angle (θ) and the vibrational frequencies. The fundamental vibrations, involving hydrogen, in a linear MHM system are shown in Figure 4.1.

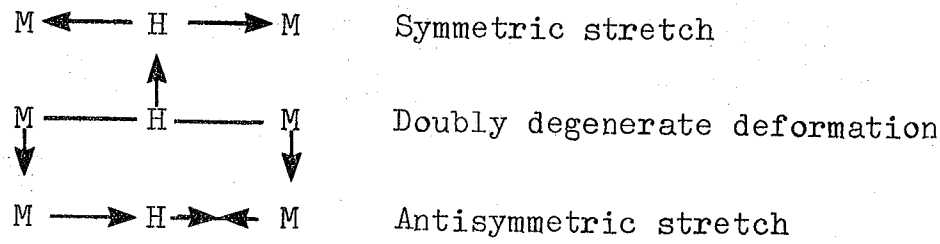

Figure 4.1

However, since most, if not all, bridged MHM species are inherently bent, a different form of vibration would be expected with the selection rules being relaxed somewhat from the linear case. In the studies of the relationship between the vibrations of the MHM bond angle and the vibrational frequencies of the MHM unit the two following vibrations have been used since, more often than not, these two have been the only hydrogen involved vibrations seen in infra-red or Raman studies. Figure 4.2 shows the anti-symmetric and symmetric stretches.

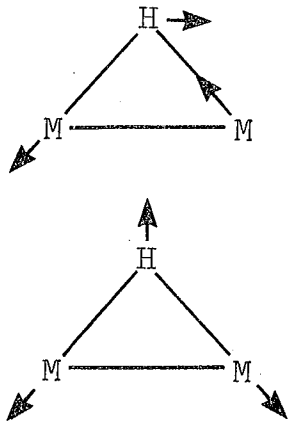

Antisymmetric stretch (υ_{as})

Symmetric stretch (υ_{s})

Figure 4.2.

Kirtley was the first to seek such structural/ vibrational correlations (36). Equations were derived for the calculation of the υ_{as} and υ_{s} stretches from the bond angle and various bond force constants using a simple valence force field approximation. The mass of the metal atoms were taken as very large compared to hydrogen thus the mass of the metal atoms are taken as being infinite. As θ decreased, υ_{s} decreased but υ_{as} increased. A plot of υ^2_{s} against $(1+\cos\theta)$ gave a straight line of slope k, where k was the MHM bridge stretching force constant, and a plot of υ^2_{as} against

$(1-\cos\theta)$, also, gave a straight line of slope k. At the time (1971) little crystallographic or vibrational data was available for a test of the correlation.

Shephard et al (43) also compared the stretching frequencies of the MHM moiety with known MHM band angles. Once again using a simple valence force field, derived from Herzberg (44), with approximations for the mass of the metal being infinitely heavier than the hydrogen atom and that the angle bending force constant $\underline{k}_\theta$ was smaller than that of the bond stretching force constant, $\underline{k}_r$. They obtained equations 4.1 and 4.2:-

$$\upsilon_{as}^2 = \underline{k}_r \sin^2(\theta/2)/2 \; \pi^2 \underline{c}^2 \underline{m}_H^2 \qquad (4.1)$$

$$\upsilon_{s}^2 = \underline{k}_r \cos^2(\theta/2)/2 \; \pi^2 \underline{c}^2 \underline{m}_H^2 \qquad (4.2)$$

where θ is the MHM bond angle and $\underline{c}$, the velocity of light. From these equations the following simple relationships were derived: $(\upsilon_{as}/\upsilon_{s}) \propto \tan(\theta/2)$ and $(\upsilon_{as}/10^3) \propto \sin(\theta/2)$.

Using data from 7 hydridocarbonyls, reasonable agreement was achieved between theoretical and experimental results so that it appeared that these empirical relationships were of some predictive value.

Katovic and McCarley (45) determined M-H bond distances in $(M_2X_8H)^{3-}$ ions where X was a halide and using this distance the bond angle could be estimated by using $d_{(M-H)} = d_{(M-M)} \left(2\sin\left[\frac{\theta}{2}\right]\right)^{-1}$. These compounds gave two infra-red bands in the 1200-1600cm^{-1} region. Once again, using a central force field approximation, the symmetric and antisymmetric frequencies were related to the force constants, the atomic weights of the atoms involved and the

MHM bond angle. Using the following approximations: that the metal-metal stretch was at a much lower frequency compared with the metal-hydrogen stretch and that the mass of the hydrogen was very much less than that of the metal atoms, allowed the following relationship to be derived equation 4.3

$$\frac{\upsilon_s}{\upsilon_{as}} = \left[M_M^{-1} + M_H^{-1}(1+\cos\theta)\right]^{\frac{1}{2}} \left[M_M^{-1} + M_H^{-1}(\cos\theta)\right]^{-\frac{1}{2}} \quad 4.3$$

where υ_s and υ_{as} are the frequencies of the symmetric and antisymmetric stretches, M_M and M_H are the atomic weights of the metal and hydrogen involved and θ is the MHM bond angle.

Cooper et al (40) also carried out a simple valence force field calculation in which the force constants were fixed and the MHM angle varied from 90^o-180^o. The variations in θ with the vibrational frequencies of the antisymmetric stretch and the doubly degenerate deformation were found for various bond angles. Figure 4.3 shows the empirical plot for the MoHMo system. The main part to note is that there is a rapid change in the vibrational frequencies as θ approaches 90^o and in fact the values cross as the backbone becomes more strongly bent.

With the general lack of information on the molecular vibrations in transition metal hydridocarbonyls, it appeared that, with the selection rules and unique properties peculiar to inelastic neutron scattering, valuable information could be determined by a study using neutrons. In crystallography, neutron diffraction techniques had been more successful than X-rays because it was a more efficient proton detecting tool. So, it is expected that those

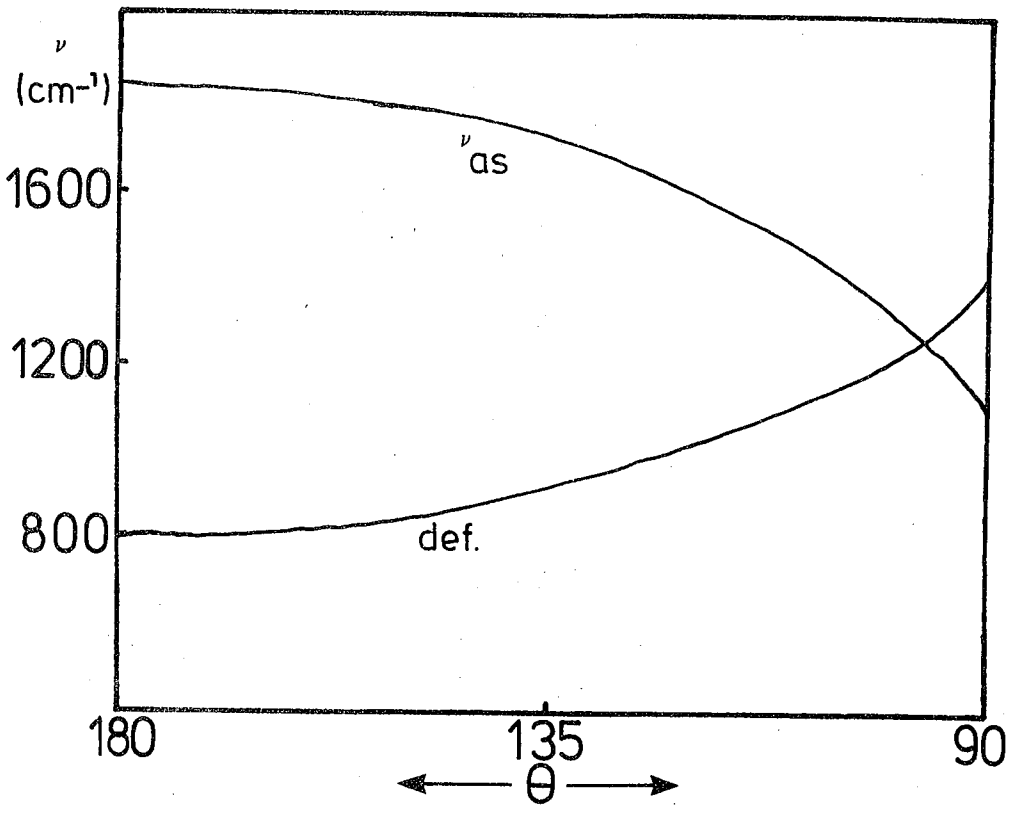

Figure 4.3

molecular vibrations involving hydrogen, which have been difficult to detect, if at all, by infra-red and Raman methods, will be more readily seen using inelastic incoherent neutron scattering spectroscopy.

Previous spectroscopic data collected on the studied compounds is discussed in the next chapter. However, it can be said that already there has been a study of transition metal hydrides by Wright using neutrons (46). Those compounds studied in the 0-400cm^{-1} region were $HOs_3(CO)_{12}PF_6$, $HRu_3(CO)_{12}PF_6$, $H_3Mn_3(CO)_{12}$, $H_3Re_3(CO)_{12}$, $HFeCo_3(CO)_{12}$ and $CsHFe_3(CO)_{11}$. Those compounds studied in the 200-900cm^{-1} region were $HCo(CO)_4$, $H_2Fe(CO)_4$, $HCo(PF_3)_4$, $KHFe_3(CO)_4$, $HMn(CO)_5$ (all with terminal hydrogen), $H_3Mn_3(CO)_{12}$ and $CsHFe(CO)_{11}$. The low frequency study was to find the effect of bridging with hydrogen on the

metal-metal bond. At the time, the position of the hydrogen in $HFeCo_3(CO)_{12}$ was not known and Wright claimed, from just low frequency data, that it lay within the ($FeCo_3$) tetrahedron, bonded to the iron atom. This has, probably, been proven incorrect from neutron and X-ray data on a derivative of the compound.

This study is not just an extension of Wright's work because the 0-2500cm^{-1} range is covered for all compounds and doubly, triply and hexacoordinated hydrogens have been studied, using higher resolution spectrometers.

4.2.4. Structural Studies: Miscellaneous Techniques

Reliable molecular weights have been measured using mass spectral techniques and, where due care has been taken, the number and types of hydrogen within the cluster have been estimated. In the hydridocarbonyls there is usually competitive loss of hydrogen and carbonyls and often, in polynuclear hydridometal complexes, hydrogen loss does not occur from the parent ion, eg the hydrogen in $HFeCo_3(CO)_{12}$ is tenaciously retained through the various carbonyl losses down to the $FeCo_3H$ unit (47).

Gas-phase ultra-violet photoelectron studies have been carried out (48) on $H_3Re_3(CO)_{12}$, $H_2Os_3(CO)_{10}$, $H_4Os_4(CO)_{12}$ and $Os_3(CO)_{12}$ as well as $H_4Re_4(CO)_{12}$ (49) in a study of the MHM bond. Bands have been found in the 8-16ev region and identified as due to -CO ligand orbitals and M-CO back-bonding orbitals. Further M-M bonds at ~ 7-8ev have been seen in $Os_3(CO)_{12}$, which are absent in the hydridocarbonyls and have been replaced by a band at ~ 12ev. This has been interpreted as indicative of a

localised three centre MHM bond.

Mossbauer spectroscopy has also been used as a tool in the characterisation of transition metal carbonyl and hydridocarbonyl complexes. The structure of $(HFe_3(CO)_{11})^-$ as observed by Mossbauer (and X-ray spectra) lead to a new assignment of the structure of $Fe_3(CO)_{12}$ (50). Further the species $(HFe_2(CO)_8)^-$ is believed related to $Fe_2(CO)_9$, as determined by its Mossbauer spectrum, in that a bridging carbonyl is replaced by a hydride ligand (51). One study of direct interest has been that of $(FeCo_3(CO)_{12})^-$ and its conjugate acid and the substituted trimethyl phosphite derivatives of it (52). Only small changes in the Mossbauer spectra were observed on protonation indicating that the high symmetry of the ion was not disrupted on moving to $HFeCo_3(CO)_{12}$ implying the hydrogen lay on the major axis.

4.3. Characterisation of the Metal-Hydrogen Bonds

4.2.1. General Formula of Studied Type

The general formula of the compounds studied is:-

$$X_a^{n+}\left[H_j\ M'_k M''_l (CO)_m \right]^{n\pm}\ Y_b^{n-} \qquad \text{where}$$

(a) the total number of hydrogen atoms is ≥ 1

(b) the total number of metal atoms is ≥ 2

(c) there may be more than one metal type in the cluster

(d) the hydridocarbonyl may be neutral and may not need a counter ion, such as X^+ or Y^-, since $a \geq 0$ and $b \geq 0$.

(e) if the hydridocarbonyl is a cation, it is balanced by a number of non-hydrogeneous anions, such as PF_6^-

(f) if the hydridocarbonyl is an anion, it is balanced by a number of non-hydrogeneous cations such as Cs^+

The compounds chosen in the study do not contain any other hydrogeneous material than the hydrogen(s) of interest i.e. no other hydrogen containing ligands or hydrogen containing counter ion. Inelastic neutron scattering would take place from such alternative sources of hydrogen and would probably make the spectrum too complex for analysis.

4.3.2. Types of Compounds Being Studied

The compounds can be classified into groups according to the method adopted by Churchill et al (53) in their study of bridging hydride ligands.

(i) Species with a single μ_2-hydride ligand between two metal atoms.

This is the (MHM) system. Various aspects of the bonding in this unit are discussed later, however, it can be said that in most cases there is still substantial direct metal-metal orbital overlap which dominates this three centre bond. Where there is no metal-metal overlap, an 'open' bond is found. Where a degree of overlap exists the system is 'closed' and can be crudely described as a protonated metal-metal single bond. Such species are represented by either of the following schematic descriptions in Figure 4.4. However, there appears to be no hard and fast distinction between these two types of bond which may only differ by degree rather than kind.

It seemed possible that a linear MHM, rather than a bent MHM system, could exist as was first postulated from work on the $(HCr_2(CO)_{10})^-$ ion (56). However, recent work seems to indicate that the hydrogen occupies various off-

(a) (54) OPEN CLOSED

(b) (55) OPEN CLOSED

Figure 4.4

centre positions but that its mean position would be at the centre of Cr-Cr bond. (It is not known whether the hydrogen passes through the centre of the Cr-Cr bond to reach these off-centre positions or merely revolves round the bond). The μ_2- hydride ligand will be represented in this study by M—H—M so that diagrams showing the unit will appear more explicit.

Those compounds which contain this unit and are studied by neutron scattering are:- $HW_2(CO)_9NO$, $HRe_3(CO)_{14}$, $H_2FeRu_3(CO)_{13}$, $H_3Re_3(CO)_{12}$, $H_3Mn_3(CO)_{12}$ and $H_4Ru_4(CO)_{12}$.

(ii) Species with two μ_2-hydride ligands bridging a pair of metal atoms

This is the (MH_2M) unit. In this case, the metal-metal overlap takes the form of a double bond which is doubly protonated. The bis-(μ_2-hydride) ligands will be represented by M(H)(H)M. In the three structurally characterised hydridocarbonyls containing $M(\mu_2\text{-}H)_2M$ systems; $H_2Os_3(CO)_{10}$, $H_2Re_2(CO)_8$ and $H_2W_2(CO)_8^{2-}$ the MM doubly-

bridged M-M bond distance is shorter than the singly bridged or non-bridged MM bond distance. For example: Os-Os in $Os_7(CO)_{21}$ is 2.806-2.935Å, $Os(\mu_2\text{-}H)Os$ in $(\mu_1\text{-}H)(\mu_2\text{-}H)Os_3(CO)_{11}$ is 2.989Å whereas $Os(\mu_2\text{-}H)_2Os$ in $(\mu_2\text{-}H)_2Os_3(CO)_{10}$ is 2.683Å (57). The only studied compound in this group is $H_2Os_3(CO)_{10}$.

(iii) Species with greater than two μ_2-hydride ligands bridging a pair of metal atoms

These are the (MH_nM) systems where $n \geq 3$. Here triply and quadruply protonated metal-metal triple and quadruple bonds are respectively found. No species were prepared from this section because the known compounds had large hydrogeneous ligands attached for stability.

(iv) Species with a single μ_3-hydrido ligand spanning three metal atoms

These are the (M_3H) units and these four centre bonds are represented by 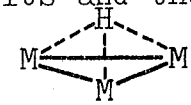 The compounds studied in this section are $H_2Ru_6(CO)_{18}$ and $HFeCo_3(CO)_{12}$.

(v) Species with more than one μ_3-hydride ligand associated with a metal-metal bond

There is only one compound known under this heading and it has been studied. It is $H_4Re_4(CO)_{12}$ which contains a tetrahedron of rhenium atoms with μ_3-hydride ligands bridging each Re_3 face. Thus, each Re-Re vector is associated with two μ_3-hydrogens.

(vi) Species with a μ_n-hydride ligand where $n \geq 3$

Only the (M_6H) system has been found where $n \geq 3$. This μ_6-hydride ligand exists at the centre of an octahedron of metal atoms. $CsHCo_6(CO)_{15}$ has been studied in this section.

4.3.3. Aspects of Bonding in Transition Metal Hydridocarbonyls

Metal clusters are discrete molecular species in which three or more metal atoms interact (bond) to form two or three dimensional arrays. In most clusters the periphery is enveloped by a set of ligands, though 'interstitial' ligands are possible, such as H in $CsHCo_6(CO)_{15}$. Common cluster ligands are halogens, sulphur, hydrogen, carbon monoxide and organic species. The cluster prototypes are the dinuclear metal entities, a structurally well defined group.

Electronically the metal clusters are closed shell structures that bear formal analogies to the polyhedral boranes and heteroboranes (58,59). The stoichiometry of most lower clusters are rationalised by an extension of the 18-electron rule and the prediction of cluster geometries can be made by skeletal electron counting. For triangular clusters, the electron requirement is $48e^-$ and all trimetal clusters obey the rule except $H_2Os_3(CO)_{10}$ (60) and $(H_3Re_3(CO)_{10})^{2-}$ (61,62) which have $46e^-$, that is they are coordinatively unsaturated and thus have a rich chemistry. The electronic requirement of tetrametals is $60e^-$ and again the exceptions are $H_4Re_4(CO)_{12}$ (22) and $H_3Ni_4Cp_4$ (62) with 56 and $63e^-$ respectively. These complexes have metal-metal bonding which is not necessarily directed along the tetrahedral edges. The $18e^-$ rule breaks down more often with higher clusters.

In hydrogen bridged complexes the $M(\mu_2\text{-}H)$ M system is known as a two-electron three-centre bond, the $M(\mu_2\text{-}H)_2M$ system as a four-electron four centre bond and the

$M_3(\mu_3\text{-H})$ system as a three-electron four-centre bond and the $M_6(\mu_6\text{-H})$ system as a twelve-electron seven-centre bond.

One of the earliest methods of estimating the position of the hydrogen in the cluster was to look at the positions of the other ligands and the lengths of the metal-metal bonds. The disposition of the other ligands has been mentioned in conjunction with diffraction data. For example, in $H_4Ru_4(CO)_{12}$, with four edge bridging hydrogens, the three terminal carbonyls are staggered with respect to the ruthenium-ruthenium edges, however, in $H_4Re_4(CO)_{12}$ the terminal carbonyls are eclipsed with respect to the rhenium-rhenium edges. In the rhenium tetrahedron the metal orbital overlap takes place over the faces of the tetrahedron where the hydrogen is found triply bonding, whereas the overlap in the ruthenium tetrahedron is along the edges where the hydrogen is found (22).

In the early X-ray study of the anion $(HCr_2(CO)_{10})^-$, with its CrHCr bridged system, the data implied that the anion had a D_4h structure with a linear CrHCr unit with eclipsed terminal carbonyls (25). (However, since this early study the $(HCr_2(CO)_{10})^-$ and $(DCr_2(CO)_{10})^-$ situation has become much more complex and will be discussed later). A study of $HW_2(CO)_9NO$ proceeded and it was expected that a similar geometry would be found with, possibly, some asymmetry caused by the isoelectronic replacement of a $(CO)^-$ group by a neutral (NO) unit in the $(HW_2(CO)_{10})^-$ anion (63). However, the overall structure of the molecule was bent, rather than linear, with staggered carbonyl groups. The hydrogen atom was expected to lie at the intersection of the two axial ligand-metal vectors Figure 4.5a. and a WHW angle of 159°

Figure (4.5)

Hydrogen positioning in MHM bonds and overlaps of orbitals in closed and open bonds.

(a) expected H position in $HW_2(CO)_8NO$

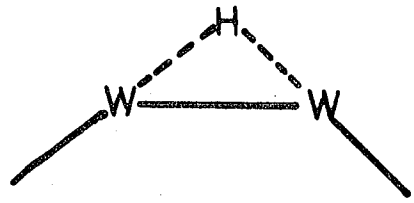

(b) actual H position in $HW_2(CO)_8NO$

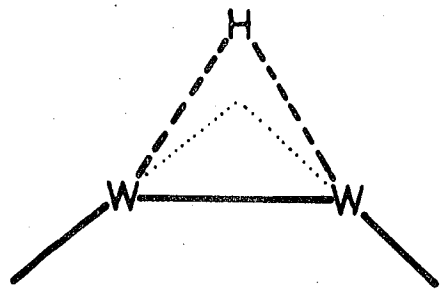

(c) orbital overlap in 'closed' bond

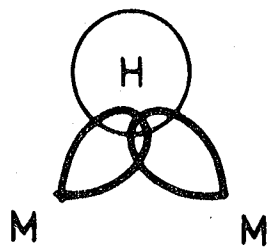

(d) orbital overlap in open bond

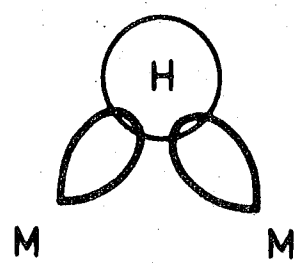

was predicted. Subsequent neutron diffraction work (55) showed the hydrogen to lie further from the W-W axis with a WHW angle of 125° Figure 4.5b. This indicated the nature of the MHM overlap was such that all orbitals merged in a common region in space with the centre of the hydrogen nucleus lying beyond this point away from the W-W axis. Thus such an overlap, as shown in Figure 4.5c. existed. The original intention of finding any asymmetry in the hydrogen position with respect to the tungsten atoms due to the -NO group was not achieved due to a packing disorder, which generated the appearance of a symmetric WHW bond. If little metal-metal interaction took place then orbital overlap would be as in Figure 4.5d.

Asymmetry has been found, though only to a small degree, in $HW_2(CO)_8NO(P(OMe)_3)$ which has W-H distances of 1.859Å and 1.894Å (64). An unsymmetrical bond has also been found in the mixed metal complex $(Cp)_2(CO)NbHFe(CO)_4$ which has an Nb-H distance of 1.91Å and an FeH distance of 1.61Å where the hydrogen is displaced towards the $16e^{-1}$ iron group and away from the $17e^{-1}$ niobium group (65). A low temperature study of $(Et_4N)^+(HW_2(CO)_{10})^-$ (at 14K), using neutron diffraction techniques, indicated W-H distances of 1.718 and 2.070Å (13). Such pronounced asymmetry, surprisingly so, points to a near donor acceptor complex, i.e. electrons of the W-H bond in $HW(CO)_5^-$ are donated to the empty orbital of the electron deficient $W(CO)_5$ moiety. This distortion may be the evidence sought to explain the high frequency anti-symmetric stretch at $1680cm^{-1}$ found for $(Et_4N)^+ (HW_2(CO)_{10})^-$ (35). Unfortunately no other bands involving hydrogen were reported in the low temperature

study which found the 1680cm^{-1} band. Thus, the effect of distortion could not be assessed upon these other vibrations. If they did change drastically at very low temperatures compared with the values at higher temperatures then the effect of distortion may be causing this though, of course, care would have to be taken to separate out any effect due to the drop in temperature alone. It must be noted that little investigative studies of this nature have been carried out on $HW_2(CO)_9NO$.

The evidence so far accumulated suggests that the MHM bond is inherently bent. Even the $(HCr_2(CO)_{10})^-$ ion has on reinvestigation turned out to be bent, contrary to the early X-ray study (25). The true picture emerging has been found by neutron diffraction studies. It was found that $(Et_4N)^+(HCr_2(CO)_{10})^-$ contained a non-linear CrHCr bond with the bridging hydrogen randomly disordered between two centrosymmetrically related sites, each equidistant from the chromium atoms and displaced, opposite each other, 0.3Å from the centre of symmetry of the ion (66). The carbonyl-chromium skeleton retains its D_{4h} symmetry while the hydrogen atom moves between these two sites. It was concluded that the potential energy surface associated with the hydrogen nucleus was so shallow to allow the easy bending of the CrHCr moiety without peturbing the non-hydrogen D_{4h} symmetry. A further neutron diffraction study of $((PPH_3)_3N)^+(HCr_2(CO)_{10})^-$ (67) could not resolve the disc-shaped hydrogen atom thermal ellipsoid, but in this case the authors postulated that either there were four centrosymmetrically related sites or that the hydrogen was radially disordered. A very recent single crystal study

of $((PPh_3)_2N)^+ (DCr_2(CO)_{10})^-$ (68) at low temperature has found that a four-fold disorder of the hydrogen was taking place and this caused the unusual hydrogen thermal ellipsoid.

The hydrogen position can also be inferred from the angular arrangement of terminal carbonyls. For example, in the anionic triangular rhenium carbonyl hydride, $(H_2Re_3(CO)_{12})^-$, characterised by Churchill et al (38), the axial terminal carbonyls are more or less regularly arranged but the equatorial terminal carbonyls are much less regular and appear to be forced apart with respect to two sides of the triangle. This is very probably due to the presence of hydrogen atoms along these two edges. Further, in this ion, the Re-Re distances are 3.173, 3.181, and 3.035Å. It would appear that the metal-metal distances are being lengthened by the hydrogens. This feature has been found in most $M(\mu_2\text{-}H)M$ complexes and is seen most significantly in the tetrahedral cluster, $H_4Ru_4(CO)_{12}$ (59). There are four long and two short ruthenium-ruthenium bond lengths. The short distances are 2.786Å and are opposite each other and are not bridged whereas the bridged Ru-Ru distances are 2.950Å, which compares favourably with hydrogen bridged Ru-Ru bond lengths in $H_2Ru_4(CO)_{13}$, 2.930Å (70) and even the triply bridged $H_2Ru_6(CO)_{18}$, 2.954Å (71). $H_2Ru_6(CO)_{18}$ contains a Ru_6 octahedron with two opposite Ru_3 faces bridged by μ_3-H ligands. There would also appear to be a metal-metal lengthening effect on placing hydrogen within an octahedral hole. The structure of the $(HCo_6(CO)_{15})^-$ ion has been resolved and shows cobalt-cobalt distances of 2.579Å whereas in the $(Co_6(CO)_{15})^-$ ion the average

cobalt-cobalt distance is 2.509Å indicating that protonation has 'swelled' the octahedron (72).

Studies have been carried out on the rearrangements that can take place in polynuclear metal carbonyl hydrides involving the migration of hydrogen, carbonyls and unsaturated organic ligands around the vertices, edges and faces of the metal framework (11). Carbonyl migration in compounds such as $Fe_3(CO)_{12}$ and $Rh_6(CO)_{16}$ is now well understood. Three types of exchange have been found: 1) rotation of the metal skeleton within a fixed carbonyl envelope, for example such a movement may take place in $Fe_3(CO)_{12}$ (73), 2) rotation of the metal skeleton accompanying a particular permutation with the ligand envelope via an intermediary or an alternative carbonyl polyhedral structure. For example in $H_2FeRu_3(CO)_{13}$, where different processes are found which are extremely temperature dependent, (74) and 3) local rearrangements within sections of the ligand envelope, with a fixed metal core, for example in $H_2Os_3(CO)_{11}$, hydrogen exchange takes place between the terminal and μ_2-bridging hydrogen positions (29, 75). N.m.r. spectra of the phosphite substituted $H_4Ru_4(CO)_{12}$(76) at ambient temperaure indicate fast proton exchange possibly via the two shorter Ru-Ru edges. Such hydride motions imply a low energy barrier to tautomerization, which may take place via several pathways. There is an argument as to whether in $H_4Co_4(CO)_4$, which has face bridging hydrogens, the migration moves by a face-edge-face mechanism (77) or by a face-terminal-face mechanism (78).

4.4. Synthesis of Transition Metal Hydridocarbonyls

There are a number of synthetic routes into transition metal hydridocarbonyls and these have been listed by Green

and Jones (3) and by Kaesz and Saillant (4).

(i) Reactions with molecular hydrogen.

(ii) Reactions of metal complexes with saline or complex hydrides.

(iii) Hydrogen transfer from solvent or metal co-ordinated group.

(iv) Hydrolysis and dehydrohalogenation.

(v) Protonation.

The following are the preparatory routes used to achieve the studied transition metal hydridocarbonyls. Analyses of each compound is given with those of the preparative authors.

The chemicals used in the preparations were supplied by the following companies: $Ru_3(CO)_{12}$, $Co_2(CO)_8$, $Fe_3(CO)_{12}$ $Os_3(CO)_{12}$, $Mn_2(CO)_{10}$, $Re_2(CO)_{10}$, $W(CO)_6$ and $NaFe(CO)_4$ by Strem Chemicals Inc; hydrogen by British Oxygen Ltd; orthophosphoric acid (90%, G.P.R. grade), hexane (synchemica grade), sulphuric acid (analar grade) by Hopkin and Williams Ltd; sodium borohydride (lab. reagent grade) and dekalin (technical grade) by British Drug Houses Ltd; tetrahydrofuran by B.A.S.F. GmbH and octane (purum grade) from Fluka AG. All solvents were purified before use by distillation and by normal drying routines. All manipulations were carried out under nitrogen on vacuum lines, glove boxes etc.

The metal content was determined using a Perkin-Elmer 403 atomic absorption spectrophotometer. The C, H and N content was determined using a Perkin-Elmer 240 elemental analyzer. The hydrogen content must be quoted with $\pm$ 0.4% error. The estimated values differ above and below

the theoretical value but in all cases remain within ±0.4%. Of the 12 compounds analyzed the hydrogen error ranges from +0.32% to -0.30%. In most cases, the authors who had originally produced the hydridocarbonyls, had the analysis carried out by independent micro-analysis laboratories. No hint was given of the method undertaken or the errors involved.

(i) Tetra-μ_2-hydridododecacarbonyltetraruthenate $H_4Ru_4(CO)_{12}$

$H_4Ru_4(CO)_{12}$ was made by the method of Knox et al (79) by the direct hydrogenation of ruthenium carbonyl, $Ru_3(CO)_{12}$ in octane at 120°C, with hydrogen.

Analysis	%	Theor.	Actual	Knox etal
	C	19.36	19.12	19.33
	H	0.54	0.25	0.54
	Yield	-	77%	88%

Quantity made = 5.44g

(ii) Di-μ_2-hydridodecacarbonyltriosmate $H_2Os_3(CO)_{10}$

$H_2Os_3(CO)_{10}$ was made by the method (79) of Knox by direct hydrogenation of the osmium carbonyl, $Os_3(CO)_{12}$, in octaneat 120°C, with hydrogen.

Analysis	%	Theor.	Actual	Knox et al
	C	14.08	14.20	Not
	H	0.23	0.25	Given
	Yield	-	83%	73%

Quantity made = 16.23g

(iii) μ_3-hydridododecacarbonylirontricobaltate $HFeCo_3(CO)_{12}$

This mixed metal hydridocarbonyl was made via a two step preparation due to Chini et al (32) which consisted

of the protonation of a carbonyl mixed metallate formed from the disproportionation of cobalt and iron carbonyls which took place in mild conditions.

Analysis	%	Theor.	Actual	China et al
	C	25.26	25.52	25.20
	H	0.20	0.09	0.14
	Co	31.04	30.90	30.85
	Fe	9.80	9.44	9.78
	Yield	-	98%	95.5%

Quantity made = 32.48g

(iv) Di-μ_2-hydridotridecarbonylirontriruthenate $H_2FeRu_3(CO)_{13}$

This compound was prepared by the two step reaction of Geoffroy and Gladfelter (80). $Ru_3(CO)_{12}$ was reacted with Na_2 $Fe(CO)_4$ and then acidified with phosphoric acid.

Conditions had to be correct to ensure a good yield of $H_2FeRu_3(CO)_{13}$. Larger quantities of $H_4Ru_4(CO)_{12}$, $H_2Ru_4(CO)_{13}$ and $Fe_2(CO)_{12}$ were produced when optimum conditions were not used.

Analysis	%	Theor.	Actual	Yawney et al (81)
	C	21.52	22.09	22.3
	H	0.28	0.54	0.43
	Yield	-	48%	49%

Quantity made = 11.57g

(v) μ_2-hydridonitrosylnonacarbonylditungstate $HW_2(CO)_9NO$

$HW_2(CO)_9NO$ was prepared in two stages. The ion $(HW_2(CO)_{10})^-$ was prepared by refluxing $W(CO)_6$ with $NaBH_4$ in T.H.F. (82) and then treated with sodium nitrite and acetic acid to produce the neutral hydridocarbonyl (55).

Analysis	%	Theor.	Actual	Olsen et al (55)
	C	16.60	16.90	16.34
	H	0.15	0.11	0.27
	N	2.15	2.50	2.28
	Yield	-	30%	40%

Quantity made = 17.95g

(vi) tri-μ_2-hydridododecacarbonyltrimanganate $H_3Mn_3(CO)_{12}$

This compound was produced by the high yield reaction of Johnson et al (83). $Mn_2(CO)_{10}$ was treated with the base, KOH, then acidified with phosphoric acid.

Analysis	%	Theor.	Actual	Johnson et al (83)
	C	28.64	29.59	Not
	H	0.59	0.34	Given
	Yield	-	69%	80%

Quantity made = 8.18g

(vii) Tetra-μ_3-hydridododecacarbonyltetrarhenate $H_4Re_4(CO)_{12}$

$H_4Re_4(CO)_{12}$ was produced by directly hydrogenating $Re_2(CO)_{10}$ in refluxing dekalin (26,84) where $H_3Re_3(CO)_{12}$ was produced as an intermediate. The reaction was terminated after ~ 50 hours refluxing due to the high quantity of rhenium metal being produced from further hydrogenation of $H_4Re_4(CO)_{12}$. Unconverted $Re_2(CO)_{10}$ and $H_3Re_3(CO)_{12}$ were removed by precipitation on cooling to 0°C. Benzene was added to the filtered solution to precipitate the $H_4Re_4(CO)_{12}$. Dekalin solvate. The $H_4Re_4(CO)_{12}$.solvate was purified by dissolving in cyclohexane and re-precipitating with benzene. The solvate moiety was removed by heating the material at 60°C at ~0.1 torr for ~30 minutes.

Analysis a) cyclohexane solvate

%	Theor.	Actual	Saillant et al (30)
C	18.49	18.45	18.84
H	1.38	1.70	1.39
Yield	-	22%	50-60%

b) after solvent removal

C	13.28	12.83	Not Given
H	0.37	0.58	(solvent not removed)
Yield	-	100%	-

Quantity made = 3.38g

(viii) Tri-μ_3-hydridododecacarbonyltrirhenate $H_3Re_3(CO)_{12}$

Direct hydrogenation, though simpler, was less desirable, due to the tendency to form rhenium metal, than the earlier method of reducing $Re_2(CO)_{10}$ with sodium tetrahydroborate in T.H.F. followed by acidification to the neutral hydridocarbonyl (85).

Analysis	%	Theor.	Actual	Huggins et al (85)
	C	16.05	14.71	16.04
	H	0.34	0.60	0.30
	Yield	-	50.1%	46%

Quantity made = 10.65g

(Note: It was felt a small amount of $Re_2(CO)_{10}$ was present in the final product).

(ix) μ_2-hydridotetradecacarbonyltrirhenate $HRe_3(CO)_{14}$

$HRe_3(CO)_{14}$ was made according to the procedure described by Fellmann and Kaesz (37). The tetracarbonyl anion $(Re(CO)_4)^-$, produced by the reduction of $Re_2(CO)_{10}$ by $NaBH_4$, was added to $Na^+Re(CO)_5^-$, produced by the reduction

of $Re_2(CO)_{10}$ by sodium amalgam. To these anions was added concentrated H_3PO_4 and the mixture was heated at 60° for 30 minutes. Cooling to -10°C led to bright yellow needles of the product. Since the yield was low, ~20%, and the IINS study needed ~30g, the experiment had to be carried out many times.

Analysis	%	Theor.	Actual	Fellmann et al (37)
	C	17.66	18.14	17.60
	H	0.11	0.30	0.35
	Yield	-	22.8	20%

Quantity made = 22.75g

(x) Caesium μ_6-hydridopentadecacarbonylhexacobaltate $CsHCo_6(CO)_{15}$

The potassium salt of $(HCo_6(CO)_{15})^-$ was produced by the procedure according to Hart et al (72). The caesium salt was gained by metathesis using CsCl in H_2O

Analysis	%	Theor.	Actual	China et al
	C	19.82	18.89	Not
	H	0.11	0.0	Given
	Co	38.99	38.65	

Quantity made = 33.26g

(Note: $CsHCo_6(CO)_{15}$ not yet reported in literature)

xi) di-μ_3-hydridooctadecacarbonylhexaruthenate $H_2Ru_6(CO)_{18}$

This compound was made via the high yield route developed by Jackson et al (86). Ruthenium carbonyl was reacted with a base to produce the $(Ru_6(CO)_{18})^{2-}$ anion, then reacted with acid to produce the diprotonated $H_2Ru_6(CO)_{18}$.

Analysis	%	Theor.	Actual	Knight & Mays (87)
	C	19.4	19.18	19.5
	H	0.18	0.48	-

Yield = 86%

Quantity made = 20.75g

4.5. Characterisation of Studied Transition Metal Hydridocarbonyls

The following is a brief description of previous studies of the individual compounds prepared for this spectroscopic investigation. Previous vibrational studies will be dealt with in the results section.

i) $H_4Ru_4(CO)_{12}$

Early studies of the above inferred bridging hydrogens and terminal carbonyls. Its infra-red spectrum contained five carbonyl stretching bonds in agreement with a postulated D_{2d} structure and the n.m.r. study showed only a single chemical shift value at 27.98 τ (79). Only weak hydrogen modes were found in the infra-red (88) whereas they were more prominent in the Raman (4). Hydride migrations have been studied in $H_4Ru_4(CO)_{12-x}(P(OMe)_3)_x$ (76) and $(H_3Ru_4(CO)_{12})^-$ (88). However, the data did not delineate the exchange mechanism used by the rapid intramolecular rearrangement. It was expected that an edge-face-edge rearrangement would take place, nevertheless, contrary to such expectations the diphosphine derivative, $H_4Ru_4(CO)_{10}(Ph_2PCH_2CH_2PPh_2)$, displayed an N.M.R. spectra consistent with an edge-terminal-edge hydride scrambling pathway.

X-ray diffraction work has been carried out on $H_4Ru_4(CO)_{12}$ (78) (as well as a number of its derivatives

which display various hydride ligand arrangements about the ruthenium tetrahedron. $H_4Ru_4(CO)_{12}$ has a distorted tetrahedral arrangement of ruthenium atoms with two short and four long bridged ruthenium-ruthenium bonds with terminal carbonyl ligands staggered with respect to the ruthenium-ruthenium bonds. Figure 4.6 shows a molecular plot of the molecule with the estimated hydrogen positions which were not located, even with image enhancing techniques, due to a packing disorder in the crystal.

(ii) $H_2Os_3(CO)_{10}$

Early studies indicated that the carbonyls were all terminal and n.m.r. data consisted of a single resonance inferring similar hydrogen environment or that they were exchanging too fast on the n.m.r. time scale to be distinguished (89). Two x-ray diffraction experiments were carried out on the compound, though both were unsuccessful in accurately locating the positions of the hydrogens (90,91). These studies showed the molecule to have approximate C_{2v} symmetry. The osmium atom opposite the bridged osmium/osmium bond has four attached terminal carbonyls and the other two osmium atoms have three each. The non-bridged osmium-osmium distances are 2.815Å whereas the bridged bond is 2.681Å and has been described as a 'doubly protonated double bond' (91). Surprisingly, these two studies were followed by two further diffraction studies, both of which used neutrons. Orpen et al (92) carried out a combined x-ray and neutron diffraction study and optimised the extraction of structural information. The Os-H-Os units were symmetrical. Broach and Williams (60) carried out

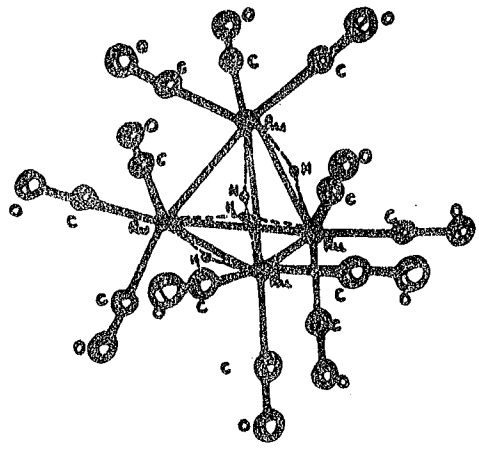

Figure (4.6)

$H_4Ru_4(CO)_{12}$

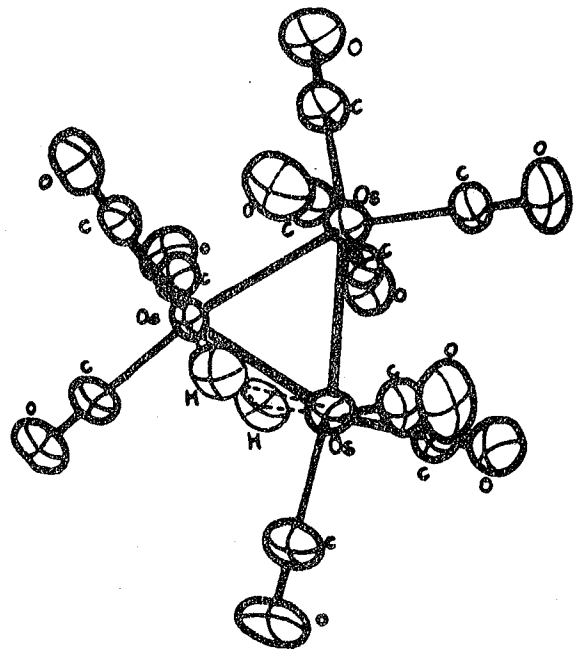

Figure (4.8)

$H_2Os_3(CO)_{10}$

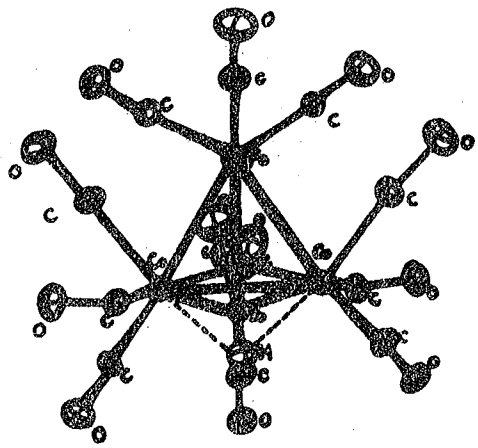

Figure (4.9)

$HFeCo_3(CO)_{12}$

a high 'precision' neutron diffraction study which showed the molecule to be very close to an ideal C_{2v} symmetry and confirmed that the hydrogens were bridging the single osmium-osmium vector. The hydrogens lie, not beyond the LMML intersection as in $HW_2(CO)_9NO$ Figure 4.7a but actually lie within the intersection towards the osmium-osmium vector. The hydrogens also lie symmetrically above and below the osmium plane as shown in Figure 4.7b

(a) $HW_2(CO)_9NO$

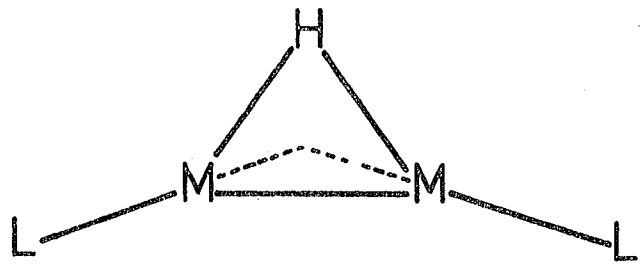

(b) $H_2Os_3(CO)_{10}$

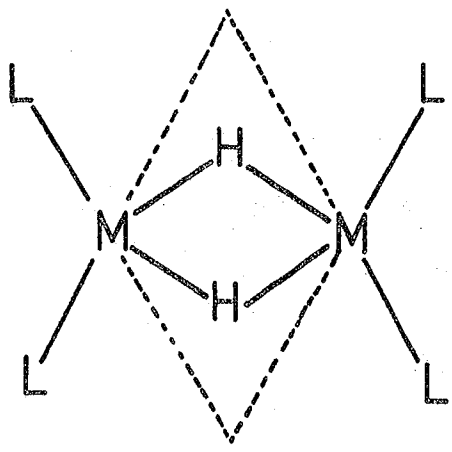

FIGURE 4.7

It was postulated that this hydrogen positioning was not due to carbonyl crowding, since no acute HOsCO(cis) or obtuse OCOsOs angles were found, nor was it due to H····H interactions, since the HH distance was 2.376Å. The hydrogens actually seem to adopt positions in which nuclear repulsive forces, metal-metal overlap and metal-hydrogen overlap are best balanced causing the hydrogens to move out of the plane normal to the osmium plane at the bridged osmiums. The measured OsHOs angles were ~93-95.5°. In such $M(\mu_2\text{-}H)_2M$ systems such as $(\mu_2\text{-}H)_2Os_3(CO)_{10}$, $(\mu_2\text{-}H)_2Re_2(CO)_8$ (93) and $((\mu_2\text{-}H)_2W_2(CO)_8)^{--}$ (94), it is seen that the doubly bridged M-M bond is shortened in direct contrast to $M(\mu_2\text{-}H)M$ systems. Broach and Williams prefer to call such bonds as four-centre four-electron rather than doubly protonated double bonds. Such a bonding concept is consistent with earlier qualitative theoretical work by Mason and Mingos (95) on such MX_2M systems. Figure 4.8 shows a molecular plot of the compound.

(iii) $HFeCo_3(CO)_{12}$

The first mixed metal carbonyl, the anion $(FeCo_3(CO)_{12})^-$ was protonated by Chini (32). However, the characterization of this compound has been very slow and, further, a number of inaccurate results have been quoted. The presence of quadropolar nuclei (eg ^{59}Co) has lead to the lack of any observed high field ^1H n.m.r. signal due to unfavourable relaxation effects (47). Early infra-red work showed that there were bridging as well as terminal carbonyls (47). Infrared data implied the existence of a metal-hydrogen bond (96). Mays and Simpson (47), on the basis of mass

spectral evidence and electron counting arguments, proposed that the hydrogen lay within the tetrahedral cage. Later, this was corroborated by White and Wright (97) on the basis of inelastic neutron scattering data, which confirmed a C_{3v} structure but they then went on to state that the hydrogen was bound to the iron atom while residing inside the $FeCo_3$ tetrahedron. Bor et al (98) again reaffirmed the C_{3v} geometry from infrared data. However, they preferred to place the hydrogen much nearer the Co_3 face. Mossbauer measurements showed no structural change round the Fe atom on deprotonation (99). It was found that more suitable crystals for diffraction work were available in the derivatives of the parent compound and to this end an X-ray study was carried out (100) on the series $HFeCo_3(CO)_{12-x}(P(OCH_3))_x$. This study showed the likelihood that the hydrogen was capping the Co_3 base plane and residing outside the tetrahedron (~ 0.75Å above the plane) with a Co-H distance of 1.5 to 1.7Å. A definitive neutron diffraction study (101) was carried out on $HFeCo_3(CO)_9P(OCH_3)_3$ which found the hydrogen lying 0.978Å above the Co_3 face and equidistant from each cobalt atom by 1.728-1.742Å. In $H_2Ru_6(CO)_{18}$ the μ_3-hydrogens lengthened the Ru-Ru bonds, however, the μ_3-hydrogen in the above compound has had no affect on the cobalt-cobalt distances compared to $Co_4(CO)_{12}$ whereas no figures are available for Co-Co distances in $(FeCo_3(CO)_{12})^-$. Logically one can infer that the hydrogen in $HFeCo_3(CO)_{12}$ is capping the Co_3 face. Some earlier results can be reexamined, such as the mass spectral data with the detection of

HCo_3^+ ions but not HFe^+ ions (98). Figure 4.9 shows a molecular plot of $HFeCo_3(CO)_{12}$ with the probable position of the hydrogen.

(iv) $H_2FeRu_3(CO)_{13}$

This compound, first prepared by Yawney and Stone (81), gave a singlet in ^1H n.m.r. suggesting the two hydrogens were in similar environments (or exchanging to fast on the n.m.r. time scale to be distinguished). The infra-red showed bridging hydrogens were present. An x-ray diffraction study (102) soon followed and the structure comprised of a tetrahedron of three ruthenium atoms and one iron atom, with three terminal carbonyl groups on each ruthenium atom and two terminal carbonyls on the iron atom. As predicted by the infra-red data (81) there were two carbonyl groups asymmetrically bridging two FeRu bonds. The hydrogens were not found but two Ru-Ru bonds were 2.890 and 2.916Å while one was in the 2.761-2.821Å range and thus one can use Churchills criterion, where the μ_2-hydrogen bridged M-M bonds are usually larger than unbridged bonds. Further, the disposition of the carbonyl groups indicate the hydrogen positions. Figure 4.10 shows a molecular plot of $H_2FeRu_3(CO)_{13}$ with estimated hydrogen positions.

(v) $HW_2(CO)_9NO$

The system $(HM_2(CO)_{10})^-$ has been studied in detail since being reported by Behrens (103). Various Group VI hydrido metal carbonyl anions were produced by Hayter (82) who saw, from the carbonyl infra-red regions, that a four

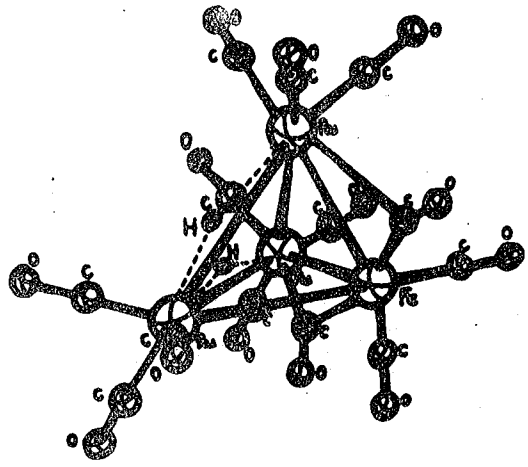

Figure (4.10)

$H_2FeRu_3(CO)_{13}$

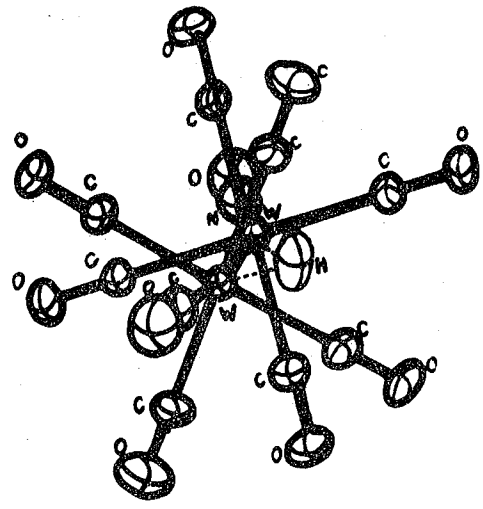

Figure (4.11)

$HW_2(CO)_9NO$

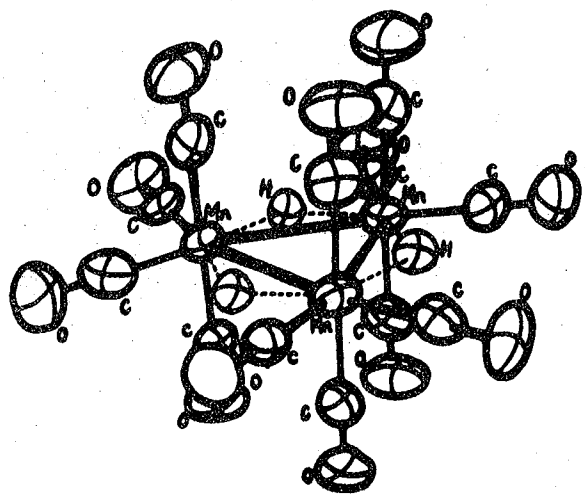

Figure (4.12)

$H_3Mn_3(CO)_{12}$

fold axis of symmetry was likely i.e. D_{4h} with eclipsed carbonyls or D_{4d} with staggered carbonyls. Dahl's first study of $(HCr_2(CO)_{10})^-$ (25) suggested the hydrogen lay on the 4 fold axis connecting the two $Cr(CO)_5$ fragments and went on to say the metal atoms were held together by the bridging hydrogen. The later studies of the $(HCr_2(CO)_{10})^-$ anion (66,67,68) found a rather different picture with the hydrogen disordered between two (68) and four (67,68) centro-symmetrically related sites.

There have been many structural studies since. The $(Et_4N)^+$ and $(PPN)^+$ salts of $(HCr_2(CO)_{10})^-$ and $(Et_4N)^+$ $(HW_2(CO)_{10})^-$ have a linear CO-MM-CO backbone, eclipsed carbonyls and MHM angles of 137-160° whereas $HW_2(CO)_9NO$, and the $(PPN)^+$ and $(Ph_4P)^+$ salts of $(HW_2(CO)_{10})^-$ have a bent CO-M-M-CO backbone with staggered carbonyls and MHM angles of 125-130°. Such asymmetry has been discussed by Darensbourg (104) and is due to either substantial crystal packing forces perturbing the anion or the perturbation is caused by the hydride ligand prefering to occupy a potential minima at a small MHM angle thus forcing the two '$M(CO)_5$' or '$M(CO)_4NO$' moeities apart. Bau et al (63) first characterised the $HW_2(CO)_9NO$ backbone by X-ray diffraction and went on to locate the hydrogen using neutrons (55). Figure 4.11 shows a molecular plot of this species.

(vi) $H_3Mn_3(CO)_{12}$

Kaesz et al (105) reported the production of a manganese hydridocarbonyl whose formulation rested on the similarity of its infra-red spectrum with that of $H_3Re_3(CO)_{12}$

and Johnson et al confirmed this (83). Mass spectral work (106,107) confirmed the parent ion $(H_3Mn_3(CO)_{12})^+$ and the hydrogens were located by an X-ray structure determination using difference Fourier techniques (26). The structure consists of an equilateral array of manganese atoms, each with four terminal carbonyl groups, modelling a D_{3h} symmetry. The presence of the 1H n.m.r. singlet at = 24.0ppm indicated the equivalence of the hydrogen environment (108). The Mn-H distances in the X-ray determination were 1.61-1.79Å with the MnHMn angles of 119°, 126° and 149° (an average of 131° with a great variation). Figure 4.12 shows a molecular plot of the compound.

(vii) $H_4Re_4(CO)_{12}$

Mass spectral data was in good agreement with the above formula and the 1H n.m.r. showed a singlet indicating the equivalence of the hydrogens positions (30). The infra-red spectrum showed only two carbonyl stretching bonds indicating a molecule of as high a symmetry as the tetrahedral $Ir_4(CO)_{12}$. A qualitative molecular orbital treatment implied that the combinations of the 'd'orbitals of the rhenium atoms were localized over the faces of the tetrahedron inferring that the Re_3 faces were bridged by hydrogens. The molecular structure of $H_4Re_4(CO)_{12}$ was found by employing a X-ray image enhancing technique which confirmed that the hydrogens were of the (μ_3-H) type (22). Eclipsed carbonyls were found, instead of the staggered variety found in $H_4Ru_4(CO)_{12}$. Figure 4.13 shows a molecular plot of $H_4Re_4(CO)_{12}$.

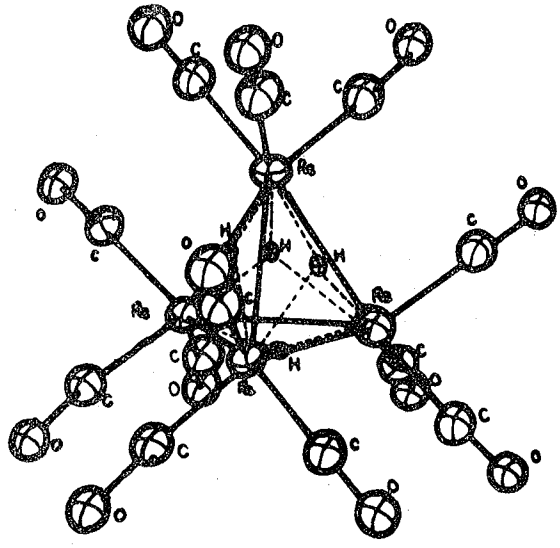

Figure (4.13)

$H_4Re_4(CO)_{12}$

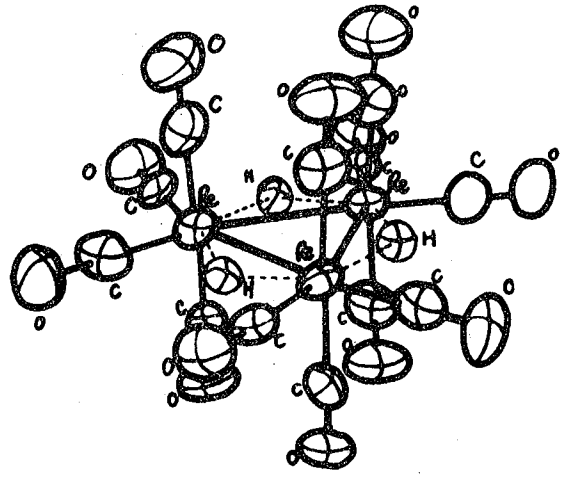

Figure (4.14)

$H_3Re_3(CO)_{12}$

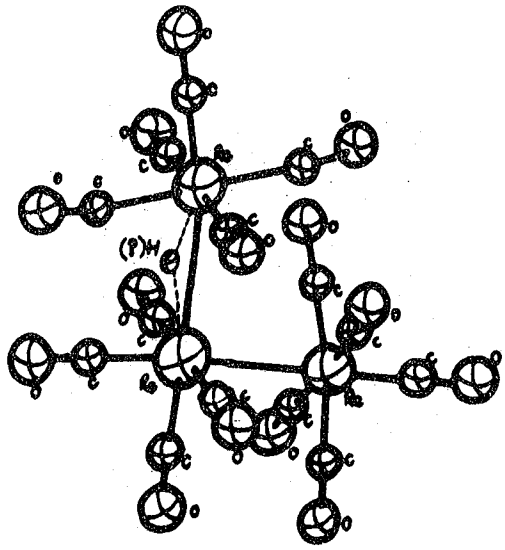

Figure (4.15)

$HRe_3(CO)_{14}$

(viii) $H_3Re_3(CO)_{12}$

Molecular weight measurements of this rhenium hydridocarbonyl indicated that a rhenium tetracarbonyl trimer was probable (85). No terminal Re-H bonds were implied from infra-red data, which also showed a D_{3h} structure. An X-ray pattern was obtained which showed that the trimer was isomorphous which a previously isolated trimer of technetium, however, a full scale diffraction study has not been possible because of the inability to grow suitable crystals. A Raman study (109) found metal-hydrogen bands in the 1100-1100cm^{-1} region which led to the first postulation about the hydrogen possibly residing between metal atoms. An n.m.r. study also indicated the equivalence of the hydrogen environments. (109 ref 5). An X-ray study of the crystalline anionic rhenium carbonyl hydride $(H_2Re_3(CO)_{12})^-$ (38), had C_{2v} symmetry with two longer rhenium-rhenium bonds and a disposition of carbonyl ligands that further enhanced the argument for Re-(μ_2-H)-Re units in $H_3Re_3(CO)_{12}$. Figure 4.14 shows a molecular plot of the compound.

(xi) $HRe_3(CO)_{14}$

Fellman and Kaesz found the compound gave only a single ^1H n.m.r. peak (37). Infra-red data in the carbonyl region indicated only terminal carbonyls present but the number of bands agreed with a C_{4v} structure found with a linear rhenium triad, instead of a triangular system as in $H_3Re_3(CO)_{12}$. Initially they placed the hydrogen exactly between two of the rhenium atoms with the carbonyls in an

eclipsed conformation. This argument was expounded further when mass spectral data was analysed showing the existence of the HRe_3^+ ion (28). Hoyano and Graham found an M-H infra-red band at 1035cm^{-1} indicating such an Re-H-Re bridge (110). Fleeting indications in the literature appeared, of a diffraction experiment carried out by Dahl et al (e.g. 111 (ref. 84)) implying that the molecule was bent like $HRe_2Mn(CO)_{14}$ (111) and that they had estimated the ReHRe angle to be 159° based on the octahedral arrangement of the carbonyl ligands about the metals and the average Re-H bridging bond length ($\sim$1.7Å) found in complexes such as $((C_6H_5)_4As)^+(H_2Re_3(CO)_{12})^-$. Bau's analysis (111) of $HRe_2Mn(CO)_{14}$ placed the hydrogen exactly between the two rhenium atoms. Dahl had estimated the bond angle in this case to be 164°. Obviously Bau's estimation is wrong but also that of Dahl is probably not valid since in $M(\mu_2\text{-}H)M$ systems the hydrogen would move beyond the octahedral coordination position as implied by the intersection of the L-M-M-L vectors. Unfortunately the structure of $HRe_3(CO)_{14}$ was never published. Figure 4.15 shows a possible molecular plot based on $HRe_2Mn(CO)_{14}$ though the hydrogen position is very much in doubt.

(x) $CsHCo_6(CO)_{15}$

Up to quite recently only $(M)_n\text{-}(\mu_n\text{-}H)$ systems have been characterised where n=1,2, or 3. No μ_4-H species are known to exist in molecular complexes though hydrogen is found in tetrahedral holes in rare earth metal hydrides such as CeH_2 and $HoH_{1.98}$ (112). It is felt that as the studies of the vibrational frequencies of hydrogen atoms

in tetrahedral and octahedral holes in these rare earths will be relevant to the present study. It will be discussed further in the appropriate place.

An early powder neutron diffraction work by Simon had shown the existence of hydrogen inside, the niobium octahedron in HNb_6I_{11} (113). $(Co_6(CO)_{15})^{2-}$ was the first anionic high nuclearity cluster to be isolated (114) and infra-red work on $Co_6(CO)_{16}$ indicated an octahedral array of cobalt atoms isostructural with the known $Rh_6(CO)_{16}$ (115). Chini (116) was the first to look at the chemistry of the $(Co_6(CO)_{15})^{2-}$ ion, which on protonation produced the $(HCo_6(CO)_{15})^-$ ion which gave an anomalously low ^1H n.m.r. chemical shift of -13.2ppm (117). The diprotonated $H_2Co_6(CO)_{15}$ species has not yet been reported. $(HRu_6(CO)_{18})^-$ also gave a low field chemical shift of -6.4ppm (118) however an X-ray study implied a symmetrical structure with the hydrogen within the octahedron. Finally, a combined X-ray and neutron diffraction study of $((Ph_3P)_2N)^+$ $(HCo_6(CO)_{15})^-$ was carried out by Chini and Bau (72). The X-ray study at 177K indicated a long Co-Co bond in the octahedron with the carbonyl atoms splayed out from it suggesting a Co-(μ_2-H)-Co system but the neutron diffraction study at 80K located the hydride at the centre of the Co_6 octahedron. The Co-Co distances, when compared with $Co_6(CO)_{16}$, seemed to show some degree of swelling on protonation. Figure 4.16 shows a molecular plot of $(HCo_6(CO)_{15})^-$. The CoH distance is compared with other metal interstitial hydrogen distances in Chapter (5).

It can be noted here that further single crystal

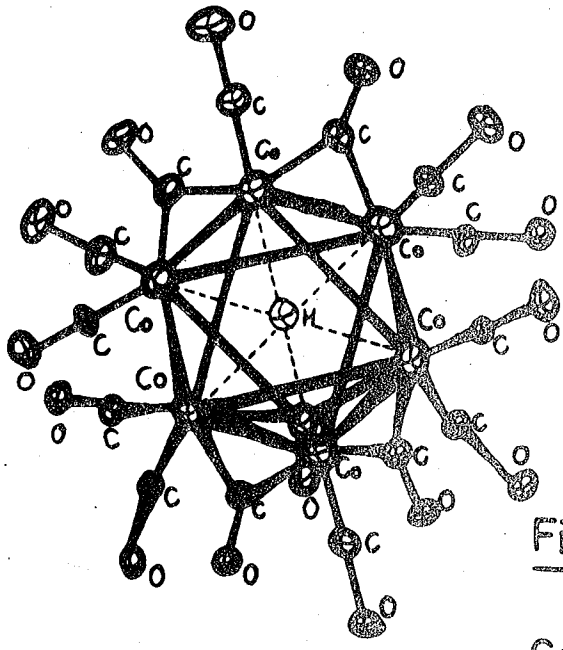

Figure (4.16)

$CsHCo_6(CO)_{15}$

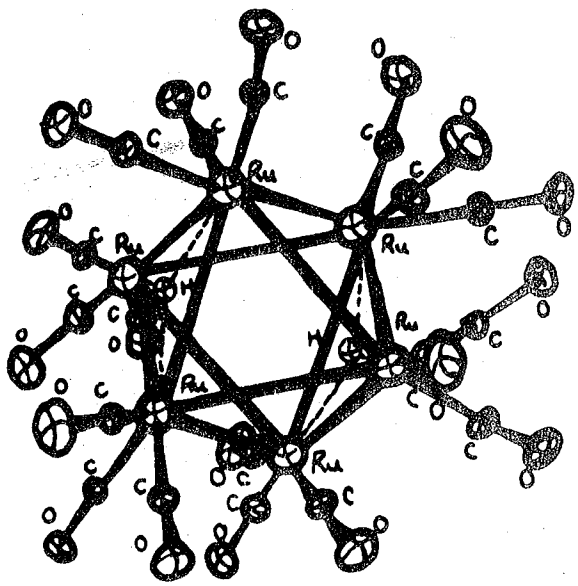

$H_2Ru_6(CO)_{18}$

Figure (4.18)

Figure (4.17)

Positions of the interstitial hydrogen atoms and increases in interlayer distances in the anions $[Ni_{12}(CO)_{21}H_{4-n}]$ (n=2,3,4) [ref:119]

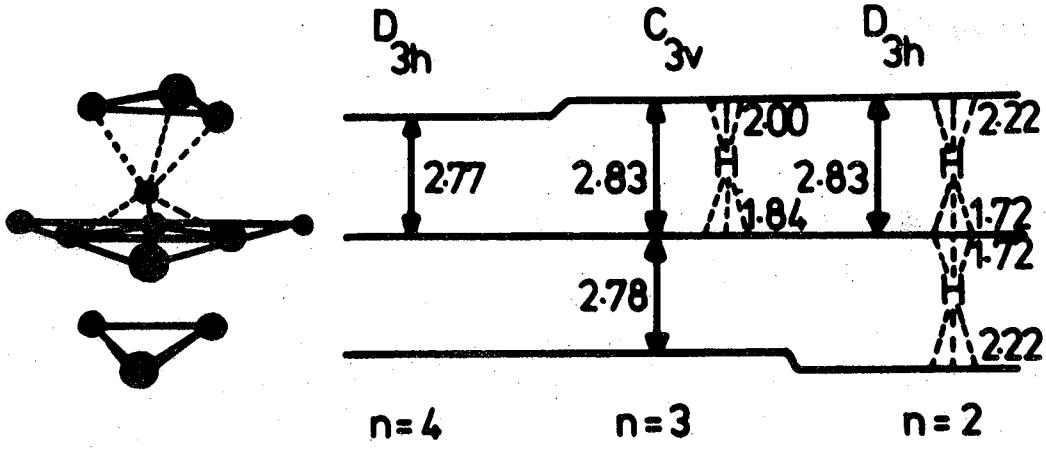

(distances in Å)

neutron diffraction studies on the $(HNi_{12}(CO)_{21})^{3-}$ and $(H_2Ni_{12}(CO)_{21})^{2-}$ anions have definitively shown the existence of H atoms inside the octahedral holes of these Ni_{12} clusters (119). However, it appears that, rather than the hydrogens lying in the centre of the holes as in the $(HCo_6(CO)_{15})^-$ anion, the hydrogens are capping a Ni_3 face from within the octahedral hole. That is the hydrogen is displaced from the centre and the capped Ni_3 face is actually found to be slightly expanded relative to uncapped Ni_3 faces. So the existence of M_6H units has been proven, however, it is not clear yet whether hydrogen can exist in a tetrahedral hole in a complex without appreciable swelling of the M_4 unit. The skeletal forms of the nickel-hydrogen cluster are shown in Figure (4.17) with relevant Ni-H distances shown. These nickel-hydrogen clusters are discussed with the cobalt-hydrogen system in Chapter(5).

(ix) $H_2Ru_6(CO)_{18}$

This hexanuclear compound, first produced by Knight and Mays(87), is a purple air-stable substance which was identified by mass spectrometry. This was carried out by identifying the molecular ions $H_2Ru_6(CO)_{18}^+$ and $D_2Ru_6(CO)_{18}^+$ and finding that the latter was two mass units higher than the former. The infra-red carbonyl stretching frequency shows three bands implying a highly symmetrical structure. An X-ray crystallographic determination (71,120) has been carried out on $H_2Ru_6(CO)_{18}$ and it has been shown that the ruthenium atoms define an octahedron, each with three terminal carbonyls. It was

postulated that the hydrogens occupied triply bridging positions on two opposite faces of the octahedron. This gave the molecule approximate D_{3d} symmetry, due to a slight distortion of the octahedron as shown by the Ru-Ru distances, on the triply-bridged faces, of 2.950-2.959Å and the Ru-Ru distances, on the non-bridged faces, of 2.850-2.874Å. Further to this swelling of the bridged faces, the carbonyls are found spread away, slightly from the truly axial postions above the larger faces of the ruthenium octahedron. Figure 4.18 shows the form of $H_2Ru_6(CO)_{18}$.

4.6. The Surface Cluster Analogy and its Relevance to this Study

This section deals briefly with the surface chemistry/cluster chemistry analogy and with the arguments advanced for the support of the proposition that discrete molecular metal clusters may be reasonable models of metal surfaces in chemisorption processes. The arguments levelled against this are stated and then the relevancy of the analogy to this study is discussed where it is hoped the hydrogen vibrations in transition metal hydridocarbonyls can be compared with already existing data on hydrogen chemisorbed on transition metal surfaces. In a later section the data gathered for benzene complexes will be compared with benzene chemisorbed on platinum and in zeolite cages.

4.6.1. Arguments for the surface/cluster analogy

In catalytic processes involving metal or metal oxide surfaces there are usually 6 steps on which information

is needed for the greater understanding of the role of the catalyst. They are the bond-making of the adsorbate to the surface, the bond-making of the coadsorbate, possibly surface diffusion of reactants, the reaction, the molecular rearrangement and the product release. Various mechanisms exist which discuss the type of reaction steps and the rate determining parts of a reaction. The Langmuir-Hinshelwood-Bonhoeffer hypothesis suggests that the reaction proceeds through the adsorption of the reactants on adjacent sites followed by interaction and desorption. The Rideal-Eley mechanism suggests that only one reactant need be adsorbed and the second species reacts from the gas phase (121). In the analysis of the intrinsic structural, stereochemical and thermodynamic features of a metal surface it appears, at first light, useful to study such features in discrete metal clusters which could act as models of metal surfaces (14,122-6). Those critical elements that have been studied in the assessment of the analogy are size, shape, coordination number, structure and stereochemistry, thermodynamic and ligand mobility (14). Apart from the many stated advantages that are known to exist in favour of cluster and single crystal models, there are many problems involved in the analysis of a 'real' surface both from a practical and theoretical viewpoint. There are no techniques available that could collect and evaluate the immense amount of data produced in a real catalytic setting, which must be described as 'dirty' compared with single crystal studies. Many adsorbate/substrate and adsorbate/adsorbate interations could be

taking place, differing mechanistic routes may be followed in the reaction due to the variability of the surface and concentration of reactants at any one point. Thus, the real surface, in a catalytic context, is not amenable to definitive analysis because it is not a discrete unit. Its structure, which may change during the course of a catalytic cycle due to the above mentioned interactions, could not be ascertained and, further, from a purely practical viewpoint the reactions, both with regards to the stoichiometric chemisorbed system and to the actual catalytic reaction could not be probed sufficiently accurately through the normal kinetic and spectroscopic means. Thus there would appear to be a need for discrete modelling.

Various synthetic routes have produced metal clusters that contain fragments of close packed arrays of metal atoms usually found in bulk metal. For example, $(Rh_{14}(CO)_{25})^{4-}$ contains a piece of a body centred cubic close packed array (127) and $(Pt_3(CO)_6)_n^{3-}$ has a structure based on stacked trigonal prisms (128). Thus, with some qualification, these clusters of metal atoms with attached ligands resemble small metal fragments or crystallites surrounded by chemisorbed species. The spatial arrangement of those peripheral ligands with respect to the metal skeleton has been compared with those of such a ligand species when chemisorbed on a metal surface e.g. terminal- and bridge- bonding has been reasonably defined in each case. Analysis of thermodynamic data shows a close comparison between bond energies for the (M-ligand) bond in molecular complexes and metal surface/chemisorbed

species complexes (14). Localized models of bonding have been qualitatively discussed where long metal-metal interactions are ignored, as well as ligand-ligand interactions (125). The mobility of ligands in molecular complexes is now more understood and such mobility would appear to be an essential part of a catalytic process.

Much work is being carried out studying clusters and highly dispersed metal particles supported on some inert matrix such as an aluminosilicate framework. Very exciting prospects exist in this field. Very recently osmium hydridocarbonyls and carbonyls have been attached to hydroxylated silica surfaces by breakage of the Si-OH bond. The species $HOs_3(CO)_{10}$ Si- has been formed in this manner (129) and has been charaterised by spectral methods. The size of clusters can approach small crystallites; the clusters stabilized by ligands, the crystallites by interactions with the support material (e.g. an oxide, zeolite frame, or matrix). The properties of both have been reviewed (130). It is evident that metal particle size influences the chemisorption properties of supported metals. For example, the stretching vibrations of NO irreversibly adsorbed on platinum is particle size dependent; the larger the size the lower the (NO) vibration (126) and the interpretation is that the back donation to the Π^* orbitals of the NO^+ depends on the collective properties of the crystallites.

4.6.2. Arguments against the surface cluster analogy

Moskovits (131) has questioned the campaign for emphasizing the surface/cluster similarities and for playing down the differences. It would seem necessary

that a quantitative bonding scheme has to be sought between an adsorbent and adsorbate. Yet the importance of such a model is not stressed since it has yet to be proven that information on the metal-adsorbate bond is the salient characteristic that determines the chemistry of adsorbate/surface interactions. Interactions between the adsorbate and the surface and other adsorbates have yet to be studied in detail and even the division between local and non-local bonding is artificial.

Since a collective effect can subtly change an adsorbate/surface vibration, one can assume that long range forces are taking part in the interaction and thus the catalytic activity could not be explained by a purely local effect description. However, if the concentration of active sites, upon which either chemisorption or the catalytic mechanism takes place, is very low then perhaps a local model may well be used, whereas on a perfect surface the collective effect must prevail.

The effect ligands have on clusters must be very large. A small cluster, with many 'bristling' ligands, must have an electron density on its surface (and below the surface) very much different from much larger bulk metal and metal oxide particles. Indeed, the metal-metal bond lengths are changed considerably when ligands bridge bond a metal-metal bond in clusters. Though it is now known that adsorbate attachment on to metal surfaces can alter the substrate surface atom structure to a large extent. Many studies have been carried out on the hydrogen/tungsten (100) system (132) where the first surface layer tungsten atom structure varies with hydrogen coverage.

Further, the catalytic activity of clusters is known to be smaller than metal surfaces because of the inherent stability of clusters where, for example, the metal atoms follow an $18e^{-1}$ rule and the ligands and metal atoms move into a 'preferred' orientation rather than a 'forced' structure.

Mobility on surfaces has yet to be studied, yet less than monolayer coverage, necessary for any motion across the surface, cannot be simulated on a cluster surface because most clusters are coordinatively saturated and, except for $(Pt_{19}(CO)_{12})^{4-}$ do not have less than one ligand per cluster metal atom. Further, because of the ligand saturated or near saturated nature of the surfaces of clusters, there must be involved ligand-ligand interactions which will be fundamentally different to those that are found on a metal surface, especially with less than a monolayer of adsorbate species. From this the types of diffusion mechanisms that exist in both may altogether be different because of the ligand geometries. For example, it is highly unlikely that a metal atom on a surface will have three or more terminally bonded adsorbate species whereas this generally occurs on clusters.

4.6.3. Relevance of the analogy to this work

The vibrational modes of adsorbates chemisorbed on metals are a direct reflection of the orientation of the molecule on the surface and its coordination geometry with respect to the array of underlying metal atoms. Therefore, vibrational spectra are sensitive to the

structure of the molecule/surface complex (among other things).

The hope is that such vibrational information can provide an insight into the chemistry generated at the surface (if the bonding principles are independent of the bulk in which the local grouping is included). Further, it is hoped that information from this study of hydrogen bonded via various mechanisms to transition metal carbonyls can be of some use in understanding hydrogen chemisorption on transition metal surfaces. This kind of modelling has already been used by Willis (133) in his experimental and analytical study of hydrogen on W(100) which, if correct, is contrary to earlier work by Ibach et al on W(100) (134). The variation in the frequency of the hydrogen modes on tungsten had been discussed by Ibach et al and they claimed that the two different surface vibrations at different coverages corresponded to two different occupied sites by hydrogen. At low coverages, the mode was associated with hydrogen in an on top site (ie W-H terminal) whereas at a higher coverage, nearer 1 monolayer, the mode was attributed to the occupation of bridge sites (ie W(μ_2-H)W). Willis had originally (135) found only an on top W-H species on W(111) for all coverages. However, Willis (133) indicated that on W(100) there was only one species - the W(μ_2-H)W unit at all coverages. The variation in frequency, attributed by Ibach et al to different sites, was due to a variation in WHW angle which changed with coverage. It was known that some reconstruction of the tungsten surface was taking place

on hydrogen adsorption as found by LEED results (136,137). The hydrogens would seem to reorder the surface atoms producing changes in the W-W distances. The magnitude of these shifts and, thus, the WHW angle variation has been compared with the variation in bond angles in molecular complexes containing $M(\mu_2\text{-}H)M$ species and the frequency dependence has been compared in each case. Use was made of the relationships derived by Shephard et al (122) and their Raman and infra-red data on transition metal hydridocarbonyls. It is thus hoped that the data from this current study may be compared with μ_2-, μ_3- and μ_6- hydrogens chemisorbed (or absorbed in the μ_6 case) on transition metals. A comparison of the vibrational frequencies of hydrogen lying in these sites will be compared with the inelastic neutron scattering data in a later chapter.

Other surface vibrational experiments of great interest are those carried out by Richardson and Bradshaw, who looked at the H/W (100) system (138). Using Ibach et al's results they calculated the vibrational frequencies of the hydrogen atom as a function of its position above a W(100) plane as it moves from a μ_1- to a μ_2- to a μ_4- site. Further, a study of hydrogen adsorbed on Pt(111) by Ibach et al (139) has shown that hydrogen is adsorbed in a 3-fold site, ie $(\mu_3\text{-}H)Pt_3$ is formed and this can be compared with inelastic neutron scattering data for hydrogen on platinum (140) black which indicated also that hydrogen was in a bridging site, though in this case, a $Pt_2(\mu_2\text{-}H)$ was preferred. Ibach also studied hydrogen adsorbed on the $Pt(S)\text{-}[6(111)X(1\bar{1}1)]$ stepped plane (141) and postulated

that, once again, $Pt_3(\mu_3\text{-H})$ moieties were found on the terraces but that hydrogen formed $Pt_2(\mu_2\text{-H})$ units along the corner of the step.

It is felt that it would be an interesting aside to compare the $(\mu_3\text{-H})$ and $(\mu_2\text{-H})$ spectra of the hydrido-carbonyls with the previous spectra of supposed $(\mu_3\text{-H})$ and $(\mu_2\text{-H})$ species found on platinum, nickel and tungsten as it would with all vibrational work of hydrogen on transition metals.

4.7. References

1. A.P. Ginsberg Transition Metal Chem. 1 (1965) 112
2. E.L. Muetterties (Ed.) "Transition Metal Hydrides" M. Dekker (NY) 1971
3. M.L.H. Green, D.J. Jones Adv. Inorg. Chem. Radiochem. 7 (1965) 115
4. H.D. Kaesz, R.D. Saillant Chem. Rev. 72 (1972) 231
5. R.B. King Progr. Inorg. Chem. 15 (1972) 287
6. K. Wade Adv. Inorg. Chem. Radiochem. 18 (1976) 1
7. T.F. Koetzle, R. Bau Energy Res. Abst. No. 26207 (1976)
8. P. Chini, B. Heaton 'Topics in Current Chemistry' 71 (1977) 1
9. P. Chini, G. Longoni, V.G. Albano Adv. Organomet. Chem. 14 (1976) 285
10. G.L. Geoffroy, J.R. Lehman Adv. Inorg. Chem. Radiochem. 19 (1977) 189
11. J. Evans Adv. Organometal Chem. 16 (1977) 319
12. R. Bau (Ed.) Adv. Chem. Ser. 167 (1978)
13. R. Bau, R.G. Teller, S.W. Kirtley, T.F. Koetzle Acc. Chem. Res. 12 (1979) 176
14. E.L. Muetterties, T.N. Rhodin, E. Band, C.F. Brucker, W.R. Pretter Chem. Rev. 79 (1979) 91
15. A.P. Humphries, H.D. Kaesz Progr. Inorg. Chem. 25 (1979) 145
16. W. Heiber Angew. Chem. 49 (1963) 463
17. W. Heiber, F. Leutert Naturwissenschaften 19 (1931) 360
18. W. Heiber Die Chemie 55 (1942) 24
19. R.V.G. Ewens, M.W. Lister Trans. Farad. Soc. 35 (1939) 681
20. F.A. Cotton, G. Wilkinson Chem. Ind. (London) (1956) 1305

21. P.G. Owston, J.M. Partridge, J.M. Rowe Acta. Cryst. 13 (1960) 246

22. R.D. Wilson, R. Bau J. Amer. Chem. Soc. 98 (1976) 4687

23. G.C. Abrahams, A.P. Ginsberg, K. Knox Inorg. Chem. 3 (1964) 554

24. G.J. La Placa, W.C. Hamilton, J.A. Ibers, A. Davison Inorg. Chem. 8 (1969) 1928

25. L.P. Handy, P.M. Treichel, L.F. Dahl, R.G. Hayter J. Amer. Chem. Soc. 88 (1966) 366

26. S.W. Kirtley, J.P. Olsen, R. Bau J. Amer. Chem. Soc. 95 (1973) 4532

27. J.R. Moss, W.A.G. Graham Inorg. Chem. 16 (1977) 75

28. H.D. Kaesz, R. Bau, M.R. Churchill J. Amer. Chem. Soc. 89 (1967) 2775

29. A.J. Deeming, S. Hasso J. Organometal. Chem. 88 (1975) C21

30. R.B. Saillant, G. Barcelo, H.D. Kaesz J. Amer. Chem. Soc. 92 (1970) 5739

31. A.J. Deeming, S. Hasso J. Organometal. Chem. 114 (1976) 313

32. P. Chini, L. Colli, M. Peraldo Gazzetta 90 (1960) 1005

33. G. Huttner, H. Lorenz Chem. Ber. 107 (1974) 996

34. A. Davison, J.W. Faller Inorg. Chem. 6 (1967) 845

35. W.F. Edgell, J.W. Fisher, G. Asato, W.M. Risen Inorg. Chem. 8 (1969) 1103

36. S.W. Kirtley (Ph.D. Thesis) Univ. of Calif. (L.A.) 1971

37. W. Fellman, H.D. Kaesz Inorg. Nucl. Chem. Letts. 2 (1966) 63

38. M.R. Churchill, P.H. Bird, H.D. Kaesz, R. Bau, B. Fontal J. Amer. Chem. Soc. 90 (1968) 7135

39. M.F. Clayton, N. Sheppard J. Chem. Soc. (D) (1969) 1431

40. C.B. Cooper, D.F. Shriver, S. Onaka Adv. Chem. Ser. 167 (1978) 232

41. C.B. Cooper, D.F. Shriver, D.J. Darensburg, J.A. Froelich Inorg. Chem. 18 (1979) 1407

42. D.C. Harris, H.B. Gray J. Amer. Chem. Soc. 97 (1975) 3073

43. M.W. Howard, U.A. Jayasooriya, S.F.A. Kettle, D.P. Powell, N. Sheppard J. Chem. Soc. Chem. Comm. (1979) 929

44. G. Herzberg 'Infra-red and Raman Spectra' Van Nostrand (1956) 168

45. V. Katovic, R.E. McCarley Inorg. Chem. 17 (1978) 1268

46. C.J. Wright (Ph.D. Thesis) Univ. of Oxford (1969)

47. M.J. Mays, R.N.F. Simpson J. Chem. Soc. (A) (1968) 1444

48. J.C. Green, D.M.P. Mingos, E.A. Seddon J. Organometallic Chem. 185 (1980) C20

49. J. Howard (Univ. of Oxford) Personal Communication (1980)

50. N.E. Erickson, A.W. Fairhall Inorg. Chem. 4 (1965) 1320

51. K. Farmery, M. Kilner, R. Greatrex, N.N. Greenwood Chem. Comm. (1968) 593

52. B.T. Huie, C.B. Knobler, H.D. Kaesz J. Amer. Chem. Soc. 100 (1978) 3059

53. M.R. Churchill, B.G. DeBoer, F.J. Rotella Inorg. Chem. 15 (1976) 1843

54. M.R. Churchill, S.W. Ni J. Amer. Chem. Soc. 95 (1973) 2150

55. J.P. Olsen, T.F. Koetzle, S.W. Kirtley, M. Andrews, D.L. Tipton, R. Bau, J. Amer. Chem. Soc. 96 (1974) 6621

56. L.B. Handy, J.K. Ruff, L.H. Dahl J. Amer. Chem. Soc. 92 (1970) 7312

57. J. Lewis, B.F.G. Johnson, Gazz. Chim. Ital. 109 (1979) 271

58. K. Wade Chem. Brit. 11 (1975) 177

59. E.L. Muetterties "Boron Hydride Chemistry" Academic Press (NY) 1975

60. R.W. Broach, J.M. Williams Inorg. Chem. 18 (1979) 314

61. M. Freni, P. Romiti, G. D'Alfonso J. Organometal Chem. 140 (1977) 195

62. R. Hoffmann, B.E.R. Schilling, R. Bau, H.D. Kaesz, D.M.P. Mingos J. Amer. Chem. Soc. 100 (1978) 6088

63. M.A. Andrews, D.L. Tipton, S.W. Kirtley, R. Bau J. Chem. Soc. Chem. Comm. (1973) 181

64. R.A. Love, H.B. Chin, T.F. Koetzle, S.W. Kirtley, B.R. Whittesley, R. Bau J. Amer. Chem. Soc. 98 (1976) 4491

65. K.S. Wong, W.R. Scheidt, J.A. Labinger Inorg. Chem. 18(1979) 4491

66. J. Roziere, J.M. Williams, R.P. Stewart, J.L. Peterson, L.F. Dahl J. Amer. Chem. Soc. 99 (1977) 4497

67. J.L. Peterson, P.L. Johnson, J. O'Connor, L.F. Dahl, J. M. Williams Inorg. Chem. 17 (1978) 3460

68. J.L. Peterson, R.K. Brown, J.M. Williams, R.K. McMullan Inorg. Chem. 18 (1979) 3493

69. R.D. Wilson, S.M. Wu, R.A. Love, R. Bau, Inorg. Chem. 17 (1978) 1271

70. D.B.W. Yawney, D.J. Doedens Inorg. Chem. 11 (1972) 838

71. M.R. Churchill, J. Wormald J. Amer. Chem. Soc. 93 (1971) 5670

72. D.W. Hart, R.G. Teller, C.Y. Wei, R. Bau, G. Longoni, S. Campanella, P. Chini, T.F. Koetzle Angew. Chem. 18 (1979) 80

73. B.F.G. Johnson J. Chem. Soc. Chem. Comm. (1976) 703

74. L. Milone, S. Aime, E.W. Randall, E. Rosenberg, J. Chem. Soc. Chem. Comm. (1975) 452

75. J.R. Shapley, J.B. Keister, M.R. Churchill, B.G. DeBoer J. Amer. Chem. Soc. 97 (1975) 4145

76. S.A.R. Knox, H.D. Kaesz J. Amer. Chem. Soc. 93 (1971) 4594

77. G. Huttner, H. Lorenz Chem. Ber. 108 (1975) 973

78. J.R. Shapley, S.I. Richter, M.R. Churchill, R.A. Lashewycz J. Amer. Chem. Soc. 99 (1977) 7384

79. S.A.R. Knox, J.W. Koepke, M.A. Andrews, H.D. Kaesz
J. Amer. Chem. Soc. 97 (1975) 3942

80. G.L. Geoffroy, W.L. Gladfetter J. Amer. Chem. Soc.
99 (1977) 7565

81. D.B.W. Yawney, F.G.A. Stone J. Chem. Soc. (A) (1969) 502

82. R.G. Hayter J. Amer. Chem. Soc. 88 (1966) 4376

83. B.F.G. Johnson, R.D. Johnston, J. Lewis, B.H. Robinson
J. Organometal. Chem. 10 (1967) 105

84. H.D. Kaesz, S.A.R. Knox, J.W. Koepke, R.B. Saillant
J. Chem. Soc. Chem. Comm. (1971) 477

85. D.K. Huggins, W. Fellman, J. M. Smith, H.D. Kaesz
J. Amer. Chem. Soc. 86 (1964) 4841

86. P.F. Jackson, B.F.G. Johnson, J. Lewis, M. McPartlin,
W.J.H. Nelson J. Chem. Soc. Chem. Comm. 17 (1979) 735

87. J. Knight, M.J. Mays J. Chem. Soc. Dalton Trans.
(1972) 1022

88. J.W. Koepke, J.R. Johnson, S.A.R. Knox, H.D. Kaesz
J. Amer. Chem. Soc. 97 (1975) 3947

89. B.F.G. Johnson, J. Lewis, P.A. Kilty J. Chem. Soc.
(A) (1968) 2859

90. V.F. Allen, R. Mason, P.B. Hitchcock J. Organometal Chem.
140 (1977) 297

91. M.R. Churchill, F.J. Hollander, J.R. Hutchinson
Inorg. Chem. 16 (1977) 2697

92. A.G. Orpen, A.V. Rivera, E.G. Bryan, D. Pippard,
G.M. Sheldrick, K. Rouse, J. Chem. Soc. Chem. Comm.
(1978) 723

93. M.J. Bennet, W.A.G. Graham, J.K. Hoyano, W.L. Hutcheon
J. Amer. Chem. Soc. 94 (1972) 6232

94. M.R. Churchill, S.W.Y. Chang Inorg. Chem. 13 (1974) 2413

95. R. Mason, D.M.P. Mingos J. Organometal Chem. 50 (1973) 53

96. J. Knight, M.J. Mays J. Chem. Soc (A) (1970) 711

97. J.W. White, C.J. Wright J. Chem. Soc.(A) (1971) 2843

98. G. Bor, G. Sbrignadello , K. Noack Helv. Chem. Acta.
58 (1975) 815

99. C.E. Cooke, M. J. Mays, J. Chem. Soc. Dalton Trans. (1975) 455

100. B.T. Huie, C.B. Knobler, H.D. Kaesz J. Chem. Soc. Chem.Comm. (1975) 684

101. R.G. Teller, R.D. Wilson, R.K. McMullan, T.F. Koetzle, R. Bau J. Amer. Chem. Soc. 100 (1978) 3071

102. C.J. Gilmore, P. Woodward Chem Comm. (1970) 1463

103. H. Behrens, W. Klek Z. Anorg. Allg. Chem. 292 (1957) 151

104. M.Y. Darensbourg, J.L. Attwood, R.A. Burch, W.E. Hunter, N. Walker J. Amer. Chem. Soc. 101 (1979) 2631

105. W. Fellman, D.K. Huggins, H.D. Kaesz Proc VIII Int. Conf. Coord. Chem. Vienna (1964)

106. J.M. Smith, K. Mehner, H.D. Kaesz J. Amer. Chem. Soc. 89 (1967) 1759

107. B.F.G. Johnson, R.D. Johnston, J. Lewis, B.H. Robinson Chem. Comm. (1966)851

108. E.O. Fischer, R. Aumann J. Organometal Chem. 10 (1967) P1

109. J.M. Smith, W. Fellmann, L.H. Jones Inorg. Chem. 4 (1965) 1361

110. J.K. Hoyano, W.A.G. Graham Inorg. Chem. 11 (1972) 1265

111. L.B. Handy, J.K. Ruff, L.F. Dahl J. Amer. Chem. Soc. 92 (1970) 7312

112. G.G. Libowitz, A.J. Maeland "Handbook of Phys. Chem. of Rare Earths" (1979) N. Holland Chapter 26

113. A. Simon Z. Anorg. Allg. Chem. 355 (1967) 311

114. P. Chini J. Chem. Soc Chem. Comm. (1967) 29

115. P. Chini Inorg. Chem. 8 (1969) 1206

116. V.G. Albano, P. Chini, V. Scatturin J. Organometal Chem. 15 (1968) 423

117. P. Chini, G. Longoni, S. Martinengo, A. Ceriotti Adv. Chem. Ser. 167 (1978) 1

118. C.R. Eady, B.F.G. Johnson, J. Lewis, M.C. Malatesta, P. Machin, M. McPartlin J. Chem. Soc. Chem. Comm. (1976) 945

119. R.W. Broach, L.F. Dahl, G. Longoni, P. Chini, A.J. Schultz, J.M. Williams Adv. Chem. Ser. 167 (1978) 93

120. M.R. Churchill, J. Wormald, J. Knight, M.J. Mays Chem. Comm. (1970) 458

121. G.C. Bond 'Catalysis by Metals' Academic Press (1962)

122. R. Ugo Catal. Rev. 11 (1975) 225

123. E.L. Muetterties Bull. Soc. Chim. Belg. 84 (1975) 959

124. E.L. Muetterties Bull. Soc. Chim. Belg. 85 (1976) 451

125. E.L. Muetterties Science 196 (1977) 839

126. M. Primet, J. M. Basset, E. Gabrowski, M. V. Matthieu J. Amer. Chem. Soc. 97 (1975) 3655

127. S. Martinengo, G. Ciani, A. Sironi, P. Chini 175th Nat. met. A.C.S. Calif. (1978) No. INOR-073

128. J.C. Calabrese, L.F. Dahl, P. Chini, G. Longoni, S. Martinengo J. Amer. Chem. Soc. 96 (1974) 2614

129. A.K. Smith, B. Besson, J.M. Bassett, R. Psaro, A. Fusi, R. Ugo. J. Organometal Chem. 192 (1980) C31

130. J.M. Bassett, R. Ugo Aspects of Homogeneous Catalysis 3 (1976) 137

131. M. Moskovits Acc. Chem. Res. 12 (1979) 229

132. R.A. Barker, P.J. Estrup Phys. Rev. Letts. 41 (1978) 1307

133. R.F. Willis Surface Sci. 89 (1979) 459

134. H. Froitzhiem, H. Ibach, S. Lehwald Phys. Rev. Letts. 36 (1976) 1549

135. C. Backx, B. Feuerbacher, B. Fitton, R.F. Willis Surface Sci. 63 (1977) 193

136. M.K. Debe, D.A. King Phys. Rev. Letts 39 (1977) 708

137. R.A. Barker, P.J. Estrup, F. Jona, P.M. Marcus Solid State Comm. 25 (1978) 375

138. N.V. Richardson, A.M. Bradshaw "Vibrations in Ads. Lay". Proc. Int. Conf. (1978) Julich 2.

139. A.M. Baro, H. Ibach, H.D. Bruchmann Surface Sci. 88 (1979) 384

140. J. Howard, T.C. Waddington, C.J. Wright Int. Symp. Neut. Inel. Scatt. Vienna (1977) IAEA-M-219/17

141. A.M. Baro, H. Ibach Surface Sci. 92 (1980) 237

C H A P T E R 5

An IINS Study of Transition Metal Hydridocarbonyls

5.1 Spectrometers Used

The IINS spectra of the transition metal hydrido-carbonyls were obtained on 3 spectrometers. The compounds were run on BFDDIDO, using neutrons scattered from the Al (111) and (311) planes in the regions of 97-419cm^{-1} and 339-911cm^{-1} respectively. Some compounds were run in the 900-2200cm^{-1} region using the Al(511) and (711) planes, however, poor results were found due to a low signal-to-noise ratio. A further disadvantage lay in the very long counting times needed to cover the 1000-2500cm^{-1} region, which was covered better by IN1B, which was used with greater success to cover the 355-790, 726-1790 and 1613-2355cm^{-1} ranges using the (200), (220) and (311) planes of the copper monochromator. The 0-400cm^{-1} region was covered by the Dido 4H5 time-of-flight instrument. In all cases the samples were sealed in silica cells, thus a background subtraction routine was used. The background scattering caused by the silica was determined by running an empty can of the same dimensions. Typical IN1B and BFDDIDO silica spectra are shown in Figure 5.1 (The % scattering from an empty can was estimated to be 2-3%). The bands resolved in the IN1B spectrum are spectrometer artifacts.

5.2 $M_2(\mu_2\text{-H})$ Systems

This sections analyses the data on $HW_2(CO)_9NO$, $HRe_3(CO)_{14}$ $H_3Re_3(CO)_{12}$, $H_3Mn_3(CO)_{12}$, $H_4Ru_4(CO)_{12}$ and $H_2FeRu_3(CO)_{13}$.

5.2.1. $HW_2(CO)_9NO$

a) Previous Results

Little vibrational work has been carried out on $HW_2(CO)_9NO$. IR and Raman bands in the CO and NO stretching regions have been listed with Raman bands in the 800-1200cm^{-1} region (1).

The Raman bands were reported at 1205(wb), 1115(mb), 1045(mb), 965(mb), 900(wb) and 790(wb)cm^{-1}. The neutron diffraction data was compared with Kirtley and Kaesz's (2) method of correlating the WHW angle with the hydrogen stretching frequency. The Raman band at 1045cm^{-1} was assigned to the WHW stretch, and from this the WHW angle was calculated to be ~140°. Neutron diffraction data showed the WHW angle was 125.5° (1).

Most related vibrational studies have been carried out on $(HW_2(CO)_{10})^-$. A comparative study of the $(Et_4N)^+$ salts of $(HW_2(CO)_{10})^-$, $(DW_2(CO)_{10})^-$ and $(W_2(CO)_{10})^{2-}$ was undertaken (3) The intense Raman active W-W stretch, found in $(W_2(CO)_{10})^{2-}$(3) at 109cm^{-1}, was found to shift to 101cm^{-1} in the protonated and deuterated species. An IR band at 1680cm^{-1} at 93K was attributed to the anti-symmetric WHW stretch in the protonated salt (4). The band intensity, involving significant hydrogen motion, was found to be temperature dependent by Cooper et al (4) who detected IR bands at 1683cm^{-1} (Et_4N^+) and 1702$cm^{-1}$$(PPN^+)$. Cooper et al list IR and Raman frequencies associated with hydrogen motion in various $M_2(\mu_2\text{-}H)$ complexes. The Raman spectra of $(HM_2(CO)_{10})^-$ species all contained bands in the 600-1100cm^{-1} region, which, according to Cooper et al, should have contained a deformation mode. However the expected number of vibrations fell short of the observed number of bands. It was thought that these extra bands could be arising due to Fermi resonance between the symmetric MHM stretch or MHM deformation (5) and the overtones or combinations involving the MC stretch or MCO deformation motions. A Raman study ensued (5) which

substituted ^{18}O for ^{16}O and shifts were found for the MC and MCO deformations. The expected shifts of 10-28cm^{-1} for the overtones and combinations would have affected the features arising from the Fermi resonance but the frequencies did not change significantly. This discounts the possibility of Fermi resonance. Other possibilities such as bands due to the hydrogen residing in differing potential wells were postulated.

Howard et al (6) later assigned bands at 1680 and 875cm^{-1} and 1520 and 1022cm^{-1} to the antisymmetric and symmetric stretches respectively in the Et_4N^+ and Ph_4P^+ salts of $(HW_2(CO)_{10})^-$. The antisymmetric stretches were found to be more prominent in the IR and the symmetric stetches more prominent in the Raman. The study by Cooper et al (4) failed to mention the possibility of a symmetric stretch in the 600-1100cm^{-1} region and the Howard et al study (6) made no mention of deformation bands in the same region.

(b) Results

Table 5.1 lists the data from this study of $HW_2(CO)_9NO$. Figures (5.2, 5.3, 5.4) show the 4H5, IN1B and BFDDIDO spectra respectively. The 4H5 spectra in this chapter are of $F(\beta)*\tilde{S}(\alpha,\beta)/\alpha$ vs. energy transfer (cm^{-1}). A time-of-flight spectrum measures the intensity of scattered neutrons both as a function of ω and $\underset{\rightarrow}{Q}$ and so it is not suitable for direct comparison with optical spectra thus one can extrapolate $S(\alpha,\beta)/\alpha$ (where $\alpha = \hbar Q^2/2MT$ and $\beta = \hbar\omega/KT$) to zero α (ie zero momentum transfer). This function has the advantage of using the data from all the angles of detection.

Table 5.1: Bands Associated With H Motion in $HW_2(CO)_9NO$

IN1B (77K)	BFDDID0 (77K)	4H5 (130K)	IR (77K)	FIR (77K)	RAMAN (RT)	RAMAN (RT)(1)	Assignments
2025(mvb)							Overtone (2x1056= 2112cm^{-1}) and/or CO stretch
1595(ms)			1600(mb)		1620(vwb)		WHW antisymmetric stretch
1404(msh)			1398(w)				Combination (1056+313=1369cm^{-1})
					1170(wb)	1205(wb)	
			1110(w)		1120(wb)	1105(mb)	
1056(s)	1075(s)		1042(wm)		1080(wb)	1045(mb)	WHW Symmetric stretch
					1020(w)		
			950(vw)			965(mb)	
			939(vw)				
927(m)	904(wb)		888(w)		896(vw)	900(wb)	2nd Overtone (3x313=939cm^{-1})
780(m)	811(m)					790(wb)	Combination (313+480=793cm^{-1})
611(ms)	628(ms)						Overtone (2x313=626cm^{-1})
					563(s)		WCO deformation
480(s)	493(s)				462(w)		i/plane WHW deformation
					439(w)		WC stretch
389(wm)	393(wm)						Combination (313+80=393cm^{-1})
	313(vs)			305(m)			o/plane WHW deformation
	249(wsh)						Unknown
	173(m)	175(wm)					CWC deformation and/or combination band
		100(m)		103(wm)	107(mb)		WW stretch
		83(mb)		85(sh)			CWC deformation
		60(wb)			62(w)		} Lattice modes
		42(sh)					

IR = Infra-red, FIR = Far infra-red i/p = in-plane o/p = out-of-plane Band strength described as s = strong m = medium w = weak b = broad sh = shoulder v = very

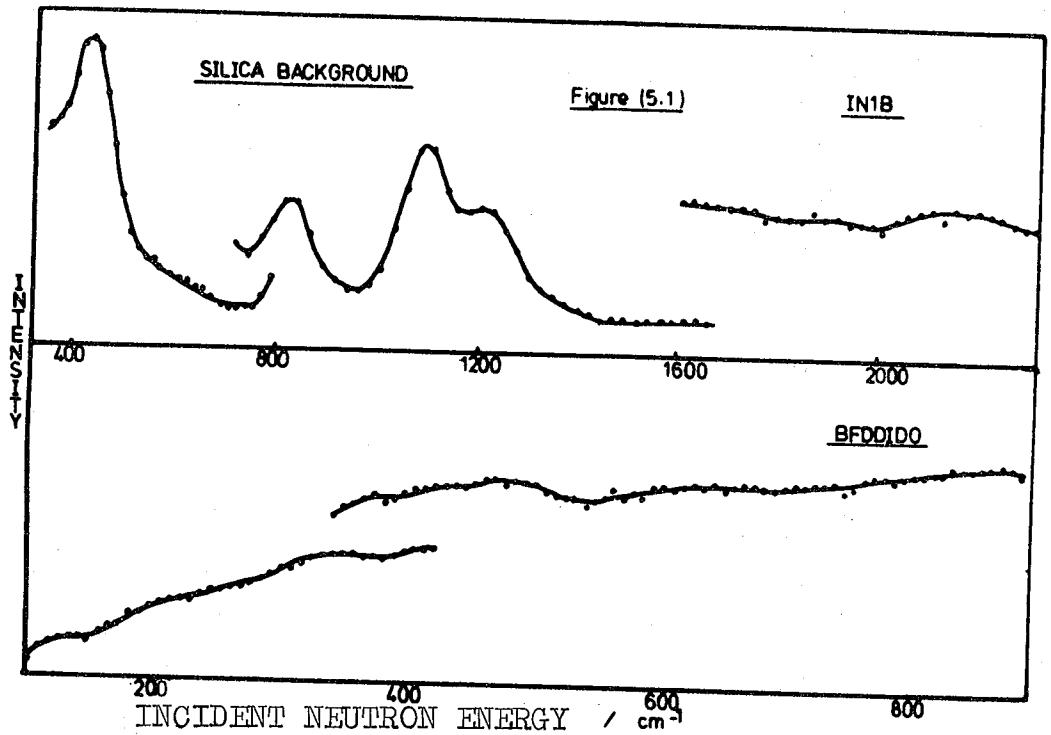
SILICA BACKGROUND
Figure (5.1)
IN1B
INTENSITY
400
800
1200
1600
2000
BFDDIDO
200
400
600
800
INCIDENT NEUTRON ENERGY / cm-1

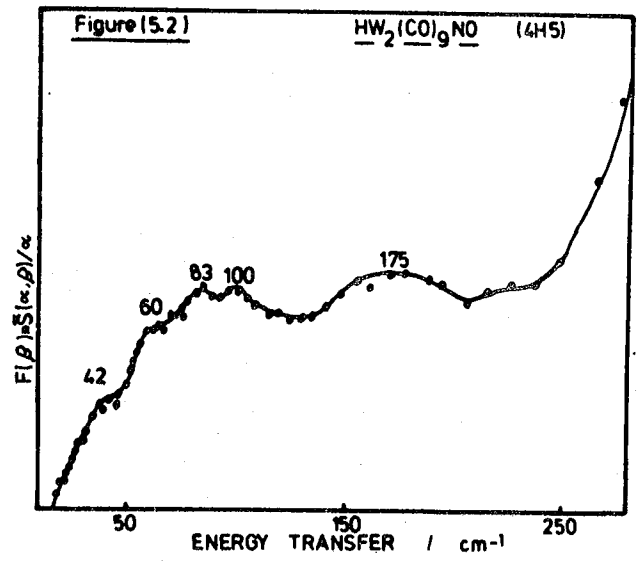
Figure (5.2)
HW2(CO)9NO (4H5)
F(β)=S(α,β)/α
42
60
83
100
175
50
150
250
ENERGY TRANSFER / cm-1

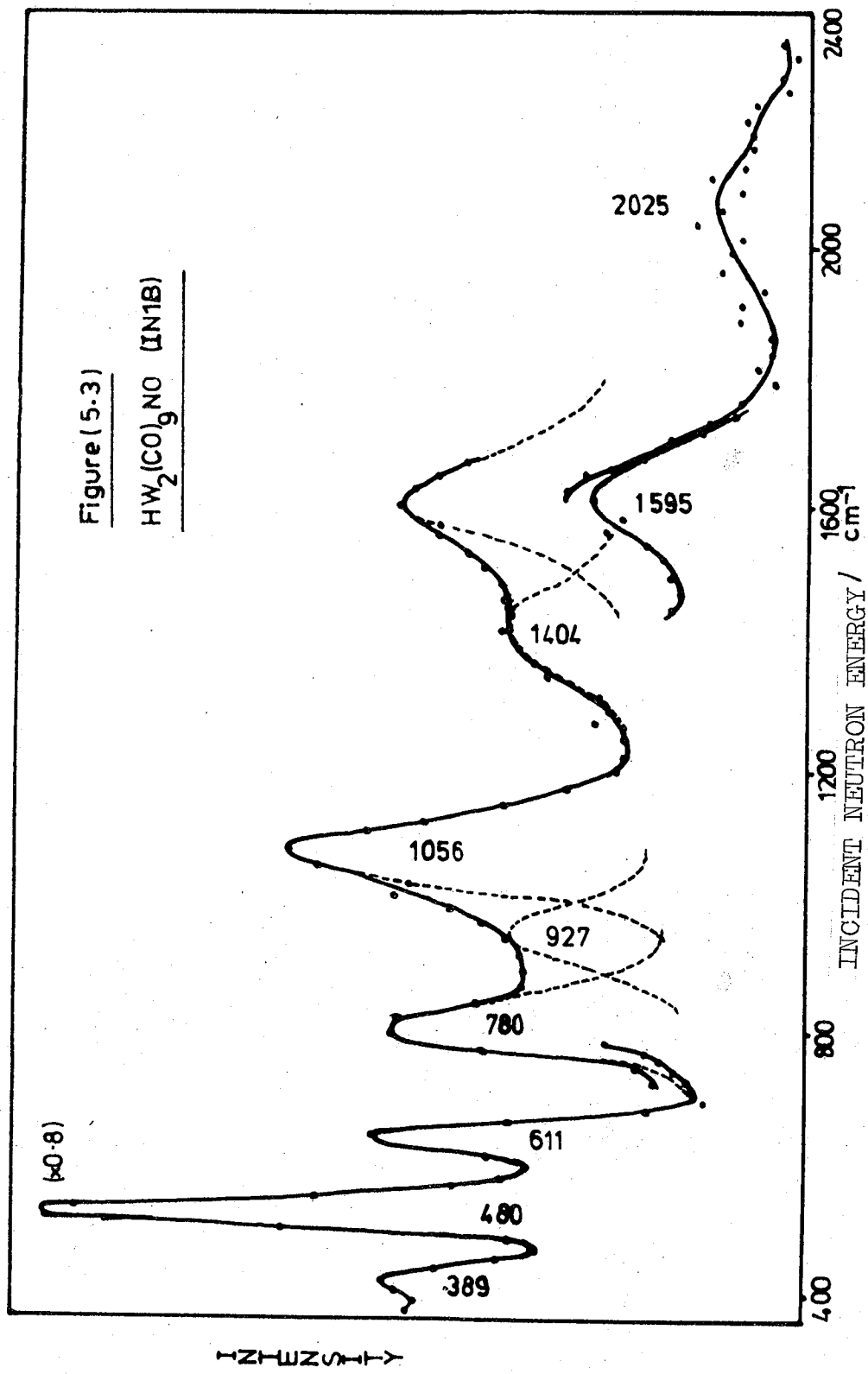
Figure (5.3)
$HW_2(CO)_9NO$ (IN1B)
(×0·8)
389
480
611
780
927
1056
1404
1595
2025
400
800
1200
1600
2000
2400
INCIDENT NEUTRON ENERGY / cm^{-1}
INTENSITY

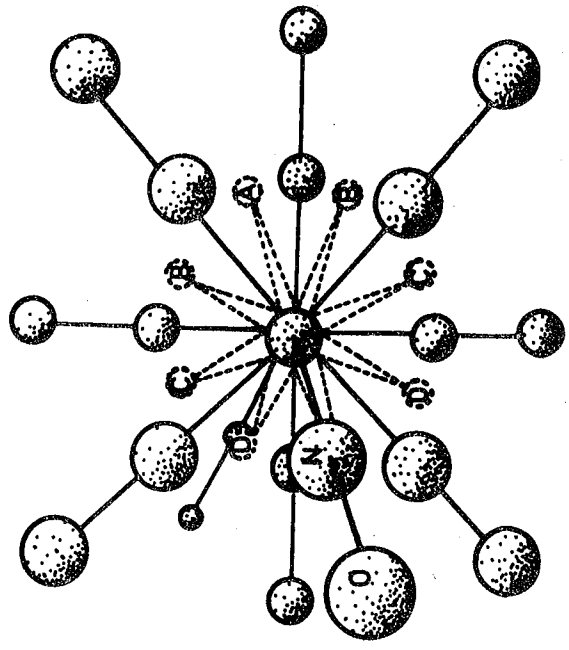

Figure(5.5) Positions hydrogen may take up in $HW_2(CO)_9NO$ (Looking along W-W axis)

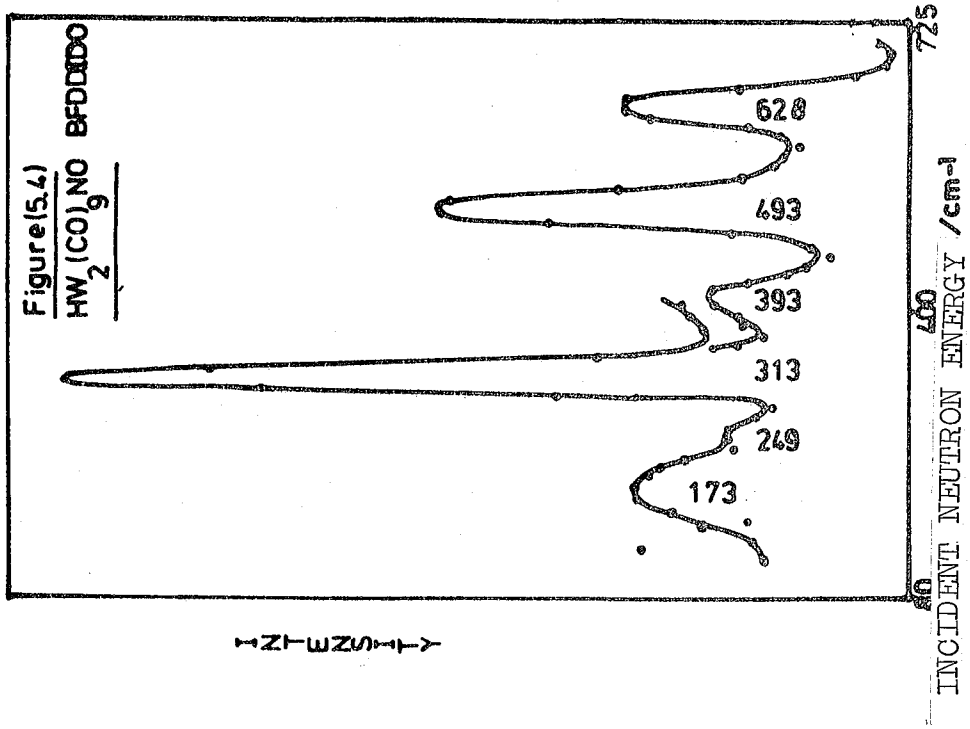

(c) Discussion

With C_s symmetry $HW_2(CO)_9NO$ is expected to have vibrations that involve hydrogen motion of the following character (Table 5.2).

Table 5.2: C_s Vibrational Analysis

Vibration	Symmetry	Activity
WHW stretch	2A'	IR and Raman
WW stretch	A'	
WHW deformation	A'	

(i) Tungsten-Tungsten Stretch Region

The WW stretching vibration is both IR and Raman active. This stretch is observed at $100cm^{-1}$ in the 4H5 spectrum, at $103cm^{-1}$ in the IR and $107cm^{-1}$ in the Raman spectrum. The perturbing influence of the hydrogen can be assessed by comparing the series $(W_2(CO)_{10})^{2-}$, $(HW_2(CO)_{10})^-$ and $HW_2(CO)_9NO$. Onaka et al (7) found the WW stretch at $110cm^{-1}$ in $(W_2(CO)_{10})^{2-}$ in their Raman study of $(M_2(CO)_{10})^{2-}$ ions. Harris and Gray (3) assigned a Raman band at $109cm^{-1}$ to the WW stretch in $(W_2(CO)_{10})^{2-}$ and at $101cm^{-1}$ in $(HW_2(CO)_{10})^-$ and $(DW_2(CO)_{10})^-$. Harris and Gray indicated that the stretch did not involve H or D motion. However, this is felt impossible since a deformation of the WH(D)W angle must take place. Further, since the W-W mode is observed in the IINS spectrum there must be associated hydrogen motion since the band is too strong to be due to tungsten atom motion alone ($\sigma_{inc}(W) = 2.8$ whereas $\sigma_{inc}(H) = 79.7$) There is a small lowering

in frequency on protonation and a similar effect on deuteration. This is expected since the shift on deuteration and protonation would be dependent on the masses of the atoms involved and the geometrical structure of the molecule. Since the mass of the W atom, compared with H and D, is so large, the effect of replacing anH atom with a D atom would be minimal. The band at $101cm^{-1}$ in the IINS spectrum in $HW_2(CO)_9NO$ is identical to that found in the Raman spectrum of $(HW_2(CO)_{10})^-$ and, therefore, there is little effect on changing an axial carbonyl group for the nitrosyl group in $HW_2(CO)_9NO$.

The IINS band at $83cm^{-1}$ is assigned to a CWC deformation mode, which is neutron active due to associated hydrogen motion. The medium broad IINS band at $175cm^{-1}$ in Figure 5.2 is more intrigueing due to its strong intensity and large FWHH. It may be due to a number of components such as a combination band ($100 + 83 = 183cm^{-1}$), lattice mode or a WWC deformation. There are features at lower frequencies in the IINS spectrum at 60 and $42cm^{-1}$. These are probably due to lattice modes. The frequencies at which they occur and their IINS intensity vary from spectrum to spectrum in the $P(\alpha,\beta)$ data ie they are angle and therefore momentum transfer dependent. IINS spectra involve appreciable momentum transfers which vary with the angle of detection. The variation depends on the angle of detection and the dispersion curve for the material being studied. If a mode is dispersive, the gradient changes from point to point so that the IINS intensity varies. When the gradient is very nearly zero then the intensity is strongest. Lattice modes show a greater

degree of dispersion than internal modes and can thus be identified in the IINS spectrum by their variations in intensity and peak position.

ii) WHW Vibrations ($>200cm^{-1}$)

With C_s symmetry, $HW_2(CO)_9NO$ is expected to have $2A'$ WHW stretching modes (the symmetric and antisymmetric stretches) and a single A' WHW deformation mode. However, such a simple spectrum was not found with at least 4 IINS bands found above $200cm^{-1}$ of sufficient intensity to imply they were fundamentals. The complexity of IR and Raman spectra of compounds with (μ_2-H) species has been discussed by Cooper et al (5) in the $800-1100cm^{-1}$ region. From our IINS spectra it would appear that the complexity is found in all parts of the spectrum. One postulate (5) was that the complexity could be caused by hydrogen residing in different potential wells. Differing bonding positions have been ascertained to exist in $(H(D)M_2(CO)_{10})^-$ species (eg (8)). $HW_2(CO)_9NO$ is isoelectronic with $(HM_2(CO)_{10})^-$ but has a distorted backbone with the separate COW and NOW axial vectors crossing at an angle of 159^o rather than 180^o found in, say, $(HCr_2(CO)_{10})^-$. With the distorted backbone only one potential well would be envisaged if the hydrogen resided at the cross-over point. However, the hydrogen resides beyond this point producing a WHW angle of 125.5^o. The hydrogen, in this case, may not be constrained by the disposition of the $W_2(CO)_9NO$ backbone and could possibly exist in other positions. Four positions were found in the $(DCr_2(CO)_{10})^-$ ion (8) though it is difficult to envisage that all the possible 8 positions available to the hydrogen in

$HW_2(CO)_9NO$ are all equally of the same potential well depth. However, in other similar compounds with bent MHM bonds the movement of the hydrogen atom from one potential well to another takes place without visibly perturbing the metal-carbonyl backbone ie there were no large thermal ellipsoids associated with the metal-carbonyl skeleton as there were with the hydrogen atom. The thermal associated with the hydrogen atoms in $HW_2(CO)_9NO$ and $HW_2(CO)_8NO(POCH_3)_3$) (9) were large, especially around about the W-W bond, which indicated a combination of hindered rotational motion about the WW bond and the packing disorder. If the rotational motion is hindered only to a small degree then Figure 5.5 will indicate the likely positions available to the hydrogen. Position A is the actual position inferred from the centre of the thermal ellipsoids from the neutron diffraction data, positions B,C and D are symmetric pairs of positions where the barrier to site occupation is likely to increase along the group to position E, the least likely occupied site. Thus the eight positions are formed by the staggered nature of the carbonyl ligands whereas the eclipsed nature of the ligands in $(H(D)Cr_2(CO)_{10})^-$ can only infer four positions, all of equal potential. Thus the complexity of the spectral situation may be caused by a certain number of hydrogen atoms residing for short lengths of time in the alternative positions.

However, the normal mode description, which allows the large number of fundamental vibrations, is an intrigueing problem. Three and recently four vibrations have been reported. The IINS spectra show at least 5 bands in

$HW_2(CO)_9NO$ and $HRe_3(CO)_{14}$, which are worthy of a fundamental description on intensity grounds alone. The following normal mode arguments are relevant to this discussion.

(a) Herzberg (10) described the vibrations of the X_3 species as:-

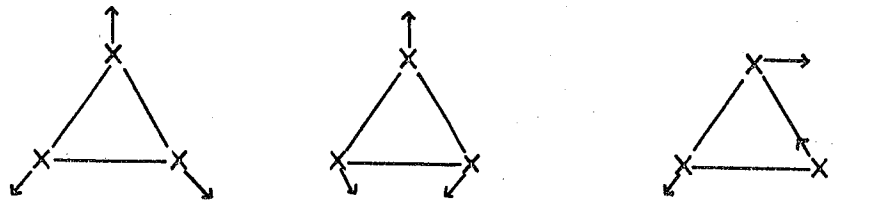

Symmetric Stretch | In-plane Deformation | Antisymmetric stretch

(b) Cooper et al (4) started from a description of the linear MHM group as shown in Figure 4.1 . On bending the MHM unit the selection rules were relaxed and the form of the normal modes changed. The authors then described the modes as an antisymmetric stretch, a deformation and the MM stretch.

(c) Howard et al (6) described the stretching vibrations as shown in Figure 4.2.

(d) Katovic and McCarley (11) described three vibrations as the MHM symmetric and antisymmetric stretches and a further mode which was either an MHM bend or an MM stretch.

(e) Andrews et al (12) postulated the following normal modes.

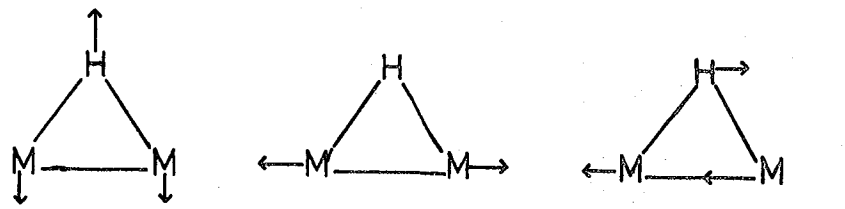

Symmetric stretch | Metal-Metal stretch | Antisymmetric stretch

(f) Cooper et al (5) later described the vibrations of the

$(HM_2(CO)_{10})^-$ species as a low frequency M-M stretch, a high frequency antisymmetric stretch and two vibrations derived from the double degenerate deformation of the linear MHM system. These would form the symmetric stretch and an out-of-plane deformation, which was derived from a rotation of the isolated MHM group.

The previous descriptions lack consistency but the final argument by Cooper et al (5) is thought to be nearer the truth. The regions of the IINS spectra in which the strong bands occur are (a) 1400-1750 (b) 800-1300 (c) 480-650 (d)300-450 and (e) 50-200cm^{-1}. From the observed frequency of the bands in the IINS spectra of the (μ_2-H) moieties, none of these can be due to a first overtone of any other band. Thus the problem must find an alternative explanation.

On protonating a species such as $M_2(CO)_m$ to $HM_2(CO)_m$ one produces three new vibrations. Two of these will be the symmetric and antisymmetric stretches and, if the masses of the M atoms is low, ie not too disimilar to that of hydrogen, then one should also get an in-plane deformation. The form of the modes will be similar to those of the ring system X_3, developed by Herzberg (10). However, as the masses of the metal atoms increases, the form of the in-plane deformation will change. The vectors describing the metal motion will move very close to the vector describing the M-M bond and thus describe, to a first approximation, an M-M stretch. It is known that M-M stretches occur in $M_2(CO)_m$-type systems. On protonation of the MM bond, the M-M stretch still takes place but the frequency can shift in the spectrum. This will be due to additional hydrogen motion and the effect of the bridging hydrogen in perturbing the MM bond

(eg. increasing the bond length). Now the hydrogen must take part in this M_2H motion and will not be decoupled from it. Since the vibrational amplitudes of the metal atoms involved in these motions is small, due to their heavy masses, then it may be possible that the vibrational amplitude of the bridging hydrogen will not be very large either, at least not to the same extent as found in, say, the stretching modes. Thus the M-M stretch still occurs at low frequency, $\sim 100\text{-}200cm^{-1}$, but involves hydrogen motion (and is thus neutron active) and must therefore be described as an in-plane deformations.

The two MHM stretching vibrations occur at high frequency (eg. 6), the M-M stretch (with additional H motion) occurs at low frequency but two further bands must be assigned in the $300\text{-}700cm^{-1}$ region. The form of one is that described by Cooper et al (5) as 'a possible out-of-plane deformation'. This is produced by a rotation of the isolated MHM moiety about the centre of gravity of the molecule, transformed into a vibration by the external ligands. This treatment of the (M_2H) core separately from that of the bulk molecule may be possible. For example, it will be seen that the carbonyl and the M-M vibrations can be desribed in terms of the point group symmetry of the the cluster in questions eg. (D_{2d} in $H_4Ru_4(CO)_{12}$, C_{2v} in $H_2Os_3(CO)_{10}$ and T_d in $H_4Re_4(CO)_{12}$) whereas the MHM vibrations (excluding the M-M stretch) can be quite convincingly described in terms of the 'local' symmetry of the hydrogen atom, (C_{2v} in $H_4Ru_4(CO)_{12}$, D_{2h} in $H_2Os_3(CO)_{10}$ and C_{3v} in $H_4Re_4(CO)_{12}$). The IINS study then places the out-of-plane deformation at $\sim 300\text{-}450cm^{-1}$. This leaves, however,

the band at 480-650cm^{-1} still to be assigned. From the frequency alone it must be a deformation mode, and in-plane since the out-of-plane mode has already been assigned. The in-plane mode must then be related to the M-M stretch in form. One alternative explanation of the mode arises from a framework $M_2(CO)_m$ vibration. Perhaps there are skeletal vibrations involving the hydrogen, due to some electronic perturbation to the M_2H unit. The IINS bands lie in the M-C stretch and M-C-O deformation regions though the forms of these vibrations are complex since they are known to mix heavily (13). The framework mode that would produce such an IINS band of medium-strong intensity is unknown in form though it produces an 'in-plane' - type deformation. Now the M-C stretches are observed in the 300-500cm^{-1} range while the M-C-O deformations dominate the 500-800cm^{-1} range according to Johnson et al (13) while Adams et al (14) describe the ranges as 300-450 and 450-700cm^{-1} respectively. So the in-plane deformation must arise from a skeletal motion which is more likely to be an M-C-O deformation than an MC stretch. Further, as noted by other studies (13,14) of metal carbonyls, the M-C-O deformations are strong in the IR and weak in the Raman spectra. So if there are IR analogues of the IINS bands this may indicate that the IINS bands arise from skeletal M-C-O deformations involving associated hydrogen motion.

Table 5.3 lists the IINS bands of interest in the 480-640cm^{-1} region and possible IR analogues for the (μ_2-H) transition metal hydridocarbonyls studied.

Table 5.3: IINS and IR Analogues in 480-640cm^{-1} Region (cm^{-1})

Compound	IINS	IR
$HW_2(CO)_9NO$	480	498(vs)
$HRe_3(CO)_{14}$	631 546	537(m), 580(vsb)
$H_3Re_3(CO)_{12}$	531	515(m), 560(m)
$H_3Mn_3(CO)_{12}$	606	605(m)
$H_4Ru_4(CO)_{12}$	619	621(vs)
$H_2FeRu_3(CO)_{13}$	639	614(sh),625(ms), 639(sh)

From the above arguments we propose that the forms of the modes which bring about the bands in the IINS spectra are shown in Figure 5.6 .

Figure 5.6: Vibrational Modes of (μ_2-H) Species

Modes of the M_2H Unit

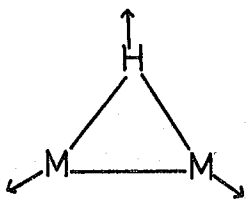

Symmetric Stretch

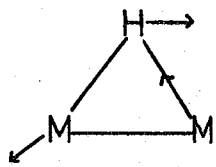

Antisymmetric Stretch

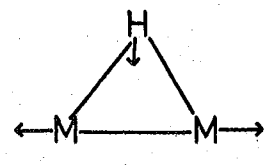

Metal-Metal Stretch (involving deformation of MHM bond angle)

Additional modes derived from skeletal modes of parent carbonyl

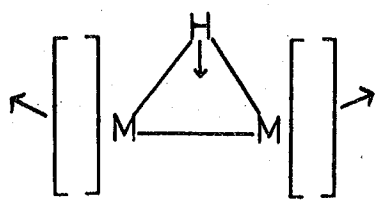

"in-plane deformation"

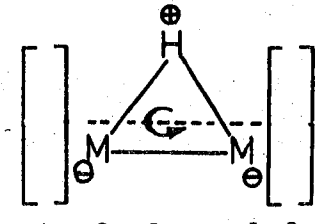

out-of-plane deformation

Cooper et al (5) and others had only evidence that metal-hydrogen vibrations existed in the 1400-1750, 800-1300 and 50-300cm^{-1} regions when they carried out their assignments. Early IINS work by White and Wright (15,16,17) seemed to go unoticed because they found very strong bands at 300 and 600cm^{-1} in their studies. No evidence pointed to the deformation mode (s) lying in the 900cm^{-1} region as previously stated by Cooper et al (5).

From a comparison with the studied $(HW_2(CO)_{10})^-$ species the assignments of the antisymmetric and symmetric stretches can be made to the IINS bands 1595 and 1056cm^{-1} respectively. These bands are the most intense above 500cm^{-1} in Figure 5.3. These values are justified by comparing the calculated WHW bond angle using the later methods (section 5.4.1.) with the known WHW angle. As expected, both bands are also seen in the IR, at 1600(mb) and 1042(w)cm^{-1}, and in the Raman at 1620(vwb) and 1080(wb)cm^{-1}. The antisymmetric stretch has a low frequency component at 1404cm^{-1}. This band may be due to the hydrogen residing in the stable environments of positions such as B, Figure 5.5. However, it could be alternatively be assigned to a combination band such as the combination of the two strong IINS bands at 313 and 1056cm^{-1}, total = 1369cm^{-1}.

The symmetric stretch region in the IR and Raman is very complex with more bands appearing in the Raman above 1000cm^{-1} and more bands appearing in the IR at less than 1000cm^{-1}. The reason for this anomaly may be that the higher frequency vibrations are of hydrogen residing in symmetric positions (nearly D_{4h}) where the A' symmetric stretch is likely to be only Raman active. At lower frequencies

the vibrations are of hydrogen in less symmetric positions (more likely C_s) where the bands become IR active and much less intense in the Raman spectrum.

The low frequency IINS spectrum below 750cm^{-1} is complex with four strong bands found where one or two WHW deformations would be expected. The two dominating bands at 313 and 480cm^{-1} are assigned to the previously discussed out-of-plane and in-plane deformation modes. The 611cm^{-1} band, of weaker intensity is assigned to the second harmonic of the313cm^{-1} band, the strongest band in the spectrum. Further, the band at 927cm^{-1} may well be a further overtone of the strong 313cm^{-1} band. The three bands at 313, 611 and 929cm^{-1} can be compared with the IINS bands found for $CsHCl_2$ and CsHClBr (18) (The fundamental bending vibration of the hydrogen bond in $CsHCl_2$ lay at 656cm^{-1}, similarly of very strong intensity. Three overtones, with diminishing IINS intensity were assigned to bands at 1250, 1810 and 2480cm^{-1}). The IINS band at 780cm^{-1} can be readily assigned to the combination of the two strong deformation modes in this low symmetry molecule (ie 313 + 480 = 793cm^{-1}). The weak band at 389cm^{-1} may be an overtone of the strong IINS band at 175cm^{-1} (if this band is due to a single component). It may also be due to a WC stretch with IINS activity caused by associated hydrogen motion. Finally, the very broad IINS band at 2025cm^{-1} is assigned to either a second harmonic of the symmetric stretch or to an IINS-activated CO stretching mode.

5.2.2. $HRe_3(CO)_{14}$

(a) Previous Results

Various studies have been carried out on protonated and deuterated analogues of $HRe_3(CO)_{14}$ (12,19). In the IR

spectrum, a band at 1035cm^{-1} in $HRe_3(CO)_{14}$ and 734cm^{-1} in $DRe_3(CO)_{14}$ was assumed to involve hydrogen motion. Bands were also reported in the Raman spectra of $HRe_3(CO)_{14}$ at 1265(vwb), 1049(mb), 965(wb) and 910(vwb) which shifted to 1110(vwb), 820(wb) and 740(sb)cm^{-1} in $DRe_3(CO)_{14}$ (19). It was postulated that the 1035cm^{-1} (IR) and 1049cm^{-1} (Raman) bands were analogous and were assigned to the ReHRe stretch. Further Kirtley reported bands in an improved Raman spectrum at 1258(wb), 1184(wb), 1097(wsh), 1041(mb), 952(mb), 904(mb) and 850(wb)cm^{-1} in $HRe_3(CO)_{14}$ and at 1122(wb), 825(mb) and 742(m) in $DRe_3(CO)_{14}$ (2,4). Parts of this Raman output were depicted by Kaesz and Saillant (20) and a band of interest occurred at 1130cm^{-1}(m) in $DRe_3(CO)_{14}$, though this may be the 1122(wb) band reported earlier. Using the H/ D ratio of 1.414 this would indicate the possibility of a band at ~1600cm^{-1} in $HRe_3(CO)_{14}$. Unfortunately this region was not depicted nor was a band reported here. This may be a prime example of the ability to see deuterated bands more easily than protonated bands in the IR and Raman. The latter are usually broader due to the greater amplitude of vibration of hydrogen (10).

(b) Results

Table 5.4 indicates those features and assignments from this vibrational study of $HRe_3(CO)_{14}$ and Figures 5.7,5.8,5.9 show the 4H5, BFDDIDO and IN1B spectra respectively.

(c) Discussion

$HRe_3(CO)_{14}$ has C_s symmetry if the H atom resides in the Re_3 plane and C_1 symmetry if it resides out of the aforesaid plane. Table 5.5 indicates the activity of the vibrations

Table 5.4: Bands Associated With H Motion in $HRe_3(CO)_{14}$

IN1B (77K)	BFDDID0 (77K)	4H5 (130K)	IR (77K)	FIR (77K)	Raman (RT)	Raman (RT)(2)	IR (RT)(19)	Assignment
2110(mvb)								Overtone($2\times1064=2128cm^{-1}$)and/or CO stretch
1604(ms)								ReHRe antisymmetric stretch
1516(wsh)								
						1258(wb)		
1209(mb)						1184(wb)		Combination($631+546=1177cm^{-1}$)
					1100(wb)	1097(wsh)		
1064(m)			1047(m)			1041(mb)	1035(wb)	ReHRe Symmetric stretch
			1010(vw)					
			965(m)			952(mb)		
			949(vw)					
919(msb)			934(w)			904(mb)		Combination (see text)
631(vs)	631(vs)							ReHRe In-plane deformation
546(vs)	546(vs)	555(sb)						(in and out of phase) (see text)
	445(vw)							ReC stretch
356(m)	365(vs)	355(ssh)		368(sh)				ReHRe out-of-plane deformation
	324(vs)	321(s)		341(w)				(in and out-of-phase)(see text)
	240(w)	230(vw)						Overtone ($2\times107=214cm^{-1}$)
				166(w)				CReC deformation
				128(w)	126(w)			CReC deformation
	107(vs)	96(m)		105(m)	100(m)			ReRe stretch
		80(m)		86(w)	85(m)			Re(H)Re stretch
		59(wsh)			60(w)			Lattice mode or ReC deformation
					52(w)			
		35(mb)						} Lattice modes

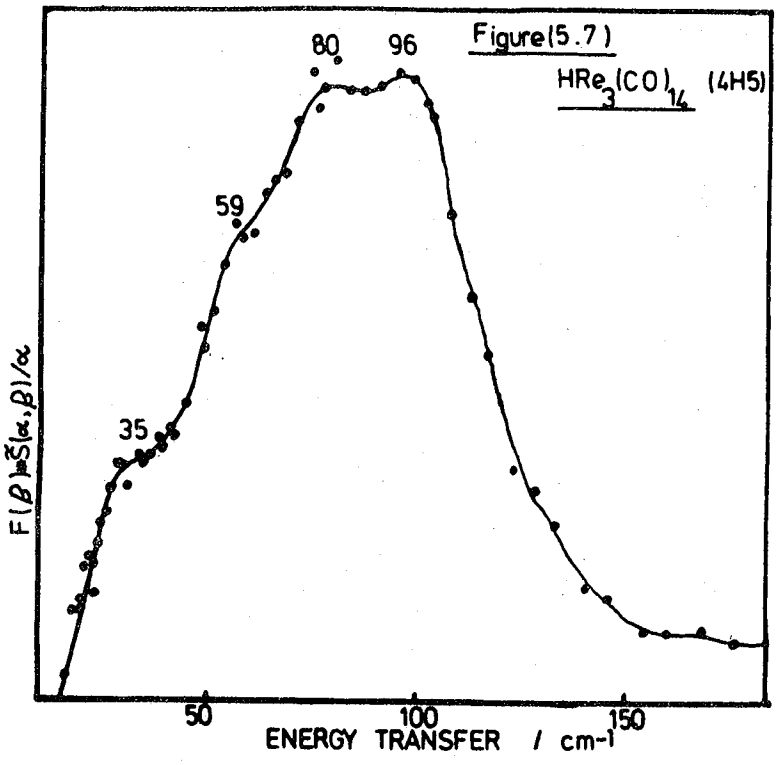
Figure(5.7)
HRe3(CO)14 (4H5)
80
96
59
35
F(β)=S(α,β)/α
50
100
150
ENERGY TRANSFER / cm-1

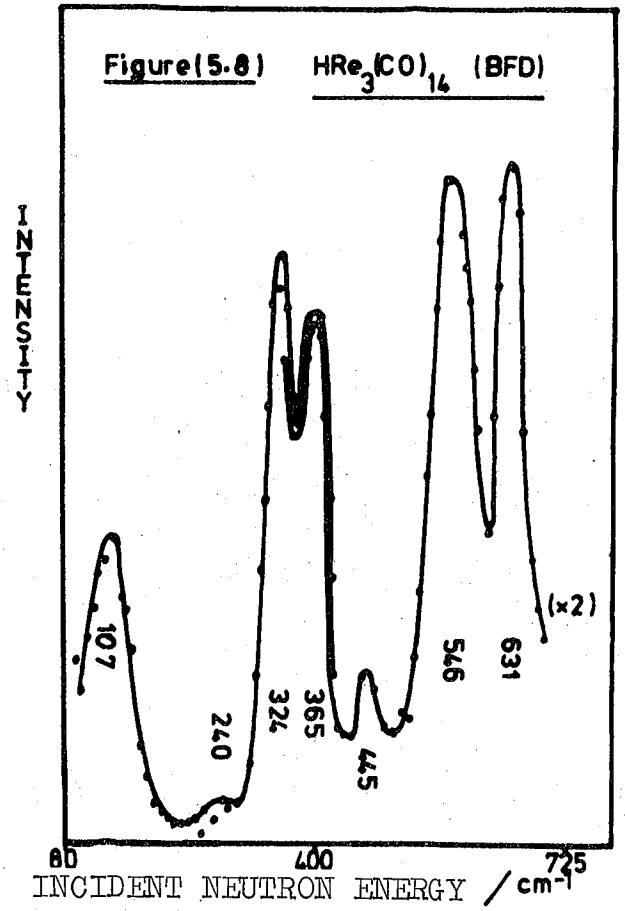
Figure(5.8)
HRe3(CO)14 (BFD)
INTENSITY
107
240
324
365
445
546
631
(×2)
80
400
725
INCIDENT NEUTRON ENERGY / cm-1

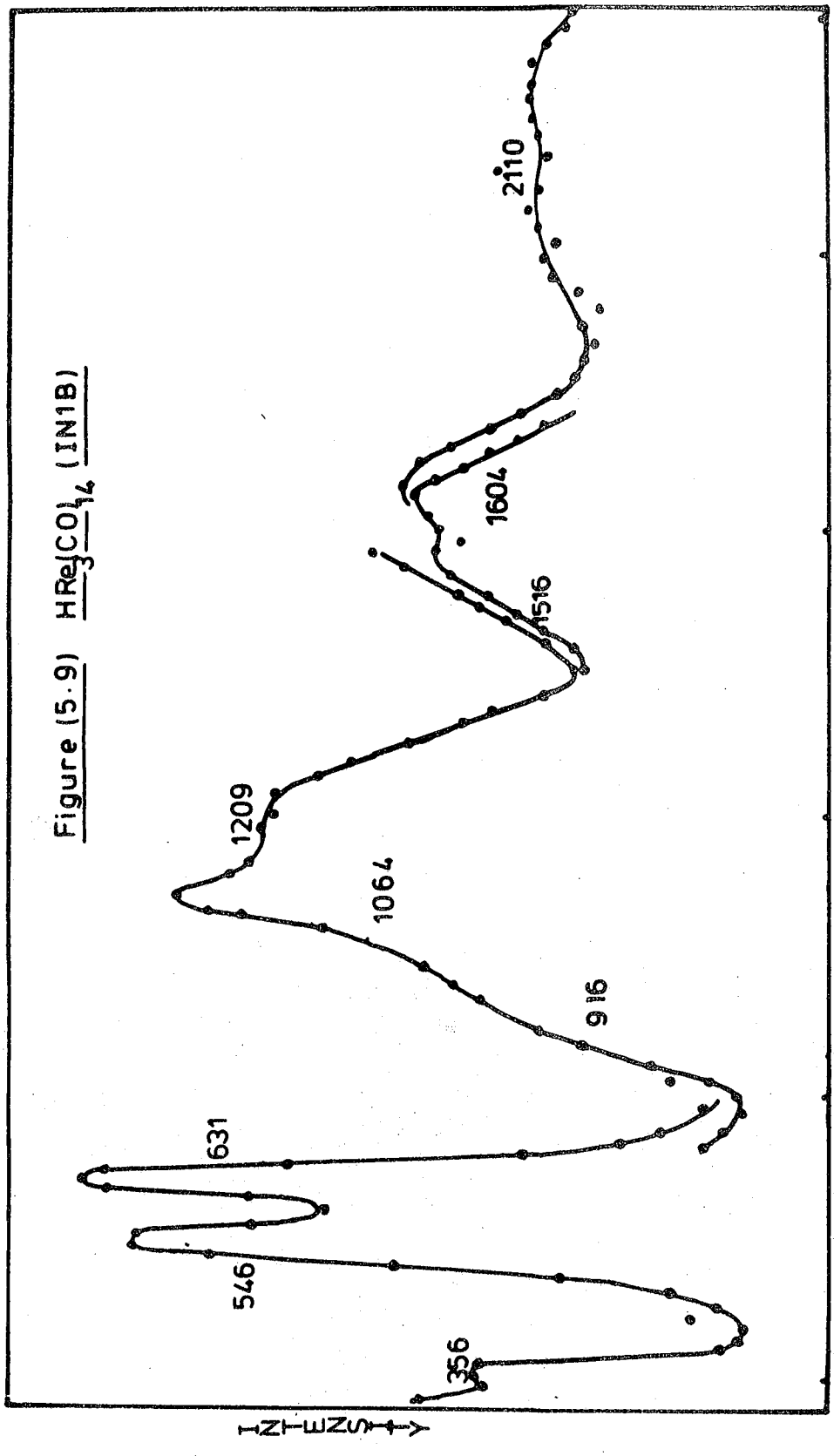
Figure (5.9) HRe_3CO_{14} (IN1B)
356
546
631
916
1064
1209
1516
1604
2110
400
800
1200
1600
2000
INCIDENT NEUTRON ENERGY / cm-1
SCATTERING INTENSITY

of the HRe_3 moiety.

Table 5.5: C_s and C_1 Vibrational Activity

Vibration	C_s System		C_1 System	
	Number and Symmetry	Activity	Number and Symmetry	Activity
ReHRe stretch	2A'	IR and Raman	2A	IR and Raman
ReHRe deformation	A'		A	
'non-bridge' Re-Re stretch	A'		A	
'bridged' Re-Re stretch	A'		A	

(i) Re-Re Stretch Region

There are two Re-Re stretches (IR and Raman active) and one mode may be described for the non-bridged and one for the bridged Re-Re bonds though this description is a crude approximation (ie that the two fragments are decoupled). The Re-Re stretch in $Re_2(CO)_{10}$ has been disputed. The arguments, from Raman studies, have favoured either a band at 129cm^{-1} from intensity grounds (eg. 22) or at 107cm^{-1} from polarisation measurements (eg. 14). In the IR and Raman spectra, bands were observed at approx. 85, 100 and 125cm^{-1} whereas time-of-flight IINS bands were observed at 96 (107cm^{-1} in the BFDDIDO spectrum) and 80cm^{-1}.

From the above evidence the IR/Raman band at 125cm^{-1} is assigned to a CReC deformation band since it is not observed in the IINS spectrum. This allows the 96cm^{-1} IINS band to be assigned to the non-bridged Re-Re stretch with

analogy to the parent carbonyl, $Re_2(CO)_{10}$. The IINS band at 80cm^{-1} in the time-of-flight spectrum is assigned to the hydrogen-bridged Re-Re stretch. This reduction in frequency from the non-bridged to the bridged entities is consistent with the increase in the M-M bond length seen on bridging with hydrogen. The frequency ratio of the two bands at 96 and 80cm^{-1} is 1.2:1 and this is larger than the average ratio of 1.1:1for the two non-bridged M-M stretches found in similar bent trimetal compounds (22).

The lower frequency IINS bands, ~70cm^{-1}, are no doubt lattice vibrations with the translatory modes to be found at lower frequencies than the libratory lattice modes (14). The very weak band at 230cm^{-1} may be due to a combination or a CReC deformation activated to some degree in the neutron spectrum in the same manner as the M-M stretches.

The IINS assignments of the ReRe stretch to the band at 96cm^{-1}(IINS)/100cm^{-1}(R) and 105cm^{-1}(IR), the Re(H)Re stretch at 80cm^{-1} (IINS) and the CReC deformation to the IINS band at 125cm^{-1} favours the assignments of Adams et al (14) on $Re_2(CO)_{10}$ for the ReRe stretch at 107cm^{-1}(R). It does not favour the Hyams et al (21) assignment at 129cm^{-1}(R).

(ii) ReHRe Vibrations

With a single H atom, three ReHRe vibrations are expected. One, the Re(H)Re stretch has already been assigned. They are all expected to be IR and Raman active. As depicted in Figures (5.8,5.9), the situation is more complex as seen with $HW_2(CO)_9NO$. The IINS spectra of μ_3- and (μ_6-H) compounds are much less complicated than the (μ_2-H) compounds. Table 5.6 indicates the possible number of hydrogen positions

that can be held in the (μ_2-H) compounds studied (from symmetry considerations).

Table 5.6: H Positions in (μ_2-H) Compounds

Species	No. of hydrogen positions about the M-M bond
$(HM_2(CO)_{10})^-$	4
$HW_2(CO)_9NO$	up to 8
$HRe_3(CO)_{14}$	2
$H_2FeRu_3(CO)_{13}$	1
$H_3Re_3(CO)_{12}$	1
$H_3Mn_3(CO)_{12}$	1
$H_4Ru_4(CO)_{12}$	1

It is believed that the hydrogen in $HRe_3(CO)_{14}$ resides in a similar position to that of hydrogen in $HRe_2Mn(CO)_{14}$. the latter compound (23) the M-M bands are nearly perpendicular to each other and the CO groups are eclipsed and lie in the Re_2Mn plane or perpendicular to it. Further, the carbonyls are not 'splayed' out as in $(H_2Re_3(CO)_{12})^{2-}$ (24), which in the latter compound allows the bridging hydrogen to reside in the Re_3 atom plane. Since it has been proven that such MHM bridges are inherently bent, two positions only would appear favourable to hydrogen bridging in $HRe_3(CO)_{14}$, with analogy to $HRe_2Mn(CO)_{14}$. Figure 5.10 shows these two positions to be ~45° above and below the Re_3 plane and bent away from the Re-Re bond. In the isolated molecule these two positions would be identical but in the crystal they may not be. The angle between these two available positions

is very similar to those occupied by the bridging hydrogen atoms in $H_2Os_3(CO)_{10}$. It is intrigueing to see that the low frequency spectra, $< 800cm^{-1}$, is similar in these compounds. The hydrogen, at the temperature of the study, may reside in either of these two positions (or potential wells). Some kind of tunnelling would be taking place or a 50:50 mixture would exist if the barrier to the site exchange were too large.

Figure 5.10: Two Identical Postions Available to Hydrogen

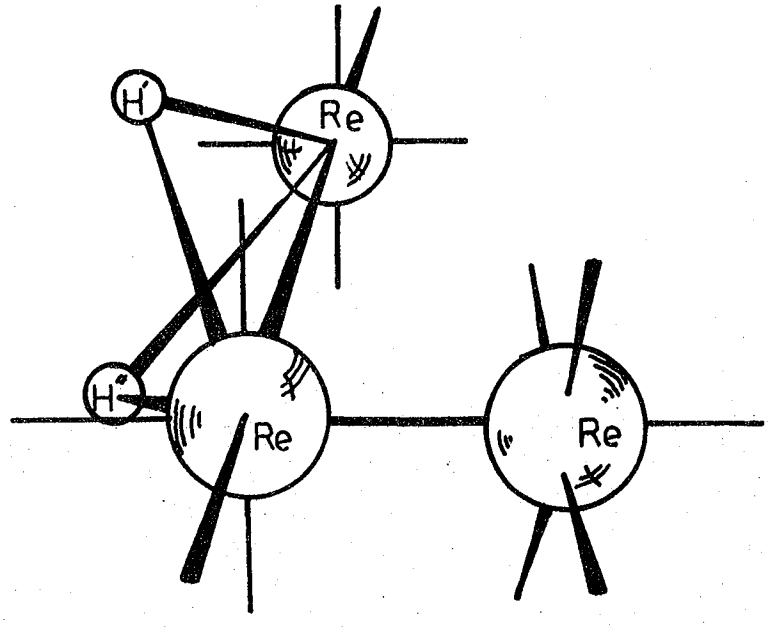

Thus any splitting of the bands in the IINS spectrum may be due to some external force, if these two positions were identical. This splitting would then be similar to the splitting due to a solid state effect, such as site symmetry where unrelated sites produce characteristic vibrations. Such splitting, as seen in the IINS spectrum of $HRe_3(CO)_{14}$,

may be explained in this way.

The assignment of the antisymmetric stretch to the IINS band at 1604cm^{-1} is based on evidence that the band is the most intense above 1200cm^{-1} and that a Raman band was found at 1130cm^{-1} in $DRe_3(CO)_{14}$. The assignment of the symmetric stretch is more difficult since three IINS bands are present in the 900-1300cm^{-1} region. Again the symmetric stretch is expected to be Raman active and the most intense Raman band lies at 1041cm^{-1} with other bands at 1258,1184, 1097,952,904 and 850cm^{-1}. The strongest IINS feature would appear, at first glance, to lie at 1064cm^{-1} in the region between 900-1300cm^{-1}. A shoulder of some intensity is seen to lie on each side of the central band. Since the Raman and IR spectra (2, 19 and this work) have the strongest band at ~1050cm^{-1} it is felt that the central IINS band at 1064cm^{-1} should be assigned to the symmetric stretch. Indeed, using the curve resolver, this band is by far the stronger if peaks are fitted at all of the Raman frequencies found by Kirtley (2). The 1064cm^{-1} IINS band is therefore assigned to the symmetric stretch. The other components on either side of the 1064cm^{-1} band in the IINS spectrum lie at 919 and 1209cm^{-1}. These bands may be assigned to combination and overtone bands. However, the possibilities are more complex in $HRe_3(CO)_{14}$ due to the splitting of the lower frequency deformations. If the lower frequency split bands are averaged (ie (324+365)/2 = ~345cm^{-1} and (546+631)/2 = ~588cm^{-1}) this may assist in the analysis. The 1209cm^{-1} shoulder may be due to the first overtone of the strongest IINS bands ie 2 x 588 = 1176cm^{-1}. The combination of the two averaged deformations could be assigned to the 919cm^{-1}

shoulder ie 345+588=933cm^{-1}.

The other postulate by Cooper et al (5) for the complexity found in these spectra is that factor group coupling is causing the fundamental bands to split by either the effect of the surrounding lattice, producing a frequency shift in non-degenerate bands and a split in degenerate vibrations of the internal and external modes or/and the effects of the internal vibrations of other molecules. In the latter event a non-degenerate fundamental can be split into a number of bands equivalent to the number of molecules in the unit cell (25). This splitting is caused by the in- and out-of-phase vibrations of the unit cell contents. The spread of the symmetric stretching vibrations appears to be too large for this effect but the low frequency region two bands which are, again in an analogy with $HW_2(CO)_9NO$, assigned to the in-plane and out-of-plane ReHRe deformations. The bands at approximately 350 and 600cm^{-1} are each split into two bands of nearly equal intensity. The lower frequency out-of-plane deformation is split by 41cm^{-1} into two bands at 324 and 365cm^{-1}, and the higher frequency in-plane deformation is split into two bands at 631 and 546cm^{-1} separated by 85cm^{-1}. This splitting may well be caused by a solid state effect such as factor group coupling or, probably more specifically, correlation field coupling. Only studies involving polarisation measurements and single crystal experiments will ensure the correct analysis of the vibrations of such compounds with regards to intermolecular coupling. The splittings are quite large for such an effect but such coupling has greater consequence in vibrations involving hydrogen, such as hydrogen bonded species (26).

Other features found in the IINS spectra are 445(w) and at 240cm^{-1}(w). The latter is very probably a weak combination or second harmonic band involving the M-M vibrations and/or the CMC deformations. The 445(w)cm^{-1} band may be a very slightly activated ReC stretching mode caused by associated hydrogen motion. The broad band at ~ 2110cm^{-1} is found in <u>all</u> the hydridocarbonyls studied and this is very intrigueing because it is felt many are just second harmonics of the very strong symmetric stretching vibrations (for example see $CsHCo_6(CO)_{15}$). However, in others there are no bands in the 1000cm^{-1} region e.g. $H_3Re_3(CO)_{12}$, $H_3Mn_3(CO)_{12}$ and $H_4Ru_4(CO)_{12}$. Though second harmonic bands are seen in some of the compounds studied there appears to be a weak broad band at 2000-2200cm^{-1} implying that the carbonyl stretching vibrations are being seen in the neutron spectrum to some degree caused by associated hydrogen motion associated with the very strong IR active carbonyl stretching vibrations.

5.2.3. $H_3Re_3(CO)_{12}$

(a) <u>Previous Results</u>

IR bands at room temperature have been reported for $H_3Re_3(CO)_{12}$ and $D_3Re_3(CO)_{12}$ (26). There appeared to be very weak features in the protonated spectrum, which shifted on deuteration and these changes were reversible. These bands were at 625(sh) and 339(w)cm^{-1} in $H_3Re_3(CO)_{12}$. A Raman study of the compounds (27) showed only one major difference in that a broad band at 1100cm^{-1} shifted to 787cm^{-1} in $D_3Re_3(CO)_{12}$. Later studies by Fontal (19) and Kirtley (2) listed ReHRe stretching vibrations in the Raman spectrum at 1098(wb) and 1170(wb)cm^{-1} and 1076(mb) and 1172(mb)cm^{-1}

respectively. Kaesz and Saillant (20) reported Raman bands at 1000(vw), 1076(vw) and 1100(vw)cm^{-1}. White and Wright looked at the low frequency region, using IINS, (15) and found a peak at 83cm^{-1}, assigned to the Re(H)Re stretch of E symmetry, and weaker bands at 101 and 151cm^{-1}. They could not decide which of these features was due to the Re(H)Re stretch of A_1 symmetry. It was postulated that a band at 320cm^{-1} was either an in-plane or out-of-plane ReHRe deformation.

(b) Results

Table 5.7 indicates those features and assignments from the vibrational study of $H_3Re_3(CO)_{12}$ and Figures 5.11,5.12, 5.13 show the 4H5, BFDDIDO and IN1B spectra.

(c) Discussion

$H_3Re_3(CO)_{12}$ has probably D_{3h} symmetry and thus will have vibrations of $10A_1' + 7A_2' + 17E' + 4A_1'' + 7A_2'' + 11E''$ symmetry of which the following, in Table 5.8, involve hydrogen motion.

Table 5.8: D_{3h} Vibrational Analysis

Vibration	Symmetry	Optical Activity
ReHRe stretch	A_1'	Raman
	A_2'	Inactive
	$2E'$	IR/Raman
ReHRe deformation	A_1'	Raman
	E'	IR/Raman
ReRe stretch	A_1'	Raman
	E'	IR/Raman

Table 5.7: Vibrational Data and Assignments for $H_3Re_3(CO)_{12}$

IN1B (77K)	BFDDID0 (77K)	4H5 (130K)	IR (77K)	FIR (77K)	Raman (RT)	Raman (RT) (2)	IR (RT) (26,27)	IINS * (25)	Assignment
1991(sb)									Combination(1675+324)or CO stretch
1675(m)			1700(wb) 1640(wb)		1745(w)				Antisymmetric ReHRe stretch
1450(wb)					1435(wb)				Combination band ($1159+324=1483cm^{-1}$)
					1170(wb)	1172(mb)			ReHRe symmetric stretch
1159(sb)	1148(wb)				1150(vwb)				
					1117(wb)	1100(vw)			
	1060(sh)				1070(wb)	1076(vw)			
					980(vwb)	1000(vw)			2nd overtone ($3x324=972cm^{-1}$)
911(wm)									Combination band (?) ($324+531=855cm^{-1}$)
845(m.av)	860(m)								Difference band(?) ($1159-324=835cm^{-1}$)
814(wm)									Overtone ($2x324=648cm^{-1}$)
623(m)	641(m)						625(vw)		ReHRe in-plane deformation
531(vs)	531(vs)	550(vs)			556(vw)				ReC stretch
405(wsh)	400(vw)			370(wsh)	372(w)				ReHRe out-of-plane def.
				342(m)					ReC stretch
	324(vs)	324(vs)		320(w)			339(vw)	320(mb)	Combination or difference band
				306(w)					CReC deformation and/or lattice mode
	242(sh)								CReC deformation
	174(sb)	156(sb)						151(w)	CReC deformation ,
				143(vw)	143(mb)				Re(H)Re stretch(A_1)
					116(sh)				CReC deformation ,
		94(m)			106(s)			101(w)	Re(H)Re stretch(E)
					90(ms)				Lattice modes
		78(m)			77(ms)			83(ms)	
		45(sh)			48(w)				
					30(m)				

av. = average

* Unknown experiment temperature

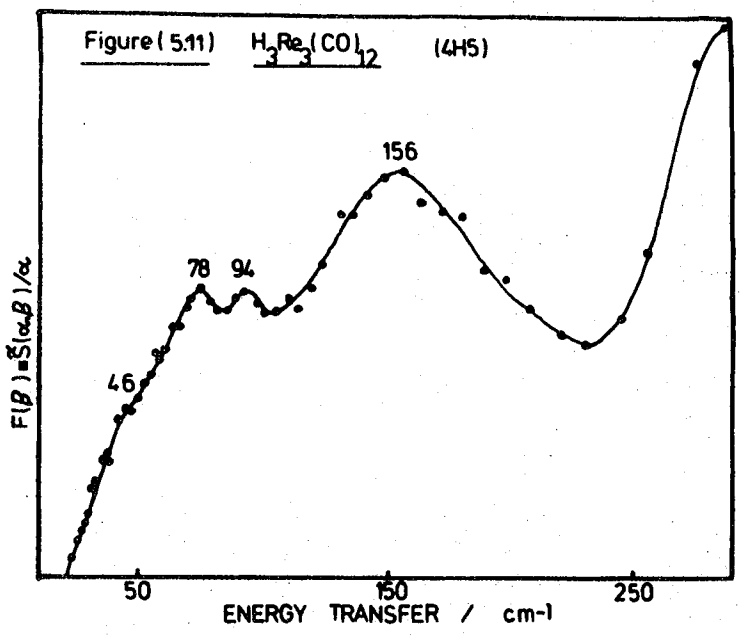
Figure (5.11) $H_3Re_3(CO)_{12}$ (4H5)
156
78
94
46
$F(\beta) = S(\alpha,\beta)/\alpha$
50
150
250
ENERGY TRANSFER / cm-1

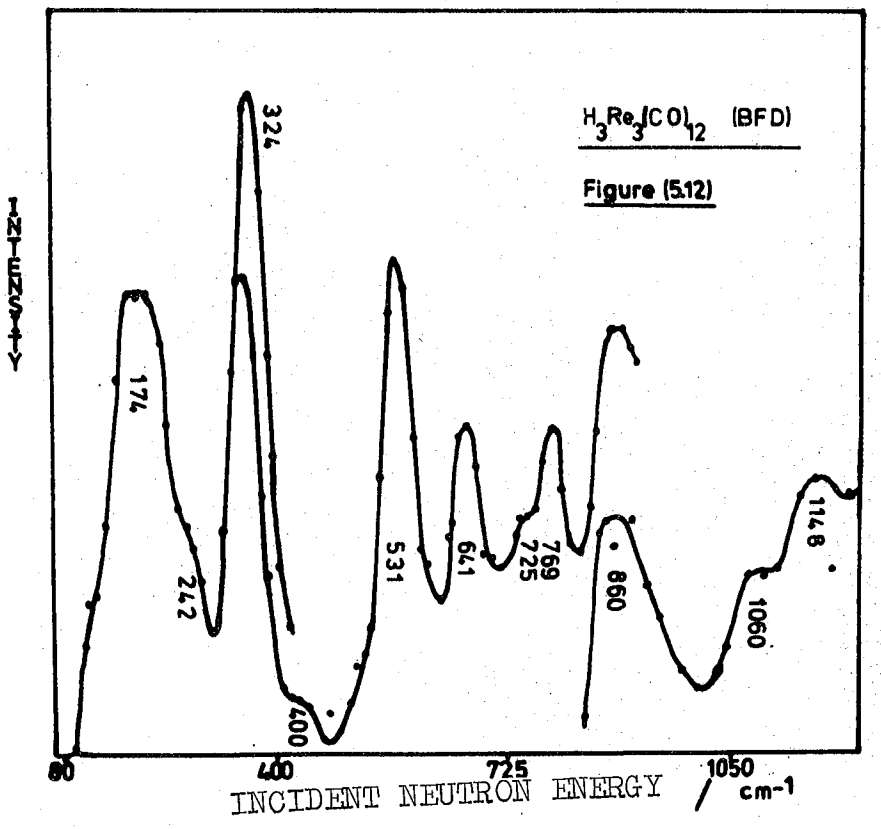
$H_3Re_3(CO)_{12}$ (BFD)
Figure (5.12)
324
174
242
100
531
641
725
769
860
1060
1148
INTENSITY
60
400
725
1050
INCIDENT NEUTRON ENERGY / cm-1

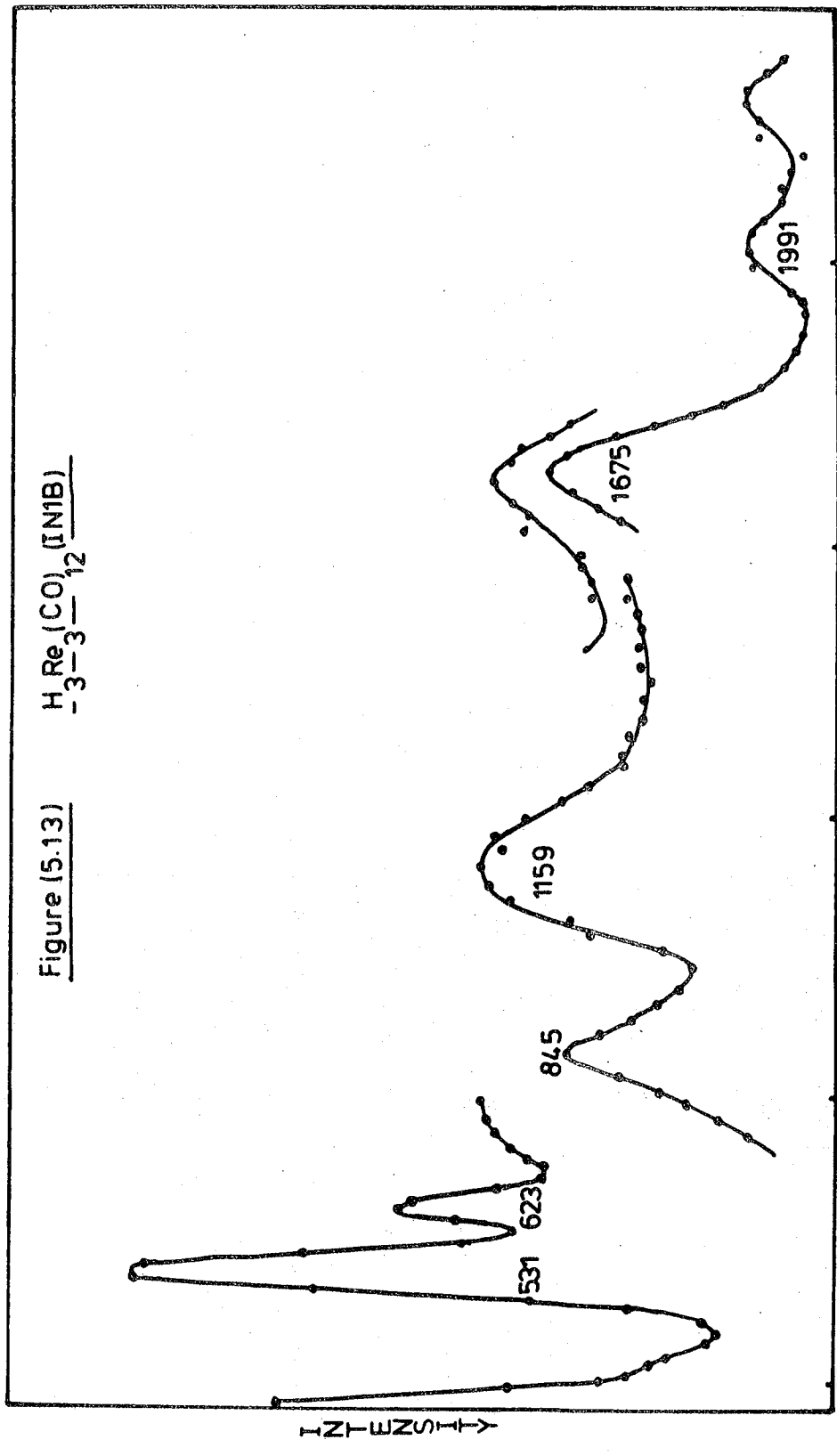

Figure (5.13) $H_3Re_3(CO)_{12}$ (IN1B)

(i) Re-Re Stretch Region

$H_3Re_3(CO)_{12}$, like $H_3Mn_3(CO)_{12}$, has D_{3h} symmetry and thus two ReRe stretches are expected to be 'neutron active', $A_1' + E'$. The predicted frequency ratio is $A_1' : E' = \sqrt{2} : 1$ from the assumption of a single valence force field (22). Figure 5.11 is dominated by three features, a strong IINS band at 156cm^{-1} with weaker bands at 94 and 78cm^{-1}. The ratio of the band positions of the former pair, 156/94, is 1.65:1 while that of the latter pair, 94/78, is 1·21:1. These ratios lie on each side of the expected ratio 1.41:1. Raman bands are also observed at 148 and 106cm^{-1}. There is only a single IR band of weak intensity in this region at 143cm^{-1}. Perhaps the ReHRe bond is similar in $H_3Re_3(CO)_{12}$ and $HRe_3(CO)_{14}$. Thus the IINS bands at 94 and 78cm^{-1} could be compared with the ReRe and Re(H)Re assignments at 96 and 80cm^{-1} in $HRe_3(CO)_{14}$. The intensity of the two IINS bands in $H_3Re_3(CO)_{12}$ is somewhat low and this may be due to heavy mixing with other modes in the same region. The IINS band at 156cm^{-1} may be a group of 'neutron-active' CReC deformations.

In the IINS spectrum the intensity of the E' mode could be crudely related to the intensity of the A_1' mode by the following consideration.

$$\frac{\text{Intensity of } E' \text{ mode}}{\text{Intensity of } A_1' \text{ mode}} \approx \frac{2}{1}$$

On this basis the assignment of the 156 cm^{-1} band to the A_1' vibration would be inconsistent since it is more intense than the lower frequency pair at 94 and 78cm^{-1} even if they have lost some intensity due to their proximity to other modes. However, the intensity comparison of the 94

and 78cm^{-1} bands is not good since they appear of similar intensity. These three IINS bands at 156, 94 and 78cm^{-1} can be compared with those of White and Wright (15) who found similar bands at 151, 101 and 83cm^{-1} and who also had difficulty in assigning the M-M stretches. From purely intensity considerations the 156cm^{-1} in our IINS spectra cannot be an Re-Re stretch and thus the 78 and 94cm^{-1} bands are assigned to the E' and A_1' Re-Re stretches respectively. These assignments are of a tentative nature due to the poor resolution of the 4H5 spectrum and to the obvious poor A_1':E' intensity ratio.

(ii) ReHRe Vibrations (>200cm^{-1})

The vibrations which involve hydrogen motion (>200cm^{-1}) cannot be desribed in terms of the $H_3Re_3(CO)_{12}$ D_{3h} point group because of the following pieces of evidence:

(i) The IN1B spectra, in particular, of those compounds with a single hydrogen atom per cluster, ie $HW_2(CO)_9NO$, Figure 5.4 , and $HRe_3(CO)_{14}$, Figure 5.9, are very similar to that of $H_3Re_3(CO)_{12}$, Figure 5.12. Bands are found in the five regions once again: ie < 200, ~ 320, ~ 530, ~ 1150 and 1675cm^{-1}. A medium intense band also exists at 845cm^{-1} but it may be alternatively assigned.

(ii) Work by Kettle and Stanghellini (28) on Os- and Ru-carbonyls has shown that inter and intra-molecular coupling may be neglected to a first approximation (with the exception of the ν(CO) region). Though it was unreasonable to accept a complete decoupling, possible applicability of an isolated $M(CO)_4$ group model was a possibility. The

assumption that a mechanical coupling between vibrations led to the predicted frequency ratio A_1' to E' of $\sqrt{2}$:1. Experimentally this was so in $M_3(CO)_{12}$ species but in $Os_{3-n}Ru_n(CO)_{12}$ species the individual vibrations could be separated. This indicated little electronic interaction between the M-M bonds. Perhaps this is also the case when the bridging takes place. Thus the ReHRe vibrations could be described in C_{2v} rather than D_{3h} symmetry.

(iii) Not only do the $HW_2(CO)_9NO$, Figure 5.4 , and $H_3Re_3(CO)_{12}$, Figure 5.12, IINS spectra look similar but under D_{3h} symmetry four ReHRe stretching vibrations would have been expected. Clearly in Figure 5.12 there are not four bands of strong intensity above ~ 800cm^{-1} that would merit such a description.

The IN1B spectrum is dominated at high frequency by a strong band at 1675cm^{-1}. Weak features are found in the IR and Raman spectra and this points to the band being the anti-symmetric stretch. This value is consistent with other transition metal hydridocarbonyls. The assignment of the ReHRe symmetric stretch was made by Kirtley (2) to a number of bands, from Raman data, in the 1000-1172cm^{-1} region. The band at 1159cm^{-1} in the IINS spectrum is thus assigned in this manner. Our Raman spectrum found similar weak bands in the 980-1170cm^{-1} region.

$H_3Re_3(CO)_{12}$ and $H_3Mn_3(CO)_{12}$ differ quite drastically in the assignment of the symmetric stretch. Bands appear in both IN1B spectra, Figures 5.12,5.17, in the 800-1400cm^{-1} region but the symmetric stretch is found at 875cm^{-1} in the latter compound to 1159cm^{-1} in the former. It may have been possible to assign the symmetric stretch of $H_3Re_3(CO)_{12}$ at

845 cm^{-1} in Figure 5.12, which would have compared quite well with the manganese cluster data. However, this did not agree with the optical data. The IINS band at 845cm^{-1} has a non-guassion shape and thus must contain a number of components. Possibilities for difference, combinations and overtones in this region are:-

(a) The second overtone of the strongest IINS band at 324cm^{-1} would lie at ~ 3 x 324cm^{-1} = 972cm^{-1}

(b) The combination of the two very strong IINS bands at 531 and 324cm^{-1} = 855cm^{-1}

(c) Another possibility lies in the assignment of a difference band e.g. 1159-324 = 835cm^{-1}. With regards the symmetric stretch assignment in $H_3Re_3(CO)_{12}$ and $H_3Mn_3(CO)_{12}$ it may be worth noting that in section 5.6 it is shown that the MHM bond angle estimating techniques are at variance with $H_3Re_3(CO)_{12}$. However, it can be shown that it is the ratio of the antisymmetric stretch to the symmetric stretch which is the important factor and that the individual frequencies cannot be used accurately. So that even though the antisymmetric stretches are similar in $H_3Mn_3(CO)_{12}$ and $H_3Re_3(CO)_{12}$, this is no guide to indicate that the symmetric stretches should also be so in such similar compounds.

The low frequency deformation region is quite complex but can be very easily related to the spectrum of $HW_2(CO)_9NO$. The strong bands at 531 and 324cm^{-1} are assigned to the deformation modes. The former being less intense and described as an 'in-plane' mode. This band is likely to be symmetric in nature and a weak Raman band was found at 556cm^{-1}. No IR analogue was observed. The out-of-plane deformation is IR active and an IR band was found at 342cm^{-1}, though it

may have been an ReC stretch. The other weak bands in the IINS spectra are at 242, 400 and 1991cm^{-1}. The former may be an overtone of the Re(H)Re stretches or a CReC deformation. The 400cm^{-1} bond is assigned to a ReC stretch activated in the IINS spectra due to associated hydrogen motion while the 1991cm^{-1} broad band may involve a number of combinations/overtones and, possibly, a CO stretch. One further point to note is that since the IINS spectra of $HW_2(CO)_9NO$ and $H_3Re_3(CO)_{12}$ are so comparable perhaps they can be compared more closely. They are virtually identical below 700cm^{-1}. However, above this frequency an 'extra' band would appear to be found in $HW_2(CO)_9NO$ at ~ 1400cm^{-1} as a weaker lower frequency component of the antisymmetric stretch at 1595cm^{-1}. A study of $H_3Re_3(CO)_{12}$, at first glance, does not show such a feature. However, if the band at 1675cm^{-1} in $H_3Re_3(CO)_{12}$ were raised in intensity so that the spectra became continuous with increasing energy transfer (ie one did not change plane) and there was a flat background running from ~ 800 to ~ 1800cm^{-1} then there is a possibility that a further broad band could be resolved at ~ 1450cm^{-1} of medium intensity which would be at a similar frequency to the 1406cm^{-1} band in $HW_2(CO)_9NO$. Figure 5.14 shows the similarities between these compounds in this energy range. The true IINS intensity of these bands and, of course, all others depends on the chosen background, an unknown factor. How the band at 1447cm^{-1} arises may be due to a combination band involving the out-of-plane deformation and the symmetric stretch. The band occurs, with varying intensity, in most compounds

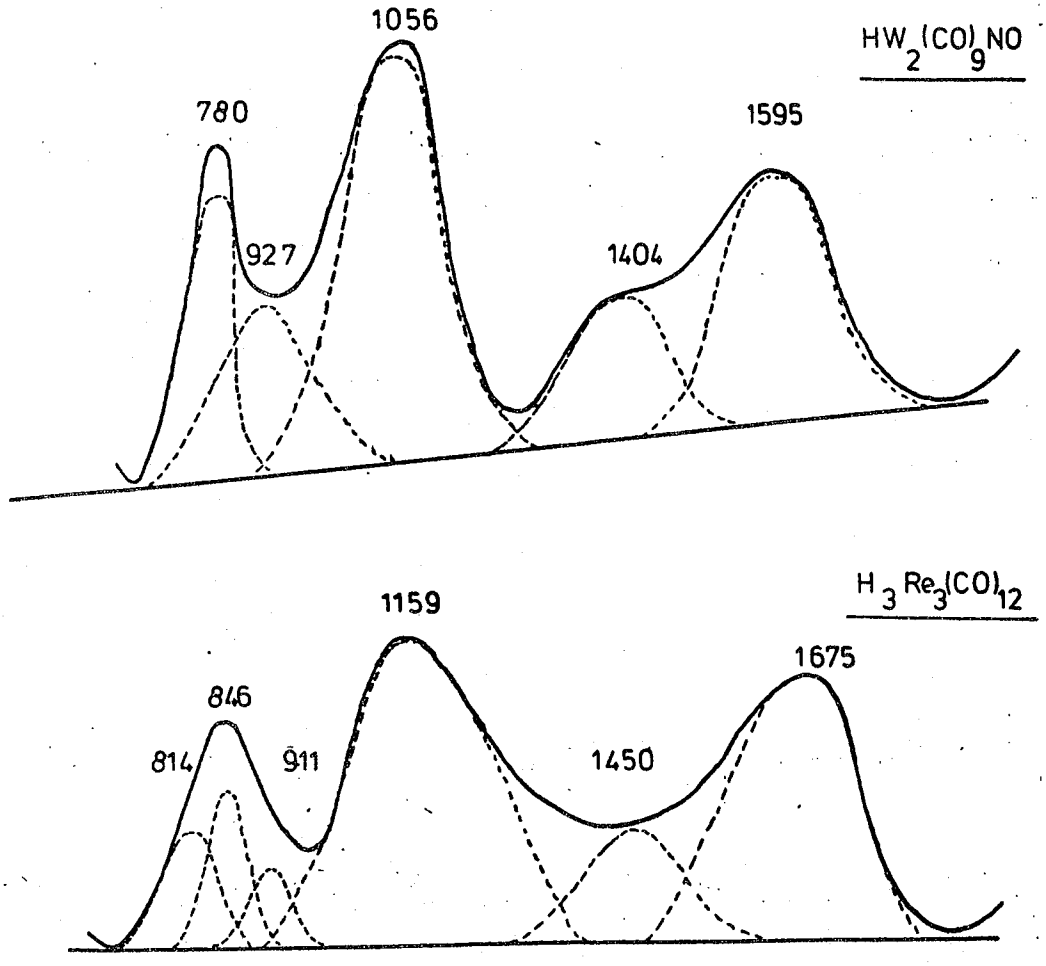

Figure(5.14) Comparison between $HW_2(CO)_9NO$ & $H_3Re_3(CO)_{12}$ IN1B Spectra in the 700-1800cm^{-1} region

e.g.	Band Frequency	Combination
$HW_2(CO)_9NO$	1404	1050+313
$H_3Re_3(CO)_{12}$	1447	1159+324
$H_3Mn_3(CO)_{12}$	1198	875+336

In $H_3Mn_3(CO)_{12}$ the band is at much lower frequency because one component, the symmetric stretch, lies at lower frequency.

It can also be noted that two IR bands were observed, of weak intensity, at 1640 and 1700cm^{-1}. This is probably a solid state effect which may also explain the split Raman bands in the region of the symmetric stretch. In fact, similar splitting of the IR bands around 1600cm^{-1} and the Raman bands around 875cm^{-1}, indicative of the antisymmetric and symmetric stretches respectively, occurred in $H_3Mn_3(CO)_{12}$. A less favoured explanation of the splitting is that there would appear to be some asymmetry (apparent) in the H positions in the related $H_3Mn_3(CO)_{12}$ (29) with one hydrogen appearing to occupy more volume than the other two producing a distorted D_{3h}------C_{2v} structure. This asymmetry was believed to be an artifact since no chemical reason could be advanced for believing anything but a D_{3h} symmetrically bridged structure. If any asymmetry is found then slightly different antisymmetric and symmetric stretches will arise due to the different bonding geometries.

5.2.4 $H_3Mn_3(CO)_{12}$

(a) Previous Studies

White and Wright (17) studied the 0-900cm^{-1} region, using IINS techniques, and compared the room temperature IINS spectrum of $H_3Mn_3(CO)_{12}$ with the IR and Raman spectra

of $H_3Re_3(CO)_{12}$ in the same frequency range. There was difficulty in finding the hydrogen modes using the latter techniques whereas two strong bands in the IINS spectrum were found at 608 and 312cm^{-1} which were assigned to MnHMn vibrations. An IINS time-of-flight spectrum of $H_3Mn_3(CO)_{12}$ (15) was found to contain two bands at 96(m) and 146(m)cm^{-1} which were assigned to the Mn(H)Mn stretching vibrations of E and A_1 symmetry respectively. They postulated that bands at 608 and 312cm^{-1} were due to the in- and out-of-plane MnHMn deformation. A later BFDDIDO spectrum of $H_3Mn_3(CO)_{12}$ was shown to have a marked similarity to that of $H_2Fe(CO)_4$ (17) in the manner and intensity of the spectral features, which were found at 670(sh), 610(ms), 550(sh), 470(w), 410(w) and 320(vs)cm^{-1}. The bands in the 600cm^{-1} region were assigned to MnHMn deformations but a study of the intensity distribution led to a justification that the 320cm^{-1} band was not an in- or out-of-plane MnHMn deformation. They went on to indicate that since there was a resemblance between the spectra of $H_2Fe(CO)_4$ and $H_3Mn_3(CO)_{12}$ then the hydrogen position, in each case, must be similar. Howard et al (6) assigned Raman bands at 1660cm^{-1} (average value) and 888cm^{-1} (average value) to the antisymmetric and symmetric MnHMn stretches respectively.

(b) Results

Table 5.9 indicates those features from the vibrational of $H_3Mn_3(CO)_{12}$ and Figures 5.15,5.16,5.17 show the 4H5, BFDDIDO and IN1B spectra.

Table 5.9: Bands Associated With H Motion in $H_3Mn_3(CO)_{12}$

IN1B (77K)	BFDDIDO (77K)	4H5 (130K)	IR (77K)	FIR (77K)	Raman (RT)	Raman * (6)	IINS (90K) (15,17)	Assignment
2233(wb) 1971(mb)								Combination/overtones or CO stretches
1661(s)			1660(vw) 1605(wb)			1660(av)		MnHMn antisymmetric stretch
1413(wb)	1363(w)		1362(w)					Combination
1198(mb)	1165(w)							Combination(875+336)overtone(2x606)
983(m)	990(mb)							2nd overtone ($3x336=1008cm^{-1}$)
875(s)	895(mb)					888(av)		MnHMn symmetric stretch
660(sh)	664(w)						670(sh)	overtone($2x336=672cm^{-1}$)
606(vs)	616(s)						610(ms)	MnHMn in-plane deformation
554(sh)	566(sh)						550(sh)	} MnCO deformations
468(wm)	480(w)						470(w)	
433(vw)	435(w)	440(w)					410(w)	MnC stretch
	336(vs)	315(s)		338(w)			320(s)	MnHMn out-of-plane deformation
				320(w)				MnC stretch
	195(wsh) 157(m)			150(m)				} CMnC deformations
		136(m)		144(m)			146(m)	MnMn stretch (A_1')
				116(vw)				CMnC deformation
		100(m)					96(m)	MnMn stretch (E_1)
		58(sh)						} Lattice modes/CMnC deformation
		45(msh)						

* Unknown experimental temperature

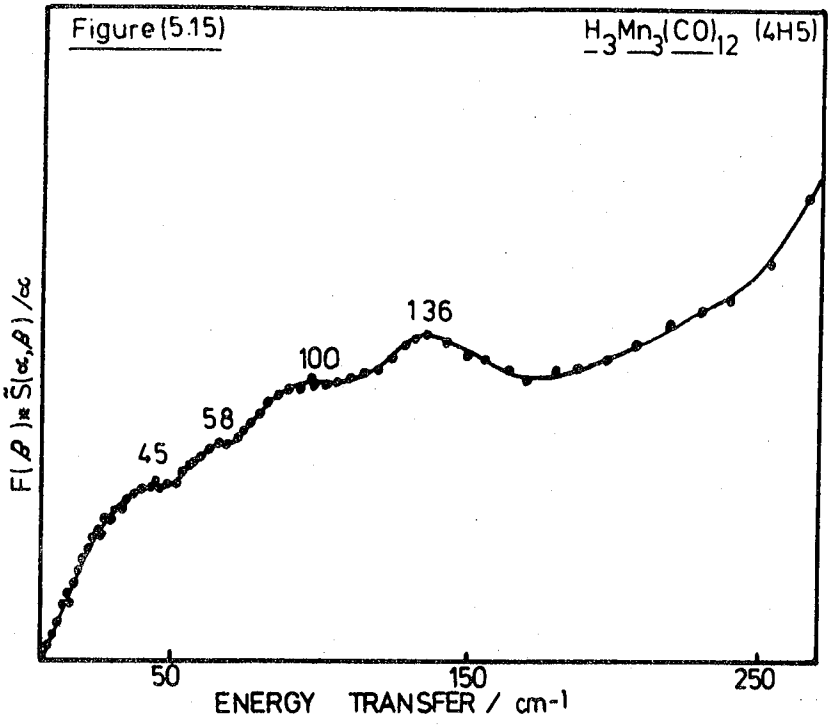
Figure (5.15)
$H_3Mn_3(CO)_{12}$ (4H5)
$F(\beta) \propto \tilde{S}(\alpha,\beta)/\alpha$
45
58
100
136
50
150
250
ENERGY TRANSFER / cm-1

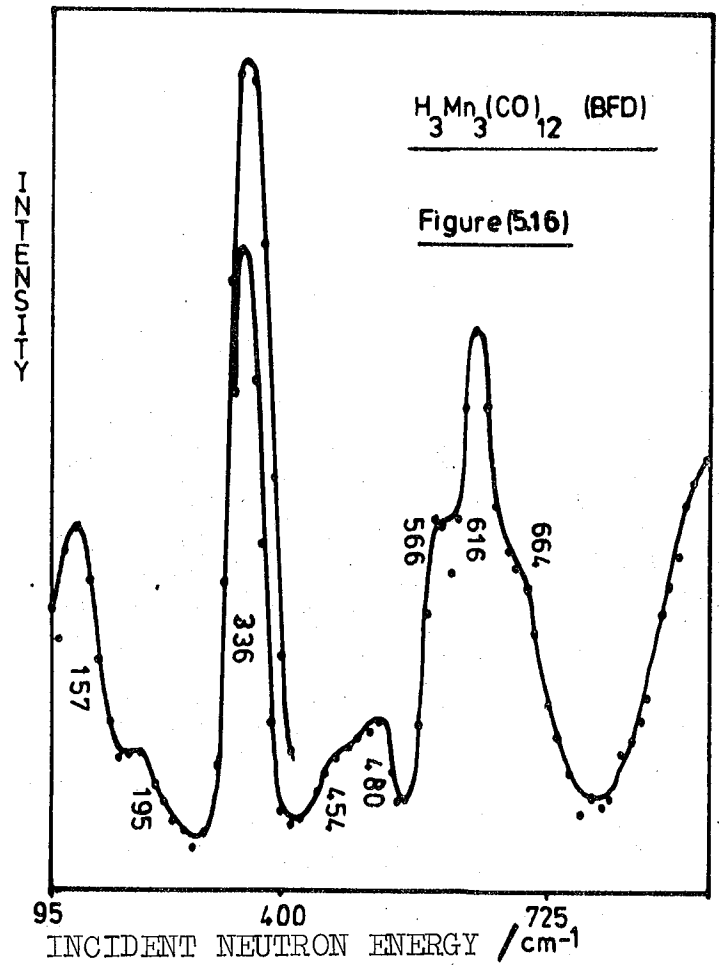
$H_3Mn_3(CO)_{12}$ (BFD)
Figure (5.16)
INTENSITY
157
195
336
454
480
566
616
664
95
400
725
INCIDENT NEUTRON ENERGY / cm-1

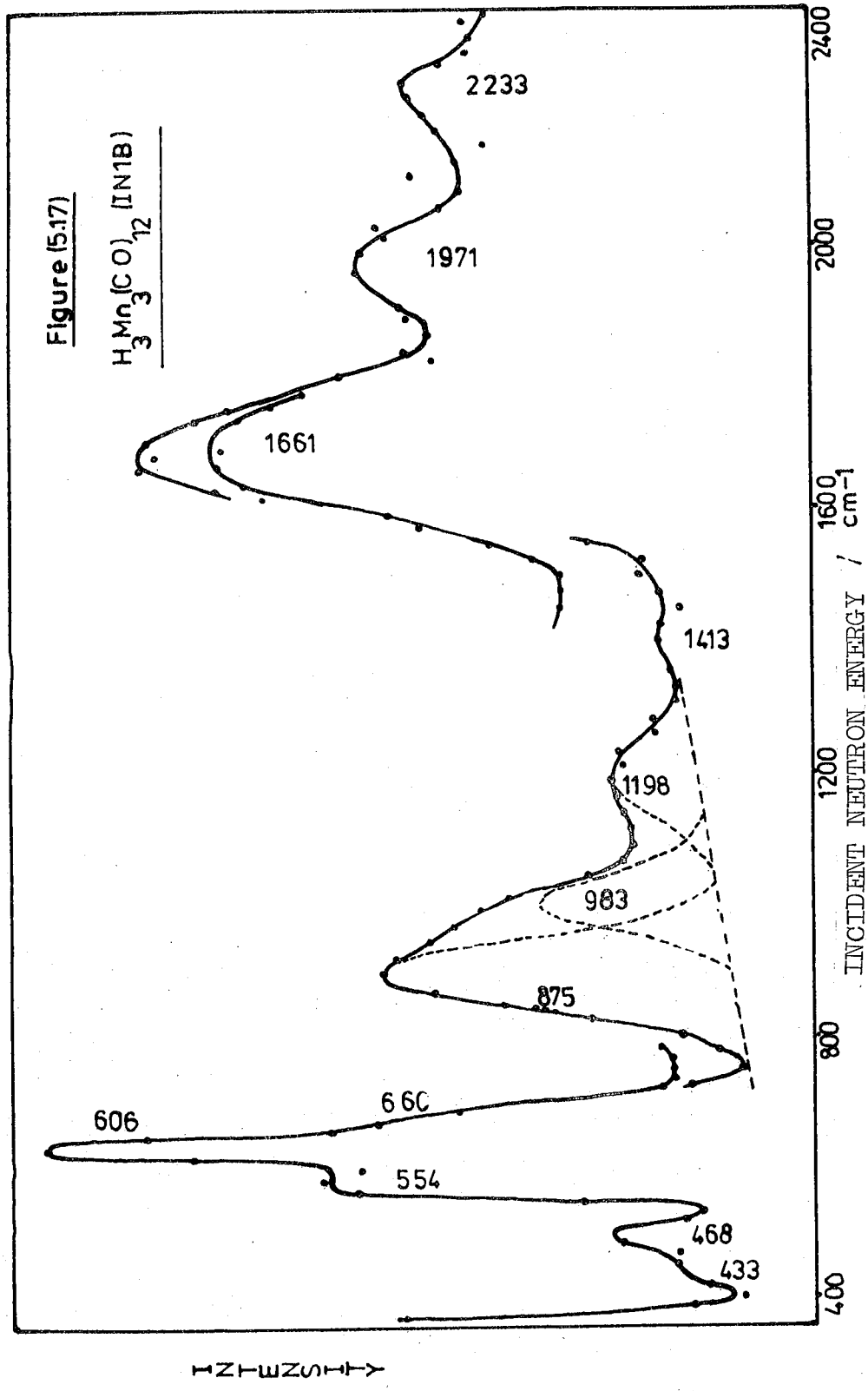

Figure (5.17)

$H_3Mn_3(CO)_{12}$ (IN1B)

(c) Discussion

(i) Mn-Mn Stretch Region

$H_3Mn_3(CO)_{12}$, like $H_3Re_3(CO)_{12}$, has D_{3h} symmetry. The A_1' and E' Mn-Mn stretches are expected to be neutron active and the predicted frequency ratio, using the simple valence force field principle, is $A_1':E' = \sqrt{2}:1$ (22). The 4H5 spectrum, Figure 5.15 is dominated by two broad peaks at 136 and 100cm^{-1} (frequency ratio is 1.36:1). Unfortunately, no Raman data is available on this compound since it decomposed very easily in a Raman beam. The IR spectrum at room temperature has a medium intense band at 146cm^{-1} which, at 90K, was resolved into a doublet at 144 and 150cm^{-1}, is near the MnMn stretch in $Mn_2(CO)_{10}$ at 157cm^{-1} (22). If the 146cm^{-1} IR band is the MnMn stretch then it is likely to be the E' IR active band. If the 136cm^{-1} IINS band is therefore assigned to the E' mode then the A' mode would be expected at $(\frac{\sqrt{2}}{1} \times 136)$cm^{-1} ie 192cm^{-1}. No IINS feature was found in this region. It is felt that the IR band at 146cm^{-1} is a CMnC deformation mode and, in fact, a Raman band is observed at 148cm^{-1} in $Mn_2(CO)_{10}$ and has been assigned to such a deformation (30). This band in $Mn_2(CO)_{10}$ is an E_2 mode and Raman active in D_{4d} symmetry ($Mn_2(CO)_{10}$) but IR active in D_{3h} symmetry ($H_3Mn_3(CO)_{12}$). The presence of this band probably leads to much mixing with the Mn-Mn stretching bands and reduces their intensity somewhat. Thus the two IINS bands at 136 and 100cm^{-1} are assigned to the Mn-Mn stretches of A' and E_1' symmetry respectively. This assignment has been carried out on the basis of the frequency ratio rather than from any IR/Raman supporting evidence.

Finally the IINS band at $45cm^{-1}$ is assigned to a lattice mode because of the bands peak frequency variability with scattering angle, whereas the $58cm^{-1}$ shoulder is assigned to another CMnC deformation.

(ii) Manganese-Hydrogen Deformation and Stretch Region

With D_{3h} symmetry, four MnHMn stretches (A_1', A_2' and $2E'$) and two MnHMn deformations (A_1' and E') are anticipated. The IINS spectra for $H_3Re_3(CO)_{12}$ and $H_3Mn_3(CO)_{12}$, are very similar, except in the assignment of the symmetric stretch. This inconsistency arises from the slightly different MHM geometries. Since the IN1B spectra indicates convincingly that only two bands of major intensity are found in the stretching region, like the previous compounds, the vibrations involving hydrogen are described in terms of their local C_{2v} symmetry rather than the D_{3h} point group. The very strong broad IINS band at $1661cm^{-1}$ is assigned to the antisymmetric stretch. The IR of this compound shows two bands at 1605 and $1660cm^{-1}$ in much the same fashion as $H_3Re_3(CO)_{12}$. The same postulate, as for $H_3Re_3(CO)_{12}$, is put forward that some asymmetry in the hydrogen position may exist and this is confirmed in the actual diffraction analysis of $H_3Mn_3(CO)_{12}$ (29). The broad IINS band at $1661cm^{-1}$ indeed could hold a weaker component in its low frequency wing. The two IR bands could be caused by the solid state effect. If this mode is split then similar splitting of other bands would be expected. In fact, as Howard et al (6) reported, the symmetric MnHMn stretch was split into two Raman bands at 860 and $888cm^{-1}$ (average value = $875cm^{-1}$). No further splitting was found in the IR/Raman spectra. In accord with the Howard et al (6)

Raman study, the IINS band centred at 875cm^{-1} is assigned to the symmetric MnHMn stretch. The broad band at 875cm^{-1} contains a high frequency shoulder and a further band exists at 1198cm^{-1}. Using the du Pont curve resolver, the shoulder component was observed at ~ 983cm^{-1}. The intensity ratio of the three bands at 875: 983: 1198cm^{-1} is approximately 2.6: 1.2: 1.0. As with $H_3Re_3(CO)_{12}$, the 983cm^{-1} feature can be assigned to the second overtone of the strongest IINS band at 336cm^{-1} (3 x 336 = 1008cm^{-1}). The first overtone is assigned at 660cm^{-1}. The band at 1198cm^{-1} could be assigned to the first overtone of the 'in-plane deformation' at 606cm^{-1} (2 x 606 = 1212cm^{-1}), however, a preferred assignment is a combination band of the out-of-plane deformation and the symmetric stretch (875 + 336 = 1211cm^{-1}). This is preferred since the combination can be readily assigned with greater confidence in $H_3Re_3(CO)_{12}$ and $HW_2(CO)_9NO$ in the 1400-1500cm^{-1} region. Perhaps both combination and first overtone produce some of the experimental IINS intensity at 1198cm^{-1}.

At lower frequency there are two very strong IINS bands which can be assigned to the in and out-of-plane deformations. The out-of-plane deformation is observed in the IR spectrum at 320-338cm^{-1}. White and Wright tentatively assigned <u>all</u> the bands at 670, 610 and 550cm^{-1} to the MnHMn deformation vibrations but did not assign the bands at 470, 410 and 320cm^{-1} (17). From the IINS intensities it would appear that the 320 and 606cm^{-1} IINS bands are fundamental vibrations whereas previously this could not be justified. Further, the band at 660cm^{-1} is assigned to the second harmonic of the out-of-plane deformation (2 x 336 = 664) with analogy to most other

hydridocarbonyls. The bands at 480 and 435cm^{-1} are assigned to either weak combinations or two MnC stretching vibrations weakly activated in the IINS spectrum by associated hydrogen motion. The weak shoulder at 566cm^{-1} could also be similarly assigned, being due to associated hydrogen motion involved in an MCO deformation mode. An alternative is that it is due to some splitting of the 'in-plane deformation'. This may be due to the same effect which produc d the two IR bands at 1605 and 1660cm^{-1} and, therefore, the broadening of the IINS band at 1661cm^{-1}. The separation of the high frequency IR bands was 55cm^{-1} whereas the separation between the two IINS bands at 566 and 616cm^{-1} is 50cm^{-1}. It must be noted though that in $HRe_3(CO)_{14}$, the splitting produced doublets of equal intensity whereas in $H_3Mn_3(CO)_{12}$ the higher frequency band, at 616cm^{-1}, is of greater intensity.

5.2.5. $H_4Ru_4(CO)_{12}$

(a) Previous Work

Johnson et al (31) found bands in the IR spectra of $H_4Ru_4(CO)_{12}$ and $D_4Ru_4(CO)_{12}$ at 1284 and 902cm^{-1} respectively and these were assigned to the Ru-H(D)-Ru stretching vibrations. It was shown that the RuHRu band was broader than the respective RuDRu band. It was also reported that the frequencies appeared higher than those found in hydrides such as $H_3Re_3(CO)_{12}$. A closer investigation of the IR spectra of $H_4Ru_4(CO)_{12}$ showed bands at 1605 and 1272cm^{-1} (32,12). A Raman study of $H_4Ru_4(CO)_{12}$, $H_2D_2Ru_4(CO)_{12}$ and $D_4Ru_4(CO)_{12}$ showed bands at 1585 and 1290cm^{-1} (H_4 form), 1587, 1291, 1156 and 909cm^{-1} (H_2D_2 form) and 1153 and 909cm^{-1}

(D_4 form) (32). This study implied that the spectrum of the H_2D_2 analogue was an exact supposition of that of the H_4 and D_4 species and from this it was postulated that the various Ru-H(D)-Ru oscillators were uncoupled (32). Andrews et al (32) went on to discuss the possible number of fundamental vibrations expected in such a system: (D_{2d}) Raman active RuHRu stretching modes (A_1, B_1, B_2 and 2E) and 3 IR active modes (B_2 and 2E). However, the Raman consisted of two bands at 1585 and 1290cm^{-1} and the IR of two bands at 1605 and 1272cm^{-1} which appeared to the authors to be noncoincident. If the Ru-H(D)Ru entities were completely uncoupled then 3 RuHRu modes were predicted ($2A_1 + B_1$) with one A_1 band at low frequency. The authors (32) suggested the form of these vibrations as shown in Figure 5.18.

Figure 5.18: Vibrational Description of Andrews et al (31)

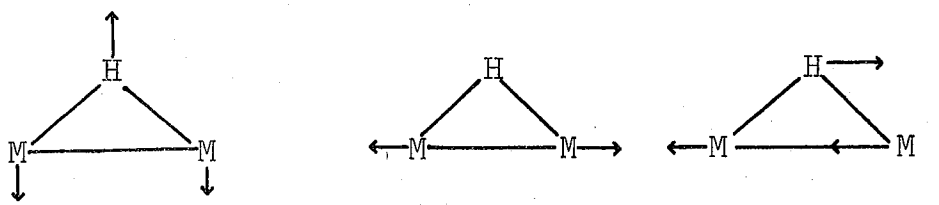

A_1(R,IR) A_1(R,IR) B_1(R,IR)

(b) Results

Table 5.10 lists the data collected from the vibrational study of $H_4Ru_4(CO)_{12}$. Figures 5.19,5.20,5.21 show the 4H5, BFDIDO and IN1B spectra of the compound.

(c) Discussion

$H_4Ru_4(CO)_{12}$ belongs to the D_{2d} point group and has vibrations of $13A_1 + 10A_2 + 10B_1 + 13B_2 + 22E$ symmetry. The

Table 5.10: Bands Associated With H Motion in $H_4Ru_4(CO)_{12}$

IN1B (77K)	BFDDID0 (77K)	4H5 (130K)	IR (77K)	FIR (77K)	Raman (RT)(32)	IR (RT)(32)	IR (RT)(31)	Assignment
2274(w) 1935(mb)								Combination bands or/ CO stretch
1600(m)			1605(w) 1585(vw)		1605(vw) 1585(w) 1310(w)	1605		RuHRu antisymmetric stretch
1294(s)	1320(mb)		1290(mb) 1260(w)		1290(m) 1272(w)	1272	1284	RuHRu symmetric stretch
1201(ms)	1176(wb)		1192(mb)					Overtone(?)(2x619=1238cm^{-1})
942(m)	936(wb)		936(w)					Combination(619+346=965cm^{-1})
673(wm)	704(wsh)		676(w)					Overtone(2x346=692cm^{-1})
623(vs)	619(vs)	600(vs)						RuHRu In-plane deformation
542(w) 472(w)	452(wb)	460(w)		369(wsh)				RuCO deformations and RuC stretches
359(vs)	346(vs)	339(vs)		352(w)				RuHRu out-of-plane deformation
				346(w)				RuC stretch
	208(w)	270(sh) 221(vw)		232(vw) 172(wm)				CRuC deformations
	121(m)	140(m)		154(m) 116(vw) 109(vw)				RuRu stretch CRuC deformations
		95(s)		101(vw) 91(vw)				Ru(H)Ru stretch
		57(m) 34(sh) 23(wsh)						CRuC deformation Lattice modes

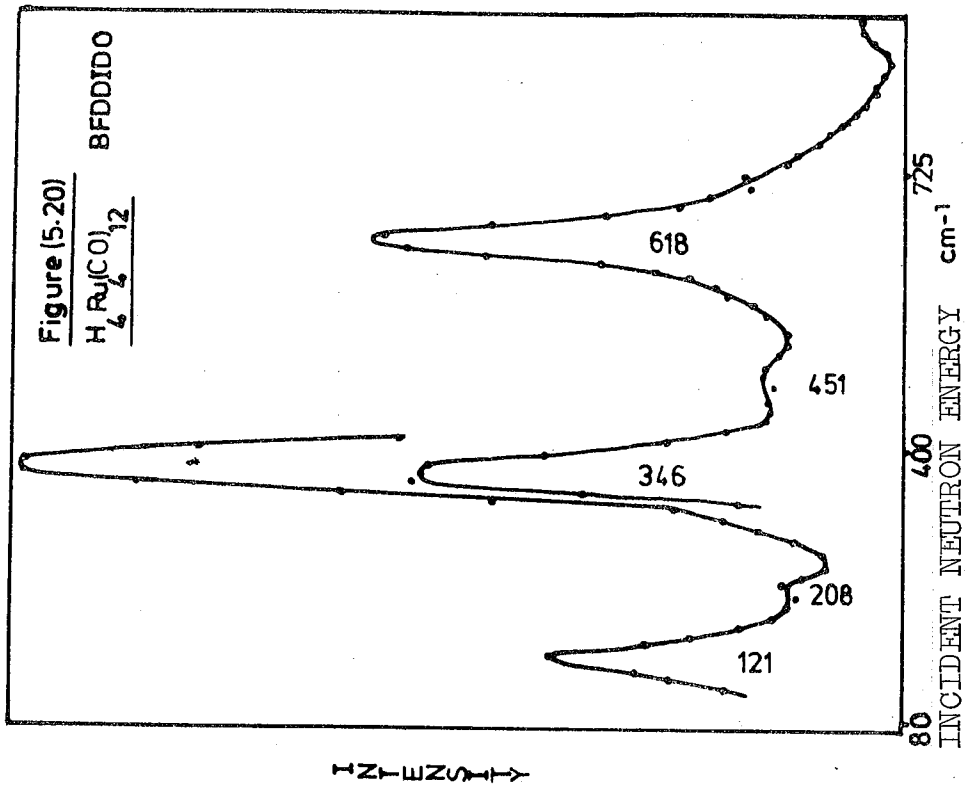
Figure (5.20)
$H_4Ru_4(CO)_{12}$
BFDDIDO
618
451
346
208
121
80
400
725
INCIDENT NEUTRON ENERGY cm-1

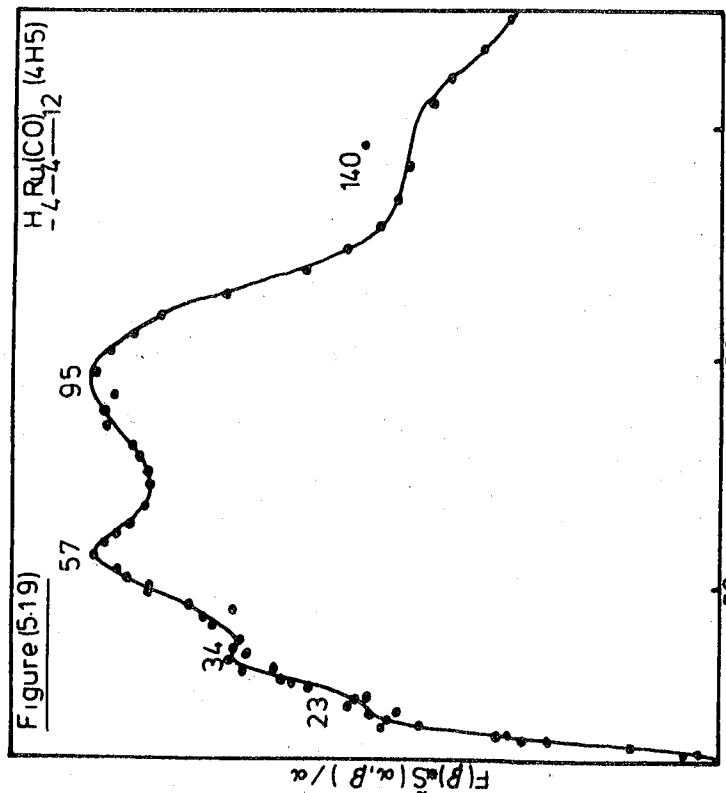
Figure (5.19)
$H_4Ru_4(CO)_{12}$ (4H5)
57
95
140
34
23
50
100
150
ENERGY TRANSFER / cm-1

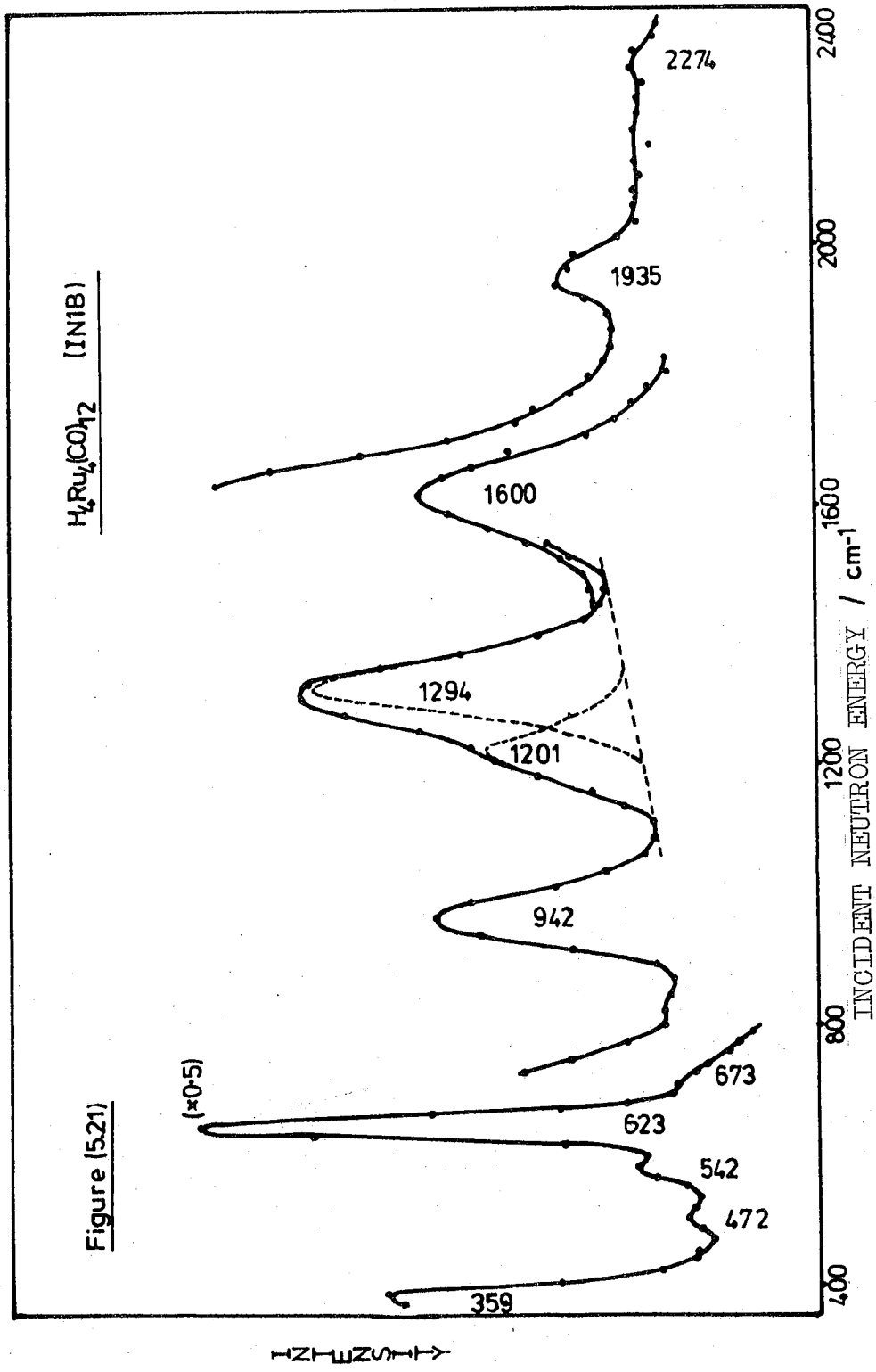
$H_2Ru_4(CO)_{12}$ (IN1B)
2274
1935
1600
1294
1201
942
673
623
542
472
359
(×0·5)
400
800
1200
1600
2000
2400
INCIDENT NEUTRON ENERGY / cm^{-1}

Figure (5.21)

vibrations involving hydrogen motion may be crudely described as shown in Table 5.11.

Table 5.11 D_{2d} Vibrational Analysis

Vibration	Symmetry	Activity
RuHRu stretch	A_1	Raman
	A_2	Inactive
	B_1	Raman
	B_2	IR/Raman
	2E	IR/Raman
RuHRu deformation	A_2	Inactive
	B_2	IR/Raman
	E	IR/Raman
'Bridged' RuRu stretch	A_1	Raman
	B_1	Raman
	E	IR/Raman
'nonbridged' RuRu stretch	A_1	Raman
	B_2	IR/Raman

(i) Ruthenium-Ruthenium Stretch Region

$H_4Ru_4(CO)_{12}$ has D_{2d} symmetry and thus 3 Ru(H)Ru (A_1+B_1+E) and 2 RuRu (A_1+B_2) stretching vibrations are expected. However, only those metal-metal stretching vibrations of the same symmetry as the RuHRu deformation vibrations, in the same low frequency ($< 700cm^{-1}$) region, are activated in the IINS spectrum. The expected deformations have A_2+B_2+E symmetry and thus only the Ru(H)Ru stretch of E symmetry and

the RuRu stretch of B_2 symmetry will be anticipated and, further, both bands are IR and Raman active. The band frequencies should also be relatively close to one another and only separated by the effect of the hydrogen bridging. This is arrived at by considering, initially, the parent "$Ru_4(CO)_{12}$" parent carbonyl of Td symmetry. In this hypothetical compound the RuRu stretches will of A_1+T_2+E (T_d) symmetry. On degrading the molecular symmetry to D_{2d} in $H_4Ru_4(CO)_{12}$ the A_1 mode transforms into another A_1 mode, the E mode into A_1+B_1 and the T_2 mode into B_2+E, by relaxation of the symmetry rules. Of these only the B_2 and E symmetry vibrations are expected to be activated in the neutron spectrum of $H_4Ru_4(CO)_{12}$. These bands are probably split to some degree because of the bridging/non-bridging situation. The 'bridging' E mode should probably be of lower frequency than the B_2 mode and of greater intensity in the IINS spectrum since there are twice as many Ru(H)Ru bonds but the likeihood of it mixing to a greater degree with CRuC deformations will work against this and reduce the IINS intensity with respect to the B_2 mode. The RuRu stretches of $Ru_3(CO)_{12}$ are found at 151cm^{-1} (E' mode) and 187cm^{-1} (A_1' mode) (28). White and Wright found similar bands in $HRu_3(CO)_{12}PF_6$, at 145 and 180cm^{-1} (15). From Figure 5.19 it can be seen that the metal-metal stretching frequencies are probably found at lower values in $H_4Ru_4(CO)_{12}$ than in either $Ru_3(CO)_{12}$ or $HRu_3(CO)_{12}PF_6$. $Ru_3(CO)_{12}$ has very strong Raman active CRuC deformations at 48 and 85cm^{-1} (28) and a band at 57cm^{-1} is assigned as such in the IINS spectrum of $H_4Ru_4(CO)_{12}$. These bands are IINS active due to associated hydrogen motion. It would also appear reasonable to assign the strongest IINS band at

102cm^{-1} to a RuRu stretch and the higher frequency broad band at 140cm^{-1} to the other stretch. There are no features above 140cm^{-1}, except the very weak band observed at ~ 170-180cm^{-1}, to indicate the RuRu stretch vibrations are similar to those found in $Ru_3(CO)_{12}$ and $HRu_3(CO)_{12}PF_6$. Further, from crude intensity considerations the E mode would be expected to be stronger in the IINS than the B_2 mode. This is, infact, the case, in Figure 5.19 where the 102cm^{-1} band is much stronger than that at 140cm^{-1}.

The very low frequency shoulders at 23 and 34cm^{-1} are assigned as lattice modes. The RuRu stretches should be visible in both the IR and Raman spectra. There are coincident IR bands at 101 and 154cm^{-1}.

(ii) Ruthenium-Hydrogen Vibration Region

Andrews et al (32) could not ascertain whether the (RuHRu) species were totally uncoupled from the molecular symmetry of D_{2d}, forming separate C_{2v} units within the whole $H_4Ru_4(CO)_{12}$ unit, from observations of weak IR and Raman features. They said that there were non-coincident peaks in the IR and Raman spectra at 1605/1585 and 1272/1290cm^{-1}. This was based on the Raman spectra shown in reference (12) and on unpublished IR work. The temperature of the studies was not stated. However, it can be shown that they are coincident and that they probably arise from the same vibrations. This is done by looking in detail at the areas of interest in the IR (our work) and Raman spectra (12). One can tentatively say 1) there is more Raman intensity in the 1585cm^{-1} band rather than the 1605cm^{-1}, 2) that there is more Raman intensity at 1290cm^{-1} rather than the 1272cm^{-1}

band 3) the IR band at 1605cm^{-1} is more intense than the 1585cm^{-1} band and 4) there is a broad feature at 1287-1292 in the IR, a weak band at 1260cm^{-1} but no feature at 1272cm^{-1}, which is contrary to that stated in (29) if the temperature of study is the same. These weak features from the actual spectra are enlarged in Figure 5.22.

Figure 5.22 (cm-1)

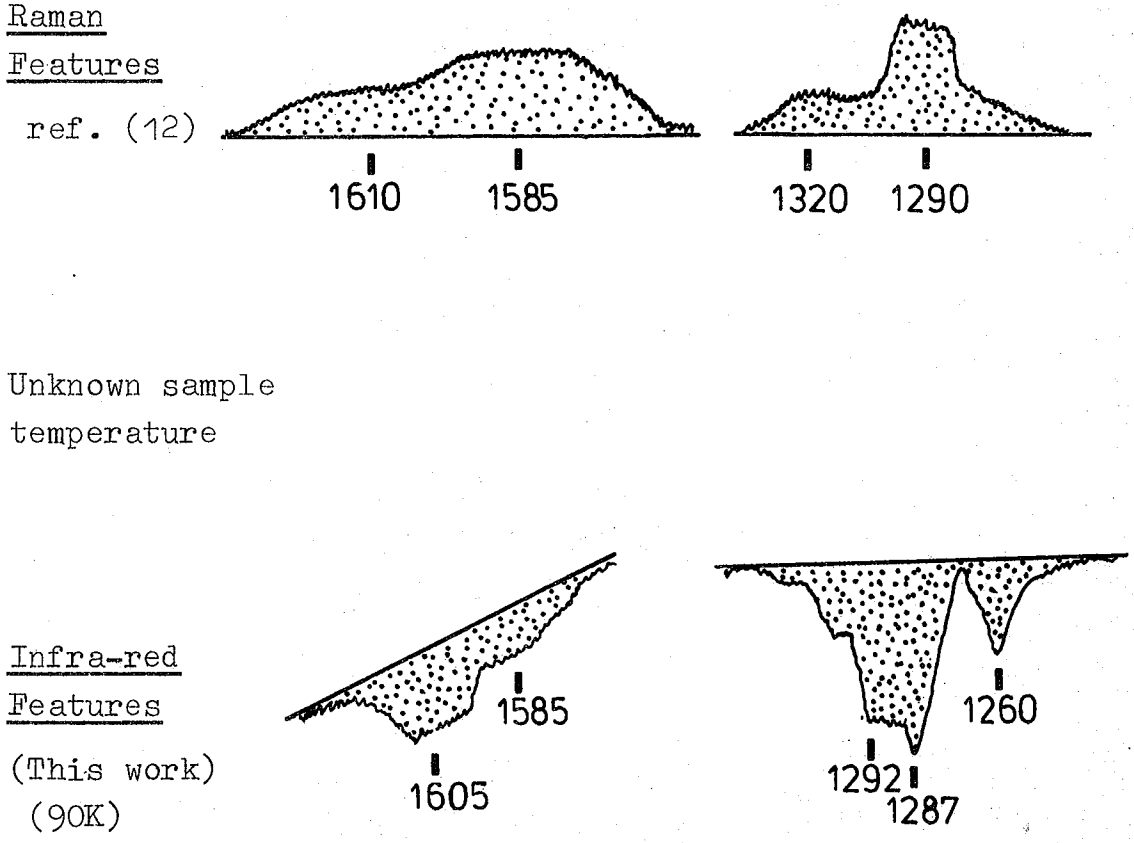

It can further be noted that the IR spectrum contains weak to medium intense features which are coincident with all the IINS bands. In the Raman spectra displayed by

Kaesz and Saillant(12,32), only the features in the 1600 and 1300cm^{-1} regions are observed and the peaks at 1217, 936 and 673 are not visible (under the conditions of the experiment). From this evidence it would appear that since all the modes were successfully observed in the IR spectrum then the symmetry rules must be being relaxed from the D_{2d} structure. Distortion of $H_4Ru_4(CO)_{12}$ may be taking place lowering the D_{2d} symmetry though there is no crystallographic evidence of this. Certain $H_4Ru_4(CO)_{12}$ derivatives have been studied showing that various structural isomers are formed, which are convertable. For example two isomers, one of C_2 or C_{2v} and one of C_{3v} symmetry are known with $((C_6H_5)_4As)(Ru_4H_3(CO)_{12})$(32) and two isomers of C_2 and C_{3v} are known with $((Ph_3P)_2N)(H_3Ru_4(CO)_{12})$ (33).

For a D_{2d} description of the $H_4Ru_4(CO)_{12}$ molecule, 6 fundamental stretching vibrations should be found above, say, 700cm^{-1} and 3 fundamental deformation vibrations should be found below this value for motions involving hydrogen. From Figure 5.20,5.21 it can be seen that this is not the case. Some IINS bands are broad and may be split to a degree due to solid state effects but the spectra only show in total two fundamental vibrations in the deformation region and 2 vibrations in the stretching region, ie five short of the D_{2d} description. If the vibrations were totally uncoupled perhaps the $(\mu_2\text{-H})M_2$ description situation could be used where it was shown that two deformations and two stretches can be indentified

The IINS band at 1600cm^{-1} is assigned to the antisymmetric stretch. From the IR and Raman studies it would appear that, possibly due to a solid state effect, that this singly

degenerate band has been split. One component after splitting appears to be more Raman active, the other more IR active. The effect may occur because a number of differing sites may exist for individual molecules within the crystal. The symmetric stretch region contains three bands of intensity at 942, 1201 and 1294cm^{-1}. The symmetric stretch is assigned to the strongest band at 1294cm^{-1} from IINS intensity considerations and from the IR and Raman data available. Again, this mode may be split to some degree as shown in the IR and Raman spectra in Figure 5.22. An intrigueing part of the IINS spectrum of $H_4Ru_4(CO)_{12}$ is the region containing the two bands at 1201 and 942cm^{-1}. These are observed in the IR spectrum at 77K but **not** in the Raman spectrum (31). There are possibly various explanations of the pair. They could be the second and third overtones of the strongest band in the spectrum Figure 5.20 at 346cm^{-1}. However, they would appear to be more intense than the 673cm^{-1} band which is assigned to the first overtone. This is therefore dismissed. The band at 1201cm^{-1} may be the first overtone of the strong IINS band at 623cm^{-1} (2 x 623 = 1246cm^{-1}). The intensity of the 942cm^{-1} IINS band indicates that it may be due to a fundamental mode involving hydrogen motion. An explanation may lie in the following. $H_4Ru_4(CO)_{12}$ has an IINS band at 1935cm^{-1} of unusual intensity, compared with other hydridocarbonyls. Perhaps, there could be a possibility that vibrations of terminally bonded hydrogen could be seen in this neutron scattering experiment. N.M.R. spectra of the related $H_4Ru_4(CO)_{10}(Ph_2PCH_2CH_2PPh_2)$ (35) are consistent with an edge-terminal-edge hydrogen scrambling pathway. Perhaps, if the hydrogen resides long enough at the terminal position, at

the temperature of the experiment, then the faster ($\sim 10^{11}$Hz as against $\sim 10^{8}$Hz in n.m.r.) neutron scattering technique may have measured its vibrational spectrum. Terminal RuH stretching frequencies are usually found in the 1900-200cm^{-1} region (36) and terminal RuH deformations occur in the 700-950cm^{-1} region (37). Peaks in the IINS spectra at 942 and 1935cm^{-1} in $H_4Ru_4(CO)_{12}$ may be indicative of this effect. A less exciting possibility of the cause of the 942cm^{-1} IINS band may be that it is a combination band of the two deformation modes, which lie at 346 and 619cm^{-1} (total = 965cm^{-1}).

The region below 700cm^{-1} in the IINS spectrum contains two strong bands at 346 and 619cm^{-1} and, with analogy to the previous carbonyls, they are assigned to the in-plane and out-of-plane deformations respectively. The weak band at 673cm^{-1} is probably the second harmonic of the strongest spectral band at 346cm^{-1}. There is little fine structure in this region and no splitting of the major bands as found in $HRe_3(CO)_{14}$ and $H_2Os_3(CO)_{10}$. The weaker features at 370, 452 and 542cm^{-1} are either (1) weak combination bands involving the strongest IINS fundamental at 346cm^{-1} and the RuRu stretches in the 50-200cm^{-1} region or (2) weakly neutron activated RuCO deformations and RuC stretching bands due to associated hydrogen motion on the the mixing of RuHRu deformation bands, at 346 and 619cm^{-1}, of high intensity in the IINS spectrum with RuCO bands, of the same symmetry. This associated hydrogen motion could well be viable since the thermal ellipsoids of the hydrogen atoms are large in this molecule and the ability for the

hydrogen to move from, say, (μ_2-H) to (μ_3-H) or (μ_1-H) positions is known to be easy. Thus, one can envisage the light hydrogen atoms being relatively free to move and, when lying in an environment where there is a dense carbonyl population, one could envisage some association of behaviour.

Thus, in conclusion, the spectra would seem to indicate that there is a decoupling of the hydrogen motions in $H_4Ru_{14}(CO)_{12}$ forming four separate C_{2v} type systems. There are certainly not enough fundamental vibrations in the IINS spectra to indicate that the vibrations involving hydrogen merit a D_{2d} symmetry description. Once again there are still too many vibrations to imply a single C_{2v} symmetry as indicated by Andrews et al (32) but, from the IINS studies of the (μ_2-H) compounds a simple C_{2v}-type spectrum is not found in the solid state. The IINS bands at 1600, 1294, 619 and 346cm^{-1} are indicative of symmetric and antisymmetric stretches and in-plane and out-of-plane deformations. Various possibilities for an explanation exist for the assignment of the 942cm^{-1} vibration of which the combination band is more likely. The form of the vibrations are the same as found in $HRe_3(CO)_{14}$ and $HW_2(CO)_9NO$. All the stretching and deformation modes are seen in the IR at 90K and this is indicative of a solid state effect.

5.2.6. $H_2FeRu_3(CO)_{13}$

(a) Previous Work

The IR spectrum of the compound has been reported (38) yet no feature, indicating a possible hydrogen mode, was found between the MCO deformation vibrations (< 650cm^{-1}) and the CO stretching vibrations (> 1850cm^{-1}).

(b) Results

Table 5.12 lists the data collected from the vibrational study of $H_2FeRu_3(CO)_{13}$. Figures 5.23, 5.24, 5.25 show the 4H5, BFDDIDO and IN1B spectra of the compound.

(c) Discussion

$H_2FeRu_3(CO)_{13}$ has C_s symmetry and, thus, the following vibrations: $47A_1 + 43A_2$. Those vibrations involving hydrogen are summarized in Table 5.13. However, it is felt that the vibrations involving hydrogen can be discussed in terms of C_{2v} symmetry.

Table 5.13: C_s Vibrational Analysis

Vibration	Number and Symmetry	Activity
RuHRu stretch	$2A_1 + 2A_2$	IR and Raman
RuHRu deformation	$A_1 + A_2$	
'bridged' RuRu stretch	$A_1 + A_2$	
'non-bridged' RuRu stretch	A_1	
'non-bridged' FeRu stretch	$2A_1 + A_2$	

(i) Metal-Metal Stretch

Since the RuHRu deformations are of A_1 and A_2 symmetry then all the M-M stretches are expected to be neutron active, though the degree of activity must be uncertain. The description of the M-M vibrations as being due to specific parts of the molecule, e.g. an A_1 mode due to an Ru(H)Ru

Table 5.12: Bands Associated With H Motion in $H_2FeRu_3(CO)_{13}$

IN1B (77K)	BFDDIDO (77K)	4H5 (130K)	IR (77K)	FIR (77K)	Assignment
2177(vw) 2009(vw)					Combination bands and/or CO stretch
1471(msh)			1465(wb) 1395(wm)		RuHRu antisymmetric stretch
1322(vs)					RuHRu symmetric stretch
1104(wb)					2nd overtone ($3 \times 362 = 1086 cm^{-1}$)
999(m)	996(w)				Combination ($362+639=1001 cm^{-1}$)
732(sh)	732(sh)				Overtone($2x362=724 cm^{-1}$)
646(vs)	639(s)				RuHRu in-plane def.
538(vw) 405(sh)	525(vw) 427(sh)				RuCO deformations and RuC stretches
	385(sh)			360(sh)	
362(s)	348(s)	370(sb)			RuHRu out-of-plane def.
	208(wsh)			212(m)	Fe(CO)Ru stretch
		160(wm)		164(wm)	FeRu stretch
				152(w)	CRuC deformation
	133(m)	130(m)		143(m)	RuRu stretch
		100(m)		100(wb)	Ru(H)Ru stretch
		70(w)			CRuC deformation

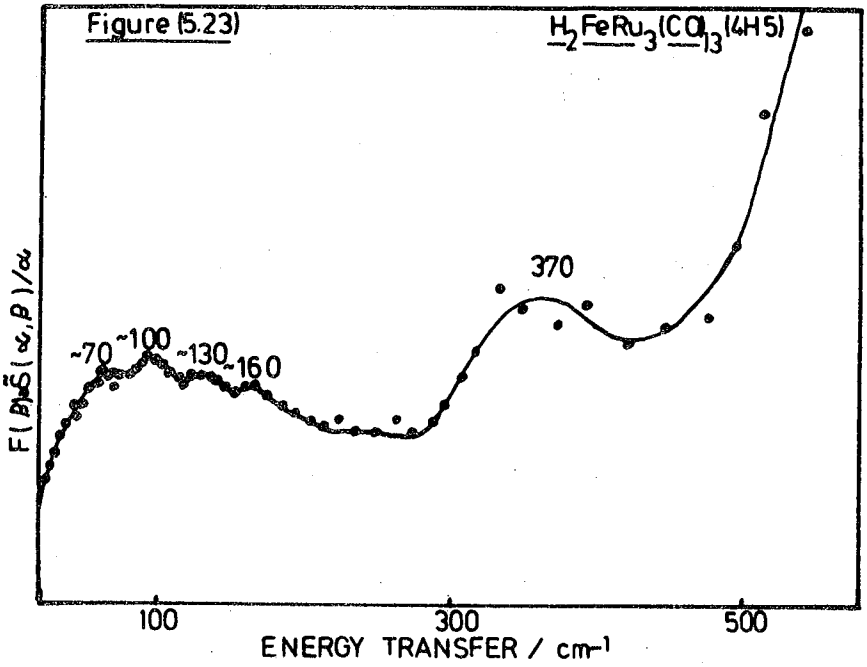
Figure (5.23)
$H_2FeRu_3(CO)_{13}$ (4H5)
$F(\beta)\tilde{S}(\alpha,\beta)/\alpha$
~70
~100
~130
~160
370
100
300
500
ENERGY TRANSFER / cm⁻¹

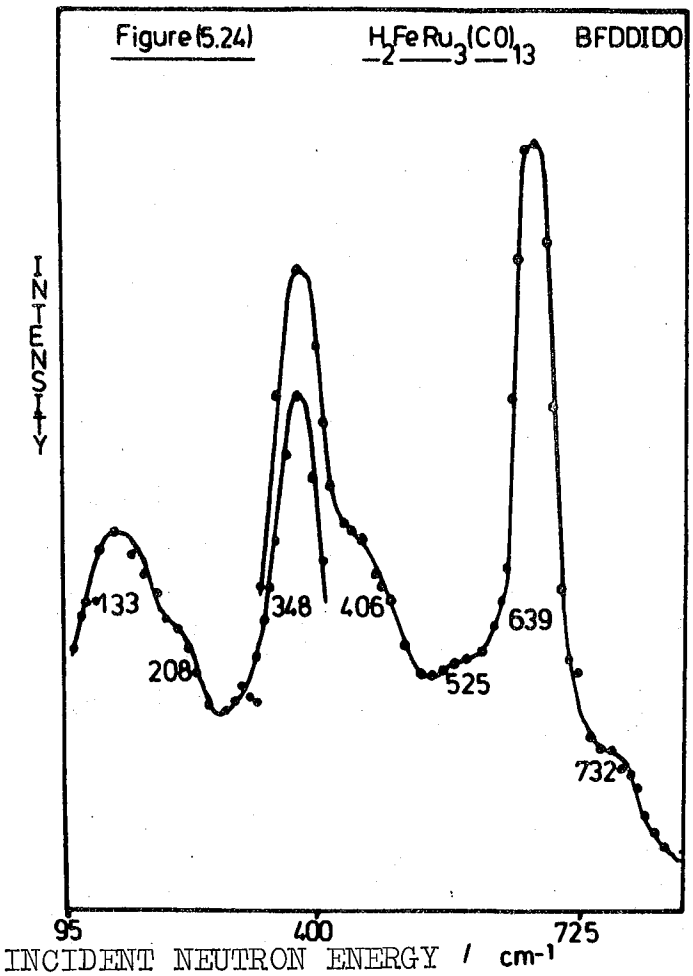
Figure (5.24)
$H_2FeRu_3(CO)_{13}$ BFDDIDO
INTENSITY
~133
208
348
406
525
639
732
95
400
725
INCIDENT NEUTRON ENERGY / cm⁻¹

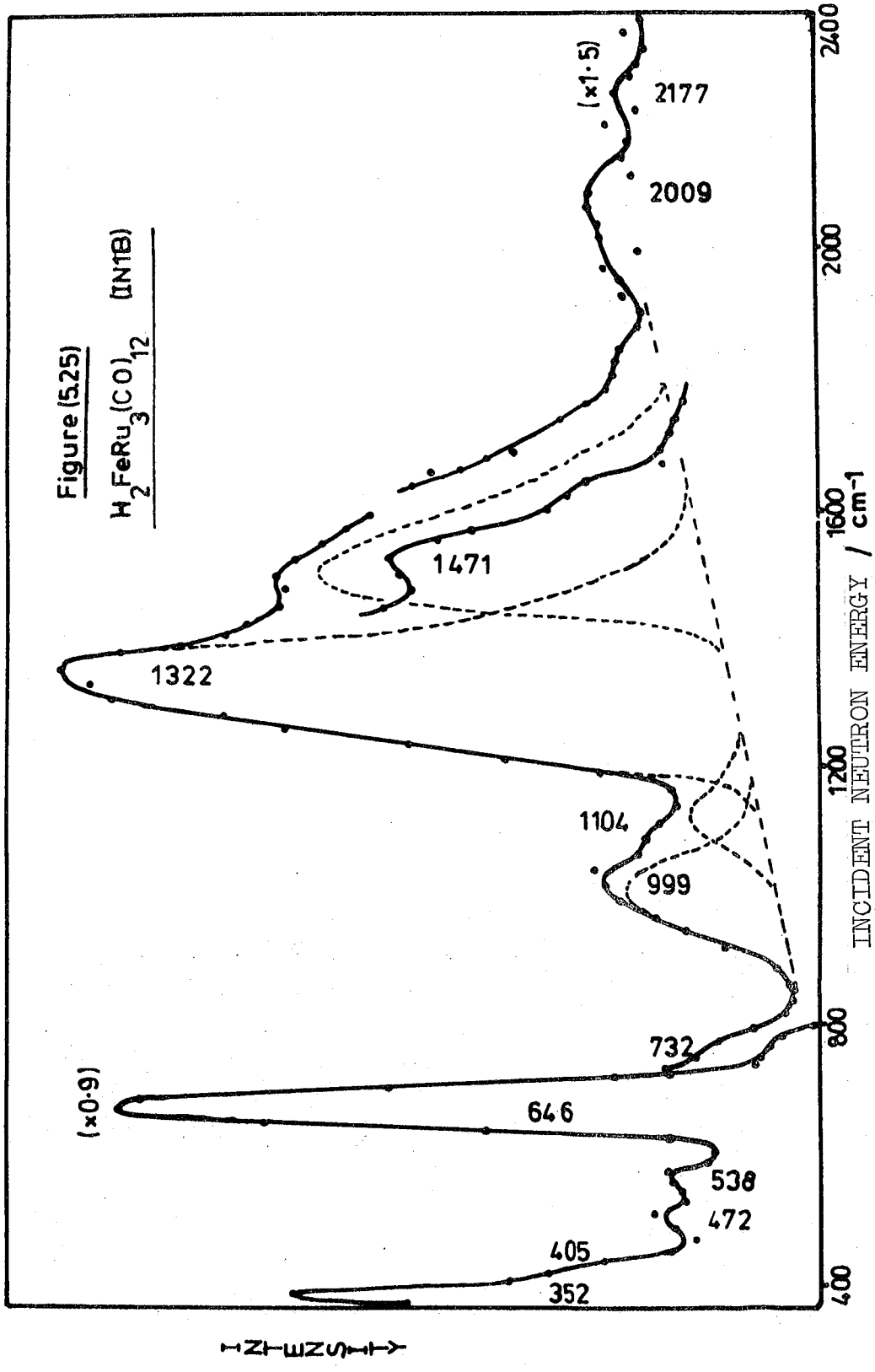

Figure (5.25)

$H_2FeRu_3(CO)_{12}$ (IN1B)

stretch, is an approximation which becomes less viable as the force constants and masses involved converge. Therefore the normal mode description is very approximate. The actual time-of-flight spectrum, Figure 5.23, consists of a broad band in the 50-200cm^{-1} region It would be consistent to assume the band at 100cm^{-1} is the Ru(H)Ru stretch, as found in $H_4Ru_4(CO)_{12}$. This assignment implies that the Ru(H)Ru bond is unaffected by the perturbation caused by the substitution of the apical Ru atom for an Fe atom and by the removal of two other hydrogens from $H_4Ru_4(CO)_{12}$. A related problem has been discussed by Kettle and Stanghellini (28) in connection with $Ru_2Os(CO)_{12}$ and $RuOs_2(CO)_{12}$ where it is thought that the effect of the odd atom, M, on the M'-M' stretch is not electronic but only mechanical and little changes are found ie. the Os-Os stretch in $Os_3(CO)_{12}$ and $Os_2Ru(CO)_{12}$ is identical. Since there is little perturbation on replacement of the Ru atom for an Fe atom then the non-bridged RuRu stretch found at ~ 140cm^{-1} in $H_4Ru_4(CO)_{12}$ would not be shifted to any degree in $H_2FeRu_3(CO)_{13}$. However, the spectrum of $H_2FeRu_3(CO)_{13}$ is poorly resolved though there may be some intensity at 130cm^{-1}. Alternatively the intensity at 160cm^{-1} could be due to this RuRu stretch. It may be expected that the FeRu stretching vibrations may be weakly neutron active. The carbonyl-bridged Fe-Fe stretch in $(\eta^5\text{-}C_5H_5)Fe_2(CO)_4$ and $Fe_3(CO)_9$ lies above 200cm^{-1} and the carbonyl-bridged RuRu stretch (e.g. in $(\eta^5\text{-}C_5H_5)_2Ru_2(CO)_4$) lies at 221cm^{-1} (39). It would appear reasonable that the carbonyl-bridged Fe-Ru stretch would then lie at such a high frequency. The weak intensity at ~ 208cm^{-1} in the BFDDIDO spectrum Figure 5.24

is assigned to this particular vibration.

(ii) Ruthenium-Hydrogen Stretching Region

In comparing the IINS spectra of $H_2FeRu_3(CO)_{13}$ and $H_4Ru_4(CO)_{12}$, Figures 5.24, 5.25, 5.20, 5.21, it is immediately seen that the antisymmetric stretch must lie at a lower and the symmetric stretch at a higher frequency in $H_2FeRu_3(CO)_{13}$. This, taken with the fact that the bridged RuRu distancesin $H_2FeRu_3(CO)_{13}$ are shorter than those that exist in $H_4Ru_4(CO)_{12}$, is indicative of the possible differing bridging geometry that may exist in both. The IINS spectrum is dominated by the double peak in the 1400cm^{-1} region comprising of a strong feature at 1322cm^{-1} and a shoulder at 1471cm^{-1}. Since these are the two strongest features above 650cm^{-1} they are assigned to the antisymmetric and symmetric stretches. Two features were found in the IR (77K) at 1395 and 1465cm^{-1}. These were not reported by Yawney and Stone (38). Unfortunately, no Raman data was collected on this deep red compound since it decomposed very readily leaving a Ru/Fe deposit even under very low laser power. The antisymmetric stretch was assigned to the 1471cm^{-1} band because if it had been assigned to the 1322cm^{-1} band a very odd bridging geometry would be implied, which would have created a very small RuHRu bond angle and, thus, an unacceptably short RuHRu bond, if the RuH bond distance was similar to that found in other (μ_2-H) complexes.

Both the bands at high frequency have very strong intensity. The use of the curve resolver in this region is, unfortunately, ambiguous due to the change in monochromator plane at ~ 1600cm^{-1}. The background level is difficult to

set in the best of circumstances and it cannot be set with confidence in this case. However, using the curve resolver, the intensity of these bands at 1471 and 1322cm^{-1} is approximately the same though the FWHH of the 1471cm^{-1} shoulder is much larger than that of the 1322cm^{-1} band. No reason can be offered to explain this phenomenon.

If the hydrogen motions are decoupled, which is very likely in a comparison with the spectra of $H_4Ru_4(CO)_{12}$, then a typical (μ_2-H) type spectrum would be expected. The lower frequency region is certainly very much like that of $H_4Ru_4(CO)_{12}$ as shown in Table 5.14 and the assignments are carried out as for $H_4Ru_4(CO)_{12}$.

Table 5.14: IINS Comparison in 300-800cm^{-1} Range

$H_2FeRu_3(CO)_{13}$	$H_4Ru_4(CO)_{12}$	Assignment
732	704	Overtone (2x362=724cm^{-1})
639	619	in-plane deformation
525	542	RuC stretches or/
427	452	RuCO deformations
385	370	
362	336	out-of-plane deformation

It is interesting to see such a close comparison between the two deformation regions especially since the stretching regions of both compounds are so different. Thus it appears that the bonding geometry has only a profound effect upon the MHM stretching vibrations and not upon the MHM deformations.

In the 1000cm^{-1} region there is a weaker band made up of two components, the stronger lying at 999cm^{-1}, the weaker at 1104cm^{-1}. Unlike the 942cm^{-1} band in $H_4Ru_4(CO)_{12}$ which was seen prominently in the IR, neither of these bands were observed in the IR. Unfortunately no convincing argument can be postulated to explain these peaks. The 999cm^{-1} band is assigned to a combination band of the two deformations which are of the same A symmetry. The 1104cm^{-1} band may be a weak second overtone of the strong 362cm^{-1} deformation band.

5.3. $H_2Os_3(CO)_{10}$

(a) Previous Results

Howard et al (6) assigned IR bands at 1228(av)cm^{-1} and 1177(av)cm^{-1} as the antisymmetric and symmetric $Os(H_2)Os$ stretches respectively. These values were used in their appraisal of a technique for estimating the MHM bond angle in $M_2(\mu_2\text{-}H)$ systems.

(b) Results

Table 5.15 shows the data collected from this study of $H_2Os_3(CO)_{10}$ and Figures 5.26, 5.27, 5.28 show the 4H5, BFDDIDO, and IN1B spectra.

(c) Discussion

$H_2Os_3(CO)_{10}$ has a symmetry of C_{2v} and vibrations are thus $22A_1$, + $13A_2$ + $16B_1$ and $18B_2$. Those involving hydrogen motion are shown in Table 5.16. If the Os_2H_2 unit in $H_2Os_3(CO)_{10}$ could be uncoupled from the rest of the molecule it may have a 'D_{2h}' (distorted) symmetry similar to the Re_2H_2 unit in $H_2Re_2(CO)_8$. The vibrations of this unit are

Table 5.15 Bands Associated With H Motion in $H_2Os_3(CO)_{10}$

IN1B (77K)	BFDDID0 (77K)	4H5 (130K)	IR (77K)	FIR (77K)	IR *(6)	Assignments
2024(sh)						Combinations and/or CO stretch
1943(wm)						
			1725(wb)			
1483(s)	1500(wb)		1515(vwb)			OsHOs Antisymmetric stretch(B_{2g})
1330(m)	1344(wb)		1363(vw)			Overtone (2x672=1344cm^{-1})
			1244(mb)			
1225(s)	1212(mb)		1224(s)		1228(av)	OsH_2Os symmetric stretch(A_g)
			1218(wsh)			
			1195(m)		1177(av)	
1112(wsh)			1118(w)			Combination (430+672=1102cm^{-1})
			1020(wb)			Unknown
			990(vw)			
	851(vw)					Overtone (2x426=852cm^{-1})
730(vs)	732(vs)		773(vs)			OsH_2Os In-plane deformation (B_{3u})
672(vs)	672(vs)		667(wm)			OsH_2Os In-plane deformation(B_{1u})
504(sh)	533(sh)	550(vs)				OsCO deformation
430(ms)	426(s)	426(vs)				OsH_2Os out-of-plane deformation(B_{1u})
	284(m)	284(w)				Combination or/OsC stretch
				206(w)		
		158(s)				OsOs stretch(A_1)
				143(s)		OsOs stretch (B_2)
		120(sh)		123(vw)		COsC deformation
				108(wm)		
		100(sb)		100(m)		Os(H_2)Os stretch
				92(wm)		COsC deformation
		70(sh)		78(msh)		
		45(m)		59(wm)		Lattice modes
		27(sh)				

* Unknown experimental temperature

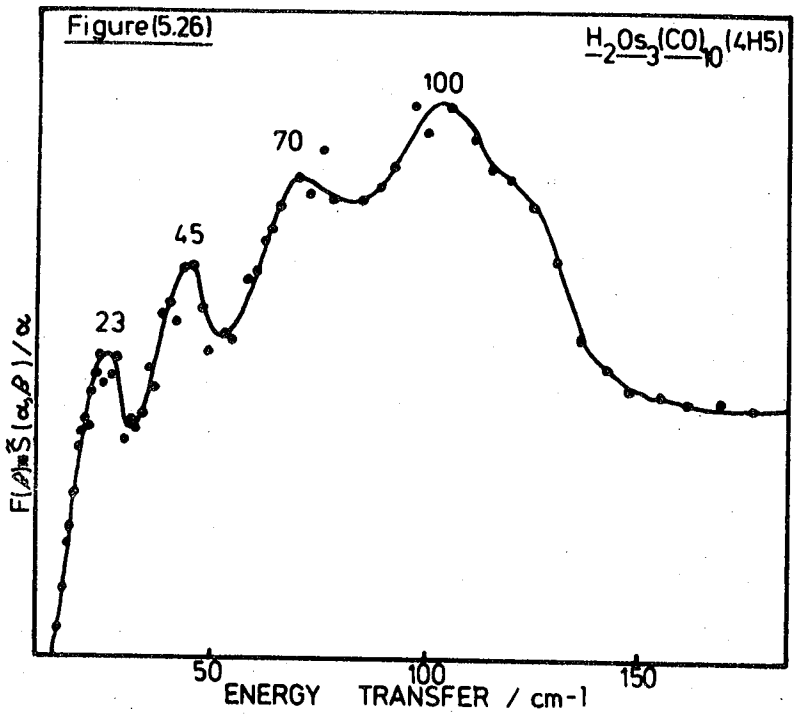
Figure(5.26)
$H_2Os_3(CO)_{10}$ (4HS)
100
70
45
23
$F(\rho)=S(\alpha,\beta)/\alpha$
50
100
150
ENERGY TRANSFER / cm-1

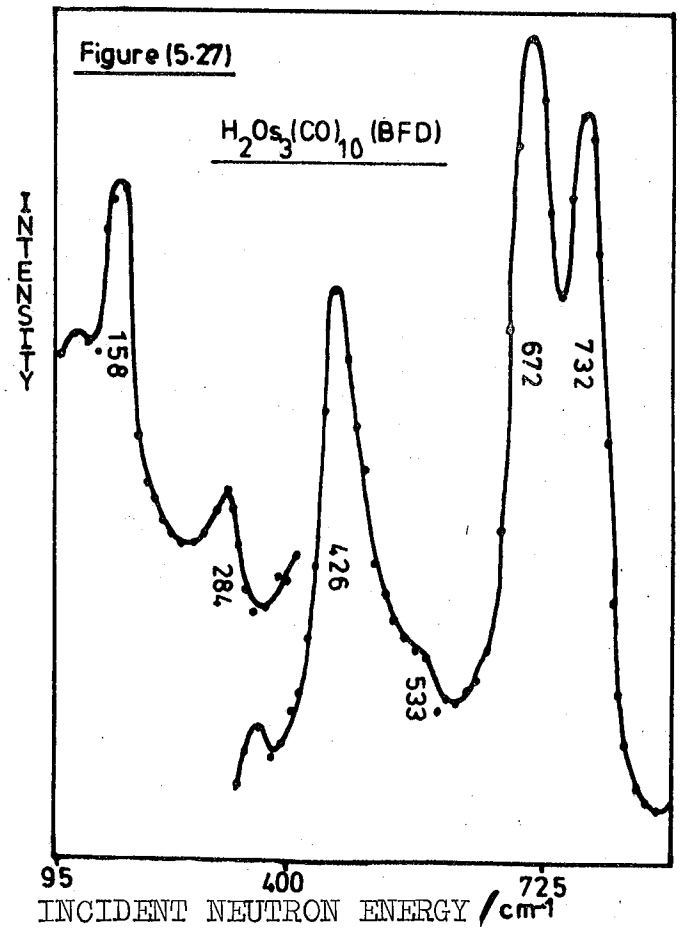
Figure (5.27)
$H_2Os_3(CO)_{10}$ (BFD)
INTENSITY
158
284
426
533
672
732
95
400
725
INCIDENT NEUTRON ENERGY / cm-1

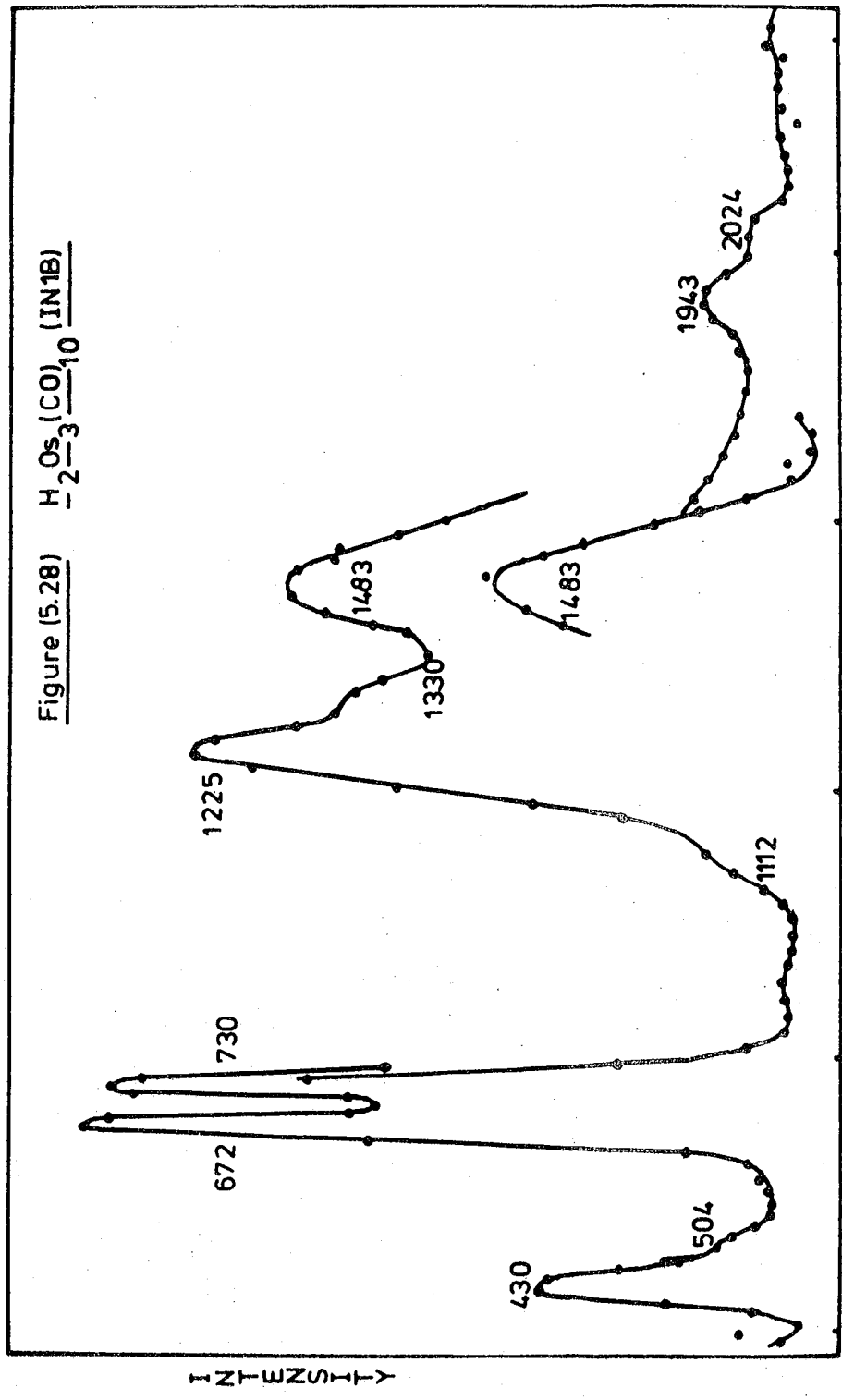
Figure (5.28) $H_2Os_3(CO)_{10}$ (IN1B)
INTENSITY
INCIDENT NEUTRON ENERGY / cm⁻¹
400
800
1200
1600
2000
430
504
672
730
1112
1225
1330
1483
1483
1943
2024

also shown in Table 5.17.

Table 5.16: C_{2v} Vibrational Analysis

Vibration	Number and Symmetry	Activity
OsH_2Os stretch	A_1	IR/Raman
	A_2	Raman
	B_1	IR/Raman
	B_2	IR/Raman
OsH_2Os deformation	A_1	IR/Raman
	B_1	IR/Raman
'bridged' OsOs stretch	A_1	IR/Raman
'non-bridged' OsOs stretch	A_1	IR/Raman
	B_2	IR/Raman

Table 5.17: D_{2h} Vibrational Analysis

Vibration	Number and Symmetry	Activity
OsH_2Os stretch	A_g	Raman
	B_{2g}	Raman
	B_{1u}	IR
	B_{3u}	IR
OsH_2Os deformation	Ag	Raman
	B_{3u}	IR
'bridged' OsOs stretch	B_{1u}	IR

(i) Metal-Metal Stretch

$H_2Os_3(CO)_{10}$ has C_{2v} symmetry and thus has $Os(H_2)Os$ deformation modes of A_1 and B_1 character. The bridged

$Os(H_2)Os$ stretch is of A_1 character and the non-bridged OsOs stretches are of A_1 and B_2 character. Thus only the A_1 symmetry modes are neutron active. The IINS spectrum Figure 5.26, is dominated by a strong band at $100cm^{-1}$ which has shoulders of medium intensity at 70 and $120cm^{-1}$.

Now $HOs_3(CO)_{12}PF_6$, also of C_{2v} symmetry, gave two bands in an IINS spectrum (15) at 160 and $112cm^{-1}$. Corresponding Raman bands were also found at 158 (A_1') and $119cm^{-1}$(E_1') in $Os_3(CO)_{12}$ (28) which has D_{3h} symmetry. White and Wright (15) postulated from this that protonation of an OsOs band had a negligible effect on the D_{3h} symmetry description of the OsOs stretches. However, in $H_2Os_3(CO)_{10}$ diprotonation of the single OsOs band takes place and two carbonyls are lost changing the osmium carbonyl skeleton from $Os_3(CO)_{12}$ to $Os_3(CO)_{10}$. This more perturbing change is reflected in the IINS bands at 100 and $120cm^{-1}$. If the $120cm^{-1}$ band is the A_1 non-bridged OsOs stretch it has obviously been greatly perturbed from the $Os_3(CO)_{12}$ situation, of $Os(CO)_4$ - $Os(CO)_4$, to an $Os(CO)_3$ - $Os(CO)_3$ bond in $H_2Os_3(CO)_{10}$. This cannot be accepted. A weak band lies at ~ $158cm^{-1}$ in the $P(\alpha,\beta)$ spectra of $H_2Os_3(CO)_{10}$ and a band lies at $158cm^{-1}$ of strong intensity in the BFDDIDO spectrum Figure 5.27. The band at $158cm^{-1}$ is assigned to the non-bridged OsOs stretch. The weaker $120cm^{-1}$ shoulder could be an OsCOdeformation. The band at $100cm^{-1}$ is assigned to the bridged OsOs stretch and it has moved from $119(Os_3(CO)_{12})$ to 112 ($HOs_3(CO)_{12}^+$) to $100cm^{-1}$ in $H_2Os_3(CO)_{10}$. Thus the protonation can be seen to be having the effect of forcing the stretch to lower frequencies.

The value of the IINS inactive B_2 symmetry OsOs stretch can be found by looking at the IR spectra of $H_2Os_3(CO)_{10}$ and other $X_2Os_3(CO)_{10}$ (22) compounds (where X_2 = $(OMe)_2$, $(OEt)_2$ and (H(OBu)). The $2A_1$ and B_2 bands have been assigned to the region of ~ 170cm^{-1} (A_1), ~ 133cm^{-1}(B_2) and ~ 100cm^{-1} (A_1) using Raman spectroscopy, however, only the latter pair were observed in the IR. The IR of $H_2Os_3(CO)_{10}$ has bands at 143(s) and three weak-medium intense features in the 92-108cm^{-1} area. With analogy to $X_2Os_3(CO)_{10}$ the medium inactive band (B_2) is assigned to the 143cm^{-1} feature in the IR. The 158cm^{-1} band is seen in the IINS spectrum but not in IR. This is because it does not gain sufficient intensity because the perturbation from the D_{3h} parent to the C_{2v} symmetry is obviously not great enough to make the original D_{3h} 'breathing' mode sufficiently IR active.

The lowest frequency bands in the IINS spectrum at 27 and 45cm^{-1} are assigned to lattice modes whereas the strong shoulder at 70cm^{-1} is assigned to an COsC deformation, which has gained some IINS intensity by associated hydrogen motion.

(ii) Os-H Vibrations (> 200cm^{-1})

Howard et al (6) reported, from IR measurements, that the average value of the antisymmetric stretch was 1228cm^{-1} and that the symmetric stretch lay at 1177cm^{-1}. Figure 5.29 shows the 1100-1400cm^{-1} region of our IR spectrum at 77K. At room temperature the peaks were reduced in intensity but no shifts were found.

The reported band at 1177cm^{-1} does not exist in our spectrum. Perhaps it has been replaced by the medium intense

Figure (5.29)
IR bands in the 1200 cm^{-1} region of $H_2Os_3(CO)_{10}$ (77K)

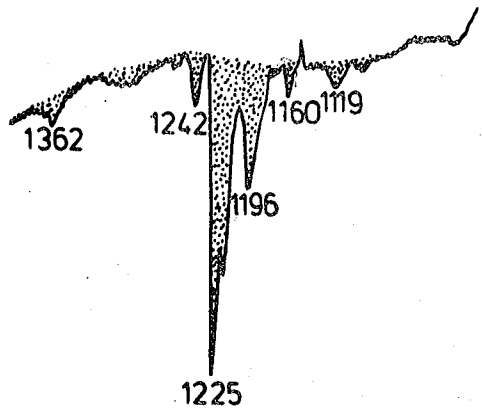

Figure (5.30) Vibrations involving hydrogen in $H_2Os_3(CO)_{10}$

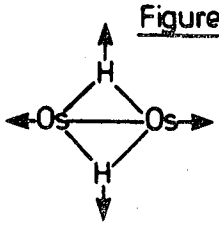

symmetric stretch
1241cm^{-1} (A_g)

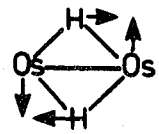

antisymmetric stretch
1483cm^{-1} (B_{2g})

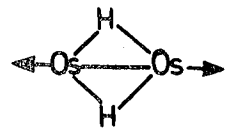

osmium-osmium stretch
100cm^{-1} (A_g)

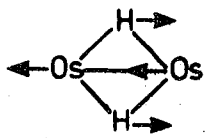

symmetric 'in-plane deformation 732cm^{-1} B_{3u}

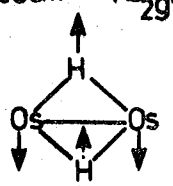

symmetric in-plane deformation 672cm^{-1} B_{1u}

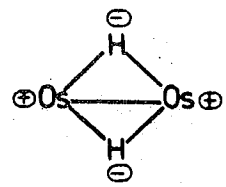

out-of-plane deformation 430cm^{-1} B_{2u}

band at 1196cm^{-1}. If the hydrogen is coupled with the rest of the molecule, which may be approximated to an Os_3H_2 fragment since both have C_{2v} symmetry, then the vibrational modes may be crudely approximated to the following:-

OsH stretches	$A_1 + A_2 + B_1 + B_2$
OsOs stretches	$2A_1 + B_2$
OsH deformations	$A_1 + B_1$
Total	9

If the hydrogen is decoupled from the molecule then the Os_2H_2 fragment need only be analysed (ie the $Os(CO)_4$ moiety is ignored). The Os_2H_2 fragment can be compared then with $H_2Re_2(CO)_8$ which has D_{2h} symmetry. The vibrational modes may be crudely approximated to the following:-

OsH stretches	$Ag + B_{2g}$
OsOs stretches	Ag
OsH deformations	$B_{1u} + B_{2u} + B_{3u}$
Total	6

The number of vibrations in the molecule obviously remains the same but the hydrogen is involved in 9 in the case of C_{2v} symmetry and 6 in the case of D_{2h} 'local' symmetry. It has already been shown that the OsOs stretching vibrations probably involve the whole Os_3 triangle and they were described by the C_{2v} molecular point group. However, 6 OsH stretches and deformations are expected with C_{2v} symmetry whereas 5 are expected with D_{2h} local symmetry. There are, in fact, 5 IINS bands of strong intensity at 426, 672, 732, 1241 and 1483cm^{-1} (though a sixth may lie at 1326cm^{-1} as a shoulder). Howard et al (6) have no real evidence apart from two peaks, with a separation of 51cm^2 in their IR spectrum

(a separation of 29cm^{-1} in this study) for supporting their assignment of the stretching vibrations. Such multiple bands occur in most hydridocarbonyls in the symmetric stretch region (800-1300cm^{-1}) and where these multiplets have been observed there has never been a separation and assignment of two fundamental modes. The Raman technique has been more successful in locating symmetric stretches whereas the IR technigue has been more successful in locating the antisymmetric stretches in bridged hydridocarbonyls, so the apparent weaker intensity of their 1177cm^{-1} and our 1196cm^{-1} band may well have indicated it was a symmetric stretch and the stronger band at 1228(1225)cm^{-1} may well have indicated an antisymmetric stretch. However, since two strong bands at 1483 and 1245cm^{-1} appear in the neutron spectrum some doubt must be thrown onto these assignments. Further, on using a curve resolver the shoulder seen between these two strong bands can be resolved into a band at 1330cm^{-1}. The relative intensities for the 1225, 1330 and 1483cm^{-1} bands are approximately 2.5:1:2.5. On considering the possible D_{2h} and C_{2v} symmetries, it can be seen that the symmetric stretch, on A_g band in D_{2h}, is only Raman active whereas in C_{2v} symmetry, as an A_1 band, it is IR and Raman active. The antisymmetric stretch, in D_{2h} symmetry, is a B_{2g} mode which is only Raman active and on relaxationto C_{2v}, degrades into an A_2 mode which, again, is only Raman active. This is overwhelming proof that whether under C_{2v} or the decoupled symmetry of D_{2h} that the antisymmetric stretch is Raman active only. Further, the symmetric stretch is only IR active in the C_{2v} symmetry. Solid state effects could

provide the necessary effect to make all the bands IR active but in this case the 1483cm^{-1} band would then be in the IR spectrum. No band was seen in this region except a very weak broad feature at 1515cm^{-1}. This may be an indication that the site symmetry is relaxed.

Thus the IR bands at 1225 and 1196cm^{-1} are assigned to the symmetric stretch. The multiplet seen cannot be due to the hydrogen residing in multiple potential wells, as in the single hydrogen (μ_2-H) compounds. This small splitting (29cm^{-1}) may be related to the slight splitting (3cm^{-1}) in the band at 732cm^{-1}. This could be due to hydrogen atoms residing in slightly different environments in the crystal and, thus, each specific site produces its own non-degenerate vibration. No degenerate species exist in C_{2v} or D_{2h} symmetry. The antisymmetric stretch is assigned to the Raman active IINS band at 1483cm^{-1}. Later, in section 5.4.1 it will be seen that with either set of stretches the results achieved with the bond angle estimation are poor indicative that the $M_2(\mu_2\text{-H})_2$ units must be treated separately from $M_2(\mu_2\text{-H})$ moieties.

There are very few other features of note in the 750-2400cm^{-1} region. The bands at 1943 and 2024cm^{-1} must again be combination bands with possibly some carbonyl stretching motion with associated hydrogen movement. The shoulder at 1112cm^{-1} may be a combination band, of the two B symmetry deformations at 672 + 430 = 1102cm^{-1} but, again, it may not be statistically significant. The band at 1330cm^{-1} may only be an overtone of very strong lower frequency bands. (In fact 2 x 667cm^{-1} = 1334cm^{-1}).

Looking at the spectra overall it may now be possible to find out whether a decoupled D_{2h} system is found or whether a whole-molecule-symmetry remains to control the vibrations involving hydrogen. From the IINS data there are 3 strong bands below 750cm^{-1} at 732, 667 and 430cm^{-1} indicating that there are 3 deformations and there are two strong high frequency bands at 1225 and 1483cm^{-1} indicating that there are two stretching modes. This seems overwhelming evidence that the vibrations involving hydrogen are decoupled from the rest of the molecule and can be explained in terms of the D_{2h} local symmetry. The form of the stretching and deformation vibrations involving hydrogen motion in the D_{2h} symmetry are shown in Figure 5.30. These modes were discussed by Andrews et al (12) for the $H_2Re_2(CO)_8$ molecule. They also depicted the Re-Re stretch which must have involved hydrogen motion producing a deformed ReHRe bond angle. In $H_2Os_3(CO)_{10}$ the single bridged Os(H)Os stretch does not strictly exist since the Os-Os vibrations appeared coupled.

At lower frequencies there are strong bands at 430, 672 and 732cm^{-1}. The lowest frequency feature at 430cm^{-1} is assigned to the out-of-plane deformation of B_{2u} character. This band is assigned to the lowest frequency deformation because it is the most antisymmetric with analogy to the other hydridocarbonyls. This value is at higher frequencies than the analogous $(\mu_2\text{-H})M_2$ out-of-plane deformations, which are found in the 300-400cm^{-1} regime. The higher frequency value may be due to the different metal-metal bond, which has been described as a double bond (38) in these $M_2(\mu_2\text{-H})_2$ species. Further, the hydrogens are already out of the plane which is perpindicular to the osmium triad. This

would possibly make the motion, shown in Figure 5.30, more difficult to execute and since the intensity of this band is much lower than in other $M_2(\mu_2\text{-H})$ species, this explanation would seem to be vindicated. The in-plane deformations will be as intense as those found in the $M_2(\mu_2\text{-H})$ system, if regarded as a decoupled D_{2h} unit. The bands at 672 and 732cm^{-1} are of great interest and they may be due to a splitting of the in-plane motion producing a doublet of equal intensity because of a correlation field coupling effect. With Z = 2 in the unit cell this splitting may have taken place. However, the separation of 59cm^{-1} will probably be too large for this effect. An alternative explanation is sought. From the similar IINS intensity of the bands at 667 and 732cm^{-1} they must be due to similar fundamental vibrations and because of their low frequency they are obviously deformation modes, thus making up the 3 deformations/2 stretch D_{2h} OsH description. The deformations of B_{1u} and B_{3u} symmetry are assigned to the bands at 732 and 667cm^{-1}. The only difference between these bands is that the 667cm^{-1} band is not as intense in the IR spectrum as the 732cm^{-1} band. Looking at their form in Figure 5.30 one could say that the B_{3u} vibration was related to the B_{2g} antisymmetric stretch in that the hydrogen direction of motion is the same. Since the heavy Os atoms will not move very far then this comparison may be valid. The B_{1u} deformation can be related to the symmetric stretch of A_g symmetry. This would seem to point to the B_{3u} band lying at 732cm^{-1} and the B_{1u} band at 667cm^{-1} because the antisymmetric motion will lie at higher frequency and further, but less convincingly, the antisymmetric motions would be expected to be, as in other hydridocarbonyl

systems, more easily seen in the IR than the symmetric motions though this is not the case for the stretching vibrations in $H_2Os_3(CO)_{10}$.

5.4. $(\mu_3\text{-H})M_3$ Species

5.4.1. $H_4Re_4(CO)_{12}$

(a) Results

No other vibrational studies have been reported on this compound. Table 5.18 shows the data and assignments from this investigation. Figures 5.31, 5.32, 5.33 depict the 4H5, BFDDIDO and IN1B spectra.

(b) Discussion

$H_4Re_4(CO)_{12}$ has vibrations of the following type $6A_1 + 2A_2 + 8E + 9T_1 + 13T_2$ Table 5.19 shows the symmetry of the vibrations under T_d symmetry.

Table 5.19: T_d Vibrational Analysis

Vibration	Symmetry T_d
CO stretch	$A_1 + E + T_1 + 2T_2$
ReC stretch	$A_1 + E + T_1 + 2T_2$
ReCO deformation	$A_1 + A_2 + 2E + 3T_1 + 3T_2$
Re_4H_4 stretch	$A_1 + E + T_1 + 2T_2$
Re_4H_4 deformation	$2A_1 + A_2 + 3E + 3T_1 + 3T_2$
CReC deformation	
$Re(CO)_3$ Rock	
$Re(CO)_3$ Torsion	

Table 5.20 shows the situation if the four Re_3H units are decoupled. The vibrations will take place under C_{3v} symmetry.

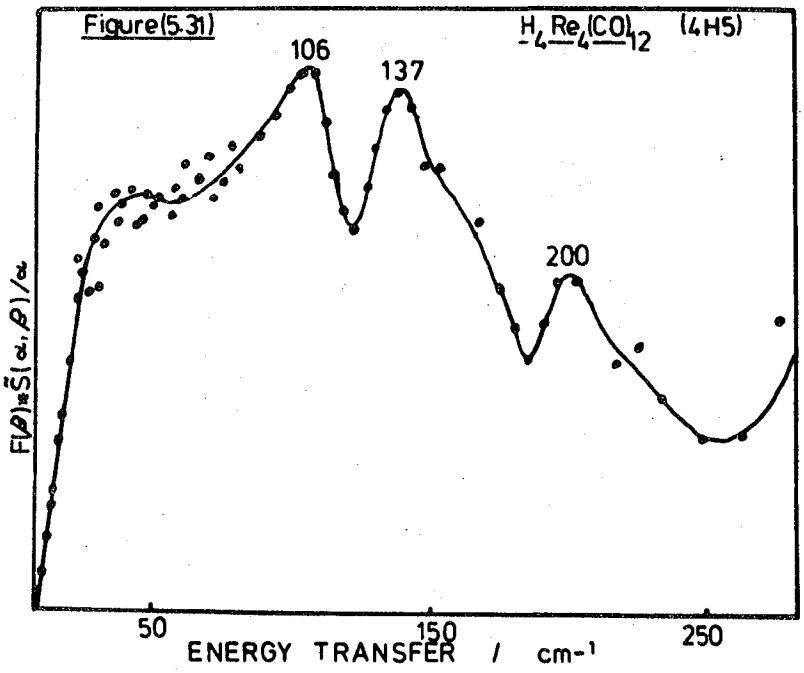
Figure(5.31)
$H_4Re_4(CO)_{12}$ (4H5)
106
137
200
$F(\beta)=\tilde{S}(\alpha,\beta)/\alpha$
50
150
250
ENERGY TRANSFER / cm-1

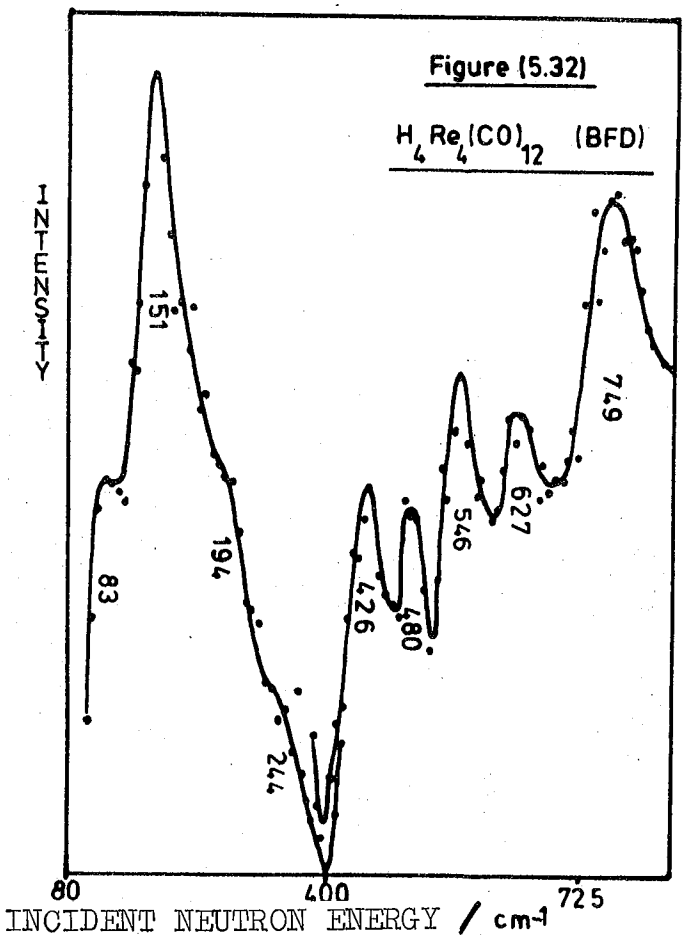
Figure (5.32)
$H_4Re_4(CO)_{12}$ (BFD)
INTENSITY
151
83
194
274
426
480
546
627
719
80
400
725
INCIDENT NEUTRON ENERGY / cm-1

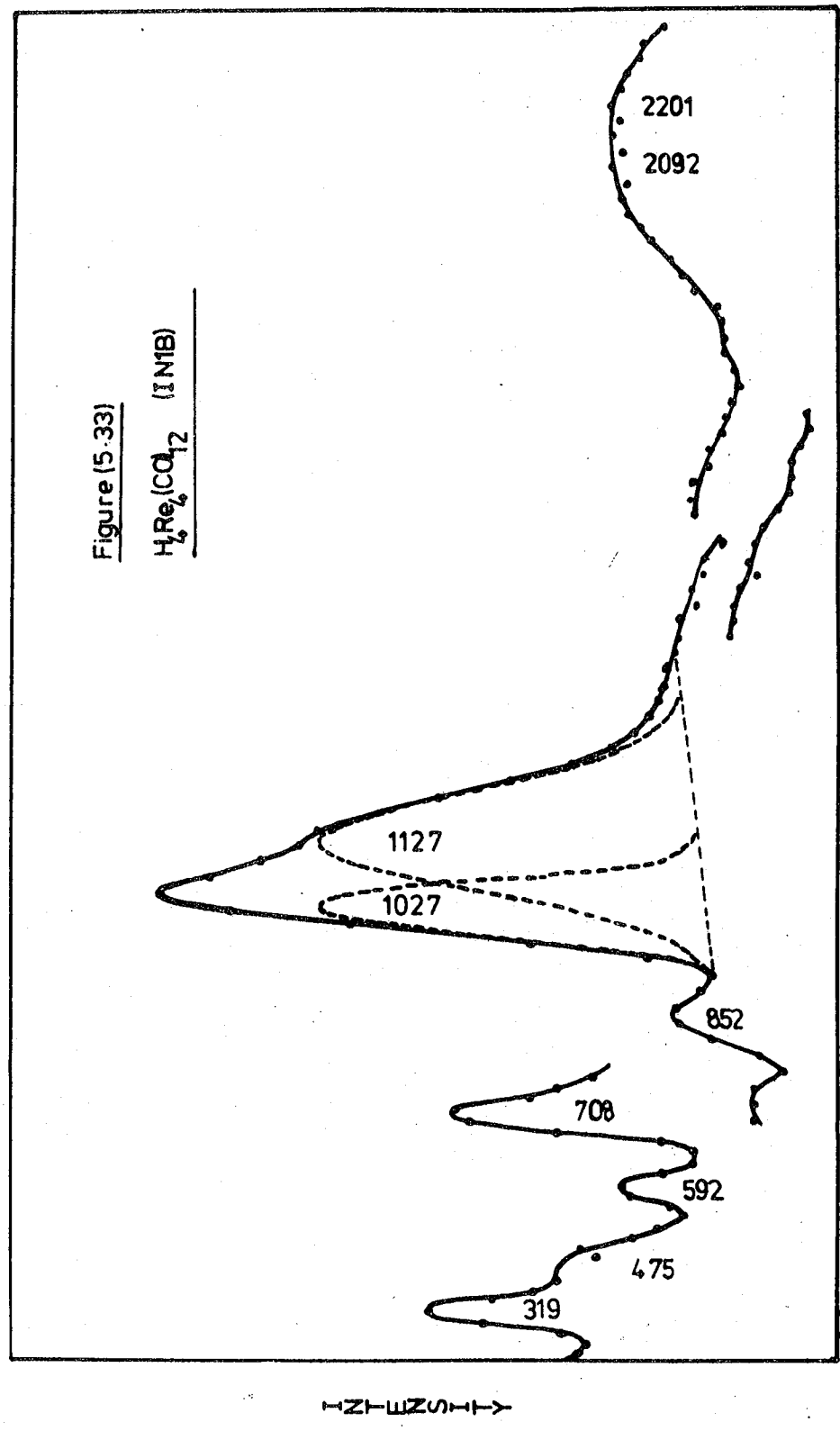

Figure (5.33)

$H_4Re_4(CO)_{12}$ (1N1B)

Table 5.20: C_{3v} Vibrational Analysis

Vibration	Symmetry (C_{3v})	Activity
Re_3H stretch	A_1	IR and Raman
	E	
Re_3H deformation	A_1	
	E	

(i) Re-Re Stretches

$H_4Re_4(CO)_{12}$ approximates to a regular tetrahedron. If the Re_4 moiety can be treated separately then vibrations of $A_1 + E + T_2$ symmetry are expected. The T_2 mode is IR active whereas they are all Raman active. Unfortunately no Raman data was collected successfully on this deep red compound since it was very easily reduced to rhenium metal. Further the 4H5 spectra is poorly resolved. The predicted frequency ratio for the vibrations, assuming a simple valence force field are $A_1:T_2:E = 2:\sqrt{2}:1$ (22). There is only a single band in the IR spectra, at 148cm^{-1}, below 300cm^{-1}. IINS bands can be observed at 200cm^{-1} (ie $1.46T_2$) and 106cm^{-1} ($0.77\ T_2$). Thus the frequency ratio is 2:1.37:1.06 which is reasonably close to the expected ratio. Unfortunately, the effect of the bonding of the 4 hydrogen atoms, to the Re_3 faces, on the ReRe stretches cannot be estimated since there has been no study of an $Re_4(T_d)$ system without H bridges (e.g. $Re_4(CO)_{16}^{2-}$). The low frequency shoulder in the IINS spectrum at 55-70cm^{-1} is assigned to a CReC deformation mode.

Table 5.18: Bands Associated With H Motion in $H_4Re_4(CO)_{12}$

IN1B (77K)	BFDDIDO (77K)	4H5 (130K)	IR (77K)	FIR (77K)	Assignment
2201(mb)					Overtones(2x1127=2254 2x1027=2054cm^{-1}) and/ or CO stretch
2092(mb)					
			1620(wb)		
1127(ssh)			1100(wb)		Re_3H antisymmetric stretch (E)
1027(vs)					Re_3H symmetric stretch (A_1)
853(m)					See text
708(m)	749(sb)				Re_3H'symmetric' deformation (A_1)
592(w)	627(m)				
	546(ms)				ReCO deformations
475(sh)	480(wm)	460(vs)			and ReC stretches
	426(m)				
319(m)		320(w)			Re_3H'antisymmetric' deformation (E)
	244(vw)				Unknown
	194(sh)	200(w)			ReRe stretch (A_1)
	151(vs)	137(m)		148(w)	ReRe stretch (T_2)
		106(mb)			ReRe stretch (E)
		55/70 (bsh)			CReC deformation

(ii) ReH Vibrations

As shown in Table 5.19 many vibrations will be expected for $H_4Re_4(CO)_{12}$ which involve hydrogen motion. However, if the HRe_3 moieties are uncoupled then under C_{3v} symmetry Re_3H stretches and deformations of A_1' and E symmetry will be

anticipated (ie. 6 vibrations total). The IINS spectrum Figure 5.33 is dominated by the large partially resolved doublet at ~1100cm^{-1}. At lower frequencies there are medium intense bands at 708 and 319cm^{-1}. From this, it would appear that there are four fundamentals indicative of a C_{3v} system. Also there is a band of weaker intensity at 852cm^{-1}.

The strong bands at 1027 and 1127cm^{-1} are assigned to the symmetric and antisymmetric stretches of the independent Re_3H units. There is a weak IR band at ~ 1100cm^{-1} and this implies that the 1127cm^{-1} IINS band is IR active. In the C_{3v} system the A_1 and E modes are both IR and Raman active but since, in general, most symmetric stretches are more often observed using the Raman technique and most antisymmetric stretches are observed with the IR technique, it appears reasonable to assign the 1100cm^{-1} IR band and the 1127cm^{-1} IINS band to the antisymmetric stretch and the IINS band at 1027cm^{-1} to the symmetric stretch. Further, if the vibrations described in C_{3v} local symmetry were derived from the overall T_d symmetry then the A_1 symmetric stretch would only be Raman active whereas the antisymmetric stretch would be an IR and Raman active T_2 mode.

It is known that the ReHRe angle is 110.8° (40) and, if a purely qualitative comparison can be made with $(\mu_2\text{-H})M_2$ species (6), such an angle would produce a higher frequency antisymmetric stretch than the symmetric stretch. To a first approximation from IINS band intensity considerations it may be reasonable to expect the intensity of the 1127cm^{-1} E mode to be twice that of the 1027cm^{-1} A_1 mode. Using the du Pont curve resolver this is found, as shown in Figure 5.33,

though once again the fitting is tentative and not unique. The integrated area ratio of the 1127 to the 1027cm^{-1} band is approximately 2:1.

At higher frequencies the bands at 2092 and 2201cm^{-1} are second harmonics of the intense stretches, 2 x 1027 = 2054cm^{-1} and 2 x 1127 = 2254cm^{-1}. If there is some carbonyl stretch activity brought about by associated hydrogen motion, as implied by earlier studies this will also be seen in the 2000-2100cm^{-1} region. The two strong bands in the IINS spectra, Figure 5.33, at 319 and 708cm^{-1} are assigned to the two deformations of E and A_1 symmetry respectively in the C_{3v} symmetrical model. The A_1 mode could possibly be described as a symmetric deformation whereas the E mode would be antisymmetric in nature. The form of the four assigned fundamentals is shown in Figure 5.34

Figure (5.34) $M_3H(C_{3v})$ Fundamental vibrations

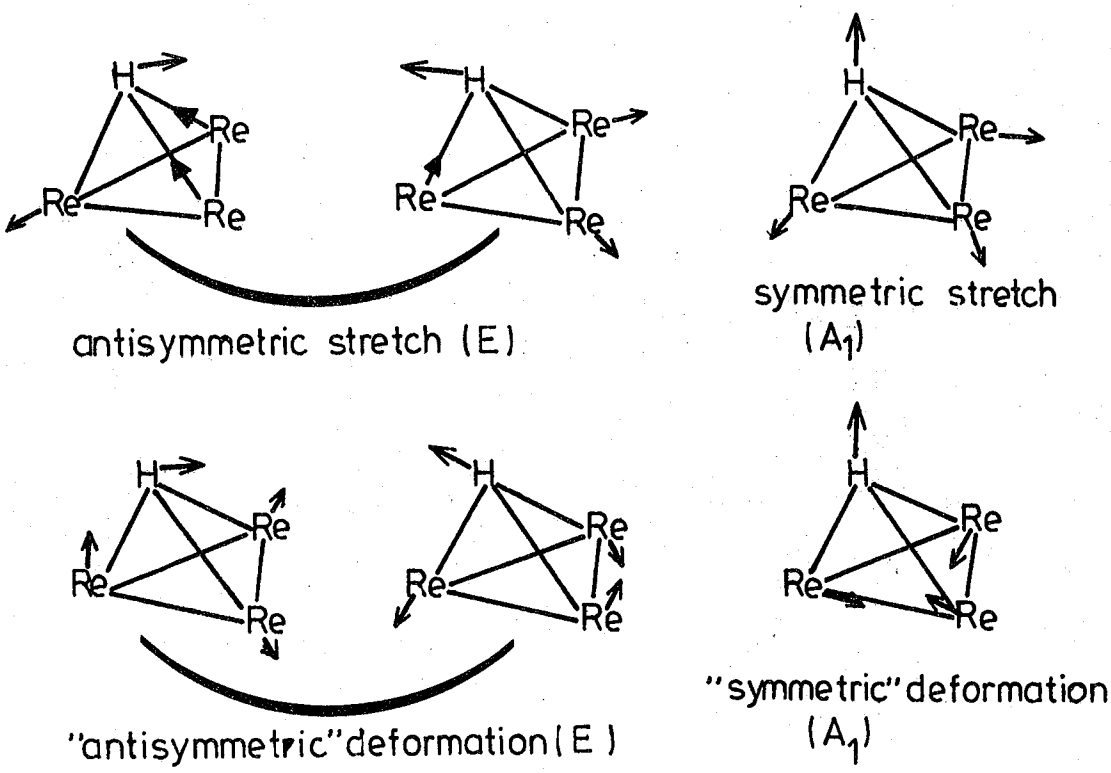

The greater complexity at lower frequencies (300 to 900cm^{-1}) Figure 5.33 compared with the other (μ_3-H)M_3 systems, $HFeCO_3(CO)_{12}$, Figure 5.36, and $H_2Ru_6(CO)_{18}$ Figure 5.38, could be due to some intramolecular hydrogen coupling motions which, in such a high hydrogen density may be quite likely. The H---H distances are 1.9Å in the $H_4Re_4(CO)_{12}$ molecule (40). There is only a single hydrogen on the $FeCo_3$ tetrahedron in $HFeCo_3(CO)_{12}$ and the two hydrogens in $H_2Ru_6(CO)_{18}$ are found on the opposite sides of the Ru_6 octahedron. Unfortunately, the data acquired from the BFDDIDO spectrometer is of poor quality. This was due to the small sample size and, thus, low hydrogen content. From the IN1B spectrum, there are a further 3 features at 475, 592 and 852cm^{-1} of weak medium intensity. The bands at 475 and 592cm^{-1} are similar to such bands found in other hydridocarbonyls and could be due to ReC stretches and ReCO deformations active in the neutron spectrum due to associated hydrogen motion. The band at 852cm^{-1} is in an area where other ligand vibrations do not take place and a comparison of all band frequencies and intensities from 0-900cm^{-1} implies that it could not be a combination vibration. Since the spectrum as a whole can be quite reasonably analysed except for this weak-medium intense band at 852cm^{-1}, it is felt that an alternative explanation, outside the C_{3v} symmetry model of the Re_3H moiety, may be found. It may be attractive to assign the band to some coupling motion of the independent Re_3H units but the form of this vibration cannot be envisaged. The band occurs in $H_4Re_4(CO)_{12}$ but not in the other (μ_3-H) complexes and this is the only evidence for the

coupling motion. Perhaps the Re_4 tetrahedron could be regarded as a metal particle and with the hydrogen coverage of the faces of the particle/cluster equal to 1 monolayer then the hydrogen atoms may move in phase in a lattice-type mode.

5.4.2. $\underline{HFeCo_3(CO)_{12}}$

(a) Previous Results

Mays and Simpson (41) found a broad weak IR band at 1114cm^{-1} for the title compound, which shifted on deuteration to 813cm^{-1}. Knight and Mays (42) later studied $HMCo_3(CO)_{12}$ complexes, where M = Os, Fe and Ru, and reported the metal-hydrogen stretch at 1118cm^{-1} for $HFeCo_3(CO)_{12}$. White and Wright (15) carried out a low frequency IINS study of this compound and concluded that it had C_{3v} symmetry but that the hydrogen lay within the $FeCo_3$ tetrahedron. They found four bands at 400, 173, 90 and 18cm^{-1}. The lowest frequency band was assigned to a lattice vibration and the highest to the hydrogen bending (E) vibration. They argued that the 173 and 90cm^{-1} bands were due to MM stretches IINS activated by mixing with M-H deformations of the same symmetry. They compared hydrogen lying in positions where the molecule retained C_{3v} symmetry or C_s symmetry, which produced 2 and 3 neutron active MM stretches respectively. With two bands being found, it implied the hydrogen lay on the C_3 axis. From calculated MM stretching force constants they postulated that the hydrogen must lie within the tetrahedron.

(b) Results

Table 5.21 shows the data from the vibrational study of $HFeCo_3(CO)_{12}$ and Figures 5.35, 5.36 show the BFDDIDO and IN1B spectra.

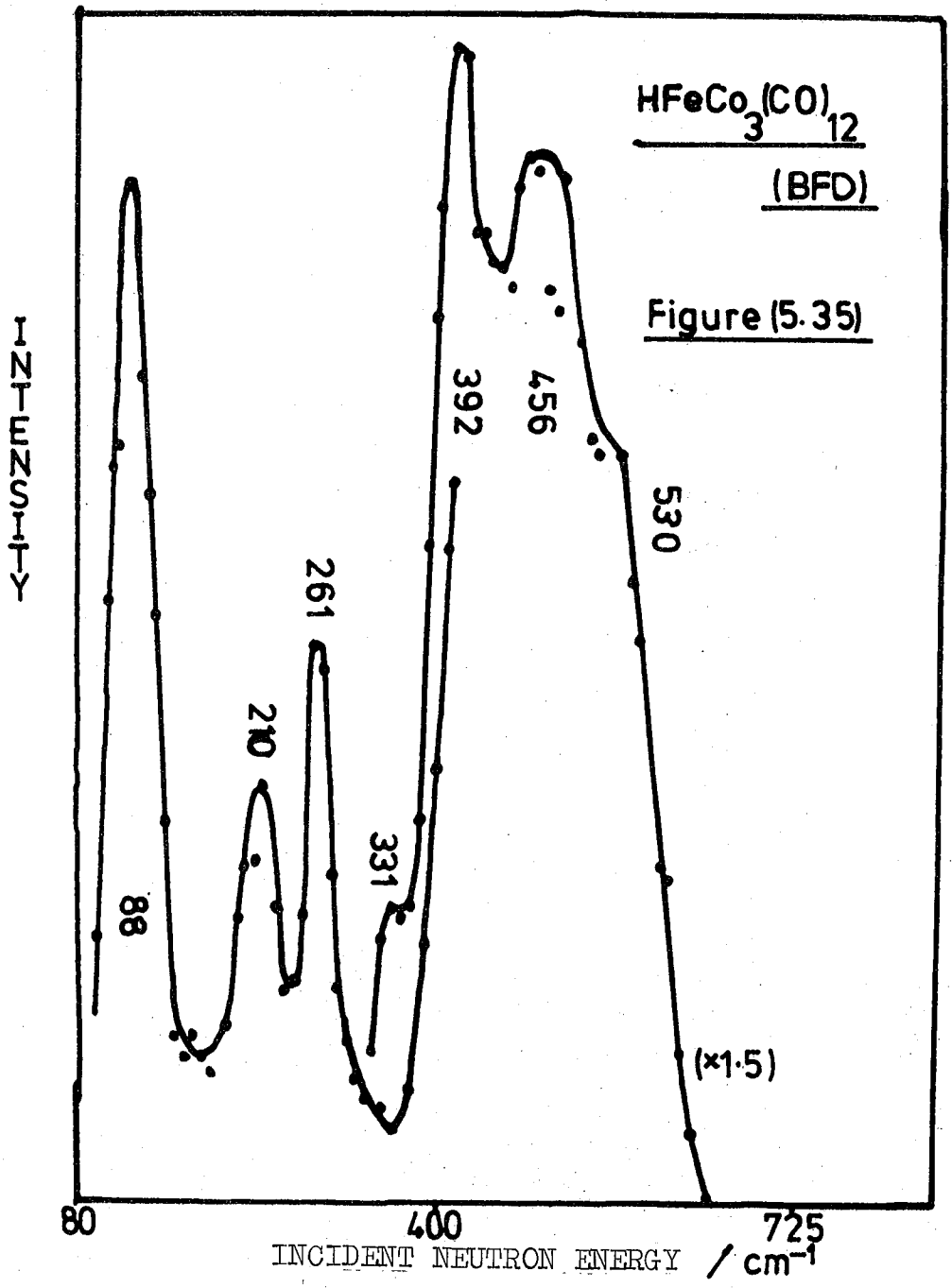
HFeCo3(CO)12
(BFD)
Figure (5.35)
INTENSITY
88
210
261
331
392
456
530
(×1·5)
80
400
725
INCIDENT NEUTRON ENERGY / cm⁻¹

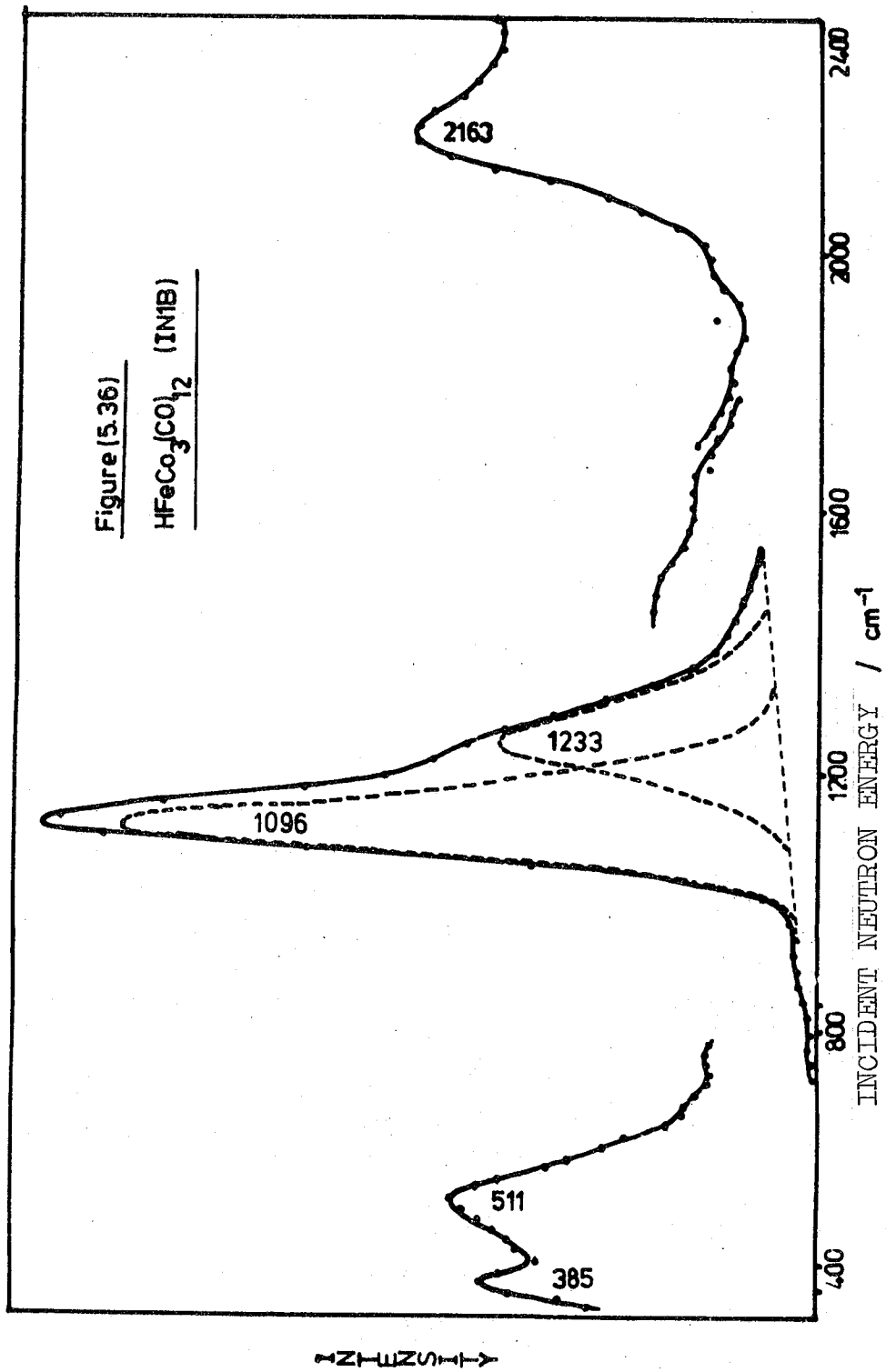

Figure (5.36)

$HFeCo_3(CO)_{12}$ (IN1B)

Table 5.21: Bands Associated With H Motion in $HFeCo_3(CO)_{12}$

IN1B (77K)	BFDDIDO (77K)	IR (77K)	IR(42) RT	IINS (15) *	Assignment
2400(sh)					Overtone(2x1233= 2466cm^{-1})
2163(sb)					Overtone(2x1096= 2192cm^{-1}) and/or CO stretch
1233(ssh)					Co_3H symmetric stretch (A_1)
1096(vs)		1112(mb)	1118(wb)		Co_3H antisymmetric stretch (E)
511(m)	521(wsh) 472(mb)				Co_3H symmetric deformation (A_1)
385(m)	392(mb)	394(wm)		400	Co_3H antisymmetric deformation (E)
	331(w)				MC stretch (?)
	261(s)				CoCo stretch
	210(m)				
				173	MM stretch
				90	
				18	Lattice mode

*Unknown Sample Temperature

(c) Discussion

$HFeCo_3(CO)_{12}$ has C_{3v} symmetry. Therefore the vibrations can be described as $19A_1 + 8A_2 + 27E$. Those involving hydrogen motion in the Co_3H moiety are shown in Table 5.20, as for Re_3H.

The IN1B spectrum, Figure 5.36, is dominated by the very strong band at 1096cm^{-1} with a strong shoulder at 1233cm^{-1}.

These bands can be assigned to the two stretches of A_1 and E symmetry. The IR spectrum (77K) has a single broad band at 1112cm^{-1} similar to that reported by Mayset al (41,42). Since the IR band is likely to be the antisymmetric stretch then the symmetric stretch is assigned to the higher frequency IINS band at 1233cm^{-1}. This reversal of the stretch frequencies (ie symmetric stretch at higher frequency) is consistent with qualitative measurements of M-H bond angles with the ratios of the symmetric and antisymmetric stretches (6) because the CoHCo bond angle is approximately 92^{o} (43). A broad shoulder was observed in the IR spectrum at 1025cm^{-1} at room temperature moiety. It was not observed at 77K. This could be evidence that at room temperature some hydrogen atoms can reside in a slightly different position. Teller et al (43) reported in their low temperature neutron diffraction study of $HFeCo_3(CO)_9(P(OCH_3)_3)_3$ that a room temperature study had been carried out (in 1975) on the compound and the analysis had been severly hampered by weak data but that the $HFeCo_3(CO)_9P_3$ skeleton was well defined. They concluded that in the solid state between 90 and 300K, there was no evidence of a change in position of the metal bonded hydrogen atom. Thus, if the peaks detected in the room temperature IR study at ~ 1110 and ~ 1025cm^{-1} are real, then the distortion will probably be only in the height of the hydrogen above the cobalt face. This would affect the antisymmetric stretch frequencies because of the change in the MHM bond angle. If the antisymmetric stretch was at 1025, as well as 1100cm^{-1}, then this must indicate some multiple site occupancy with some molecules lying in sites similar to that found at 77K and

some others in sites producing the 1025cm^{-1} band. This lower antisymmetric stretch value indicates that the CoHCo bond angle must be less than 92^{o} ie. the hydrogen atom residing further away from the cobalt face. The assignments can be tested by using a curve resolver to determine the integrated areas of the two IINS components at 1096 and 1233cm^{-1}. As shown in Figure 5.36 the most intense band is centred at 1096cm^{-1} and the weaker at 1233cm^{-1}. The ratio of the areas is 68:32 ie approximately 2:1. This confirms the assignment of the E mode and A_1 modes.

Above 1233cm^{-1} in the IINS spectrum there is a strong broad band at ~ 2163cm^{-1} with a broad shoulder at 2400cm^{-1}. This latter band may be due to an increasing background whereas the former is probably an overtone of the very strong IINS band at 1096cm^{-1}. Unlike $H_4Re_4(CO)_{12}$ the region between 500 and 1100cm^{-1} is devoid of peaks in the neutron spectrum. The BFDDIDO spectrum is confusing in the 400-600cm^{-1} region and the quality must be questionable. Nevertheless the IN1B spectrum shows two medium intense features at 385 and 511cm^{-1} (392 and 472/521cm^{-1} in BFDDIDO). These are assigned to the 'antisymmetric' and 'symmetric' deformations of E and A_1 symmetry respectively. The former band is seen in the IR at 395cm^{-1}. This IR band has weak intensity at room temperature, but at 77K it is much more intense and the increase in intensity is noticeably greater than the increase in the MCO deformation and MC stretches found in the same frequency region. The 385cm^{-1} deformation will be the 400cm^{-1} band detected by White and Wright in their IINS study (15). The BFDDIDO spectrum shows bands at 261 and 210cm^{-1} which may

involve metal-metal stretches. For example, the Co-Co stretch in $Co_2(CO)_8$ (CO- bridged) occurs at 229cm^{-1} and the Co-Co (CO-bridged) stretch in $Co_4(CO)_{12}$ occurs at 250cm^{-1} whereas the non-bridged stretch occurs at 185cm^{-1} (39). The White and Wright study of $HFeCo_3(CO)_{12}$ did not find any vibrations between 173 and 400cm^{-1} (15). Unfortunately, the MM stretch region was not studied in this thesis because of the lack of time-of-flight beam time. The form of the Co_3H vibrations are shown in Figures 5.34 and are identical to the decoupled Re_3H vibrations in $H_4Re_4(CO)_{12}$.

5.4.3. $H_2Ru_6(CO)_{18}$

(a) Results

No previous work has been carried out on this compound. Table 5.22 lists the data and assignments from this study. Figures 5.37, 5.38 show the BFDDID0 and IN1B spectra.

(b) Discussion

$H_2Ru_6(CO)_{18}$ has D_{3d} symmetry and thus vibrations of the following type: $13A_{1g} + 8A_{2g} + 21E_g + 9A_{1u} + 12A_{2u} + 21E_u$. If the Ru_3H moieties are totally uncoupled then each will have C_{3v} symmetry and have vibrations of the type shown in Table 5.20 for Re_3H.

$H_2Ru_6(CO)_{18}$ has a quite complex spectrum. $HFeCo_3(CO)_{12}$ had C_{3v} symmetry and the (Co_3H) moeity could be treated as a simple XY_3 entity. The spectrum due to $H_4Re_4(CO)_{12}$ indicated that again the (Re_3H) moeities could be treated as independent XY_3 entities though some coupling may have taken place. $H_2Ru_6(CO)_{18}$ does not have any strong IINS bands between 650 and 1000cm^{-1} and such coupling, across the Ru_6

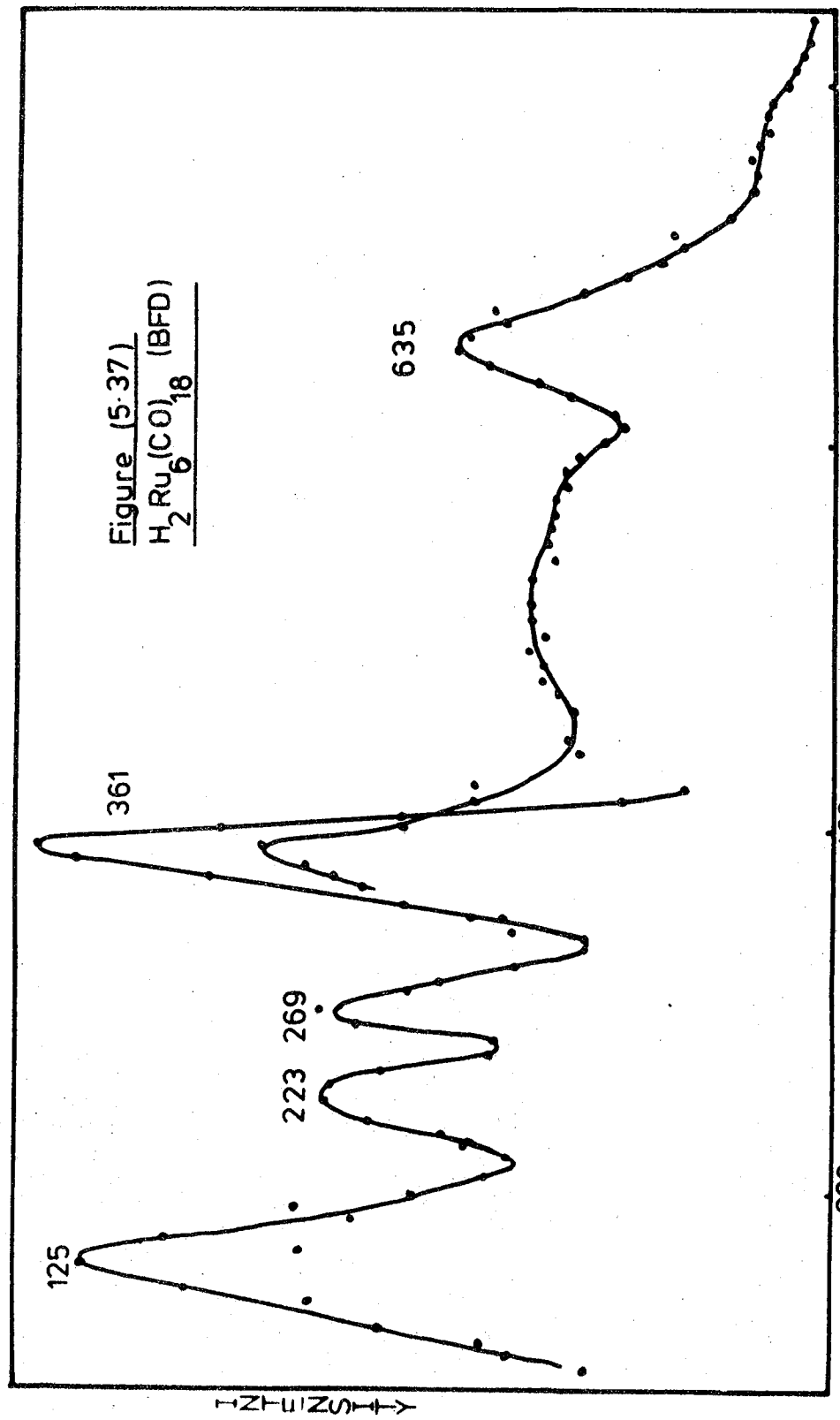
Figure (5·37)
$H_2Ru_6(CO)_{18}$ (BFD)
125
223
269
361
635
200
400
600
800
INCIDENT NEUTRON ENERGY / cm^{-1}
INTENSITY

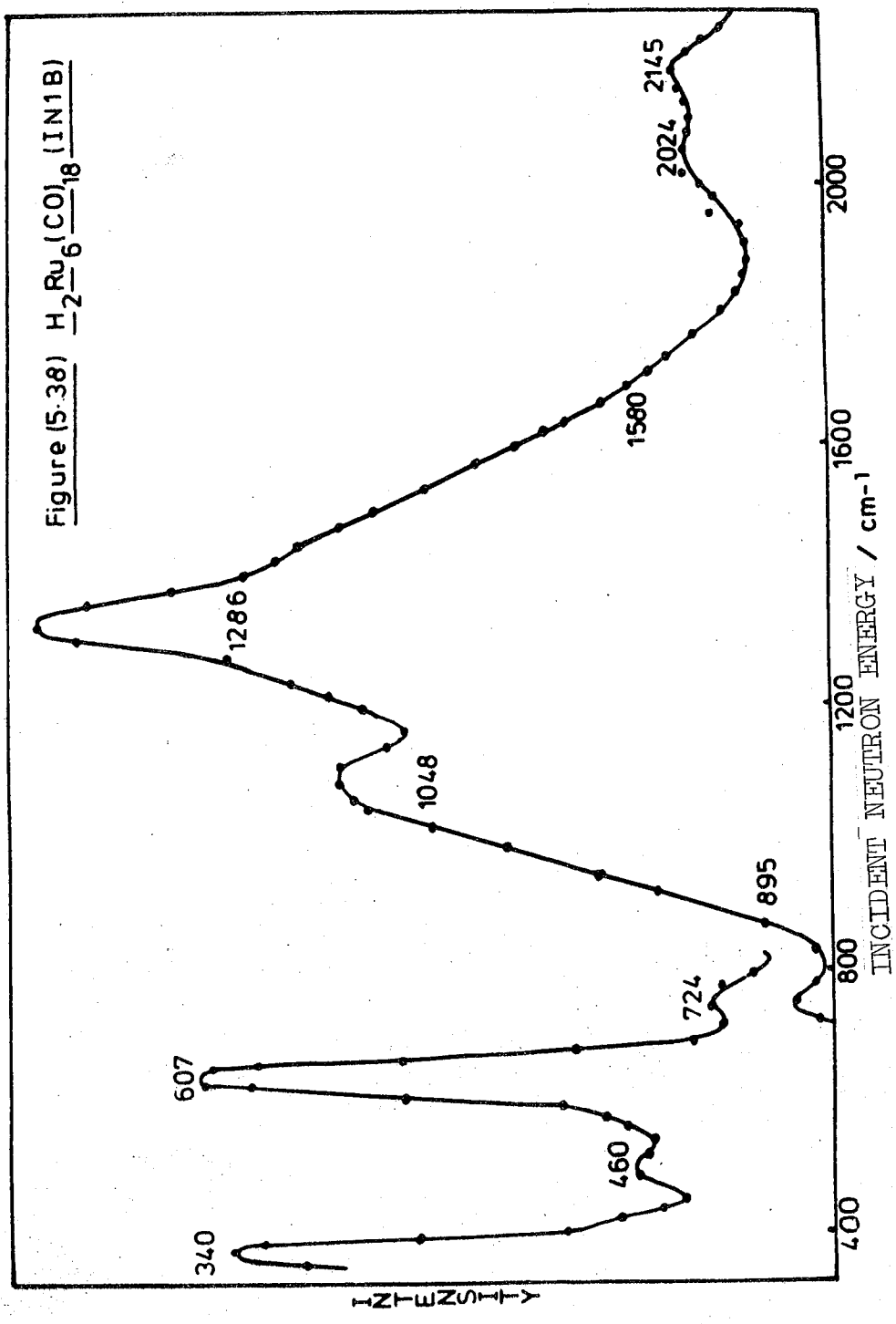
Figure (5-38) $H_2Ru_6(CO)_{18}$ (IN1B)
INTENSITY
INCIDENT NEUTRON ENERGY / cm^{-1}
340
460
607
724
895
1048
1286
1580
2024
2145
400
800
1200
1600
2000

octahedron would appear to be inconsistent. $H_2Ru_6(CO)_{18}$ has two medium intense IINS bands at 607 and 367cm^{-1} and these can be assigned to the 'symmetric' and antisymmetric' deformations of A' and E symmetry, analogous to $HFeCo_3(CO)_{12}$ and $H_4Re_4(CO)_{12}$. The weaker IINS band at 486cm^{-1} is probably a RuC stretching motion with associated hydrogen movement. The IINS band at 733cm^{-1} is assigned to a second harmonic band of the strong E_1 deformation at 361cm^{-1} (2 x 361 = 722cm^{-1}).

Table 5.22: Bands Associated With H Motion in $H_2Ru_6(CO)_{18}$

IN1B (77K)	BFDDIDO (77K)	IR (77K)	Assignment
2133(wmb) 2032(wmb)			Overtone (2x1048=2096cm^{-1}) and/or CO stretch
1580(m) 1330(w)			Unknown
1270(vs)		1238(w) 1130(wb)	Ru_3H antisymmetric stretch
1048(s) 895(w)		1030(wb)	Ru_3H Symmetric stretch
724(w)	733(vwb)		RuCO deformation
607(s)	635(m)	612(w)	Ru_3H symmetric deformation
460(w)	486(vwb)		RuC stretch
340(s)	361(ms)		Ru_3H Antisymmetric deformation
	269(w) 223(w)		Unknown
	125(m)		RuRu stretch

The assignment of the antisymmetric and symmetric stretches is more difficult since the 1000-1600cm^{-1} region of the IINS spectrum, Figure 5.38, is dominated by an intense band

with a complex shape. Using the du Pont curve resolver, a number of possible fits can be made which vary in the position and number of the weaker components. However, since two weak IR bands (77K) exist at 1238 and 1030cm^{-1} the fitting procedure was initiated using two peaks centred at these frequencies and two very strong bands were fitted with a number of weaker components to form the complex band. The relative intensities of the bands at 1286, 1048 895, 1330 and 1580cm^{-1}, shown in Figure 5.38, are 51:25:2:3:15. From intensity considerations the antisymmetric stretch, an E mode, can be assigned to the strongest IINS band at 1286cm^{-1} whereas the singly degenerate A_1 vibration is assigned to the IINS band at 1048cm^{-1}. How the weaker components arise is not apparent. A worthwhile task would be to rerun the compound on IN1B in the 800-1700cm^{-1} region to check the exact band shape. The IINS bands at 2032 and 2133cm^{-1} are possibly overtones of the stretch bands and, again, due to CO stretches.

Once again the vibrations of this compound can be tentatively assigned using the decoupled model ie the $(\mu_3\text{-H})M_3$ treatment.

5.5. $M_6(\mu_6\text{-H})$ Systems: $CsHCo_6(CO)_{15}$

(a) Previous Vibrational Studies

No previous vibrational work has been reported on the species $(HCo_6(CO)_{15})^-$, however, an IR study of the related $(HRu_6(CO)_{18})^-$ system has been carried out (44). At room temperature a strong broad IR doublet was detected at 825cm^{-1}, which at 95K was resolved into bands at 806 and

845cm^{-1}. It was thought that only a single triply-degenerate mode would be observed. Thus the two equally intense bands seemed rather odd since any site group effect would reasonably split band into a doublet of 2:1 relative intensity if the dipole changes were equal. The authors postulated the splitting was due to Fermi-resonance taking place, between a combination or overtone of a lower lying Ru-C stretch or C-O deformation, with the Ru-H band.

A comparison can be made between hydrogen lying in six-coordinate holes within metal clusters and hydrogen in similar positions in metal hydrides. IINS studies of the lattice dynamics of metal hydrides, containing six-fold hydrogen, have observed vibrational bands, using the time-of-flight technique, in the 400-650cm^{-1} region. For example a low concentration of hydrogen in Pd produced a band at 496-528cm^{-1} with a possible overtone at 1080cm^{-1} (45). At higher concentrations a shift was seen to 448 and 896cm^{-1} respectively. $CeD_{2.12}$ was studied and found to have a well defined band at 424cm^{-1} (15) which compared well with the 592cm^{-1} band in $CeH_{1:98}$ (47). Considerable scattering was observed peaking at approximately 760cm^{-1} in the deuterated sample though not explained. Splitting of vibrational bands involving hydrogen motion in such octahedral holes was found, using IINS and IR techniques, in alkaline earth hydrides. This was explained as due to the slight displacement of the hydrogen from a purely six-coordinate position towards one involving 1,2 or 3 nearest neighbours. Such asymmetry appeared to produce broadening and band splitting in the dihydrides CaH_2, BaH_2, SrH_2 and YBH_2 (48). Similar effects were found in asymmetrically positioned hydrogen in tetra-

hedral holes producing 3 nearest neighbours (49).

(b) Results

Table 5.23 contains the data from this vibrational study of $CsHCo_6(CO)_{15}$ and Figures 5.39, 5.40 show the BFDDIDO and IN1B spectra.

(c) Discussion

From Figure 5.40 it can be seen that the spectrum is dominated by the single peak at 1056cm^{-1} which shows no secondary components.

Table 5.23: Bands Associated With H Motion in $CsHCo_6(CO)_{15}$

IN1B (77K)	BFDDIDO (77K)	IR (77K)	Assignment
2129(mb)			Overtone (2x1056=2112cm^{-1})
1224(w)			Instrument artifact
1056(vvs)		1038(vbw)	Co_6H stretch ($T_{1u}+T_{2u}$)
864(w) 727(w) 606(w)	 619(msh)	 725(vvw)	Instrument artifact
497(m) 370(vw)	500(sb) 422(w) 380(m) 305(wsh)	 430(vw) 395(w)	Possibly CoC stretches
	250(w) 143(sh) 100(vs)		CoCo stretches

Unlike the $(HRu_6(CO)_{18})^-$ entity which has perfect octahedral symmetry in the spatial arrangement of the 18 terminal carbonyl groups (43), $(HCo_6(CO)_5)^-$, due to its particular bonding scheme which has terminal and bridging

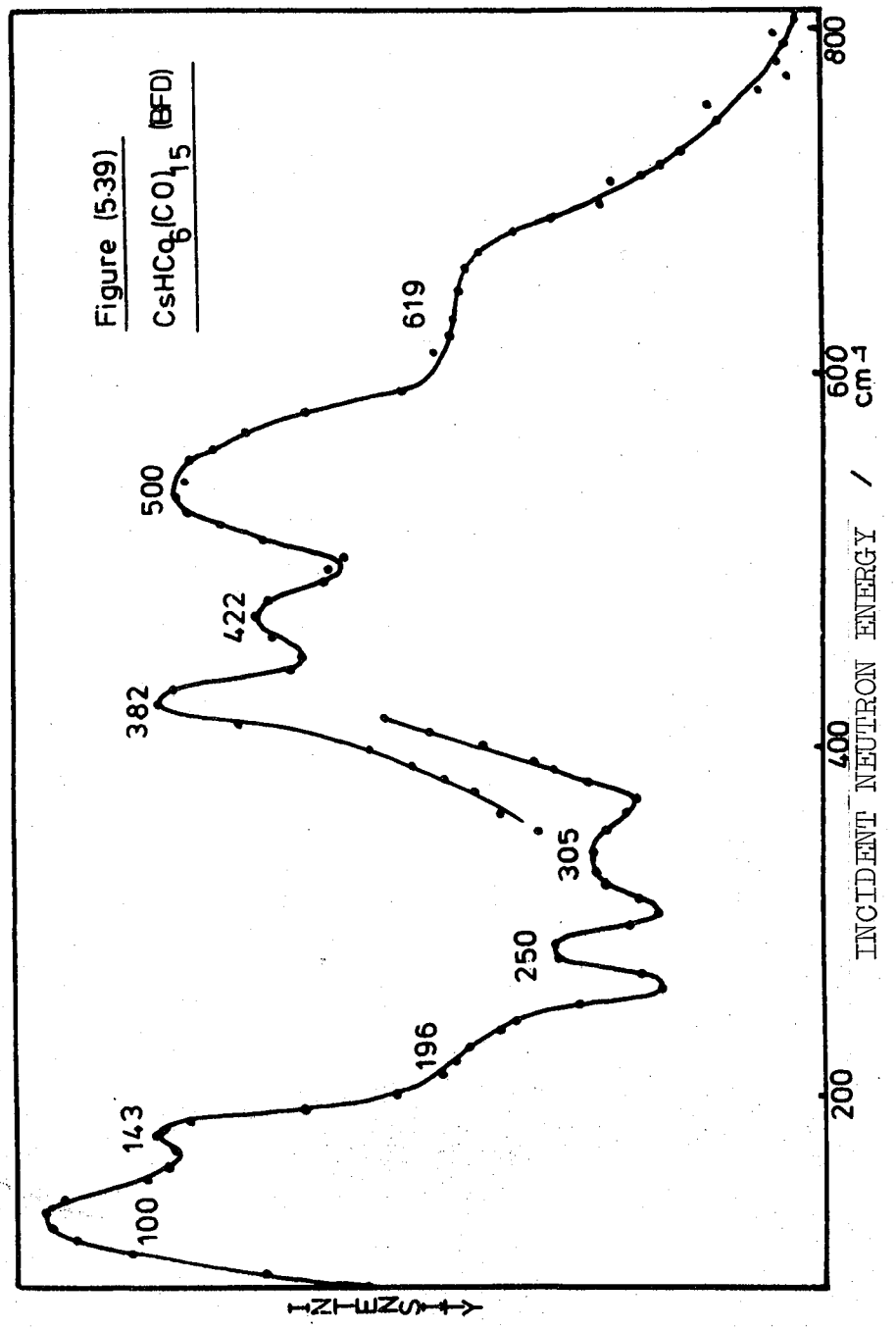
Figure (5.39)
CsHCo6(CO)15 (DFD)
INTENSITY
INCIDENT NEUTRON ENERGY / cm-1
100
143
196
250
305
382
422
500
619
200
400
600
800

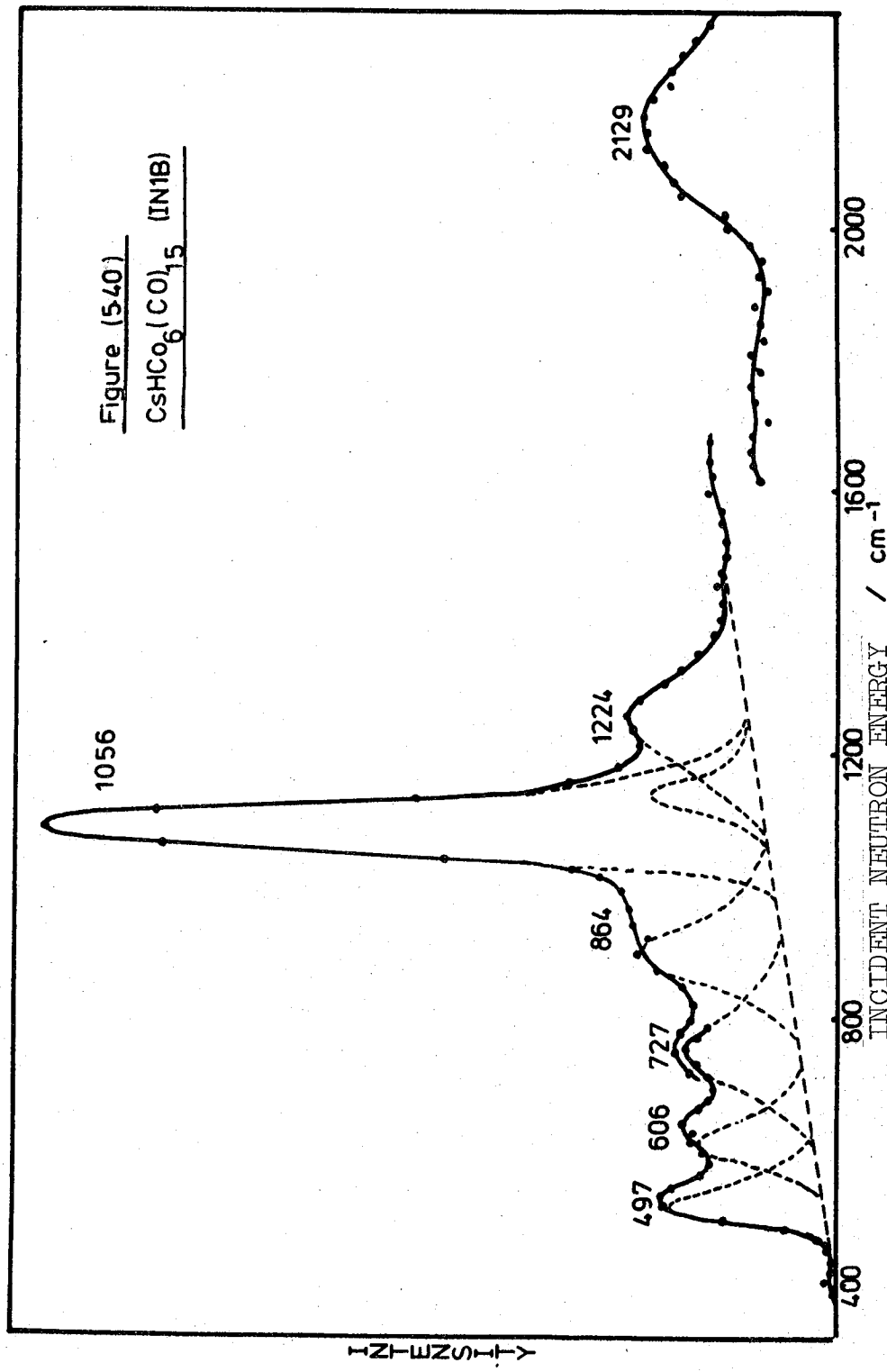
Figure (5.40)
$CsHCo_6(CO)_{15}$ (IN1B)
1056
1224
864
727
606
497
2129
400
800
1200
1600
2000
INCIDENT NEUTRON ENERGY / cm^{-1}
INTENSITY

carbonyls, has only C_s symmetry (50). However, the carbonyl cloud is probably not static and the motions that involve hydrogen are possibly uncoupled from the carbonyl vibrations. This will be dependent on the relative timescales in which these motions operate. The molecule may then be split into parts which independently vibrate. It is postulated that one need only consider the Co_6H unit to characterise the vibrations that involve hydrogen. The total representations of the Co_6H moiety are $A_{1g} + E_g + T_{2g} + 2T_{1u} + T_{2u}$. Only the T_{1u} symmetry group contains vibrations that involve hydrogen motion with respect to the metal octahedron. Dederichs et al (51) studied the vibrations of an interstitial atom with an octahedral hole. Figure 5.41 depicts the T_{1u} vibrations which involve hydrogen motion in Co_6H.

Figure 5.41: $2T_{1u}$ Vibration in Co_6H (51)

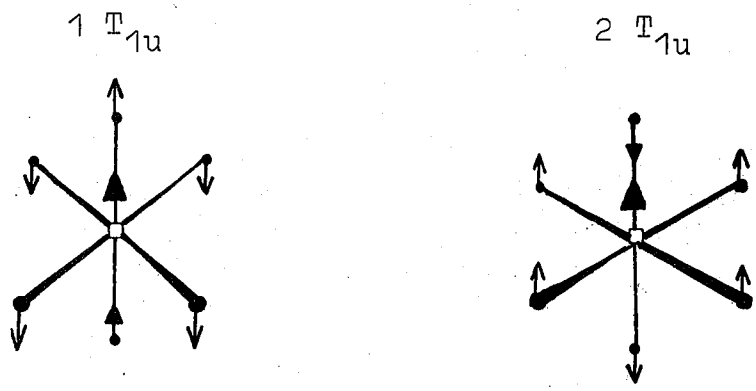

Oxton et al (44) expected only a single triply degenerate IR active band but two should have been anticipated using the descriptions of Dederichs et al (51). However, in $CsHCo_6(CO)_{15}$, only one band is found in the IR spectrum at 77K whereas two were found by Oxton et al at 95K with $(HRu_6(CO)_{18})^-$. Perhaps the two IR bands of $(HRu_6(CO)_{18})^-$ are those T_{1u} bands.

Since the vibrations resemble each other then this could explain their similar intensity. If this is the case then the bands must be strongly temperature dependent and even more so in $CsHCo_6(CO)_{15}$ where no splitting was seen even at 77K. The splitting could be evidence for the hydrogen residing away from the centre of the octahedron of Ru atoms in $(HRu_6(CO)_{18})^-$ whereas pure Oh symmetry may still remain in $(HCo_6(CO)_{15})^-$. This asymmetry was refuted by Oxton et al (44) who also ruled against a site group effect or factor group coupling. They postulated Fermi resonance but there is evidence that this effect does not take place in $M_2(\mu_2\text{-H})$ compounds whereas no evidence is available to support the postulate. There are splittings of IINS and IR bands known for metal hydrides (48,49) and the explanation was put forward that the hydrogen was residing further away from one of the metal atoms in the octahedron producing either a quasi- $M_5(\mu_5\text{-H})$ species similar to hydrogen residing in an four-fold symmetric hole on a metal surface or a quasi- $M_3(\mu_3\text{-M})$ species similar to hydrogen residing over a three-fold symmetric hole on a metal surface. It would be interesting to study the vibrational spectra of the $(Ni_{12}(CO)_{21}H_{4-n})^{n-}_{ions}$ (n = 2,3,4), which contain hydrogen considerably displaced from the octahedral hole centre (see Figure 4.17). This indicates that the hole available to the hydrogen is bigger than necessary. In $(Ni_{12}(CO)_{21}H_2)^{2-}$ the NiH distances are 2.22 and 1.72Å from neutron diffraction studies (52). The average NiH distance would be ~ 1.97Å with movement of 0.25Å to the 1.72Å position. The MH distances are 2.03 and 1.82Å in the Ru and Co clusters. This would appear to indicate that the

hydrogen in the Ru_6 octahedron would have more room than necessary whereas it would be more constrained in the Co_6 octahedron. Therefore, there would be a greater likelihood of band splitting in $(HRu_6(CO)_{18})^-$ than $(HCo_6(CO)_{15})^-$. Further arguments along these lines are developed in section 5.8. It would therefore appear that in the cobalt instance the two T_{1u} vibrations are coincident at 77K whereas they are coincident at 300K in $(HRu_6(CO)_{18})^-$ but not at 95K. The T_{1u} vibrations must be very similar. As shown in Figure 5.41 it is observed that the metal atom movement is similar in each case with the hydrogen atom moving in an opposite direction to two and four metal atoms. The distances travelled by the hydrogen will be greater in the $1T_{1u}$ vibration because it moves against the greater number of Ru atoms. Therefore the 845cm^{-1} band in $(HRu_6(CO)_{18})^-$ (44) can be tentatively assigned to $1T_{1u}$ vibration and the 806cm^{-1} band to the $2T_{1u}$ vibration.

The rest of the IINS spectrum of $CsHCo_6(CO)_{15}$ is composed of weak features. The band at 2129cm^{-1} is very probably the second harmonic of the stretch at 1056cm^{-1} (2 x 1056 = 2112). Looking at the 400-1200cm^{-1} region it may be possible that the background level in Figure 5.40 has increased somewhat giving the impression of many bands at 497, 606, 727, 864 and 1224cm^{-1}, all of weak-medium intensity. It is felt this was due to an instrument of artifact. For example, the 864 and 1224cm^{-1} band could not involve any ligand motions which have been activated through an associated hydrogen motion because there are no carbonyl vibrations between 600 and 1750cm^{-1}. The bands below 300cm^{-1} probably involve CoCo stretching modes.

It can be seen that the intensity in the 400cm^{-1} region compared with the band at 500cm^{-1} differs in the BFDDIDO and IN1B spectra. The IN1B spectrum shows a decrease in intensity below 500cm^{-1} whereas the BFDDIDO spectrum shows a prominent peak at 380cm^{-1}. This may be explained because it was known that when the compound was run on BFDDIDO the quality of spectra collected were very poor. The instrument was not functioning as well as could have been expected at that time.

5.6. The (μ_2-H) System

(a) Introduction

Seven techniques, known to have some value in evaluating the hydrogen position in transition metal hydridocarbonyls, using vibrational data, are used to estimate the hydrogen location in those compounds, in the present study, on which this information is not available. These estimates are standardised by compounds on which structural and vibrational data is available. Table 5.24 indicates the methods of bond angle evaluation.

Those compounds studied, in this, thesis, on which structural information is known are $HW_2(CO)_9NO$, $H_3Mn_3(CO)_{12}$ and $H_2Os_3(CO)_{10}$ whereas $H_4Ru_4(CO)_{12}$, $H_2FeRu_3(CO)_{13}$, $HRe_3(CO)_{14}$ and $H_3Re_3(CO)_{12}$ do not have their hydrogen positions characterised. Structural and vibrational data on $H_2Os_3(CO)_{10}$ $H_2Os_3(CO)_9CCH_2$, $Ph_4PHW_2(CO)_{10}$, $Et_4NHW_2(CO)_{10}$ and $Et_4NHCr_2(CO)_{10}$ was also available to calibrate the various plots (6).

Table 5.24: Methods of Bond Angle Evaluation

Method	Plot	Ref.
1	(ν_s/ν_{as}) vs. $(M_M^{-1}+M_M^{-1}(1+\cos\theta))^{\frac{1}{2}}(M_M^{-1}+M_M^{-1}(1-\cos\theta))^{\frac{1}{2}}$	11
2	(ν_{as}/ν_s) vs $\tan(\theta/2)$	6
3	ν_{as} vs $\sin(\theta/2)$	6
4	ν_{as}^2 vs $(1+\cos\theta)$	2
5	ν_s^2 vs $(1+\cos\theta)$	2
6	ν_{as} vs θ	4
7	ν_s vs θ	4

(b) Results

Table 5.25 contains all the information used in the various plots in this study of the relationship between the anti-symmetric and symmetric stretches and the hydrogen position. Figures 5.42-5.47 show the various plots used to estimate the hydrogen positions in $HRe_3(CO)_{14}$, $H_2FeRu_3(CO)_{12}$, $H_3Re_3(CO)_{12}$ and $H_4Ru_4(CO)_{12}$. Table 5.26 shows the information gained from each technique. In the diagrams the curves drawn are the best for the experimental data. The fitted lines are not related to the predicted lines, from a force field calculation, as in the case of theoretical line of Howard et al (6). Thus the order of the polynomial in each is decided purely by the fit.

The different techniques can be compared and it can be seen that they differ in the complexity of the θ factor. Cooper only plots the vibrational frequencies against θ whereas

Table 5.25: Data Used in Estimating Plots

Compound	υ Antisymmetric	υ^2 Antisymmetric ($\times 10^{-6}$)	υ Symmetric	υ^2 symmetric ($\times 10^{-6}$)	θ	$\tan(\theta/2)$	$\sin(\theta/2)$	$(1+\cos\theta)$	$(1-\cos\theta)$	** Katovic Number	Plot Number
$HRe_3(CO)_{14}$	1604	2.573	1064	1.132	-	-	-	-	-	-	-
$HW_2(CO)_9NO$	1595	2.544	1056	1.115	125.5	1.937	0.889	0.419	1.581	0.518	1
$H_2FeRu_3(CO)_{13}$	1471	2.164	1322	1.748	-	-	-	-	-	-	-
$H_3Re_3(CO)_{12}$	1675	2.806	1159	1.343	-	-	-	-	-	-	-
$H_3Mn_3(CO)_{12}$	1661	2.759	875	0.766	131	2.194	0.910	0.344	1.656	0.465	2
$H_4Ru_4(CO)_{12}$	1660	2.560	1294	1.674	-	-	-	-	-	-	-
$H_2Os_3(CO)_{10}$	1483	2.199	1225	1.501	94.3	1.080	0.733	0.930	1.070	0.928	-
$HOs_3(CO)_{10}CHCH_2$	1392	1.938	1286	1.654	101.5	1.222	0.775	0.801	1.199	0.826	3
$H_2Os_3(CO)_9CCH_2$	1411	1.991	1313	1.724	103.5	1.266	0.786	0.767	1.233	0.798	4
$Ph_4PHW_2(CO)_{10}$	1520	2.310	1022	1.045	123.3	1.853	0.880	0.451	1.549	0.561	5
$Et_4NHW_2(CO)_{10}$	1680	2.820	875	0.766	137.2	2.552	0.931	0.266	1.734	0.423	6
$Et_4NHCr_2(CO)_{10}$	1720	2.958	818	0.669	158.9	5.365	0.983	0.067	1.933	0.212	7
$H_3Mn_3(CO)_{12}$	1660	2.756	888	0.789	131	2.194	0.910	0.344	1.656	0.465	-
$H_2Os_3(CO)_{10}$	1228	1.508	1177	1.385	92.6	1.046	0.723	0.955	1.045	0.956	-

** The Katovic number is $[M_M^{-1} + M_M^{-1}(1+\cos\theta)]^{\frac{1}{2}}[(M_M^{-1} + M_H^{-1}(1-\cos\theta)]^{-\frac{1}{2}}$

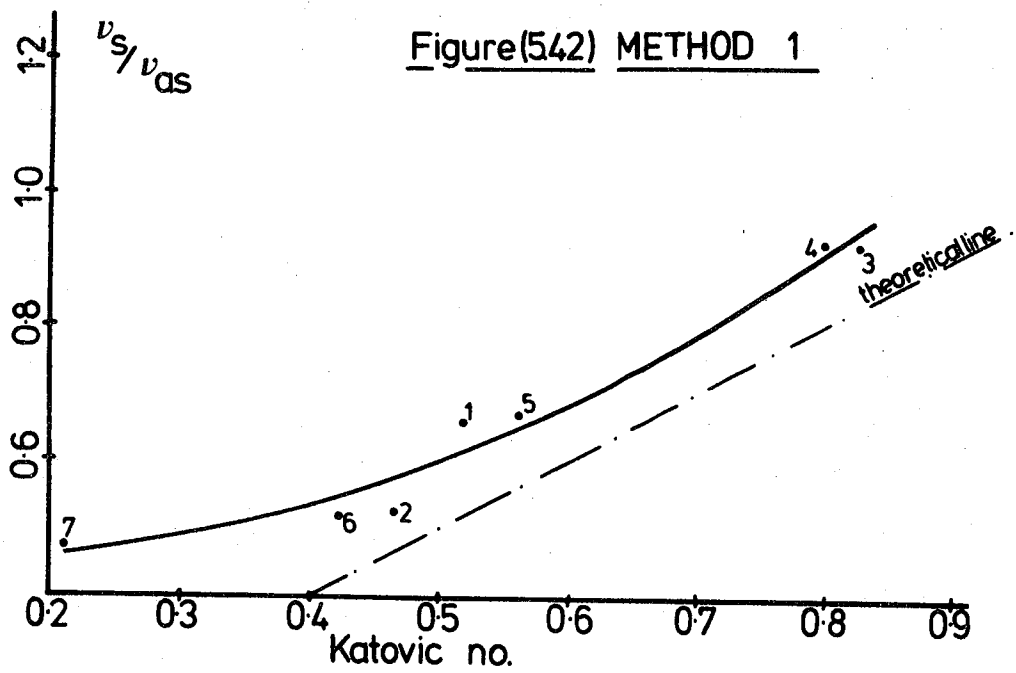

Figure(5.42) METHOD 1

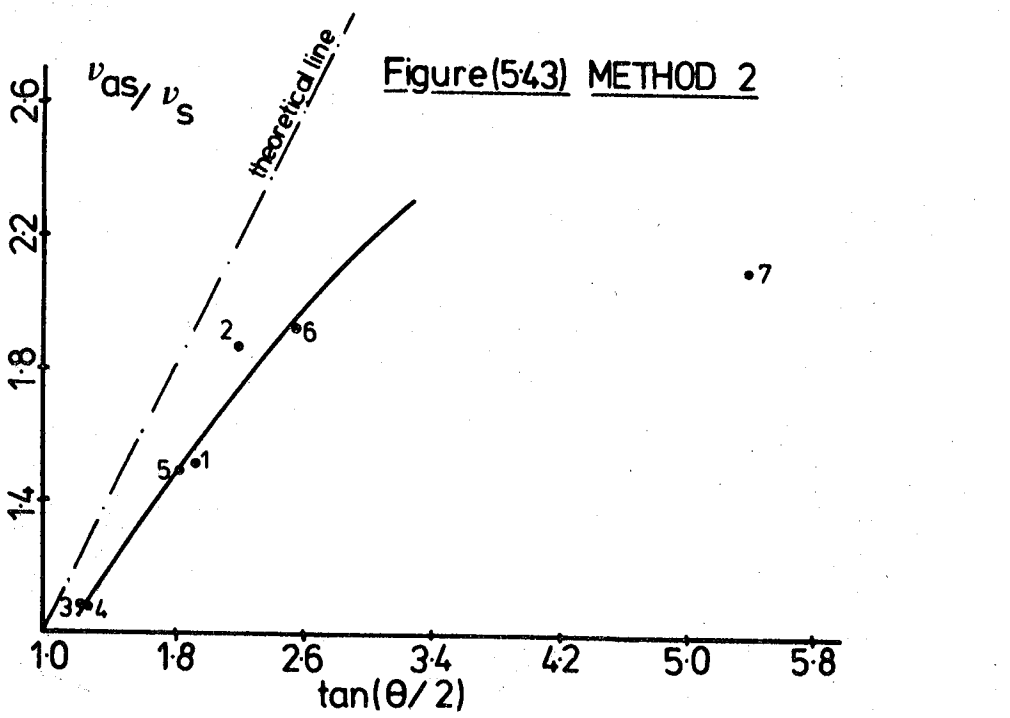

Figure(5.43) METHOD 2

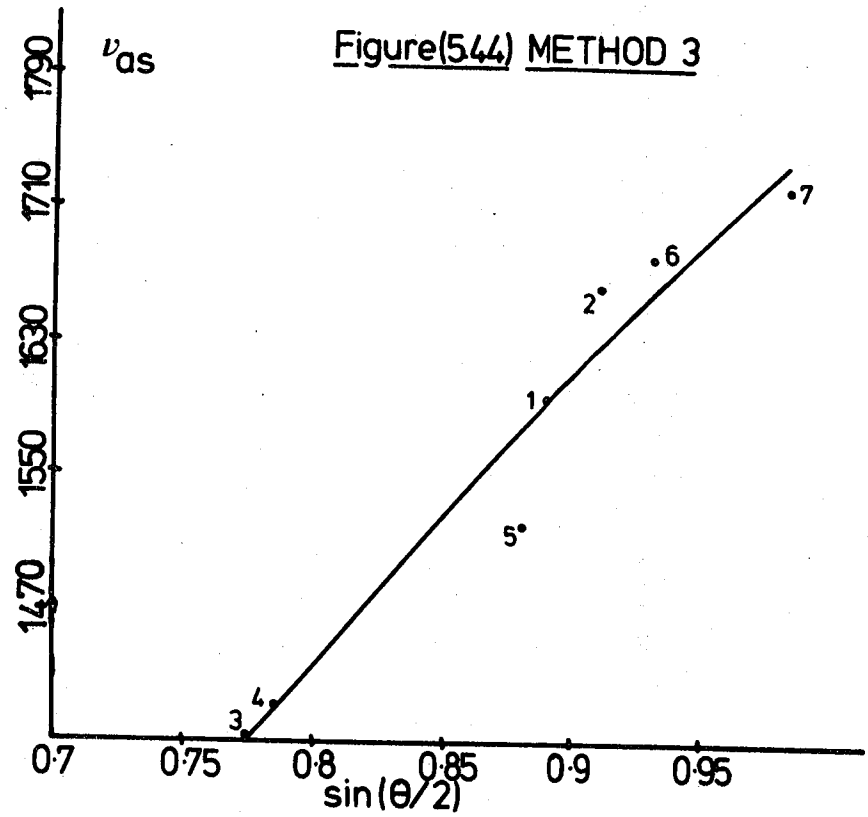

Figure(544) METHOD 3

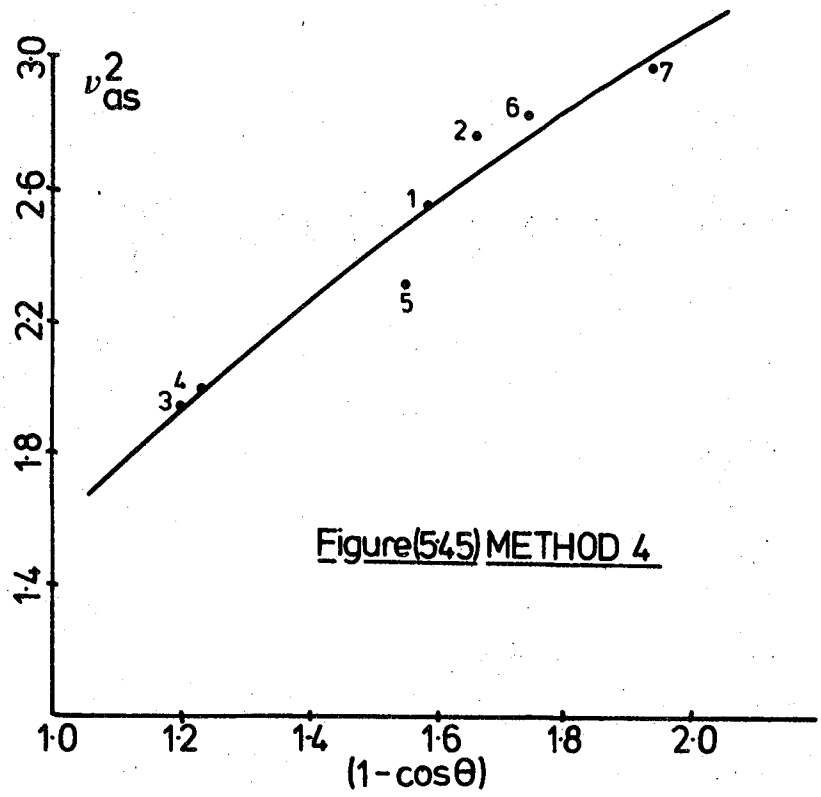

Figure(545) METHOD 4

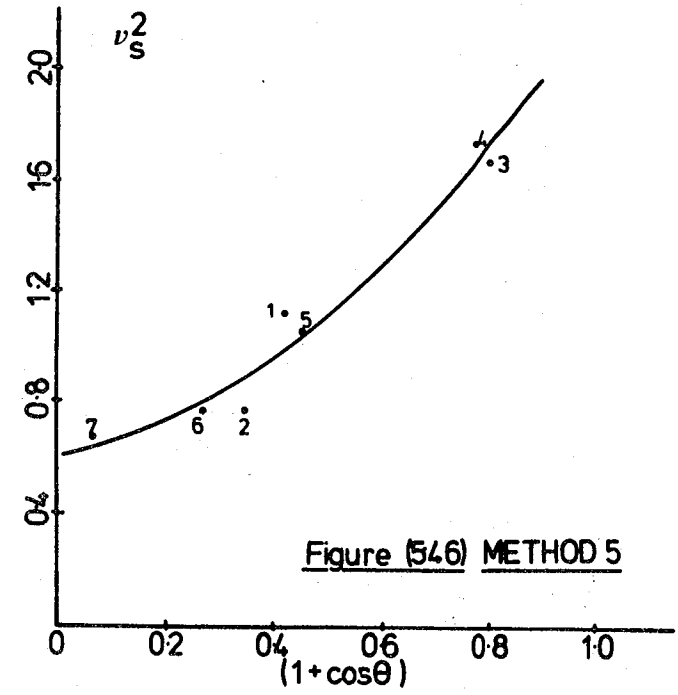

Figure (546) METHOD 5

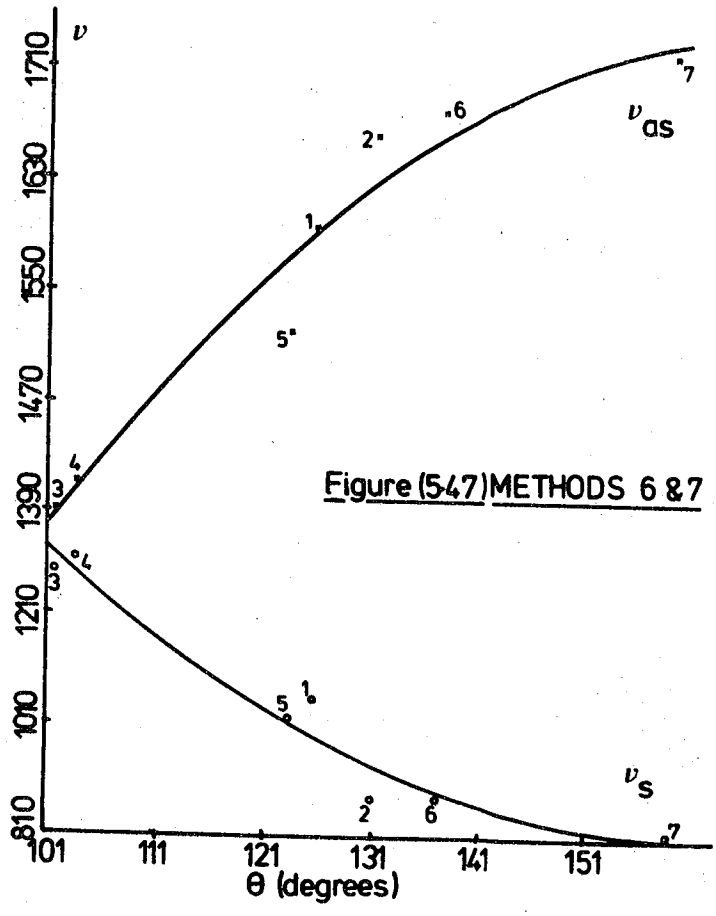

Figure (547) METHODS 6 & 7

Howard et al and Kirtley use simple valence force fields to described the 'M_2H entity' with suitable approximations. These were that the mass of the metal atoms were of infinite value compared to the hydrogen atom mass and that the angle deformation force constant was much smaller that the bond

Table 5.26: MHM Angles Derived From Relationship (^{o})

Method	$HRe_3(CO)_{14}$	$H_2FeRu_3(CO)_{13}$	$H_3Re_3(CO)_{12}$	$H_4Ru_4(CO)_{12}$
1	120.6	103.8	118.7	113.6
2	123.0	105.6	120.6	115.0
3	127.0	109.8	141.2	126.4
4	126.1	108.0	140.4	126.8
5	119.4	101.6	113.0	103.3
6	126.3	110.0	139.5	126.0
7	17.7	102.0	111.0	103.0

stretching force constant. The method due to a Katovic and McCarley goes a little further in taking the mass of the metal atoms to be a finite value. It can be seen from the plots that the Katovic technique, Figure 5.42, would appear to reflect the angle situation more realistically. There is a greater spread in the points in the plots 3 to 7. The methods 1 and 2 (at small bond angles) will be used in the following sections in the evaluation of the MHM

bond angles in clusters and of hydrogen on metal surfaces. In plot 2, Figure 5.43, at larger values of θ, the deviation from the theoretical line increases rapidly. In a central force field model with $\theta = 180^{\circ}$ then ν_s should be zero but in the valence force field this extreme situation is never met because the angle deformation constant, which was taken as much smaller than the stretching force constant, becomes more important. Hence as θ increases, the observed ν_{as}/ν_s ratio tends to a value less than that stated in the equation which governs method 2. ($\nu_{as}/\nu_s = \tan \theta/_2$)

The equations of the curves in plots 1 - 7 are shown in Table 5.27. These points were fitted using a curve fitting computer program.

Table 5.27: Equations of Curves in Figures 5.42-5.47

Figure	Method	Equation of Curve
5.42	1	$y = 0.463 - 0.203\,x + 0.958\,x^2$
5.43	2	$y = 0.203 + 0.622\,x + 0.0968x^2 - 0.0273x^3$
5.44	3	$y = -768 + 3660\,x - 1128\,x^2$
5.45	4	$y = -0.699 + 2.629\,x - 0.369\,x^2$
5.46	5	$y = 0.607 + 0.384\,x - 1.172\,x^2$
5.47	6	$y = -509 + 26.77x - 0.0798\,x^2$
5.47	7	$y = 4565 - 46.71\,x + 0.145\,x^2$

(c) Discussion

(i) Position of H Atoms in $H_2Os_3(CO)_{10}$

It is felt that one cannot be justified in comparing the vibrational data on $H_2Os_3(CO)_{10}$, which contains the $M_2(\mu_2\text{-}H)_2$ moiety, with that of $M_2(\mu_2\text{-}H)$ compounds. It has

been shown that the character of the $(\mu_2\text{-H})_2M_2$ system differs from that of the $M_2(\mu_2\text{-H})$ system. For example, $(\mu_2\text{-H})Os_2$ and $(\mu_2\text{-H})_2Os_2$ species differ in the type of Os-Os bonding and this is shown in the differing Os-Os bond lengths. $Os_3(CO)_{12}$ has no bridged hydrogen and has an Os-Os bond length of 2.877Å (53) whereas the following compounds all have similar non-bridged Os-Os distances but singly-bridged bond lengths of 3.061Å in $H_2Re_2Os_3(CO)_{20}$ (54), 2.989Å in $H_2Os_3(CO)_{11}$ (55) and 2.963Å in $H_4Os_4(CO)_{11}CNMe$ (56). $H_2Os_3(CO)_{10}$ has a doubly-bridged Os-Os distance of only 2.68Å indicating the Os=Os 'double-bond' character. Thus $H_2Os_3(CO)_{10}$ can only be compared with like-species such as $H_2Re_2(CO)_8$ and $(H_2W_2(CO)_8)^{2-}$. The OsHOs bond angles estimated using the data from our work lie in the 106-111° range ie at least 12° higher than the actual value of 94.3°. Using the vibrational assignments of Howard et al (6), which are thought incorrect, one gets an OsHOs bond angle of between 88-111° (using methods 1 and 2 (average) using our data OsHOs = 108.6°, using their data OsHOs = 100°.)

(ii) Position of hydrogen atoms in the related pair $H_2FeRu_3(CO)_{13}$ and $H_4Ru_4(CO)_{12}$

$H_4Ru_4(CO)_{12}$ was studied by x-ray diffraction techniques (57), however, due to partial molecular disordering, only an inconclusive hydrogen site was found. The measured Ru-H distance was 1.76Å though no significance was placed on this figure. This distance indicated an RuHRu angle of 116.7°. This can be compared with the average RuHRu bond angles of 115.2° found in $H_4Ru_4(CO)_{10}(Ph_2PCH_2CH_2PPh_2)$ by an X-ray

analysis by Shapley et al (35). In Table 5.26 it can be seen that the bond angles derived from the seven methods varies from 103.0° to 126.8°. However, as discussed earlier, methods 3,4 and 6 always give too high an estimate whereas methods 5 and 7 always underestimate (The average of the 7 values is 116.3°). Since more confidence can be placed on methods 1 and 2, an average of the two is taken as a reasonable estimate of the bond angle. This is calculated to be 114.3°

Now $H_2Ru_4(CO)_{13}$ has bridged Ru-Ru distances of 2.93Å and non-bridged Ru-Ru distances of 2.78Å (58) which can be compared with 2.911Å and 2.79Å respectively for $H_2Ru_3Fe(CO)_{13}$ (59). This would appear to indicate that the Ru_3 triad in $H_2FeRu_3(CO)_{13}$ is not seriously perturbed by the replacement of an Ru atom by an Fe atom. $H_4Ru_4(CO)_{12}$ has bridged Ru-Ru bond lengths of 2.996Å and unbridged distances of 2.772Å (57). Here the bridging hydrogen lengthens the Ru-Ru bond by 8.08% whereas an increase of only 4.30% was found in $H_2FeRu_3(CO)_{13}$. Now if the Ru-H distance is comparable in $H_2FeRu_3(CO)_{13}$ and $H_4Ru_4(CO)_{12}$, as indicated with reference to $H_2Ru_4(CO)_{13}$, then the expected RuHRu angle should be smaller than that found in $H_4Ru_4(CO)_{12}$ and is calculated to be 104.9°. The average estimate using all the methods is 106.0° whereas the average between methods 1 and 2 is 104.7°, which is entirely reasonable with the above arguments.

(iii) Hydrogen positions in $HRe_3(CO)_{14}$ and $H_3Re_3(CO)_{12}$

No structural work has been carried out on $H_3Re_3(CO)_{12}$. It has been indicated that Dahl carried out an X-ray study of $HRe_3(CO)_{14}$, eg (60), and found the bridged Re-Re distance was 3.295Å. An estimate of 159° was made for the ReHRe bond

angle. It is felt that the value of 159° in $HRe_3(CO)_{14}$, using an ReH distance of 1.7Å (approx) is much too large since Dahl bases his conclusions on the octahedral array of ligands. However, now it is known that, for a single $M_2(\mu_2\text{-H})$ system, the hydrogen prefers to reside beyond the LReReL 'crossing point'. Thus, a larger Re-H distance would be expected. It is known that the ReH distance in $H_4Re_4(CO)_{12}$ is 1.77Å (40) and in $H_8Re_2(PEt_2Ph)_4$ is 1.878Å (61). Unfortunately no other Re-H distances are known. Using the more appropriate (μ_2-H) Re distances of 1.878Å and the 3.295Å Re-Re distance, the ReHRe angle in $HRe_3(CO)_{14}$ may be 122.6°, which can be compared with the values derived from the vibrational frequencies: average of 7 methods = 122.9° whereas the more reasonable average between methods 1 and 2 = 121.8°. It would appear therefore that simple geometric considerations can also be used with careful choice of M-M (bridged) and M-H distances. For example the X-ray study of $HRe_2Mn(CO)_{14}$ (23) did not find the hydrogen atom but using the measured Re-Re distance of 3.392Å and the possible ReH distance of 1.828Å, the ReHRe bond angle can be shown to be 129.1°. This value differs considerably from the 164° evaluated by Dahl's 'octahedral array' technique. This further weakens the case for using the axial MCO vectors in evaluating a hydrogen position.

$H_3Re_3(CO)_{12}$ seems to differ greatly from the above examples and it can be seen from Table 5.26 that the estimated bond angles differ from technique to technique and form two distinct groups. Those with MHM values of ~ 120° and those of ~ 140°. This has arisen because of the evidence in favour of the 1159cm^{-1} bond as the symmetric stretch, instead of the

845cm^{-1} band. If the 845cm^{-1} band had been taken as the symmetric stretch, a consistent value of ~142° would be found. However, the preferred assignment indicates that the more correct estimating techniques are those involving the ratio of the antisymmetric stretch to the symmetric stretch and vice versa rather than the individual values. The value of the ReHRe angle, as estimated by method 1 and 2, is 118.7° and 120.6°, much more similar to other ReHRe angles than the higher value of ~145°. If a value of ~1.88Å is taken for the ReH distance, one can calculate the Re-Re (bridged) distance in the case of the 140° value to be approximately 3.53Å, an unbelievably long distance, especially compared with the hydrogen bridged distances in $(H_2Re_3(CO)_{12})^-$ (62) of 3.18Å and in $(HRe_3(CO)_{12})^{2-}$ (2) of 3.14Å. The value calculated using the ReHRe angle of 119.7° (av.) is 3.25Å, a more reasonable value.

(5.7) The (μ_3-H) Systems

An attempt will be made to compare the structural and vibrational data for the three (μ_3-H) compounds and to present a method by which possible (μ_3-H) species on transition metal surfaces can be structurally evaluated from suitable vibrational data. However, caution must be expressed since only 3 compounds were studied, of which structural data is only available for two of them. The hydrogen position has been found in $H_4Re_4(CO)_{12}$ (40) and $HFeCo_3(CO)_9(P(OCH_3)_3)_3$ (43) and, though an X-ray analysis has been carried out on $H_2Ru_6(CO)_{18}$, the exact location has yet to be determined (64). The 'estimating' techniques have shown that quite reasonable MHM bond angles can be calculated from credible MH distances

and known MM distances. In the case of $H_2Ru_6(CO)_{18}$, the Ru-Ru (bridged) distance is known to be 2.95Å (64). From the change in Re-H bond lengths from (μ_2-H) to (μ_3-H) entities, an estimate of the Ru-H bond distance can be obtained from known Ru-(μ_2-H) systems. This value of 1.72Å can thus give an Ru-(μ_3-H)-Ru angle of 118°. This value will be used with those of the other (μ_3-H) compounds.

The two preferable techniques; methods 1 and 2, of estimating the MHM bond angle will be used. Once again it must be stated that the $M_3(\mu_3$-H) systems, like $H_2Os_3(CO)_{10}$, cannot be compared with the $(\mu_2$-H)M_2 systems because of the essential bonding differences though the techniques may lend themselves to the individual systems chosen. Table 5.28 shows the data used in the plots of (υ_{as}/υ_s) vs. tan ($\theta/2$), Figure 5.48, and (υ_s/υ_{as}) vs. $(1/M_M+1/M_H(1+\cos\theta))^{\frac{1}{2}}(1/M_M + 1/M_H(1-\cos\theta))^{-\frac{1}{2}}$, Figure 5.49.

Table 5.28: Data Used for $M_3(\mu_3$-H) Study

Compound	υ_{as}	υ_s	θ^o	$\frac{\upsilon_{as}}{\upsilon_s}$	$\frac{\upsilon_s}{\upsilon_{as}}$	$\tan(\frac{\theta}{2})$	Katovic No.
$HFeCo_3(CO)_{12}$	1102	1240	92	0.889	1.125	1.032	0.966
$H_2Ru_6(CO)_{18}$	1270	1048	118(e)	1.212	0.825	1.670	0.604
$H_4Re_4(CO)_{12}$	1128	1032	110.8	1.093	0.915	1.450	0.692

It is noted that the best line drawn in these figures is straight whose equations are: Figure 5.48 y=0.8x+0.35 and Figure 5.49 y = 0.49x + 0.385. Once again the same general trends are shown, in each case, as those seen in the $M_2(\mu_2$-H) comparison. From the data it can be seen that at low MHM angles the υ_s value is greater than the υ_{as} value. This

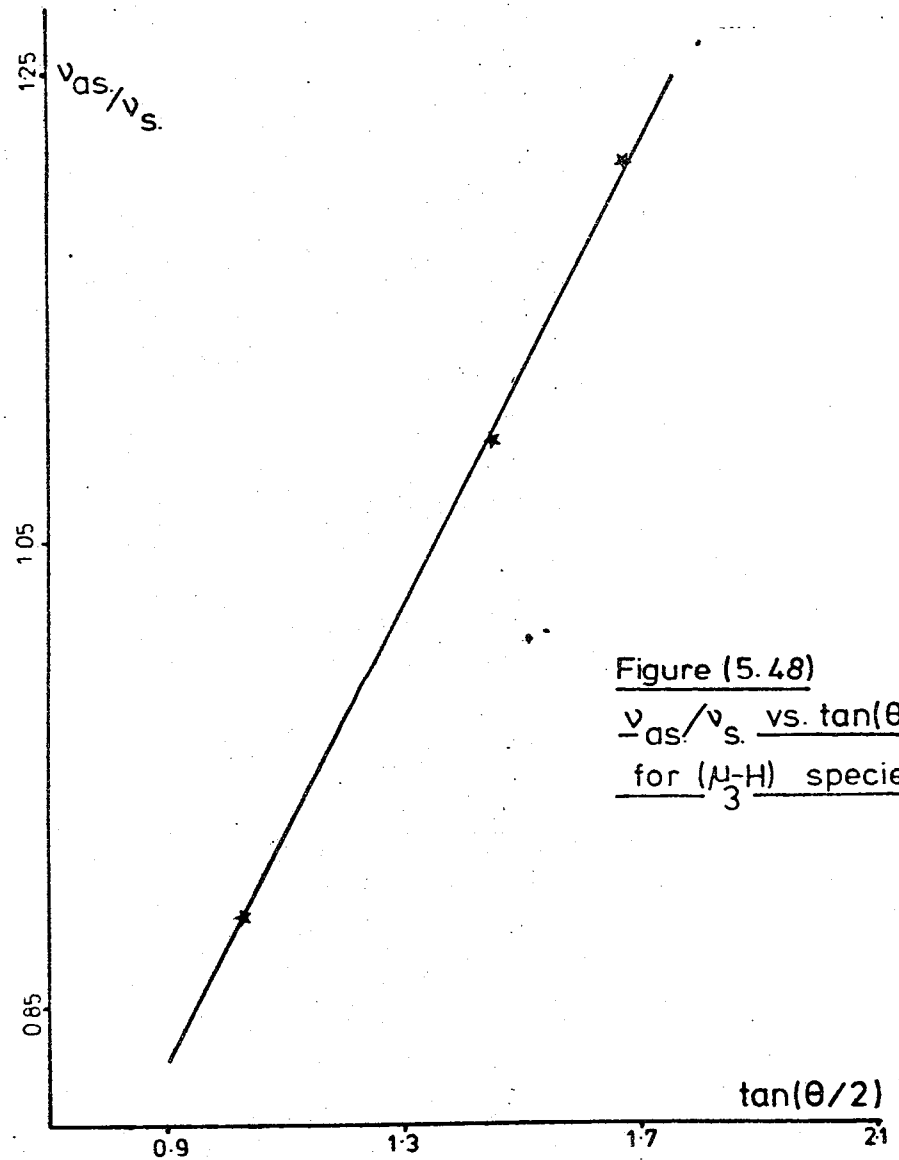

Figure (5.48)
$\nu_{as.}/\nu_{s.}$ vs. tan(θ/2)
for $(\mu_3\text{-H})$ species

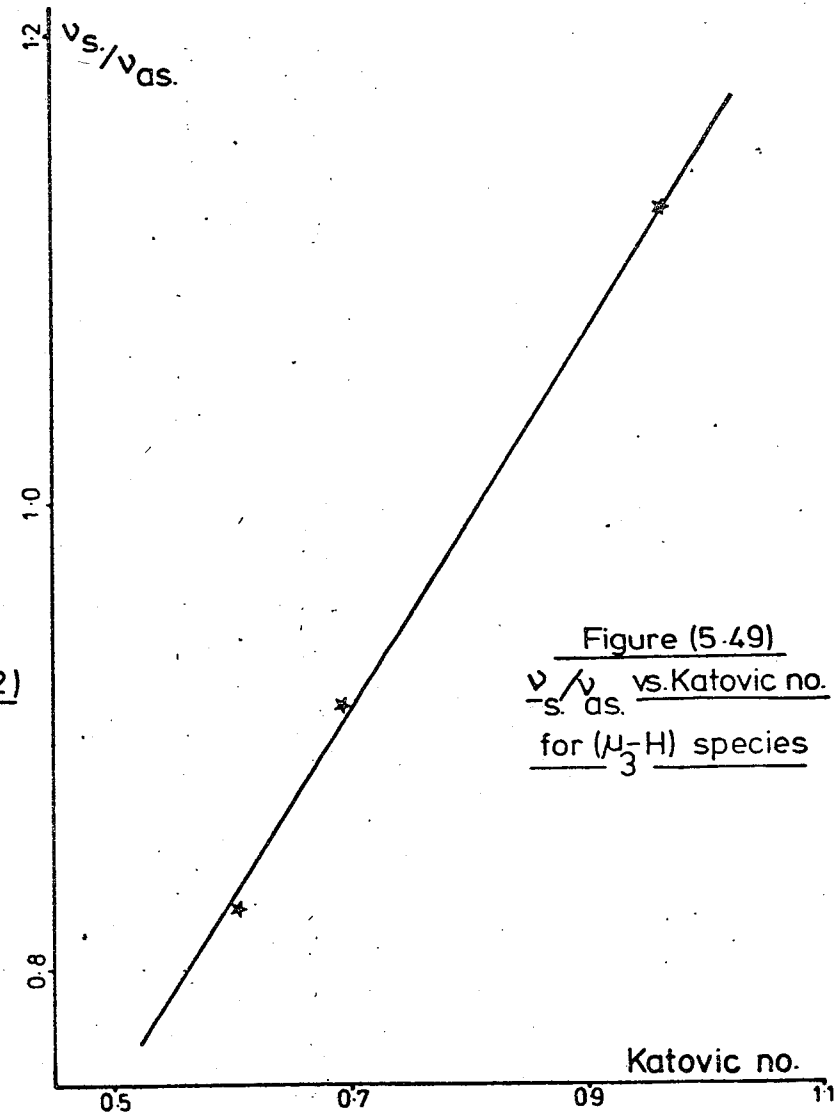

Figure (5.49)
$\nu_{s.}/\nu_{as.}$ vs. Katovic no.
for $(\mu_3\text{-H})$ species

'cross-over' point occurs at an MHM angle of ~100° which can be compared with the $(\mu_2\text{-H})M_2$ data, Figure 5.47, where a similar 'cross-over' point was found at 100°. Data from this $(\mu_3\text{-H})$ comparison will be used in section 5.5 to test possible $(\mu_3\text{-H})$ assignments on transition metal surfaces. It can be noted that the large RuHRu angle of 118° means that the hydrogen is residing quite close to the Ru_3 plane resulting in an Ru_3(surface)-H distance of 0.22Å (The H to Re_3(surface) in $H_4Re_4(CO)_{12}$ is 0.3Å) (40). The maximum MHM angle in such a situation would be 120° when the hydrogen would reside in the metal triad plane.

5.8. The $(\mu_6\text{-H})$ system

Unfortunately there are only vibrational data available on two $(\mu_6\text{-H})$ transition metal clusters, $(HRu_6(CO)_{18})^-$ (44) and $(HCo_6(CO)_{15})^-$ though structural data are available on other clusters which contain hydrogen in octahedral holes, such as $(HNi_{12}(CO)_{21})^{3-}$ and $(H_2Ni_{12}(CO)_{21})^{2-}$ (52). One may compare the structural and vibrational data available on these compounds with metal hydrides containing hydrogen. Table 5.29 contains data on MH bond lengths (d_{M-H}), M_6H vibrational frequencies (ν_{MH}) and the respective metal and hydrogen electronegativities. Figure 5.50 shows a plot of ν_{M-H} against d_{M-H} and Figure 5.51 shows a plot of log (ν_{M-H}) vs log (d_{M-H}). The equation of the curve drawn in Figure 5.50 is $y = 5x - 0.0055x^2$ whereas in Figure 5.51, a straight line was drawn whose equation is $y = -1.931x + 2.131$. It can be seen that there is a definite trend in the increase in vibrational frequency, ν_{MH}, with a decrease in the MH distance, d_{M-H}. There would also appear to be an increase

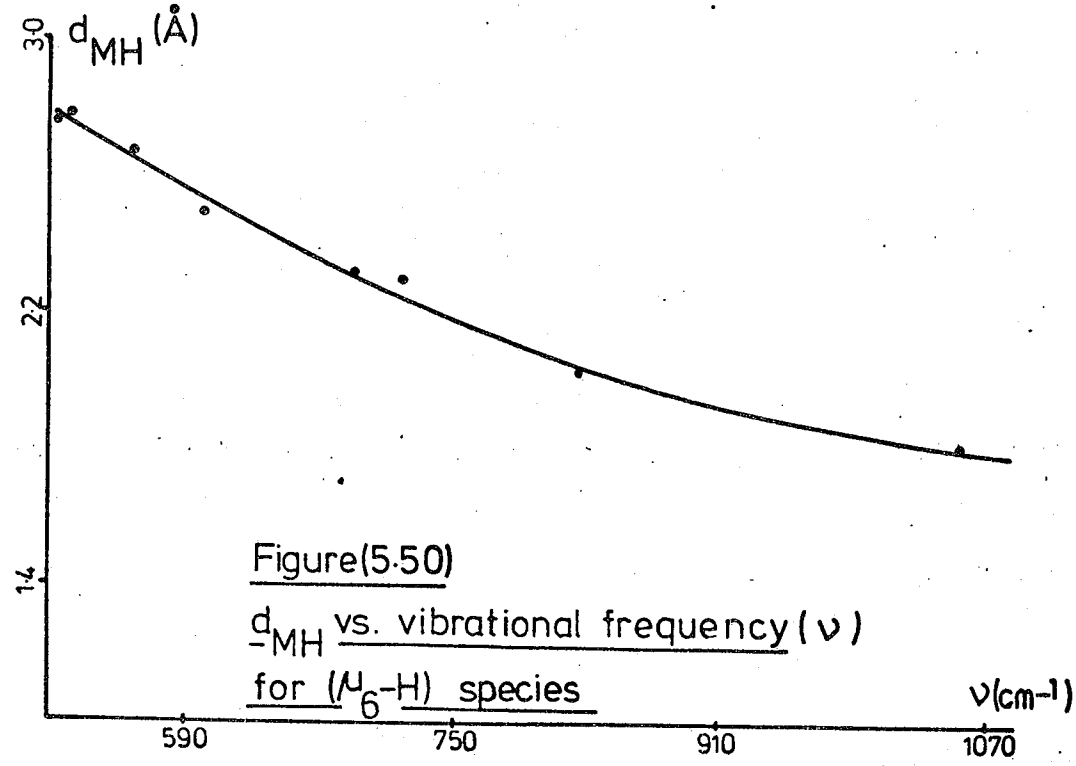

Figure(5·50)
d_{MH} vs. vibrational frequency (ν)
for (μ_6-H) species

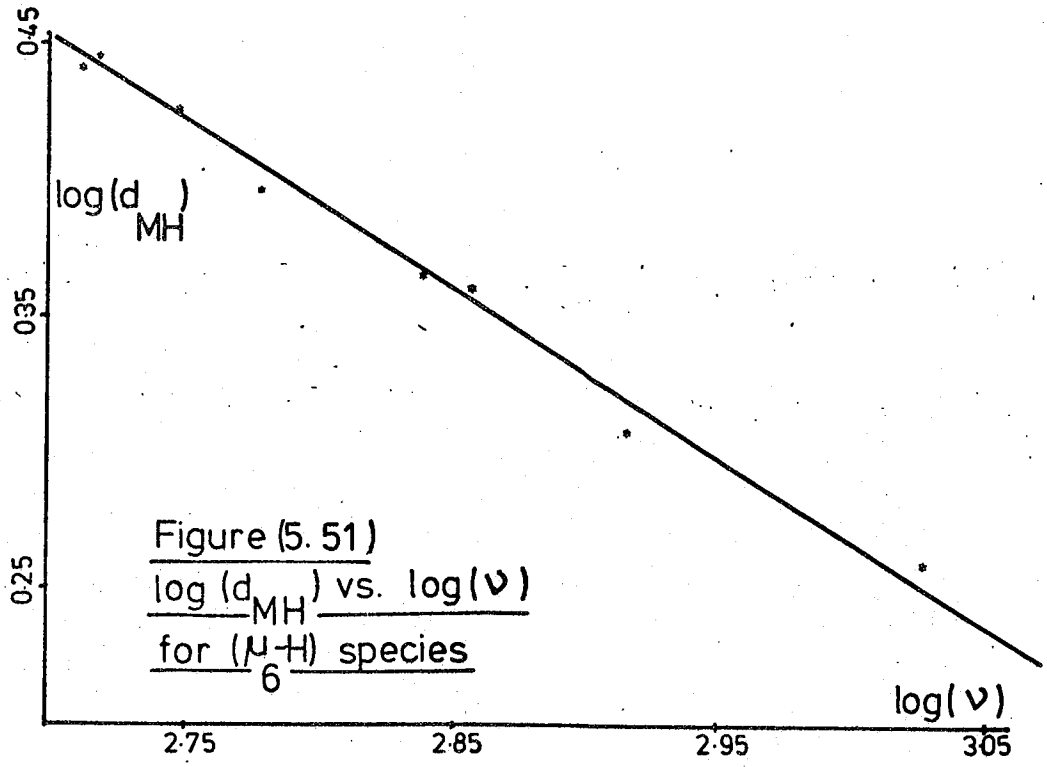

Figure (5. 51)
log (d_{MH}) vs. log(ν)
for (μ_6-H) species

in the electronegativity of the metal atom as the d_{M-H} decreases and υ_{M-H} increases. Chini (64) discussed various

Table 5.29: Data For (μ_6-H) Systems

System	d_{M-H}(Å)	υ_{M-H}(cm^{-1})	Metal Electronegativity
$(HCo_6(CO)_{15})^-$	1.82 (50)	1056	1.70
$(HRu_6(CO)_{18})^-$	2.03 (44)	* 825 (44)	1.42
YbH_2	2.30 (48)	720(48)	1.06
CaH_2	2.32 (48)	690 (48)	1.04
SrH_2	2.49 (48)	600 (48)	0.99
BaH_2	2.67 (48)	560 (48)	0.97
$LaH_{2.97}$	2.76 (64)	516 (65)	1.10
$CeH_{2.80}$	2.78 (64)	524 (65)	1.06
H	-	-	2.10

* $825cm^{-1}$ is an average value (44)

features of simple metal interstitial hydrides and it would seem that the lanthanum and cerium hydrides are the most electron rich, in this study, and they give up a large, but partial negative charge in favour of the more electronegative interstitial atom whereas the much more electronegative cobalt atoms would rather hold onto the electronic charge thus reducing the charge on the interstitial atom. Various theoretical cluster models of the electronic structure and bonding mechanisms of interstitial hydrogen have been developed by Adachi and Imoto (66) and Messmer et al (67) for the groups Sc-Cu and Ni-Pt respectively. In both models electron transfer takes place, to a certain degree, between

the M_6 octahedron and the proton with the resulting formation of a bond between the H is orbital and the M 'spd' orbitals of correct symmetry, in this case the symmetric A_{1g} orbitals. The resulting orbital is quite stable and lies well below the metal 'd' band. This band will probably be more ionic in the Co_6H species and more covalent in the case of the rare earth hydrides. Further, the higher vibrational frequency exhibited by the Co_6H entity would appear to indicate a stronger, more stable, bond than that taking place in the Ru_6H analogue. Further evidence for this lies in the fact that a stabilising effect is known to take place when bridging ligands are found on the exterior of the metal octahedron, for example, (μ_3-I) species in HNb_6I_{11}. Four bridging (μ_2-CO) species are found in $(HCo_6(CO)_{15})^-$ whereas all the carbonyls in $(HRu_6(CO)_{18})^-$ are terminal. Also the vibrational spectrum of $(HCo_6(CO)_{15})^-$ contains only a single peak possibly indicating an octahedral hydride whereas a more complex situation perhaps is found in $(HRu_6(CO)_{18})^-$ indicative of a less symmetric structure.

This trend in ν_{MH} and d_{MH} for M_6H systems has been mirrored in tetrahedral M_4H moieties. Ross et al (47,69) measured ν_{MH} for hydrogen in tetrahedral holes in metals and plotted the peak frequency against d_{MH}. Figures (5.52,5.53) show the trend where there is a fall in peak frequency with an increase in d_{MH}. Sakamoto (68) derived for such systems a potential relationship which quantified this trend where ν_{MH}, for sites of a given geometry (eg. Td or Oh), could be correlated with d_{MH}. The Sakamoto line is shown in Figure 5.52. Ross et al (69) postulated that deviations from the

Figure (5·52) Relationship between d(M-H) and (M H) vibrational frequency (69)

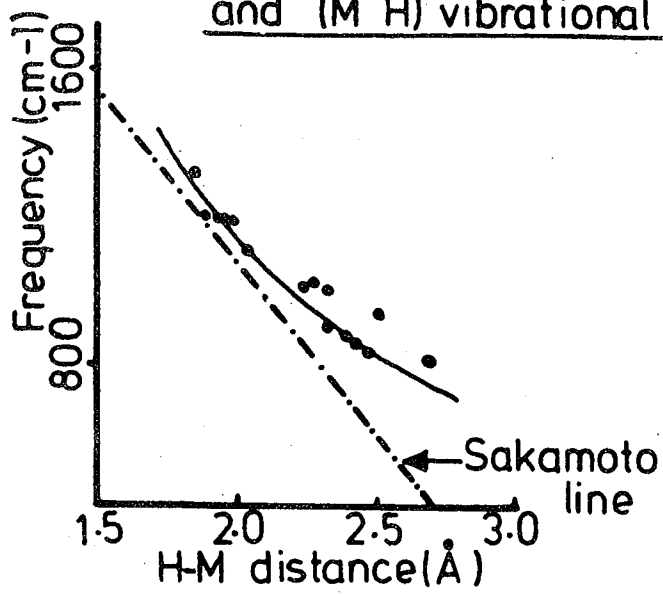

Figure(5.53) Relationship between d(M-H) and (M-H) vibrational frequency (47)

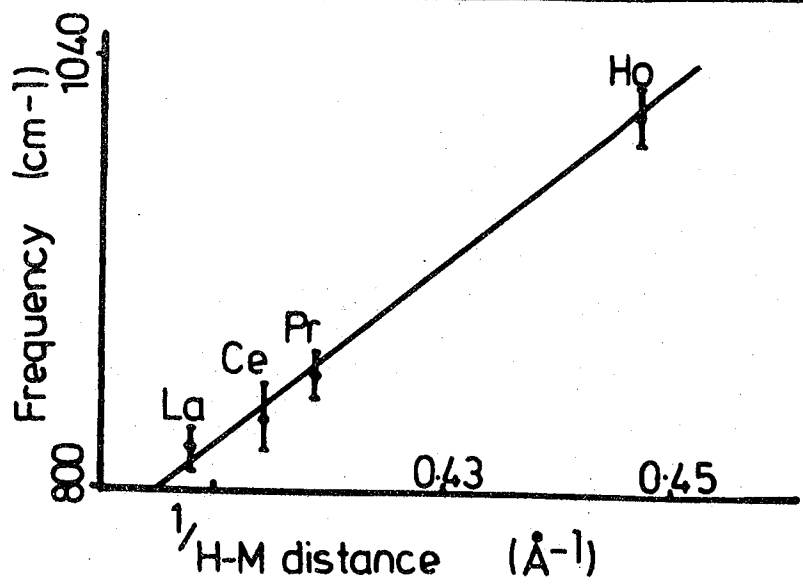

general trend could be an indication of instability. It can be noted that there is a similar trend in Figures 5.50, 5.51). As the frequency falls, d_{MH} moves further away from the Sakamoto line which would appear to be adhered to at high frequencies and low M-H distances. Thus, in Figure 5.50 (frequency versus d_{M-H} for the octahedral species) if the Sakamoto line operates similarly then the data on the cluster compounds will lie nearer the line whereas the rare-earth interstitial systems will move away from possible ideality.

As noted by Ross et al (69) some datum points were found to deviate from the main trend. This also occurs in the octahedral systems. If one considers the Pd-H system where vibrational frequencies have been reported at 549cm^{-1}, in the α-phase, and 460cm^{-1}, in the β-phase (70) and the Pd-H distance is 2Å (64). No convincing argument can be advanced to explain this.

5.9. Hydridocarbonyls: Relationships between vibrations of hydrogen in transition metal hydridocarbonyls and hydrogen chemisorbed on transition metal surfaces

5.9.1. Introduction

As already discussed in Chapter 4 there can be virtue in comparing characterised model compounds with adsorbate/adsorbent systems, especially if the latter have been difficult to characterise or where conflicting data has been found. The use of vibrational data on model compounds, such as transition metal hydridocarbonyls, has been put to use by Jayasooriya et al (71) and Willis (72) to describe the arrangement of atomic hydrogen atoms bonded to the (100), (110) and (111) planes of tungsten. This was carried out by using the

MHM stretches of $(\mu_2\text{-H})M_2$ systems which followed trends in the variation of the MHM bond angle. This section will review pertinent experimental work carried out on the H/W, H/Ni and H/Pt systems. This will be done on the basis that not only is more data available on other $(\mu_2\text{-H})M_2$ systems, which have been further characterised, but now data is available on $(\mu_3\text{-H})M_3$ species and, also, hydrogen in octahedral holes. These latter groups could not be used in the analysis carried out by Jayasooriya et al (71) and Willis (72) since no data was available on such model compounds.

5.9.2. Hydrogen and Nickel

(a) Previous Work

Renouprez et al (73,74) carried out studies of hydrogen adsorbed on Raney nickel using IINS techniques. A low frequency time-of-flight spectrum (73) showed bands at 202, 242cm^{-1}, assigned to Ni lattice bands, 726, 1049 and 1170cm^{-1}. The latter pair were interpreted as a NiH vibration centred at 1121cm^{-1}, whereas no explanation was offered for the 726cm^{-1} band. The 1121cm^{-1} band was assigned as a hydrogen motion relative to the Ni surface and it was postulated that a $(\mu_1\text{-H})Ni_1$ group was formed. Later (74), the IN1B instrument was used to study the higher frequency region. At a coverage of 0.42θ bands were found at 950 and 1130cm^{-1} which were repeated at a higher coverage of 1θ. At higher coverage, a weaker band appeared at 640cm^{-1}. The spectra from this paper are shown in Figure 5.54. It can be seen that the arrow pointing to the 640cm^{-1} band in spectrum 2 is, infact, pointing at the minima between the weak peak and the 950cm^{-1} band but this is an error as the weak peak is at 640cm^{-1} (~ 79 meV)

Figure(5.54) IINS study of the Raney nickel-H_2 system (74)

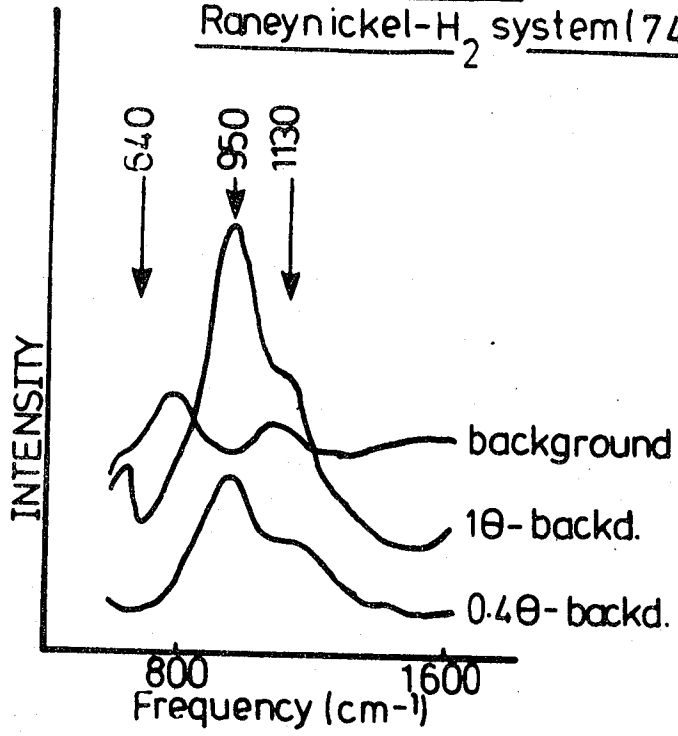

Figure (5.55) EELS study of the Ni(111)/H_2 system (81)

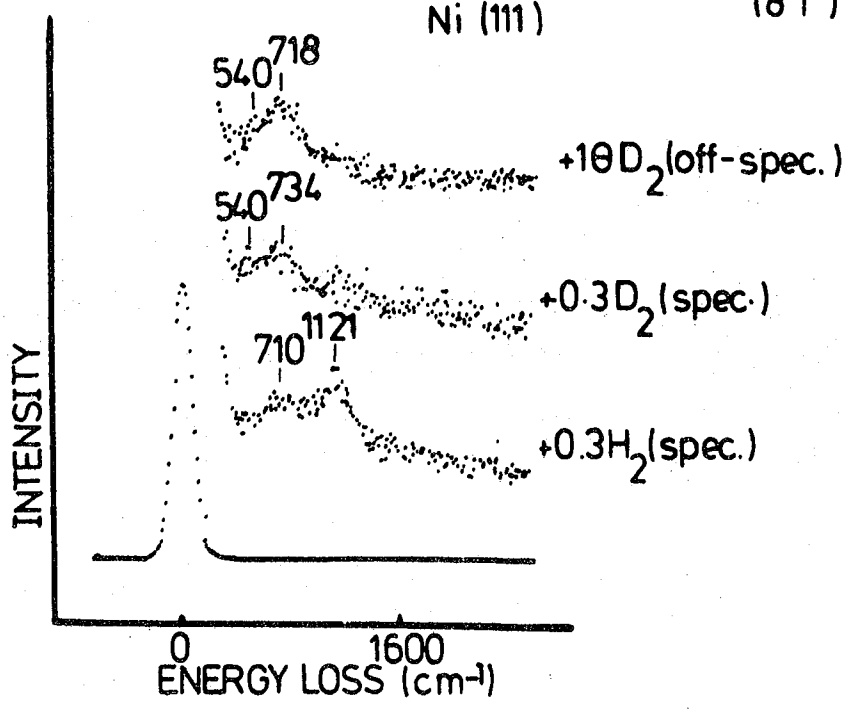

using the frequency scale. Bands at higher frequency, ~2175cm^{-1}, were also found. The band at 640cm^{-1} was not interpreted (This peak obviously has an analogue in the time-of-flight spectrum at 726cm^{-1}). It was felt that the vibrations at 950 and 1130cm^{-1} were indicative of hydrogen in a multiple bonded situation, but the exact stoichiometry could not be decided upon. From intensity measurements, the bands at 1930 and 2175cm^{-1} were assigned to second harmonics and to a vibration due to terminally bonded hydrogen as was postulated in the lower frequency experiment. Wright (75) offered an alternative explanation for the IN1B data of Renouprez et al (74) and insisted that the proposed multiple bonding model did not explain the predicted experimental intensities. His alternative model reverted back to the original Ni (μ_1-H) entity at all hydrogen coverages.

Very recently a LEED study of hydrogen on the Ni(111) plane showed that (μ_3-H)Ni$_3$ species were formed and that the hydrogen was estimated to lie 1.15Å above the surface, with a NiH band length of 1.84Å (75). Demuth (77) carried out photoemission studies on hydrogen bonded to Ni (111) and concluded that this occurred primarily via the nickel 's' orbitals with some 'd' and 'p' orbital participation. These results were entirely consistent with work by Messmer et al on hydrogen in tetrahedral holes in nickel (67) which strongly suggested that such chemisorption of hydrogen could lead to the 'incorporation' of the hydrogen into the tetrahedral interstices under (111) surfaces.

The chemisorption of atomic hydrogen on large nickel clusters has been studied theoretically, using Hartree-Fock

calculations (78). The cluster consisted of the low index (100), (110), (111) and (112) planes. The vibrational frequencies of the hydrogen atoms relative to the surface was found to change with respect to the number of nearest neighbours. As n increased from 1 to 4 in $Ni_n(H)_1$ the calculated frequencies were 2218, 1371, 1210 and 589cm^{-1}. Bonding was shown to be quite unfavourable in the $Ni_1(\mu_1\text{-H})$ system since a more covalent bond was expected whereas the $(\mu_3\text{-H})Ni_3$ grouping was more probable than the $(\mu_2\text{-H})Ni_2$ group. Electron energy loss spectroscopy (EELS) has been utilised by Andersson(79) in an inspection of the H/Ni (100) interaction. On this plane 3 possible sites could be expected for atomic hydrogen to occupy: hydrogen in one, two and four fold positions. The EELS data showed a band at 597cm^{-1} which agreed well with the calculated frequency of 589cm^{-1}, (78) for hydrogen residing in a four fold site. Further, an investigation by Reider et al (80), using helium diffraction, studied the H/Ni (110) system. On this plane 4 sites were possible: $(\mu_1\text{-H})$, $(\mu_2\text{-H})$ and $2x(\mu_4\text{-H})$ positions. If the nickel surface did not reconstruct, the $(\mu_2\text{-H})$ moiety was preferred with a NiH bond length of 1.65Å whereas if the nickel surface was rumpled, on hydrogen adsorption the preferred sites would be four-fold. From previous LEED studies (77) it was postulated that adsorption had led to lateral displacement of the nickel atoms to form pairs.

Finally, recent EELS studies of hydrogen on Ni(111) were made by Ho et al (81) at 170K. Two peaks were shown in the spectra, Figure 5.55, at 710 and 1121cm^{-1} at all coverages. The Ni(111) plane contains three coordinate sites distinguished

by the presence or absence of a nickel atom beneath the surface hole. The author suggested that the 1121cm^{-1} band was due to hydrogen lying above an 'open' hole, ie a (μ_3-H) position, and the 710cm^{-1} due to hydrogen in a near -(μ_4-H) site. However, since the scattering intensity was so low in both the specular and non-specular directions this implied little dipole moment in the vibrations and that the hydrogen atom was embedded in the surface layer in a screened position. Another postulate was that the hydrogen was embedded and that the 710 and 1121cm^{-1} bands were due to the symmetric and antisymmetric stretches respectively.

5.5. Analysis of previous work

The spectrum 'shape' of the data collected by Renouprez et al (74), from IN1B, Figure 5.54, for hydrogen on Raney nickel, at 0.42 and 1.0 monolayers, is remarkably similar to that of the (μ_3-H) transition metal hydridocarbonyl complexes that are studied in this thesis. There is a strong doublet in the 1000-1100cm^{-1} region with a weaker band at lower frequencies and a broad feature at 2100cm^{-1}. With the LEED data (76), the theoretical study (78) and the EELS (79) evidence favouring the hydrogen residing in a highly co-ordinated position, it may be possible to show that hydrogen holds such a position on Raney nickel, as postulated by Renouprez, from this study of (μ_3-H)M_3 complexes. The possibility that hydrogen is terminally bonded to nickel can be ruled out since the spectrum is much too complex and such a bonding mechanism could not explain the appearance of the 640cm^{-1} band or the presence of a doublet around 1000cm^{-1}. The existence of only two bands of any intensity, at 950 and 1130cm^{-1} would tend

to rule out the viability of a (μ_2-H) system especially since there is a total lack of a vibration in the 1200-1700cm^{-1} region indicative of an antisymmetric NiHNi stretch. The weaker band at 640cm^{-1} (IN1B)/726cm^{-1} (IN4) can be assigned by comparing the data with the lower frequency regions of (μ_3-H) compounds. In $H_2Ru_6(CO)_{18}$ the strong band at 607cm^{-1} is assigned to the symmetric deformation. This band occurs at 511cm^{-1} in $HFeCo_3(CO)_{12}$ and at 708cm^{-1} in $H_4Re_4(CO)_{12}$. Thus the 640cm^{-1} band is assigned to the deformation of the Ni_3H system. This will be a symmetric vibration with the hydrogen atom vibrating normal to the nickel surface. The bands at 950 and 1130cm^{-1} are assigned to the antisymmetric and symmetric stretches. The problem then lies in which band is which motion. From the study of the (μ_3-H) complexes and the fact that the 950cm^{-1} band on nickel is more intense than the 1130cm^{-1} band it can be inferred, initially, that the 950cm^{-1} band is the antisymmetric stretch from intensity consideration where the intensity of the IINS band, of E symmetry (ie the doubly degenerate antisymmetric stretch), will be approximately twice the intensity of the A symmetric mode (ie the symmetric stretch). This hypothesis can be tested by regarding the LEED data which showed a NiH bond length of 1.84Å and a NiNi bond length of 2.492Å. From this a NiHNi bond angle of 85.2° can be calculated. From the (μ_3-H) comparison test (section 5.7) it was shown that a 'cross-over' point in the values of ν_{as} and ν_s was possible in the same was as ν_{as} and ν_s 'cross-over' in value in $M_2(\mu_2$-H) species (4). Thus the assignment to the 950cm^{-1} band as the antisymmetric

stretch would seem entirely consistent if the bond angle is of the same magnitude as 85°. Using methods (1) and (2), the NiHNi angle on the Raney nickel can be evaluated using Figures 5.48, 5.49 with $(\nu_{as}/\nu_s) = 0.841$ and $(\nu_s/\nu_{as}) = 1.189$. This gives bond angles of approximately 89.0° and 84.4°. These bond angles are reasonably close to those calculated from the Christmann data (75). This has thus shown the likelihood that the hydrogen was residing in three-fold sites on the Raney-nickel, at high coverage. It can also be noted that $H_3Ni_4(Cp)_4$ has been studied by neutron diffraction techniques by Koetzle et al (82). The three hydrogen atoms were found to be triply bridging three nickel faces and that the NiH bond lengths were 1.69Å and the NiHNi bond angle 93.9°. The HNi surface distance of 0.9Å compares well with the 1.15Å determined by the LEED data (75), as do the other measurements, so that the structures of the surface systems and the models can be seen to be comparable.

Finally, the data of hydrogen + Ni(111) from Ho et al (81) can be analyzed in the same manner. Very poor data was collected, as shown in Figure 5.55. However, the band at ~139meV in the lower spectrum is quite broad and would appear to have a shoulder at lower frequency at ~125meV. (At high coverage of deuterium in the top spectrum the band at 89meV would appear to have a strong component at ~104meV). Now these other weaker components could well be due to motions parallel to the surface whereas the stronger bands at 88 and 139meV are due to motions normal to the surface. This is very reasonable for specular measurements. Thus the strongest band at 139meV can be assigned to the symmetric stretch, the 88meV band to the symmetric deformation and the weaker 125meV band to the in-plane antisymmetric stretch for triply co-ordi-

nated hydrogen. (The in-plane antisymmetric deformation will be at too low a frequency for the EELS technique). With ν_s = 1121cm^{-1} and ν_{as} = 1008cm^{-1} the bond angle can be estimated to be 92.9° (method 1) and 88.6° (method 2) which fit in with the general trend. The argument by Ho et al (81) that the 710 and 1121cm^{-1} bands could be due to two symmetric stretches of two (μ_3-H) type species is not convincing. The argument postulates that they are due to the absence and presence of a nickel atom below the triply co-ordinate position. In (μ_3-H) transitionmetal hydridocarbonyls these situations can be compared with (μ_3-H) in $H_2Ru_6(CO)_{18}$, which has the absence of a lower metal atom (ν_s = 1048cm^{-1}), and in $H_4Re_4(CO)_{12}$ and $HFeCo_3(CO)_{12}$ there are present underlying metal atoms (ν_s = 1032 and 1240cm^{-1} respectively). There is no such difference in frequency as suggested by Ho et al. Table 5.30 summarises the results for H + Ni.

Table 5.30: Summary of H/Ni studies

System	Technique	Bond Angle (°)	ν_s	ν_{as}	δ_s (cm^{-1})
H + Raney Ni	IINS (74)	84.4,89.0	1130	950	640
H + Ni(111)	LEED (76)	85.2	-	-	-
$H_3Ni_4(Cp)_4$	Neutron (82) Diffraction	93.9	-	-	-
H + Ni(111)	EELS (81)	92.9,88.6	1121	1008	710

5.9.3. Hydrogen and Tungsten

(a) Previous Work

The W/H system has been thoroughly studied yet it was not until recently that concern was expressed over the random

assignments made for vibrations involving hydrogen (71,72).

The previous work first started with the H/W (100) system using EELS (83,84). Two energy loss peaks were observed at 560 and 1090cm^{-1}. These were assigned to motions of atomic hydrogen relative to the surface, however, the instrumental resolution was very poor (~ 400cm^{-1}). Both reports implied single sites were occupied at all coverages. This was refuted by Froitzheim et al (85) who also used EELS. Two vibrations were found, one at low coverage, 1250cm^{-1}, which was gradually replaced by a band at 1049cm^{-1} at high coverage. This was postulated to be due to two sites. At low coverage the 'on-top' (μ_1-H)W system was inferred and this was replaced by (μ_2-H)W_2 entities.

Many theoretical and experimental studies over the years of hydrogen on tungsten have postulated nearly every possible configuration of hydrogen upon the surface due to one reason or another. For example:-

a) H+W(111): Tamm favoured W_2H(80) from desorption measurements

b) H+W(110): Blanchet favoured a bridge site (88) from surface reflectance expts.
Collins favoured W_2H (88) from emission microscopy expts.
Tamm favoured W_3H or W_4H (86) from desorption Kinetics

c) H+W(100): Estrup favoured W_2H (89) on the basis of LEED patterns
Collins favoured W_2H (89) from emission microscopy expts.
Tamm favoured W_4H (90) due to LEED and desorption data

Weinberg favoured W_1H (91) from M.O. calculations

Anders favoured W_1H (92) from M.O. calculations

Jaeger favoured W_4H (93) @ low θ } electron stimulated desorption studies

Jaeger favoured W_2H (93) @ high θ }

Madey favoured W_1H (94) @ low θ } electron stimulated desorption studies

Madey favoured W_2H (94) @ high θ }

Viswanath favoured W_4H (95) from desorption studies.

Some of these systems vary with hydrogen coverage and some indicate that two species may exist at once. It appears consistently that possibly two states are present on the (110), (100) and (211) planes whereas more may be present on the more open (111) plane (96,97).

Studies by Backxet al (98) on the H/W (111) system, using EELS, found a single peak at 1290cm^{-1} and, with analogy to Froitzheim, assigned it to the 'on-top' hydrogen system, $W_1(\mu_1\text{-H})$.

Richardson et al used IR and EELS for the H/W (100) system (99). They showed that 3 vibrations were possible due to the 3 hindered translations of the adsorbate. The actual site symmetry would indicate the actual number of expected active vibrations. They discussed the variation in the frequency of the WH vibrations, due to the translations in the x,y and z planes, with the positioning of the hydrogen atom in three sites with respect to the unit cell of the W(100) surface (ie in $W(\mu_1\text{-H})$, $W_2(\mu_2\text{-H})$ and $W_4(\mu_4\text{-H})$ situations.) Vibrational bands were discussed at 2097, 1290, 1048 and 645cm^{-1} and were assigned to an overtone, a $W_1(\mu_1\text{-H})$ stretch, a $W_2(\mu_2\text{-H})$

bridge stretch and to a deformation mode of the $W_2(\mu_2\text{-H})$ moiety respectively. Willis et al also studied the above system (100) using EELS and at saturation coverage found a peak at 1049cm^{-1} but they then carried out some out-of-plane specular beam scattering and further features were found at 645, 1290 and 2097cm^{-1} (The same values as for (99)). However, they insisted that the assignments were a deformation mode (645cm^{-1}), a symmetric stretch (1049cm^{-1}), an antisymmetric stretch (1290cm^{-1}) and a second harmonic (2x1049) which were all indicative of a $W_2(\mu_2\text{-H})$ system, at monolayer coverage. (In specular detection the detection takes place at a reflected angle which is the same as the incident angle. Those vibrational bands which have a band intensity maximum at this angle are those which have a perpendicular dipole such as the symmetric stretch. A further scattering process- Impact scattering - can be detected at reflected angles at other than the incident angle. This allows those vibrational processes involving vibrations parallel to the surface to be excited and detected. The consequence is that the limitations imposed by the 'surface selection rule' are lifted whereby only those vibrations involving a perpindicular-to-the-surface dipole are observed).

Willis went on to measure the variation with coverage (72,101) and found that as a monolayer was built up, the symmetric stretch decreased in value from 1250 to 1049cm^{-1}, the antisymmetric stretch increased from 968 to 1291cm^{-1} whereas the deformation mode increased from 440 to 686cm^{-1}. Using Howards example (6) it appeared reasonable that a $W_2(\mu_2\text{-H})$ existed at all coverages but that the WHW angle was

varying and recent LEED measurements (103) on tungsten surfaces had indicated that reconstruction of the surface tungsten atoms took place on adsorption of an adsorbate producing a stable 'puckered' surface. WHW angles were originally quoted as 89° and 108° for the low and high coverages (101) then quoted as 80° and 100° in the later publication (72) which seemed to indicate some uncertainty.

Jayasooriya et al (71) reviewed this pre-1979 data on WH vibrations and went on to assign most bands to WHW vibrations in $W_2(\mu_2\text{-H})$ moieties with variations in the vibrational frequencies due to reconstruction of the W atoms producing variations in the WHW angle. The 'on-top' vibrations reported earlier were dismissed since the 1200-1300cm^{-1} bands assigned as such, occurred at too low a frequency compared with similar terminal hydrides in model complexes. Finally, Ho et al (81) very recently published work on H/W(100) and found exactly the same results as Willis and others and analysed the data in the same vein.

(b) Alternative view of previous data

The 'on-top' site of Froitzheim et al (85) assigned at 1250cm^{-1} is incorrect because such a frequency is too high to be a deformation and too low to be stretch for a terminal hydride. Froitzheim quite reasonably can say the 1056cm^{-1} band is due to a stretch of the $W_2(\mu_2\text{-H})$ species at high coverage. The band at 1250cm^{-1} must also be due to this species. The explanation due to Willis (72) and Jayasooriya et al (71) is valid. The reason for the lack of an anti-symmetric stretch must be due to the fact that only an out-of-specular beam study would have seen it. If the symmetric

stretches are at 1250 and then 1056cm^{-1} then WHW angles of approximately 90^{o} and 112^{o} respectively will be found.

Backxet al (98) studied hydrogen on tungsten (111) and assigned the band at 1290cm^{-1} to an 'on-top' system. This is again unreasonable. The data is very poor and the band at 1290cm^{-1} could well, with better resolution, have been resolved into more components. On the evidence given, either a (μ_2-H) or (μ_3-H) is found with the (μ_3-H) moiety more favoured on this particular plane.

Willis et al (101), again, studied hydrogen on tungsten (100) as did Froitzheim (85). Froitzheim, it must be noted, saw the 1250cm^{-1} band at low coverage using a specular beam measurement whereas at high coverage the 1056cm^{-1} band was observed. Willis, at high coverage, saw only a band at 1049cm^{-1} with a further band at 1290cm^{-1} in out-of-specular beam measurements. Obviously these bands are different. The Froitzheim 1250cm^{-1} band could well be the symmetric stretch but if Willis has found the band at 1290cm^{-1} then it should be the antisymmetric stretch. Used in conjunction with methods (2) and (3), after Howard et al (6), and method (1), after Katovic and Macarley (11), reasonably consistent WHW angles should be attained. This does not happen. The sin(θ/2) plot gives WHW = 88^{o}, the tan(θ/2) plot gives 114.4^{o} and the Katovic N^{o}. plot gives 85.3^{o}. Especially since the latter two differ by so much, it is felt that the W_2(μ_2-H) system cannot describe the moiety which has produced vibrations at 1290 and 1056cm^{-1}. The alternatives to a (μ_2-H) system on the W(100) plane are (μ_1-H), which has already been rejected, and (μ_4-H), a system favoured by many. Unfortunately no real data is available on compounds containing hydrogen in

four-fold positions. The (μ_3-H) system could be considered to prevail with the hydrogen lying in a near-four-fold site but with the atom distorted towards two of the tungsten stoms and being bonded to them and the next tungsten atom in the layer below the surface. Methods (1), (2) and (3) give reasonably consistent WHW angles of 122.6°, 120.5° and 122.6° but obviously the angle cannot be greater than 120°, a geometrically impossible situation. Since (μ_1-H), (μ_2-H) and (μ_3-H) cannot be acceptable then the (μ_4-H)W_4 system must be favoured, on the basis of the above results. Thus the model of Tamm and Schmidt (86,90) is further enhanced rather than that of Estrup and Anderson (89). Figure 5.56 shows the two proposed models of Tamm and Schmidt, and Estrup and Anderson. At high coverage the Tamm and Schmidt model has 50% of sites occupied by H atoms and 50% of sites occupied by H_2 molecules. Figure 5.57 depicts the (μ_4-H) position.

Willis et al (72) in the more detailed study then relates results which differ from those of Froitzheim et al (85). Froitzheim et al showed that with increasing θ, the 1250cm^{-1} band slowly disappeared and the 1056cm^{-1} grew whereas Willis showed the 1250cm^{-1} band moving down in frequency, with coverage, to the 1049cm^{-1} band. Indeed, these results are not compatible. However, Willis (72) postulates at low coverage: the antisymmetric stretch is at 968cm^{-1} and the symmetric stretch at 1226cm^{-1}, at high coverage: the antisymmetric stretch is at 1291cm^{-1} and the symmetric stretch at 1008cm^{-1}. Table 5.31 shows the results of a test of this hypothesis. Willis calculated at low coverage and high coverage that the WHW angle was 80° and 100° respectively. The table shows those results calculated for the W_2(μ_2-H) system and the

Figure(556) Models of H/W(100) system

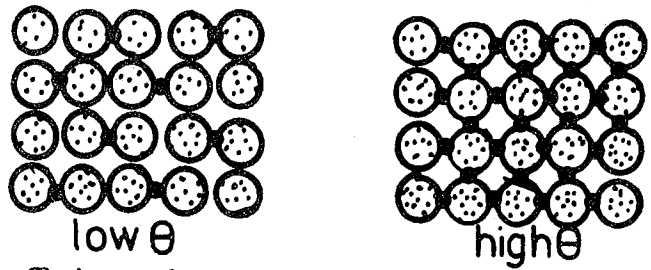

Estrup & Anderson model (89)

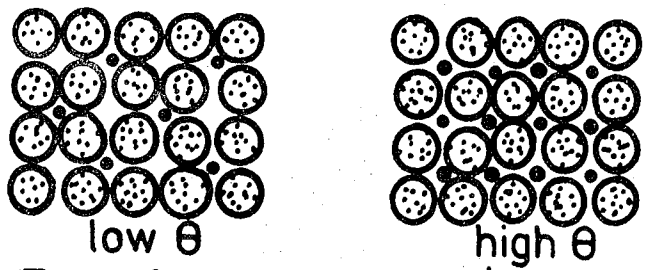

Tamm & Schmidt model (86.90)

Figure (557)

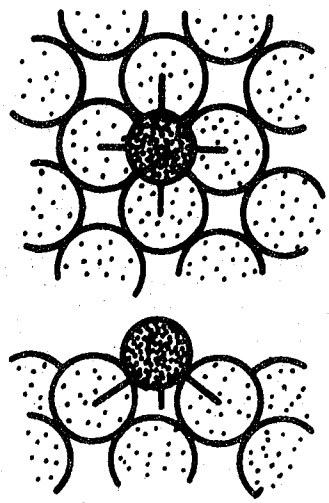

fcc(100)
hollow site

possible $W_3(\mu_3\text{-H})$ system using Howards techniques (6), 2 and 3, and the Katovic and McCarley technique (11), which has been shown to be reliable. Once again a large spread in results is found with the $(\mu_2\text{-H})W_2$ system whereas the $(\mu_3\text{-H})W_3$ moiety gives more consistent results. Though once again at high coverage unacceptable WHW bond angles are found with the $W_3(\mu_3\text{-H})$ system.

Table 5.31: Estimated Bond Angles in $W_2(\mu_2\text{-H})$ and $W_3(\mu_3\text{-H})$ Systems

System	At Low Coverage (o)	At High Coverage (o)	Method
$W_2(\mu_2\text{-H})$	68.8	94.6	1
	91.6	116.4	2
	82.4	113.0	3
$W_3(\mu_3\text{-H})$	78.1	131.0	1
	75.4	127.4	2
	76.9	129.9	3

It is therefore suggested that the evidence up to now is not conclusively in favour of any one system. The $(\mu_1\text{-H})W_1$ moeity can be ruled out, as can the $(\mu_3\text{-H})W_3$ unit at high coverage. From the spread in WHW angles attained from the Willis values for the antisymmetric and symmetric stretches and the fact that the spectrum is not entirely unlike the $(\mu_3\text{-H})M_3$ model compounds, one cannot contend that the $W_2(\mu_2\text{-H})$ is present. At this moment on the W(100) plane two models exist for the structure of atomic hydrogen: the Tamm and Schmidt (86,90) system of four-fold hydrogen and the Estrup and Anderson (89) model of two-fold hydrogen. From

the above evidence it would appear that the four-fold situation is favoured. However, since no data is available on hydrogen cluster species containing (μ_4-H) moieties (they have yet to be prepared!), one must look forward to a LEED study in the same vein as that for H/Ni(111) (76). Until then it appears unsatisfactory that analyses are being presented of the H/W(100) situation on the basis of vibrational structural data available on only μ_1-and(μ_2-H) cluster compounds when other popular models for the surface structure are known.

5.9.4. Hydrogen and Platinum

(a) Previous Results

Many studies have been carried out on the H/Pt system. Difficulties abound in the analysis of data where a number of 'states' are found. Arguments have been presented for the number of states being caused by the same number of different sites for hydrogen whereas other have indicated that only one site is occupied by the adsorbate and that the number of states indicates the types of interactions between these identical sites varying with coverage. LEED, Thermal desorption, EELS and contact potential measurements have been used (eg. 103-105) and, generally, two 'states' have been seen on the (100), (111), (110) and (997) planes though some studies have found more complex results than others. IINS methods have been used by Howard et al (106, 107) to study hydrogen vibrations on Pt black. Low frequency data (106) found a band at 400cm^{-1} which was assigned to a PtH motion. This value was lower than that of hydrogen on Raney-Ni (73) and it was postulated that this was a consequence of the increased density of 'd' electrons at the Pt surface leading to a metallic rather than a covalent bonding of the adsorbed

hydrogen. Higher frequency work (109) found, at low and high coverage, bands at 500, 622 and 812cm^{-1} and, at higher coverage, new bands at 936 and 1296cm^{-1}. The 3 bands at low coverage were assigned to the 3 distinct hydrogen atom vibrations which arise from the 3 degrees of translational freedom of the proton. This implied a two-fold site was held by the hydrogen atom upon the platinum surface. Only 2 vibrations would have been expected for μ_3- and (μ_4-H) species, the deformation and antisymmetric stretch being degenerate. Terminal hydrides were ruled out because a comparison with Pt(μ_1-H) model compounds revealed bands at 900 and ~ 2000cm^{-1}. At greater coverage the existence of the 936cm^{-1} band and some intensity in the 2000-2300cm^{-1} region were postulated as due to such terminal hydrogens. Candy et al (108) studied hydrogen on Pt, supported on MgO, and found similar results. A reversibly bound hydrogen species formed IR bands at 2100cm^{-1} and an irreversibly form gave a band at 950cm^{-1}. The former was assigned to a Pt_1 (μ_1-H) group and the latter as a (μ_2-H)Pt_2 group from a comparison with the vibrational bands at ~1100cm^{-1} in $H_3Re_3(CO)_{12}$.

Baro et al (109) studied hydrogen adsorbed on Pt(111) using the in- and out-of-specular beam techniques of EELS. In-the-beam spectra gave a broad peak at 550cm^{-1} which increased in intensity with coverage. Out-of-the-specular-beam spectra also gave a broad band at ~ 1230cm^{-1}, which increased in intensity with coverage, and a weak band at 860cm^{-1}. Since only two bands were seen, a(μ_3-H)Pt_3 system was favoured at all coverages with the antisymmetric stretch at 1230cm^{-1} and the symmetric stretch at 550cm^{-1}. The (μ_4-H) species was not ruled out. Further, the 860cm^{-1} band was assigned to a

possible distorted (μ_3-H).....(μ_2-H) intermediate. The Pt-H bond length was calculated to be 1.76Å giving a PtHPt angle of 104.3°. Baro et al (110) then studied adsorption on the stepped Pt(S) (6(111) x (111)) plane using HREELS. At low coverage bands at 500 and 1130cm^{-1} appeared, the latter strongly intense, implying early saturation, and a weak feature at 1270cm^{-1} was also seen. At high coverage the 500cm^{-1} band was saturated, the 1130 and 1270cm^{-1} bands were still observed. Using the out-of-specular-beam technique the 1270cm^{-1} band was found to be strong at all coverages. It is suggested that the new band found at 1130cm^{-1} was due to hydrogen being adsorbed in $Pt_2(\mu_2$-H) sites. This was presumed to take place at the steps and to happen at early coverages. Thus the 500cm^{-1} band was assigned to the symmetric stretch and the 1270cm^{-1} band to the antisymmetric stretch of triply bridging hydrogen and the 1130cm^{-1} band to the symmetric stretch of the Pt(μ_2-H)Pt moiety. Since an out-of-specular beam measurement was undertaken they should have also observed the antisymmetric stretch of this Pt(μ_2-H)Pt moiety. It is possible that they did not observe it because the dipole was not large enough but no reason was given by the authors.

(b) Alternative views on previous results

At low hydrogen coverage, in the IINS study by Howard et al (107), it is difficult to believe that the PtH stretches arising from 2 hindered translations of the hydrogen atom are in the 500-800cm^{-1} region since they are at too low a frequency though the deformation mode could well be assigned to one. If a large PtHPt angle was found then the symmetric stretch could be at 812cm^{-1}, however, the technique should then have found the antisymmetric stretch in the 1500-

1800cm^{-1} region. This may have occurred because a band lay at ~1750cm^{-1} (220 meV) in the spectrum. The authors thought some water may have been co-adsorbed and this band was removed when the spectrum was normalised to remove any feature due to water. Figure 5.58 shows the spectrum (top) of the adsorbed hydrogen at low coverage. Features exist at 500, 622, 812 and 1715cm^{-1}. From the study by us of (μ_2-H) metal hydridocarbonyls, using IINS spectroscopy, there were usually 4 strong bands found above ~ 200cm^{-1} (e.g. see Figure 5.21 for $H_4Ru_4(CO)_{12}$) which are indicative of the in and out-of-plane deformations and symmetric and antisymmetric stretches. Table 5.32 compares the assignments of these modes in $H_3Mn_3(CO)_{12}$ (section 5.2.4) with the suggested assignments for Pt black and H_2 at low coverage.

Table 5.32: MHM Assignments in $H_3Mn_3(CO)_{12}$ and Pt(black)1H_2

Mode	$H_3Mn_3(CO)_{12}$	PtBlack+H_2(lowθ)(107)
Antisymmetric stretch	1661	~ 1750
Symmetric stretch	875	812
'in-plane deformation	606	622
'out-of-plane deformation	336	500

These assignments are readily comparable with those by Howard et al (6) for $Et_4NHCr_2(CO)_{10}$ where the symmetric and antisymmetric stretches were assigned at 818 and 1750cm^{-1}. In the latter complex a CrHCr bond angle of 158.9° has been found by X-ray diffraction techniques. This implies that a large PtHPt angle exists at low coverage. The intensities of the IINS bands in Figure 5.58 can be compared with IINS

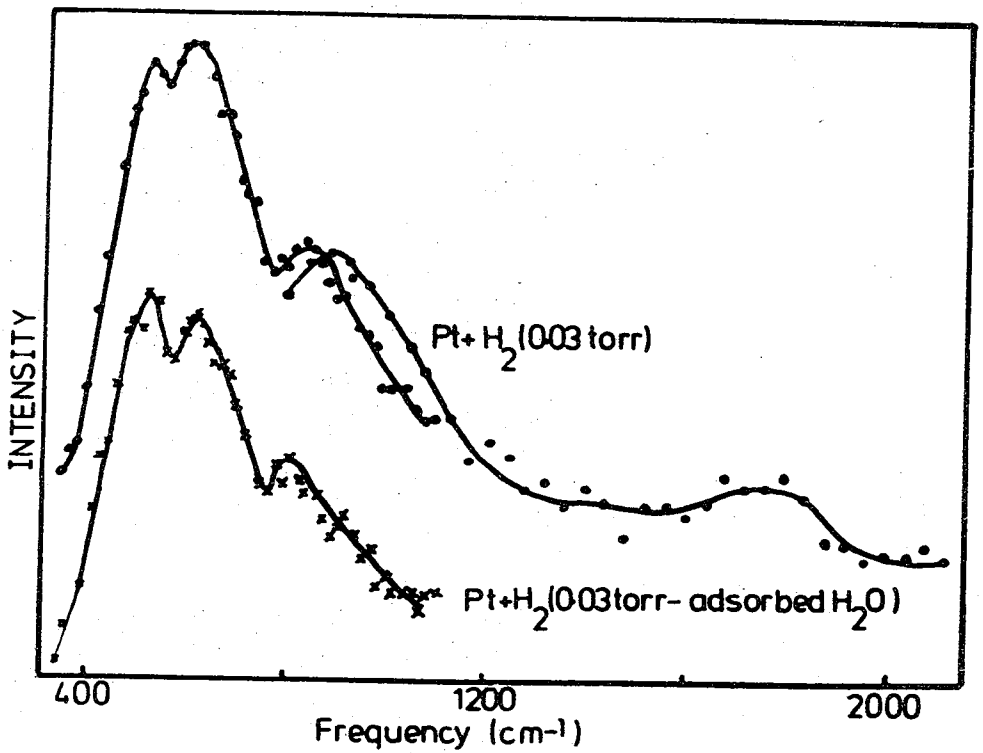

Figure (5.58) Pt black + H_2 system (107)

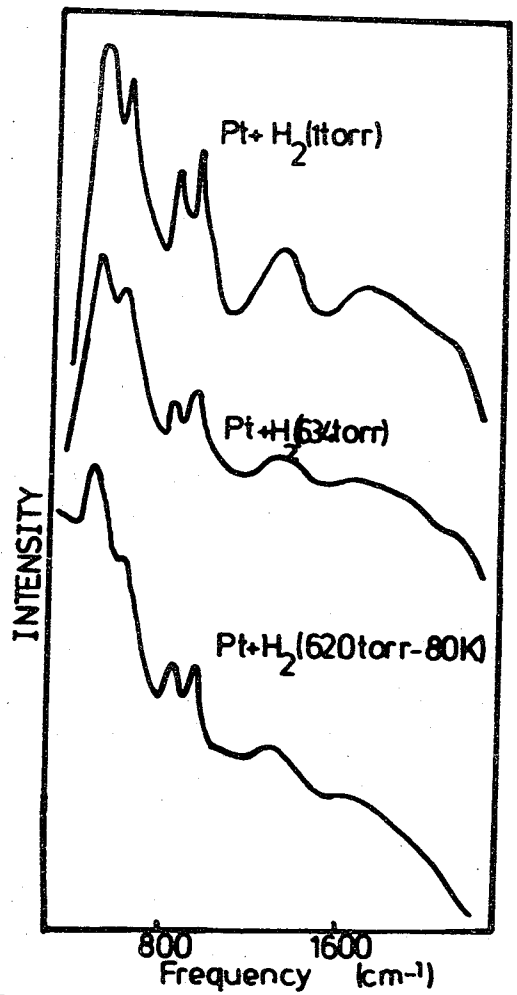

Figure (5.59) Pt black + H_2 system (107)

data on the hydridocarbonyls. No quantitative comparisons can be made due to the lack of a confident background level in the spectra. However, as the frequency increases the bands tend to broaden and loose some intensity. Thus at low coverage there seems to be a chance that Pt_2 (μ_2-H) species exist, if there was not a lot of water present on the sample, in agreement with the conclusions of Howard et al (107) that hydrogen lay in the bridged position.

The new bands which appeared at higher hydrogen coverage Figure 5.58 were those at 936, 1296 and 2000-2250cm^{-1}. The bands at 496, 616 and 848cm^{-1} did not change very much from the values found at low coverage. The band at 1656cm^{-1} may be the band at 1750cm^{-1} which has shifted to lower frequencies with an increase in coverage. The spectra at higher coverage are much better resolved from those at low coverage. Howard et al (107) suggested that the new bands at 916 and 2000-2250cm^{-1} were indicative of the production of a Pt(μ_1-H) species on the surface. However, it is felt that the argument must involve the strong band at 1296cm^{-1} which was not satisfactorily explained by Howard et al. A strong IINS band at 1296cm^{-1} could be indicative of a (μ_3-H) species (symmetric or antisymmetric stretch) or indicative of a (μ_2-H) species (symmetric stretch). However the IINS spectra in Figure 5.59 can be readily compared with the of $H_4Ru_4(CO)_{12}$, Figure 5.21. Table 5.33 shows the comparable features in each.

It can be seen that the similarities between the two systems are extant. The intensity of the bands at 1656 and 1296cm^{-1} implies that these bands are due to the antisymmetric

Table 5.33: IINS Bands in $H_4Ru_4(CO)_{12}$ and Pt(black)+H_2

$H_4Ru_4(CO)_{12}$	Pt(black)+H_2 (107)
2274 (W)	2000-2250 (wb)
1935 (m)	
1600 (m)	1656
1294 (ms)	1296
942 (m)	936
	848
623 (vs)	616
359 (vs)	496

and symmetric stretches respectively of (μ_2-H) bridging moieties. Thus the PtHPt band would have appeared to have changed in character with increased coverage. This argument is the only one which can satisfactorily explain the frequency and intensity of the 'new' band at 1296cm^{-1} and the frequency shift from 1750 to 1656cm^{-1}. Using the estimating techniques (methods 1 and 2) the PtHPt bond angle can be gauged to be 111.2° (method 1) and 114° (method 2). Therefore on increased coverage of hydrogen the PtHPt bond angle has been reduced from ~160° to 111-114°. The major point of discussion is whether the other new bands at 936 and 2000-2250cm^{-1} are indicative of the new species Pt(μ_1-H) as directed by Howard et al (107). In $H_4Ru_4(CO)_{12}$ there were bands at 1935 and 2274cm^{-1} which were probably due to combinations whereas the band, of medium intensity at 942cm^{-1} could be described in terms of combinations and overtones of the low frequency deformations. Such overtones and combinations of the bands at 616 and 496cm^{-1} though

do not adequately describe the IINS bands at 848 and 936cm^{-1} in the spectra, Figure 5.59. So therefore a Pt(μ_1-H) may exist on the surface with the Pt_2(μ_2-H) species described earlier. (It is further noted that an argument was given in section (5.2.5) that the IINS bands in $H_4Ru_4(CO)_{12}$ at 942 and 1935cm^{-1} were possibly due to Ru(μ_1-H) species).

The EELS results of Ibach et al (109) are in contrast to the above where it would appear a (μ_3-H)Pt_3 species is favoured on the (111) plane. The spectra, shown in Figures 5.60,5.61 are poorly resolved. the band at 550cm^{-1} is quite broad whereas the 1230cm^{-1} band has a lower frequency component at ~1150cm^{-1}. The symmetric stretch at 550cm^{-1} does not compare at all with those found in the (μ_3-H) model compounds. The symmetric stretch is therefore assigned to the shoulder at 1150cm^{-1} whereas the antisymmetric stretch, from the out-of-specular beam study, is assigned to the band at 1230cm^{-1}. The band at 550cm^{-1} was assigned to the symmetric stretch by Ibach et al because it was so intense in the in-beam study but the band itself contains a strong component at ~ 480cm^{-1}, shown in Figure 5.60, due to CO contamination. The subtraction of this component would remove some intensity from the band centred at 550cm^{-1}. However, the remaining intensity at ~ 550cm^{-1} after the CO contaminant had been subtracted would be due entirely to the symmetric deformation mode which would be detected in the specular measurements since the hydrogen motion in this mode is very similar to the hydrogen motion in the symmetric stretch, ie normal to the surface. At higher frequency a band in the specular measurements can be made out at ~ 1000cm^{-1}

Figure (5.60) Specular EELS study of the Pt(111)+H_2 system (109)

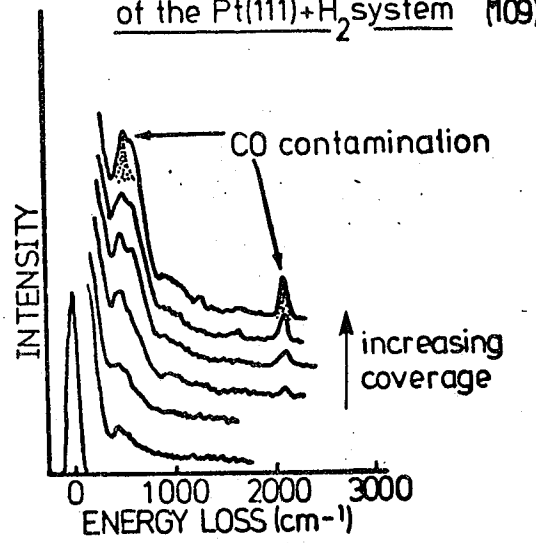

Figure (5.61) Non—specular EELS study of the Pt(111)+H_2 system (109)

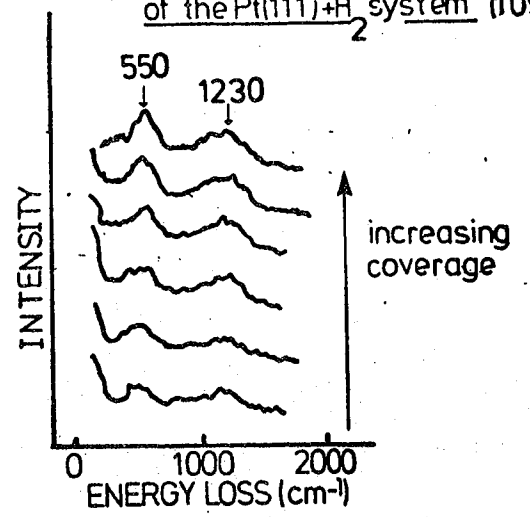

which is very poorly resolved but could be assigned to the symmetric stretch. Further, at low coverage the band at 860cm^{-1} can be compared with the spectrum of $H_4Re_4(CO)_{12}$ which has a band at 852cm^{-1} due, possibly, to a coupling motion of the hydrogen atoms on the saturated surface. Since the band is found at low coverage on platinum, this must indicate that the hydrogen atoms, after the dissociation of the H_2 molecules, are chemisorbed in close proximity to each other and are, probably, bonded in triply co-ordinated positions separated only by a Pt-Pt bond (ie in $H_4Re_4(CO)_{12}$ they are separated by an Re-Re bond). There appeared to be little change in the band positions with coverage implying little change in the position of the hydrogen above the surface with coverage increase. Baro et al (109) calculated the PtHPt angle to be 104.3°. The bond angle is estimated using Figure 5.49, (Katovic method) to be 108.2° whereas using, Figure 5.48, (tan(θ/2) method) it is 107.2°. Thus these estimations compare quite well with the value calculated by Baro et al (109). Unfortunately no Pt-H vibrational/ structural model compound data has been reported that could assist in this analysis. Few hydrogen-bridged Pt compounds exist. The compound $(PtH(\mu_2\text{-}H)(PCy_3))_2$ was studied by Green et al (111) and the Pt-H stretch was assigned at 1550cm^{-1}. However, this was a $(\mu_2\text{-}H)_2Pt_2$ compound and cannot be compared with the $(\mu_2\text{-}H)_2M$ systems.

It is felt that the Baro et al (110) study on stepped platinum (111) surfaces is just a better resolved version of their earlier (46) study on Pt(111). Further, the appearence of $(\mu_2\text{-}H)Pt_2$ should have allowed the antisymmetric stretch, of such a system, to be observed in the out-of-specular beam mode.

5.10 Conclusion

This IINS, IR and, where possible, Raman study of transition metal hydridocarbonyls has shown that the vibrations of hydrogen lying in μ_2-, μ_3-, and μ_6- positions can be quite adequately described in terms of the 'local' metal-hydrogen symmetry e.g. C_{2v} in $H_4Ru_4(CO)_{12}$, D_{2h} in $H_2Os_3(CO)_{10}$, C_{3v} in $H_4Re_4(CO)_{12}$ and O_h in $CsHCo_6(CO)_{15}$. The (μ_2-H) complexes, however, show a more complex IINS spectrum than the others and it is suggested that the vibrational description must take into account skeletal metal-carbonyl deformations which have associated hydrogen motion.

The vibrational data from the 11 studied systems has been used to characterise the μ_3-, μ_3- and (μ_6-H) moieties so that one can predict structural and vibrational data. The (μ_2-H) systems have been studied in greater depth using 7 methods of estimating MHM bond angles. New bond angle estimates are given for $H_4Ru_4(CO)_{12}$, $H_3Re_3(CO)_{12}$, $H_3Mn_3(CO)_{12}$ and $H_2FeRu_3(CO)_{13}$. A means is also provided for estimating MHM bond angles in (μ_3-H) moieties whereas a method for calculating the MH distance for hydrogen in octahedral holes has been developed along similar lines to previous studies of hydrogen in tetrahedral holes.

The above work has been used effectively to study, with more confidence, previous vibrational data on hydrogen/transition metal surface systems. Overwhelming evidence implies the existence of (μ_3-H) species on all Ni surfaces whereas (μ_2-H) and (μ_3-H) species have been confirmed on Pt black and Pt(111) surfaces. A more complex situation would

seem to prevail on tungsten surfaces. Previous studies have favoured either μ_2- or (μ_4-H) sites for adsorbed hydrogen. It is felt that the (μ_2-H) model does not confidently describe the vibrational spectra and since the (μ_4-H) model has yet to be characterised then no firm descriptions of the H/W system can be made.

5.11 References

1. J.P. Olsen, T.F. Koetzle, S.W. Kirtley, M. Andrews D.L. Tipton, R. Bau J. Amer. Chem. Soc 96 (1974) 6621
2. S.W. Kirtley, Ph.D. Thesis U.C.L.A. (1971)
3. D.C. Harris, H.B. Gray J. Amer. Chem. Soc. 97 (1975) 3073
4. C.B. Cooper, D.F. Shriver, S. Onaka Adv. Chem. Ser. 167 (1979) 232
5. C.B. Cooper, D.F. Shriver, D.J. Darensbourg, J.A. Froelich Inorg. Chem. 18 (1979) 1407
6. M.W. Howard, U.A. Jayasooriya, S.F.A. Kettle, D.B. Powell N. Sheppard, J. Chem. Soc. Chem. Comm. (1979) 18
7. S. Onaka, C.B. Cooper, D.F. Shriver Inorg. Chim. Acta. Letts. 37 (1979) L467
8. J.L. Peterson, R.K. Brown, J.M. Williams, R.K. McMullen Inorg. Chem. 18 (1979) 3493
9. R.A. Love, H.B. Chin, T.F. Koetzle, S.W. Kirtley, B.R. Whittlesley, R. Bau J. Amer. Chem. Soc. 98 (1976) 4491
10. G. Herzberg 'Infra-Red and Raman Spectra of Polyatomic Molecules' Van Nostrand (1945)
11. V. Katovic, R.E. McCartey Inorg. Chem. 17 (1978) 1268
12. M.A. Andrews, S.W. Kirtley, H.D. Kaesz Adv. Chem. Ser. 167 (1978) 213
13. J.R. Johnson, D.M. Duggan, W.M. Risen Inorg. Chem. 14 (1975) 1053
14. D.M. Adams, M.A. Hooper J. Organometal Chem. 181 (1979)131
15. J.W. White, C.J. Wright J. Chem. Soc (A) (1971) 2843
16. J.W. White, C.J. Wright J. Chem. Soc. Chem. Comm. (1970)711
17. J.W. White, C.J. Wright J. Chem. Soc. Farad. Trans. II 68 (1972) 1423
18. J. Howard, T.C. Waddington, J. Tompkinson Chem. Phys. 42 (1979) 113
19. B. Fontal Ph.D. Thesis U.C.L.A. (1969)

20. H.D. Kaesz, R.B. Saillant Chem Rev. 72 (1972) 273

21. I.J. Hyams, D. Jones, E.R. Lippincott J. Chem. Soc(A) (1967) 1987

22. M.J. Ware 'Essays in Structural Chemistry' (MacMillan) London (1971) 404

23. M.R. Churchill, R. Bau Inorg. Chem. 6 (1967) 2086

24. M.R. Churchill, P.H. Bird, H.D. Kaesz, R. Bau, B. Fontal J. Amer. Chem. Soc. 90 (1968) 7135

25. P.M.A. Sherwood 'Vibrational Spectroscopy of Solids' Cambridge Univ. Press (1972)

26. D.K. Huggins, W. Fellmann, J.M. Smith, H.D. Kaesz J. Amer. Chem. Soc. 86 (1964) 4841

27. J.M. Smith, W. Fellmann, L.H. Jones Inorg. Chem. 4 (1965) 1361

28. S.F.A. Kettle, P.L. Stanghellini Inorg. Chem. 18 (1979) 2749

29. S.W. Kirltey, J.P. Olsen, R. Bau J. Amer. Chem. Soc. 95 (1973) 4532

30. D.M. Adams, M.A. Hooper, A. Squire J. Chem. Soc. (A) (1971) 71

31. B.F.G. Johnson, J. Lewis, I.G. Williams J. Chem. Soc. (A) (1970) 901

32. S.A.R. Knox, J.W. Koepke, M.A. Andrews, H.D. Kaesz J. Amer. Chem. Soc. 97 (1975) 3942

33. J.W. Koepke, J.R. Johnson, S.A.R. Knox, H.D. Kaesz J. Amer. Chem. Soc. 97 (1975) 3947

34. P.F. Jackson, B.F.G. Johnson, J. Lewis, M.McPartlin, W.J.H. Nelson J. Chem. Soc. Chem. Comm. (1978) 920

35. J.R. Shapley, S.I. Richter, M.R. Churchill, R.A. Lashewycz J. Amer. Chem. Soc. 99 (1977) 7384

36. G.L. Geoffroy, J.R. Lehman Adv. Inorg. Chem. Radiochem. 19 (1977) 189

37. M.L.H. Greem, D.L. Jones Adv. Inorg. Chem. Radiochem. 7 (1965) 115

38. D.B.W. Yawney, F.G.A. Stone J. Chem. Soc (A) (1969) 502

39. D.F. Shriver, C.B. Cooper Adv. Infra-Red Raman Spec. 6 (1978) 127

40. R.D. Wilson, R. Bau J. Amer. Chem. Soc. 98 (1976) 4687

41. M.J. Mays, R.N.F Simpson J. Chem. Soc (A) (1968) 1444

42. M. Knight, M.J. Mays J. Chem. Soc. (A) (1970) 711

43. R.G. Teller, R.D. Wilson, R.K. McMullan, T.F. Koetzle, R. Bau J. Amer. Chem. Soc. 100 (1978) 3071

44. I.A. Oxton, S.F.A. Kettle, P.F. Jackson, B.F.G. Johnson, J. Lewis J. Chem. Soc, Chem. Comm. (1979) 687

45. W. Drexel, A. Murani , D. Tocchetti, W. Kley, I. Sosnowska, D.K. Ross J. Phys. Chem. Solids 37(1976)1135

46. C.J. Glinka, J.M. Rowe, J.J. Rush, G.G. Libowitz, A. Maeland Solid State. Commun. 22 (1977) 541

47. D.G. Hunt, D.K. Ross J. Less Common Metals 45 (1976)229

48. A.J. Maeland J. Chem. Phys. 52 (1970) 3952

49. J.J. Rush, H.E. Flotow J. Chem. Phys. 48 (1968) 3795

50. D.W. Hart, R.G. Teller, C.Y. Wei, R. Bau, G. Longoni, S. Campanella, P. Chini, T. Koetzle Angew. Chem. 18 (1979)80

51. P.H. Dederichs R. Zeller, K. Schroeder Springer Tracts in Modern Phys. 87 (1979) 83

52. R.W. Broach, L.F. Dahl, G. Longoni, P. Chini, A.J. Schulz, S. Martinengo Adv. Chem Ser. 167 (1978) 93

53. M.R. Churchill, B.G. DeBoer Inorg. Chem. 16 (1977) 878

54. J.R. Shapley, G.A. Pearson, M. Tachikawa, G.E. Schmidt, M.R. Churchill, F.J. Hollander, J. Amer. Chem. Soc. 99 (1977) 8064

55. J.R. Shapley, J.B. Keister, M.R. Churchill, B.G. DeBoer J. Amer. Chem. Soc. 97 (1975) 4145

56. M.R. Churchill, F.J. Hollander Inorg. Chem. 19 (1980)309

57. R.D. Wilson, S.M. Wu, R.A. Love, R. Bau Inorg. Chem. 17 (1978) 1271

58. D.B.W. Yawney, R.J. Doedens Inorg. Chem. 11 (1972) 838

59. C.J. Gilmore, P. Woodward J. Chem. Soc. Chem. Comm. (1970) 1463

60. M.R. Churchill, B.G. DeBoer, F.J. Rotella Inorg. Chem. 15 (1976) 1843

61. R. Bau, W.E. Carroll, R.G. Teller, T.F. Koetzle J. Amer. Chem. Soc. 99 (1977) 3872

62. M.R. Churchill, P.H. Bird, H.D. Kaesz, R. Bau, B.Fontal J. Amer. Chem. Soc. 90 (1968) 7135

63. M.R. Churchill, J. Wormald J. Amer. Chem. Soc. 93 (1971) 5670

64. P. Chini, G. Longoni, S. Martinengo, A. Ceriotti Adv. Chem. Ser. 167 (1978) 1

65. G.G. Libowitz, A.J. Maeland "Handbook of Phys. of Rare Earths" N. Holland (1979) Chap. 26

66. H. Adachi, S. Imotu J. Phys. Soc. Japan 46 (1979) 1194

67. R.P. Messmer, D.R. Salahub, K.H. Johnson, C.Y. Yang Chem. Phys. Letts. 51 (1977) 84

68. M. Sakamoto J. Phys. Soc. Jap. 19 (1961) 1862

69. D.K. Ross, P.F. Martin, W.A. Oates, R. KhodaBaksh Z. Phys. Chem. (NF) 114 (1979) 221

70. M.R. Chowdhury, D.K. Ross Solid Stat. Commun. 13 (1973)229

71. U.A. Jayasooriya, M.A. Chesters, M.W. Howard, S.F.A. Kettle D.B. Powell, N. Sheppard Surface Sci. 93 (1980) 525

72. R.F. Willis Surface Sci. 89 (1979) 457

73. R. Stockmeyer, H.M. Conrad, A. Renoprez, P. Fouilloux Surface Sci. 49 (1975) 549

74. A.J. Renouprez, P. Fouilloux, G. Goudourier, D. Tocchetti R. Stockmeyer J. Chem. Soc. Farad I 73 (1977) 1

75. C.J. Wright J. Chem. Soc. Farad II 73 (1977) 1497

76. K. ChristmannBull. Soc. Chim. Belg. 88 (1979) 519

77. J.E. Demuth J. Coll. Int. Sci. 58 (1977) 184

78. T.H. Upton, W.A. Goddard Phys. Rev. Letts 42 (1979)472

79. S. Andersson Chem. Phys. Letts. 55 (1978) 185

80. K.H. Reider, T. Engel Phys. Rev. Letts 43 (1979) 373

81. W. Ho, N.J. DiNardo, E.W. Plummer J. Vac. Sci. Technol. 17 (1980) 134

82. T.F. Koetzle, R.K. McMullen, R. Bau, D.W. Hart, R.G. Teller, D.L. Tipton, R.D. Wilson Adv. Chem Ser. 167 61

83. F.M. Propst. T.C. Piper J. Vac. Sci. Technol. 4 (1967) 53

84. E.W. Plummer, A.E. Bell J. Vac. Sci. Technol. 9 (1972)583

85. H. Froitzheim, H. Ibach, S. Lehwald Phys. Rev. Letts. 36 (1976) 1549

86. P.W. Tamm, L.D. Schmidt J. Chem. Phys. 54 (1971) 4775

87. G.B. Blanchet, P.J. Estrup, P.J. Stiles Phys. Rev. Letts. 44 (1980) 171

88. R.A. Collins, B.H. Blott J. Appl. Phys. 40 (1969) 5390

89. P.J. Estrup, J. Anderson J. Chem. Phys. 45 (1966) 2254

90. P.W. Tamm, L.D. Schmidt J. Chem. Phys. 51 (1969) 5352

91. W.H. Weinberg J. Vac. Sci. Technol. 10 (1973) 89

92. L.W. Anders, R.S. Hansen, L.S. Bartell J. Chem. Phys. 59 (1973) 5277

93. R. Jaeger, D. Menzel Surface Sci. 63 (1977) 232

94. T.E.Madey, J.J.Czyzewski, J.T. Yates Surface Sci. 49 (1974) 465

95. Y. Viswanath, G. Sanders, L.D. Schmidt Surface Sci. 59 (1976) 297

96. H. Wise "Surface Chemistry and Colloids" Ser. 1 Vol. 7 Buterworths (1972) 225

97. L.D. Schmidt Topics in Appl. Phys. Vol. 4 Springer-Verlag (1975) 63

98. C. Backx, B. Feuerbacher, B. Fitton, R. F. Willis Surface Sci. 63 (1977) 193

99. N.V. Richardson, A.M. Bradshaw Julich Conf. (1978) 'Vibrations in adsorbed layers'

100. R.F. Willis, W. Ho. E.W. Plummer Surface Sci. 80 (1979) 593

101. M.R. Barnes, R.F. Willis Phys. Rev. Letts. 41 (1978)1729

102. R.A. Barker, P.J. Estrup Phys. Rev. Letts. 41 (1978)1307

103. A.E. Morgan, G.A. Somorjai Surface Sci. 12 (1968) 405

104. K. Christmann, G. Ertl, T. Pignet Surface Sci. 54 (1976) 365

105. D. Bullett Surface Sci. 68 (1977) 149

106. J. Howard, T.C. Waddington, C.J. Wright J. Chem. Phys. 64 (1976) 3897

107. J. Howard, T.C. Waddington, C.J. Wright Int. Symp. Neutr. Inelastic Scatt. Vienna (1977)

108. J. Candy, P. Fouilloux,M.Primet Surface Sci. 72 (1978)167

109. A.M. Baro, H. Ibach, H.D. Bruchmann Surface Sci. 88 (1979) 384

110. A.M. Baro, H. Ibach Surface Sci. 92 (1980)

111. M. Green, J.A.K. Howard, J.L. Spencer, F.G.A. Stone, C.A. Tsipis J. Chem. Soc. Chem. Comm. (1976) 671

CHAPTER 6

ORGANOMETALLICS

(i) Tropyllium

6.1 Methods of Synthesis

All compounds in this study were prepared by literature methods. $Mo(CO)_6$, $W(CO)_6$, $Cr(CO)_6$ were supplied by Strem Chemicals, C_7H_8 by Koch-Light Labs Ltd (and freshly distilled before use), CH_3CN from Fluka AG. The source of $TaCl_5$ was unknown but was checked before use. (Chlorine analysis gave 49.9% (Theoretical value = 49.51%)). Triphenyl carbinol was supplied by B.D.H. Ltd.

$C_7H_7Mo(CO)_3BF_4$ was prepared by reacting C_7H_8 with $Mo(CO)_6$ to form $C_7H_8Mo(CO)_3$, which on reaction with $(C_6H_5)_3CBF_4$ (prepared from triphenylcarbinol and fluoroboric acid) precipitated the tropyllium salt (1).

Analysis (%)	Actual	Theoretical
C	34.1	33.5
H	2.2	2.0
Mo	26.8	26.8

$C_7H_7Cr(CO)_3BF_4$ was prepared by the same methods as above using $Cr(CO)_6$ (2,3).

Analysis (%)	Actual	Theoretical
C	37.8	38.2
H	1.9	2.2
Cr	20.1	20.2

The tungsten analogue was made from $W(CO)_6$ via $(CH_3CN)_3W(CO)_3$ and $C_7H_8W(CO)_3$ and, again $(C_6H_5)_3CBF_4$ (4,5).

Analysis (%)	Actual	Theoretical
C	26.6	26.9
H	1.8	1.6

$C_7H_7MO(CO)_2I$ was formed by reacting $C_7H_7Mo(CO)_3BF_4$ with NaI (6).

Analysis (%)	Actual	Theoretical
C	28.6	29.2
H	1.9	1.9
Mo	25.3	26.9

$(C_7H_7)_2TaCl_3$ was prepared by the reaction of $TaCl_5$ with C_7H_8 in benzene (7).

Analysis (%)	Actual	Theoretical
C	34.9	35.8
H	3.6	3.0
Cl	22.6	22.5

Finally, $C_7H_7BF_4$ was prepared by reacting C_7H_8 with $(C_6H_5)_3CBF_4$ in acetic anhydride (8).

Analysis (%)	Actual	Theoretical
C	45.9	47.2
H	4.0	3.9
F	42.6	42.7

6.2. Structures of Complexes

The tropyllium complex $C_7H_7BF_4$ was studied so that the intra-molecular vibrational modes could be indentified in this D_{7h} planar regular heptagon. The tropyllium cation, $(C_7H_7)^+$, has been known variously as cycloheptatrienylium, tropenylium and tropenium. (9) This seven carbon six π-electron cyclic cationic system was predicted by Huckel theory (10) to be a planar regular heptagon with greater resonance energy than benzene. The cation is stabilised by resonating between 7 structures which exist as shown in Figure 6.1 (11). This structure was found by various X-ray crystallographic studies of the $(C_7H_7)^+$ ion (12,13).

The compounds $(C_7H_7)M(CO)_3BF_4$ (where M = Mo, Cr, W) have all, probably, the same structure. An X-ray diffraction investigation of the molybdenum analogue was carried out at room temperature (14) and the $(C_7H_7Mo(CO)_3)^+$ cation has a 'piano stool' arrangement as shown in Figure 6.2.

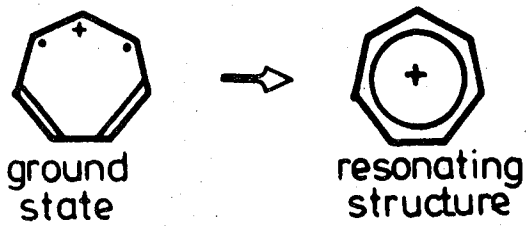

THE TROPYLLIUM ION

Figure (6.1)

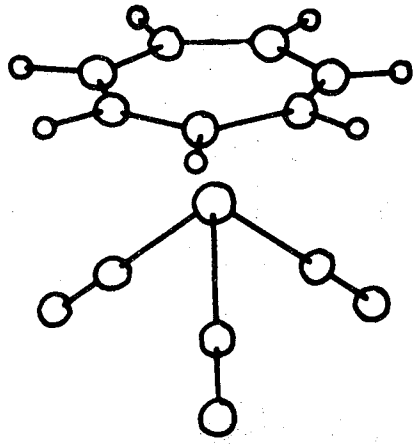

Figure (6.2)

$(C_7H_7)Mo(CO)_3BF_4$

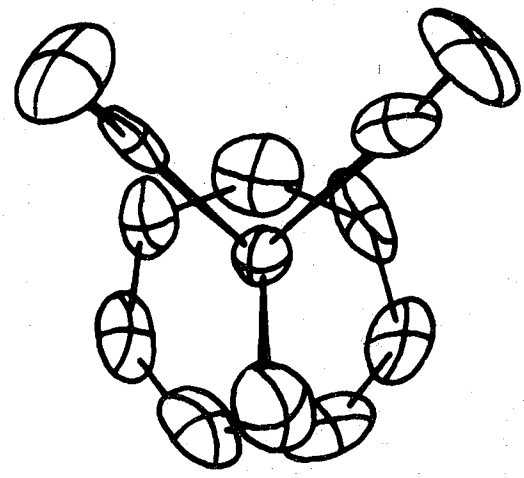

Figure (6.3)

$(C_7H_7)Mo(CO)_2I$

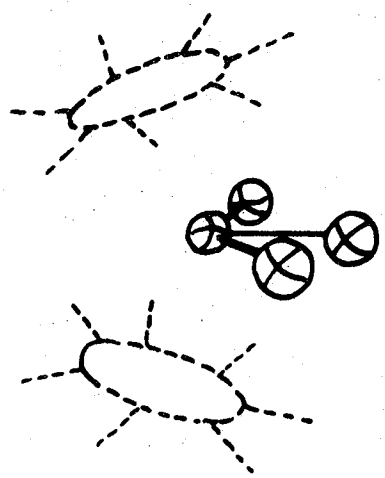

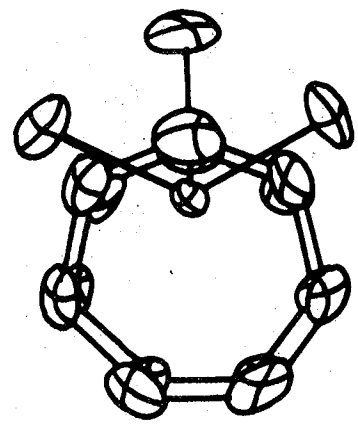

Figure (6.4) POSSIBLE FORM OF $(C_7H_7)_2TaCl_3$

The structure of $C_7H_7Mo(CO)_2I$ can be inferred from the crystal structure determination by Zeigler et al (15) on the chloride and bromide analogues. Again, a 'piano stool' arrangement has been found to exist with some asymmetry caused by the replacement of one carbonyl group with the single halide atom, as shown in Figure 6.3. A structural determination has not been carried out on $TaCl_3(C_7H_7)_2$ but it may be inferred from a study of $TaH_3(C_5H_5)_2$ by Bau et al (16) which confirmed a bent C_{2v} structure with a planar TaH_3 fragment. Figure 6.4 shows the proposed structure of $TaCl_3(C_7H_7)_2$.

The ligand cycloheptatriene has also been studied by an electron diffraction method by Traetteberg (17) who confirmed that a 'boat' shape of C_3 symmetry existed in the gas phase.

6.3. Cycloheptatriene

6.3.1. Previous results

Evans and Lord (18) studied cycloheptatriene but, at the time, the structure was in doubt. The position of the methylene CH_2 group was unknown. From the I R and Raman data they postulated that the molecule was C_{2v} and was planar but that the CH_2 group may have been slightly out of the C_6H_6 plane. La Lau and De Ruyter (19) re-examined the infra-red spectrum of C_7H_8 and C_7D_8 and found that a planar form was not compatible with the data. They suggested that the CH_2 group lay out of the molecular plane with the hydrogen atoms in dissimilar positions giving the molecule C_s symmetry. They further reassigned the I R bands at 657 and 589 cm^{-1}. Table 6.1 summarises

Table 6.1: Vibrations and Assignments for C_7H_8

Raman	IR		IINS			
Evans/ Lord (18) RT	Evans/ Lord (18) RT	La Lau (19) 303K	4H5 128K	BFD 77K	Vib. No. (18)	Assignment
			50(msh)			Lattice
			60(m)			Vib.
			82(s)			
			150(sh)	150(sh)		
223(m)	-	-	235(w)	230(s)	14	Ring def.
291(m)	-	-	282(w)	282(s)	20	Ring puck.
355(m)	353(ms)	-	-	355(m)	39	Ring puck.
405(m)	-	406(wb)	-		17	CH o/p def.
421(s)	410(s)	420(sb)	-	461(sb)	13	Ring def.
-	428(s)	-	-		38	Ring puck.
-	-	-	-	451(sh)	-	2 x 14
588(w)	590(s)	589(ms)	-	588(w)	37	CH o/p def.
657(vw)	656(s)	657(ws)	-	667(sh)	36	CH_2 rock.
712(vw)	705(vvs)	710(vvs)	-	741(mb)	35	CH o/p def.
743(vw)	740(vs)	743(vs)	-		34	CH o/p def.

o/p = out-of-plane, def. = deformation, puck. = puckering

s = strong, m = medium, w = weak, v = very, b = broad

the results of Evans and Lord (18), La Lau and De Ruyter (19) and the I I N S results obtained in this study. The I I N S bands have been assigned with reference to the above works.

6.3.2. Results

Cycloheptatriene was run on the 4H5 spectrometer at 128K. Figure 6.5 shows the C_7H_8 spectrum gathered at the scattering angles of 82^o and 90^o. Figure 6.6 depicts the BFDDIDO spectrum of C_7H_8 at liquid nitrogen temperature. Table 6.1 shows relevant features from these spectra.

6.3.3. Discussion

The bands below $150cm^{-1}$ are assigned to the lattice vibrations of C_7H_8. From the BFDDIDO spectrum it can be seen that the four strongest bands lie in the $230-420cm^{-1}$ region. These bands are the deformations and puckerings of the boat-shaped ring and, obviously, involve considerable hydrogen motion compared with the out-of-plane CH deformations found at higher frequency.

6.4. Tropyllium Tetrafluoroborate

6.4.1. Previous results

Fately et al (12) presented infra-red and Raman spectra for C_7H_7Br and from the data postulated that a D_{7h} planar form of the cation must exist. Aida (20) calculated the frequencies of the inactive vibrations of $(C_7H_7)^+$, using force constants derived from benzene data. Sourisseau and Hervieu (21) reported the vibrational spectra and structure of crystalline $C_7H_7PCl_6$ at 100K. The infra-red vibrations were quite intense in contrast to the weak Raman data.

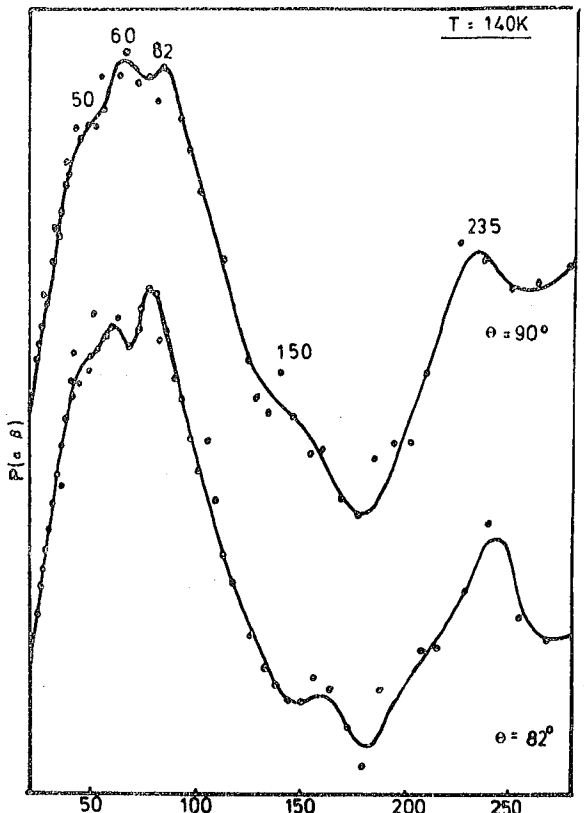

Figure(6·5) P(α β) data for C_7H_8

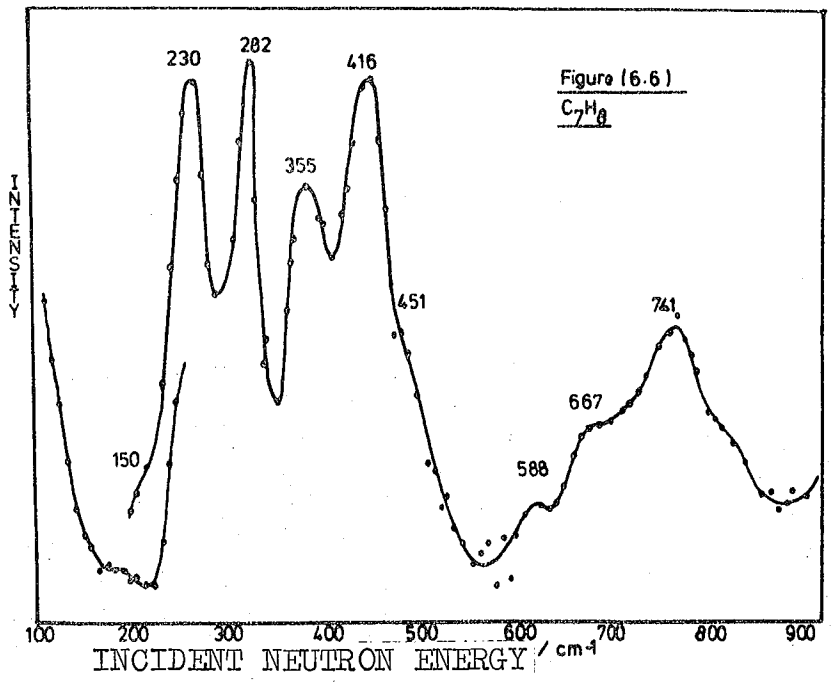

Figure (6.6)
C_7H_8

The authors thought that the crystalline state would allow all the bands to be infra-red active but not all were observed. In general, the inactive vibrations were found to be quite different in value from those calculated by Aida (20). Sourisseauet al (21) felt from the vibrational frequencies, compared to those of benzene, that the $(C_7H_7)^+$ ring was much more difficult to distort than the C_6H_6 ring. The assignment of Sourisseau and Hervieu also differed from those of Fately et al (12). For example they assigned an out-of-plane ring deformation to the strong IR band at 635cm^{-1} which was previously assigned to a CH out-of-plane deformation by Fately et al. Table 6.2 lists the data of Fately et al, Sourisseau and Hervieu and Aida in the region of interest.

6.4.2. Results

Table 6.3. lists the results gained from this study of $C_7H_7BF_4$. Figure 6.7. shows the BFDDIDO spectrum of $C_7H_7BF_4$ gained at liquid nitrogen temperature.

6.4.3. Discussion

The Raman active bands of this planar D_{7h} cation, $C_7H_7^+$, are $2A_1' + 1E_1'' + 4E_2''$ whereas those infra-red active bands are of $1A_2''$ and $3E_1'$ symmetry.

There are a number of points of interest to come out of this study of $C_7H_7BF_4$ especially in a comparison with the work on $C_7H_7PCl_6$ (21). The following points are taken from the work of Sourisseau and Hervieu on their study.

i) They could not decide whether a band of weak intensity, in the infra-red, had E_2'' or E_3'' symmetry. Thus only 34 of the 36 vibrations were in fact assigned.

Table 6.2: Vibrational Studies on the $(C_7H_7)^+$ cation (cm^{-1})

C_7H_7Br (12)			Calculated values (20)	$C_7H_7PCl_6$ (21)						Assignment
				IR			RAMAN			
IR RT	RAMAN RT	Assignment		300K	100K	Sol.	300K	100K	Sol.	
					1033(w)					
			1211,914	1025(w)	1029(w)					E_2'' or E_3'' CH o/p def.
					1024(w)					
					996(sh)					
992(wm)		E_1' CH i/p def.		993(m)	993(m)					E_1' CH i/p def.
	925(w)			892(vw)	890(m)		892(vw)	890(vw)		E_1'' CH o/p def.
					885(sh)					
	868(vs)	A_1' Ring breathing		870(w)	873(m)		869(ms)	870(s)	867(s)	A_1' Ring breathing
					870(m)					
			1148	768(w)	772(m)					E_3' i/p ring def.
					667(sh)					
658(m)		Combination band (see text) (433+225cm^{-1})		661(vs)	659(vs)					A_2' CH o/p def.
					653(sh)					
633(s)		A_2'' CH o/p def.	625	635(vs)	637(vs)	636(vs)				E_3'' o/p ring def.
					620(w)					
	433(m)	E_2' i/p ring def.					430(wm)	432(m)	430(m)	E_2' i/p ring def.
			389	353(w)	356(w)					E_2'' o/p ring def.
				214(vw)	216(vw)					PCl_6 def. (?)
					105(m)					
				88(m)	84(m)		78(s)	89		
					54(w)		35(sh)	39		
							26(s)			

Table 6.3: Vibrational Data and Assignments for $C_7H_7BF_4$

BFDDIDO (97K)	IR (97K)	FIR (77K)	RAMAN (RT)	
	876(wb)		879(s)	A_1': Ring breathing
776(w)				E_3': i/p Ring deformation
	748(vw)			A_1: BF_4 symm. def.
	696(w)			-
685(s)	675(s)			A_2'': o/p CH deformation
665(m)	652(m)			Combination (438+238=676)
562(s)				E_3'': o/p CH deformation
	530(wm)			-
	520(s)			T_2: BF_4 deformation mode
438(m)			436(vw)	E_2': i/p Ring def.
335(wm)	338(w)	353(w)	340(vw)	E_2'' or E_3'': o/p Ring def.
238(vs)	230(sh)	238(sh) 233(m)		E_2'' or E_3'': o/p Ring Def.
		127(sh)	136(w)	Lattice Modes
		119(sh)	119(s)	
112(sb)		112(m)	110(sh)	
		106(m)		
		98(sb)	95(sh)	
80(m)		87(s)		
		83(s)		

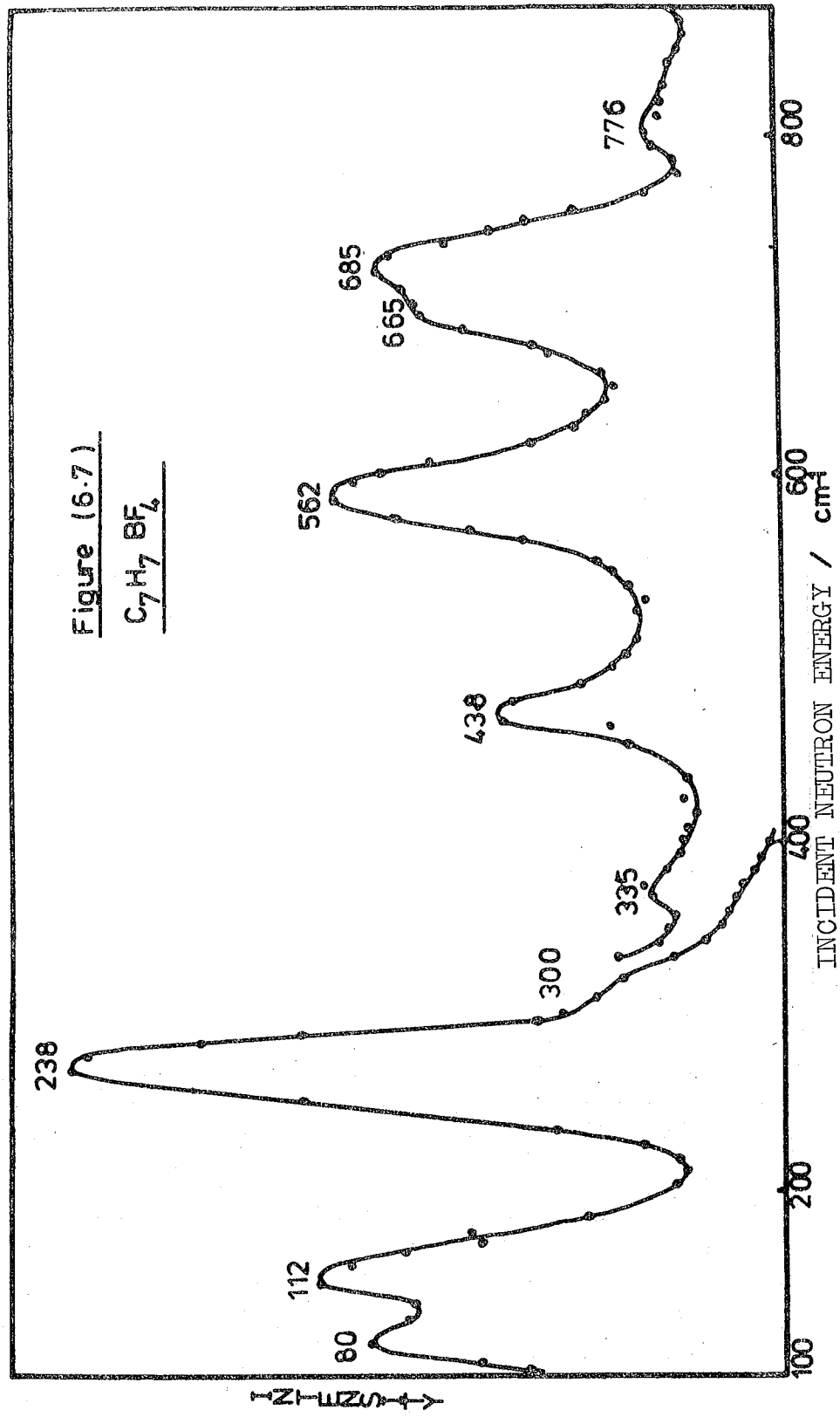
Figure (6.7)
$C_7H_7BF_4$
238
112
80
300
335
438
562
665
685
776
100
200
400
600
800
INCIDENT NEUTRON ENERGY / cm^{-1}
SCATTERING

ii) They very tentatively assign an IR band at 216cm^{-1} to a forbidden PCl_6^- vibration (not seen in other PCl_6^- studies).

iii) They do not carry out a normal co-ordinate analysis on the E_2'' or E_3'' symmetry blocks since they were unsure of the frequencies.

iv) An infra-red band at 586cm^{-1} was tentatively assigned to a decomposition product of PCl_6^-.

In this IINS study of $C_7H_7BF_4$ strong bands exist at 562 and 238 cm^{-1}, which from intensity grounds alone are probably fundamental vibrations. It is postulated that the band at 238cm^{-1} in the IINS, which is also seen in the infra-red in the same manner as the 216cm^{-1} infra-red band of $C_7H_7PCl_6$, can be assigned to an out-of-plane ring deformation mode. Figure 6.8 shows the 238cm^{-1} infra-red band of $C_7H_7BF_4$. The quite low frequency assignment is reasonable since a ring deformation mode exists at 223cm^{-1} in C_7H_8 (18). However, it may not be appropriate to compare the vibrations of the C_7H_7 planar moiety with the bent C_7H_8 molecule. Further evidence is provided later in this section for this assignment. The IINS band at 562cm^{-1} is not observed in either the infra-red or Raman spectra of $C_7H_7BF_4$. Thus it is obviously a forbidden mode and inactive even in the crystalline state. It may be an out-of-plane CH or ring deformation because of the high IINS intensity associated with the vibration.

Now Fately et al (12) estimated the inactive E_2'' out-of-plane ring deformation to be at 225cm^{-1} in C_7H_7Br by assigning the infra-red band at 658cm^{-1} to a combination band of the E_2'' vibration with the E_2' normal mode at

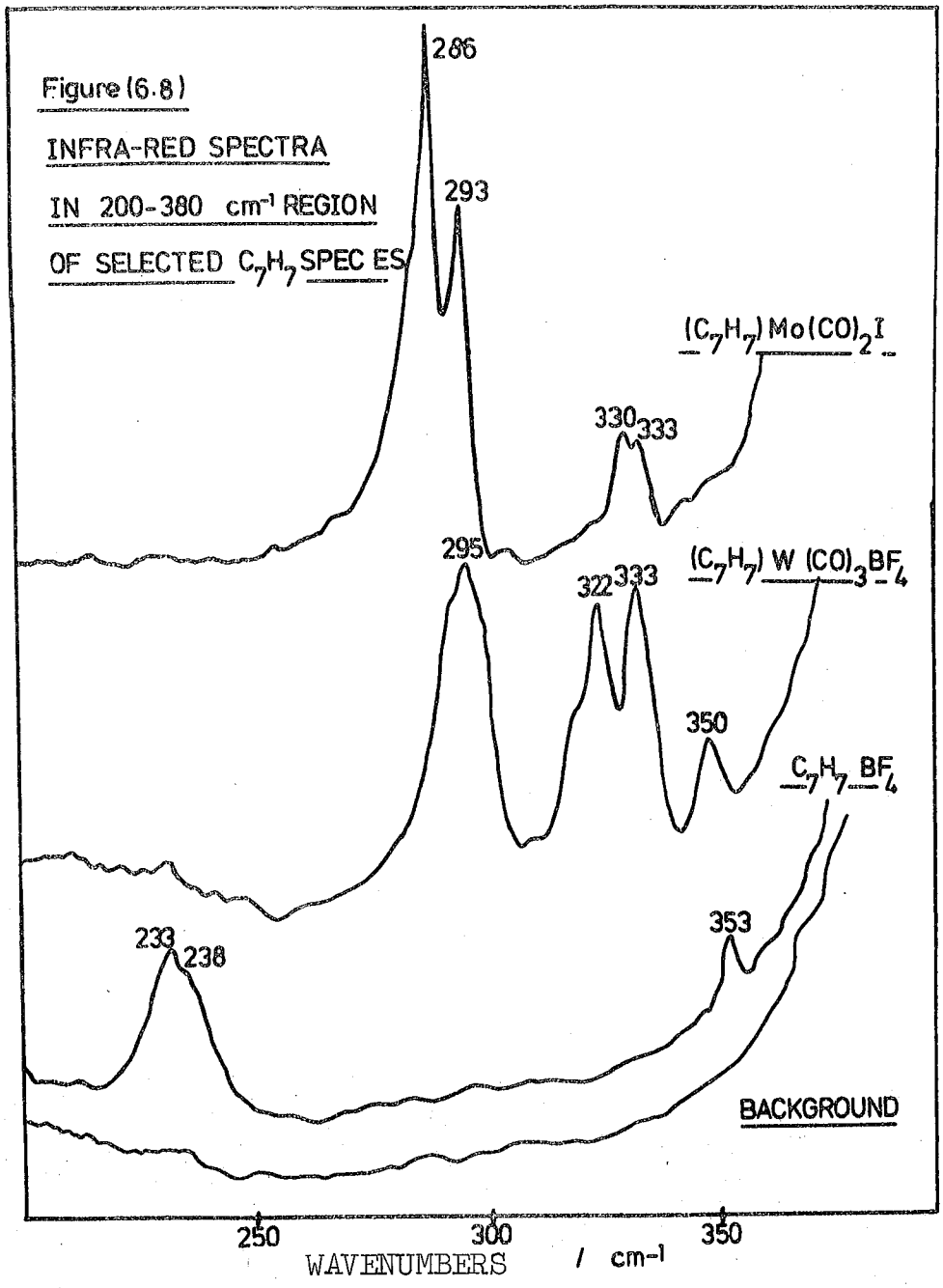
Figure (6.8)
INFRA-RED SPECTRA
IN 200-380 cm⁻¹ REGION
OF SELECTED C_7H_7 SPECIES
286
293
$(C_7H_7)Mo(CO)_2I$
330
333
295
322
333
$(C_7H_7)W(CO)_3BF_4$
350
$C_7H_7BF_4$
233
238
353
BACKGROUND
250
300
350
WAVENUMBERS / cm-1

433cm^{-1} (225 + 433 = 658cm^{-1}). An interesting test of this would be to extend the hypothesis to $C_7H_7PCl_6$ and $C_7H_7BF_4$.

$C_7H_7PCl_6$:	216 + 430 = 646cm^{-1}	There are IR bands at 661 and 635cm^{-1}
$C_7H_7BF_4$:	238 + 438 = 676cm^{-1}	There is an IINS band at 665cm^{-1} and an IR band at 652 and 665cm^{-1}.

The possibility thus arises that the 238cm^{-1} IINS band in $C_7H_7BF_4$ (and at 216cm^{-1} in $C_7H_7PCl_6$(21)) is an out-of-plane ring deformation as implied by the study of Fately et al (12) of C_7H_7Br. This would mean that possibly the infra-red bands at 658cm^{-1} in C_7H_7Br, 661cm^{-1} or 636cm^{-1} in $C_7H_7PCl_6$ and 665cm^{-1} in $C_7H_7BF_4$ are combination bands and not fundamental vibrations as implied by the study Sourisseau et al (21). If this were the case then another fundamental vibration has to be assigned elsewhere in the data of Sourisseau et al (ie the extra mode from the 1025cm^{-1} band and the assignment of the 661/635cm^{-1} to a combination band). These two extra normal modes which had not been correctly assigned by Sourisseau et al, are assigned to the IINS bands of strong intensity at 238 and 562cm^{-1} in $C_7H_7BF_4$.

The IINS data on $C_7H_7BF_4$, it would appear, is much more amenable to the analysis carried out by Fately et al (12) than that of Sourisseau et al (21), of the $C_7H_7^+$ intramolecular modes. The actual assignments in the region of interest, are carried out as follows. The strong Raman band at 879cm^{-1}, beyond the range of the IINS study, is assigned to the Raman active ring breathing mode. Similar

assignments had been made to Raman bands in C_7H_7Br and $C_7H_7PCl_6$. In C_7H_7Br, the strongest infra-red band lay at 633cm^{-1} and the $C_7H_7BF_4$ analogue was found at 675cm^{-1}. This band is assigned to the A_2'' CH out-of-plane deformation, which has its benzene counterpart at 671cm^{-1} of similar infra-red activity. The IINS analogue of the infra-red band at 675cm^{-1} lies at 685cm^{-1}. The weaker IINS b nd at 665cm^{-1}, a shoulder to the stronger 685cm^{-1} deformation mode, is assigned to the combination mode as described by Fately et al (12).

The strong IINS band at 562cm^{-1}, which may have a $C_7H_7PCl_6$ infra-red counterpart at 586cm^{-1} (21), is assigned to the E_3'' out-of-plane CH deformation, which had been previously assigned by Sourisseau et al to the weak infra-red 1025cm^{-1} in $C_7H_7PCl_6$ (21). This arises because there are only two types of vibration that are incorrectly assigned by Sourisseau et al: the E_2'' and E_3'' out-of plane ring deformations and the above CH deformation. Since the ring deformations are more likely to be at lower frequency, then the CH deformation, of E_3'' symmetry, is assigned at higher frequency, i.e. 562cm^{-1}. The weak Raman band at 436cm^{-1} in $C_7H_7BF_4$ is straight forwardly assigned, in the same manner as Fately et al (12) and Sourisseau et al (21) to the E_2' Raman active in-plane ring deformation.

The weak-medium IINS band at 335cm^{-1} has only weak infra-red and Raman analogues. This could indicate that the normal mode is infra-red and Raman inactive. Since the Raman band can be alternatively assigned, the infra-red activity may arise due to a solid state effect. The

IINS bond is assigned to a low frequency out-of-plane ring deformation mode. The IINS band at 238cm^{-1} is also assigned similarly. This band must be an out-of-plane ring deformation since the lowest fundamental intramolecular frequencies of such planar aromatic systemsgenerally take this form e.g. ~400cm^{-1} in benzene. Unfortunately, no such low frequency data areavailable on the $C_8H_8^{2-}$ ion since vibrational studies, up to the present, have only been qualitative in nature and far from complete. Further, Fately et al (12) estimated that the normal mode would be of such a low frequency from their combination band argument.

Since the band has E_2'' or E_3'' symmetry, it is formally infra-red and Raman inactive, however, weak-medium intense bands are found in the infra-red. The assignment of the two low frequency out-of-plane ring deformations at 238 and 335cm^{-1} (both formally infra-red and Raman inactive) to either E_2'' or E_3'' symmetry, or vice versa, cannot be differentiated on the evidence at hand. Fately et al (12) and Sourisseau et al (21) assigned the E_2'' band at 225 and 335cm^{-1} respectively whereas the latter assigned the E_3'' band at 636cm^{-1}. This latter assignment is rejected. Evidence from the study of the $C_7H_7M(CO)_3^+$ species indicates that probably the assignment by Fately et al (12) was correct.

Further evidence for the assignment of the two out-of-plane ring deformations, of E_2'' and E_3'' symmetry, at 238cm^{-1} and 335cm^{-1} and for the CH out-of-plane deformation at 562cm^{-1} arises from the study of the tropyllium-metal complexes. In all the IINS spectra and in some of the infra-red data, vibrational bands exist at all of these frequencies, ~230, ~330 and ~560cm^{-1}.

The BF_4^- vibrations are of $A_1 + E + 2T_2$ symmetry since BF_4^- is tetrahedral. All are Raman active whereas only the T_2 vibrations are infra-red active. Bands have been previously assigned at 769, 353, 1016 and 529 cm^{-1} respectively from IR and Raman studies (22, 23). Infra-red and Raman bands are found in these regions and the following assignments can be made in $C_7H_7BF_4$.

Tetrafluoroborate ion Vibrations

Vibration	Cm^{-1}	Activity
A_1 stretch	748	IR (vw)
T_2 deformation	520	IR (s)
E deformation	353	IR (w) R (w)

The other T_2 symmetry band at ~1000cm^{-1} was not definitely located since it lay in a region of many infra-red active tropyllium intra-molecular modes. Sourisseau et al (21), however, do not observe any Raman bands arising from this source in this region (900-1100cm^{-1}) and so a weak Raman band observed at 1045cm^{-1} in $C_7H_7BF_4$ may be due to this final BF_4 vibration of T_2 symmetry.

Figure 6.8. shows the low frequency E deformation of the BF_4^- anion in $C_7H_7BF_4$.

6.5. $C_7H_7M(CO)_3BF_4$ (M = Cr, Mo, W)

6.5.1. Previous studies

No vibrational studies have been carried out on the low frequency vibrations of this series (< 700cm^{-1}). Fritz (24) listed the seven infra-red active normal vibrations of some π-C_7H_7 complexes which included the chromium and molybdenum analogues. The lowest frequency vibrations of interest in the region studied were the ring breathing

mode, which had shifted in frequency from 876cm^{-1} in $C_7H_7BF_4$ to 860cm^{-1} in the complexes, and the CH out-of-plane deformation which shifted from 690cm^{-1} to 810cm^{-1}. This latter vibration has as its benzene analogue, ν_{11}, which also, on complexing, usually shifts up in frequency by ~100cm^{-1} (see Chapter 7,8 and 9). King listed infra-red vibrations of the tungsten compound above 700cm^{-1} but no assignments were made (5).

6.5.2. Results

The vibrational spectra of the tropyllium complexes have been studied by IINS spectroscopy, using 4H5, BFDPLUTO and BFDDIDO spectrometers, infra-red, far infra-red and Raman spectroscopy. The beryllium filter and infra-red studies were carried out at liquid nitrogen temperature whereas the 4H5 studies were at 133-140k.

The Raman studies were performed at room temperature with the samples held in thin sealed glass tubes. The laser power used was 8mW.

The IINS, Raman and infra-red results are summarised in Table 6.4 and the neutron spectra are shown in Figures 6.9 - 6.13.

6.5.3. Discussion

The structures of the chromium and tungsten analogues are assumed to be similar to the 'piano stool' arrangement of $(C_7H_7Mo(CO)_3)^+$ and thus they are all of C_s symmetry. The symmetries of the fundamental modes of the complexes are shown in Table 6.5

Table 6.4: Vibrational Data and Assignments for the $C_7H_7M(CO)_3BF_4$ Species

$C_7H_7Cr(CO)_3BF_4$						$C_7H_7Mo(CO)_3BF_4$						$C_7H_7W(CO)_3BF_4$						Assignment
4H5 (133K)	BFDDIDO (77K)	IR (77K)	FIR (77K)	IR(24) (RT)	RAMAN (RT)	4H5 (130K)	BFDDIDO (77K)	IR (77K)	FIR (77K)	IR(24) (RT)	RAMAN (RT)	4H5 (133K)	BFDDIDO (77K)	IR (77K)	FIR (77K)	RAMAN (RT)	IR(5) (RT)	
		967(wm)		970	958(w)		992(m)	957(m)		958								E_1 CH o/p deformation
		863(w)		864			882(m)	860(m)		861	865(s)		854(s)	863(m)		865(wm)	862(w)	A_1 Ring breathing
		814(s)		816			833(sh)	806(s)		807	812(w)		820(sh)	811(s)			814(w)	A_1 CH o/p deformation
		725(vw)			725(wb)						709(wm)					696(vw)	721(w)	A_1 symmetric BF_4 stretch
													682(w)					Unknown (possibly (2x336 - 652cm^{-1})
	627(w)						640(wm)											Unknown (possibly (2x325 - 650cm^{-1})
		606(vs)																M-C-O deformations
		565(vs)						561(vs)										
	547(mb)						558(ms)						544(sb)					E_3 CH o/p deformation
		536(m)			532(wb)			513(m)			503(w)			560(m)		555(wb)		T_2 BF_4 deformation
														519(m)				M-C-O deformation
		498(ms)						492(s)						477(s)				M-C stretches
								475(s)						455(sh)				
	474(m)					460(w)	471(sh)					470(m)	471(m)					E_2 in-plane ring def.
		448(s)						407(s)						416(ms)				M-C stretches
		420(w)						395(sh)	391(m)									
	368(sh)						378(sh)						375(sh)					E_2 or E_3 o/p ring def.
		351(vw)	350(vw)		353(m)				353(w)		352(wm)				350(m)	370(w)		E BF_4 deformation
		327(w)	325(m)				325(vs)	330(sh)	328(m)		325(msh)		326(vs)	336(m)	333(ms)	325(w)		Metal-C_7H_7 stretches and tilts
	314(vs)	319(w)	315(m)		316(sh)	317(s)			319(w)			320(s)			322(m)			
	298(m)	307(w)	304(m)		305(s)		294(s)	309(ms)	307(s)		311(vs)		299(m)	296(ms)	295(s)	298(s)		
																293(sh)		
	204(wm)				240(w)	220(w)	208(wm)	210(w)			210(vw)	220(w)	219(m)			220(vs)		E_2 or E_3 o/p ring def.
												160(m)						Unknown (possibly overtone band)
									139(m)						143(w)			C-M-C deformation
138(s)	135(ms)					114(m)	110(s)					119(ms)	118(m)			122(wm)		Metal C_7H_7 deformation
					120(mb)						107(sb)					108(msb)		C-M-C deformation
			100(wb)						85(vs)				100(sh)		95(wb)			
						75(ms)						76(s)						Metal- C_7H_7 torsion
75(s)	64(s)					62(msh)												
66(sh)									58(w)									Lattice modes (intermolecular)
43(sh)					40(w)	38(mb)				43(w)		40(sh)				51(wm)		

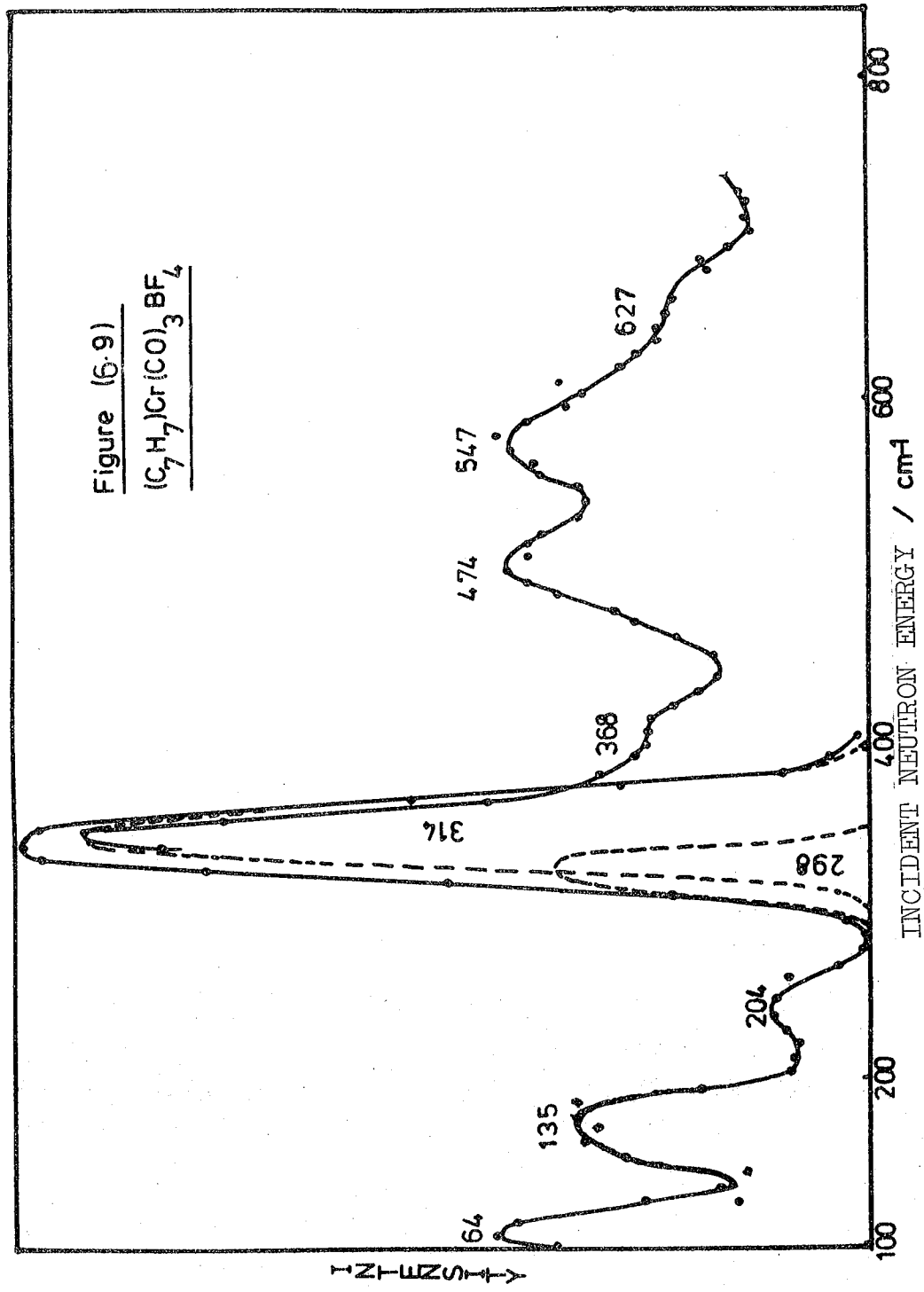
Figure (6.9)
$(C_7H_7)Cr(CO)_3BF_4$
INTENSITY
INCIDENT NEUTRON ENERGY / cm-1
100
200
400
600
800
64
135
204
298
314
368
474
547
627

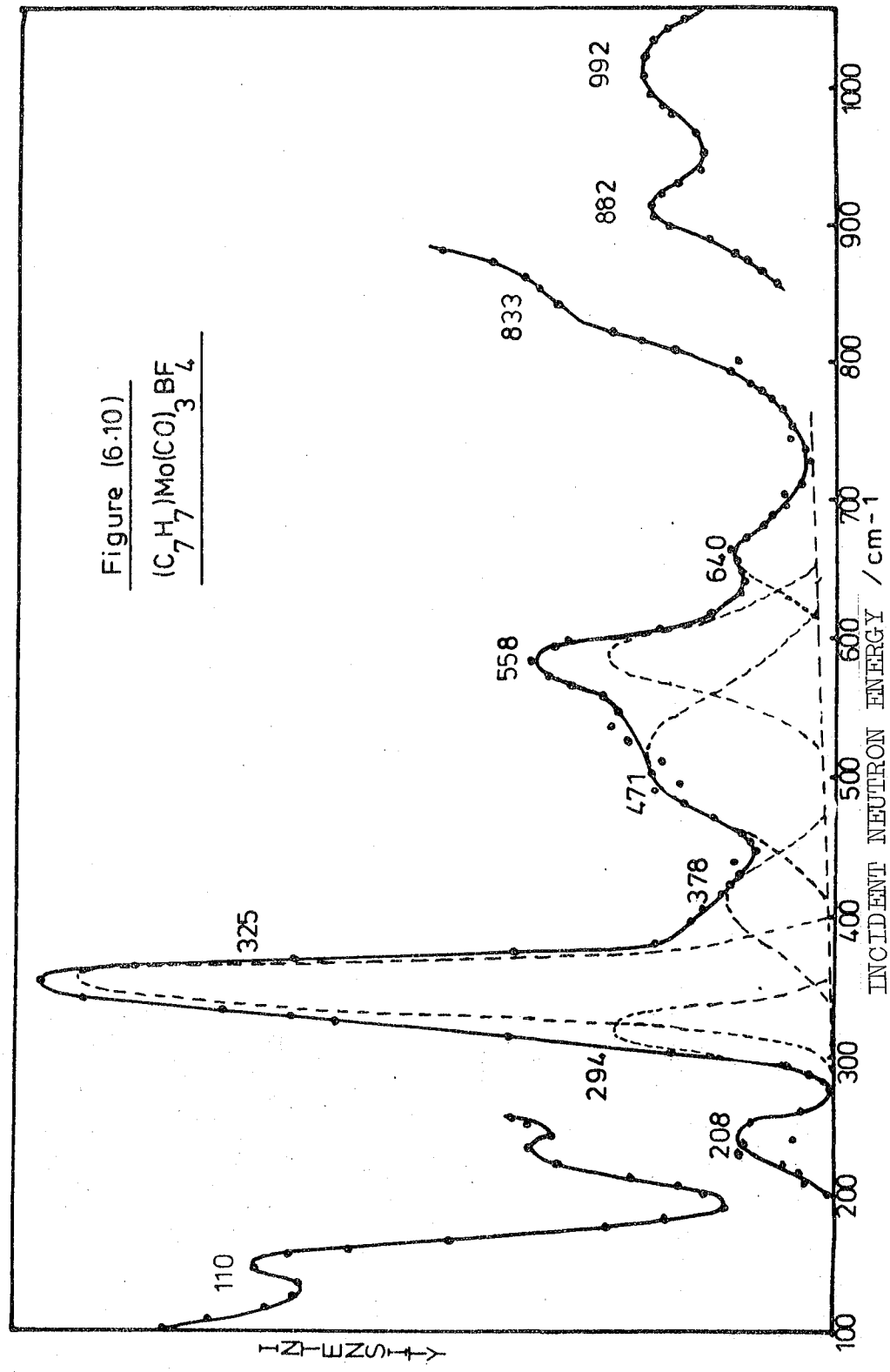
Figure (6.10)
$(C_7H_7)Mo(CO)_3BF_4$
INTENSITY
INCIDENT NEUTRON ENERGY /cm-1
100
200
300
400
500
600
700
800
900
1000
110
208
294
325
378
471
558
640
833
882
992

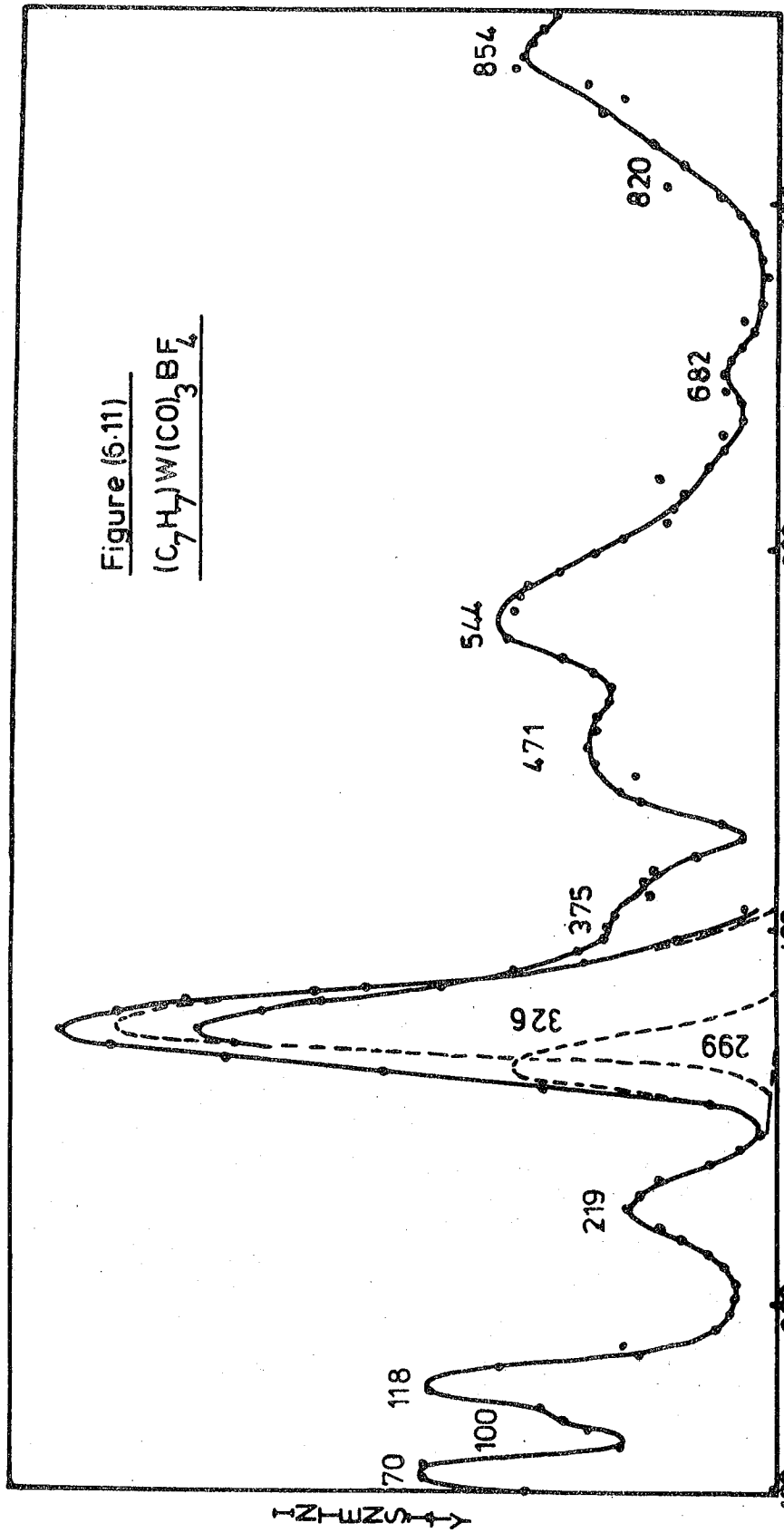
Figure (6.11)
$(C_7H_7)W(CO)_3BF_4$
INTENSITY
INCIDENT NEUTRON ENERGY /cm⁻¹
100
200
400
600
800
70
118
100
219
326
299
375
471
544
682
820
854

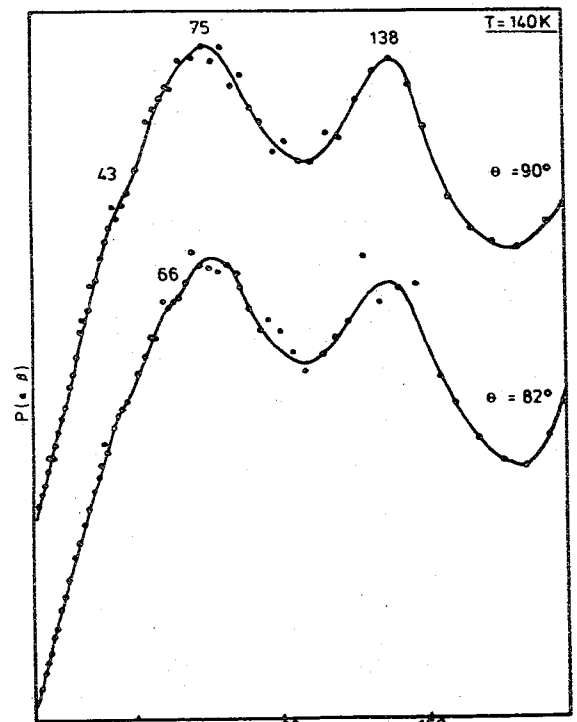

Figure(6·12) P(ε β) data for $(C_7H_7)Cr(CO)_3BF_4$

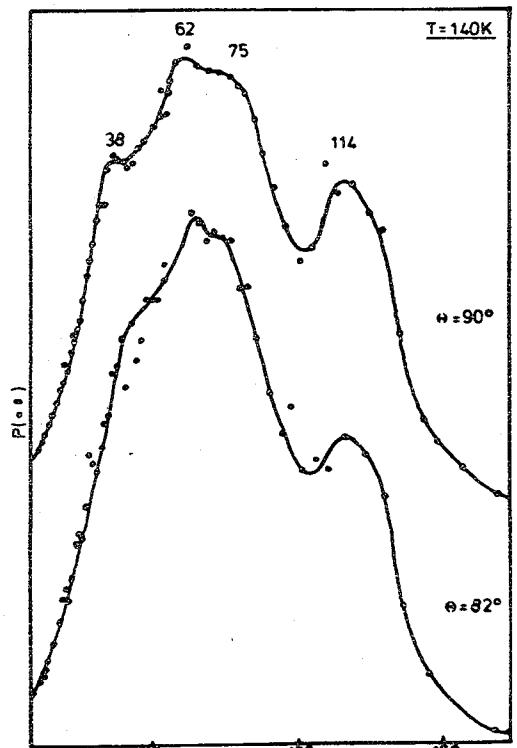

Figure(6·13) P(ε β) data for $(C_7H_7)Mo(CO)_3BF_4$

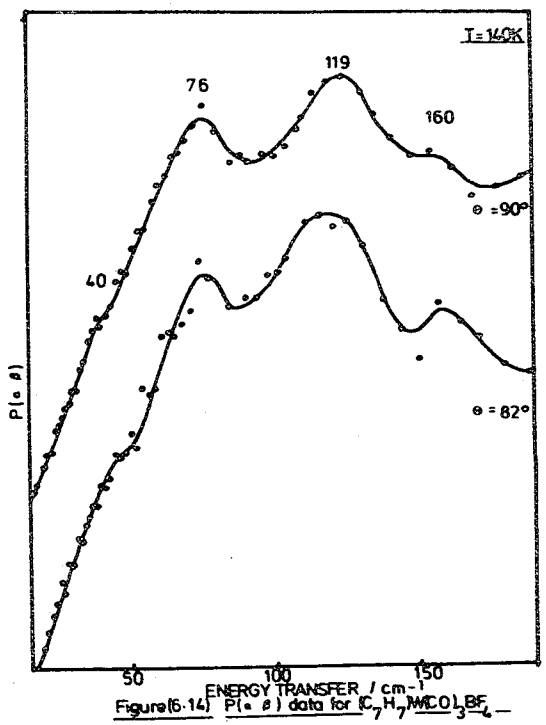

Figure(6·14) P(ε β) data for $(C_7H_7)W(CO)_3BF_4$

Table 6.5: C_s Vibrational Analysis

C_s	$C_7H_7Mo(CO)_3^+$	$M(CO)_3$	C_7H_7	C_7H_7-M skeletal vibrations	Activity
A'	31	9	19	3	IR/R
A''	26	6	17	3	IR/R

With the formal C_s symmetry, all modes are infra-red and Raman active and there should be no doubly degenerate species but this will not necessarily be the case. The tropyllium ring must be considered as a perturbed D_{7h} system which retains its seven-fold symmetry and thus has C_{7v} local symmetry. The one-sided bonding to the metal, and, therefore the absence of σ_h and the seven C_2's of the $D_{7h}(C_7H_7)$ point group, causes the lowering of the symmetry.

The co-ordination of the tropyllium to the $M(CO)_3$ unit results in six new modes, of 3A' and 3A'' symmetry under C_s symmetry. These bands arise from the rotations and translations of the free $(C_7H_7)^+$ ligand. The form of these motions is depicted in Figure 6.15.

As shown in Figure 6.15 there are two pairs of deformations and tilts. These will be doubly degenerate if the metal-ligand vibrations could be treated under C_{7v} symmetry. However, if the metal-ligand vibrations are strictly described under C_s symmetry then some splitting of the doubly degenerate bands would be expected. Whether this would be visible in the IINS spectra would lead to some conjecture.

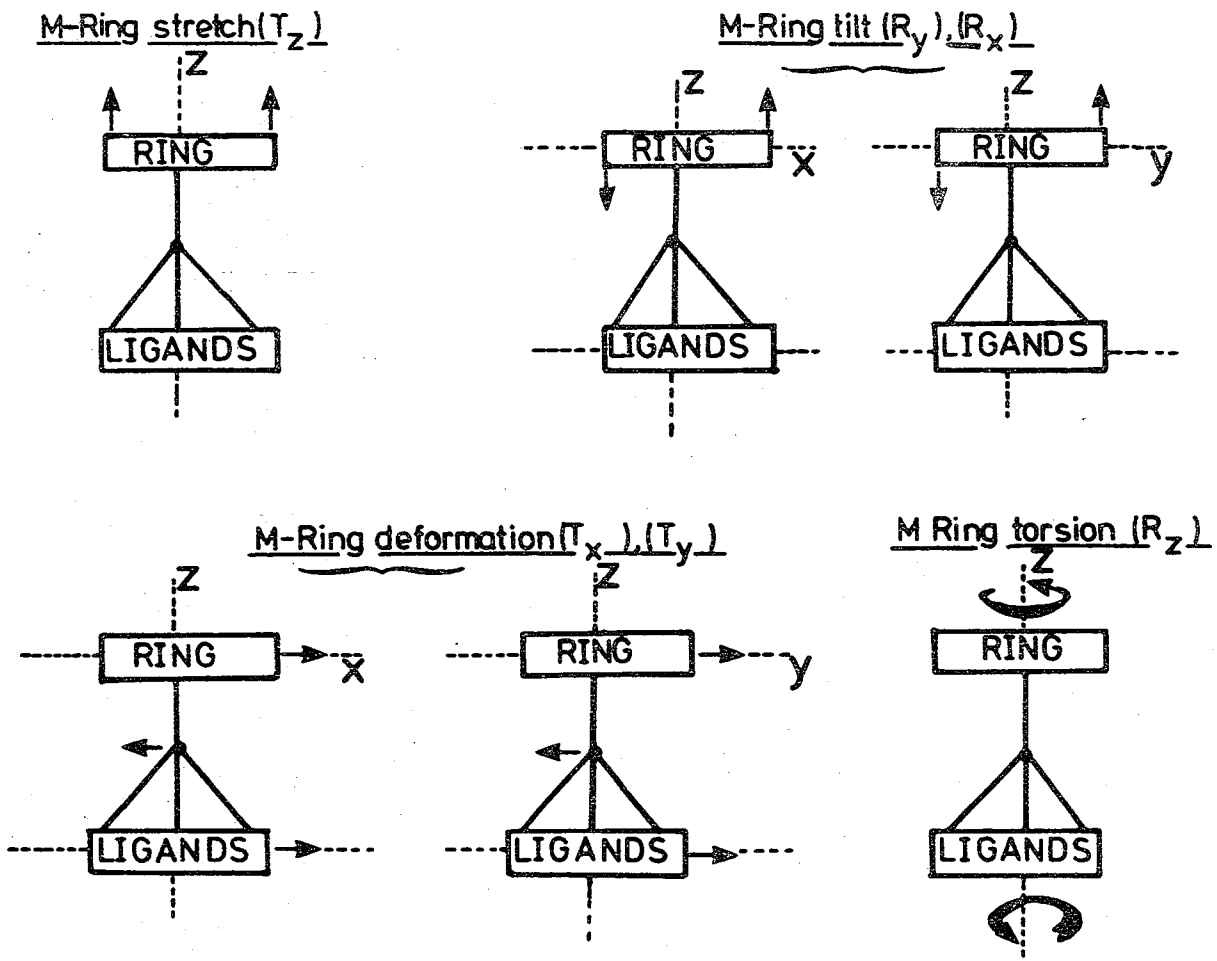

Figure(6·15) Skeletal vibrations of C_nH_n(ring)-Metal-(ligand) system

The spectral expectations for a C_7H_7 M species holding C_{7v} symmetry is shown in Table 6.6.

Table 6.6: C_{7v} Vibrational Analysis

C_{7v}	C_7H_7M	C_7H_7	M-ligand	Activity
A_1	4	3	stretch	IR/R
A_2	1	1	-	-
E_1	5	4	Deformation	IR/R
E_2	6	6	-	R
E_3	6	6	-	-

Vibrations above $200cm^{-1}$

Above $200cm^{-1}$ the following five types of vibration are found:-

i) Tropyllium intramolecular fundamental modes

ii) M-C stretches in the $M(CO)_3$ unit

iii) M-C-O deformation in the $M(CO)_3$ unit

iv) BF_4^- vibrations

v) High frequency skeletal motion (stretch and tilts)

The counter ion, BF_4^-, has T_d symmetry and thus vibrations of $A_1 + E + 2T_2$ symmetry. All are Raman active whereas only the triply degenerate vibrations are infra-red active. The bands have previously been assigned to features in the infra-red and Raman of $NaBF_4$ at 769, 353, 1016 and $529cm^{-1}$ (22,23). In the BF_4^- complexes, Raman bands were found at 353 and $698cm^{-1}$ and a medium-intense band at $510-560cm^{-1}$. Thus the following assignments can be made in Table 6.7 in the same manner as $C_7H_7BF_4$. (Once again the band at

~1000cm^{-1} is difficult to assign due to the intramolecular tropyllium modes).

Table 6.7: BF_4^- Vibrations in $C_7H_7M(CO)_3BF_4$ Complexes

$C_7H_7BF_4$ analogue	Frequency Range in BF_4^- salts	Raman Activity	Infra-red Activity	Assignment
748	690 - 730	wm	vw	(A_1) stretch
520	500 - 560	w	ms	(T_2)deformation
353	350 - 370	wm	w	(E) deformation

There are another set of vibrations which are not IINS active and they involve the $M(CO)_3$ group. The vibrations of this group have been assigned in many π-organometallic species, such as $C_6H_6M(CO)_3$ (25) and $C_7H_8M(CO)_3$ (26). The M-C stretches and M-C-O deformation fall within the region of interest. Even though they are not formally neutron active, some activity may arise due to the mixing of these modes with strong IINS active bands in the same areas of the IINS spectrum. That is, they acquire IINS activity due to associated hydrogen motion. These $M(CO)_3$ vibrations can be assigned on the basis of their local C_{3v} symmetry and are usually strongly infra-red active and sometimes of medium intensity in the Raman spectrum. Strong infra-red bands in the 350-700cm^{-1} region, without IINS analogues, are so assigned, as shown in Table 6.4.

The ligand vibrations can be assigned from a comparison with $(C_7H_7)^+$ salts and, in particular, the IINS spectrum

of $C_7H_7BF_4$. Above 800cm^{-1} similar IINS and infra-red bands exist at the same frequencies as the assignments of Fritz (24). Table 6.4 shows these infra-red active vibrations of C_7H_7 described in terms of the C_{7v} symmetry. For the C_{7v} symmetry, the vibrations of $3A_1 + 4E_1$ symmetry are infra-red active whereas the Raman active bands are of $4A_1 + 5E_1 + 6E_2$ symmetry.

The A_1CH out-of-plane deformation in the complexes has shifted to higher frequency on complexation and been reduced slightly in intensity. This situation was paralleled in the C_6H_6 + Pt black experiment where υ_{11} had shifted to higher frequency and similarly reduced in intensity from that found in benzene alone. (The intensity increased markedly as the benzene coverage was increased and it returned to its non-complexed frequency). This CH out-of-plane deformation is also strongly infra-red active and the IR bands at ~810cm^{-1} can be assigned. In all the tropyllium complexes there are medium intense bands in the 540-560cm^{-1} region which are assigned to the E_3 CH out-of-plane deformation. Because of the medium-strong IINS intensity, the band describes a vibration involving large hydrogen vibrational amplitudes. This tends to add further evidence for this band involving an out-of-plane motion and that it is a fundamental intramolcular tropyllium mode. In D_{7h} symmetry in the $C_7H_7^+$ salts, the band had E_3'' symmetry and was infra-red and Raman inactive. In C_{7v} symmetry it has E_3 symmetry and, thus, again is infra-red and Raman inactive. No infra-red or Raman analogues of this IINS band were found.

The IINS BFDDIDO spectra only show one vibration in the 400-500cm^{-1} region. This lies at 471-474cm^{-1}. It can be straightforwardly correlated with the in-plane deformation

of the tropyllium ring, which was assigned at 438cm^{-1} in $C_7H_7BF_4$. The intensity is approximately the same in the non-complexed and complexed state. The frequency increase on complexing was $\sim$ 35cm^{-1}. This band of E_2' (D_{7h}) symmetry in $C_7H_7BF_4$ is only Raman active and in C_{7v} symmetry this is also the case of this E_2 mode and no infra-red analogues were found at the IINS frequency. Unfortunately, no Raman bands were discovered either and complexation must have reduced the polarizability change of this in-plane mode. This may be reasonable since the fixing of the C_7H_7 entity by π-complexing would reduce the in-plane vibrational amplitudes somewhat if the complexing is quite strong.

The lower frequency C_7H_7 intramolecular modes in these $C_7H_7M(CO)_3^+$ compounds involve out-of-plane ring deformations. Now with the $C_7H_7^+$ salts these bands were of E_2'' and E_3'' symmetry and both were infra-red and Raman inactive and thus it was difficult to determine their individual symmetry even though the 238cm^{-1} band was observed in the infra-red spectrum of $C_7H_7BF_4$ and, possibly 216cm^{-1} in $C_7H_7PCl_6$. The symmetry of these respective normal modes, E_2'' and E_3'', is lowered to E_2 and E_3 in C_{7v} symmetry respectively and thus E_2 and E_3 are again still infra-red inactive though the former E_2 mode becomes Raman active. If there are Raman analogues of one of these bands in the $C_7H_7M(CO)_3^+$ complexes then the E_2 and E_3 symmetries in the C_{7v} complexes will be resolved and this will help assign the E_2'' and E_3'' species in D_{7h} symmetry. In all three Cr, Mo and W compounds there exists weak Raman bands at $\sim$ 250cm^{-1} analogous to weak IINS bands whereas the higher fre-

quency IINS bands at 370cm^{-1} did not have infra-red or Raman analogues. Perhaps, then this is an indication that the lower frequency band in $C_7H_7M(CO)_3^+$ has E_2 symmetry and in $C_7H_7^+$ has E_2'' symmetry whereas the higher frequency band in $C_7H_7M(CO)_3^+$ has E_3 symmetry and in $C_7H_7^+$ has E_3'' symmetry. Once again this argument is amenable to the analysis of Fately et al (12) on C_7H_7Br since they felt a band at 225cm^{-1} existed and that it had E_2'' symmetry. Sourisseau et al (21), it is felt incorrectly, assigned the E_2'' band at 335cm^{-1} in $C_7H_7PCl_6$ and the E_3'' band at 636cm^{-1}.

The BFDDIDO/PLUTO spectra show only one further feature that has not been assigned above 200cm^{-1}. In these $C_7H_7M(CO)_3^+$ species. There is a broad IINS band around 320cm^{-1}, which has a weaker component on its low frequency side. There are expected three high frequency skeletal modes of which two may be degenerate. They are tilt 1 (R_x) and tilt 2 (R_y) while the other is the symmetric stretch derived from the translation in the x axis.

The infra-red and Raman bands in this region are quite complex. On removal of the intra-molecular C_7H_7, BF_4^- and M-C stretching vibrations, there remains three Raman bands which are coincident with three infra-red bands. The lowest frequency Raman and infra-red band is quite intense whereas the two at higher frequency are of approximately the same frequency. The lowest frequency band is assigned to the symmetric stretch. This is reasonable since the metal-ring stretch is more intense in the infra-red and Raman spectra than the tilting motions. This greater intensity arises because it involves a larger dipole moment change and a larger polarizability change. The pairs of

bands at higher frequency may be due to the individual tilting modes which have been split due to either a site effect or to the C_s point group of the molecule. The splittings are small, shown in Table 6.8, and will not be seen in the IINS spectrum since the separation is not as large as the full width of half height (FWHH) of IINS bands at ~300cm^{-1}, using the (311) monochromator plane.

Table 6.8: Skeletal Vibrations in the IR/RAMAN Spectra of $C_7H_7M(CO)_3BF_4$ Complexes (cm^{-1})

	$C_7H_7Cr(CO)_3BF_4$		$C_7H_7Mo(CO)_3BF_4$		$C_7H_7W(CO)_3BF_4$	
	IR	R	IR	R	IR	R
Tilt	325(m)	316(sh)	328(m)	329(m)	333(m)	325(w)
	315(m)	310(w)	319(w)	323(w)	322(m)	320(sh)
Splitting	10	6	9	6	11	5
Stretch	304(m)	305(s)	307(s)	311(s)	295(s)	298(s)

The infra-red spectrum of $C_7H_7W(CO)_3BF_4$ is depicted in Figure 6.8 as an example of the splitting of the metal-ligand tilt and the greater intensity of the metal-ligand stretch. Further, it can be noted that the weak band at 350cm^{-1} is indicative of the BF_4^- E deformation mode, found in $C_7H_7BF_4$, whereas the E_2'' $C_7H_7^+$ intra-molecular vibration is noticeably absent at ~230cm^{-1}.

In the interpretation of the beryllium filter detector neutron spectra of compounds such as these, considerable insight was gained with the use of a du Pont 310 curve resolver.

Guassi n-shaped functions similar to IINS peaks were visually generated and superimposed on the spectrum being analysed. Their size, width and position controlled to produce differing combinations. Various conditions were taken into account, e.g. band centres from infra-red and Raman data and the resolution of the instrument at that frequency. The band centres in this study of tropyllium complexes were taken as the average of the infra-red and Raman data in Table 6.8 whereas the full width at half height, FWHH, was calculated to be not less than $35cm^{-1}$, using the 311 monochromator at $300cm^{-1}$. Table 6.9 indicates the data achieved from the fitting procedure using these parameters. Rough criteria for expected IINS peak intensities and the peak numbers in each case were used to reduce the fitting possibilities. In all cases, the general flat background level of the spectrum was taken as the baseline for the curve resolver. Clearly the method can be quite useful but not infallible. Close fits to the experimental spectra were obtained but should be treated with some reservation.

From this study it can be seen that the intensity of the doubly degenerate tilt is much greater (3-4 times) than that of the singly degenerate metal-ligand stretch.

Vibrations less than $200cm^{-1}$

The 4H5 spectra, collected at 140K, are used in conjunction with the infra-red and Raman data to characterise the low frequency vibrations of these tropyllium complexes. The 4H5 spectra are dominated by two strong bands at $60-80cm^{-1}$ and at $110-140cm^{-1}$. No assignments

Table 6.9: M-C_7H_7 Stretch and Tilt Data for $C_7H_7M(CO)_3BF_4$ Complexes

Skeletal Motion	Technique and IINS FWHH	$C_7H_7M(CO)_3BF_4$ Compound (cm^{-1})		
		M=Cr	M=Mo	M=W
Tilt	R/IR(av)	316	325	325
	IINS	314	325	326
	FWHH(cm^{-1})	47	48	50
Stretch	R/IR(av)	304	309	297
	IINS	298	294	299
	FWHH	35	35	40

have been carried out before on these vibrations. It would be expected that the two low frequency tropyllium-metal skeletal vibrations would be intense in the IINS system. The deformation would be expected to be seen in the infra-red and Raman spectra but the torsion would be unlikely due to the very small, if any, changes in dipole moment and polarizibility that would arise from such a vibration in these planar π-arene organometallics. The torsion takes place about the C_7 axis of the tropyllium ring and if the two rotors, CC_7H_7 and $M(CO)_2$), librate independently in this vibration in their external field and if the internal field is zero (27) then one would expect only to see the torsion of the C_7H_7 movement in the IINS spectrum because the scattering cross-section of the $M(CO)_3$ group would, in comparison, be very small. Since the deformation mode

is usually found at higher frequencies than the torsion, the band in the 110-140cm^{-1} region is assigned to the doubly degenerate deformation whereas the lower frequency peak is assigned to the torsion. The intensities are comparable. In the infra-red or Raman spectra, there are a number of vibrational bands non-coincident with the skeletal vibrations found in the IINS spectra. They are assigned to C-M-C deformations which have been similarly assigned to other tricarbonyl species. It is noteworthy that no other features, except lower than the torsional frequency, are depicted in the time-of-flight spectra. This is an indication that the C-M-C deformations are not mixing with the skeletal vibrations to any great extent in these $C_7H_7M(CO)_3^+$ species. If it had happened then weaker bands would have been found in the IINS spectra due to associated hydrogen motion. The 63cm^{-1} band may be due to this effect in $C_7H_7Mo(CO)_3^+$ as will the 66cm^{-1} shoulder in the chromium analogue. However, since these bands vary in frequency with scattering angle in the time-of-flight spectra, they are more likely to be due to lattice vibrations (intermolecular modes).

Calculation of torsional barriers

The barrier can be assumed to be of the form:

$$V = \frac{Vo}{2} (1-\cos N\theta)$$

and by making the harmonic oscillator approximation, the calculation of the effective force constant $(\frac{N^2V_B}{2})$ can be calculated from $(\frac{N^2V_B}{2}) = \frac{4\pi^2 I_R \bar{\nu}^2 c}{h}$ where N = barrier multiplicity and I_R = moment of inertia of the (C_7H_7) group (assuming the barrier to rotation is external.

Using the crystal structure of $C_7H_7Mo(CO)_3BF_4$ (14), the moment of inertia can be calculated to be 446.95 x $10^{-40}gcm^2$. Thus the effective force constant and the barrier to torsion, V_B, can be calculated. The barrier multiplicity is not known but can be reasonably estimated to be 7. The moment of inertia of the (C_7H_7) ring in the molybdenum compound is used in conjunction with the chromium and tungsten analogues. Table 6.10 lists the results. These calculated values are discussed in more detail on page 343.

Table 6.10: Calculated EFC and Torsional Barriers of the $C_7H_7M(CO)_3BF_4$ Complexes

Compound	(cm^{-1}) Torsional Frequency	($kJmol^{-1}$) Effective force constant (EFC)	($kJmol^{-1}$) Torsional barrier
$C_7H_7Cr(CO)_3BF_4$	75	537	21.9
$C_7H_7Mo(CO)_3BF_4$	75	537	21.9
$C_7H_7W(CO)_3BF_4$	76	552	22.5

6.6. $C_7H_7Mo(CO)_2I$

No previous vibrational studies have been carried out on this type of tropyllium complex.

6.6.1. Results

Table 6.11 summarises the IINS and infra-red data collected for the compound. Raman data was not achieved because of the purple-black colour of the complex. Figure 6.16 summarises the 4H5 spectra, at 133K, gathered at scattering angles of 90° and 82°. Figure 6.17 depicts the BFDDIDO spectrum, at liquid nitrogen temperature.

Table 6.11: Frequencies and Spectral Assignments of $C_7H_7Mo(CO)_2I$

4H5 (133K)	BFDDIDO (77K)	IR (77K)	FIR (77K)	Assignment
		792(vs)		A_1: o/p CH def.
520(s)	554(s)	553(s)		E_3: o/p CH def.
		511(m)		M-C-O def.
		496(vs)		M-C stretch
460(m)	475(m)	467(w)		E_2: in-plane ring def.
		418(vs)		M-C stretch
	391(m)			E_3: o/p ring def.
			333(w)	Tilt 2
340(vs)	344(s)	330(w)	330(m)	
			293(m)	Tilt 1
290(vs)	295(vs)	287(m)	286(vs)	Mo-C_7H_7 symmetric stretch
	215(w)			E_2: o/p ring def.
			169(s)	Mo-I stretch
			166(sh)	
162(m)	177(w)			2 x torsion or/ Mo-I stretch
			139(wb)	C-Mo-C def.
118(s)	114(m)		120(m)	Mo-C_7H_7 def.
			112(m)	"
71(s)	70(m)			Torsion
			52(w)	Lattice modes
40(m)				

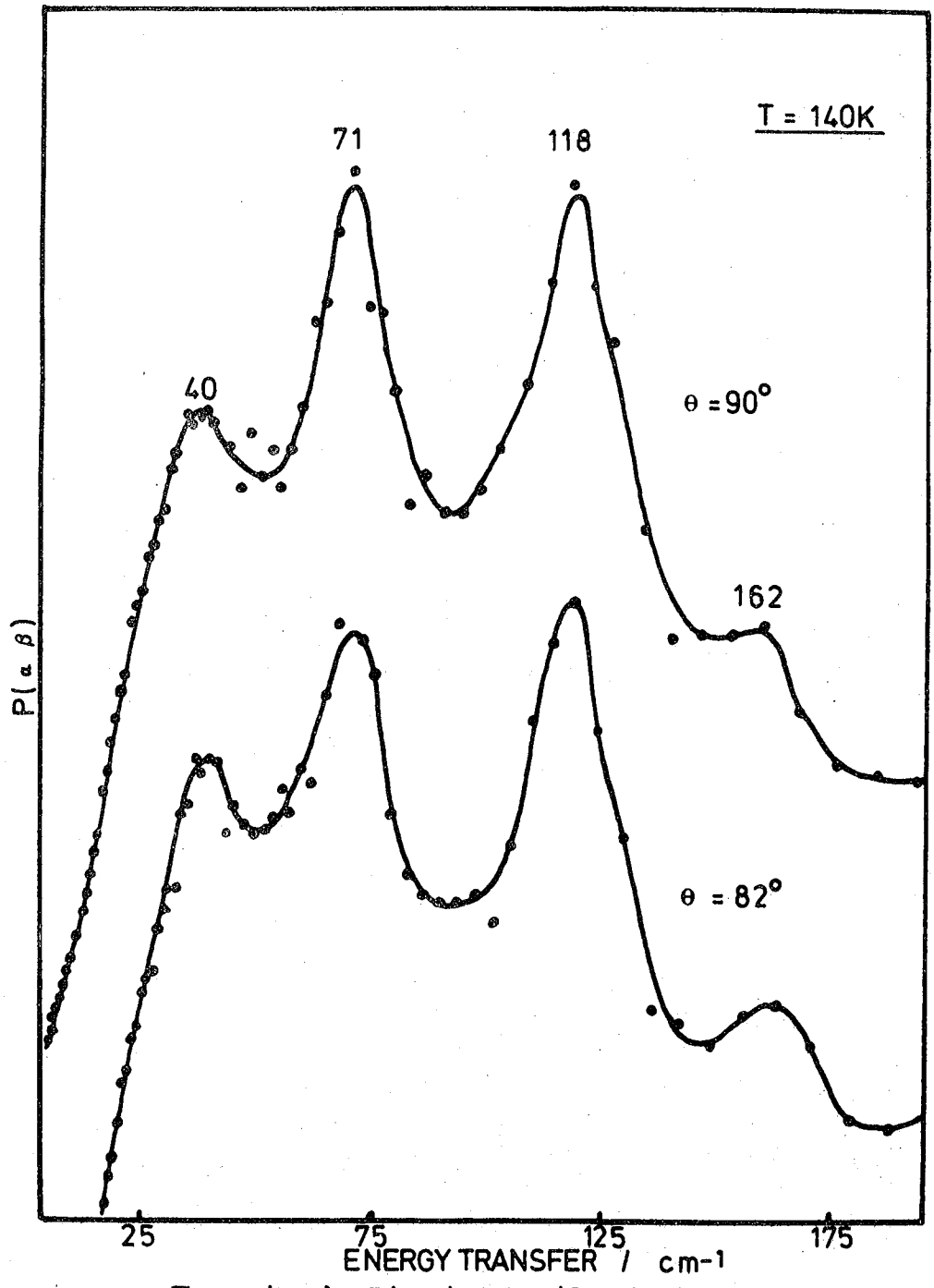

Figure (6.16) P(α β) data $(C_7H_7)Mo(CO)_2I$

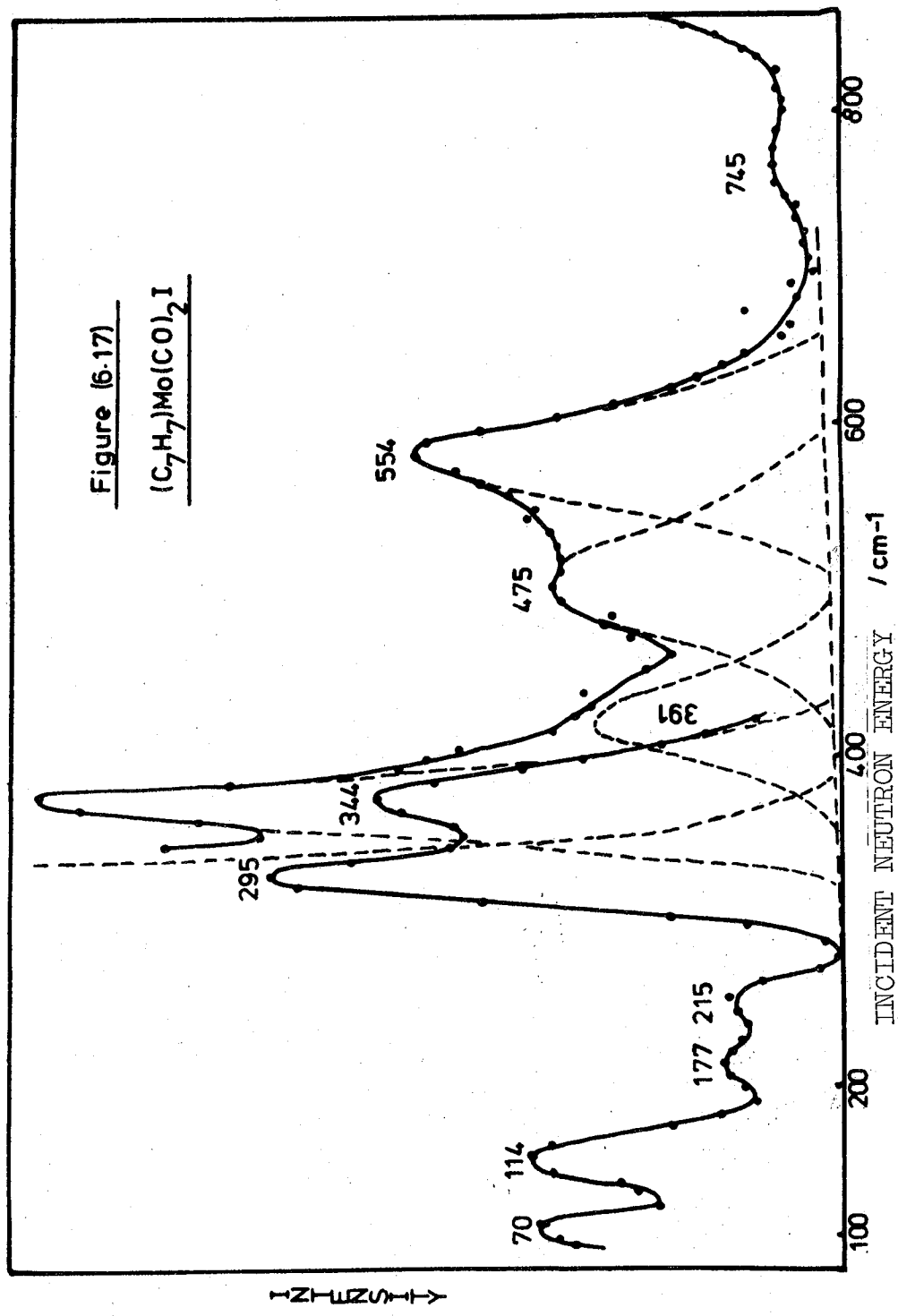
Figure (6.17)
$(C_7H_7)Mo(CO)_2I$
554
475
391
344
295
745
177 215
114
70
100
200
400
600
800
INCIDENT NEUTRON ENERGY / cm-1
INTENSITY

6.6.2. Discussion

In $C_7H_7Mo(CO)_2I$, one carbonyl group of the $C_7H_7Mo(CO)_3^+$ ion has been replaced by the iodine atom. This has produced electrical neutrality. This study is carried out to observe whether any perturbation of the molecule, caused by the iodine atom, has caused splitting of the doubly degenerate bands and, especially the effect on the skeletal motions.

The vibrations may be separated into the following groups:-

i) Mo - I stretch
ii) $Mo(CO_2)$ vibrations
iii) (C_7H_7)-Mo-$(CO)_2I$ skeletal vibrations
iv) C_7H_7 internal vibrations

Analysis of the vibrations of $C_7H_7Mo(CO)_2I$, which has only C_s symmetry, is shown in Table 6.12. However, it is expected that the intramolecular vibrations of the tropyllium ring will be described in terms of C_{7v} symmetry, as in the BF_4^- salts.

Table 6.12: C_s Vibrational Analysis

C_s	$C_7H_7Mo(CO)_2I$	$Mo(CO)_2I$	C_7H_7	C_7H_7-M skeletal vibrations	Activity
A'	29	7	19	3	IR/R
A''	25	5	17	3	IR/R

The Mo-I stretch is expected in the 100-200cm^{-1} region and to be quite intense in the infra-red since Clark and Crosse found such a band, in $Mo(CO)_5I$, at 146cm^{-1} (28). There are a number of infra-red bands in $(C_7H_7)Mo(CO)_2I$ in this

region. The most intense are at 112/120cm^{-1} and at 169cm^{-1}. Much weaker features lie at ~139cm^{-1} and 208cm^{-1}. The latter is assigned to the lowest frequency out-of-plane deformation of tropyllium. The bands at 112 and 120cm^{-1} can be assigned to a skeletal vibration (see later). From intensity reasons the infra-red band at 169cm^{-1} is assigned to the Mo-I stretch whereas the very weak feature at 139cm^{-1} may be due to a deformation of the Mo-$(CO)_3$ system. Some splitting of the 169cm^{-1} band is found at liquid nitrogen temperature, since a shoulder appears at ~166cm^{-1}. There is a band at 162cm^{-1} in the 4H5 spectrum and this may either be a second harmonic of the strong band at 71cm^{-1}, though this is not favoured, or it may be due to the Mo-I stretch. Although formally not involving any hydrogen motion, since it involves the heavy iodine atom, the motion could modify the electron density of the molecule so that the Mo-ring distance also changes and thus in the IINS spectrum the band at 162cm^{-1} (177cm^{-1} in the BFDDIDO spectrum) is due to associated hydrogen motion.

The metal-carbonyl vibrations, Mo-C stretches and Mo-C-O deformations are likely to fall in the same regions as the tricarbonyl complexes and are strongly infra-red active but formally not active in the IINS spectrum. However, it can be noted that weak IINS bands were found in the 300-600cm^{-1} region of the transition metal hydridocarbonyls (Chapter 5) and were assigned to these vibrations due to associated hydrogen motion similar to the Mo-I stretch above. Due to the broad bands in the IINS spectrum, Figure 6.17, no weak features similar to those in Chapter 5

were observed. Accordingly, the infra-red bands at 418, 496 and 511cm^{-1}, which did not have IINS counterparts, were assigned to metal-carbon stretches and metal-carbonyl deformation modes.

The assignment of the tropyllium intra-molecular modes is carried out in the same manner as those in the BF_4^- complexes. No anomalies were found and Table 6.13 summarises the data from $C_7H_7BF_4$, $C_7H_7Mo(CO)_3BF_4$ and $C_7H_7Mo(CO)_2I$. The symmetry is described in terms of C_{7v} symmetry.

One point to note is that the E_3'' (D_{7h}) CH out-of-plane deformation, which is infra-red inactive is D_{7h} symmetry, and should be also infra-red inactive in C_{7v} symmetry, lies at 554cm^{-1}. A coincident strong infra-red band exists at 553cm^{-1}. This will surely be a coincidence and the infra-red band must be due to a carbonyl deformation mode and not due to the infra-red inactive $E_3(C_{7v})$ vibration, though some of the intensity may be due to this vibration because of a solid state effect. If the E_3 mode at 554cm^{-1} had been infra-red active, the other E_3 mode at 391cm^{-1} in the IINS spectrum would probably have had an infra-red counterpart. This was not the case .

As expected little change has been found between the complexes. It may be of interest to note the slightly lower A_1CH out-of-plane frequency in $C_7H_7Mo(CO)_2I$ compared with $C_7H_7Mo(CO)_3BF_4$. Studies of this vibrational band in other ring systems have implied that as the frequency shift increases from that found in the noncomplexed state (i.e. in $C_7H_7BF_4$) then the strength of the ring-metal bond

Table 6.13: C_7H_7 Intramolecular Vibrational Assignments

$C_7H_7BF_4$	$C_7H_7Mo(CO)_3BF_4$	$C_7H_7Mo(CO)_2I$	Assignment
685	806	792	A_1 CH o/plane def.
562	561	554	E_3 CH o/plane def.
440	471	475	E_2 i/plane ring def.
335	378	391	E_3 o/plane ring def.
238	217	215	E_2 o/plane ring def.

increases. If this is so in this case then perhaps the Mo-C(C_7H_7) distance would be lower in $C_7H_7Mo(CO)_2I$. However, no difference between the two systems was found.

	Mo-C(C_7H_7) distance (Å)	
$C_7H_7Mo(CO)_3BF_4$	2.28 - 2.34	(14)
$C_7H_7Mo(CO)_2Br$, Cl	2.31 ± 0.06	(15)

Unfortunately, no Raman data was available, but again, infra-red bands were not found at 391 and 215cm^{-1} where IINS bands were observed indicative of the low frequency out-of-plane ring deformations. Thus, the intramolecular tropyllium bands appear to be described in C_{7v} symmetry in the same manner as the tetrafluoroborate complexes.

Finally, the skeletal vibrations can be assigned. It is seen that the IINS spectrum in the 300cm^{-1} region is very different from the $(C_7H_7)M(CO)_3BF_4$ species. This must be due directly or indirectly to the replacement of

the carbonyl group with the iodine atom. The BFDDIDO spectrum is dominated by the two bands at 295 and 344cm^{-1} of which the 295cm^{-1} band is the more intense. This could be an indication that the tilt, a doubly degenerate band, has been split quite drastically. Figure 6.18 shows how possibly these motions became split. The rotation about the y axis is relatively similar to that found in the $M(CO)_3$ situation but in the x axis the motion is hindered by the large heavy iodine atom. This alternative involves a direct iodine/ring interaction.

Another alternative, which is more possible since the iodine/tropyllium interaction is only tentative, is that in $C_7H_7Mo(CO)_2I$ the molybdenum atom lies well off the C_7H_7 C_7-axis, as shown in figure 6.19. This is not the case in $C_7H_7Mo(CO)_3BF_4$ where the molybdenum lies virtually on the C_7 axis. The actual molybdenum -(C_7) axis distance in the iodine complex is ~ 0.4Å calculated from the diagram in reference (15). This asymmetry will certainly bring about such a splitting of the tilts. The cause of the asymmetry was probably the iodine atom so that in this case the iodine only indirectly causes the loss of degeneracy.

The strongest infra-red band, in figure 6.8, is expected to be due to the symmetric metal-ring stretch and a very strong band was observed at 286cm^{-1} whereas two medium intense features exist at 293cm^{-1}, as a shoulder, and at 330cm^{-1}. This latter band has been split slightly. The 286cm^{-1} infra-red band is assigned to the Mo-C_7H_7 symmetric stretch and the two bonds at 293 and 330cm^{-1} are assigned to the singly degenerate tilting motions. Therefore, the strongest IINS band at 295cm^{-1} is assigned to the

Figure (6.18)

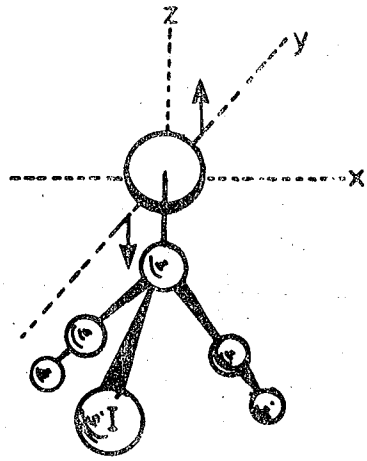

Rotation about x axis hindered by iodine - tilt 1

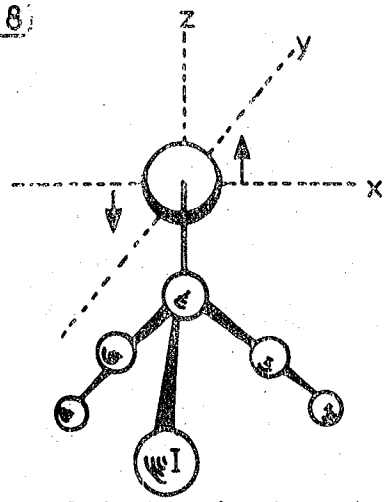

Rotation about y axis not hindered to same extent by iodine - tilt 2

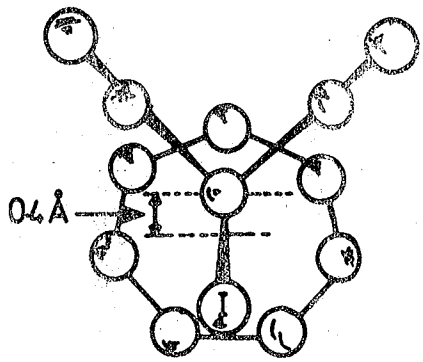

Figure (6.19)
Molybdenum asymmetry in $[C_7H_7]Mo(CO)_2I$

symmetric stretch and to one of the tilts whereas the less intense band at 344cm^{-1} is assigned to the other tilt.

Vibrations less than 200cm^{-1}

The IINS spectrum in figure 6.16 is dominated by three bands of 40, 71 and 118cm^{-1} with a weaker shoulder at 162cm^{-1} which has already been assigned. The band at 40cm^{-1} is expected to be a lattice mode and varies in frequency with scattering angle, though at 82° and 90° the frequencies are the same.

The strong IINS bands at 71 and 118cm^{-1} are assigned to the torsion and deformation bands. The relative intensities are approximately the same, as found in the BF_4^- complexes. These assignments are resonable since the torsion is usually at lower frequency than the deformation. Further, it would be expected that the torsion of this planar π-arene ring about the central axis would not be seen in the infra-red spectrum since there would be a negligible change in the magnitude of the dipole moment, even though, in a C_s symmetrical molecule, the torsion would be formally active, being of A' symmetry. This would contrast with the (C_7H_7)-Mo-$(CO)_2$I deformation which would be formally infra-red active and should produce a relatively larger dipole moment change and thus produce an observable infra-red band. There are two infra-red bands at 112cm^{-1} and 120cm^{-1}, which are assigned to the doubly degenerate deformation which has been split. This would have occured due to the same effect that split the tilt mode. The asymmetry of the molybdenum is preferred to the iodine/

ring interaction. The two medium intense bands at 112 and 120cm^{-1} are indicative of the loss in degeneracy, which has produced differing vibrations, due to the translation of the ring in the x and y directions. Since the resolution of the IINS experiment is not as good as that in the infra-red, the splitting of only 8cm^{-1} would not have been resolved. The splitting of the tilt, however, was observed because it amounts to 37cm^{-1}.

The assignment of the torsion to the 70cm^{-1} IINS band can lead to an estimate of the effective force constant, $(\frac{N^2V_B}{2})$. Using the atomic co-ordinates of the (C_7H_7) ring in the analogous Br compound (15), the moment of inertia of the (C_7H_7) ring in the $(C_7H_7)Mo(CO)_2I$ can be evaluated. This produces an effective force constant (E F C) of 474.8kJmol^{-1}. This can be compared with the E F C of the $C_7H_7Mo(CO)_3BF_4$ salt which was 552kJmol^{-1}. The smaller value in $C_7H_7Mo\ CO)_2I$ would seem to indicate a weaker interaction and must be contrary to the model of an iodine/ ring interaction which would have produced an increase in the E F C. From the crystal structure, it would be reasonable to estimate N, the multiplicity, to be 7 and thus the barrier to rotation, V_B, would be 19.4kJmol^{-1}

A number of E.F.C. values and torsional barriers have now been calculated using inelastic neutron scattering data. Table 6.14 presents a relevant selection of calculated values on C_nH_nM species acquired from this study and from others.

As it can be seen in this study of C_nH_n complexes, as n increasesfrom 4 to 7, the effective force constants

Table 6.14: Comparison of Torsional Data for some C_nH_n-M Species

Compound/ System	Torsional Frequency (cm^{-1})	EFC ($kJmol^{-1}$)	Multi-plicity	Torsional Barrier (V_B)	Ref.
$C_4H_4Fe(CO)_3$	60	87.8	4	11.0	(29)
$(C_5H_5)_2Fe$	50	172	5	13.8	"
$NiHg_2(SCN)_6C_6H_6$	63	250	6	13.9	This work
$C_6H_6Co_4(CO)_9$	75	273	6	15.1	"
C_6H_6 + Pt black	121	922	6	51.2	"
$C_7H_7Cr(CO)_3BF_4$	75	537	7	21.9	"
$C_7H_7Mo(CO)_3BF_4$	75	537	7	21.9	"
$C_7H_7W(CO)_3BF_4$	76	552	7	22.4	"
$C_7H_7Mo(CO)_2I$	71	475	7	19.4	"

and the torsional barriers generally increase. This, however, would appear to be independent of actual torsional frequency. Even though there would seem to be a trend, there are a number of points which would refute any further worthwhile comparisons. The multiplicity in each case is taken as equal to the number of protons per arene ring. This will not always be so since in $C_6H_6M(CO)_3$ species, for example, the actual multiplicity may be equal to three due to the three carbonyl ligands. Thus the barrier to rotation would change drastically in this case with N=3 compared to N=6. Also in the three benzene systems, it can be seen that the Pt black/benzene system is very much different from the two complexes. This shows that the ligand-metal

interaction can vary so much, due to many system parameters that any further general comparisons cannot be made.

6.7. $(C_7H_7)_2TaCl_3$

6.7.1. Previous Results

Sharma et al (7) listed the infra-red absorptions of the compound, in nujol, at room temperature and only found one weak band, below 1000cm^{-1}, at 720cm^{-1}. In the present infra-red study, in a KBr disc, at liquid nitrogen temperature, there is a dominating band centred at ~720cm^{-1} with maxima at 820, 770, 687 and 635cm^{-1}.

6.7.2. Results

Table 6.15 shows the spectral results for the compound with assignments. Figures 6.20, 6.21 depict the 4H5 and BFDDIDO IINS spectra collected at 130K and liquid nitrogen temperature respectively. Figure 6.20 shows a plot of the frequency distribution function plotted against energy transfer. The Raman data was collected at room temperature with a laser power of 7mW.

6.7.3. Discussion

This sandwich compound can be estimated to have C_{2v} symmetry if it has the form shown in Figure 6.4. With C_{2v} symmetry the vibrations of the unit are listed in Table 6.16

The $(C_7H_7)_2TaCl_3$ skeletal vibrations have $2A_1+2A_2+4B_1+4B_2$ symmetry. Whether or not they are totally non-degenerate (e.g. the symmetric tilts are split) is a matter of conjecture in this compound.

Table 6.15: Vibrational Features and Assignments of $(C_7H_7)_2TaCl_3$

4H5 (130K)	BFDDIDO (77K)	IR (77K)	FIR (77K)	RAMAN (RT)	Assignment
		820(vs)		820(wm)	A_1: o/p CH Def.
	774(w)	770(vs)			$TaCl_3$ vib. with slight H motion
	717(msh)				Combination (297+407=704cm^{-1})
		687(s)			
	656(s)	655(w)		670(mb)	Antisymmetric tilt
		635(s)		625(wb)	
	554(ms)			530(wb)	E_3: o/p CH def.
420(mb)	447(s)	440(w)		460(wb)	E_2: in-plane ring def.
	443(w)				(2x221cm^{-1}) Second harmonic
	407(msh)			385(w)	Symmetric tilt
	297(m)	306(vvs)	300(sb)	312(wm)	Antisymmetric stretch
220(ms)	221(vs)			210(wb)	Symmetric stretch
			160(sb)		$TaCl_3$ vibration
111(m)	109(sh)		100(vw)		Deformation
68(s)	75(s)			60(w)	o/p torsion
40(m)					in phase torsion

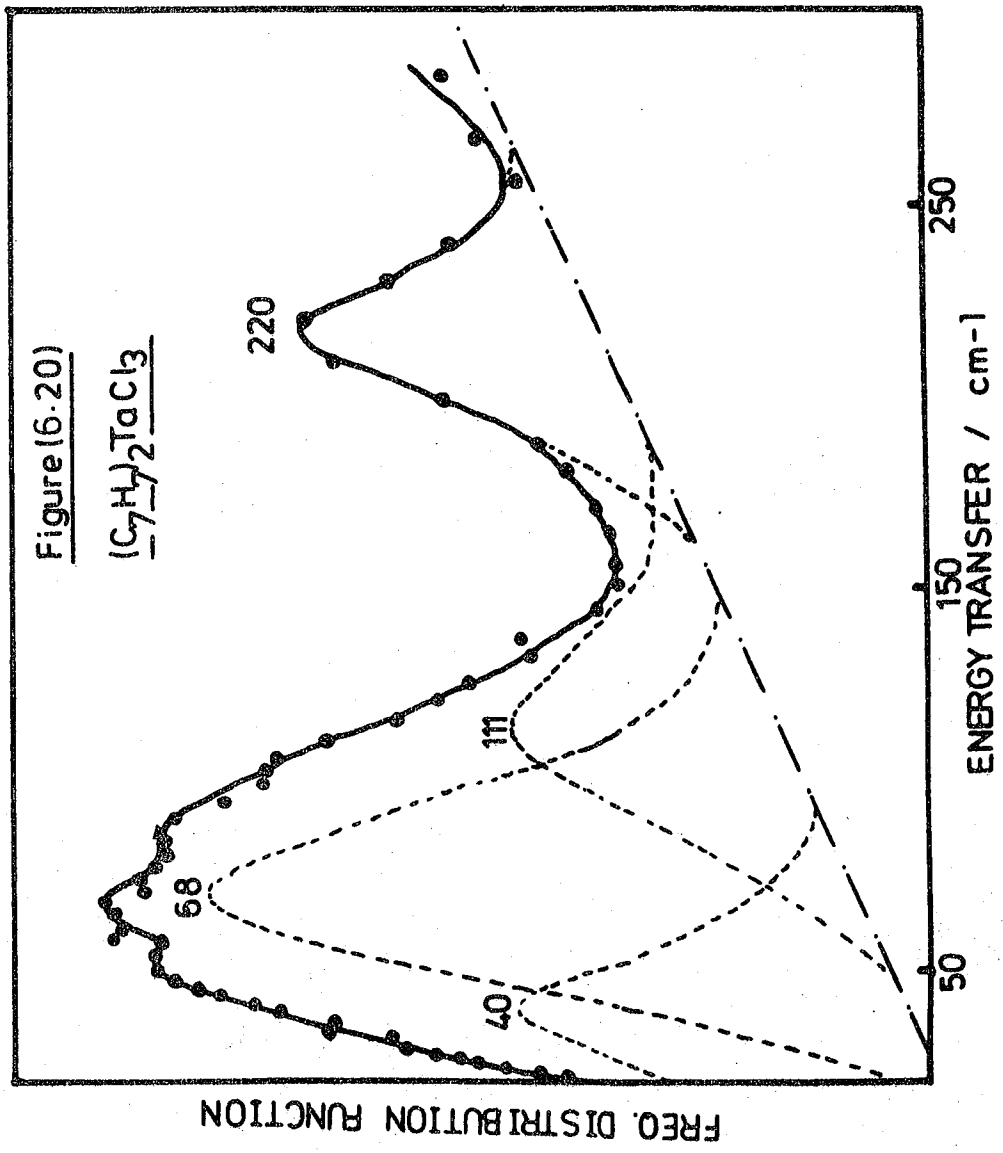
Figure (6.20)
$(C_7H_7)_2TaCl_3$
220
111
68
40
50
150
250
ENERGY TRANSFER / cm-1
FREQ. DISTRIBUTION FUNCTION

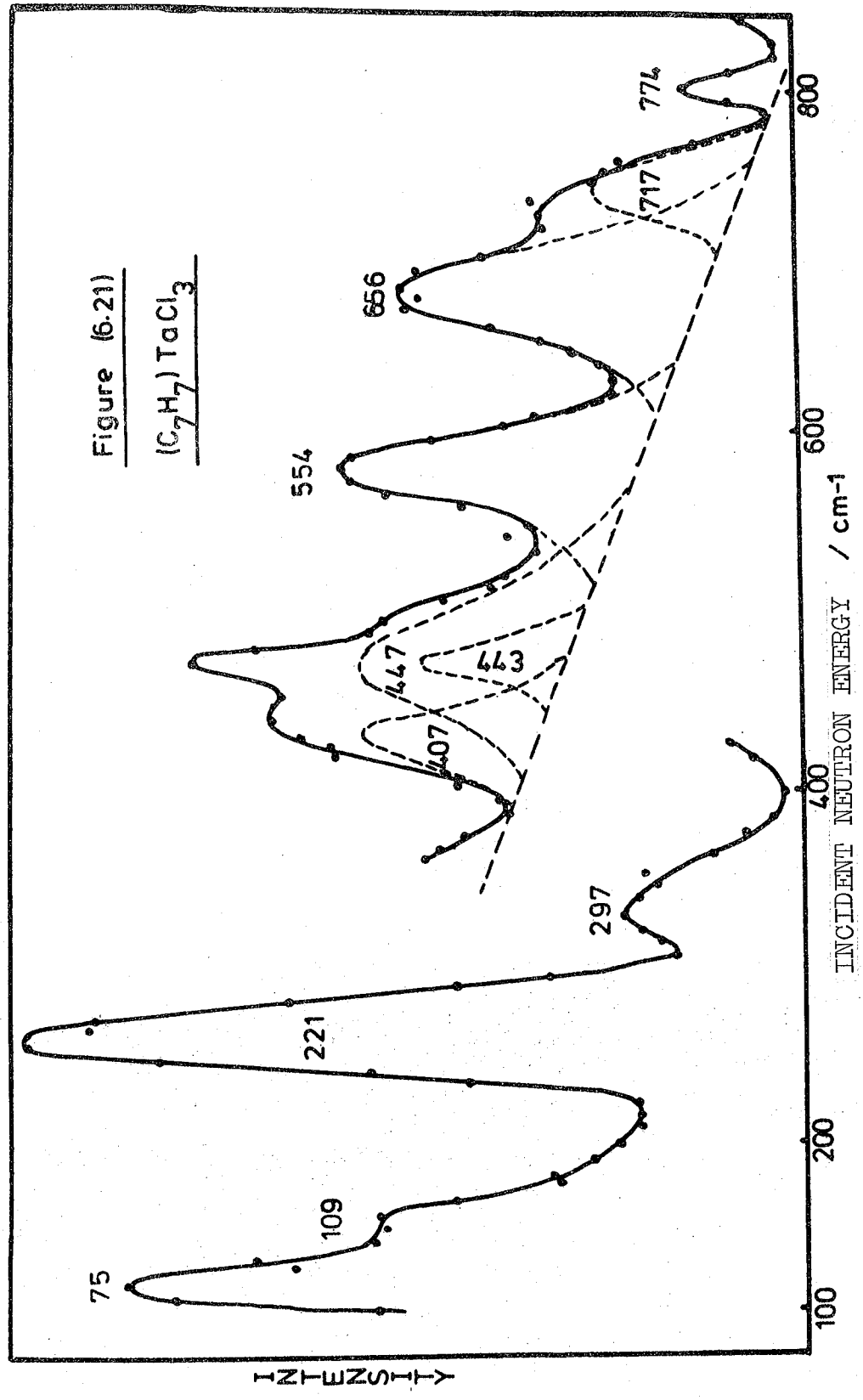
Figure (6.21)
$(C_7H_7)TaCl_3$
INTENSITY
INCIDENT NEUTRON ENERGY / cm-1
100
200
400
600
800
75
109
221
297
407
447
443
554
656
717
774

Table 6.16: C_{2v} Vibrational Analysis

C_{2v}	$TaCl_3(C_7H_7)_2$	$TaCl_3$	C_7H_7	C_7H_7	Skeletal normal modes	Activity
A_1	25	3	10	10	2	IR/R
A_2	20	-	9	9	2	-/R
B_1	23	1	9	9	4	IR/R
B_2	22	2	8	8	4	IR/R

Table 6.17 indicates the symmetry of the skeletal motions that should be found in the IINS spectrum and their relative infra-red and Raman activity. Some splitting of the E modes, that would be found a symmetric dibenzene chromium-type sandwich, may take place due to the angular form of the tropyllium ligands.

Table 6.17: Skeletal Vibration Activity in $(C_7H_7)_2TaCl_3$ With C_{2v} Symmetry

Framework Vibration	Symmetry (C_{2v}) and Activity	
Torsion (in-phase)	B_1	IR/R
Torsion (out-of-p ase)	A_2	R
Symmetric stretch	A_1	IR/R
Antisymmetric stretch	B_2	IR/R
Deformation	B_1+B_2	IR/R
Antisymmetric tilt	A_2+B_2	IR(B_2 only) /R
Symmetric tilt	A_1+B_1	IR/R

Vibrations less than 200cm^{-1}

The 4H5 frequency distribution spectrum is dominated by two broad bands at ~220cm^{-1} and ~70cm^{-1}. Using the curve resolver rather tentatively in this very poorly resolved latter region, it is possible to separate out these low frequency components at 40, 68 and 111cm^{-1}. Now the infra-red spectrum shows only two features below 200cm^{-1} at 100(w)cm^{-1} and 160(sb)cm^{-1}. In $TaCl_5$, at 100K. there have been observed a number of bands, assigned to in-plane deformation modes, of medium-strong intensity in the IR at 144 and 169cm^{-1} (30). The authors felt the assignments were tentative. However, since there was no IINS analogue of the strong 160cm^{-1} infra-red band in $(C_7H_7)_2TaCl_3$, then it is felt that one can conclude that the 160cm^{-1} infra-red band is due to a $TaCl_3$ deformation mode.

The torsions and the deformation skeletal modes are expected to be at a low frequency. The latter deformation bands have B symmetry and are, thus, infra-red and Raman active. The weak infra-red band at 100cm^{-1} is assigned to this framework vibration. Following from this assignment, the band at 111cm^{-1} in the neutron spectrum can be likewise assigned. (In the fitting of the curves, the bands at 111 and 68cm^{-1} were originally centred at the beryllium filter detector frequencies of 109 and 75cm^{-1}). The out-of-plane torsional band has A_2 symmetry and therefore is not infra-red active. This band would involve a negligible dipole moment change and would probably not be observed, even if it was active in the infra-red spectrum. The in-phase torsion is formally infra-red active but

again it may not be observed. There is a weak Raman band at 60cm^{-1} in $(C_7H_7)_2TaCl_3$ but this may be lattice mode. Since the in-phase torsion is usually found at a lower frequency than the out-of-phase torsion then the two medium-strong IINS bands at 40 and 68cm^{-1} may be assigned to these particular skeletal modes. Both are quite intense in the IINS spectrum due to the large hydrogen vibrational amplitudes involved.

The 4H5 resolution is very poor so that these conclusions are made with some reservations especially since a number of curve fits may be produced. One worthwhile experiment would be to run this compound on the Grenoble IN4 time-of-flight instrument. The much better resolution of IN4 cannot be disputed.

Vibrations greater than 200cm^{-1}

Above 200cm^{-1} the intramolecular tropyllium vibrations can be assigned initially. At 820cm^{-1} the strong infra-red and weak-medium Raman bands are assigned to the out-of-plane CH deformation which has moved up in frequency from 685cm^{-1} found in the $C_7H_7^+$ salts on complexing. This increase compares well with the increase found in other (C_7H_7) complexes as shown in Table 6.18.

The other tropyllium intramolecular vibrations are assigned by comparison with the other C_7H_7 complexes. At 554cm^{-1}, the E_3 out-of-plane CH deformation is found with only a slight decrease in frequency on complexing. This trend was found in all the other π-C_7H_7 complexes. Similarly assigned is the in-plane ring deformation at 447cm^{-1}. The expected weakly IINS active E_2 out-of-plane

Table 6.16: Increase in $A_1(C_{7v})$CH Out-of-Plane Deformation in Tropyllium Complexes

Compound	Increase in CH out-of-plane deformation (A_1)
$C_7H_7Cr(CO)_3BF_4$	+129
$C_7H_7Mo(CO)_3BF_4$	+121
$C_7H_7W(CO)_3BF_4$	+126
$C_7H_7Mo(CO)_2I$	+113
$C_7H_7)_2TaCl_3$	+135

ring deformation, at ~220cm^{-1} in the other complexes, was not observed because of a strong IINS band at 221cm^{-1}, which must be a skeletal mode with a large hydrogen vibrational amplitude. It may be noted that no splitting of the intramolecular tropyllium vibrations could be found in the infra-red. This could have arisen due to a $(C_7H_7)\cdots(C_7H_7)$ ring interaction. However, such splitting of the infra-red bands, at low temperature was also found in the $C_7H_7^+$ salts, such as $C_7H_7PCl_6$(21).

There are four types of skeletal framework vibrations that occur above 200cm^{-1}. They involve the motions, described in Figure 6.22, as the antisymmetric tilt and stretches and the symmetric tilt and stretches. The tilt modes could be split if the vibrations are formally described under C_{2v} symmetry. The splitting, if it takes place, will not be observed in the infra-red for the antisymmetric tilt since one component is infra-red

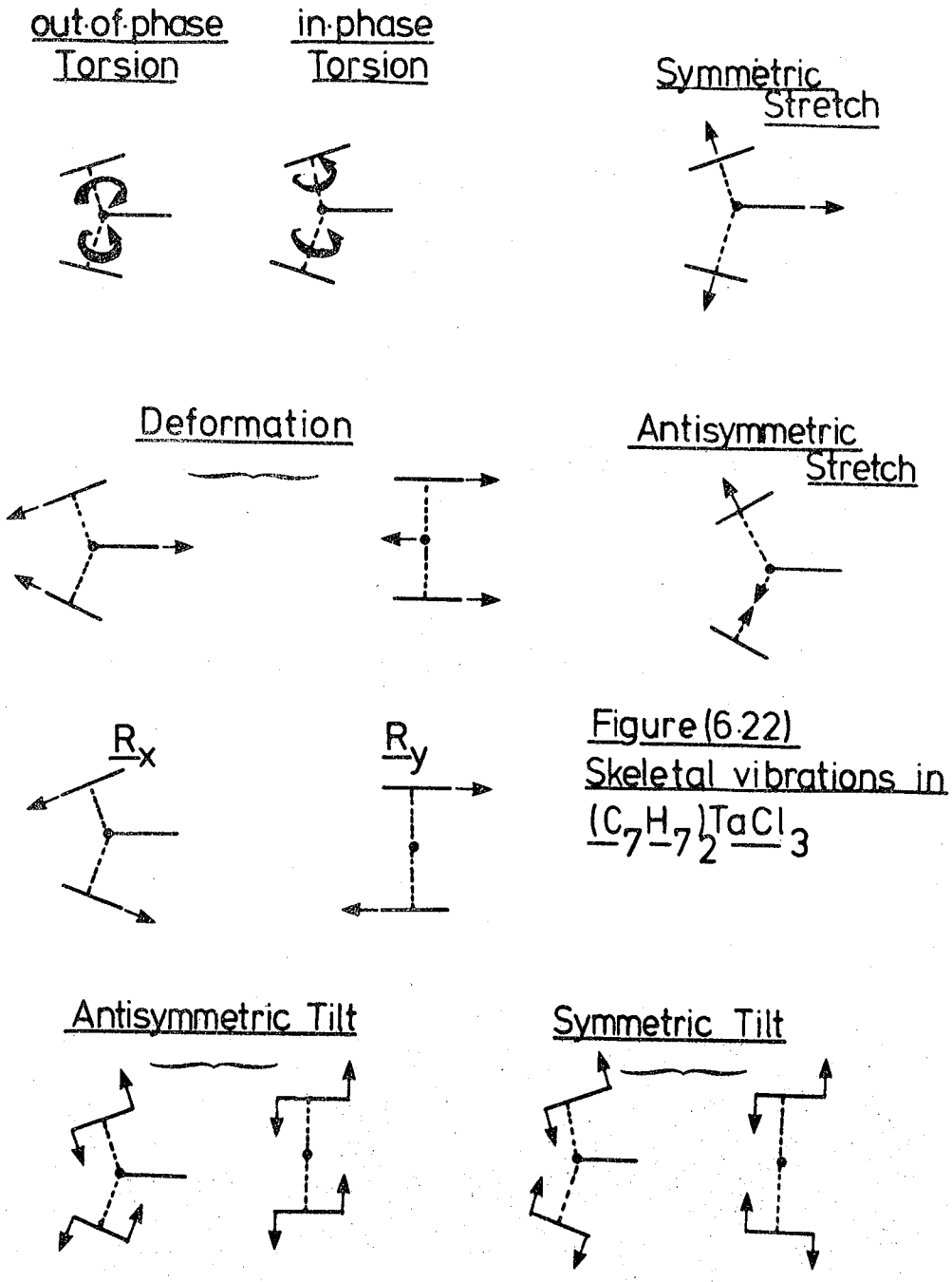

Figure (6.22)
Skeletal vibrations in $(C_7H_7)_2TaCl_3$

inactive (the A_2 mode). The order in which the frequencies of these vibrations occur is of interest since in $(C_6H_6)_2M$ species, the antisymmetric tilt has been reported at highest frequency, the antisymmetric stretch lies next and then at lower frequency comes the symmetric tilt and, finally, the symmetric stretch (31). In $(C_8H_8)_2M$ species the assignment of the antisymmetric stretch and symmetric tilt have been reversed (31). It must be noted that these studies were carried out on symmetric sandwich bis-arene complexes.

There are IINS bands, in Figure 6.21, which have yet to be assigned to particular vibrations at 656, 407, 297 and 221cm^{-1}. They have very strong to medium intensity. Only the 297 and 656cm^{-1} bands have strong infra-red analogues. This is entirely reasonable since the antisymmetric modes are more likely to be seen in the infra-red rather than the symmetric modes. For example, the stretch will involve little change in dipole moment if the individual $C_7(C_7H_7)$ axis are nearly coincident. A similar lack of dipole moment change will ensue in the symmetric ring tilt. Thus, from the infra-red activity of these bands the assignments can be made as summarised in Table 6.19

In $(C_7H_7)_2TaCl_3$ there are Raman bands at 210, 312, 385 and 670cm^{-1}. All the skeletal bands are Raman active though the symmetric stretch and tilt theoretically should be more intense. However, all the bands had weak-medium intensity.

An indication of the large hydrogen atom vibrational amplitude engaged in the symmetric stretch, found at 221cm^{-1}

Table 6.19: Comparison of Tilt and Stretch Assignments in Sandwich Compounds

	IINS Band	IR Band	Typical $(C_8H_8)_2M(31)$ Species	Typical $(C_6H_6)_2M(31)$ Species
Antisymmetric tilt	656(s)	687(s) 655(w) 635(s)	~ 690	~ 480
Symmetric tilt	407(msh)	-	~ 390	~ 300
Antisymmetric Stretch	297(m)	300(sb)	~ 250	~ 420
Symmetric stretch	221(vs)	-	~ 225	~ 280

in the IINS spectrum, can be found by comparing the band with its analogue in $C_nH_nM(CO)_3$-type complexes. In the bis-arene, the IINS intensity is large but negligible infra-red activity is found. Contrary to this in $C_nH_nM(CO)_3$ complexes, the M-C_nH_n stretch has weak-medium IINS intensity but strong infra-red activity, due to a large dipole moment change.

The order of the skeletal vibrations with increasing frequency can be compared with the $(C_6H_6)_2M$ and $(C_8H_8)_2M$ assignments (31). The order depicted in Table 6.19 parallels that found in the C_8H_8 complexes rather than the C_6H_6 sandwich compounds.

The other weaker IINS spectral features may be tentatively assigned. The 443cm^{-1} band is probably the second harmonic of the very strong 221cm^{-1} symmetric

stretch. The 774cm^{-1} band could be a $TaCl_3$ vibration, involving some associated hydrogen motion, and the 717cm^{-1} band may be a combination of the symmetric tilt and the antisymmetric stretch (297 + 407 = 704cm^{-1}).

The torsional barriers can be estimated for this compound which probably contains two indentical rotors. The potential energy variation on rotation can be described in terms of the external and internal fields (32).

External field: $V_i = \frac{V}{2}(1-\cos N'\theta_i)$ i = 1 or 2

Internal field: $V = \frac{V_I}{2}(1-\cos N''(\theta_1 + \theta_2))$

Thus $\omega_1^2 = \frac{N^2V_E + 2N^2V_I}{2I_R}$ and $\omega_2^2 = \frac{N'^2V_E}{2I_R}$

One can evaluate $N''V_I$ and N'^2V_E from

$\omega_1^2 - \omega_2^2 = \frac{V_I N''^2}{I_R}$ where ω_1 = out-of-phase torsion = 68cm^{-1}

and ω_2 = in-phase torsion = 40cm^{-1}

The value of I_R, the moment of inertia, is taken as an average of the value calculated from the atomic co-ordinates of other (C_7H_7) complexes. (444 x 10^{-40}gcm^2). Thus the value of the effective force constant due to the external field, N'^2V_E, has a value of 170kJmol^{-1} whereas the effective force constant due to the internal field is calculated to be 161kJmol^{-1}. The two force constants are therefore similar. They are quite small compared to the other tropyllium complexes and this may be an indication why no splitting of the intramolecular tropyllium vibrations was found in the infra-red spectrum due to a tropyllium-tropyllium interaction.

6.8. Conclusion

The assignments from the IINS study of $C_7H_7BF_4$ agree with those of Fately et al (12) rather than Sourisseau et al (21) for the $C_7H_7^+$ intramolecular modes. This is the case especially in the assignment of an out-of-plane ring deformation at very low frequency ($238cm^{-1}$ in $C_7H_7BF_4$).

In the study of $C_7H_7M(CO)_3^+$ complexes, the C_7H_7-M skeletal tilts and stretches were observed at similar frequency to those found in $C_6H_6M(CO)_3$ species ($\sim 300cm^{-1}$). As found in other π-complexes, the intramolecular C_7H_7 vibrations of E symmetry were not split by the complex point group symmetry or even a solid state effect. The doubly degenerate tilt was found to split in the IR and Raman spectra ($5-11cm^{-1}$) but this was not observed in the IINS spectra. However, the splitting was much greater in $C_7H_7Mo(CO)_2I$ ($40-50cm^{-1}$) where it was observed in the IINS spectra. It is suggested that this is caused by C_7H_7-Mo asymmetry due to the iodine atom.

The study of $(C_7H_7)_2TaCl_3$ revealed a typical 'sandwich' compound and a bent sandwich symmetry is preferred. The C_7H_7-M-C_7H_7 skeletal vibration assignments resembled those for C_8H_8 rather than C_6H_6 sandwich complexes.

6.9. References

1. R.B. King *Organometallic Synthesis* (Academic Press) 1 (1965)
2. E.W. Abel, M.A. Bennett, R. Burton, G. Wilkinson *J. Chem. Soc.* (1958) 4559
3. J.D. Munro, P.L. Pauson *J. Chem. Soc.* (1961) 3475
4. C.P. Tate, J.M. Augl, W.R. Knipple *Inorg. Chem.* 1 (1962) 433
5. R.B. King, A. Fronzaglia *Inorg. Chem.* 5 (1966) 1837
6. G. Hoch, R. Panter, M.L. Ziegler *Z. Naturforsch* 31B (1976) 294
7. K.M. Sharma, S.K. Anand, R.K. Multani, B.D. Jain *J. Organometallic Chem.* 21 (1970) 389
8. H.J. Dauben, L.R. Honnen, K.M. Harmon *J. Org. Chem.* 35 (1960) 1442
9. K.M. Harmon "Carbonium Ions" J. Wiley (1973) 1579
10. E. Hückel *Z. Physics* 70 (1931) 204
11. H. Fischer, J.N. Murrell *Theoretica Chimica Acta* 1 (1963) 463
12. W.G. Fately, B. Curnutte, E.R. Lippincott *J. Chem. Phys.* 26 (1957) 1471
13. A.I. Kitaigorodskii, Y.T. Strutchkov, T.L. Khotsyanova, M.E. Vol'pin, D.N. Kursanov *Izv. Akad. Nauk. SSSR.* (1960) 32
14. G.R. Clark, G.J. Palenik *J. Organometallic Chem.* 50 (1973) 185
15. M.L. Ziegler, H.E. Sasse, B. Nuber *Z. Naturforsch* 30B (1975) 26
16. R.D. Wilson, T.P. Koetzle, D.W. Hart, A. Kvick, D.L. Tipton, R. Bau *J. Amer. Chem. Soc.* 99 (1977) 1775
17. M. Traetteberg *J. Amer. Chem. Soc.* 86 (1964) 4265
18. M.V. Evans, R.C. Lord *J. Amer. Chem. Soc.* 82 (1960) 1876

19. C. La Lau, H. DeRuyter Spectrochimica Acta. 19 (1963) 1559

20. K. Aida Sci. Rpts. Res. Inst. Tohuku Univ. A8 (1956) 361

21. C. Sourisseau, J. Hervieu Spectrochimica Acta. 34A (1978) 881

22. J. Goubeau, W. Bues Z. Anorg. Allg. Chem. 268 (1952) 221

23. N.N. Greenwood J. Chem. Soc. (1959) 3811

24. H.P. Fritz Adv. Organometallic Chem. 1 (1964) 239

25. R. Cataliotti, A. Poletti, A. Santucci, J. Mol. Stuc. 5 (1970) 215

26. H. Gabelein, J. Ellerman Z. Anorg. Allg. Chem. 458 (1979) 95

27. C.J. Ludman, C.I. Ratcliffe, T.C. Waddington J. Chem. Soc. Farad. II 72 (1976) 1741

28. R.J.H. Clarke, B.C. Crosse J. Chem. Soc(A) (1969) 224

29. J. Howard, T.C. Waddington Spectrochimica Acta. 34A (1978) 445

30. G.L. Carlsson Spectrochimica Acta. 19 (1963) 1291

31. E. Maslowski "Vibrational Spectra of Organometallic Compounds" J. Wiley (1978)

32. J. Howard, Ph.D. Thesis Durham (1976)

C H A P T E R 7

ORGANOMETALLICS

(ii) Benzene Complexes

7.1 Introduction

This chapter continues our IINS, IR and Raman study of π-arene transition metal complexes. Not only was this study of benzene complexes carried out for a better understanding of the vibrational spectra, as in the case of the tropyllium complexes (Chapter 6), but also to assist in the vibrational analysis of benzene adsorbed on platinum black (Chapter 9) and in zeolite supercages (Chapter 8).

7.2. IINS Study of Benzene

7.2.1. Introduction and Experimental

This section deals only with the IINS spectrum of benzene, C_6H_6. No new work has been carried out though a comparison with previous work has been made. From this study a greater understanding of the inter- and intramolecular vibrations of solid benzene has been achieved.

The low frequency region was covered by the 4H5 time-of-flight instrument at peak neutron flux (5.3Å) whereas BFDDIDO was used for higher frequencies. Benzene was held at 141 and 77K respectively during data collection. The region covered, 0-900cm^{-1}, coincided with the organometallic and chemisorbed benzene studies.

Figure 7.1 shows the spectra summed over all the scattering angles, from the time-of-flight experiment. The scattering function sum F $(\beta)*\tilde{S}(\alpha,\beta)/\alpha$ is plotted against energy transfer (0-200cm^{-1}). Figure 7.2 shows the BFDDIDO spectrum of scattered neutron intensity against energy transfer (80-900cm^{-1}). Table 7.1 indicates the data from these studies and the assignments arrived at

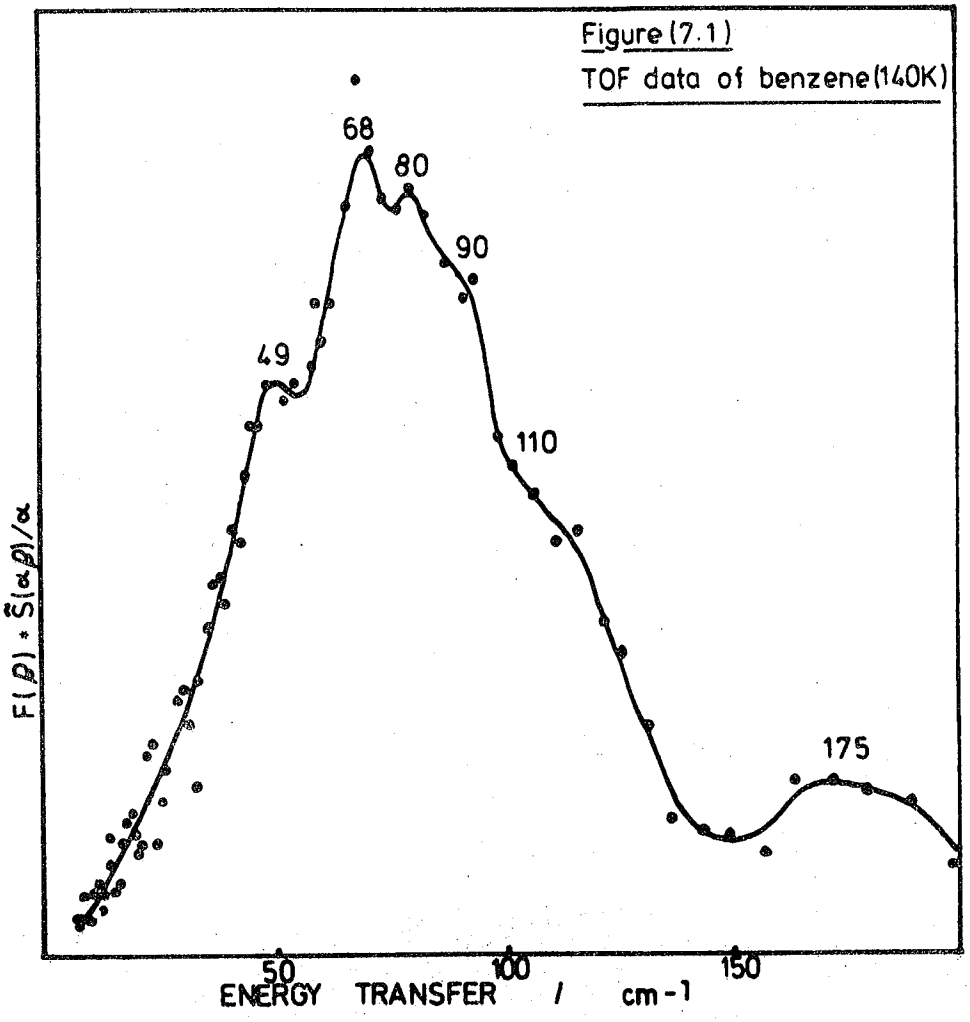
Figure (7.1)
TOF data of benzene (140K)
68
80
90
49
110
175
50
100
150
ENERGY TRANSFER / cm-1
F(β) * S(αβ)/α

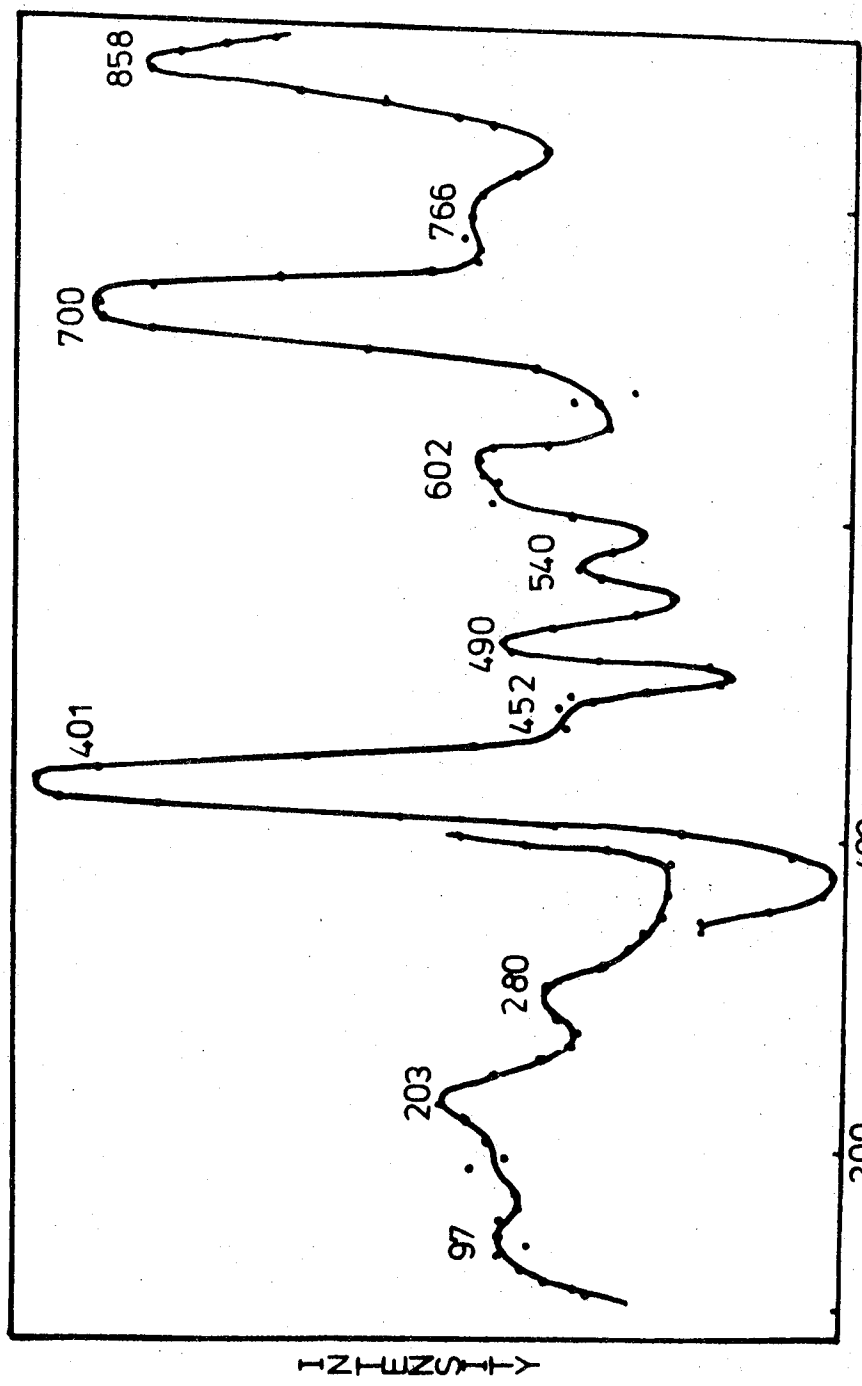

Figure(7.2) BFDDIDO data of benzene

by a comparison with previous IINS, IR and Raman work.

Table 7.1: IINS Spectral Features and Assignments for Benzene (cm^{-1})

4H5 (140K)	BFDDIDO (77K)	Assignments
49(m)		
68(vs)		A_g; B_{1u}
80(msh)		A_g; B_{2u}
90(wsh)	97(msh)	B_{1u}; A_g; B_{2g}; B_{3g}
110(m)		B_{2u}; B_{3u}; $2B_{1g}$; $2B_{3g}$
175(mb)	149(m)	No previous assignments — eg.(2xlattice modes)
	203(mb)	eg.(602-401=201cm^{-1})
	280(wb)	eg.(700-401=299cm^{-1})
	401(vs)	ν_{16} (E_{2u}) out-of-plane ring def.
	452(w)	eg.(858-401=457cm^{-1})
	490(m)	No previous assignments — eg.(401+90=491cm^{-1})
	540(w)	eg.(602-68=534cm^{-1})
	602(mb)	ν_6 (E_{2g}) in-plane ring def.
	700(vs)	ν_{11} (A_{2u}) out-of-plane CH def.
	766(w)	ν_{11}+lattice modes (700+68=768cm^{-1})
	858(s)	ν_{10} (E_{1g}) CH out-of-plane def.

inter-molecular lattice modes

def. = deformation

7.2.2. Discussion

7.2.2.1. Time-of-Flight Data

Since the lowest intramolecular benzene fundamental vibration occurs at 400cm^{-1}, the time-of-flight consists of benzene lattice vibrations and some disputed combination

and difference bands. The low frequency vibrations of benzene have been studied by IINS, IR and Raman techniques and the samples have been at a variety of temperatures and in various 'states' such as 'glassy' or crystalline, liquid and also in matrices.

Various IINS studies have been carried out with increasing success in resolving low frequency motions in benzene. Tarina (1) measured the time-of-flight spectrum and could only find a very broad band at ~ 105cm^{-1} which increased in intensity from 298 to 77K. Logan et al (2) carried out experiments at 77, 141 and 270K but suffered from poor instrument resolution. At 141K, features were found at ~ 26, ~47, ~ 72cm^{-1} with very weak bands at 95 and 125cm^{-1}.

Recently an attempt was made by Bokhenkov et al (3) to compare an experimental IINS spectrum of benzene, at 80K with a number of calculated density of phonon states spectra. Figure 7.3a shows the time-of-flight spectrum of Bokhenkov et al compared with two calculated spectra using different sets of structural data, Figures 7.3b,c. The spectrum was run at 80K on the KDSOG-1 time-of-flight spectrometer (Dubna) and is summed over all seven scattering angles (30°-150°). The incident neutron energy used was 39.5cm^{-1}. A comparison can be made with the spectrum run at 141K in Figure 7.1 on the 4H5 instrument at a neutron peak flux wavelength of 5.3Å (23.5cm^{-1}). This spectrum was summed over 13 angles (13°-90°). The spectra cannot be strictly compared though the peak frequencies are similar. Figure 7.3b is a spectrum calculated by Bokhenkov et al using averaged bond lengths and angles given by Cox (4). Figure 7.3c is a calculated

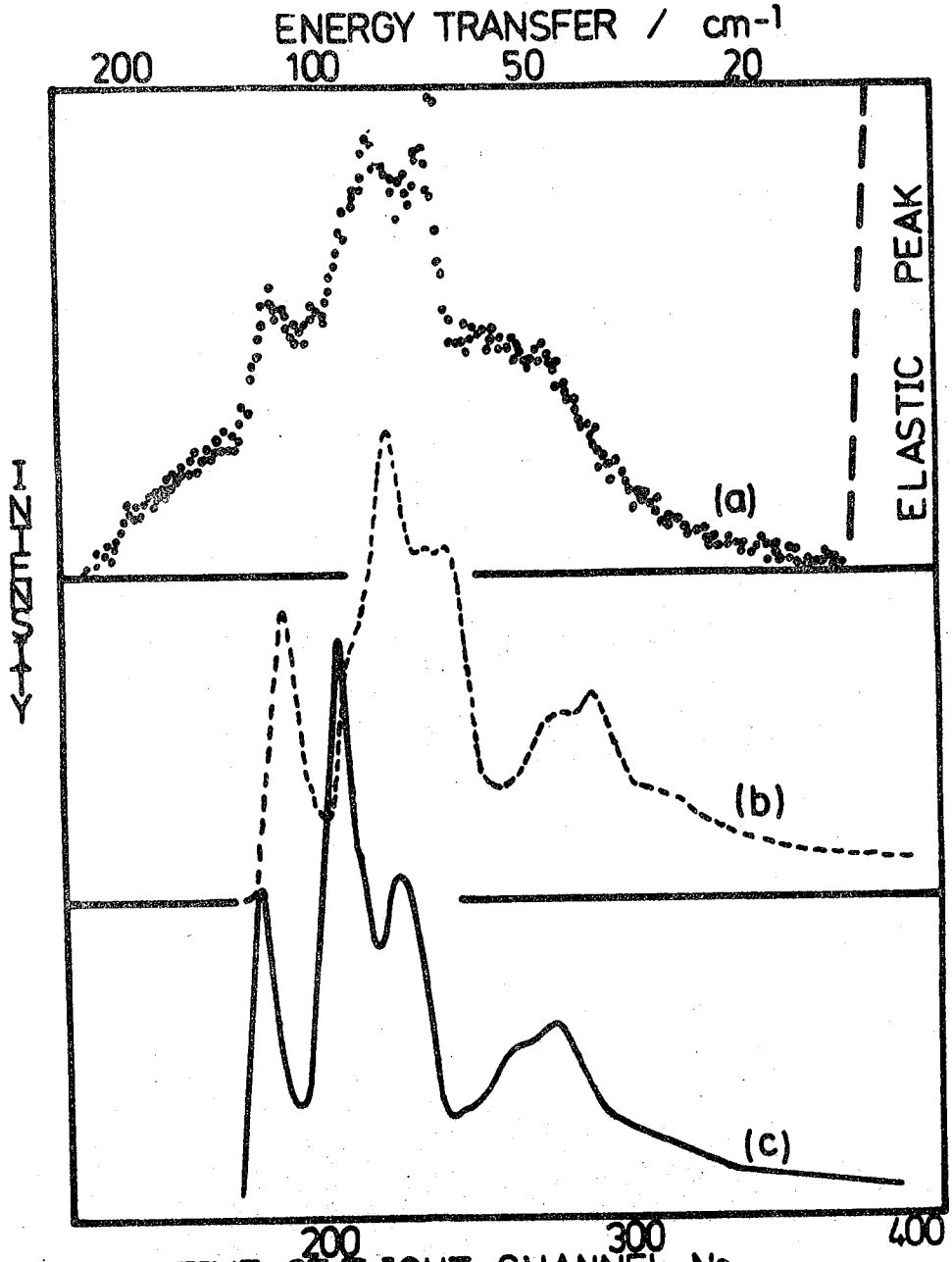

Figure(7.3) TOF data of BOKHENKOV et al [3]

spectrum based on the C_i site symmetry determined by the neutron diffraction work of Bacon et al (5). Table 7.2 lists the data of Bokhenkov et al with that from this study.

Table 7.2: Features in the Time-of-Flight Studies of Benzene After Bokhenkov et al (3) and This Study

This Study (141K)	Bokhenkov et al (80K) (3)
49(m)	50(sh)
68(vs)	72(s)
80(ms)	78(w)
90(msh)	90(s)
110(msh)	110(sh)
-	123(m)
175(mb)	170(sh)
203(mb)	220(wsh)

Bokhenkov et al said that better agreement at lower frequency would have been attained with their spectrum if it had been run at ~ 138K (The calculated spectra were produced from structural data collected at 138K so that the comparison of the present time-of-flight data collected at 141K is more reasonable).

Far-IR (6,7,8) and Raman work (8,9,10,11,12) has been carried out at a number of temperatures for the solid benzene phase. However, this present study can be compared with the IR work of Harada et al (6) and the Raman work of Bonadeo et al (12) which were carried out at 140K. Further, Ito and Shigeska (9) studied the temperature dependence of the

vibrations between 4.2 and 273K and frequencies are estimated for 140K from their data, using calibration graphs. Table 7.3 compares the optical data with our IINS data.

Table 7.3: Comparison of IINS Data With Optical Data of Other Workers

Raman Data		IINS Data	Infra-red Data
(12) 140K	(9) 140K	141K	(6) 140K
		49(m)	
			53(w)(B_{3u})(9)
57,61(w)(A_g^*,B_{1g},B_{3g})	58(m)(A_g)	68(s)	57(w)(A_g)
			70(s)(B_{1u})
79(s)(A_g^*,B_{2g})	78(vs)(A_g^*,B_{2g})	80(ms)	79(sh)(A_g)
90,92(wm)(A_g^*,B_{2g},B_{3g})	90(w)(A_g^*,B_{2g},B_{3g})	90(msh)	85(vs)(B_{1u})
			90(w)(B_{3g})
100(w)(B_{1g})	98(w)(B_{1g})(9)	110(sh)	94(vs)(B_{2u},B_{3u})
128(s)(B_{1g},B_{3g})	125(s)(B_{1g},B_{3g})		126(vw)(B_{1g},B_{3g})

* Asterisk represents the principal component in these groups.

Benzene crystallizes in the orthorhombic system of space group D_{2h}^{15} (4,5) with four molecules per unit cell lying on inversion centres. There are expected 12 Raman active librational lattice modes and 9 infra-red active translatory lattice modes of A_g, B_{1g}, B_{2g}, B_{3g} and A_u, B_{1u}, B_{2u}, B_{3u} symmetry respectively. These motions are rotational and translational oscillations of the molecules in the unit cell about or around their principal axes of inertia. Schettino and Califano (8) list previous data on the calculated and

observed lattice frequencies and their relative IR and Raman intensities. Table 7.4 lists IINS bands and their symmetry assignment based on previous data on the frequencies and intensities. Table 7.5 indicates the form of the actual vibration taking place.

Table 7.4: Assignment of IINS Time-of-Flight Features

IINS Band (cm^{-1})	Principal components (from IR/Raman Studies eg (8))	Possible Other Components
40(m)	-	-
68(s)	A_g, B_{1u}	B_{1g}, B_{3g}
80(ms)	A_g	B_{2g}
90(msh)	B_{1u}, A_g	B_{2g}, B_{3g}
110(sh)	B_{1g}, B_{3g}, B_{2u}, B_{3u}	

Table 7.5: Possible Forms of Lattice Vibrations

IINS Band (cm^{-1})	Motion
49	Unknown
68	A_g- rotation about 6 fold molecular axis B_{1u}- Translation in 'c' direction of unit cell
80	A_g - rotation about 2 fold molecular axis (about b axis)
90	A_g - rotation about 2 fold axis in molecular plane B_{1u}- translation in 'c' direction of unit cell
110	B_{1g}, B_{3g} - rotations about 2 fold axis in molecular plane. B_{2g}, B_{3u} - translation in 'a' and 'b' direction of unit cell

7.2.2.2 BFDDIDO Data

Between the frequencies of the lattice modes and the fundamental modes (130-380cm^{-1} region) there are a number of bands found at 203 and 280cm^{-1} in our IINS data. A further band may exist at ~175cm^{-1}, which has not been resolved in the BFDDIDO data (It is much better resolved in the 4H5 data). Little analysis of the 130-380cm^{-1} region has been carried out. Schrotter et al (11) listed IR bands in gaseous benzene at 265, 302 and 362cm^{-1} which were assigned to $\upsilon_{17} - \upsilon_4$ (975-707=268cm^{-1}), $\upsilon_4 - \upsilon_{16}$ (707-403=304cm^{-1}) and $\upsilon_{17} - \upsilon_6$ (975-606=369cm^{-1}) respectively. The IINS spectrum of Bokhenkov et al (3) displayed shoulders at ~150 and ~200cm^{-1}. These bands cannot be fundamental lattice vibrations if the previous assignments are correct. They may be due to the second harmonics of the lattice vibrations or difference bands involving the intramolecular benzene vibrations.

The fundamental intramolecular vibrations of benzene have been often discussed before. The form of these motions are shown in Figure 7.4. The numbering of the vibrations is after Wilson (13). The form of the vibrations is after Varsanyi (14). Table 7.6 summarises the IR and Raman data for the liquid and solid forms of benzene at various temperatures.

There are a further set of vibrations found in the IR and Raman spectra in the region 400-1000cm^{-1} which are combination or difference bands and all are of weak intensity. The IR bands lie at 447(vw)cm^{-1} and 769/788/816(vw)cm^{-1}. They have been assigned as $\upsilon_{10} - \upsilon_{16}$ (849-403) and υ_{11} + torsional lattice modes (15). Schrotter et al (11) found

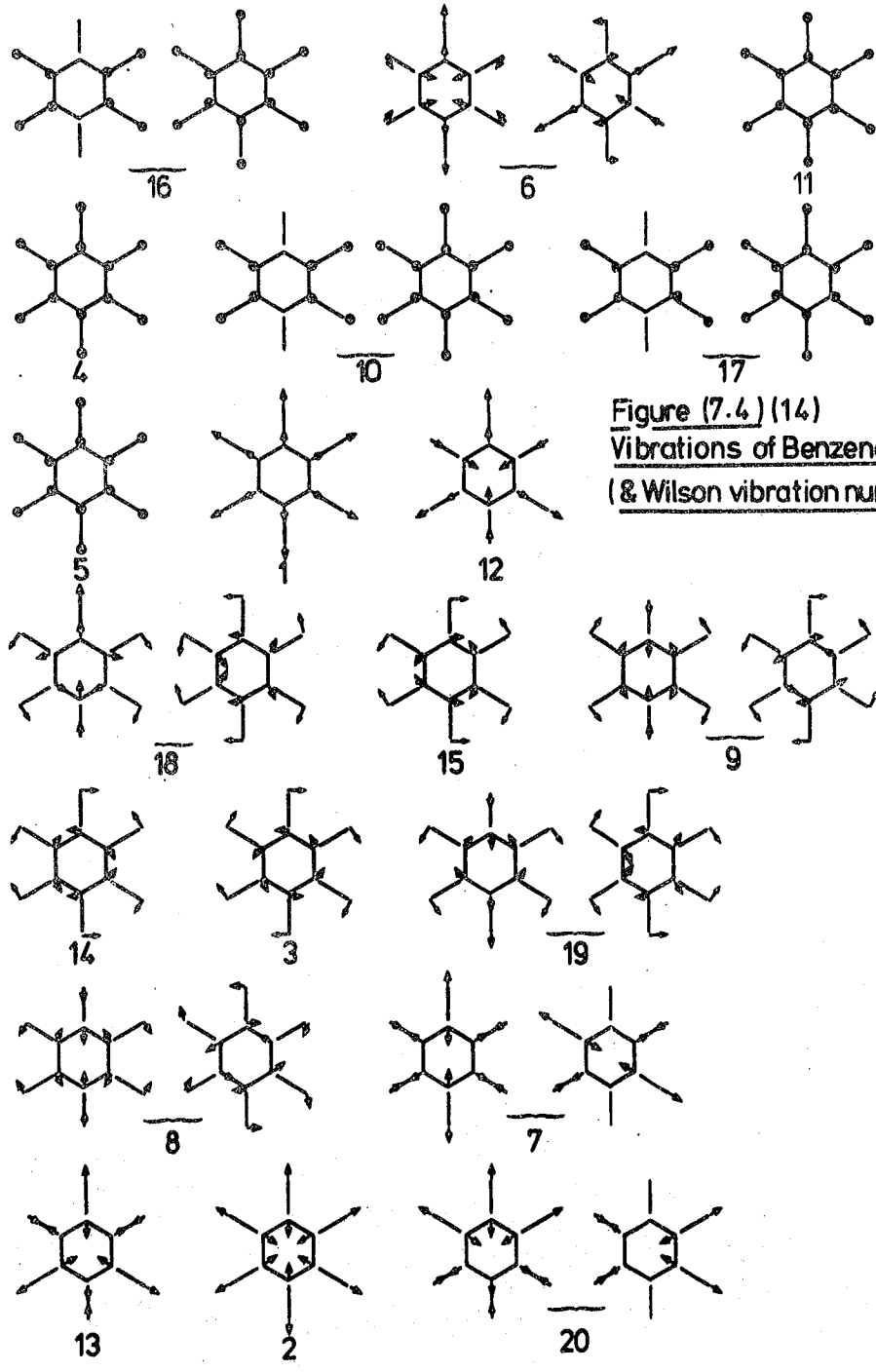

Figure (7.4) (14)
Vibrations of Benzene
(& Wilson vibration number)

Table 7.6: Previous IR and Raman Data on the Fundamental Intramolecular Benzene Vibrations.

Wilson No.	Symmetry	Motion	Liquid (14)		Solid		
			IR	R	IR (261K) (15)	IR (103K) (15)	Raman (4K) (9)
16	E_{2u}	o.p. ring def.	404(vw)	-	-	400(w) 419(vw)	-
6	E_{2g}	i.p. ring def.	-	606(s)	-	-	607(m)
11	A_{2u}	o.p. CH def.	671(s)	-	685(s)	687(s)	-
4	B_{2g}	o.p. ring def.	-	-	-	-	-
10	E'_{1g}	o.p. CH def.	-	849(m)	-	-	856(m)
17	E_{2u}	o.p. CH def.	975(w)		975(wm) 982(wm)	975(wm) 987(wm)	
5	B_{2g}	o.p. CH def.	-	-	-	-	1177(m) 1183(w)
1	A_{1g}	i.p. ring breath.	-	992(s)	-	-	992(vs)
12	B_{1u}	i.p. ring def.	1010(w)	-	1010(wm)	1009(wm)	-
18	E_{1u}	i.p. CH def.	1038(s)	-	1036(s)	1035(s)	-
15	B_{2u}	i.p. CH def.	1150(w)	-	1147(wm)	1147(wm)	-
9	E_{2g}	i.p. CH def.	-	1178(s)	-	-	-
14	B_{2u}	i.p. ring def.	1310(w)	-	1311(w)	1312(w)	-
3	A_{2g}	i.p. CH def.	-	1326(vw)	-	-	-
19	E_{1u}	i.p. ring def.	1478(s)	-	1478(s)	1478(s)	-
8	E_{2g}	i.p. ring stretch	-	1606(s)	-	-	-
7	E_{2g}	CH stretch	-	3047(s)	-	-	3044(s) 3049(s)
13	B_{1u}	CH stretch	3068(vw)	-	3070(vw)	3070(vw)	-
2	A_{1g}	CH stretch	-	3062(vs)	-	-	3064(vs)
20	E_{1u}	CH stretch	3080(s)	-	3087(ms)	3085(ms)	-

i.p. = in-plane o.p. = out-of-plane def. = deformation

Raman bands at 781(vw), 804(vw) and 824(vw)cm^{-1} which were assigned to $\nu_9-\nu_{11}$ (1178-671), $2\nu_{16}$ (2x403) and $\nu_{19}-\nu_{11}$ (1485-671) respectively. The bands in the BFDDIDO spectrum are assigned from the evidence above. The only major difference between the IR/Raman work and the IINS data is that ν_{11} lies at 700cm^{-1}, slightly higher in frequency than found in the infra-red. The final assignments are made in Table 7.1.

Finally, it can be noted that there are IINS bands at 490 and 540cm^{-1} that have not been observed previously. They must be combination or difference bands which never gain sufficient intensity to be seen by IR or Raman techniques. One possibility is that they involve a very strong IINS active intramolecular benzene vibration and the strong lattice modes.

eg. $401 + 90 = 491cm^{-1}$
$602 - 68 = 534cm^{-1}$

7.3 Methods of Synthesis: Benzene Complexes

All the compounds were prepared by literature methods. $Co_2(CO)_8$ was supplied by Strem Chemicals Inc. UCl_4 and $PdCl_2$ by Alpha-Ventron, $RuCl_3.3H_2O$ from Pierce Chemicals, Cu_2O and $AlCl_3$ from B.D.H. Ltd, $SbCl_3$ and $Hg(NO_3)_2H_2O$ from Hopkin and Williams Ltd., and 1,3-cyclohexadiene from the Aldrich Chemical Co. The $AlCl_3$ was freshly sublimed before use.

$(PdAl_2Cl_7C_6H_6)_2$ and $(PdAlCl_4C_6H_6)_2$ were prepared (16) by reacting $PdCl_2$ with C_6H_6(dry), freshly sublimed $AlCl_3$ and dried aluminium dust. The ratio of $PdCl_2$ to $AlCl_3$ had to be controlled to achieve the above stoichiometry.

	$(PdAl_2Cl_7C_6H_6)_2$		$(PdAlCl_4C_6H_6)_2$	
Analysis	Actual	Theoretical	Actual	Theoretical
C	13.81	14.85	19.62	20.40
H	1.37	1.23	1.75	1.70
Cl	50.7	51.4	38.90	40.60
Al	11.28	11.3	-	7.7
Pd	20.35	21.3	29.0	29.4

$RuCl_3.3H_2O$ was reacted with 1,3cyclohexadiene to form $(RuCl_2C_6H_6)_2$ (17). This compound was reacted with NaBr to form the bromo-derivative.

	$(RuCl_2C_6H_6)_2$		$(RuBr_2C_6H_6)_2$	
Analysis	Actual	Theoretical	Actual	Theoretical
C	28.62	28.82	20.77	21.26
H	2.58	2.42	2.03	1.78
X	28.10	28.35	47.4	47.14

UCl_4, freshly sublimed $AlCl_3$, Al dust and benzene were reacted to produce $C_6H_6\ U(AlCl_4)_3$. (18)

Analysis	Actual	Theoretical
C	6.82	8.75
H	0.74	0.73
Cl	51.30	51.80

Benzene was reacted with $Co_2(CO)_8$ to produce $C_6H_6Co_4(CO)_9$ (19).

Analysis	Actual	Theoretical
C	30.45	31.88
H	0.83	1.06
Co	39.75	41.70

$SbCl_3$ was dissolved in a slight excess of benzene then the excess was slowly removed by vacuum (20) to produce $(SbCl_3)_2C_6H_6$.

Analysis	Actual	Theoretical
C	14.47	15.36
H	1.36	1.10
Sb	44.8	44.61
Cl	38.58	38.94

The Co and Ni analogues of $MHg_2(SCN)_6.C_6H_6$ were made by adding benzene and the metal nitrate to an aqueous mixture of $Hg(NO_3)_2$ and KSCN (21).

	$CoHg_2(SCN)_6C_6H_6$		$NiHg_2(SCN)_6C_6H_6$	
Analysis	Actual	Theoretical	Actual	Theoretical
C	16.38	16.23	15.96	16.23
H	0.38	0.68	0.75	0.68
Co	6.53	6.65		
Ni			6.49	6.65
N	9.67	9.47	9.54	9.47
Hg	45.00	45.32	45.12	45.32

7.4 Structures of the Studied Systems

The structures of the Pd-C_6H_6 complexes have been determined by X-ray diffraction methods by Allegra et al (16,22). Both molecules are centrosymmetric with the mid point lying between the Pd atoms. The two C_6H_6 rings are π-bonded to the Pd atoms giving rise to an unusual sandwich structure. $(PdAl_2Cl_7C_6H_6)_2$, shown in Figure 7.5, has a partial statistical disorder at 300K. A low temperature analysis at 173K (22) showed the C_6H_6 to be lying in one of two orientations either eclipsed or staggered 30° apart. $(PdAlCl_4C_6H_6)_2$, shown in Figure 7.6, has C_{2h} symmetry.

The structure of $(C_6H_6)U(AlCl_4)_3$ has been determined by X-ray techniques (18), Figure 7.7. The U atom co-ordinates to three $(AlCl_4)$ tetrahedra, through UClAl bridges, and to a C_6H_6 ring found above the U atom parallel to the plane of the bridging U atoms.

$C_6H_6Co_4(CO)_9$ has been studied by X-ray methods (19) and consists of a Co_4 tetrahedral cluster with one Co atom π-bonded to a C_6H_6 ring, Figure 7.8. The distance from the apical Co atom to the C_6H_6 ring centre is 1.603Å. The CO-groups are bonded to the three basal Co atoms.

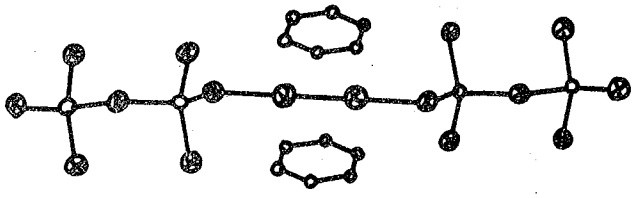

Figure (7. 5)(16)

$(PdAl_2Cl_7C_6H_6)_2$

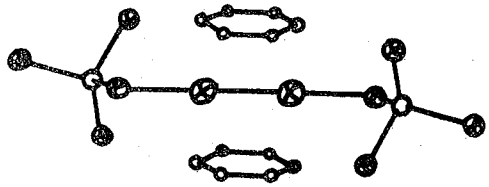

Figure (7.6)(16)

$(PdAlCl_4C_6H_6)_2$

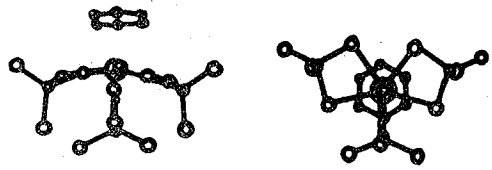

Figure (7. 7)(18)

$(C_6H_6)U(AlCl_4)_3$

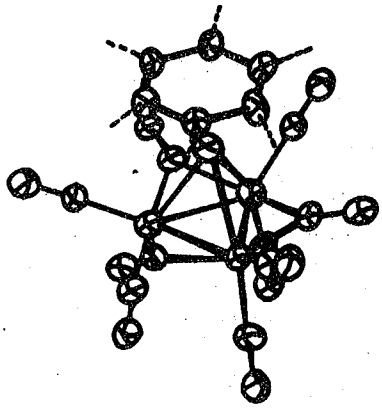

Figure (7.8)(19)

$(C_6H_6)Co_4(CO)_9$

The $(RuX_2C_6H_6)_2$ complexes have been studied by n.m.r. techniques (X=Cl or Br) (17,23). Only a single peak was found (300K) implying that the hydrogen atoms were equivalent in the molecule, as found in the similar dimeric species $(MCl_2(C_5Me_5)_2$ (24). The structure, shown in Figure 7.9, has been supported by Bennett et al (23) and by Zelonka and Baird (17) from analytical results, IR and optical spectra, n.m.r. and mass spectral measurements and from chemical properties.

$(SbCl_3)_2\ C_6H_6$ has been well studied. Unfortunately the crystal structure has yet to be analysed though other $(SbCl_3)_2$ arene complexes have been characterized (25,28). Fairly constant $Sb\text{-}C_{arene}$ distances were found (3.0-3.5Å). Two possible forms of the benzene complex are shown in Figure 7.10.

The benzene clathrates, $MHg_2(SCN)_6C_6H_6$, were shown to contain an $Hg(C_6H_6)Hg$ sandwich by an X-ray study (29). Layers of the composition $(MHg_2(SCN)_6)_n$ were found to be separated by C_6H_6 molecules held between two Hg atoms at an Hg-C distance of 3.6Å Figure 7.11.

7.5 $MHg_2(SCN)_6C_6H_6$ (M=Ni,Co)

7.5.1. Previous Studies

Fritz and Manchot (30) studied the IR spectra of these benzene clathrates with M=Cd, Co and Ni. They assigned the C-S stretches and S-C-N deformations and overtones of the strong IR active S-C-N deformations (see Table 7.7). ν_{11} was observed at $702cm^{-1}$. This implied to the authors that a weak π-complex was formed compared to, say $C_6H_6Cr(CO)_3$ (ν_{11} @ $784cm^{-1}$). From the number and type of observed benzene

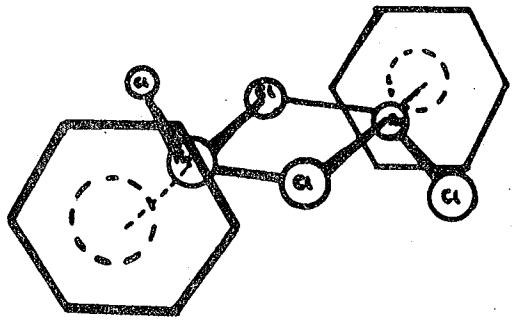

Figure (7.9)
$(RuX_2C_6H_6)_2$ (X=Cl, Br)

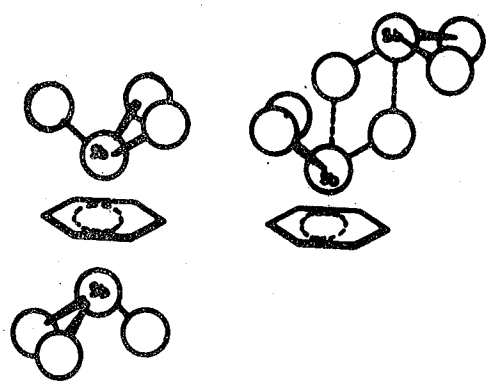

Figure (7.10)
TWO POSSIBLE FORMS
OF $(SbCl_3)_2C_6H_6$

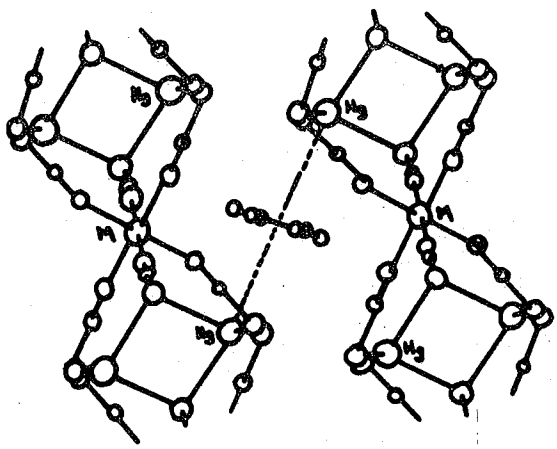

Figure (7.11)(29)

$MHg_2(SCN)_6.(C_6H_6)$
(M=Ni, Co

intramolecular modes the authors suggested that the benzene vibrations could be described in terms of D_{3d} symmetry.

7.5.2. Results

Only $NiHg_2(SCN)_6.C_6H_6$ was studied by the time-of-flight technique (130K) because of the lack of available beam time. Figure 7.12 shows the spectra from the 90° and 82° scattering angles. The scattering function $P(\alpha,\beta)$ is plotted against energy transfer (cm^{-1}). Figures 7.13 shows the BFDDIDO spectra of the nickel and cobalt analogues run at liquid nitrogen temperature. The Raman spectra were collected using a laser power of 100mW (Ni) and 200mW (Co) at room temperature. The IR spectra were run at liquid nitrogen temperature. Only a nujol spectrum of the cobalt analogue could be gained because the thorough grinding needed to produce a good alkali halide disc removed the benzene from the clathrate. This was known because the pink colour of the clathrate changed to dark blue due to the formation of $CoHg(SCN)_4$ and $Hg(SCN)_2$. Table 7.7 shows the spectral features and assignments for both compounds. Successful IR spectra (nujol) were collected for the compounds by simply placing a small quantity of the fine powder onto a KBr disc, adding a small amount of nujol and then pressing the plates together. The sample was then placed in the beam just before the region of interest (eg. 750-650cm^{-1}) to reduce any affect due to heating.

7.5.3. Discussion

The vibrations of $MHg_2(SCN)_6C_6H_6$ clathrates may be split into those involving the $MHg_2(SCN)_6$ moiety, the benzene intramolecular and the benzene-host skeletal vibrations.

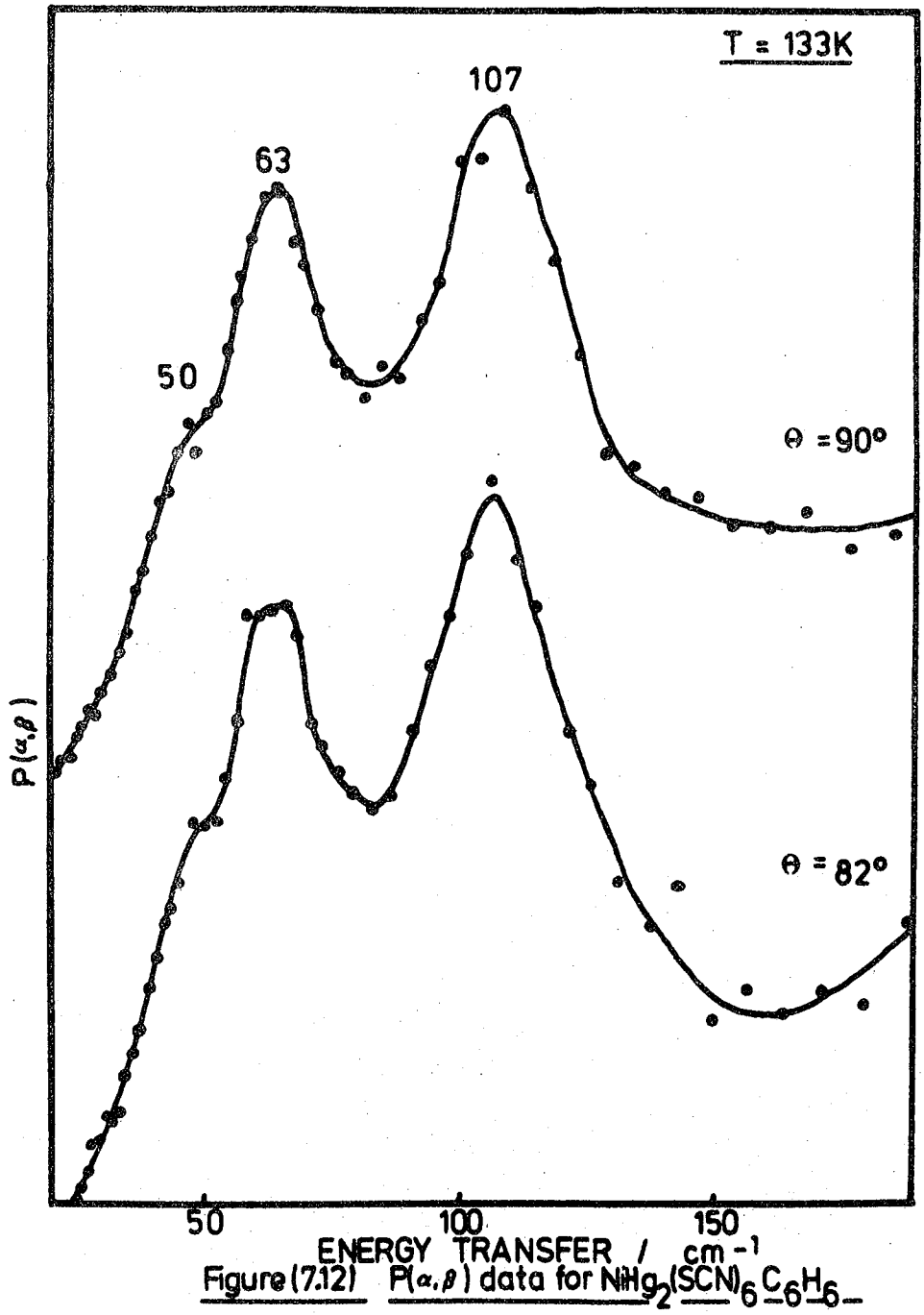

Figure (7.12) P(α,β) data for $NiHg_2(SCN)_6C_6H_6$

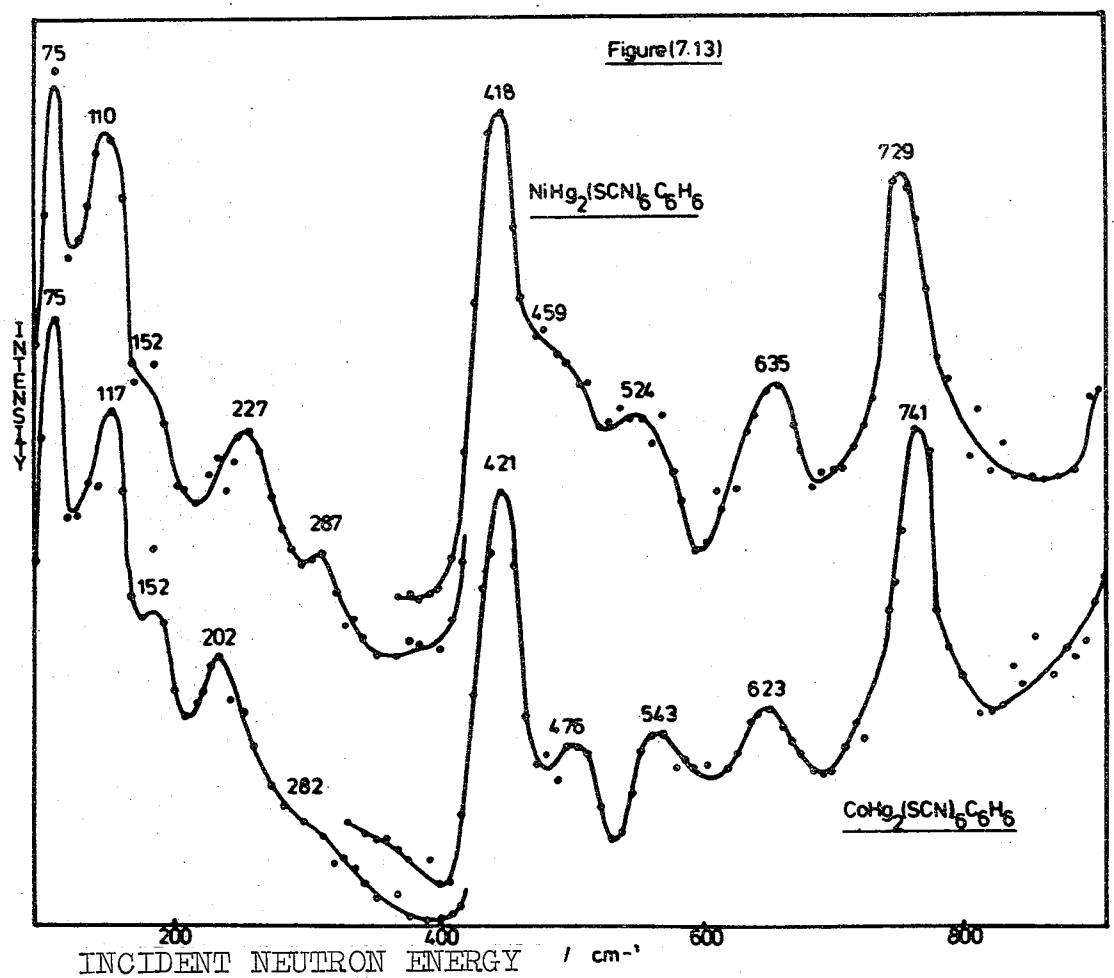
Figure(7.13)
75
110
418
729
NiHg2(SCN)6C6H6
459
635
524
741
75
117
227
421
287
152
202
623
543
476
282
CoHg2(SCN)6C6H6
INTENSITY
200
400
600
800
INCIDENT NEUTRON ENERGY / cm-1

Table 7.7: Vibrational Data on $NiHg_2(SCN)_6C_6H_6$ Clathrates

$NiHg_2(SCN)_6C_6H_6$						$CoHg_2(SCN)_6C_6H_6$					Assignment
4H5 (133K)	BFDDIDO (77K)	IR (77K)	FIR (77K)	Raman (RT)	IR(?0) (RT)	BFDDIDO (77K)	IR (RT)	FIR (77K)	Raman (RT)	IR (?0) (RT)	
		866(w)			871(w)						$2 \times 435cm^{-1}$
					772(vw)		773(vw)			773(vw)	C - S stretches
		755(w)			754(w)		754(w)			752(w)	
		740(w)			738(w)		735(w)			736(w)	
	729(s)	705(s)			702(s)	741(vs)	705(s)			702(ms)	ν_{11} (A_{2u}) CH out-of-plane deformation
	635(m)			600(w)		623(m)			620(wb)		ν_6 (E_{2g}) in-plane ring deformation
									570(mb)		Unknown
						543(m)					Benzene intramolecular/lattice mode combination/difference bands
520(s)	524(m)					476(m)					
	459(sh)										
		467(m)			467(m)		466(m)			466(m)	SCN deformations + $M(SCN)_2$ deformations
		439(msh)			446(sh)		440(sh)			444(sh)	
		435(m)			437(m)		435(m)			437(m)	
400(s)	418(s)					421(s)					ν_{16} (E_{2u}) out-of-plane ring deformation
		392(w)	392(m)								Unknown
	287(wm)	291(w)	292(m)			282(wm)		284(s)			Stretch skeletal
				267(s)					260(vs)		M-N stretches
			267(mb)					259(sh)			
		258(vs)	256(mvb)					245(sb)			Hg-S stretches
			249(sh)					239(s)			
			242(sh)					234(sh)			
			230(w)					224(w)			
210(w)	227(m)	225(wsh)	221(s)	219(s)		202(ms)		207(vs)	200(sb)		Tilt skeletal
			192(m)								
			184(ms)					180(sb)			HgSC deformations
			166(m)					156(m)			
	152(sh)			150(w)		152(msh)			153(w)		SHgS deformations
				141(w)				143(m)			
			130(w)					125(sb)	130(wb)		
			112(msh)	109(w)		117(s)		113(m)	110(w)		Deformation stretch
107(vs)	110(s)		92(ms)	92(m)				92(s)	95(m)		SHgS deformations
			81(w)	84(m)		75(m)		80(s)			Torsion skeletal
63(vs)	75(s)			60(vs)					60(vs)		
			50(m)					60(s)			Intermolecular lattice modes
50(msh)				45(m)					41(m)		

(a) Vibrations of the $MHg_2(SCN)_6$ host

From a review of vibrational studies involving the components found in the host, the following can be used to assist in the analysis of the $MHg_2(SCN)_6$ moiety. (IR review).

i) M-N stretches: (M in octahedral symmetry) Ni-N stretches in $(Ni(NCS)_6)^{4-}$ are found at ~ 240cm^{-1} (31).

ii) Hg-S stretches: The Hg-S stretch in $CoHg(SCN)_4$ group bidentate to Hg and Co atoms) lies at ~ 220cm^{-1}(31).

iii) C-S stretch: The C-S stretch in octahedral compounds such as $M_3Cr(NCS)_6$ lies at 820cm^{-1} (32) and are usually of weak intensity.

iv) N-C stretch: These vibrations exist at 2000cm^{-1}

v) N-C-S deformations: In $(M(NCS)_6)^{3-}$ ions, these bands occur at ~480cm^{-1} (32).

vi) S-M-S. deformations: These deformations have been assigned in the 80-120cm^{-1} region (33).

vii) M-S-C deformations: These bands occur in the 150-190cm^{-1} region (33)

viii) N-M-N deformations: These bands usually are observed, at higher frequency than the M-N stretch, in the 400-500cm^{-1} region (34).

Previously, Fritz and Manchot (30) assigned, in their IR study of $MHg_2(SCN)_6C_6H_6$ complexes, the strongly IR active C-S stretches and S-C-N deformations to the 700-800 and 400-500cm^{-1} regions. From these general areas of assignment, the majority of the strong IR bands of the nickel and cobalt chathrates can be readily assigned. The group of weak IR bands in the 700-750cm^{-1} region are assigned, in the manner of Fritz and Manchot (30) to C-S stretches. Similar weak

bands were found in the IR study of $M'_3M''(NCS)_6$ species by Keller et al (35). The bridging effect on the C-S stretch frequency in the $MHg_2(SCN)_6C_6H_6$ complexes has produced a fall in the vibrational frequency compared with $M'_3M''(NCS)_2$ species. The medium intense IR bands around 450cm^{-1} are assigned to SCN deformations, in agreement with Fritz and Manchot (30) and the assignments of Bennett et al (32). Also in this region lie the $M(NCS)_2$ deformations.

The Co-N and Ni-N stretches are assigned to the strong 284 and 267cm^{-1} IR bands. There are also Raman bands at similar frequencies. In the octahedral $M(NCS)_6^{n-}$ ions the single M-N stretch was of T_{1u} symmetry and only IR active. Perhaps this band has been split in the $MHg_2(SCN)_6C_6H_6$ compounds due to a lowering of symmetry which has also allowed Raman activity. There is a further group of IR bands around 230cm^{-1} and these are assigned to Hg-S stretching vibrations in agreement with the IR work on $CoHg(SCN)_4$ (31). At less than 200cm^{-1} there are many strong IR bands. Some of these are assigned to various deformation modes from a comparison with work of Knox et al (34) and Ferraro (33). The lowest frequency bands involve intermolecular vibrations (lattice vibrations).

(b) Intramolecular benzene vibrations

The following assignments, in Table 7.8, of the intramolecular benzene vibrations are made from a comparison with IINS data of benzene. A comparison of the vibrational frequencies is made with IR and Raman data on Hofmann-type clathrates with benzene as a guest. (The values in brackets are the approximate relative intensities of the IINS bands in benzene and the $MHg_2(SCN)_6C_6H_6$ clathrates).

Table 7.8: Intramolecular Benzene Vibrations in Various Clathrates

Vibration (Wilson No.)	Benzene Solid IINS	(i)			(ii)			(iii) (36,37)	
		IINS	IR	R	IINS	IR	R	IR	R
ν_{11}	700(34)	729(34)	705	-	741(39	700	-	700-705	-
ν_6	602(14)	635(18)	-	600	623(12)	-	620	-	608
ν_{16}	401(48)	418(48)	-	-	421(50)	-	-	405-410	-

i) = $NiHg_2(SCN)_6C_6H_6$

ii) = $CoHg_2(SCN)_6C_6H_6$

iii) = $M(NH_3)_2Ni(CN)_4 2C_6H_6$

ν_{11}, the CH out-of-plane deformation, strongly IR active, is assigned to the $700cm^{-1}$ bands in the IR spectra of both compounds. However, it must be noted that the strong IINS bands indicative of ν_{11} lie at slightly greater frequency, 729 and $741cm^{-1}$ in the nickel and cobalt analogues. It was possible that the IINS technique, being non-destructive, was measuring the spectra of the compound whereas the IR techniques measured the spectrum of the decomposed or partially decomposed compound. However, the $NiHg_2(SCN)_6C_6H_6$ clathrate was not decomposed, even by grinding to form a KBr disc. The KBr disc spectrum was very similar to that obtained by pressing the clathrate gently between KBr discs with a small amount of nujol. Further this latter method did not breakdown the less stable pink cobalt clathrate since no colour change was found after pressing or after the IR spectrum. The frequency of ν_{11} was not found to change in all the conditions

used for each compound. Thus this small difference between the IR and IINS spectra cannot be explained by a decomposition of the clathrate.

In the 620-640cm^{-1} region of the BFDDIDO spectra there is a medium intense IINS band, with a weak Raman counterpart, which is assigned to the ν_6 in-plane ring deformation (E_{2g}: benzene symmetry). This band is only Raman active in the D_{6h} 'free' benzene symmetry. At 420cm^{-1}, the strongest IINS band is assigned to the IR and Raman inactive ν_{16} out-of-plane ring deformation (E_{2u}). No Raman or IR counterparts were found for this band in the nickel and cobalt clathrates.

For the three discussed benzene intramolecular modes, at ~700, ~600 and ~420cm^{-1}, the symmetry in the free molecule is A_{2u}, E_{2g} and E_{2u} respectively. However, this symmetry would appear to occur in the clathrates as well. Fritz and Manchot (30) believed D_{3d} symmetry was found but this would have allowed the E_{2u} modes to become IR active. ν_{16} (E_{2u}) was not observed in our IR spectra of the clathrate nor was it reported by Fritz and Manchot (30). Thus, if the intramolecular modes of benzene can be described in terms of D_{6h} symmetry, which is reasonable since the 'Hg-C_6H_6-Hg' moiety has approximate D_{6h} symmetry, then only the A_{2u} and E_{1u} bands are formally IR active. In our IR spectra of the complexes (up to 4000cm^{-1}) strong bands at ~700, 1035, and 1475cm^{-1} indicative of $\nu_{11}(A_{2u})$, $\nu_{18}(E_{1u})$ were easily assigned. Other <u>very</u> weak features existed at 866, 930, 985 and 1010cm^{-1}. However, some of these features may be due to the framework (eg. 2x435cm^{-1} = 870cm^{-1}) whereas the very weak nature of the 985 and 1010cm^{-1} bands could be

due to a solid state affect causing some IR activity of $\nu_{17}(E_{2u})$ and $\nu_{12}(B_{1u})$.

Two other weak bands are found the IINS spectra of the two clathrates at 460 and 530cm^{-1}. Two bands were found in the IINS spectrum of solid benzene at similar frequencies, and they were assigned to combination and difference bands involving IR and Raman inactive intramolecular and lattice modes. Perhaps the clathrate vibrations can also be explained in this way though the lattice vibrations of solid benzene and the guest/host lattices will be very different. The two low frequency intense IINS bands at 75 and 110/117cm^{-1} (BFDDIDO) may be involved.

eg. $NiHg_2(SCN)_6C_6H_6$: 110 + 418 = 528cm^{-1}

2 x 227 = 454cm^{-1}

$CoHg_2(SCN)_6C_6H_6$: 117 + 421 = 538cm^{-1}

75 + 421 = 496cm^{-1}

(c) 'Hg-C_6H_6-Hg' skeletal vibrations

The form of the 'Hg-C_6H_6-Hg' vibrations that involve benzene motion are shown in Figure 7.14. Now the symmetry, from the intramolecular benzene vibrations, is D_{6h} and if this symmetry can describe the skeletal vibrations then the vibrations, derived from the rotational and translational degrees of freedom of the benzene molecule (ie $R_{x,y+z}$ and $T_{x,y+z}$), will have the activity and symmetry shown in Table 7.9.

In the IINS spectra there are 5 BFDDIDO features at lower frequency than ν_{16} @ 400cm^{-1}. Above ~120cm^{-1} there are surprisingly no strong IINS bands indicative of the tilts and stretch vibrations usually associated with arene

Figure (7.14) Skeletal modes of M- C_6H_6 -M species.

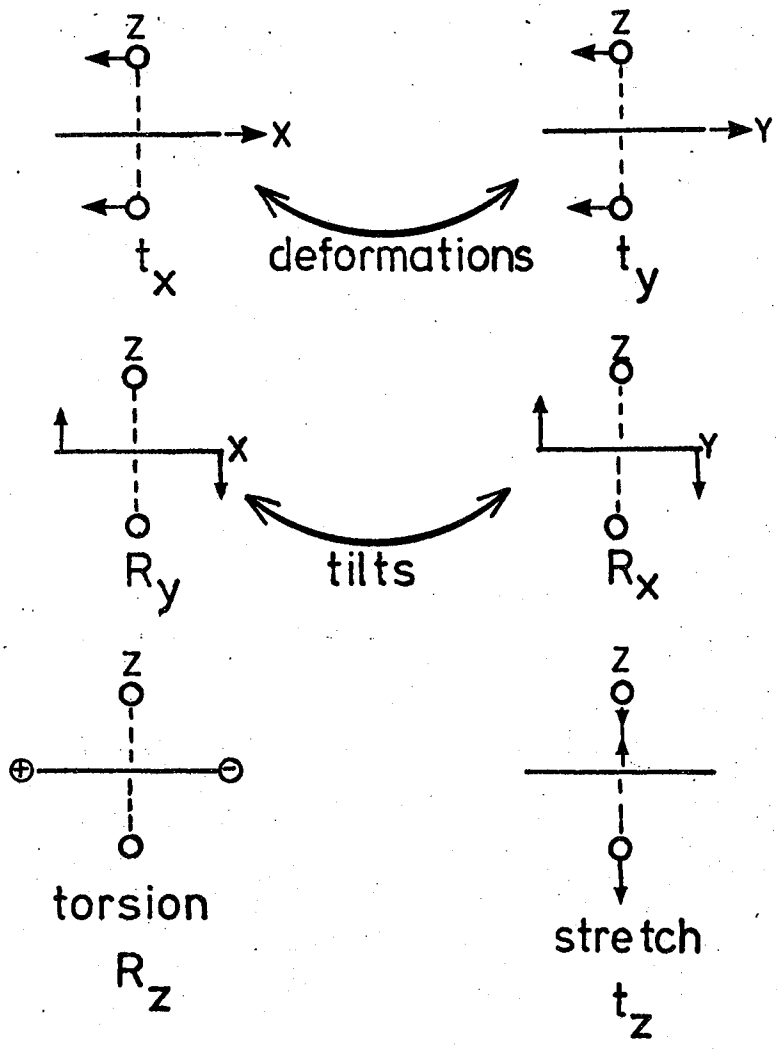

Table 7.9: Symmetry and Activity of the HgC_6H_6Hg Skeletal Vibrations

Vibration	Derived from C_6H_6	Symmetry	Activity
Deformation	(T_x, T_y)	E_{1u}	IR
Torsion	R_z	A_{2g}	Inactive
Tilt	(R_x, R_y)	E_{1g}	Raman
Stretch	T_z	A_{2u}	IR

IINS spectra (eg. in the tropyllium complexes in the previous chapter). There are, however, medium strength IINS bands at 202 and 287cm^{-1} in $CoHg_2(SCN)_6C_6H_6$ and at 227 and 287cm^{-1} in $NiHg_2(SCN)_6C_6H_6$, of which the former band has greater intensity. In the cobalt analogue, the IINS band at 282cm^{-1} is very poorly resolved. Now the tilt and stretch modes are generally at higher frequency than the torsion and deformations. The IR and Raman activity of these bands is indicated in Table 7.10.

As shown in Table 7.10 the bands at 200-230cm^{-1} can be assigned to the doubly degenerate tilt mode. This is reasonable since it is expected to be stronger in the IINS spectrum than the stretch. The tilt is expected to be Raman active and strong Raman bands were found. Coincident IR bands were also observed but it is possible that these IR bands are only coincident bands since there are very many IR bands in the 50-300cm^{-1} range. If they are not coincidental bands, then they may be due to a solid state effect. The stretch skeletal mode is assigned to the

Table 7.10: IR and Raman Bands Analogous to IINS Bands in 200-300cm^{-1} Region

Compound	IINS	IR	Raman
$CoHg_2(SCN)_6C_6H_6$	282(wm)	284(s)	-
	202(ms)	207(vs)	200(sb)
$NiHg_2(SCN)_6C_6H_6$	287(wm)	292(m)	-
	227(m)	221(s)	219(s)

weaker IINS band in the 280-290cm^{-1} region. This mode is only IR active and a strong IR counterpart exists at similar frequencies.

If the torsion and deformation can be similarly observed then it is possible that the D_{6h} symmetry description can describe the skeletal modes. At lower frequency there are two strong time-of-flight bands in $NiHg_2(SCN)_6C_6H_6$ Figure 7.12, at 63 and 107cm^{-1}. There is no IR or Raman analogue of the 63cm^{-1} band and thus it is reasonable to assign it to the torsional mode. The IINS band at 107cm^{-1} in $NiHg_2(SCN)_6C_6H_6$ and at 117cm^{-1} in the cobalt analogue is assigned to the IR active doubly degenerate deformation. They have IR analogues at 112 and 113cm^{-1} respectively. There are also weak Raman counterparts to these bands but these may only be coincidental since there are many Raman features in the 40-150cm^{-1} region.

There is a weak IINS feature at ~152cm^{-1} in both spectra. This is assigned to an Hg-S_2 deformation mode which has affected the electron density of the system so that the Hg-C_6H_6 distance has changed, and thus, allowed some associated proton motion to be observed in the IINS spectrum.

The torsion, assigned at 63cm^{-1} in $NiHg_2(SCN)_6C_6H_6$, is at a lower frequency than R_z, the torsion about the six fold axis in solid benzene assigned at 68cm^{-1} (section 7.2.2.) This may be reasonable if the intermolecular distances in solid benzene are somewhat larger than in the clathrate. The effect would to lower the torsional frequency, if the C_6H_6-Hg metal bonding was weak and if the benzene was able to move more easily in the clathrate void. In fact, the intermolecular distances in solid benzene calculated by Harada and Shimanouchi (6) from the crystal data of Bacon et al (5) are C·····H 2.85Å and H·····H 2.51Å whereas in $MHg_2(SCN)_6C_6H_6$ the Hg-$C_{C_6H_6}$ distance is 3.55Å (29). This would appear to give the benzene in the clathrate substantially more room.

The torsional mode of the benzene - Hg system can be used to calculate the effective force constant (EFC). Using the derived formula

$$\frac{N^2V_B}{2} = \frac{4\pi^2 I_r \bar{\nu}^2 C}{h}$$

$\frac{N^2V_B}{2}$, the effective force constant (EFC), can be calculated, though only for the nickel analogue since no time-of-flight data was available for the cobalt complex. The X-ray structure by Groenback and Dunitz (29) did not report C-C or C-H distances for the clathrate benzene and, thus, the atomic co-ordinates used by Favrot et al (38) are used to estimate the reduced moment of inertia, I_r. If C-C = 1.397Å and C-H = 1.084Å then $I_r = 295 \times 10^{-40}$gcm^2. Thus the EFC for the compound = 250kJmol^{-1}. It would be reasonable to give the multiplicity, N, a value of 6 from a study of the crystal structure. Thus the torsional barrier to rotation, V_B, can be estimated from the EFC ($N^2V_B/2$) to be 13.9kJmol^{-1}.

7.6 $C_6H_6Co_4(CO)_9$

7.6.1 Previous Results

Bor et al (39) studied the IR C-O stretching region of (arene)$Co_4(CO)_9$ compounds. This has been the only related vibrational study of this compound.

7.6.2. Results

Table 7.11 show the vibrational data from the study of $C_6H_6Co_4(CO)_9$. Unfortunately no Raman data was collected since the compound was black. Figure 7.15 shows 4H5 P(α,β) spectra collected at 130K. The scattering angles are 90° and 82°. Figure 7.16 is a BFDDIDO spectrum collected at liquid nitrogen temperature.

7.6.3 Discussion

$C_6H_6Co_4(CO)_9$ has C_{3v} symmetry and the vibrations of the molecule can be described as shown in Table 7.12

Table 7.12: C_{3v} Vibrational Analysis

C_{3v}	$C_6H_6Co_4(CO)_9$	$Co_4(CO)_9$	C_6H_6	M-C_6H_6	Activity
A_1	20	12	7	1	IR/R
A_2	12	8	3	1	-
E	32	20	10	2	IR/R

Thus the C_6H_6-($Co_4(CO)_9$) vibrations are described by $A_1 + A_2 + 2E$ symmetry. The form of these vibrations will be the torsion (A_2), deformation (E), tilt(E) and stretch (A_1). Unless the site symmetry implies otherwise, then no splitting of the double degenerate bands should be achieved

either in the framework vibrations or the benzene intramolecular vibrations.

Table 7.11: Vibrational Features of $C_6H_6Co_4(CO)_9$

4H5 (130K)	BFDDIDO (77K)	IR (77K)	FIR (77K)	Assignments
	737(m)	720(m)		ν_{11} CH o/plane deformation
	623(m)	614(vw)		ν_6 i/p ring deformation
		545(m)		Co-C-O deformation
		526(m)		Co-C-O deformation
	513(m)	510(w)		Difference band
		480(w)		Co-C-O deformation
	434(sh)			Unknown
		422(m)		Co-C stretch
	393(ms)	401(w)		ν_{16} o/plane ring deformation
		320(vw)	319(w)	Co-C stretch
	269(s)			Tilt (E)
	223(s)	220(m)	231(s)	Stretch (A_1)
185(mb)	177(sh)		183(w)	$Co_4(CO)_9$ deformations
140(w)			147(w)	
105(s)			97(w)	Deformation (E)
66(m)				Torsion (A_2)
40(msh)				Lattice mode

The vibrations of the molecule may be split into those involving the $Co_4(CO)_9$ moiety, the benzene intramolecular vibrations and the benzene-system skeletal vibrationals.

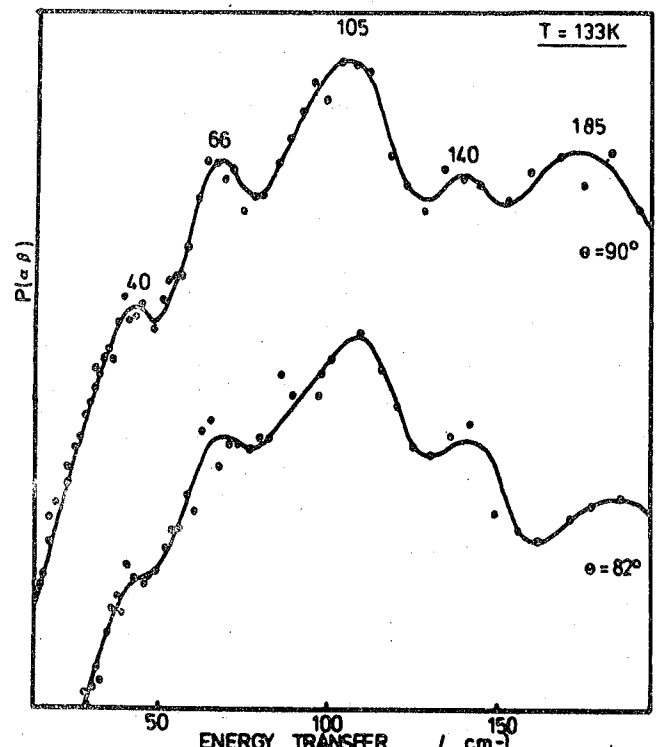

Figure(7.15) P(α β) data for $C_6H_6Co_4(CO)_9$

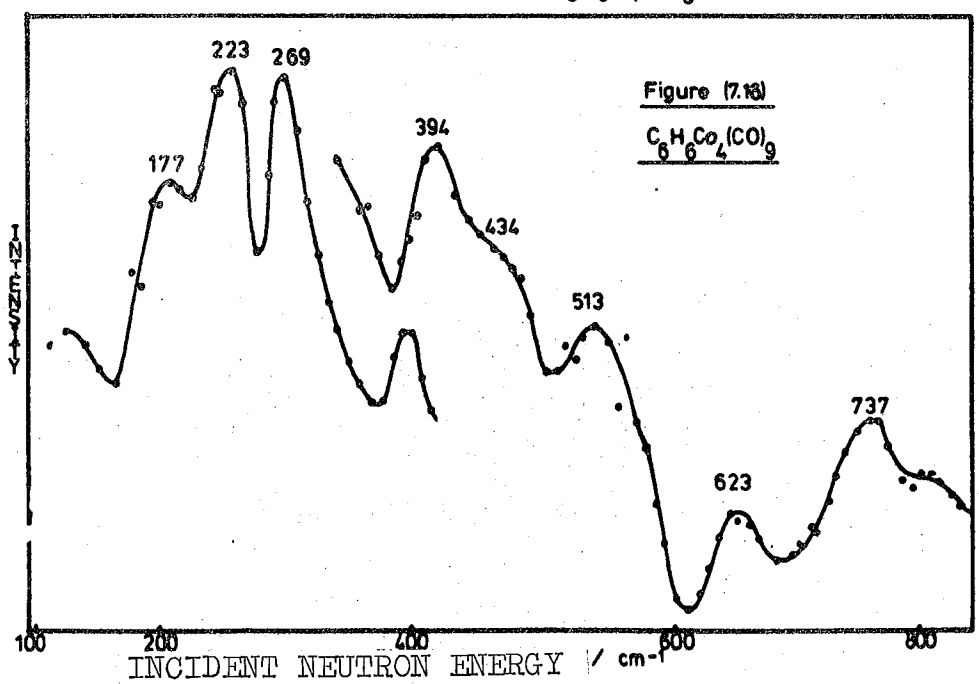

Figure (7.16)

$C_6H_6Co_4(CO)_9$

(a) Vibrations involved in the '$Co_4(CO)_9$' moiety

The carbonyl stretching vibrations lie outside the region of interest in the 1800-2100cm^{-1} range. In the IR spectrum, there are a number of bands indicative of MCO deformations and M-C stretches. They fall in the 450-700 cm^{-1} and 300-450cm^{-1} ranges respectively (33). The IR bands at 320 and 422cm^{-1} are tentatively assigned to MC stretches whereas the bands at 480, 526 and 545cm^{-1} are assigned to MCO deformations. These bands do not have IINS analogues. To achieve a full analysis of this region a single crystal study would have been necessary in the same manner as the $Re_2(CO)_{10}$ analysis by Adams and Hooper (40).

(b) Intramolecular benzene vibrations

The following assignments, in Table 7.13, of the benzene intramolecular vibrations, are made from a comparison with IINS data on benzene.

Table 7.13: Intramolecular Benzene Vibrations

Benzene IINS	$C_6H_6Co_4(CO)_9$		Assignment
	IINS	IR	
700(34)	737	720	ν_{11}
602(14)	623	614	ν_6
401(52)	394	401	ν_{16}

In the IR spectrum there is a medium intense band at 720cm^{-1} with a moderately intense IINS counterpart at 737cm^{-1} which is readily assigned to ν_{11}. This band is IR active under C_{6v} and C_{3v} symmetry where it is an A_1 mode. This

value of 737cm^{-1} is comparable with assignments of ν_{11} in Co-C_6H_6 matrices at 77K (41) where ν_{11} was measured at 765cm^{-1}. Since the Co-$C_{C_6H_6}$ distance in $C_6H_6Co_4(CO)_9$ was only 2.1Å (19) (the shortest M-$C_{C_6H_6}$ distance in these studied benzene complexes), then if this meant a strong M-C_6H_6 π-bond existed, a larger increase in ν_{11} would have been expected. In $C_6H_6Cr(CO)_3$ the Cr-$C_{C_6H_6}$ distance is approximately 2.2Å (42) but the increase in ν_{11} is ~113cm^{-1}. Thus the M-$C_{C_6H_6}$ distance cannot be taken as a true indication of the M-C_6H_6 bond strength in this instance. From our studies of $C_6H_6Co_4(CO)_9$ it was noticed that over a period of time the compound decomposed. This was shown by the black colour being replaced by a pink-blue colour due to oxidation. Thus it appeared that the benzene could be easily replaced in this novel compound. The small increase in ν_{11}, + 64cm^{-1}, may be an indication of a weak π-bond.

At lower frequency, a medium intense band in the IINS spectrum is assigned to ν_6 at 623cm^{-1}. This is an in-plane deformation which does not shift far from the free benzene value of 606cm^{-1}. This band is IR inactive in D_{6h} and C_{6v} symmetry but becomes IR active (E) under C_{3v} symmetry. The analogous 614cm^{-1} band in the IR spectrum is assigned to ν_6 indicating that the symmetry has been lowered. The strong IINS band at 394cm^{-1} is assigned to the out-of-plane ring deformation ν_{16} (E mode). It is IR inactive in D_{6h} and C_{6v} symmetry but active in C_{3v} symmetry. A weak IR analogue at 401cm^{-1} is tentatively assigned to ν_{16}.

It may be noted that there is a novel relative IINS intensity distribution in the 300-800cm^{-1} region of Figure 7.16

compared with the other benzene organometallic complexes studied. In the latter the relative IINS intensities of ν_{16}: ν_6: ν_{11} were approximately 50:10:40 and the FWHH of ν_{11} and especially ν_{16} were small in comparison with $C_6H_6Co_4(CO)_9$. The relative intensities are not given for $C_6H_6Co_4(CO)_9$, since it is difficult to select a flat background over the 300-800cm^{-1} range, however, it can be seen that the bands are not very well resolved. One possible reason is that, with only C_{3v} symmetry, there has been heavy mixing of the low frequency benzene intramolecular modes with M-C stretches and MCO deformations of the same symmetry in the 300-800cm^{-1} region producing a more complex spectrum.

(c) C_6H_6-$Co_4(CO)_9$ skeletal vibrations

In the IINS spectrum there are two strong bands at 269 and 223cm^{-1} which, because of strong intensity, are probably fundamental vibrations. The C_6H_6-$Co_4(CO)_9$ tilt is an E mode whereas the stretch is an A_1 mode. The latter will have a strong IR analogue since it involves a large dipole moment change. No IR activity was observed at 270cm^{-1} whereas a strong IR band was found at 231cm^{-1}. Thus the tilt is assigned to the 269cm^{-1} IINS band and the stretch to the 223cm^{-1} band in the IINS spectrum.

The IINS time-of-flight spectrum is quite complex with bands at 40,66,105,140 and 185cm^{-1}. The 40cm^{-1} feature varies in frequency with differing scattering angles and is assigned to a lattice mode. The 105, 140 and 185cm^{-1} bands all have IR counterparts so it is reasonable to assign the 66cm^{-1} band to the torsion, which is an A_2 mode and, therefore, IR inactive. It must be noted that the IINS intensity is not very high as usually associated with a torsional mode

in the IINS spectrum. The deformation, an E mode, is assigned to the strongest time-of-flight feature at 105cm^{-1}. The weaker bands at 140 and 185cm^{-1} are possibly deformation modes of the $Co_4(CO)_9$ unit with associated proton motion.

The low torsion frequency at 66cm^{-1} is reasonable since Gilson and Bernard reported that the barrier to rotation was very low (19(ref. 29)). They reported a value of less than 2.7kcalmol^{-1} (< 11.5kJmol^{-1}). The method by which this barrier was calculated was not stated.

The barrier to rotation can be estimated using the IINS data and the carbon co-ordinates of Bird and Fraser (19) and the average C-H band length used by Favrot et al (38). Using the equation (2.57) developed in Chapter 2 and, using a reduced moment of inertia of 293 x 10^{-40}gcm^2, the value of the effective force constant of the torsion can be calculated to be 273kJmol^{-1}. If the multiplicity, N, is estimated to be 6, the barrier to rotation, V_B, can be calculated to be 15.1kJmol^{-1} which is higher than the value of Gilson and Bernard. (To produce a value of V_B of < 11.5kJmol^{-1} one would need a torsional frequency of <55cm^{-1})

7.7 $C_6H_6U(AlCl_4)_3$

7.7.1 Previous Results

Cesari et al (18) measured the IR spectrum (nujol) at room temperature. Benzene intra-molecular vibrations were assigned to the 667,682 and 740cm^{-1} bands whereas bands at 480 and 550cm^{-1} were assigned to bridging halogen vibrations.

7.7.2 Results

Table 7.14 lists the data from our study and from that of Cesari et al (18).

Unfortunately no time-of-flight data was collected on $C_6H_6U(AlCl_4)_3$. The Raman spectrum was run at 8mW at room temperature. The IR and BFDDIDO spectra were collected at liquid nitrogen temperature. Figure 7.17 shows the BFDDIDO spectrum.

7.7.3 Discussion

C_6H_6 U $(AlCl_4)_3$ has C_s symmetry and thus $43A' + 35A''$ vibrations. Under C_s symmetry the following analysis is made in Table 7.15

Table 7.15: C_s Vibrational Analysis

C_s	$C_6H_6U(AlCl_4)_3$	$U(AlCl_4)_3$	C_6H_6	M-lig	Activity
A'	43	23	17	3	IR/R
A''	35	19	13	3	IR/R

The vibrations of the compound may be separated into those involving the $U(AlCl_4)_3$ group, the benzene intramolecular vibrations and the C_6H_6-$U(AlCl_4)_3$ skeletal framework modes.

(a) $U(AlCl_4)_3$ Vibrational analysis

The tetrahedral ion $(AlCl_4)^-$ has four Raman bands at 349, 146, 575 and 180cm^{-1} of $A_1 + E + 2T_2$ symmetry (43). Jones and Wood (44) reassigned the 575cm^{-1} (T_2) band to 495cm^{-1} and this was supported by IR work of Carlsson (45) which found a band at 495cm^{-1}. Nakamoto (46) and Ferraro(33) list data on the bridging and terminal stretching chloride vibrations. Generally the former stretches are found at

Table 7.14: Vibrational Data and Assignments for $(C_6H_6)U(AlCl_4)_3$

BFDDIDO (77K)	IR (77K) (KBr)	IR (RT) (Nujol)	FIR (77K)	Raman (RT)	IR (RT) (18)	Assignment
790(s)	806(s)	800(m)				ν_{11}CH o/p def.
733(sh)	740(w)	740(w)			740	
	690(s)	680(m)			682	$AlCl_4$ vibs.
		671(s)			667	
610(ms)	600(wsh)			600(mb)		ν_6 i/p ring def.
	566(ms)	560(sh)		558(w)	550	$AlCl_4$ vib. (split T_2)
	492(s)			494(w)	480	
534(m)						Difference band (C_6H_6)
479(wsh)						
414(vs)	415(sh)			408(w)		ν_{16} o/p ring def.
	385(sh)					$AlCl_4$ vib. (A_1)
	342(m)		340(mb)			
287(w)						Combination (202+75)
202(vs)						Tilt skeletal (E)
183(m)			180(wb)	188(wm)		Stretch skel. (A_1)
			170(w)	169(m)		$AlCl_4$ vib.(T_2)
			150(wb)	150(w)		$AlCl_4$ vib.(E)
104(sh)			109(mb)	109(s)		Def. Skel.(E)
75(s)						Torsion skel. (A_2)

lower frequency because the sharing of the halogen between two metals causes the bond to be weaker than found in terminal M-Cl bonds. However, in this study it will not

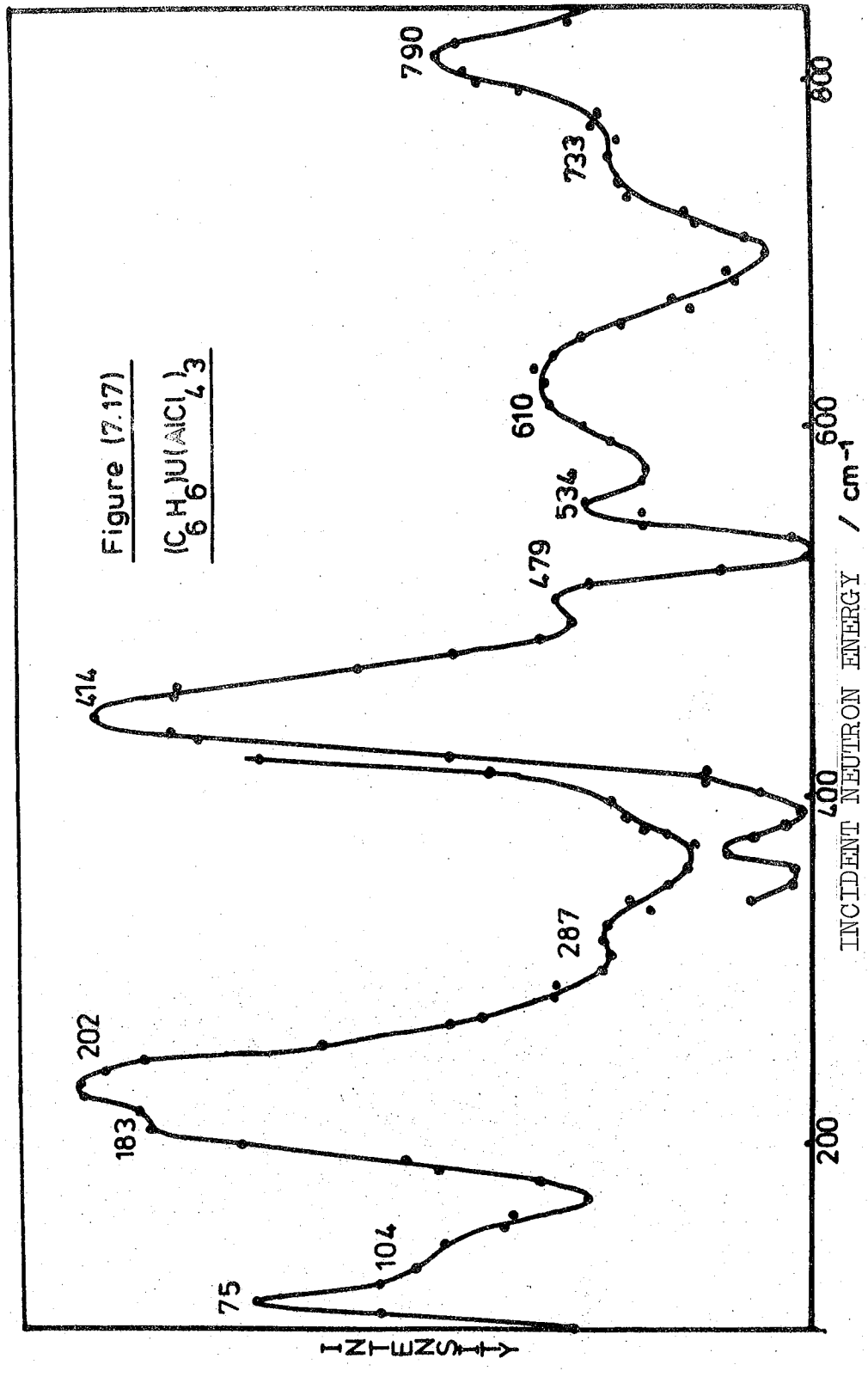
Figure (7.17)
$(C_6H_6)U(AlCl_4)_3$
INTENSITY
INCIDENT NEUTRON ENERGY / cm^{-1}
200
400
600
800
75
104
183
202
287
414
479
534
610
733
790

be strictly correct that one could split the vibrations of the '$AlCl_4$' unit up into specific individual stretches, ie. terminal and bridging motions. Harrison et al (47) assign IR bands at 496, 293 and 287 cm^{-1} indicative of Al-Cl modes in $C_5H_5SnClAlCl_3$. The authors believed the compound contained one Sn-Cl-Al bridge. Rytter et al (48) studied alkali metal-$AlCl_4$ species. The bonding to the cation destroyed the Td symmetry of $AlCl_4^-$ producing a local C_{2v} symmetry. This split the high frequency T_2 mode. They observed Raman bands at 512,498 473,348,182 and 119cm^{-1} in this species which contained two M-Cl-Al bonds.

Cesari et al (18) assign strong IR bands at 480 and 550cm^{-1} to U-Cl-Al stretches. It is felt that, more correctly, these vibrations, found in our study at 492 and 566cm^{-1}(KBr) are assigned to the split IR active T_2 mode derived from the $AlCl_4$(Td) species and are Al-Cl stretching vibrations of the $AlCl_4$ system rather than just the bridging chloride part. However, only two bands were found in the IR spectrum whereas three were identified by Rytter et al in the study of M($AlCl_4$) species (48). The two lower frequency IR bands at 340 and 385cm^{-1} are assigned to the A_1 Al-Cl stretch which has been split into two bands due to the two types of bridging chloride present in the molecule. At even lower frequency IR and Raman bands at 170 and 150cm^{-1} are assigned to the two $AlCl_4$ deformation bands derived from the E and T_2 modes from $(AlCl_4)^-$. The lowering of the symmetry to a local (C_{2v}) or molecular (C_s) description allows the bands to be IR and Raman active.

It may also be noted that bridging UClU vibrations have been assigned in the 170-220cm^{-1} IR/Raman region of

$UCl_4 2(CNCl)$ (49) at a similar frequency to the bands at 170 and 150cm^{-1} in $(C_6H_6)U(AlCl_4)_3$.

(b) Intramolecular benzene vibrations

The following assignments, in Table 7.16, of the benzene intramolecular vibrations are made from a comparison with IINS data on benzene alone.

Table 7.16: Intramolecular Benzene Vibration (cm^{-1})

Benzene Only IINS	$C_6H_6U(AlCl_4)_3$			Assignment
	IINS	IR	Raman	
700(34)	790(26)	806	-	ν_{11}
606(14)	610(19)	600	600	ν_6
400(52)	414(55)	415	408	ν_{16}

The values in brackets are an indication of the relative intensities, in %, of the bands in each IINS spectrum.

The very strong dominating IINS band at 416cm^{-1} is assigned to ν_{16}, the out-of-plane ring deformation. In D_{6h} symmetry this band is totally inactive but is totally active in C_{3v} or C_s symmetry. Weak IR and Raman bands at 415 and 408cm^{-1} respectively are an indication of the loss in symmetry. The medium intense IINS band at 610cm^{-1} can be readily assigned to ν_6, the in-plane ring deformation, which has only very slightly moved up in frequency from free benzene. In D_{6h} symmetry, this band is Raman active only and a medium intense Raman band was observed at 600cm^{-1} coincident with a weak IR band which is again possibly

indicative of the lowering of the benzene symmetry. In the IINS spectrum a strong band was observed at 790cm^{-1} which is assigned to ν_{11}, the out-of-plane CH deformation found at 700cm^{-1} in solid benzene (IINS) and at 671cm^{-1} in benzene vapour (IR). This large shift of 117cm^{-1} is due to complexation. The U-$C_{C_6H_6}$ distance is 2.91Å, much longer than the Co-$C_{C_6H_6}$ distance in $C_6H_6Co_4(CO)_9$, however, ν_{11} increased in frequency by only 64cm^{-1} in the latter case. The benzene is possibly more perturbed in the uranium complex because the available uranium 5'd' orbitals will be spatially more extensive than the 3'd' orbitals of cobalt. A strong IR counterpart of the 790cm^{-1} IINS band exists at 806cm^{-1}. This was expected since the band is strongly IR active under all symmetries.

There are a number of weaker IINS features which can be tentatively assigned. The two bands at 479 and 534cm^{-1} may be due to difference bands involving intramolecular benzene vibrations and lattice vibrations. Similar bands have been assigned in the same region in solid benzene and in the other benzene complexes. The weak broad IINS band at 730cm^{-1} has a weak IR counterpart. No comparable IINS band has been discovered in this region in the other benzene complexes.

(c) Benzene - $U(AlCl_4)_3$ skeletal vibrations

These vibrations will take the form shown in Figure since the molecule could be approximated to C_6H_6 UX_3. At low frequencies in the IINS spectrum, Figure 7.17, the broad band centred at ~ 200cm^{-1} is found to dominate. Using the du Pont 310 curve resolver, two components can be determined

with the stronger at 202cm^{-1} and the weaker at 183cm^{-1}. Of the skeletal vibrations, the C_6H_6-UX_3 stretch is expected to be strongly IR and Raman active due to large changes in polarizability and dipole moment. No IR or Raman bands exist at ~200cm^{-1} though there are such bands at 180 and 188cm^{-1} respectively. Therefore the doubly degenerate tilt mode can be assigned to the IINS band at 202cm^{-1} and the stretch to the weaker IINS band at 183cm^{-1} and in the IR and Raman spectra at 180 and 188cm^{-1}. At lower frequency the doubly degenerate deformation is tentatively assigned to the weaker 104cm^{-1} IINS shoulder whereas the greater intensity at 75cm^{-1} is assigned to the torsion of the C_6H_6 about the C_6H_6-U bond. The latter is IR and Raman inactive in C_{3v} symmetry since it is an A_2 mode whereas there are weak IR and Raman components of the deformation. No calculations are carried out on the torsional barrier due to the tentative nature of these final assignments due to the lack of IINS time-of-flight data.

(d) Further discussion

Since no splitting of the intramolecular benzene vibrations was found, especially in the infra-red, it is felt that the benzene must be 'seeing' at least C_{3v} symmetry rather than the overall C_s molecular symmetry. Thus the vibrations can be interpreted in the context of a $C_6H_6UX_3$ molecule.

Finally, it must be noted that there would appear to be an anomaly in the 660-700cm^{-1} region of this study. Cesari et al (18) reported IR (nujol) bands at 667 and 682cm^{-1} indicative benzene modes. Similar IR(nujol) bands existed in our study at 671 and 680cm^{-1}. In the IR (KBr) spectrum only a single strong broad band at 690cm^{-1} was found. No

relevant bands existed at these frequencies in the IINS spectrum and ν_{11} was readily assigned at 790cm^{-1}. The possible explanations of these bands in the 660-700cm^{-1} region are (i) They involve the $U(AlCl_4)_3$ moiety (one stretching band derived from the T_2 $AlCl_4$(Td) unit was not observed at lower frequency (ii) They involve ν_{11} in free benzene caused by the decomposition of the compound (The compound is immediately decomposed in air and by moisture). Studies of $(PdAlCl_4C_6H_6)_2$ and $(PdAl_2Cl_7C_6H_6)_2$ (section 7.10) show the presence of similar IR bands in the 700cm^{-1} range. In $(PdAlCl_4C_6H_6)_2$ similar bands exist at less than 600cm^{-1} indicative of '$AlCl_4$' species and extra bands also appear at 671 and 755cm^{-1}. In $(PdAl_2Cl_7C_6H_6)_2$ bands can be assigned at less than 670cm^{-1} indicative of 'Al_2Cl_7' species yet extra bands were found at 672, 690 and 752cm^{-1}. Unfortunately, no supporting vibrational work has appeared in the literature concerning complexed '$AlCl_4$' and 'Al_2Cl_7' since studies have been concentrated on $AlCl_4^-$ and $Al_2Cl_7^-$ ions. However, since these extra bands appear in these compounds at similar frequencies and because, in both cases, they do not have IINS analogues, they are assigned to vibrations of the complexed '$AlCl_4$' and 'Al_2Cl_7' species.

7.8 $(RuX_2C_6H_6)_2$ X = Cl, Br

7.8.1 Previous Results

Bennett and Smith (23) listed the RuCl stretching frequencies in the IR spectrum for $(RuCl_2C_6H_6)_2$. These bands were comparable to those reported by Zelonka and Baird (17), who also listed the RuBr stretching frequencies for

$(RuBr_2C_6H_6)_2$. Winkhaus and Singer (50) also reported the IR spectrum of the chloride analogue in the 290-3040cm^{-1} range. From these studies it was postulated that there were terminal and bridge bonded chlorine atoms and that the benzene was π-bonded to the Ru atoms.

7.8.2. Results

Again no 4H5 data was collected on these two complexes. Table 7.17 lists the IINS, IR and Raman data from this study and from that of the other studies (17,23,50). The Raman laser power used was 8mW. The BFDDIDO spectra are shown in Figure 7.18.

7.8.3. Discussion

Unfortunately, no crystal structure analyses have been carried out on these species but they have been characterized (29) and the structure, shown in Figure 9.6, is suggested to have C_{2h} symmetry. An analysis of the vibrations under this symmetry is presented in Table 7.18.

Table 7.18: Vibrational Analysis of $(RuX_2C_6H_6)_2$ Under C_{2h} Symmetry

C_{2h}	$(RuX_2C_6H_6)_2$	C_6H_6(x2)	Ru_2X_4	$C_6H_6(Ru_2X_4)C_6H_6$	Activity
A_g	25	18	5	2	R
B_g	17	12	1	4	R
A_u	18	14	2	2	IR
B_u	24	16	4	4	IR

The vibrations can be categorised into the Ru_2X_4 vibrations, the intramolecular C_6H_6 vibrations and the C_6H_6 - Ru skeletal modes.

Table 7.17: Vibrational Data on $(RuX_2C_6H_6)_2$ Complexes

$(RuCl_2C_6H_6)$							$(RuBr_2C_6H_6)_2$					
BFDDIDO (77K)	IR (77K)	FIR (77K)	Raman (RT)	IR(50) Nujol	IR(17) Nujol	IR(23) Nujol	BFDDIDO (77K)	IR (77K)	FIR (77K)	Raman (RT)	IR(17) Nujol	Assignments
870(s)	842(s)			842(s)			866(s)	833(s)				ν_{11} CH out-of-plane deformation (2 x 380/387cm^{-1})
	800(wsh)							800(wsh)				
										755(m)		Unknown
	721(w)							723(w)		710(w)		(2 x 370/380 cm^{-1})
635(s)	610(w)		611(vw)	616(s)			631(s)	611(w)		610(w)		ν_6 in-plane ring deformation
439(vs)	440(w)		450(vw)	439(wm)			439(vs)	437(w)		445(w)		ν_{16} out-of-plane ring deformation
										396(m)		Unknown
387(vs)	385(m)			383(vs)			380(vs)	372(m)	362(m)			Tilt skeletal mode
	330(w)			333(s)								RuCl stretch/RuBr stretch
	296(m)	300(sb)		315(sb)								Stretch skeletal mode
	285(sh)	286(ssh)		292(mb)	295	295			282(s)			RuCl stretch/RuBr stretch
287(m)			272(m)				273(w)			271(w)		Stretch skeletal mode
	263(w)	263(vs)	263(m)		256	259			264(m)			RuBr stretch (I. Red)
	250(w)	250(s)			248	248		257(wsh)	257(w)			RuClRu stretch (I. Red)
			244(mb)									RuClRu stretch (Raman)
223(m)							206(m)					Combination band (?)
									209(vs)			RuBrRu stretch (I. Red)
									206(sh)		203	
										200(w)		RuBrRu stretch (Raman)
									190(vs)			RuBrRu stretch (I. Red)
									183(sh)		182	
										168(w)		Ru-BrRu stretch (Raman)
168(ms)		163(m)	163(wm)				150(m)		157(m)			Deformation skeletal mode
142(sh)		151(vs)					139(sh)		146(m)			RuX deformation
		126(vs)							117(vs)			
									105(m)	103(wm)		RuX deformations
			91(m)						89(sh)	88(m)		
		68(ssh)							82(s)	81(ms)		
							67(s)					Torsion skeletal mode
67(s)			38(s)							56(s)		Lattice mode

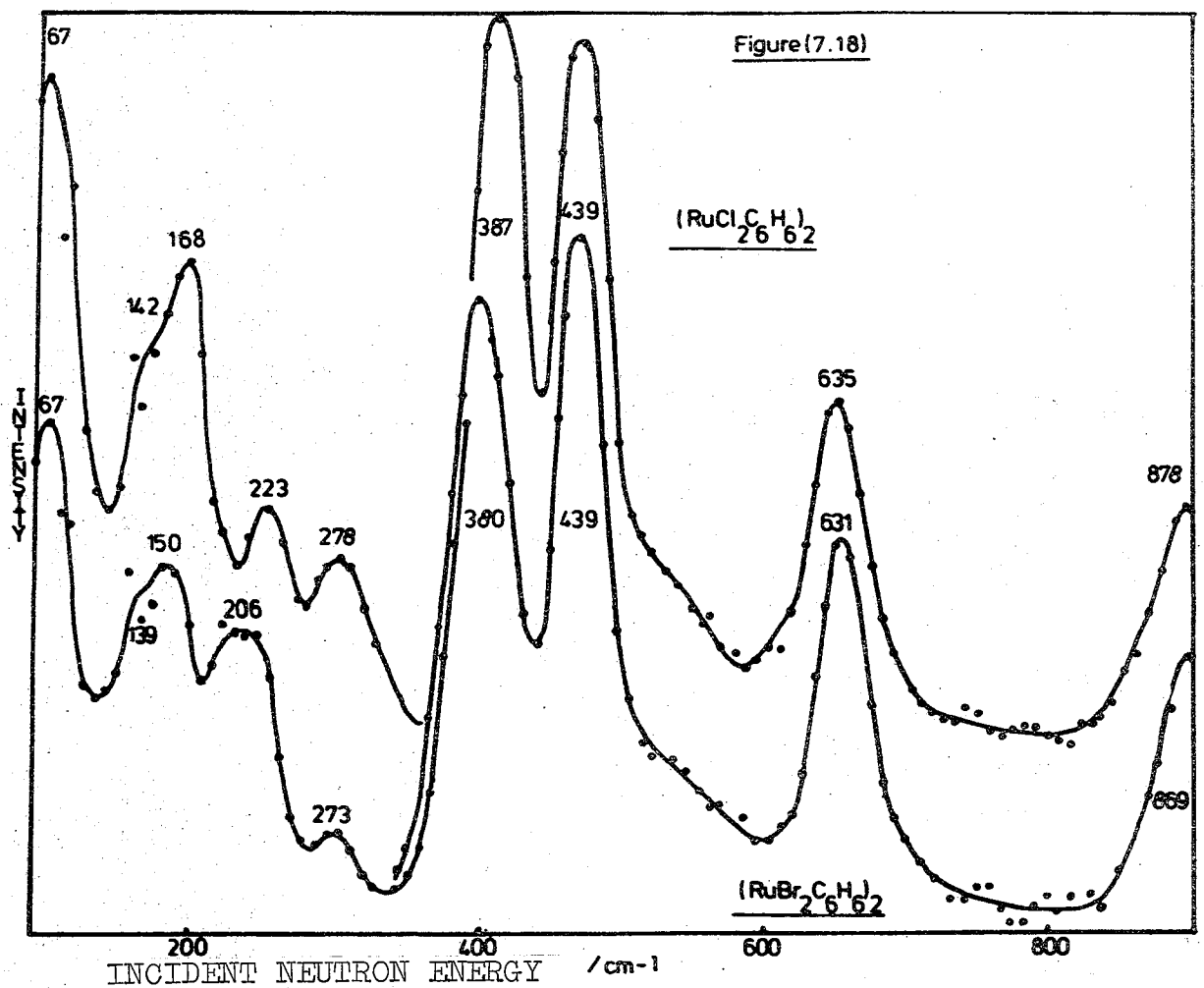
Figure (7.18)
67
168
142
67
223
278
150
139
206
273
387
439
380
439
635
631
878
869
(RuCl2C6H6)2
(RuBr2C6H6)2
INTENSITY
200
400
600
800
INCIDENT NEUTRON ENERGY /cm-1

(a) Vibrations of the Ru_2X_4 moiety

For the Ru_2X_4 it may not be strictly correct that the vibrations of the M-X-M and M-X species could be described independently since, no doubt, any one particular stretch will probably involve motion of the other type. However, generally from a review of M-X and M-X-M vibrations (33) the following can be surmised:-

Stretches	Region (cm^{-1})
M-Cl (terminal)	250-380
M-Br "	200-280
M-Cl-M (bridged)	250-330
M-Br-M "	180-220

Further for any one system, the bridging halide vibrations are found at lower frequency than the respective M-X (terminal) stretches. This was substantiated by the IR study of $(Ru(CO)_3X_2)_2$ species (51) (of C_{2h} symmetry) where X = Cl or Br. The following assignments were made:

	terminal	Bridged (cm^{-1})(51)
$(Ru(CO)_3Cl_2)_2$	331	290, 260
$(Ru(CO)_3Br_2)_2$	234	211, 195

An examination of the above ranges in the IR and Raman spectra of the arene compounds indicates that the bands are non-coincident (except for the 263cm^{-1} bands in $(RuCl_2C_6H_6)_2$). This is further evidence that the molecule can be described in terms of C_{2h} symmetry as postulated by previous authors (17,23). The non-coincidence of the bands implies that there is a centre of symmetry within the molecule. The IR work of Zelonka et al (17) and Bennett et al (23), on $(RuCl_2C_6H_6)_2$, only found 3 IR bands in the 180-340cm^{-1} range whereas this

work found 5 IR bands and 2 Raman bands of which only one was coincident ($263cm^{-1}$). Zelonka et al (17) reported only 2 IR bands in the $150-300cm^{-1}$ range in the bromo analogue but this work found 4 IR bands and 2 non-coincident Raman bands. The Raman bands in $(RuBr_2C_6H_6)_2$ were weaker than in $(RuCl_2C_6H_6)_2$. Table 7.19 lists the assignments made using the above previous data.

Table 7.19: IR and Raman Ru-X Stretch Bands

Stretch	$(RuCl_2C_6H_6)_2$		$(RuBr_2C_6H_6)_2$	
	Our Work	Previous Work (17,23)	Our Work	Previous Work (17)
'Terminal' Ru-X stretch	330(IR) 296(IR) 285(IR) 263(R)	295(IR)	282(IR) 257/264(IR) 206/209(IR)	203(IR)
'Bridged' RuXRu stretch	263(IR) 250(IR) 244(R)	256(IR) 248(IR)	200(R) 183/190(IR) 168(R)	182(IR)

At lower frequency there are a number of strong IR and Raman bands in the $70-150cm^{-1}$ region. They are non-coincident in the chloride compound, though coincident in the bromide. No IINS bands are found in this region and they are thus tentatively assigned to RuX_BRu and X_tRuX_B deformation bands (B = bridging, t = terminal). No similar assignments were discussed in the literature. However in L_2MX_2 species XMX deformations have been found at $\sim 170cm^{-1}$ in IR spectra. For example, in Py_2PdBr_2 at 99 and $122cm^{-1}$ and Py_2PdCl_2 at

122 and 166cm^{-1} (52,53).

(b) Intramolecular benzene vibrations

The intramolecular benzene vibrations are assigned in Table 7.20. This was achieved by comparing the IINS data with that of benzene. The values in brackets are the relative intensities of the bands in each spectrum.

Table 7.20: Intramolecular Benzene Vibrations

Benzene Only	$RuCl_2C_6H_6$			$RuBr_2C_6H_6$			Assignment
IINS	IINS	IR	R	IINS	IR	R	
700(34)	870(24)	842	-	866(26)	833	-	ν_{11}
602(14)	635(28)	610	611	631(28)	611	610	ν_6
401(52)	439(48)	440	450	439(46)	437	445	ν_{16}

The most notable point is that ν_{11} can be assigned at such a high frequency. The evidence for this is that there is only a single band in the IINS spectrum above ν_6 at ~630cm^{-1}. Further, the strongest IR band occurs @ 840cm^{-1} indicative of the IR active ν_{11}.

ν_6, assigned to the strong IINS bands at 630-635cm^{-1}, has IR and Raman equivalent bands. This $D_{6h}(E_{2g})$ band is only Raman active in D_{6h} and C_{2h} symmetry. Thus the benzene intramolecular modes would appear to be 'lying' in a different symmetry. It would be quite plausible that it could be C_{3v} since each benzene is part of a '$C_6H_6RuCl_3$' unit because each ruthenium is co-ordinated to three chloride atoms. This is further supported by the assignment of ν_{16} to 440cm^{-1} in the IINS, Raman and IR spectra. In D_{6h} symmetry this

band is an E_{2u} mode which is Raman and IR inactive, in C_{2h} symmetry it should be only IR active but in C_{3v} symmetry this mode is IR and Raman active. Thus C_{3v} (or less) symmetry must prevail in the solid state to describe such intramolecular benzene vibrational activity rather than the true overall molecular C_{2h} symmetry.

(c) C_6H_6-(Ru_2X_4) skeletal vibrations

Table 7.21 shows the activity of the skeletal vibrations under C_{6v}, C_{2h}, C_{3v} and C_s symmetry. These vibrations will take the form shown in Figure 6.15. It is presumed that the motions of the benzene units are not coupled.

Table 7.21: Skeletal Vibration Symmetry and Activity

Skeletal Vibration	C_{6v}	C_{2h}	C_{3v}	C_s
Torsion	A_2(-)	A_g(R)	A_2(-)	A"(IR/R)
Symmetric Stretch	A_1(IR/R)	A_g(R)	A_1(IR/R)	A'(IR/R)
Deformation	E_1(IR/R)	'2Bu'(IR)	E(IR/R)	A'+A"(IR/R)
Tilt	E_1(IR/R)	'2Bu'(IR)	E(IR/R)	A'+A"(IR/R)

The tilt and stretch modes are expected to lie at higher frequency than the torsion and deformation modes. Further, the tilt and torsion bands will have greater IINS intensity. In the IINS spectra there are strong bands at 380-390cm^{-1} and medium intense bands at ~280cm^{-1}. There is a strong IR analogue of the higher frequency IINS band but no Raman counterpart whereas there is a Raman analogue of the medium intense IINS band but no IR counterpart. This

non-coincidence in the IR and Raman spectra implies that the skeletal modes can be described in terms of C_{2h} symmetry. Further, from the particular activity and IINS intensity of these vibrations it can be assumed that the IINS bands at 380-390cm^{-1} can be assigned to the doubly degenerate tilt modes and the ~ 280cm^{-1} IINS bands to the stretching mode. With C_{2h} symmetry there was a possibility that some splitting of the tilt mode could take place but this was not observed in the IR or IINS spectra.

In C_{2h} symmetry then the deformation would be only IR active. This band is expected in the 100-200cm^{-1} IINS region and to be of some intensity, since it is an E mode. The IINS bands at 168cm^{-1} and 150cm^{-1} are assigned to the deformation in the chloride and bromide complexes respectively. Each has a medium strength IR congener. Since the tilt mode was not split in any way it is felt that the doubly degenerate deformation would also not split, so the weak shoulder in the BFDDIDO spectra at 140cm^{-1} in the complexes, which has strong IR counterparts is probably due to some associated proton motions due to mixing with a ruthenium-halide deformation. In the IINS spectra, a band of weak-medium intensity is found at 220cm^{-1} in both spectra which is not IR or Raman active. This band is assigned to a difference band involving, for example, the two skeletal E modes, ie. 387-168 = 219cm^{-1} and 380-150=230cm^{-1}.

The assignement of the torsional mode, due to the rotation of the benzene about their six-fold axes, cannot be made due to the lack of time-of-flight data. There does appear to be some intensity at ~67cm^{-1} in both IINS spectra, but these bands cannot be assigned with confidence.

In conclusion, the molecules seem to show C_{2h} symmetry characteristics in the Ru_2X_4 and skeletal vibrations whereas the intramolecular benzene vibrations are exercised under C_{3v} symmetry.

7.9 $(SbCl_3)_2 C_6H_6$

7.9.1 Previous Studies

$(SbCl_3)_2C_6H_6$ had been studied by many methods but the structure is still a matter of much conjecture.

N.M.R. studies (54) showed that there was no rotation of the benzene ring, about any axis, due to the lack of change in the line width with temperature in the -40-190°C range. The authors suggested that the benzene molecules were isolated from one another by an $SbCl_3$ lattice and that negligible complexing took place. N.Q.R. studies (55) analyzed the degree of $SbCl_3$ pyramidal distortion but no change on complexing was found. It was postulated that the chlorine atoms were not bonded to the benzene molecule. An Sb shift suggested an Sb-C_6H_6 interaction through the π-orbitals. Further studies (56) indicated that two inequivalent Sb positions were taken up in the complex and that two SbCl bands were different from the other four. C_i or C_1 symmetry was assigned to the molecule. They suggested the chlorine atoms took part in the complexation.

The first vibrational study postulated the $SbCl_3$-C_6H_6 complex (57) and this was followed by Raskins work (58-60) which looked at the intramolecular benzene vibrations in $(SbCl_3)_2C_6H_6$. It was suggested that an Sb-C_6H_6 π-complex was formed. Daasch (61) postulated the complex had C_{2v} symmetry from the intensification of certain IR bands of

the complex, in solution and as a solid. Another IR study (62) found little spectral difference between solid benzene and solid $(SbCl_3)_2C_6H_6$. C_s, C_{2v} or C_1 symmetry were postulated. Corriu et al (63) reviewed the earlier work and from their own n.m.r. and IR studies showed that the complex was asymmetrical with probably C_s symmetry, shown in Figure 9.8. The authors did note that different dipole moments for the C_6H_6-$SbCl_3$ system had been found and that they lay in the 3.75-3.93 debye region whereas $SbCl_3$ itself had a dipole moment which had been reported in the region of 2.5-4.1 debye. Corriu et al felt that the dipole moment in $(SbCl_3)_2C_6H_6$ indicated an asymmetrical structure. Contrary to this, a recent study of $SbCl_3$ in various media including benzene implied that a dipole-free quasi-molecule with the $SbCl_3$ units arranged in a 'ethane-like' way was formed in solution (64). Unfortunately, no comment was made on earlier studies in the solid state.

7.9.2 Results

Table 7.22 shows the data from this study and of others. The time-of-flight data was collected at 130K. The BFDDIDO and IN1B spectra were collected at liquid nitrogen temperature. The Raman laser power was 100mW at room temperature. Figure 7.19 shows the 4H5 time-of-flight data collected at 82° and 90° scattering angles. Figures 7.20 and 7.21 show the BFD spectra.

7.9.3 Discussion

The vibrations of the complex can be split into those involving $SbCl_3$ 'lattice', the benzene intramolecular modes and the benzene-$(SbCl_3)_2$ framework vibrations. Previous

Table 7.22: Vibrational Data on $(SbCl_3)_2C_6H_6$

$SbCl_3$			$(SbCl_3)_2C_6H_6$					$(SbCl_3)_2C_6H_6$							Assignment
IR (65)	Raman (66)	Raman (58)	IR (62)	IR (63)	IR (61)	Raman (67)	Raman (59)	AH5 (130K)	BFDDIDO (77K)	INIB (77K)	IR (77K)	FIR (77K)	Raman (RT)	IR(RT) Nujol	
				1176(m)										1177(m)	υ_9 in-plane CH deformation
			1151	1150(m)										1151(m)	υ_{15} in-plane CH deformation
				1145(w)	1142(m)					1116(vsb)					υ_{18} in-plane CH deformation
				1030(s)										1030(sh)	υ_{12} in-plane CH deformation
			1008	1015(w)	1008(m)									1010(sh)	υ_1 in-plane ring deformation
					990(sh)					993(vs)					
			985	985(m)	987(m)		988(vs)							985(m)	
				980(m)	970(sh)									978(sh)	υ_{17} out-of-plane CH deformation
				875(s)						861(s)				873(m)	υ_{10} out-of-plane CH deformation
				870(w)			870(vw)							862(w)	Unknown
				795(s)			734(vw)							773(w)	
			713	700(vs)					723(vs)	721(vs)				725(vs)	υ_{11} out-of-plane CH deformation
														672(sh)	2 x 333cm^{-1}
							603(m)		615(m)	604(m)				614(sh)	υ_6 in-plane ring deformation
							578(w)								Unknown
								390(vs)	401(vs)	416(vs)				409(w)	υ_{16} out-of-plane ring deformation
						363(m)	360(wm)					369(m)			
377	360	375				349(vs)	350(s)					351(m)	359(sh)		$SbCl_3$ stretches
						340(m)	340(m)					346(m)	344(vw)		
						324(m)	322(m)				330(sh)	333(vs)			
356	320	343				312(m)	311(ms)				310(sh)	312(s)	319(vs)		
						306(m)						303(msh)			
											270(mb)	270(sh)			Tilt and stretch skeletals
								240(vw)	236(w)						(E) (A)
													172(vs)		
164	165	164				160(ms)	161(m)					163(s)			$SbCl_3$ deformations
													152(s)		
												144(ms)			
						141(sh)	140(m)		142(sh)			138(ms)	140(s)		
128	134	134				136(m)									
						130(vw)									
						124(vw)	120(vw)	124(s)	125(s)						deformation skeletal (E)
						108(w)	103(w)								
													96(m)		$SbCl_3$ deformations
						86(w)	86(w)	88(w)				87(m)	84(w)		
						74(m)									Torsion skeletal (A_2)
						67(vw)	69(m)	65(m)					64(vs)		
						54(m)		50(m)				58(m)	51(vs)		
						47(m)	43(m)						38(vs)		Lattice modes
							23(w)	27(sh)							

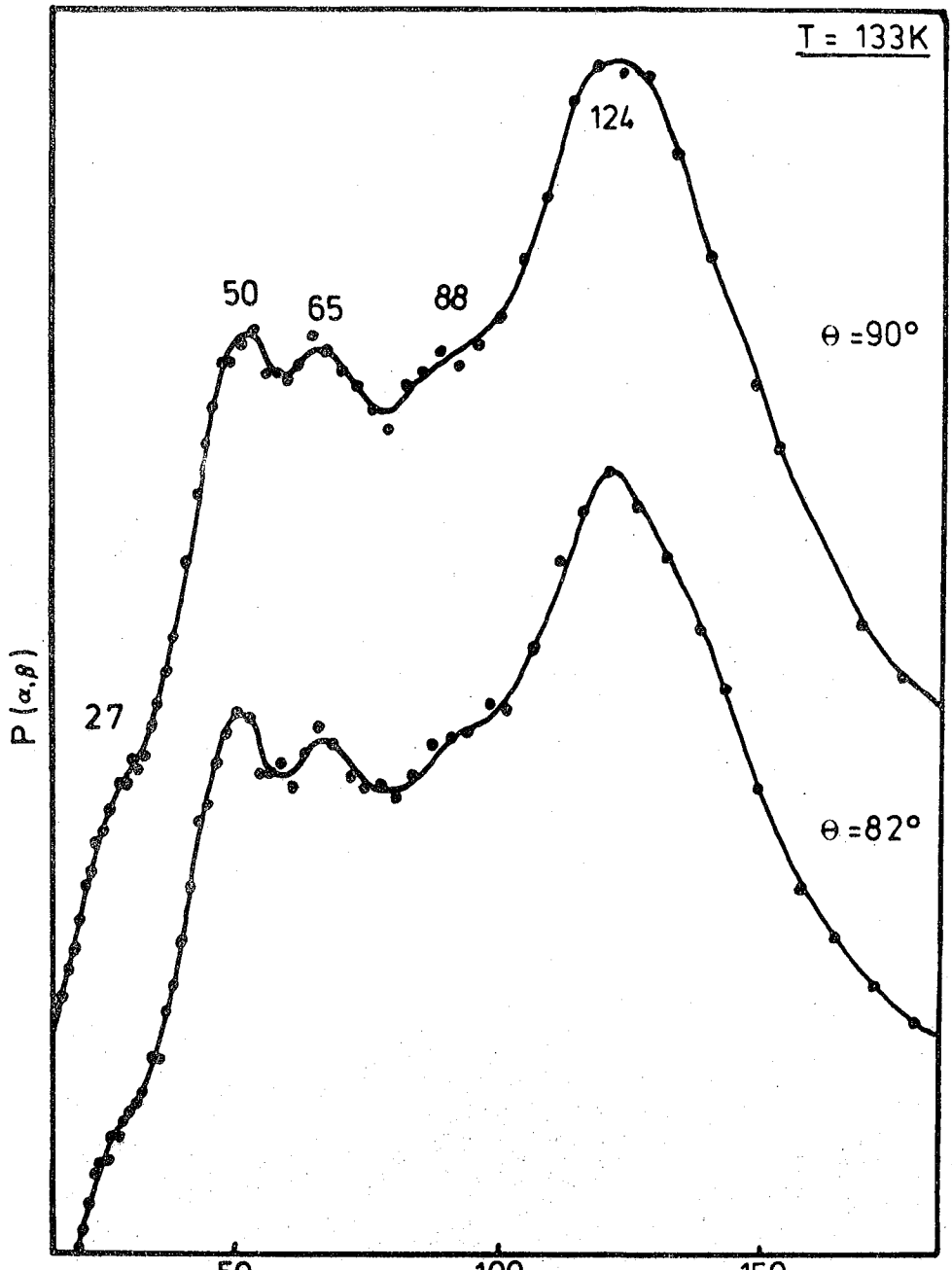

Figure(7·19) P(α,β) data for $(SbCl_3)_2C_6H_6$-

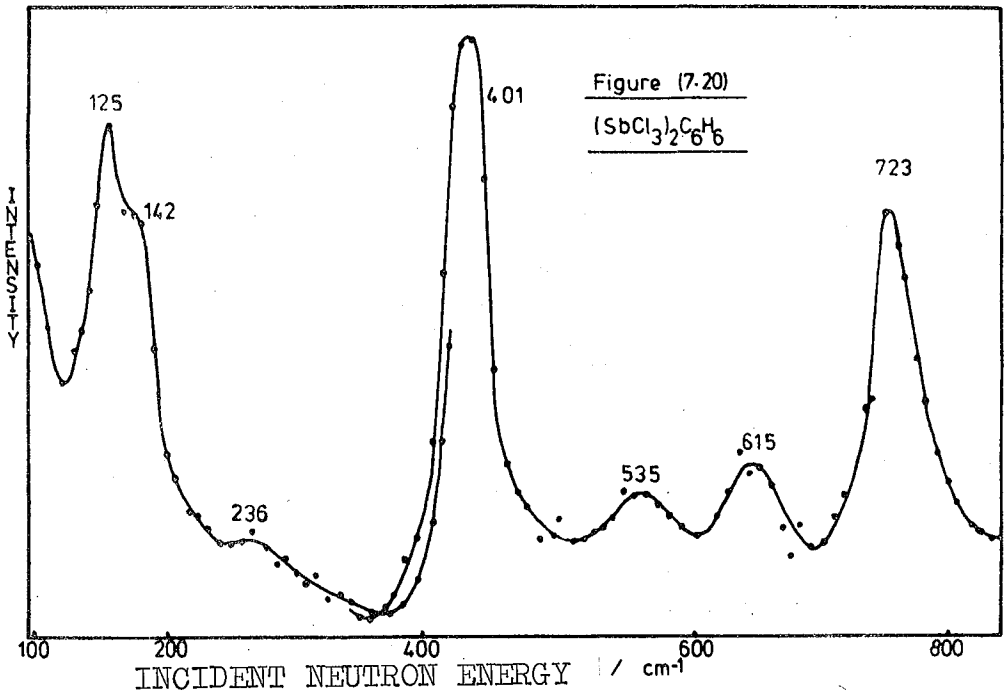

Figure (7.20)

$(SbCl_3)_2C_6H_6$

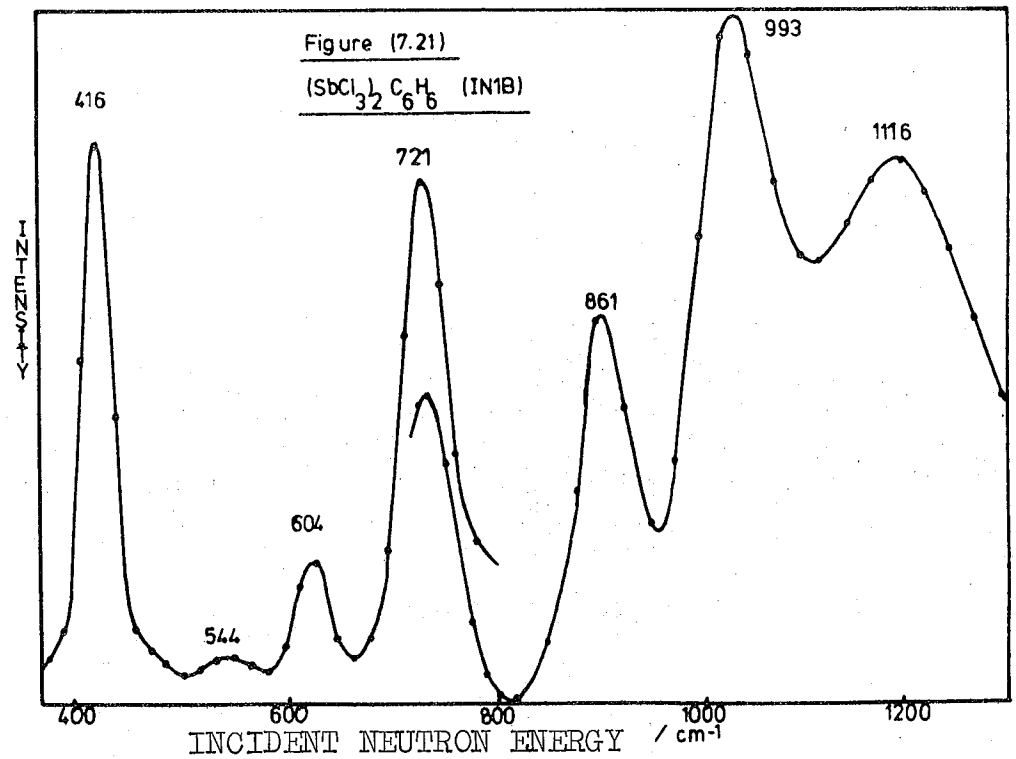

Figure (7.21)

$(SbCl_3)_2 C_6H_6$ (IN1B)

work presented favours a low complex symmetry. If the structure has C_s symmetry then the following analysis is true, in Table 7.23 for the structure of Corriu et al (38).

Table 7.23: C_s Vibrational Analysis

C_s	$C_6H_6(SbCl_3)_2$	C_6H_6	$(SbCl_3)_2$	SbC_6H_6	Activity
A'	31	17	11	3	IR/R
A''	23	13	7	3	IR/R

The C_s symmetry will arise from the asymmetrical structure favoured by Corriu et al (63). There are two 'ethane-type' forms which have been suggested. When the two $SbCl_3$ moieties on each side of the benzene are eclipsed then D_{3h} symmetry prevails. It is D_{3d} symmetry when they are staggered.

(a) $SbCl_3$ vibrations

The IR and Raman spectra of the complex differ from that of pure $SbCl_3$. There is a great increase in the number of lines, which according to Kozulin et al (67) is greater than the number expected. $SbCl_3$ gives 4 Raman bands in the gaseous state which increase to 6 in the solid state. There are many others in the complex caused by the removal of degeneracy, $SbCl_3$ units lying in different positions and solid state effects which can split even non-degenerate vibrations. Thus all the IR and Raman bands in the 136 to 369cm^{-1} region can reasonably be assigned to $SbCl_3$ vibrations in comparison with earlier studies (58,59,65-67). At lower frequencies

there are strong IR and Raman bands that could be assigned to ClSbCl deformations in accord with previous studies.

(b) Intramolecular benzene vibrations

The assignments, described in Table 7.24, along with the relative IINS band intensities of ν_{11}, ν_6 and ν_{16} (in brackets) are achieved by a comparison with IINS data on benzene.

Table 7.24: Assignments of Intramolecular Benzene Vibrations, ν_{16} ν_6 and ν_{11}, in $(SbCl_3)_2C_6H_6$

Benzene IINS	$(SbCl_3)_2C_6H_6$			Assignment
	IINS	IR	R	
401(52)	416(55)	409	-	ν_{16}
602(14)	604(12)	614	-	ν_6
700(34)	721(33)	725	-	ν_{11}
858	861	873	-	ν_{10}

Only a very poor halide disc IR spectrum could be attained with $(SbCl_3)_2C_6H_6$. The above IR results are from a nujol spectrum, as described in section 7.5 for $MHg_2(SCN)_6C_6H_6$. In a comparison of the spectra of $(SbCl_3)_2C_6H_6$ it can be seen that the vibrational frequencies are very similar yet the IR activity of the intramolecular benzene modes is very different. In $MHg_2(SCN)_6C_6H_6$ complexes the vibrations could be described in terms of D_{6h} symmetry (where only the E_{1u} and A_{2u} vibrations were IR active). The majority of the benzene vibrations were observed in

$(SbCl_3)_2C_6H_6$ in the manner of Corriu et al (63). So it appears beyond doubt that the benzene molecule is lying in a position of low symmetry, probably C_s. This is also reasonable since measurements in the solid state showed the presence of a dipole moment.

A further comparison of the IINS spectra of $(SbCl_3)_2C_6H_6$ and $MHg_2(SCN)_6C_6H_6$ species shows a great degree of similarity. It could be surmised that the benzene lies in a similar environemnt as in the Hg-(C_6H_6)-Hg complexes with the benzene lying between two metal atoms. In $MHg_2(SCN)_6$-C_6H_6 the benzene was lying in a 'supercage' similar to a zeolite with two mercury atoms in similar positions to zeolite cations. However, though the crystal structure of $(SbCl_3)_2C_6H_6$ has not been analysed, related $SbCl_3$ complexes have been studied by Lipka and Mootz (25-27) and by Hulme and Mullen (28). The latter pair studied $(SbCl_3)_2C_6H_4Me_2$ (p-xylene complex) at -110°C. The $SbCl_3$ moieties were in a 'dimer' configuration with the shortest Sb-$C_{C_6H_4Me_2}$ distance 3.18Å. The structure was basically the same as that postulated by Corriu et al for the benzene analogue (63). The essential feature of the structure was the layer-like nature of the constituents: layers of $SbCl_3$ separated by layers of p-xylene. The $SbCl_3$ entities were too far apart to form formal Sb-Cl-Sb bridge bonds (3.24Å). The Sb-Cl distances in $SbCl_3$ indicated one was longer by 0.06Å. We propose that the $(SbCl_3)_2C_6H_6$ complex is similar to $(SbCl_3)_2C_6H_4Me_2$ in structure and that the benzene is layered and separated by $SbCl_3$ units. The Sb-$C_{C_6H_6}$ distance (3.18Å) would be substantially shorter than the Hg-$C_{C_6H_6}$ distance in

$MHg_2(SCN)_6C_6H_6$ complexes (3.6Å). It is likely that the benzene in the layered compound 'sees' the environment, in which it lies, to a greater extent than as a guest in the clathrate. Therefore, though the IINS spectra are similar, it is the IR and Raman spectra which indicate to a greater extent, in these weak complexes, the effect of the environment on the benzene intramolecular vibrations.

(c) The benzene - $(SbCl_3)_x$ skeletal vibrations

The strength of the complex can be gauged by the skeletal vibrations. If the complex can be described with only one Sb-C_6H_6 interaction (C_s symmetry) then the vibrations will take the form shown in Figure 6.15. However, due to the possible layering affect then perhaps the vibrations could be described as shown in Figure 7.14. Overall they should consist of a doubly degenerate tilt and deformation and a singly degenerate stretch and torsion (about the benzene z axis). In accord with the weak benzene complexes there no strong IINS bands indicative of the tilt above 200cm^{-1}, as found in the stronger benzene complexes. There are, however, bands at 50, 65, 88 and 124cm^{-1} (from the 4H5 study) and a shoulder at 142cm^{-1} and a broad medium - weak band at 236cm^{-1} (from the BFDDIDO study).

In the Raman study of Kozulin et al (67) of $(SbX_3)_2C_6H_6$ (X = Cl or Br) weak bands were observed at 124 and 130cm^{-1} in the chloride analogue amongst the $SbCl_3$ deformations and lattice vibrations. In the bromide analogue these latter vibrations were shifted down in frequency below 120cm^{-1} but still weak bands were found at 126 and 131cm^{-1}. We propose that these bands are of a skeletal nature which are weakly

Raman active in the solid state. The 124/126cm^{-1} Raman band has a strong IINS analogue at 124cm^{-1}.

At lower frequency the band due to the torsion is expected to be IR and Raman inactive since it does not involve a dipolemoment or polarisability change. Also in the weak $MHg_2(SCN)_6C_6H_6$ complexes it was readily assigned at 63cm^{-1}. Thus the IINS band at 65cm^{-1}, in Figure 7.19, is reasonably assigned to the torsion. The lower frequency bands at 50 and 27cm^{-1} are assigned to the lattice modes on the grounds of their displayed dispersiveness. The weaker band at 88cm^{-1} and the shoulder at 142cm^{-1} may be indicative of $SbCl_3$ deformation modes (There are IR and Raman analogues at 87/84cm^{-1} and 138/140cm^{-1} respectively). Since the chlorine has a modest incoherent scattering cross-section and with 6 chlorine atoms per $(SbCl_3)_2C_6H_6$ moiety this then may bring about some weak scattering intensity from the chlorine atoms.

At higher frequency there are IINS bands at 124/142cm^{-1} and at 236cm^{-1} without IR or Raman analogues. The 236cm^{-1} band could be a second harmonic of the strong 124cm^{-1} band (2 x 124 = 248cm^{-1}). However, with comparison to the $MHg_2(SCN)_6C_6H_6$ complexes, again, it was noted that the tilt and stretches had very much reduced IINS intensity. It is felt that this is also the case in $(SbCl_3)_2C_6H_6$. The tilt and stretch would be assigned to the ~236cm^{-1} region. It is seen that since the IINS intensity is weak then the hydrogen vibration amplitudes engaged in these motions must be very small. Therefore, the modes will involve very small changes in dipole moment and polarizability and

thus be very weakly active in the IR and Raman spectrum. The strong IINS band at 124cm^{-1} is assigned to the doubly degenerate deformation. It would appear that the torsion, in the 4H5 spectrum, is less intense than the deformation mode. This is not usual but has been reported for a number of organometallic π-complexes. Howard et al (68) assign a strong IINS band at 85cm^{-1} to the deformation (E) in $C_4H_4Fe(CO)_3$ and the torsion (A_2) to a weaker band at 60cm^{-1}.

The final assignments for $(SbCl_3)_2C_6H_6$ are shown in Table 7.22. Using the torsional frequency of 65cm^{-1} and the reduced moment of inertia of benzene, the effective force constant, EFC, can be calculated to be 255kJmol^{-1}. If the multiplicity, N, can be gauged to have a value of 6 then the torsional barrier to rotation, V_B, would be 14.8kJmol^{-1}. This value is slightly larger than that found for $NiHg_2(SCN)_6$-C_6H_6, 13.9kJmol^{-1}. This is reasonable if the benzene is perturbed to a greater extent in the $SbCl_3$ lattice.

7.10 $(PdAlCl_4C_6H_6)_2$ and $(PdAl_2Cl_7C_6H_6)_2$

7.10.1 Previous Results

Allegra et al (16) listed IR bands in the 200-3000cm^{-1} region (nujol) of these two complexes. No analysis of the results was carried out.

7.10.2 Results

Table 7.25 lists the vibrational data on both benzene bis-arene complexes. Figure 7.22 shows the BFDDIDO spectra, again, of both complexes which were run at liquid nitrogen temperature. The IR spectra were run at this temperature

Table 7.25: Vibrational Data on $(PdAlCl_4C_6H_6)_2$ and $(PdAl_2Cl_7C_6H_6)_2$

$(PdAlCl_4C_6H_6)_2$						$(PdAl_2Cl_7C_6H_6)_2$							Assignments
BFDDIDO (77K)	IR (77K)	FIR (77K)	Raman (RT)	IR(RT) (Nujol)	IR(RT) (Nujol)(16)	IN4 (10K)	BFDDIDO (77K)	IR (77K)	FIR (77K)	Raman (RT)	IR(RT) (Nujol)	IR(RT) (Nujol) (16)	
	1030(m)			1020(m)	1016(m)			1030(m)			1030(wb)	1030(m)	ν_{18} i/p CH deformation
	990(mb)			995(w)	990(m)					1005(w)			ν_1 Ring breathing
				981(s)	978(m)			975(ms)			975(w)	978(w)	ν_{17} o/p CH deformation
	950(w)			951(s)	950(m)			950(m)			910(w)	946(m)	Unknown
							874(s)						ν_{10} o/p CH deformation
798(s)	800(m)			800(s)	800(s)		785(vs)	780(s)			775(s)	780(s)	ν_{11} o/p CH deformation
	755(wsh)			757(vs)	755(s)					750(mb)	759(vs)	752(vs)	
								740(mb)			739(s)		'AlCl$_4$'/'Al$_2$Cl$_7$' modes
								690(sh)			699(m)	690(vs)	
	675(s)			675(s)	671(s)			675(s)			672(m)	672(vs)	
							620(ms)						ν_6 i/p Ring deformation
615(m)													Difference band
554(msh)							554(wm)						
	600(s)				592(m)			589(mb)				570(vs)	'AlCl$_4$'(T_2)/'Al$_2$Cl$_7$' vibration
	530(sh)				520(vs)			540(msh)				542(vs)	
							473(ssh)	481(m)				450(sb)	Antisymmetric tilt skeletal
474(sh)	483(sh)												
430(s)	430(mb)				430(s)		439(s)	431(m)					ν_{16} o/p Ring deformation
406(sh)	400(m)						397(sh)	377(s)				380(w)	Antisymmetric stretch skeletal
								356(w)	348(m)			356(m)	'AlCl$_7$'(A_1)'Al$_2$Cl$_7$' vibration
									342(m)			331(m)	
	340(mb)	340(mb)			339(s)								
							303(ms)	306(w)	307(m)	315(w)			Symmetric tilt skeletal
315(ms)	320(wb)	320(wb)											
235(m)		235(ms)			228(s)	239(m)	227(m)		230(sb)	235(m)		225(m)	Symmetric stretch skeletal
						194(w)			196(m)				Unknown
									186(m)				
		185(s)											'AlCl$_4$'(T_2)/'Al$_2$Cl$_7$' vibration
		172(sh)											
													Deformation skeletal
147(m)		145(m)				170(wsh)	164(sh)		168(ms)				
		155(m)							156(sh)				'AlCl$_4$'(T_2)/'Al$_2$Cl$_7$' vibration
													out-of-phase torsion skeletal
125(ssh)						135(msb)	125(s)		127(w)				
		117(w)				106(w)			104(vw)	106(w)			'AlCl$_4$'(E)/'Al$_2$Cl$_7$' vibration
		102(wm)							89(w)				
													in-phase torsion skeletal
						72(m)	75(m)						
79(m)									58(m)	59(vs)			
										41(m)			Lattice modes
										30(m)			

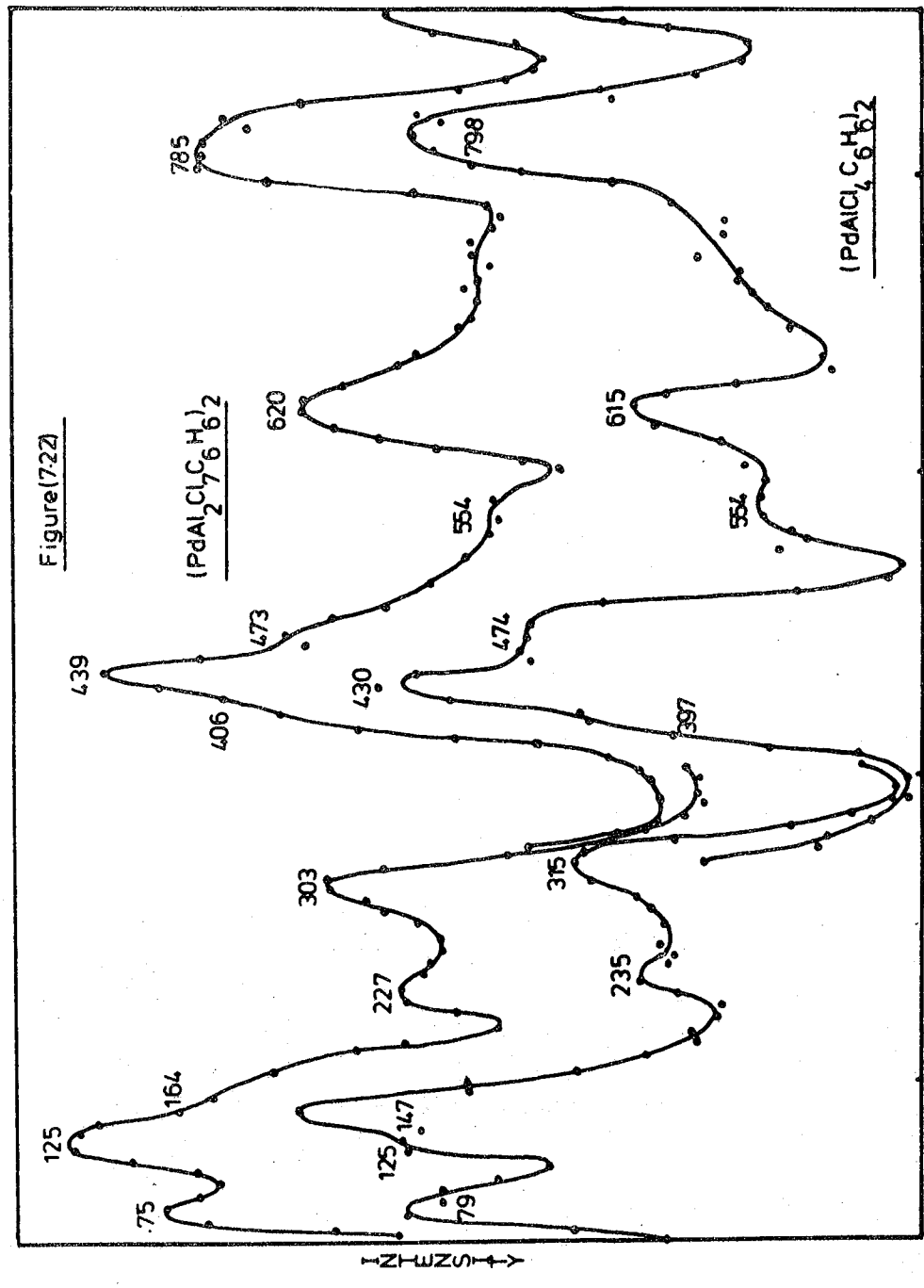
Figure(722)
(PdAl2Cl7C6H6)2
(PdAlCl4C6H6)2
INTENSITY
INCIDENT NEUTRON ENERGY /cm-1
200
400
600
800
75
125
164
125
147
79
227
303
315
235
439
406
430
473
554
620
474
397
554
615
785
798

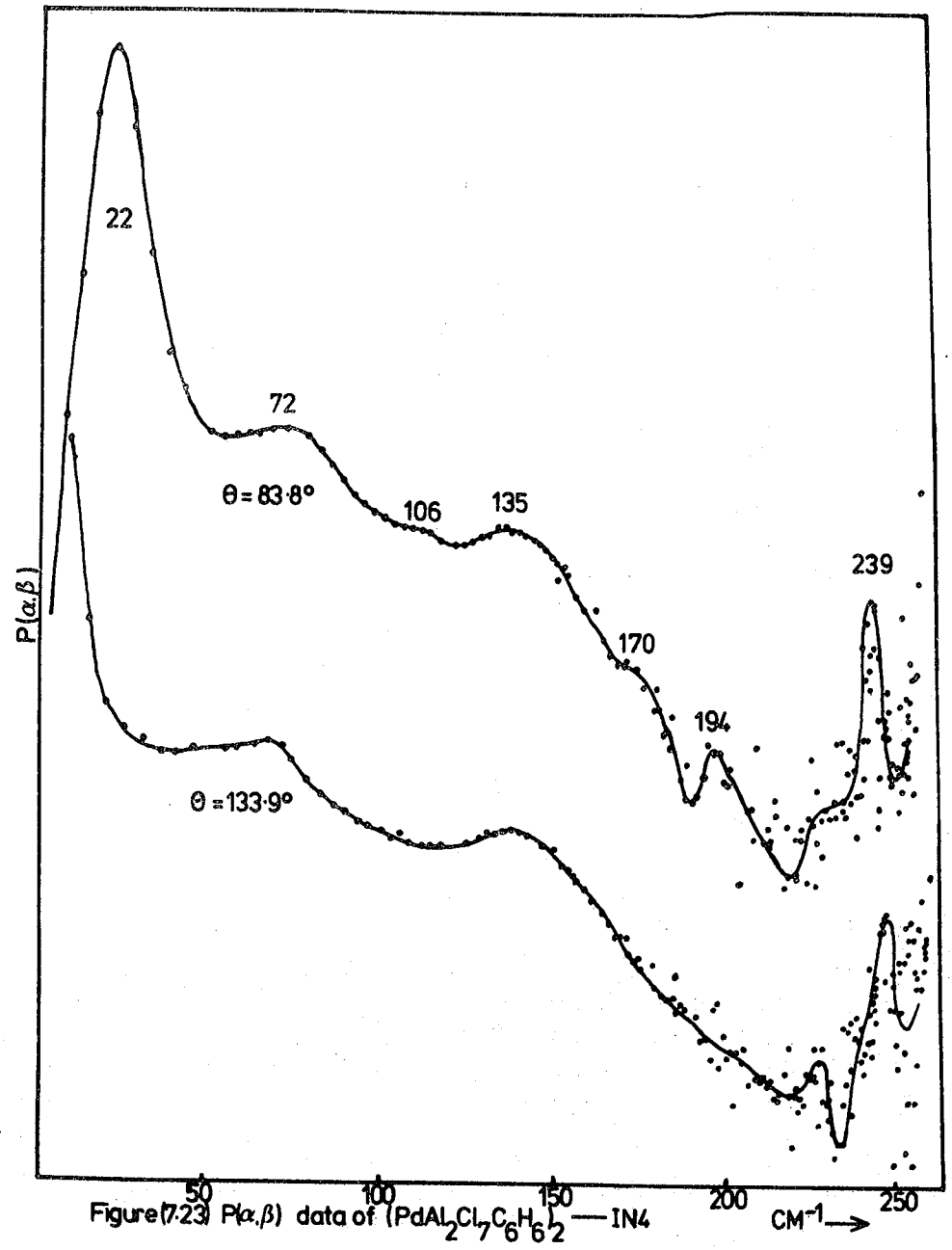

Figure (7·23) P(α,β) data of $(PdAl_2Cl_7C_6H_6)_2$ — IN4

whereas the Raman spectrum was run at room temperature a laser power of 8mW. Figure 7.23 shows P(α,β) IN4 spectra of $(PdAl_2Cl_7C_6H_6)_2$ run at 10K using an incident neutron energy of 287cm^{-1}. Each spectrum is summed over 5 angles.

7.10.3 Discussion

The two complexes can be described, to a first approximation in the case of $(PdAl_2Cl_7C_6H_6)_2$, in terms of C_{2h} symmetry. Tables 7.26 and 7.27 describe the vibrational analysis of both systems.

Table 7.26: Vibrational Analysis of $(PdAlCl_4C_6H_6)_2$

C_{2h}	Whole Molecule	$(PdAlCl_4)_2$	$(C_6H_6)_2$	$Pd_2(C_6H_6)_2$	Activity
A_g	28	10	16	2	R
B_g	23	5	14	4	R
A_u	24	6	16	2	IR
B_u	27	9	14	4	IR

Table 7.27 Vibration Analysis of $(PdAl_2Cl_7C_6H_6)_2$

C_{2h}	Whole Molecule	$(PdAl_2Cl_7)_2$	$(C_6H_6)_2$	$Pd_2(C_6H_6)_2$	Activity
A_g	35	17	16	2	R
B_g	28	10	14	4	R
A_u	29	11	16	2	IR
B_u	34	16	14	4	IR

Thus the skeletal vibrations have $2A_g+4B_g+2A_u+4B_u$ symmetry. The form of these vibrations can be related to the vibrations of $(C_7H_7)_2TaCl_3$, Figure 6.22, which is also

a sandwich complex.

(a) Vibrations of the $(PdAlCl_4)_2$ and $(PdAl_2Cl_7)_2$ species

The vibrations of these complexes may be separated into those involving the $(PdAlCl_4)_2$ and $(PdAl_2Cl_7)_2$ units, the intramolecular benzene vibrations and the benzene-skeletal motions. Initially $(PdAlCl_4)$ is discussed. The $(AlCl_4)^-$ ion has Raman vibrations at 349, 146, 495 and 180cm^{-1} due to A_1, E and $2T_2$ symmetries respectively. Only the 495cm^{-1} band is IR active (43,44). The $AlCl_4$ species in the bis-arene complexes still retains this tetrahedral shape. As shown in the study of $(C_6H_6)U(AlCl_4)_3$, the high frequency (T_2) Al-Cl stretch is expected to split as in the manner of the M-$AlCl_4$ species, studied by Rytter et al (48), because of the destruction of the Td symmetry due to complexing. Rytter et al observed Raman bands at 512, 498, 473 (due to the split T_2 mode), 348 182 and 119cm^{-1}. Bands in the vibration spectra of $(C_6H_6)U(AlCl_4)_3$ were similarly assigned, at 566, 492, 385, 340, 169 and 150cm^{-1}. In $(PdAlCl_4C_6H_6)_2$ the strong IR bands at 600 and 530cm^{-1} are assigned to the split T_2 mode. The IR band at 340cm^{-1} can be assigned to the symmetric stretch, of A_1 symmetry in the Td group. At lower frequency the deformation bands may be assigned at 185 and 117cm^{-1}. (The band at 155cm^{-1} may also be assigned in this manner but this would involve some splitting of these deformation modes and this was not observed by Rytter et al (48).) At high frequency, IR bands are found at 671 and 755cm^{-1}, similar in frequency and intensity to those found in $(C_6H_6)U(AlCl_4)_3$. They are thus assigned to the complexed '$AlCl_4$' group.

The $(Al_2Cl_7)^-$ ion has been studied by Raman spectroscopy (69). Bands were found at 429, 316 and 97cm^{-1}. A similar Raman study observed bands at 432, 312, 164 and 99cm^{-1}. However, the structure of the ion has been inferred to be $(Cl_3AlClAlCl_3)^-$ (48) with only one AlClAl bridge whereas the X-ray study of $(PdAl_2Cl_7C_6H_6)_2$ has shown the Al_2Cl_7 unit to have two AlClAl and two PdClAl bridges on each side of the molecule (ie 2 x $PdCl_2AlCl_2AlCl_3$). A study of Al_2Cl_6 (70), with two AlClAl bridges, observed Raman bands at 606, 506, 340, 284, 217, 164 and 112cm^{-1} and IR bands at 625, 484 and 420cm^{-1} and calculations indicated others existed in the same region. Thus, in this complex situation those IR and Raman bands without IINS analogues are assigned to the complexed 'Al_2Cl_7' species. Similarly the high frequency bands at 672, 690 and 752cm^{-1} are assigned as in the manner of $(C_6H_6)U(AlCl_4)_3$ and $(PdAlCl_4C_6H_6)_2$. It will be noticed that in the assigned regions that there are more bands associated with the 'Al_2Cl_7' species than the '$AlCl_4$' species.

(b) Intramolecular benzene vibrations

The low frequency intramolecular benzene vibrations are assigned from a comparison with IINS data on solid benzene in Table 7.28.

ν_{18}, ν_1 and ν_{17} are assigned above 900cm^{-1} due to their relative IR and Raman activity. Generally the symmetric vibrations are Raman active e.g. ν_1 whereas the asymmetric are IR active. ν_{10} is assigned to the strong IINS band in $(PdAl_2Cl_7C_6H_6)_2$ at 874cm^{-1}. This band is of E_{1g} symmetry (D_{6h}) and thus is only Raman active in a molecule with a

centre of symmetry. There is however, no Raman or IR analogue of the IINS band.

Table 7.28: Intramolecular Benzene Vibrations (cm^{-1})

Benzene (solid) IINS	$(PdAlCl_4C_6H_6)$			$(PdAl_2Cl_7C_6H_6)_2$			Assignment
	IINS	IR	R	IINS	IR	R	
401(52)	430(38)	430	-	439(44)	431	-	ν_{16}
602(14)	615(15)	-	-	620(16)	-	-	ν_6
700(34)	798(47)	800	-	782(40)	775	-	ν_{11}
858	-	-	-	874	-	-	ν_{10}

The region in which υ_{11} resides in the IR spectrum is quite complex in these bis-arene complexes, however, strong IINS bands exist at 780-800cm^{-1} which have strong IR counterparts. These frequencies mean that υ_{11} has increased by more than 100cm^{-1} due to complexing. These values will be compared with other complexes in section (7.11).

In the IINS spectra there are bands at ~ 620cm^{-1} which can be assigned to υ_6. A Raman counterpart was expected but no band was found in the rather poor quality Raman spectrum of the dark brown/black $(PdAl_2Cl_7C_6H_6)_2$. The strong IINS bands at ~ 430cm^{-1}, with medium intense IR analogues, are assigned to the out-of-plane ring deformation, υ_{16}.

Now also it is noted that the IR and Raman techniques did not locate υ_{10} and υ_6 which have E_{1g} and E_{2g} symmetry but that υ_{16} (E_{2u}), υ_{11} (A_{2u}), υ_{18} and υ_{17}, of E_{1u} symmetry, were found to be IR active. Further, υ_1 of A_{1g} symmetry

was assigned to a Raman band at 1005cm^{-1} in $(PdAl_2Cl_7C_6H_6)_2$. This trend indicates that the intra-molecular benzene vibrations can be described in terms of C_{2h}.

(c) C_6H_6-M_2-C_6H_6 skeletal vibrations

Table 7.29 indicates the symmetry of the skeletal vibrations in D_{6h} (as in a symmetric $(C_6H_6)_2M$ complex), C_{2h} and a further possible D_{2h} symmetry. The D_{2h} symmetry arising from the $Pd_2(C_6H_6)_2$ core.

Table 7.29: Skeletal Vibration Activity

Skeletal Motion	D_{6h} System	D_{2h} System	C_{2h} System
Torsion 1	A_{2g}(-)	B_{1g}(R)	A_g(R)
Torsion 2	A_{2u}(IR)	B_{1u}(IR)	A_u(IR)
Sym. str.	A_{1g}(R)	A_g(R)	A_g(R)
Antisym. str.	A_{2u}(IR)	B_{1u}(IR)	A_g(IR)
Deformation	E_{1u}(R)	'B_{2u} + B_{3u}'(IR)	2B (IR)
Antisym. tilt	E_{1u}(R)	'B_{2u} + B_{3u}'(IR)	2B (IR)
Symm. tilt	E_{1g}(R)	'B_{2g} + B_{3g}'(R)	2B (R)

Both D_{2h} and C_{2h} have the same activity so they cannot reasonably be separated.

Above 500cm^{-1} there are no bands in the IINS spectra that could be indicative of skeletal vibrations. The strong band in the IINS spectra assigned to υ_{16} has two components at lower and higher frequency, that are not fully resolved from it. The stronger band lies at 475cm^{-1} with the weaker

band at ~400cm^{-1}, and both have IR counterparts of medium-strong intensity. These IINS bands are thus assigned to the antisymmetric tilt (at ~475cm^{-1}) and antisymmetric stretch (at ~400cm^{-1}) and this is reasonable on intensity grounds since the tilt is adoubly degenerate mode. No splitting was apparent in the IR of the tilt.

At lower frequency in the IINS spectra there are two medium-strong bands of which the stronger is at 303cm^{-1} in $(PdAl_2Cl_7C_6H_6)_2$ and 315cm^{-1} in $(PdAlCl_4C_6H_6)_2$. These bands are assigned to the doubly degenerate symmetric tilt. An analogous Raman band was found in $(PdAl_2Cl_7C_6H_6)_2$ at 315cm^{-1}. (No Raman spectrum was successfully run for $(PdAlCl_4C_6H_6)_2$). A breakdown in the selection rules may have occurred since weak IR bands are also found at these frequencies. This may be a solid state effect. The weaker IINS band at 230cm^{-1} in both compounds is assigned to the singly degenerate symmetric stretch. A Raman band was found at 235cm^{-1} in $(PdAl_2Cl_7C_6H_6)_2$ of medium intensity and an IR analogue was also found.

The doubly degenerate deformation, an antisymmetric mode is assigned to the 147cm^{-1} $(PdAlCl_4C_6H_6)_2$ band and the 170cm^{-1} feature in $(PdAl_2Cl_7C_6H_6)_2$. Both have medium-strong IR components at 145 and 168cm^{-1}. In the former case the stronger IINS band appears at 147cm^{-1} but using the curve resolver it is centred at 125cm^{-1} with the 147cm^{-1} peak due to a weaker component. The analogue of the 125cm^{-1} $(PdAlCl_4C_6H_6)_3$ band is at 135cm^{-1} in $(PdAl_2Cl_7C_6H_6)_2$. They are assigned to the out-of-phase torsion (torsion 2). The IINS intensity of the torsional bands is usually greater than the deformation. The in-phase torsion (torsion 1) is

tentatively assigned to the lower frequency IINS bands at 75-80cm^{-1}.

In the IN4 spectrum (θ=83.8°), Figure 7.23, the very strong band at 22cm^{-1} could well be an artifact since it is absent from the other spectrum (θ = 133.9°). Table 7.30 lists the IINS data on the two bis-arene complexes with the other well-studied bis-arene, $(C_6H_6)_2Cr$. The assignments are surprisingly comparable even though the bonding situations are not.

Table 7.30: Vibrational Comparison of Bis-Arene Complexes

Vibration	$(C_6H_6)_2Cr$ IR/Raman (71,72)	$(PdAlCl_4C_6H_6)_2$ (This Work)	$(PdAl_2Cl_7C_6H_6)_2$ (This work)
Antisymmetric stretch	490	406	397
Symmetric stretch	277	235	227
Antisymmetric tilt	459	474	473
Symmetric tilt	335	315	303
Deformation	171	147	170
Out-of-phase torsion	152	125	135
ν_{16}	409	430	439
ν_6	604	615	620
ν_{11}	794	798	782
ν_{10}	811	-	874
ν_{17}	-	981	975
ν_1	-	-	1005
ν_{18}	999	1030	1030

The analysis of the vibrations for the two compounds has shown that they can be described in C_{2h} synmetry terms though the $Pd_2(C_6H_6)_2$ unit could be described in D_{2h} symmetry.

It is possible to calculate the torsional barriers, or at least the effective force constants of the internal and external fields in the same manner as $(C_7H_7)_2TaCl_3$, using the derived equations $\omega_1^2 - \omega_2^2 = \frac{V_I N''^2}{I_R}$ and $\omega_2^2 = \frac{N'^2 V_E}{2I_R}$ where ω_1 = out-of phase torsion and ω_2 = in-phase torsion. With the I_R value of 295 x 10^{-40}gcm ^{2}, the effective force constant of the internal and external fields can be calculated. Further, if the multiplicity is estimated to be 6 then the actual barrier V_I and V_E can be estimated in each case:-

($kJmol^{-1}$)	Internal field (N'^2V_I)	Barrier V_E	External field (N''^2V_E)	Barrier V_C
$(PdAlCl_4C_6H_6)_2$	331	9.2	368	10.2
$(PdAl_2Cl_7C_6H_6)_2$	440	12.2	366	10.2

The temperature of our study using IN4 was 10K. A related X-ray study of the rotational disorder observed in solid $(PdAl_2Cl_7C_6H_6)_2$ (22) was carried out at 173K. The authors estimated that the energy difference between the two orientations, 30° apart, was not more than 0.5kcalmole^{-1} (2.1kJmol) from the probabilites of the occurrence of any one particular orientation in the X-ray study. If the multiplicity, N, is thus 12 in the case of $(PdAl_2Cl_7C_6H_6)_2$ (ie 30° jumps) then the internal barrier to rotation is

estimated to be 3.1kJmol^{-1} using the IINS data (10K) which is not too dissimilar from the estimate from the X-ray data (173K) (22).

7.11 Conclusion

This short section indicates that there are a number of trends that can be seen to run through the results of this study of benzene complexes. Table 7.31 lists the frequencies of ν_{16}, ν_6 and ν_{11} (benzene intramolecular modes) the tilts, stretches, deformations and torsions (benzene-system skeletal modes) and, where the torsions have been confidently assigned, the effective force constants and the barrier to rotation, about the benzene z axis. (The skeletal bands of the two Pd compounds are not listed because they differ due to coupling). A brief comparison is made with the well studied $C_6H_6M(CO)_3$ complexes (73).

Though the results can be studied in greater depth, the main trends from the frequencies listed are that as ν_{11} increases down in the table, from that found in solid benzene (700cm^{-1}) to that found in $(RuCl_2C_6H_6)_2$ (870cm^{-1}, an increase of 24%):-

(a) ν_{16}, another out-of-plane mode, also increases but the increase is more modest (~9%). (An anomaly lies at 384cm^{-1} in $C_6H_6Co_4(CO)_9$)

(b) No similar trend was observed in the frequency of the in-plane mode, ν_6, though they generally increased by up to 5.5% (except for ν_6 on $C_6H_6W(CO)_3$ at 600cm^{-1}).

(c) The frequency of the tilt would also appear to increase down the table and as this takes place the intensity of this doubly degenerate bond also rises. In

Table 7.31: Frequencies of Skeletal and Intramolecular - Benzene Vibrations In Studied Systems

System	ν_{11}	ν_6	ν_{16}	Tilt	Stretch	Deformation	Torsion	EFC ($kJmol^{-1}$)	V_B ($kJmol^{-1}$)
Benzene (solid)	700(34)	602(14)	401(48)	-	-	-	-	-	-
$(SbCl_3)_2C_6H_6$	721(33)	604(12)	416(55)	236		124	65	266	14.8
$NiHg_2(SCN)_6C_6H_6$	729(34)	635(18)	418(48)	227	287	107	63	250	13.9
$CoHg_2(SCN)_6C_6H_6$	741(39)	623(12)	421(50)	202	282	117	-	-	-
$C_6H_6Co_4(CO)_9$	737	623	394	269	223	105	66	273	15.1
$C_6H_6Mo(CO)_3$ (73)	764	615	423	312	264	-	-	-	-
$C_6H_6W(CO)_3$ (73)	775	600	424	316	267	-	-	-	-
$C_6H_6Cr(CO)_3$ (73)	786	611	422	332	301	-	-	-	-
$(PdAl_2Cl_7C_6H_6)_2$	785(40)	620(16)	439(44)	-	-	-	-	-	-
$C_6H_6(AlCl_4)_3$	790(26)	610(19)	414(55)	202	183	104	75	-	-
$(PdAlCl_4C_6H_6)_2$	798(47)	615(15)	430(38)	-	--	-	-	-	-
$(RuBr_2C_6H_6)_2$	866(26)	631(28)	439(46)	380	273	150	-	-	-
$(RuCl_2C_6H_6)_2$	870(24)	635(28)	439(48)	387	278	168	-	-	-

$(SbCl_3)_2C_6H_6$ it has weak IINS intensity whereas in the $(RuX_2C_6H_6)_2$ complexes it has approximately the same intensity as ν_{16}.

(d) The frequency of the stretch mode varies in frequency within the 183-301cm^{-1} region. No trend is found but in the weak complexes it can be at higher frequency than the tilt and in the stronger complexes it is at lower frequency.

(e) Unfortunately there are not enough data to analyse confidently for the deformation and torsion modes but tentatively the deformation mode would appear to increase in frequency.

(f) Finally there would not appear to be any trend in the IINS band intensities of ν_{11}, ν_6 and ν_{16} in the systems studied

7.12 References

1. V. Trevino J. Chem. Phys. 46 (19) 3273
2. K.W. Logan, S.F. Trenino, H.I. Prask, J.D. Gault J. Chem. Phys. 53 (1970 3417
3. E.L. Bokhenkov, V.G. Fedotov, E.F. Sheka, I. Natkaniec M. Sudnik-Hrynkiewicz, S. Califano, R. Righini Il Nuovo Cimento 44BN2 (1978) 3241
4. E. G. Cox Rev. Mod. Phys. 30 (1958) 159
5. V.E. Bacon, N.A. Curry, S.A. Wilson Proc. Roy. Soc. 279A (1964) 98
6. I. Harada, T. Shimanouchi J. Chem. Phys. 46 (1967) 2708
7. Y.A. Sataty, A. Ron, M. Brith Chem. Phys. Letts. 23 (1973) 500
8. V. Schettino, S. Califano J. Chim. Phys. 76 (1979) 197
9. M. Ito, T. Shigeoka Spectrochimica Acta 22 (1966) 1029
10. A.V. Korshunov, L.I Mamizerova Opt. Spektrosk 31 (1971)450
11. H.W. Schrotter, J. Bofilias, H.J. Falge, H.H. Hacker, J. Brandmuller Vijnana Perishad. Anus. Patrika 14 (1971)31
12. H. Bonadeo, M.P. Marzocchi, E. Castelluci, S. Califano J. Chem. Phys. 57 (1972) 4299
13. E.B. Wilson Phys. Rev. 45 (1934) 706
14. G. Varsanyi 'Vibrational Spectra of Benzene Derivatives' (Academic Press) (NY) (1969)
15. R.D. Mair, D.F. Hornig J. Chem. Phys. 17 (1949) 1236
16. G. Allegra, G.T. Casagrande, A. Immirzi, L. Porti, G. Vituli J. Amer. Chem. Soc. 92 (1970) 289
17. R.A. Zelonka, M.C. Baird Canad. J. Chem. 50 (1972) 3063
18. M. Cesari, U. Pedretti, A. Zazzetta, G. Lugii, W. Marconi, Inorg. Chim. Acta. 5 (1971) 439
19. P.H. Bird, A.R. Fraser J. Organometal Chem. 73 (1975)103
20. B.N. Menshutkin Z. Russ. Phys. Chem. Ob. 43 (1911) 395
21. R. Baur, M. Schellenberg, G. Schwarzenbach Helv Chim. Acta. 91(1962)775

22. G. Nardin, P. Delise, G. Allegra Gazz. Chim. Ital. 105 (1975) 1047

23. M.A. Bennet, A.K. Smith J. Chem. Soc. Dalton Trans. (1974) 233

24. J.W. Kang, K. Moseley, P.M. Maitlis J. Amer. Chem. Soc. 91 (1969) 5970

25. V.A. Lipka, D. Mootz Z. Anorg. Allg. Chem. 440 (1978) 217

26. V.A. Lipka, D. Mootz Z. Anorg. Allg. Chem. 440 (1978) 224

27. V.A. Lipka, D. Mootz Z. Anorg. Allg. Chem. 440 (1978)231

28. R. Hulme, D.J.E. Mullen J. Chem. Soc. Dalton Trans. (1976) 802

29. R. Gronbaek, J.D. Dunitz Helv. Chim. Acta. 47 (1964)1889

30. H.P. Fritz, J. Manchot Chem. Ber. 96 (1963) 1891

31. D. Forster, D.M.L. Goodgame Inorg. Chem. 4 (1965) 715

32. M.A. Bennett, R.J.H. Clark, A.D.J. Goodwin Inorg. Chem. 6 (1967) 1625

33. J.R. Ferraro "Low Frequency Vibrations of Inorganic and Coordination Compounds" Plenum Press (1971)

34. G.F. Knox, T.M. Brown Inorg. Chem. 8 (1969) 1401

35. R.N. Keller, N.B. Johnson, L.L. Westmoreland J. Amer. Chem. Soc. 90 (1958) 2729

36. S. Akyuz, A.B. Dempster, R.L. Morehouse Spectrochemica Acta. 30A (1974) 1989

37. J.E.D. Davies, A.B. Dempster, S. Suzuki Spectrochimica Acta. 30A (1974) 1183

38. J. Favrot, P. Caillet, M-T Forel J. Chim. Phys. 71 (1974) 1337

39. G. Bor, G. Sbrignadello, F. Marcati J. Organometal Chem. 46 (1972) 357

40. D.M. Adams, M.A. Hooper J. Organometal Chem. 181 (1979) 131

41. H.F. Efner, D.E. Tevault, W.B. Fox, R.R. Smardzewski J. Organometal Chem. 146 (1978) 45

42. M. F. Bailey, L.F. Dahl Inorg. Chem. 4 (1965) 1314

43. H. Gerding, H. Hautgraaf Rec. Trav. Chim. 72 (1953) 21

44. D.E.H. Jones, J.L. Wood Spectrochimica Acta (1967) 2695

45. G.L. Carlsson Spectrochimica Acta 19 (1963) 1291

46. K. Nakamoto 'IR Spectra of Inorganic and Coordination Compounds' J. Wiley (1963)

47. P.G. Harrison , J.A. Richards J. Organometal Chem. 108 (1976) 35

48. E. Rytter, H.A. Øye, S.J. Cyvin, B.N. Cyvin, P. Klaeboe Acta Chem. Scand. 25 (1971) 559

49. J. MacCordick, G. Kaufmann Bull. Soc. Chim. France (1972) 23

50. G. Winkhaus, H. Singer J. Organometal Chem. 7 (1967) 487

51. E. Benedetti, G. Braca, G. Sbrana, F. Salvetti, B. Grassi J. Organometal Chem. 37 (1972) 361

52. J.R. Durig, B.R. Mitchell, D.W. Sink, J.N. Willis, A.J. Wilson Spectrochimica Acta 23A (1967) 1121

53. R.A. Walton J. Chem. Soc (A) (1969) 61

54. Yu. I. Rozenberger, N.E. Ainberger Sov. Sol. State Phys. 12 (1970) 641

55. V.S. Grechiskin, I.A. Kyuntsel Opt. Specktrosk 16 (1964)87

56. T. Okuda, A. Nakao, A. Shiroyama, H. Negita Bull. Chem. Soc. Jap. 41 (1968) 61

57. M.S. Ashkanazi, P.V. Kursonova, V.S. Finkelstein Zh. Fiz. Khim. 7 (1936) 438

58. Sh.Sh. Raskin Doklady. Akad. Nauk. SSSR 100 (1955) 485

59. Sh.Sh. Raskin Optika Specktrosk 1 (1956) 516

60. Sh.Sh. Raskin Doklady Akad. Nauk. SSSR 141 (1961) 915

61. L.W. Daasch Spectrochim. Acta 9 (1959) 726

62. H.H. Perkampus, E. Baumgarten Z. Phys. Chem. N. Folge 39 (1963) 1

63. R. Corriu, C. Coste, A. Sournia Bull. Soc. Chim. France. 8-9 (1970) 2998

64. A.T. Kozulin, A.V. Gogolev, V.I. Karmanov Zh. Prikl. Specktrosk 26 (1977) 7936

65. P.W. Davis, R.A. Oetjen J. Molecular Spec. 2 (1958) 253

66. G. Herzberg 'Infra-red and Raman Spectra' Vol. 2 Van Nostrand (1960) 167

67. A.T. Kozulin, N.V. Bogoslovskii, V.I. Karmanov Zh. Prikl. Specktrosk. 22 (1975) 797

68. J. Howard, T.C. Waddington Spectrochimica Acta 34A (1978) 445

69. R. Huglen, G. Mamantov, G.M. Begun, C.P. Smith J. Raman Spec. 9 (1980) 188

70. T. Onishi, T. Shimanouchi Spectrochimica Acta 20 (1964) 325

71. L. Schafer, J.F. Southern, S.J. Cyvin Spectrochimica Acta 27A (1971) 1083

72. S.J. Cyvin, J. Brunvoll, L. Schafer J. Chem. Phys. 54 (1971) 1517

73. B.V. Lokshin, E.B. Rusach, V.S. Kaganovich, V.V. Krivykh, A.N. Artemov, N.I. Sirotkin Zh. Struct. Khim. 16 (1975) 553

C H A P T E R 8

An IINS Study of Benzene Adsorbed on Ag and Na13X Zeolites

8.1. Zeolites: A General Introduction

It is well known that the activity of the heterogenous catalysts, zeolites and metals, is centred in the cavities and tunnels and on the surface interface. This study concerns the interaction between benzene, a simple arene which plays a major part in catalytic reactions as a main or secondary reactant or as an intermediate or product, with zeolite cages. The zeolite forms chosen are Na13X and the 100% silver exchanged form, hereafter called Ag13X.

Zeolites form a diverse group of porous crystalline adsorbents with an aluminosilicate skeletal framework which occur in nature but have been augmented by the more important group of synthetic zeolites.

The uses of synthetic zeolites are manifold in industry and research. For example, they are widely used as adsorbents and drying agents for gases and liquids and as sieves in the separation of differing molecules and the purification of mixtures. Due to their high cation-exchange capacities they can show selectivity in ion-exchange reactions and also exhibit high activity as catalysts in various reactions. Over the years a number of general articles on zeolite properties have been published (1-4).

8.2. Zeolites: Structures

The building block of the zeolite skeleton is the tetrahedral unit formed by four oxygen atoms with a silicon or aluminium atom at the centre. Each oxygen atom has two negative charges whereas the silicon and aluminium atoms have four and three positive charges respectively. Thus with the

silicon atom at centre of the tetrahedron electrical neutrality is formed. However, with each aluminium atom in the tetrahedral network, the neutrality must be balanced by a cationic charge. These additional ions are rather loosely held and may be exchangeable.

The general formula of the zeolites is $M_{x/n}(AlO_2)_x(SiO_2)_y.ZH_2O$ where y/x is in the range of 1 to 5 and n is the cation valency. The framework forms a honeycomb structure, with long-range order, made up of SiO_4 and AlO_4 tetrahedra. Polyhedral units such as cubes, prisms, cubo-octahedrons etc can be made up producing internal voids into which guest molecules may diffuse and possible reside by bonding.

Many zeolite types exist, both naturally and synthetically, however, only a few are of industrial importance. The stability of zeolites is a very important factor since many uses need a framework free of guest molecules, such as water, and thus the framework must be able to survive a process such as dehydration without skeletal collapse.

The zeolite type used in this study is a synthetic form whose structure compares favourably with the naturally occurring mineral faujasite (1,5,6,7). The 13X zeolite has the following general formula $M_{86}(AlO_2)_{86}(SiO_2)_{106}.ZH_2O$ where M in this study is chosen to be Na^+ or Ag^+ with an Si/Al ratio of 1.23. Many other exchangeable forms do exist. A typical value of Z, the water content, would be 264. If the Si/Al ratio was increased or decreased the number of cations for electrical neutrality would decrease or increase respectively.

The X-type structure has cubic symmetry and consists of combinations of truncated octahedra and hexagonal prisms

so arranged to produce large voids. Each truncated octahedron consists of 24 silicon or aluminium atoms at the vertices interconnected with 36 oxygen atoms and has 6 square faces and 8 hexagonal faces of which 4 are connected to other hexagonal faces of the four nearest truncated octahedra forming 4 small hexagonal prisms. These prisms consist of 12 silicon or aluminium tetrahedra. This arrangement of truncated octahedra and prisms forms a large cavity, known as a supercage, which has four large windows opening into four tetrahedrally arranged similar supercages. One supercage with attendant octahedra and prisms is shown in Figure 8.1 (8). There are eight supercages per unit cell and each cell occupies approximately 15000$\AA^3$.

The zeolite chosen in this study has a low Si/Al ratio and thus a high proportion of cations are necessary. These cations can be found in various sites in the unit cell and Figure 8.2 (9) shows a supercage-octahedron-prism moiety with various sites identified, though not all have been crystallographically found. Figure 8.2 shows the vertices of the tetrahedral units, ie the aluminium and silicon atoms, whereas the interlinking oxygen atoms lie off the straight lines drawn joining the vertices. With the high number of ions present, a large number of the various sites should be occupied. Table 8.1 shows the site occupancies and the types of site available to the cation in a dehydrated Na13X and K13X sample (7). These cation positions can also vary radically with the degree of dehydration. Since only dehydrated samples are used in these experiments, it is felt a comparison with hydrated zeolites is not necessary.

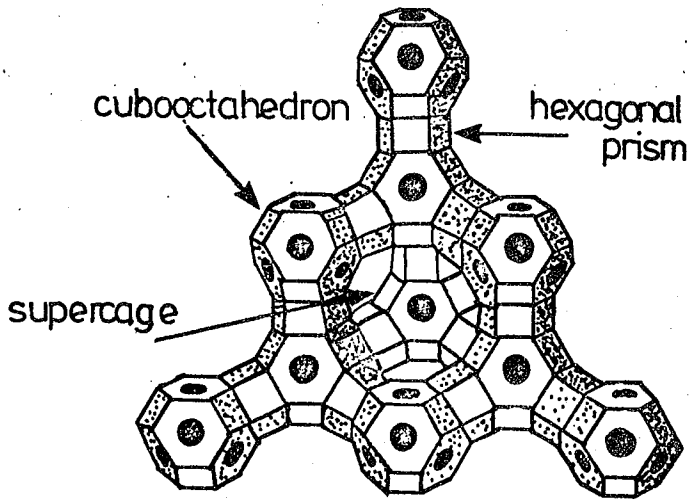

Figure(8.1)
Model of a Faujasite structure (8)

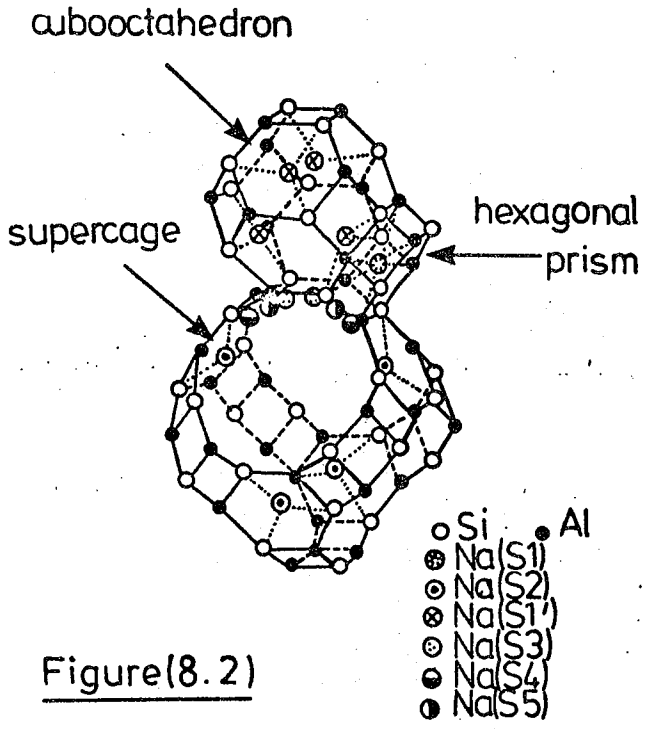

Figure(8.2)

Cation positions in Faujasites(9)

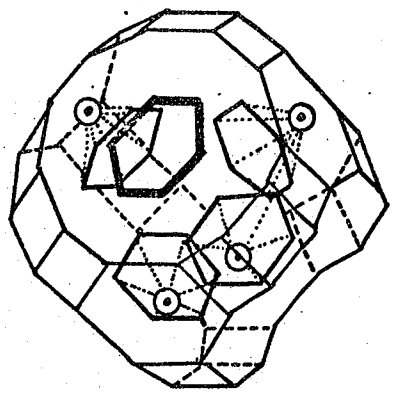

Figure(8.3)

Possible arrangement of benzene molecules in a Faujasite supercage.(27)

Table 8.1: Cation Site Occupancies in Na13X and K13X Zeolites (dehydrated)

Site	Type of Site	No. of cations per unit cell	
		Na13X	K13X
1	Inside hexagonal prism	4	9.2
1'	Inside truncated octahedra	32	13.6
2	Inside supercage	32	25.6
3	Between truncated octahedra and supercage	4	38.2
4 5	Between hexagonal prism and supercage	12	

A further comparison can be made with Na^+, K^+ and Ag^+ positions in Y zeolites. Y zeolites are a synthetic type, similar to X zeolites, and are also based on the faujasite structure. The main difference between X and Y zeolites exists in the cation distribution about the various sites in the unit cell. Table 8.2 shows the occupancy of sites 1, 2 and 3 of the Na^+, K^+ and Ag^+ cations (10). The number of site 2 positions drops from Na^+ through to Ag^+ whereas the trend is vice versa in site 3 positions.

Only those cations which lie in the supercages or in the windows of the supercage are involved in this study of benzene adsorbed in Na13X and Ag13X zeolites because benzene cannot enter the truncated octahedron or the hexagonal prism.

Table 8.2: Cation Positions in Various Y Type Zeolites

Site	No. of Cations Found Per Unit Cell		
	Na^+	K^+	Ag^+
1	30	30	28
2	19.5	14	10
3	7.5	12	16
Total found	56	56	54

Benzene has a length of 7.4Å though it could possibly fit through a 6.5Å hole, and this size constraint only allows movement in the supercage. So sites 1 and 1' are not used leaving sites 2 and the less localized sites. The site 3, 4 and 5 cations probably exist further into the supercage and, thus, interact to a smaller extent with the supercage walls than the site 2 cations. As a result any interaction with a guest molecule will be weaker with a site 3, 4 or 5 cation than with a site 2 cation.

No crystal structure studies of the AgX zeolite have been carried out. H wever, the studies of Yates (11) and Huang (10) have led to an estimate of the cations lying in specific adsorption sites from studies of ethylene and carbon monoxide adsorption. They are that $2Ag^+$ are in S1 positions, none in S1' positions, 4.75 are distributed on the supercage walls in S3, S4 and S5 positions on 4 are in the hexagonal windows in site 2 positions.

8.3. Benzene/Zeolites: Previous Work

(i) Adsorption/Desorption Studies

A temperature programmed desorption of benzene from Na13X zeolite found two desorption maxima at 75° and 160° implying that possibly two forms of adsorbed benzene were present in the supercages (13).

Adsorption isotherm data was recorded for various benzene/zeolite 13X systems and in all cases the benzene was rapidly adsorbed at low pressures (14,15,16,17). Calorimetric adsorption data (16) was used to study the possible π-interaction between the benzene and the cations, the localization of the cation and the interactions expected between benzene molecules in the same cage. The heat of adsorption of benzene was found to be greater than that of n-hexane and it was suggested that this was due to a π-interaction between the benzene and the cations in the supercages. As the benzene coverage was increased, the heat of adsorption ($\Delta H_{ads.}$) remained constant till ~ 4 benzene molecules were adsorbed per supercage then $\Delta H_{ads.}$ fell till ~ 5.5 benzene molecules per supercage had been adsorbed. It was postulated that the final ~ 1.5 benzene molecules per supercage were not forming π-bonds to the S2 cations though they may have interacted with the non-localized cations forming weaker bonds.

(ii) Kinetic Studies

The sorption cavities of Na13X were found to be readily accessible to benzene (18) and the rate of diffusion was found to be determined by diffusion through the intracrystalline secondary pores between the supercages. A comparison

between CaX and NaX zeolites was carried out by using benzene kinetic and adsorption data (19). In CaX, an isosteric break occurred in a plot of $\Delta H_{ads.}$ against coverage at 3 C_6H_6/supercage whereas $\Delta H_{ads.}$ rose very slightly in NaX till approximately 4 benzene molecules were adsorbed per supercage. The Ca^{++}-C_6H_6 interaction was found to be twice as strong as the Na^{+}-C_6H_6 interaction. A benzene-sodium π-interaction was preferred to any other.

(iii) C.N.D.O. Calculations

The benzene-cation interaction energy was studied (20) using C.N.D.O. calculation. The benzene was found to prefer to be π-bonded to Na^{+} and Mg^{++} ions at distances of 3.1 and 2.3Å respectively.

(iv) N.M.R. Studies

The majority of studies of the C_6H_6/zeolite systems have been carried out using the n.m.r. technique.

The temperature dependence of the proton relaxation time of C_6H_{12}, C_6H_{10}, C_6H_8 and C_6H_6 in NaI3X showed a marked shift of the minimum to high temperatures in the above order (21). It was postulated that the molecules were adsorbed specifically at the cation sites but by a single π-bond in each case whereas, with cyclohexane, the adsorption site was not localized. Benzene had it appeared, a more restricted rotation than the other adsorbed molecules.

The behaviour of the proton magnetic resonance of adsorbed benzene in the supercages of faujasites was measured (22). At low temperatures evidence indicated that at low coverages the adsorbed benzene rotated about a C_2 axis in the plane of

the molecules. This would take place with relative ease if the benzene was bonded to Na^+ ions by a single CC π-bond as suggested in (21). At higher coverages, ~ 5.4 benzene molecules per supercage, this rotation was hindered and a six-fold rotation took place implying that benzene was bonded to the sodium which lay on the six fold axis immediately below the arene ring. At higher temperatures an additional mobility was observed indicating that jumps were taking place between benzene sorption sites.

Wide line proton n.m.r. spectral measurements were carried out on benzene adsorbed on NaX and NaY zeolites at 77K (23). The second moment of benzene was found not to be dependent on coverage (between θ = 0.2 ·····0.85). This was accounted for by a six fold rotation of benzene and an interaction between the sodium ions and the aromatic π-electrons. It was thought the alternative 2-fold rotation models postulated in (21,22) would give a marked intermolcular contribution to the second moment and were thus dismissed. Further, C.N.D.O. calculations inferred that a C_6H_6-Na^+ interaction would be preferred with the sodium lying below the benzene on a six fold axis.

An n.m.r. study of benzene adsorption dependence on the type of cation in faujasites found that Ca^{2+} formed a stronger interaction that Na^+ with benzene (24). La^{3+} zeolites contained no benzene-La^{3+} interacting species since La^{3+} was not found in the supercages. There appeared to be more mobility in the Ca^{2+} zeolites after approximately 3 benzenes had been adsorbed. Further mobility was found with high Si/Al ratio zeolites due to the lack of fixing ions.

A later paper (25) by Lechert et al, contrary to earlier work (22) which had postulated that from θ =0 to 0.8 the benzene was adsorbed via a single C=C interaction with Na^+, found that at all coverages the benzene rotated about a six-fold axis. This was, once again, shown by C^{13} n.m.r. theoretical shift calculations to be correct due to the preferred model of the overlap of free cation electron orbitals with the orbitals of the benzene (26,8) Lechert et al went on to discuss further n.m.r. results and showed that above 200K most benzene mobility in Nal3X took the form of translational diffusion, at 200K or less intercavity motion took place whereas at much less than 200K rotation about a six-fold axis was the only form of motion (27). When the coverage was less than 4 benzene molecules per supercage (ie when each benzene was bonded to a cation) jumps took place between S2 sites and the jumps were preceeded by a tipping motion about a two fold axis. The arrangement of 4 benzene molecules inside a supercage above the S2 cations is pictured in Figure 8.3 according to Lechert et al who went on to discuss the position of the remaining ~ 1.5 benzene molecules in the supercage when saturation took place. Three models for position of the fifth molecule were discussed: lying in the centre of the supercage or lying perpendicular or parallel to the plane of a window between two supercages. The contributions of the second moment of the nuclear-proton resonance were calculated and compared with experimental results and evidence was overwhelmingly in favour of the fifth benzene molecule lying parallel to the supercage window. This position would also allow a sixth molecule to fit into

the supercage. The position of the four localized $Na^+-C_6H_6$ moieties and the fifth benzene molecule are depicted within the supercage in Figure 8.3.

(vi) Vibrational Spectroscopic Studies

The first infra-red vibrational study was carried out on benzene adsorbed in sodium and calcium faujasites. This study looked at the state and properties of the adsorbed molecules, the displacement of the vibrations, changes in intensities and any infringement of the infra-red selection rules (28). On adsorption ν_{19}, a CC stretching mode at 1486cm^{-1}, was increased in intensity tenfold compared to other infra-red bands. Also a band appeared at 730cm^{-1} which was postulated to be ν_{16}, a forbidden in-plane ring deformation. Combination bands in the 1800-2000cm^{-1} region of benzene were also shifted to higher frequency on adsorption. However, the infra-red active ν_{11}, a CH out-of-plane deformation was difficult to assign because of zeolite framework bands in the same region. The authors went on to suggest that these changes were due to the cation electrostatic field and the π-electrons of the benzene interacting. It was noted that greater changes were found with the calcium form than the sodium form.

A more detailed infra-red study of benzene adsorbed on various type Y zeolites was carried out and no visible difference was noted between Mg, Na, Zn, La, Ce, Ag and CoY types in the measured range of 1400-3100cm^{-1} (29). The authors found that the out-of-plane benzene vibrations shifted to higher frequencies whereas in-plane vibrations did not shift. Similar conclusions were gained from deuteration

experiments. The authors differed from (28) in the interpretation of the 730 and 1850cm^{-1} bands, suggesting that the former band was of zeolite framework origin and that the latter was due to another combination band found at 1854cm^{-1} in liquid benzene. The authors admitted that the π-complexing model was attractive but noted that similar spectral changes occurred in benzene on solidification. They thus felt that the cations were not involved in bringing about these changes and shifts. Further, since the same changes occurred when M^{+} and M^{++} exchanges forms were used, it appeared that the bonding must be similar in each case and that the benzene-benzene interactions were of prime importance.

A laser Raman study has been carried out on alkali X and Y type zeolites with adsorbed benzene (30). It was noted that sample fluorescence was difficult to remove and sample cooling was necessary at low frequencies. The results indicated that the ring breathing and in-plane vibrations moved to lower frequency and that the ring breathing mode, ν_1, formed a doublet which was better resolved in the zeolites with the larger cations, Cs^{+} and Rb^{+}, than those with K^{+} and Na^{+}. On increasing the coverage, the band splitting occurred implying a second adsorption site was available to benzene in the CsX and RbX types. Previous work had indicated that the intensities of the bands varied whereas the band positions did not, on increasing the coverage, and this study corroborated this at high θ. At low θ, the CC bond strength appeared to decrease due to a drop in frequency of the in-plane modes whereas the out-of-plane modes increased. It was postulated that the first two benzene molecules complexed to cations in site 3 positions then the final 3-4 benzene molecules

bonded in site 2 positions, which in Cs^+ and Rb^+ types were obviously quite energetically distinct. This appears to be contrary to all the earlier kinetic, adsorption and n.m.r. work which implied the first four benzene molecules were bonded strongly on site 2 sodium ions and that the final 1-2 benzene molecules were weakly held in position over the intercavity windows. The authors went on to indicate that each of the first two adsorbed molecules may be bonded to <u>two</u> cations then on further coverage the molecules only involve single cation-benzene interactions.

8.4. <u>The Benzene-cation Interaction</u>

The M^{n+}-benzene interaction is expected to differ when M is Ag^+ or Na^+. If the electrostatic field at the aromatic nucleus is increased on increasing the cation ionic radius in the confines of the 13X supercage, then since the ionic radius of Ag^+ is 1.26Å, a much more spatially extensive effect is expected than with Na^+, since it has ionic radius of only 0.97Å.

Further, the initial π-bond between the filled $2p_z$ π-orbitals of the benzene and the cation orbitals of suitable symmetry can lead to a further enhancement of the bonding. The accumulated negative charge on the silver cation being back donated by the d orbitals of the cation to the low lying π-acceptor orbitals of the benzene. This produces π-bonding and antibonding orbitals and hybridized metal orbitals. This model is described in terms of the Chatt-Dewar model (31,32).

The removal of the benzene electrons from the π-bonding orbitals and the donation into the π-antibonding orbitals tends to weaken the C-C benzene bond and should perturb the

intramolecular benzene vibrations in the Ag^+ situation further from the 'free' benzene vibrations than found in the Na^+system. Figure 8.4 shows the bonding concepts in the Na^+ and Ag^+ system. The barrier to rotation, created by the fixing of the cation onto the zeolite supercage wall and the fixing of the benzene to the cation, will be a function of the degree of π-bonding. Thus, a less hindered rotation about the C_6 axis would be obtained in the Na^+ zeolite than in the Ag^+ analogue due to significant π-overlap in the latter case. It must be noted that this simple model neglects other interactions that may be possible in the zeolite supercage, e.g. the $H\cdots\cdots O_{zeolite}$ $_{C_6H_6}$ interaction.

8.5. NaI3X and Benzene

8.5.1. Experimental and results

The type X zeolite was dehydrated and treated as discussed in Chapter 3. Incoherent inelastic neutron scattering spectra of benzene adsorbed on NaI3X zeolite were measured. The dehydrated zeolite, before adsorption was nearly transparent to neutrons, thus on adsorption, the total sample scattering cross-section increased due to the hydrogeneous adsorbed material. The NaI3X was white before adsorption and became white-grey on benzene adsorption. This contrasted with the AgI3X zeolite, which was light grey before dehydration. Pretreatment produced a bright yellow colour which became grey-white on benzene adsorption.

The IINS measurements of the NaI3X/$C_6H(D)_6$ system were carried out on the time-of-flight and beryllium filter detector spectrometers at A.E.R.E. Harwell. The 4H5 experiment was

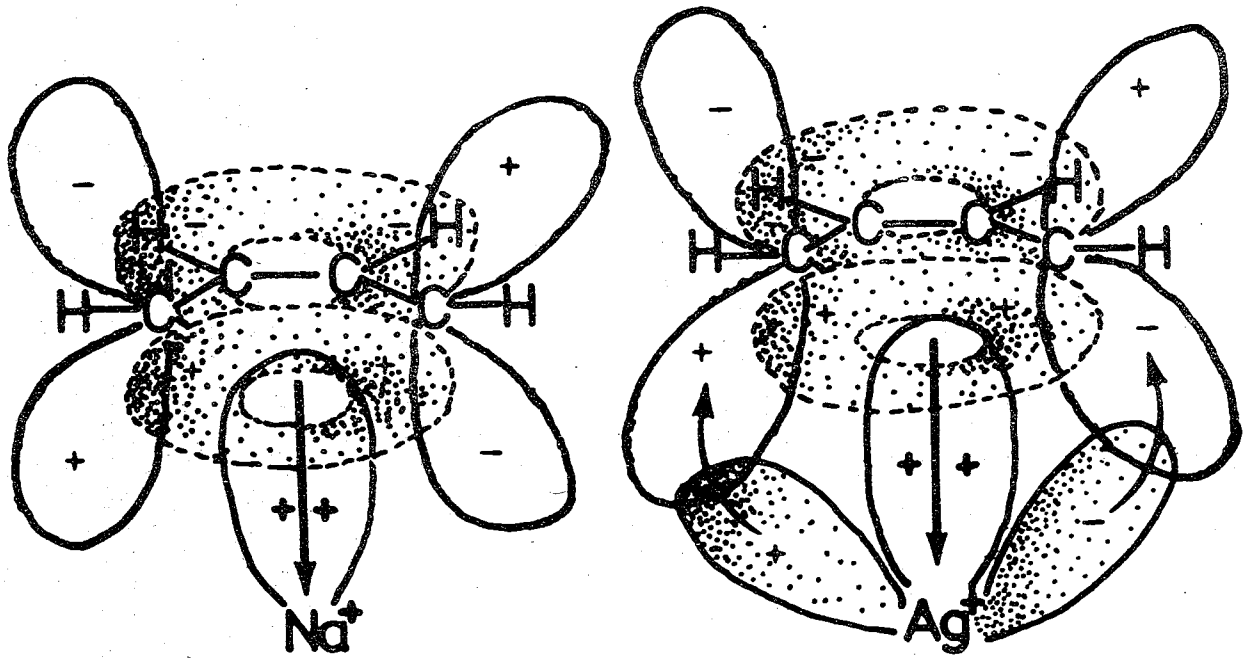

Figure (8.4) Orbital Interaction between Benzene and zeolite Cation

recorded at 113K whereas the BFDDIDO and BFDPLUTO spectra were recorded ta liquid nitrogen temperature. All the spectra were analyzed and had the zeolite background subtracted. Table 8.3 indicates the experiments carried out

Table 8.3: IINS Experiments on the Na13X/Benzene System

Adsorbate	Spectrometer	Temp. (K)	Over pressure of benzene (torr)	Approx. No. of C_6H_6 per supercage
C_6H_6	BFDDIDO	77	30	3
C_6H_6	BFDDIDO	77	100	5.4
C_6H_6	4H5	113	30	3
C_6H_6	4H5	113	100	5.4
C_6D_6	BFDPLUTO	77	100	5.4

Figure 8.5 shows the two BFDDIDO protonated adsorption spectra. Figure 8.6 depicts the BFDPLUTO deuterated adsorption and Figure 8.7 the $P(\alpha,\beta)$ data plotted against energy transfer at a scattering angle of 82^{o} for the Na13X background only, Na13X+~3 benzene molecules per supercage and Na13X +~5.4 benzene molecules per supercage (before background subtraction). It will benoted that in Figure 8.7 the spectrum of the Na13X background and after ~3 benzene molecules per supercage had been adsorbed appear very much the same, in contrast to that with 5.4 benzene molecules adsorbed per supercage. It cannot be concluded that the

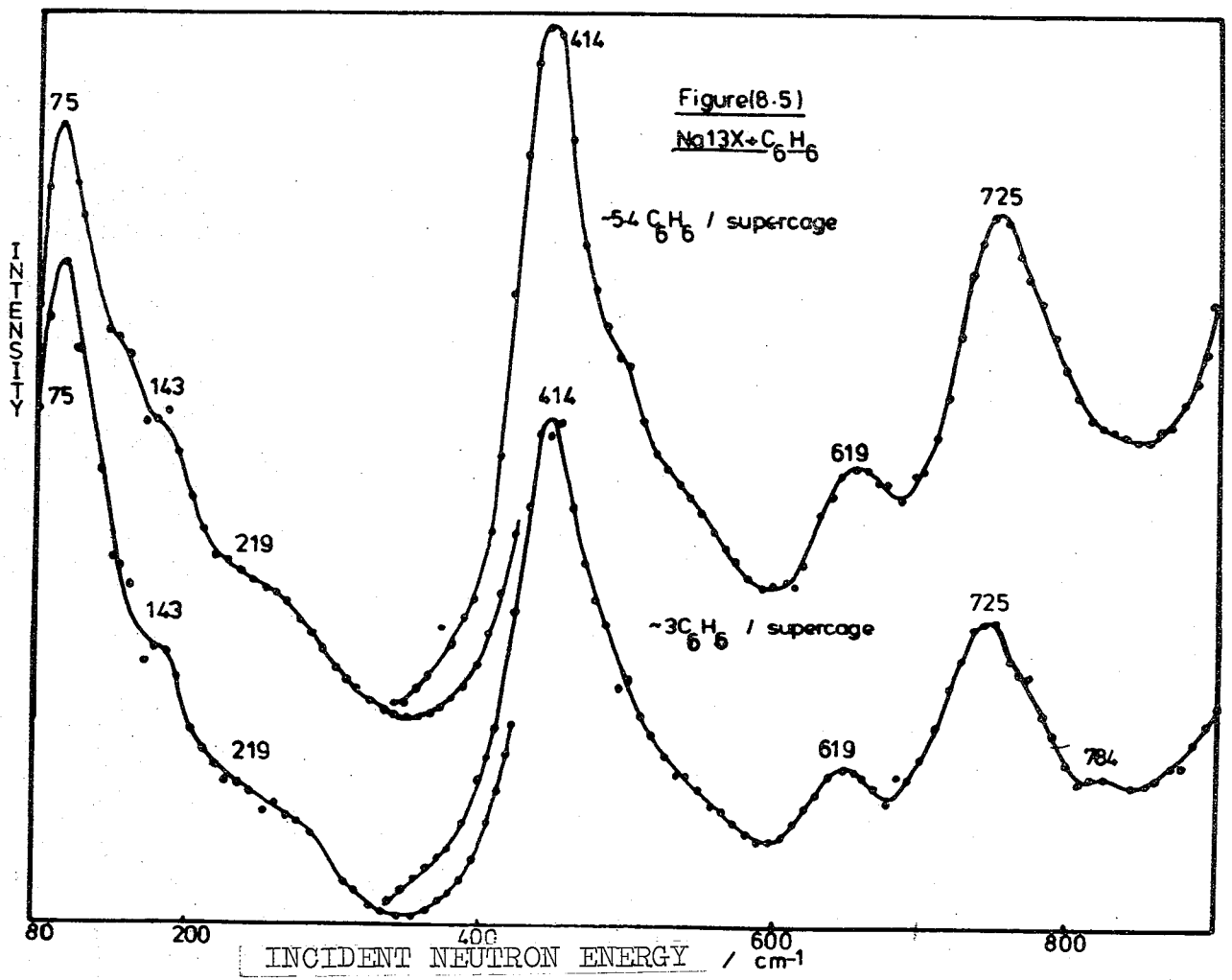
Figure(8.5)
Na13X+C6H6
~54 C6H6 / supercage
~3C6H6 / supercage
INTENSITY
INCIDENT NEUTRON ENERGY / cm-1
75
143
219
414
619
725
784
80
200
400
600
800

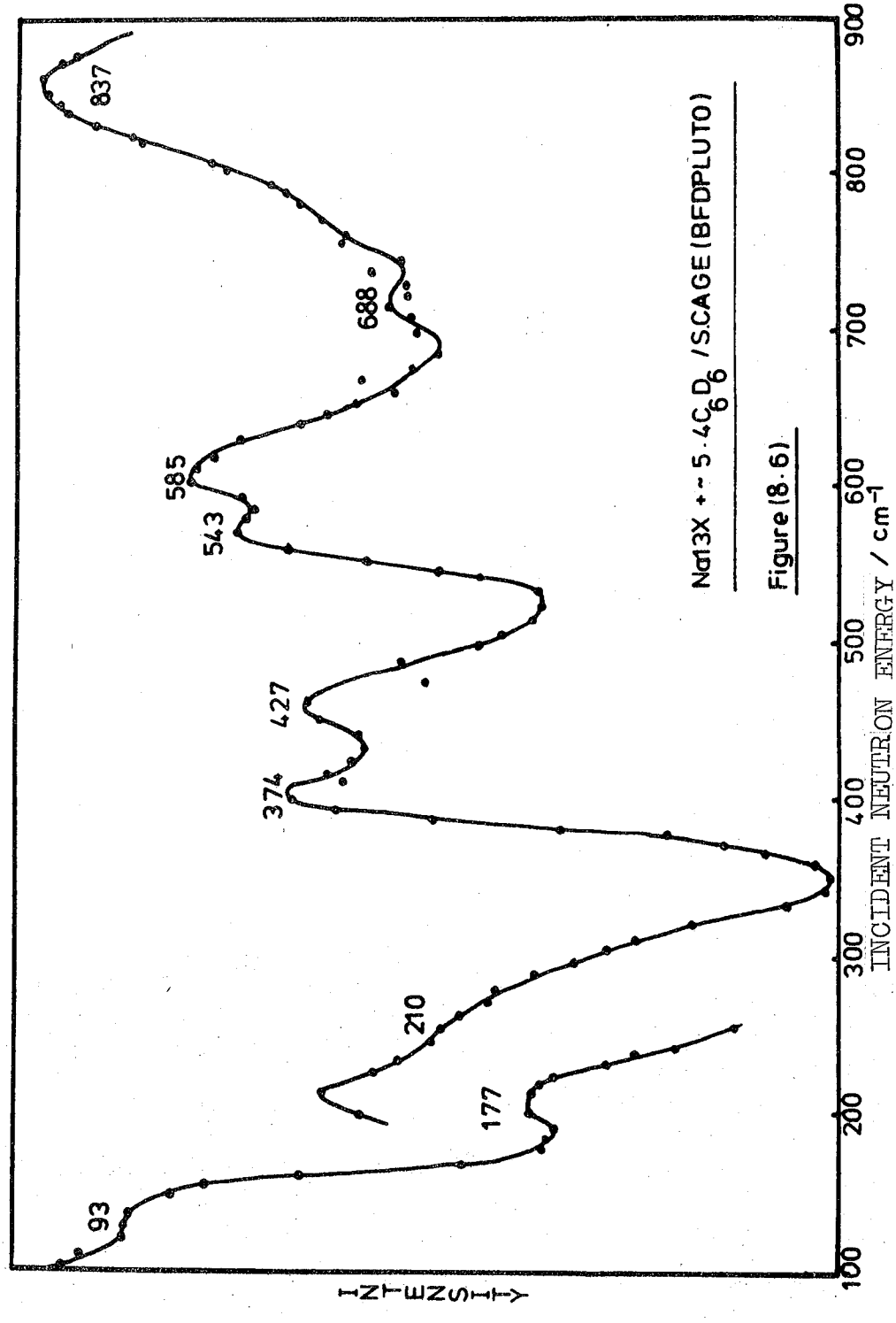
INTENSITY
INCIDENT NEUTRON ENERGY / cm⁻¹
100
200
300
400
500
600
700
800
900
93
177
210
374
427
543
585
688
837
Na13X + ~ 5.4 C6D6 /S.CAGE (BFDPLUTO)

Figure (8.6)

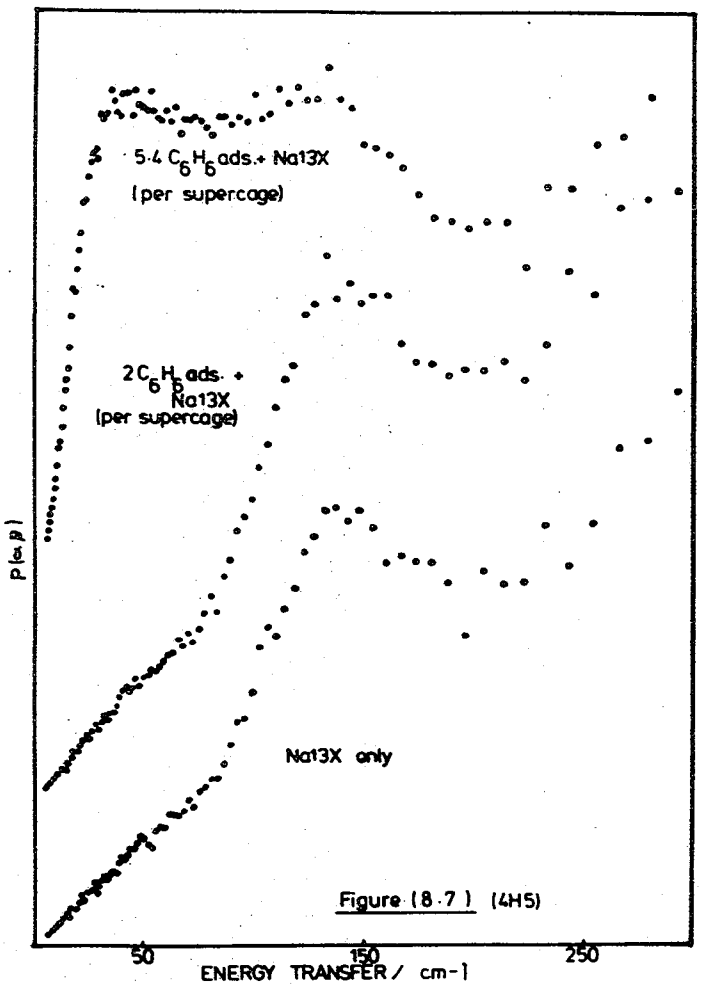

Figure (8·7) (4H5)

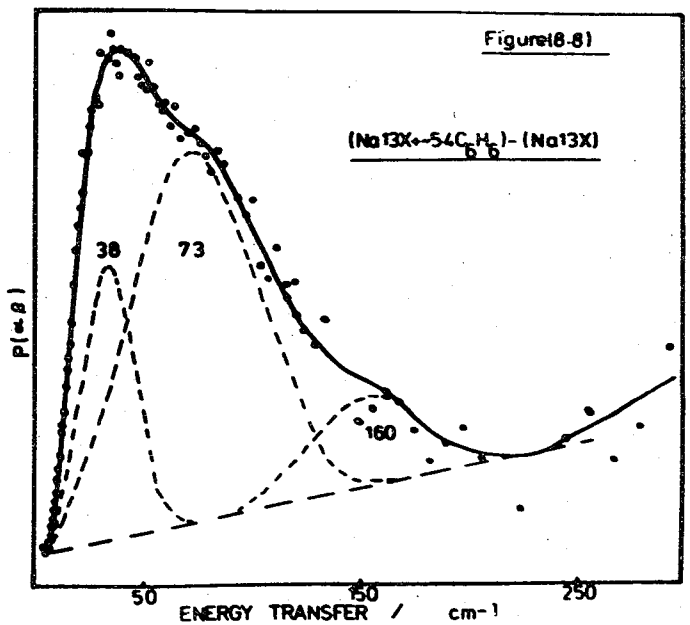

adsorption had not taken place since there was a small colour change after adsorption. Further, the zeolite sample appeared saturated with benzene after the second adsorption to ~5.4 benzene molecules per supercage. However, no significant scattering was found due to the adsorbed benzene only (~ $3C_6H_6$/supercage) after the NaI3X background had been subtracted. No explanation can be offered for this. Figure 8.8. shows the $P(\alpha,\beta)$ data at the higher benzene coverage (~ $5.4C_6H_6$/supercage) with the NaI3X background subtracted. Table 8.4 shows the data acquired from these experiments.

From the exact quantities of benzene adsorbed by the various samples, overall, saturation of the zeolite supercages occurred at ~5.4 benzene molecules in accordance with previous published data.

8.5.2. Discussion

It would be reasonable to expect that the intramolecular benzene vibrations would not be perturbed to any great extent from those found in 'free' benzene. This arises because of the type of π -interaction that is likely to take place between the sodium cation and the benzene and also due to the possible long Na-C_6H_6 (plane) distance of ~3.1Å (20). This makes the Na-$C_{(C_6H_6)}$ distance 3.4Å, which can be compared with the M-$C_{C_6H_6}$ distance in the weak benzene π -complexes discussed in Chapter 7 (3.59Å in $MHg_2(SCN)_6C_6H_6$ and 3.0-3.5Å in $(SbCl_3)_2C_6H_6$). This weak interaction arises from the lack of sodium 'd' orbitals.

Surprisingly, no changes are found at all in the two spectra recorded at different C_6H_6 coverages, in Figure 8.5.

Table 8.4: IINS Vibrational Features of C_6H_6 and C_6D_6 Adsorbed on Na13X Zeolite

Adsorbed C_6H_6			Adsorbed C_6D_6	Assignment
3 C_6H_6 adsorbed per supercage	5.4 C_6H_6 adsorbed per supercage		5.4 C_6D_6 adsorbed per supercage	
BFDDIDO (77K)	BFDDIDO (77K)	4H5 (110K)	BFDPLUTO (77K)	
		38(m)		Torsion (in-phase)
75(s)	75(s)	73(s)		Torsion (out-of-phase)
148(sh)	148(sh)	160(m)	93(vs)	Deformation
			177(m)	Tilt
219(w)	219(wm)	-	210(ssh)	Stretch
414(s)	414(s)	-	374(ms)	ν_{16} o/p Ring Def.
-	-		427(ms)	Overtone band (2 x 210cm^{-1})
725(ms)	725(ms)	-	543(m)	ν_{11} o/p CH Def.
619(m)	619(m)	-	585(m)	ν_6 i/p Ring Def.
-	-	-	688(w)	ν_{10} o/p CH Def.
-	-	-	837(vs)	ν_{17}, ν_{18}, ν_{15}, ν_5 -composite band

i/p = in-plane, o/p = out-of-plane Def. = Deformation

In both spectra ν_{16}, ν_6 and ν_{11} of the intramolecular vibrations can be assigned at 414, 619 and 725cm^{-1} from a comparison with the IINS spectra of benzene (solid) and benzene organometallic complexes. In solid benzene these fundamentals were found at 401, 602 and 700cm^{-1}. The bands have therefore shifted by up to 25cm^{-1} to higher frequency on adsorption. Since the increase, if significant, took place at low and high coverage then it can be postulated that the effect of steric crowding, within the supercage, due to the increased loading of benzene, is having a negligible affect upon the intramolecular benzene vibrations. This is contrary to the suggestion by Angell and Howell (29) which was that the changes in the benzene spectrum were brought about by the benzene-benzene interaction rather than any benzene-cation or benzene-supercage wall interaction. Thus, if the benzene-benzene interactions had been paramount in perturbing the benzene molecules then some change would have been expected with an increase in benzene coverage.

Freeman and Unland (30) thought that at low benzene coverage, in alkali monovalent cation X and Y type zeolites, the vibrational bands primarily dependent on the C-C bond strength, ie the in-plane ring vibrations, were lowered in frequency on adsorption, and that the out-of-plane vibrations increased in frequency. These trends were also discussed by Angelland Howell (29). In the present study the three assigned intramolecular vibrations all increased in frequency including ν_6, the in-plane ring deformation which increased from 606 to 619cm^{-1}. However, it must be noted that Freeman

and Unland reported ν_6 in the C_6H_6/NaX system at 607cm^{-1}, contrary to their predictions.

Abramov et al (28) assigned ν_{11} in the C_6H_6/NaX system using infra-red spectroscopy at 692cm^{-1} and a band at 731cm^{-1} to ν_{12} (which has been subsequently assigned 1010cm^{-1} (29). Angell and Howell (29) suggested that the 730cm^{-1} band was a zeolite infra-red band. However, since ν_{11} can be quite confidently assigned at 725cm^{-1} from these IINS studies, it is felt that the assignment of ν_{11} and the zeolite band should be reversed in the work of Abramov et al and not reassigned in the manner of Angell and Howell.

At lower frequency in the BFDDIDO spectra, there are weaker bands at 75, 148 and 219cm^{-1} which compare with the time-of-flight features at 38, 73 and 160cm^{-1}. The 4H5 spectrum was resolved using the du Pont curve resolver (model 310). Due to the shape of the spectrum in Figure 8.8 a unique fitting could not be achieved. A band could be centred at 73cm^{-1} similar to the BFDDIDO band at 75cm^{-1}. The strongest band could alternatively lie at 38 or 73cm^{-1} depending on the particular fitting chosen. Due to the strong IINS intensity of these two bands, compared with IINS features at higher frequency, they can be reasonably assigned to the two torsional bands expected for the systems studied. Only one benzene organometallic compound, $(PdAl_2Cl_7C_6H_6)_2$, has been studied (Chapter 7) where the in-phase and out-of-phase torsions have been assigned. The in-phase and out-of-phase torsions arise because the torsions of each benzene entity are coupled within the molecule. Thus the barrier to rotation includes an internal and external component. Due to the large hydrogen amplitudes of vibration in such a vibration,

these bands are found to have a strong IINS intensity. Further, the in-phase torsion can be assigned at lower frequency than the out-of-phase torsion. Lechert and Wittern (27) from n.m.r. studies reported that benzene rotation only took place about the hexagonal axis below 200K.

The assignment of the other skeletal motions: the $Na^+-C_6H_6$ deformation, $Na^+-C_6H_6$ stretch and the doubly degenerate tilt mode is more difficult. The low frequency band at $148cm^{-1}$(BFDDIDO)/$160cm^{-1}$(4H5) could reasonably be assigned to the deformation mode. The tilt and stretch may be found in the $219cm^{-1}$ broad feature in the BFDDIDO spectrum though this region was not very well defined in the time-of-flight spectrum. The weak nature of the $Na^+-C_6H_6$ complex allows it to be compared with the weak clathrate type complexes (Chapter 7). The 100-$300cm^{-1}$ region in each is very similar where the assignment of the metal-benzene tilt and stretch become difficult due to the lack of IINS intensity, usually associated with such motions in complexes such as $C_6H_6Cr(CO)_3$ and $(C_6H_6RuX_2)_2$. Table 8.5 lists the skeletal and lower frequency intramolecular benzene vibrations of these related systems and it can be seen that the similarities are extant.

A further test of the assignments is to compare the relative intensities of υ_{16}, ν_6 and ν_{11} in the IINS spectra of the adsorbed species with the relative intensities of these bands in solid benzene and in the organometallic species (Chapter 7) which have comparable band frequencies.

Table 8.5: Comparison of Intramolecular Vibration in Various Organometallic Complexes, the NaI3X/ Benzene System and in Benzene Only

	$NiHg_2(SCN)_6C_6H_6$	$CoHg_2(SCN)_6C_6H_6$	$C_6H_6Co_4(CO)_9$	$(SbCl_3)_2C_6H_6$	NaI3X + C_6H_6 (Both Coverages)	Benzene Only		
						gas	liquid	solid
Torsion	63	(?)	66	65	75	-	-	-
Deformation	110	117	105	124	148	-	-	-
Stretch	287	282	223	{236	{219	-	-	-
Tilt	227	202	269					
ν_{16}	418	421	394	401	414	404	404	407
ν_6	635	623	623	615	619	606	606	607
ν_{11}	729	741	737	723	725	671	675	687

Table 8.6 shows this comparison where the relative intensities for the three bands, within a particular system are expressed as a percentage of the total intensity of the three bands. A further comparison is made by comparing ν_{11} and ν_{16}, the two strongest intramolecular benzene vibrations.

Overall the comparison of the relative intensities of ν_{16}, ν_6 and ν_{11} from the IINS spectra of the weak benzene complexes, solid benzene and the NaI3X/C_6H_6 system, is quite good. This adds further weight to the above assignments and for the assertion that the NaI3X/C_6H_6 system resembles weak

complexes. The slight difference in the C_6H_6/Ag13X system is discussed in section 8.5.

Table 8.6: Relative IINS Intensities of ν_{16}, ν_6 and ν_{11} in Various Benzene-Containing Systems (%)

(L.C. = Low Coverage H.C. = High Coverage

System	ν_{16}	ν_6	ν_{11}	ν_{16}/ν_{11}
Solid Benzene	52	14	34	1.53
$NiHg_2(SCN)_6C_6H_6$	48	18	34	1.41
$CoHg_2(SCN)_6C_6H_6$	50	12	39	1.28
$C_6H_6(SbCl_3)_2$	54	12	34	1.67
C_6H_6 + Na13X: L.C.	56	8	36	1.56
" " : H.C.	50	10	40	1.25
C_6H_6 + Ag13X: L.C.	36	12	51	0.71
" " : H.C.	53	6	41	1.29
$(PdAlCl_4C_6H_6)_2$	38	15	47	0.81
$(PdAl_2Cl_7C_6H_6)_2$	44	16	40	1.10

The deuterated benzene experiment produced similar results. The deutero-benzene intramolecular vibrations increased from those found in the free non-complexed state. ν_{16}, ν_6, ν_{11} and ν_{10} increased from 351,579,497 and 663cm^{-1} to 374,585,543 and 688cm^{-1} respectively on adsorption, at the satuaration coverage of ~5.4 C_6D_6 per supercage. Table 8.7 shows the calculated deuteration shifts in benzene and in the adsorbed state. The ratios of the protonated frequency to the deuterated frequency are very similar in each case.

Table 8.7: Frequency Ratios of C_6H_6 and C_6D_6 in the Vapour Phase and When adsorbed onto NaI3X Zeolites

Wilson No.	Free Benzene (vapour)		Frequency ratio C_6H_6/C_6D_6	NaI3X + Benzene		Ratio (actual) C_6H_6/C_6D_6
	C_6H_6	C_6D_6		$+C_6H_6$	$+C_6D_6$	
16	404	351	1.15	414	374	1.11
6	606	579	1.05	619	585	1.06
11	671	497	1.35	725	543	1.34
10	849	663	1.28	-	688	-

The IINS band, in Figure 8.6, at 427cm^{-1} could not be reasonably explained, except as a combination or difference band or possibly a second harmonic (e.g. 2 x 219cm^{-1}). The low frequency bands at 93,177 and 210cm^{-1} could not be assigned with confidence due to the lack of deuterated benzene/NaI3Xzeolite time-of-flight data. However, the skeletal benzene-cation vibrations derived from the rotational degrees of freedom of the free benzene can be estimated for the deuterated system. The ratios of ($I_{C_6H_6}/I_{C_6D_6}$), where I is the moment of inertia of the rotating hydrocarbon about the x,y and z axes, can be used to predict to expected shifts on deuteration. Table 8.8. shows the calculated values of the moments of intertia and the ratio of the protonated and deuterated values for the three torsional modes τ_x, τ_y and τ_z.

Table 8.8: Moments of Inertia of C_6H_6 and C_6D_6 About the x, y and z Axes ($\times 10^{-40} gcm^2$)

Axes	$I_{C_6H_6}$	$I_{C_6D_6}$	Ratio $\frac{I_{C_6H_6}}{I_{C_6D_6}}$
x	294.7	355.8	0.828
y	88.7	106.9	0.830
z	88.7	106.9	0.830

Table 8.9 shows the prediction for the C_6D_6/Na13X system compared with the observed values calculated from the ratio of the moments of inertia.

Table 8.9: Observed and Predicted Torsional Frequencies For The Na13X/$C_6H(D)_6$ systems (cm^{-1})

Torsion	C_6H_6+Na13X Observed	C_6D_6+Na13X	
		Predicted	Observed
τ_z: in-phase torsion	38	32	-
τ_z: out-of-phase torsion	73	61	-
τ_x, τ_y } Tilt	219	181	177

Of the low frequency BDFPLUTO bands, Figure 8.6, at 93, 177 and 210cm^{-1}, the band at 93cm^{-1} could be assigned to the deformation mode of the Na^+-C_6D_6 entity whereas the torsional bands can be estimated to lie at lower frequency beyond the region of the BFDPLUTO study from the predicted

values of 32 and 61cm^{-1} estimated in Table 8.9. The 177cm^{-1} IINS band has greater IINS intensity than the 210cm^{-1} band. Therefore the doubly degenerate tilt could be assigned to the 177cm^{-1} band. This is reasonable since an estimation using the C_6H_6/Na13X data tentatively predicted a frequency of 181cm^{-1}. Once again the C_6D_6-Na^+ stretching frequency is assigned at the higher frequency of 210cm^{-1}. This reversal of the tilt and stretch assignments was found in $(SbCl_3)_2C_6H_6$ (Chapter 7). This was also the case in $Cu_4(CF_3CO_2)_4$ $(C_6H_6)_2$, another benzene organometallic species where the tilt could be assigned from an IINS study at 219cm^{-1} and the stretch at 269cm^{-1} (unpublished results).

8.6 Ag13X + Benzene

8.6.1. Experimental and Results

The incoherent inelastic neutron scattering spectra of benzene adsorbed on Ag13X zeolite were measured using the IN4, BFDDIDO and BFDPLUTO spectrometers. Table 8.10 lists the experiments carried out and the conditions under which they were recorded.

The measured maximum uptake of benzene, in molecules per supercage, by the silver zeolite was found to be approximately 4.5.

Only a low coverage of benzene was measured using BFDDIDO. The run at low coverage, was carried out in a liquid helium cryostat. On removing the sample from the cryostat, the sample, probably due to some condensed nitrogen within the sample can caused by a leaking glass-metal seal, exploded.

Table 8.10: IINS Experiments on the $Ag13X/C_6H(D)_6$ System

Adsorbate	Spectrometer	Temp. (K)	Approx. No. of benzene molecules per supercage	Over pressure of benzene (torr)
C_6D_6	BFDPLUTO	77	2-3	10
C_6D_6	BFDPLUTO	77	saturated	50
C_6H_6	BFDDIDO	15	2	5
C_6H_6	BFDPLUTO	77	saturated	100
C_6H_6	IN4	6	2.6	100
C_6H_6	IN4	6	4.5	100

BFDDIDO runs were later carried out in a liquid nitrogen cryostat due to this possible effect. The IN4 experiment was run at 6K using an incident neutron energy of $280cm^{-1}$.

Figure 8.9 shows the BFDDIDO and BFDPLUTO spectra of the protonated benzene adsorbed on the Ag13X zeolite at low and high coverage and Figure 8.10 the spectra from a BFDPLUTO deuterated benzene adsorption experiment.

Figure 8.11 shows the $P(\alpha,\beta)$ IN4 data of the background and two benzene coverages and Figure 8.12 depicts the two coverages of benzene with the Ag13X background subtracted. All the IN4 spectra are from the average scattering angle of 131.5^{o} (average of seven angles 121^{o}-139.5^{o}). The spectra in Figure 8.12 have the points above 15meV grouped in threes. Tables 8.11,8.12 list the relevant data from the protonated and deuterated experiments respectively

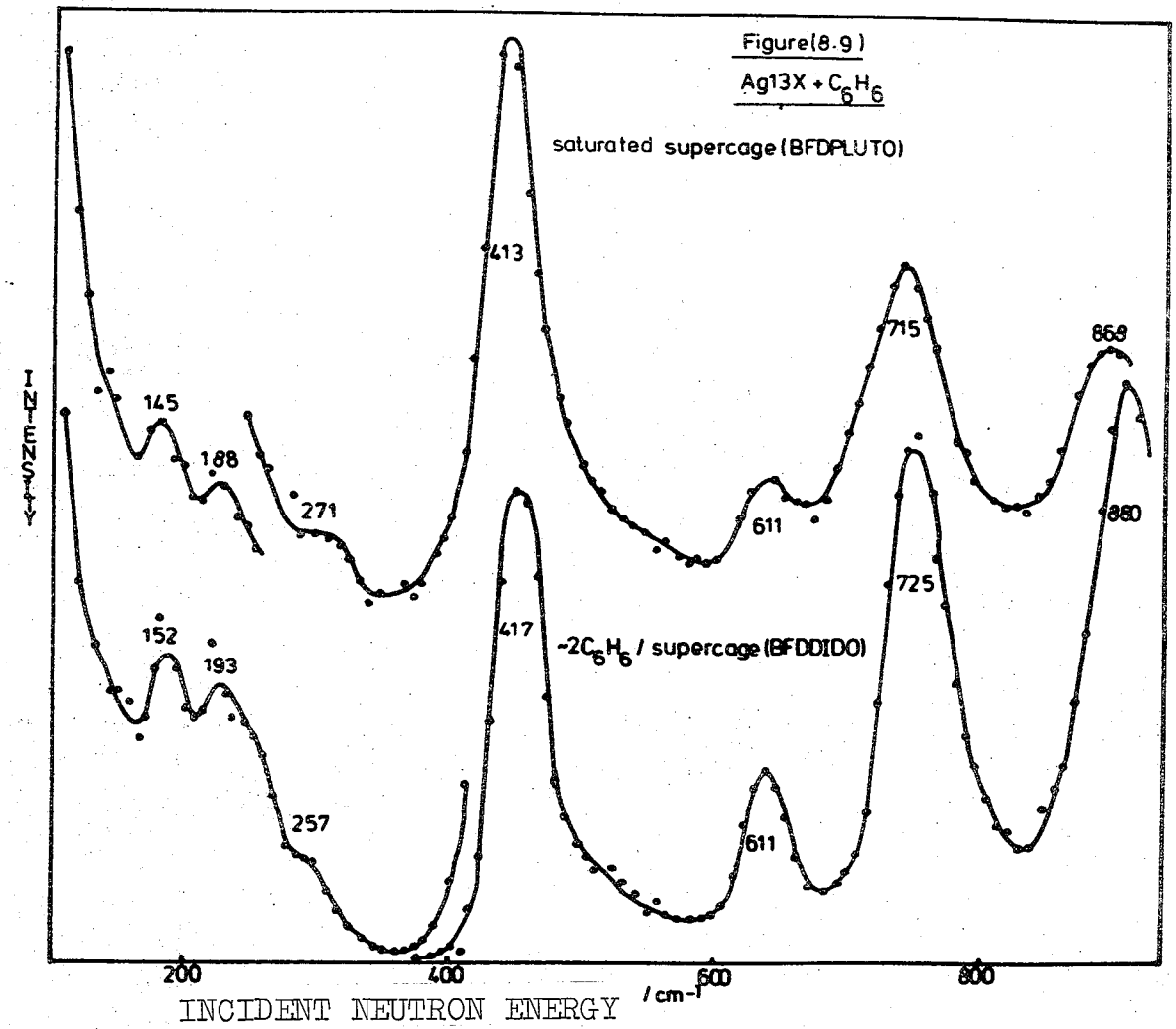
Figure(8.9)
Ag13X + C6H6
saturated supercage (BFDPLUTO)
-2C6H6 / supercage (BFDDIDO)
INTENSITY
145
188
271
413
611
715
868
152
193
257
417
611
725
880
200
400
600
800
INCIDENT NEUTRON ENERGY /cm-1

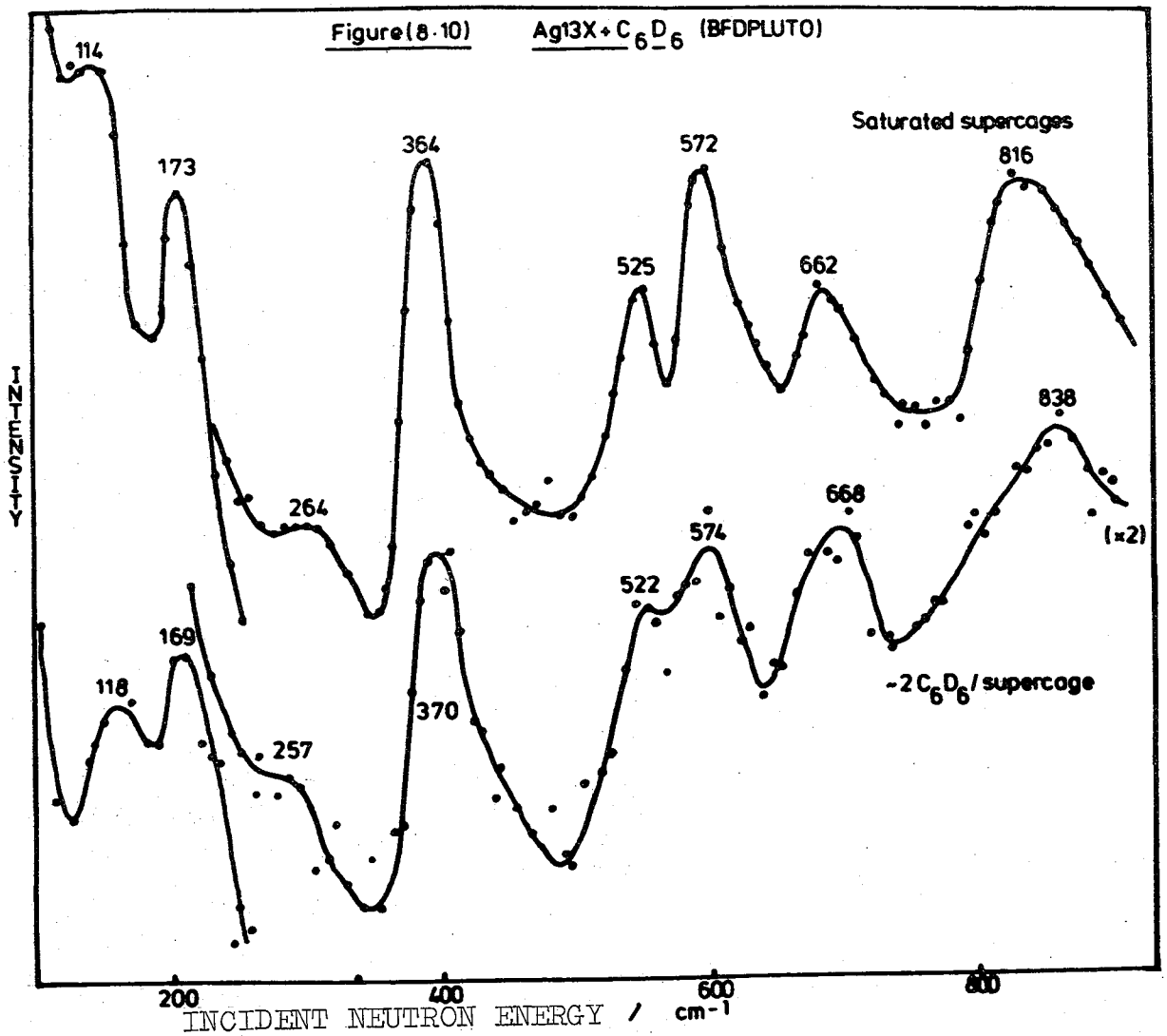
Figure (8·10)
Ag13X + C6D6 (BFDPLUTO)
Saturated supercages
114
173
264
364
525
572
662
816
838
668
574
522
169
118
257
370
(×2)
~2 C6D6 / supercage
INTENSITY
200
400
600
800
INCIDENT NEUTRON ENERGY / cm-1

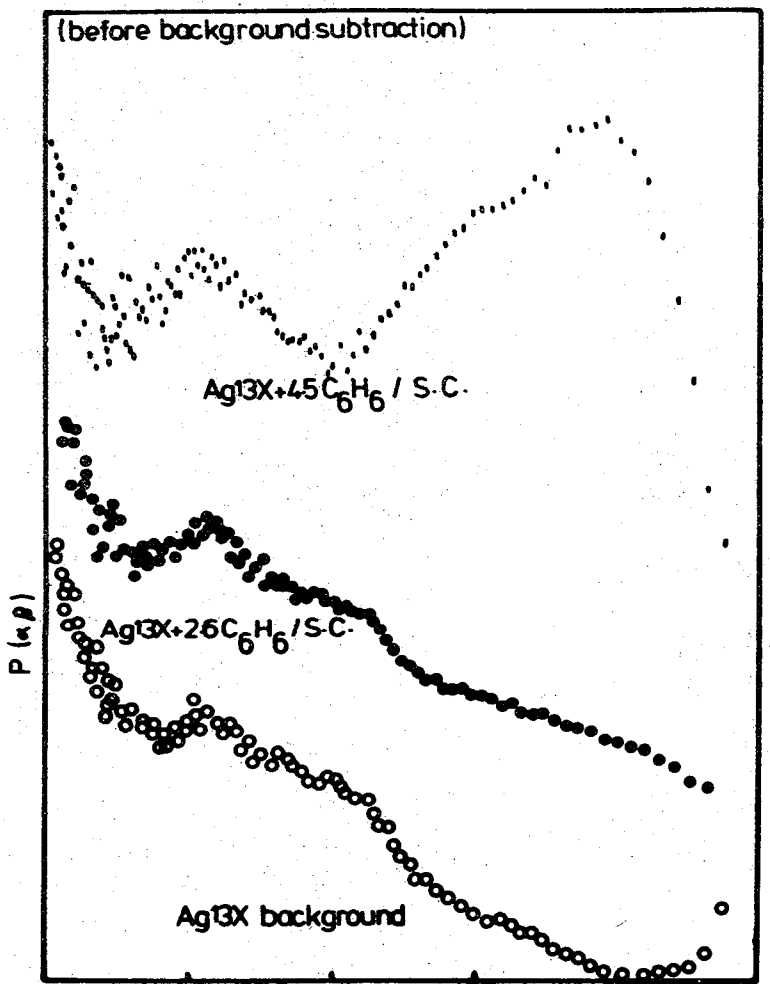

Figure(8.11) P(α β) data(IN4) – C_6H_6 / Ag13X
(S.C.= supercage)

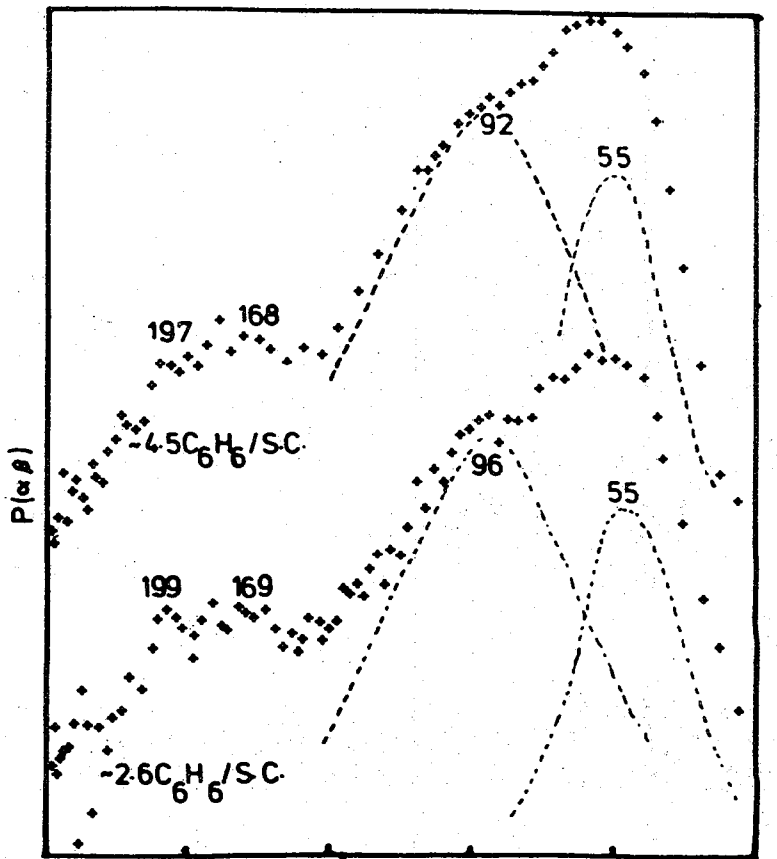

Figure(8.12) P(α β) data(IN4) – C_6H_6 / Ag13X
(S.C.=supercage)

Table 8.11: Spectral Assignments of C_6H_6/Ag13X System (Data From BFDDIDO, BFDPLUTO, IN4 and 4H5)

BFDDIDO $2C_6H_6$/ supercage	BFDPLUTO saturated supercage	IN4 2.6 C_6H_6/ supercage	IN4 saturated supercage	Free Benzene	Assignment
		55(m)	55(m)		Torsion (in phase)
		96(vs)	92(s)		Torsion (out-of-phase)
152(m)	145(wm)	169(m)	168(m)		Deformation
193(m)	188(wm)	199(m)	197(wm)		Tilt
257(sh)	271(msh)				Stretch
417(vs)	413(vs)			404	ν_{16} o/p Ring Deformation
611(m)	611(m)			606	ν_6 i/p Ring Deformation
725(vs)	715(s)			673	ν_{11} o/p CH Deformation
880(vs)	866(s)			849	ν_{10} o/p Deformation

i/p = In-plane o/p = Out-of-plane

Table 8.12: BFDPLUTO Data on C_6D_6/Ag13X System (BFDPLUTO)

'Free' Benzene Frequency	Approx. $2C_6D_6$/ supercage	Saturated supercage	Assignment
	118(m)	114(m)	Deformation
	169(m)	173(m)	Tilt
	257(wb)	264(wb)	Stretch
345	370(m)	364(s)	ν_{16} o/p Ring Deformation
503	522(sh)	525(m)	ν_{11} o/p Ch Deformation
579	574(m)	572(s)	ν_{6} i/p Ring Deformation
659	668(m)	662(m)	ν_{10}
808			ν_{18}
829	838(mb)	816(s)	ν_{5}
824			ν_{15}
787			ν_{17}

o/p = Out-of-plane i/p = In-plane

8.6.2. Discussion

As in the Na13X experiments, the Ag13X experiments were designed (i) to study the effect of benzene bonded to cations, probably in site 2 positions in the supercages. This was achieved by adsorbing enough benzene to achieve ~2-3 benzene molecules per supercage. (ii) to study the effect on the neutron spectra of saturating the supercage with benzene. This would have meant up to 4 C_6H_6-Ag^+(site 2) interactions with the excess molecules either attached to site 3,4 or 5 type cations in less localized bond situations or lying in similar positions to the excess 1.4 benzene molecules in the Na13X supercage parallel to the supercage windows. However, in the benzene adsorption on Ag13X it was found that the maximum uptake per supercage was 4.5 C_6H_6 molecules. Thus the second effect would have been negligible due to benzene on S3, 4 or 5 positions. This contrasted with the Na13X studies where ~5.4 benzene molecules were taken up at saturation. Since the higher coverage BFDDIDO spectrum was not recorded, it had to be repeated and this took place using BFDPLUTO at a later stage. Thus care has to be taken in comparing the two sets of data in Figure 8.9 since two different samples, sample temperatures and spectrometers were facilitated. From the results, it is apparent that the effect of coverage is quite small upon the benzene intramolecular vibrations as in the case of the Na13X experiments. The only change would appear to be a decrease in the shift, from the non-complexed frequencies, at higher coverage of benzene. This applies only to the out-of-plane vibrations shown in Table 8.13. These changes are very small and may

not be significant though they are consistent.

Table 8.13: Frequency Changes at Low and High Benzene Coverage on Ag13X Zeolite Compared to Free Benzene

Vibration	Difference from 'free' Benzene (cm^{-1})	
	$2.6C_6H_6$/ supercage	$4.5C_6H_6$/ supercage
ν_{16}(out-of-plane)	+13	+9
ν_6(in-plane)	+5	+5
ν_{11}(out-of-plane)	+52	+42
ν_{10}(out-of-plane)	+35	+21

It is proposed that <u>if</u> this is a real effect then the perturbation to the benzene molecule must be caused by the π-bonding to the Ag^+ ions and that it would appear to be relaxing somewhat at higher coverage and, therefore the benzene molecules are bound less specifically possible due to increased benzene-benzene interactions at higher coverage weakening the Ag-C_6H_6 bond.

A relevant comparison is between the Na13X and Ag13X zeolites. Surprisingly there is little difference between the two systems. This parallels the conclusions of Angell and Howell (29) who found a similar situation with benzene adsorbed onto mono-, di- and trivalent cation exchanged zeolites. It can be surmised that the Na^+ and Ag^+ cations, in the benzene/zeolite systems, studied by us, are having the same effect

upon the intra-molecular benzene vibrational modes. However, Angell and Howell suggested that the cations were not necessarily involved in the interaction that brought about the changes in the benzene spectrum. This was postulated because the changes found in all the zeolite systems studied resembled those found in going from benzene in the vapour to the solid state. With their model, the changes found on increasing the coverage should have parallelled the changes shown in Table 8.5, for benzene, gas to solid. This was not found whereas it appeared the intra-molecular benzene vibrations resembled to a greater degree those in weak benzene organometallic species. From the comparative Na13X+ benzene and organometallic data in Table 8.5 and the Ag13X assignments in Table 8.11 it can be seen that the intra-molecular vibrations of benzene adsorbed on the zeolites can be compared quite well with the organometallic benzene data and not so well with the change found in the solidification of benzene alone where ν_{11} has only increased marginally from 671 to 687cm^{-1}, ν_6 has remained at 606cm^{-1} whereas an increase of only 3cm^{-1} to 407cm^{-1} was found with ν_{16}. In the benzene organometallic complexes and of the benzene/zeolite systems ν_{11} has increased further in frequency to greater than 710cm^{-1}, ν_6 has increased to more than 610cm^{-1} whereas ν_{16} has generally increased by 10cm^{-1}. Thus, it is felt that though the changes are comparable in both cation exchanged zeolites, they both involve a cation-benzene interaction similar to those benzene-metal interactions in the weaker benzene complexes such as the $MHg_2(SCN)_6C_6H_6$ clathrates, $(SbCl_3)_2C_6H_6$ etc. and not with the stronger

benzene complexes such as $C_6H_6M(CO)_3$, $(RuX_2C_6H_6)_2$ etc. which show greater changes in the frequencies of ν_{16}, ν_{11} and ν_6.

Further it can be noted that in Table 8.6, which shows the relative intensities of ν_{11}, ν_6 and ν_{16}, (the three major low frequency intramolecular benzene vibrations) that the relative intensities found in the benzene/Ag13X system at low coverage are somewhat different from those found at higher coverage, solid benzene and in the clathrates. However, they are comparable to those found in $(PdAl_2Cl_7C_6H_6)_2$ and $(PdAlCl_4C_6H_6)_2$ which contain benzene bonded to more than one transition metal. Freeman and Unland (30) suggested that at low benzene coverage that each benzene may have been associated with more than one cation. Perhaps, this indicates a similar bonding situation.

The deuterated benzene studies can be treated in the same manner as those for the Na13X system. Table 8.14 compares the changes found in free benzene (vapour) with those in the Ag13X system. Again, very good comparisons can be made between the changes found in free benzene and in the adsorbed state. This adds further evidence for the assignments.

The skeletal Ag^+-C_6H_6 vibrations, which would take the form depicted in Figure 6.15, if a simple M-C_6H_6 interaction takes place, may reflect a stronger cation-benzene interaction than found in the Na13X/benzene system. The shift in the benzene intramolecular vibrations did not show this. IINS vibrations exist in the data, from the IN4 and BFDDIDO/BFDPLUTO experiments, at approximately 250, 190, 160, 90 and 60cm^{-1}. No particular trend was found with increasing

Table 8.14: Frequency Ratios of Protonated and Deuterated Benzene in the Vapour Phase and When Adsorbed Onto Ag13X Zeolite

Wilson No.	Frequency Ratio in Free Benzene C_6H_6/C_6D_6	Ag13X+ 2 molecules per supercage		Frequency Ratio C_6H_6/C_6D_6	Ag13X+Saturated supercage		Frequency ratio C_6H_6/C_6D_6
		C_6H_6	C_6D_6		C_6H_6	C_6D_6	
16	1.15	417	370	1.13	413	364	1.13
6	1.05	611	574	1.06	611	572	1.07
11	1.35	725	522	1.39	715	525	1.36
10	1.28	880	668	1.32	866	662	1.31

benzene coverage. This situation is difficult to understand since the number of benzene molecules per supercage increases from 2 to 4. Perhaps if two benzene molecules in a supercage interact to such an extent then also four benzene molecules in the supercage would also interact and if the resulting vibrational spectrum is complex at the lower coverage it may be difficult to observe any increase in spectrum complexing at higher coverage.

Unfortunately, no crystal structure has been carried out on the benzene/M13X zeolite system and, further, since the actual cation site is in doubt then the actual H------H and C---H intermolecular distances cannot be judged with any confidence. Therefore, the extent of any intermolecular interaction cannot be gauged

To understand the benzene-cation skeletal vibrations the coverages are approximated to 2 and 4 benzene molecules per supercage. (One obvious experiment involving a single benzene molecule per supercage would be worthwhile. This would indicate the type of bonding ie the number of cations associated with each benzene molecule. Also the intermolecular benzene-benzene interactions, if any, would be zero in such a case). With two benzene molecules adsorbed in the supercage an in-phase and out-of-phase torsion would be expected. From the studies of benzene complexes containing more than one benzene per molecule which interact (Chapter 7), e.g. $(PdAl_2Cl_7C_6H_6)_2$, the torsional bands were found to exist at low frequency ($<150cm^{-1}$). The complexity of the situation increases at 4 molecules per supercage and resembles that found in organometallic species such as $Ir(C_2H_4)_4Cl$, which

has been studied by IINS techniques by Howard and Waddington (33). However, in this compound one C_2H_4 ligand could be described as axial whereas the other three ligands were equatorial and equivalent. If the 4 benzene molecules are arranged in the tetrahedral manner of Lechert et al (27) then all four are arranged in an equivalent manner within the supercage.

The vibrational spectrum could, in theory, be very complex because bands may be split by interactions between the four equivalent benzene molecules. If they were not equivalent than a further complexity would arise due to the different bonding situations. Now studies of complexes containing equivalent ligands, such as in $(PdAlCl_4C_6H_6)_2$ (Chapter 7) have shown that the interactions between the ligands does not lead to splitting of the ligand internal modes but is evident only in the splitting of the skeletal $(M\text{-}C_6H_6)_n$ vibrations, such as the torsion about the metal-ligand axis ie the cation-benzene C_6 axes in the zeolite case. Splitting of the intramolecular benzene bands was not observed. The torsional frequencies will be described at both coverages in terms of an in-phase and an out-of-plase form. The latter usually is found at higher frequency.

From the IN4 experiments two bands at lower frequency can be assigned from IINS intensity grounds to be the torsions. Using a curve resolver (du Pont 310) a medium intense band can be observed at $55cm^{-1}$ at both coverages whereas a stronger band can be found to exist at $96cm^{-1}$ (low coverage) and $92cm^{-1}$ (high coverage).

The uniqueness of this curve fitting may be in doubt.

However, it is felt that the fitted curves are reasonable since there is little evidence available to assist in the fitting and only in $(PdAl_2Cl_7C_6H_6)_2$ is evidence available to indicate that the two torsions were at a low frequency ($\sim$80 and 125cm^{-1}). The frequency decrease (if it is significant) in the band at 96cm^{-1} to 92cm^{-1} as the coverage is increased may be due to a steric crowding effect.

At higher frequency weaker IN4 IINS bands exist at 169 and 199 cm^{-1} which do not vary significantly with an increase in coverage. A BFDDIDO band also exists at 260cm^{-1}. These bands are assigned to the other benzene-cation framework vibrations. The benzene-cation tilt band is expected to be more intense in the IINS spectrum than the benzene-cation stretch. These bands are also expected at higher frequency than the deformation mode which will be less intense than the torsional bands. It is difficult to differentiate the intensity of the IINS bands in the $\sim$190 and 260cm^{-1} regions. Thus their assignment is rather tentative. In the BFDPLUTO and BFDDIDO spectra it would appear that the bands at higher frequency, $\sim$260cm^{-1}, are weaker than those at $\sim$190cm^{-1}. Thus in accord with the weaker benzene organometallic complex assignments the tilt is assigned to the band at $\sim$190cm^{-1} whereas the stretch is assigned at higher frequency. The band at $\sim$150cm^{-1} is assigned to the deformation mode.

The skeletal benzene-cation vibrations, derived from the rotational degrees of freedom, can be estimated for the C_6D_6 experiments as in the manner of the Na13X/C_6D_6 comparison. This may assist in the assignment of the tilt skeletal vibration. The ratios of $(I_{C_6H_6}/I_{C_6D_6})$, where I is the

moment of inertia, can be calculated for the modes τ_x, τ_y and τ_z. It was found surprisingly that in each case the ratio was found to be virtually the same, at 0.83. (The intramolecular distances were taken as: CC = 1.397Å, CH = 1.084Å and CD was estimated to be 1.07Å (34). Table 8.8 indicates the calculated moments of inertia of C_6H_6 and C_6D_6 about the x,y and z axes.

Thus the predicted value of the tilt can be compared with that found by the BFDPLUTO study of the C_6D_6/Na13X system. Table 8.15 shows the predictions

Table 8.15: Observed and Predicted Torsional Frequencies for the Ag13X/$C_6H(D)_6$ Systems (cm^{-1})

Torsion	C_6H_6 + Ag13X Observed	C_6D_6 + Ag13X	
		Predicted	Observed
τ_x: in-phase	55	46	-
τ_z: out-of-phase	96(LC)	80	-
	92(HC)	76	-
τ_x Tilt	199(LC)	165	169
τ_y Tilt	197(HC)	164	173

LC = Low Coverage HC = High Coverage

The only torsional skeletal motion that can be compared, the tilt, compares quite well with the predicted value. This adds further evidence to the preferred assignments.

8.7 References

1. D.W. Breck 'Zeolite Molecular Sieves' Wiley Inter-Science (1973)
2. a. Molecular Sieve Zeolites Adv. Chem. Ser. 101 (1971)
   b. Molecular Sieve Zeolites Adv. Chem. Ser. 121 (1973)
3. K. Vaidyanathan Chem. Ind. Dev. 12 (1978) 15
4. R.M. Barrer "Zeolites and Clay Minerals as Sorbents and Molecular Sieves" Academic Press (1978)
5. D.H. Olson, G.T. Kokotailo, J.F. Charnell Nature 215 (1967) 270
6. D.W. Breck J. Chem. Ed. 41 (1964) 678
7. W.J. Mortier, H.J. Bosmans, J.B. Utterh even J. Phys. Chem. 76 (1972) 650
8. H. Pfeifer Phys. Reps. 26 (1976) 293
9. H. Lechert, W. Haupt, H. Kacirek Z. Naturforsch 30A (1975) 1207
10. G.R. Eulenberger, D.P. Shoemaker, J.G. Keil J. Phys. Chem. 71 (1970) 1812
11. D.J.C. Yates J. Phys. Chem. 70 (1966) 3693
12. Y-Y. Huang J. Catal. 32 (1974) 482
13. J. Latzel, H. Noller Z. Naturforsch 32B (1977) 790
14. A. Ciembroniewisz Chemia Strosowana 15 (1971) 479
15. D.M. Ruthven, I.H. Doetsch AIChE Journal 22 (1976) 882
16. N.N. Avgul, A.V. Kiselev, A.A. Lopatkin, I.A. Lygina, M.V. Zerbodov Kolloidn. Zh. 25 (1963) 111
17. B.H.Ha, D. Barthemoef, V. Trambouze J. Chim-Phys. Phys-Chim. Biol. 70 (1973) 463
18. N.I. Alekseeva, D.P. Timofeev, E.M. Sharifova Zh. Fiz. Khim. 40 (1966) 238
19. H. Blank, M. Bulow, W. Schirmer Z. Phys. Chem. (Leipzig) 260 (1979) 395

20. C. Doberenz, D. Geschke, W.D. Hoffman Z. Phys. Chem. (Leipzig) 255 (1974) 666

21. M. Nagel, H. Pfeifer, H. Winkler Z. Phys. Chem. (Leipzig) 255 (1974) 283

22. H. Lechert, H.J. Hennig Z. Naturforsch 29A (1974) 1065

23. W.D. Hoffmann Z. Phys Chem. (Leipzig) 257 (1976) 315

24. H. Lechert, W. Haupt, K. P. Wittern J. Catal. 43 (1976) 556

25. H. Lechert, K.P. Wittern, W. Schweitzer, W. Haupt, Magn. Reson. Relat. Phen. (Heidelberg) (1976) 491

26. D. Geschke, W.D. Hoffmann, D. Deininger Surface Sci. 57 (1976) 559

27. H. Lechert, K.P. Wittern Ber. Bunsenges Phys. Chem. 82 (1978) 1054

28. V.N. Abramov, A.V. Kiselev, V.I. Lygin Russ. J. Phys. Chem. 37 (1963) 613

29. C.L. Angell, M.V. Howell J. Coll. Int. Sci. 28 (1968) 279

30. J.J. Freeman, L.L. Unland J. Catal. 54 (1978) 183

31. J. Chatt, L.H. Duncanson J. Chem. Soc. (1953) 2939

32. G.E. Coates, M.L.H. Green, P. Powell, K. Wade. 'Principles of Organometallic Chemistry' Metheun (1971)

33. J. Howard, T.C. Waddington J. Chem. Soc. Farad. Trans II 74 (1978) 1275

34. J. Favrot, P. Caillet, M.T. Forel, J. Chim. Phys. 71 (1974) 1337

CHAPTER 9

An Inelastic Neutron Scattering Study of Benzene Adsorbed on Platinum Black

9.1 Introduction

This is a study of the inelastic neutron scattering results obtained from benzene adsorbed on the surfaces of cleaned platinum black. The study of adsorbate-substrate interactions is of great importance with regards to the catalytic function of surfaces. To help understand, in particular, the mechanism of hydrocarbon catalysis taking place on transition metal surfaces a simple aromatic system, benzene, is adsorbed onto platinum black surfaces. In the conclusions it is hoped that the type of interaction can be derived from the vibrational spectra. The interaction is further studied at different coverages.

The geometry of the adsorbate registered on the substrate surface and the degree of perturbation of the aromatic ring, caused by the interaction, is discussed. To help in this study of the benzene/platinum system, the inelastic neutron scattering spectra of benzene and of some benzene organometallic species (Chapter 7) have been analysed so that the intra- and inter-molecular benzene vibrations and typical benzene-metal skeletal framework vibrations can be understood.

9.2. Previous Work

(i) Kinetic Studies

Kinetic flow measurements found a rapid benzene coverage of alumina supported platinum in the 26-470°C range (1). The authors postulated that the molecules lay parallel to the platinum surface. Quantitative measurements indicated that from the benzene losses from the flow system that

~ 0.22C_6H_6/platinum atom occurred. However, since benzene has a surface area of ~43.6$Å^2$, which produces ~0.185C_6H_6/ platinum atom, a higher density packing arrangement was implied leading to H·····H interactions and possible dehydrogenation. Now total dehydrogenation would give ~0.33C_6H_6/ platinum atom and therefore partial dehydrogenation was suggested. Hydrogen was reported in the gas phase (the detecting technique used was not reported) though the authors were unsure of the source. Work by others had indicated dehydrogenation on metals took place and the ideas were extended to $C_6H_6/Pt(Al_2O_3)$. No possibility was mentioned of the benzene lying at any other angle to the surface, which would have dramatically increased the ratio. A theoretical study of the reaction rates and activation energies in the C_6H_6(gas)/C_6H_6(adsorbed) exchange reaction at a platinum black surface (2) indicated that π-complexing took place between the C_6H_6 π-orbitals and the inner 'd' orbitals of the surface atoms producing a stable surface complex in the same manner as described in Figure 8.4 .

(ii) Low Energy Electron Diffraction Studies (LEED)

A study of benzene adsorbed on Pt(111) and (100) planes showed ready adsorption took place (3). A poorly ordered layer was initially produced on Pt(111) but on further exposure an ordered layer, L1, was formed which on further coverage produced L2. The unit cell of L1 contained 8C_6H_6 (2x4) having hexagonal symmetry lying at some angle or possibly parallel to the surface. Structure L2 contained benzene molecules reorientated at an angle or even perpindicular to the surface. The authors suggested L2 consisted

of singly dehydrogenerated species covalently bonded to the platinum surface in 5 x 2 unit cells. Only disordered layers were observed on Pt(100). Figure 9.1 shows the dimensions of the benzene molecule (Van der Waal radii). Figure 9.2, 9.3 show the suggested L1 and L2 structures though the exact C_6H_6/Pt configuration was unknown. The exact coverage at which the L1→L2 transition took place was not given. However, it appeared that L1 and L2 were found at less than or equal to one monolayer coverage. The change from L1 to L2 occurred more rapidly with increased benzene over pressure. A later study was carried out on stepped platinum planes. The steps were found to act as sites for the nucleation of carbonaceous growths and some disordered carbon structures were found on the terraces. It was postulated that the steps had broken the CH bonds (4).

Benzene adsorption on Pt(111) was repeated (5). At low coverage each benzene molecule was observed to lie parallel to the plane above a single Pt atom. A further structure was seen but no change in the Pt-C distance was found, contrary to the earlier report (4). Auger measurements and the unit cell size implied that inclined molecules existed in the second structure. A LEED study of benzene multilayers, grown on platinum and silver substrates to a depth of 1000Å observed domaines with different unit cells (6). Overall the molecules lay parallel to the surface, though somewere inclined. Large amplitudes of vibration were found due to the rotation of the benzene molecules about their 6-fold axes. Even at 1000Å some surface character was found though the appearance was becoming very similar to solid benzene.

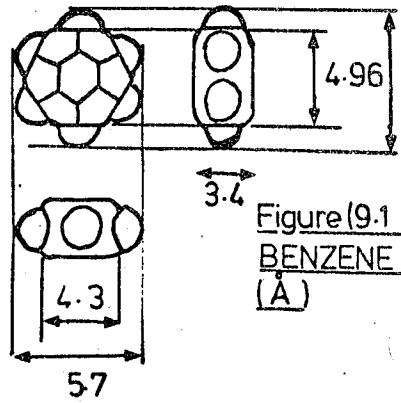

Figure (9.1)
BENZENE structure
(Å)

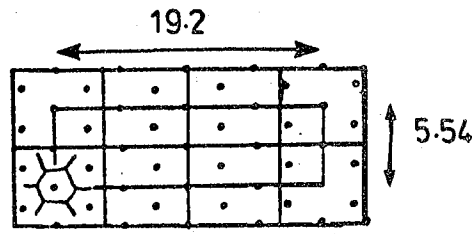

Figure (9.2) Schematic diagram of
$Pt(111)-C_6H_6$-'L1' (3)

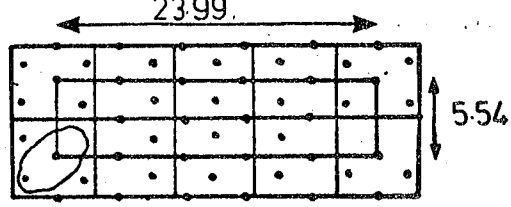

Figure (9.3) Schematic diagram of
$Pt(111)-C_6H_6$-'L2' (3)

(iii) IR Studies

The benzene/silica supported platinum system was studied (7) in the CH stretching region and the authors postulated that dissociation took place since cyclohexane was detected by infra-red. A study (8) looked in particular at the C-C stretching frequency of ν_{19}, which appeared at 1485cm^{-1} in liquid benzene and at 1430cm^{-1} in $(C_6H_6)_2Cr$. This band was found at 1390cm^{-1} an alumina supported platinum which implied to the authors that a stronger π-complex was formed on platinum than found in $(C_6H_6)_2Cr$. However, with such supports of an acidic nature, much could happen that would not be found on platinum alone. For example (9) on supported platinum, benzene was found to form many types of alkanes and cyclic compounds from another study of the CH stretching region.

(iv) Photoemission Studies

A related study of benzene adsorbed on Pd(100) found only weak $C_6H_6\cdots\cdots C_6H_6$ interactions took place. (The coverage or temperature of study were not stated though it could be assumed that monolayer coverage and room temperature prevailed). A strong Pd-C_6H_6 π-interaction took place with down shifts in the energy of the benzene π-bonding orbitals. The unit cell structure was postulated to contain two C_6H_6 molecules at right angles to each other (10).

(v) Electron Energy Loss Spectroscopy (EELS)

This section includes related benzene-nickel studies as well as those involving platinum. Bertolini et al (11) carried out the first benzene-nickel(111) and (100) study using LEED and EELS. Equivalent carbon positions were

found which were identified with the strongest infra-red active fundamentals of benzene. Table 9.1 lists their results.

Table 9.1: Results and Assignments of Bertolini et al (11) For The C_6H_6/Ni(111), (100) Systems at θ =1 (cm^{-1})

(o/p = out-of-plane i/p = in-plane)

C_6H_6 + Ni(100)	C_6H_6 = Ni(111)	Assignment(40)	Liquid Benzene Frequency
761	769	υ_{11}CH o/p def.	671
1001	1041	υ_{18}CH i/p def.	1038
1441	1401	υ_{19}CC Stretch	1478
3003	2987	υ_{20}CH Stretch	3080

In a comparison with liquid benzene, Table 7.6 , υ_{11} can be seen to have shifted markedly to higher frequencies, whereas υ_{19} and υ_{20} have shifted down. Bertolini et al postulated a 'crabbed' benzene structure with the hydrogens lying closer to the nickel surface than the carbon skeleton. Such an interaction would necessarily rehybridise the nickel 'd' orbitals available for bonding. Lehwald et al (12) criticised this work due to its lack of resolution and non-use of the EELS surface selection rule which led to incorrect assignments. Bertolini et al (13) repeated the study at higher resolution. Table 9.2 shows their results and assignments.

Similar energy losses were found on both planes which implied similar bonding and that the plane character was not affecting the actual Ni-C_6H_6 interaction. Bertolini et al

Table 9.2: Results and Assignments of Bertolini et al (13) For the C_6H_6/Ni(111), (100) Systems at θ =1 (cm^{-1})

Experimental loss peak C_6H_6 + Ni	Tentative Assignment	Liquid Benzene Frequency
750	ν_{11}	671
845	ν_1	992
1115	ν_9, ν_{17}	1170,977
1325	(ν_8)	1585
1425	ν_8	1585
3025	ν_2, ν_7	3062,3047

thought the benzene was either bonded to a single nickel atom or lay above a two fold hollow between two nickel atoms. These configurations are shown in Figure 9.4. They also carried out an out-of-specular beam measurement. This did not produce any new peaks but enhanced the low intensity bands at 845, 1115, 1325 and 1425cm^{-1} with respect to the main loss peak at 750cm^{-1}. Their analysis used the EELS 'surface selection rule'. At metal surfaces the potential of dipoles oriented parallel to the surface is very effectively screened by their image dipole. Thus vibrations parallel to the surface are not observed. Those vibrations with a perpindicular component are dipole active at the surface since no symmetry plane exists parallel to the surface. Thus, EELS active

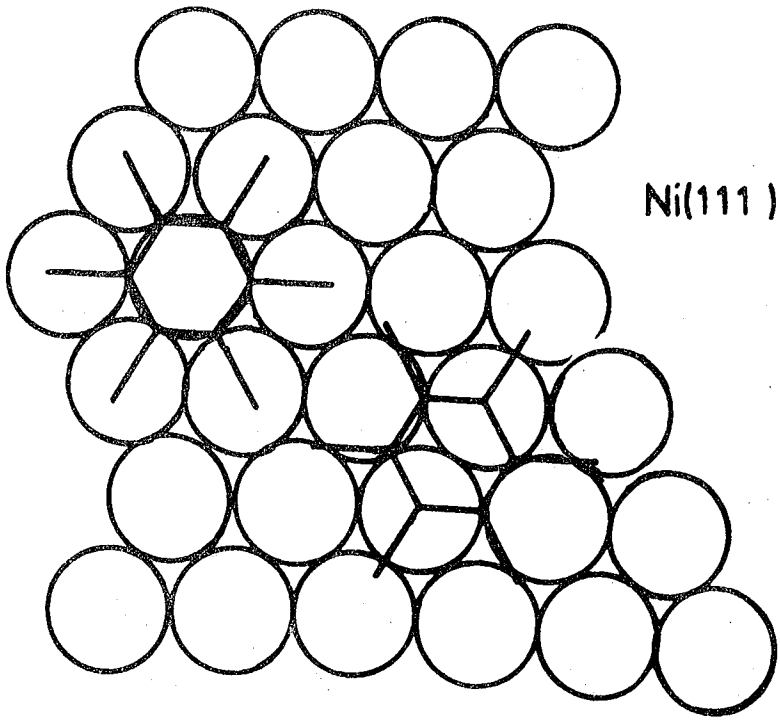

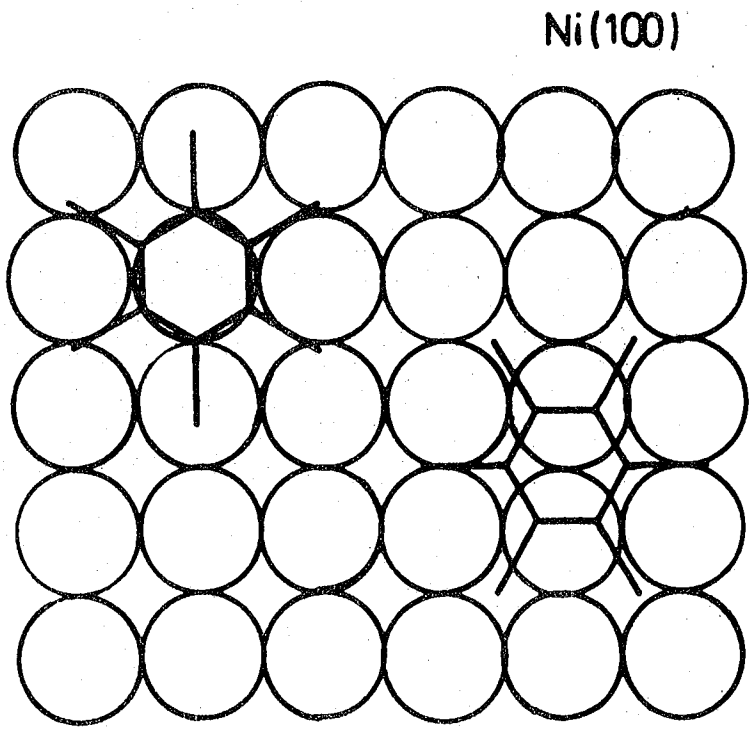

Figure(9.4)

Benzene positions on Ni(111) & (100)[13]

modes are those belonging to the A_1 representation of the surface complex point group. This rule has been generally found to be valid within 2^o of the specular beam. Using the out-of-specular measurements allowed the assignment of modes which involved a dipole moment parallel to the surface. It is notable that neither studies found metal-benzene vibrations at all. This is odd since the translation in the z axis (ie the Ni-C_6H_6 stretch) would be EELS active in C_{6v}, C_{3v} and C_{2v} configurations. Lewald et al (12) carried out an EELS study on the N(111) plane at various temperatures and coverages and reported two states of benzene. They applied the surface slection rule to their analysis and all spectra were recorded in the specular beam. The vibrational bands detected are shown in Table 9.3 with their assignments.

Table 9.3: Results and Assignments of Lehwald et al (12) for C_6H_6 + Ni(111) at θ =1 (cm^{-1})

Experimental loss Peak C_6H_6 + Ni(111)	Assignment C_{3v} Symmetry	C_6H_6 Liquid Frequency
320	C_6H_6-Ni stretch (A_1)	-
730	υ_{11}(on-top site)(A_1)	673(A_{2u})
820	υ_{11}(above 3 fold hollow)	
1130	υ_{15} (A_1)	1150
1430	υ_{14} (A_1)	1310
3000	υ_2 (A_1)	3062

At 292K the band at 730cm^{-1} was more intense whereas at 135K the 820cm^{-1} band was stronger. Further the 730/820cm^{-1}

intensity ratio decreased towards saturation coverage. Since all the other bands did not change, the authors suggested that the behaviour was due to two forms of adsorbed benzene, an 'on-top' and a 3-fold hollow type, and that the 730 and 820cm^{-1} bands were due to the same normal vibration, ν_{11}, the CH out-of-plane deformation. The application of the surface selection rule to the specular measurements only allowed the assignment of symmetric A_1 representations of the symmetry point group in which the surface-benzene complex was found. The symmetry implied by the above study was C_{3v}. It is notable that they observed a band at 320cm^{-1} which was assigned to the benzene-nickel stretch.

Lehwald et al (12) also studied the C_6H_6/Pt(111) system by EELS in the 140-230K range. Evidence showed the benzene ring was parallel to the surface and π-bonded. It was postulated that the benzene was perturbed more strongly on platinum than an nickel due to the greater shift in ν_{11}. The results and assignments are shown in Table 9.4.

Al low coverage, $<1\theta$, the spectrum was dominated by the loss at 830cm^{-1} with a shoulder at 920cm^{-1}. At high coverage, $>1\theta$, these bands were replaced by a very intense band at 720cm^{-1} and a shoulder at 850cm^{-1}, probably due to the chemisorbed phase of benzene which disappeared at greater coverage. The spectra did not change with the temperature of adsorption, or with cooling and heating, contrary to the C_6H_6/Nickel system.

The measurements were carried out in the specular beam and from the number and type of vibrations found in the

Table 9.4: Results and Assignments by Lehwald et al (12) On the Pt(111)/C_6H_6 System at Θ=1 (cm^{-1})

C_6H_6 + Pt (111)		Assignment	C_6H_6(liq.)
Low	High		
360	320	C_6H_6-Pt stretches	-
570	-		-
-	700	Bulk Benzene, ν_{11}	673
-	850	Chemisorbed benzene, ν_{11}	
830	-	'on-top' site, ν_{11}	
920	-	'above 3-fold hollow', ν_{11}	
1130	1030	ν_{12}	1010
-	1170	ν_{15}	1150
1420	-	ν_{14}	
-	1500		1486
3000	3060	ν_2	3063

spectra, indicated that at <1 monolayer coverage benzene was lying in 'on-top' sites (ν_{11} @ 830cm^{-1}) and 'above-3-fold sites' (ν_{11}@ 920cm^{-1}). At high coverage, the 700cm^{-1} band was assigned to ν_{11} from the benzene overlayers. The greater shifts in ν_{11} were seen as an indication that the benzene-platinum interaction was stronger than found on nickel. As the 5'd' orbitals of the platinum are spatially more extensive than the 3'd' orbitals of nickel, then a weaker interaction of the benzene with the nickel orbitals was expected if the benzene position above the surface was similar in each case. At low coverage two bands existed in

the EELS spectrum at 360 and 570cm^{-1}. These bands were assigned to 'C-Pt' vibrations. Presumably, since the vibrations must involve a dipole moment change perpindicular to the surface, then these two bands must be due to C_6H_6-Pt stretching vibrations when the benzene molecules lie in 'on-top' and 'above- 3-fold-hollow" sites. How these bands arose was not discussed.

(vi) Other Spectroscopic Techniques

Renouprez, Jobic and Krasser et al studied benzene adsorption on Raney nickel and silica-supported nickel by IINS (14) and Raman (15,16) spectroscopy. The IINS experiment, performed on IN1B at 77K, was compared with a calculated spectrum, using a force field developed by Favrot and Caillet (17). Excellent agreement was found and all intramolecular vibrations of chemisorbed benzene were assigned. ν_{11} was found to increase to 710cm^{-1} whereas other out-of-plane modes decreased by 40-120cm^{-1}. It was decided that ν_{16} did not split and that benzene was bonded to a single nickel atom. Nickel-benzene skeletal vibrations were assigned at 529 and 459cm^{-1}. From this study the following can be noted: (i) before the calculation of the force field, they assigned the modes which involved the greatest hydrogen vibrational amplitudes (ii) ν_{11} was not resolved from ν_{10} in the observed spectrum of adsorbed benzene (iii) the greatest modifications to the vibrations due to complexation occurred in ν_{11} and ν_{10} (iv) the authors assigned ν_{11} and ν_{10} 30 and 60cm^{-1} less than those frequencies reported on the Ni(111) and (100) planes (11,12). (v) They stressed the poor IINS resolution but it must have been better than the

EELS techniques which were being compared with it. (vi) ν_{11} was calculated to be half the intensity of ν_{10} in the force field of the adsorbed benzene. Finally (vii) ν_5 and ν_{17} were assigned at 868 and 857cm^{-1}, a shift down in frequency of ~100cm^{-1}. In Chapter 7 in the study of benzene complexes the following observations were made: (i)strong bands were always found in the 700-800cm^{-1} region indicative of ν_{11} (ii) a strong band was always found in the 820-880cm^{-1} region of the IINS spectra which could be assigned to ν_{10} (iii) ν_5 and ν_{17} were usually found in the IR/Raman at >950 cm^{-1} (iv) it is felt that ν_{10} does not shift down to 770cm^{-1} as directed by Jobic et al (14) (v) that ν_{11} does increase to greater than 714cm^{-1} in the complexed state (vi) that ν_{11} and ν_{10} can be readily resolved using BFDDIDO and BFDPLUTO spectrometers (vii) and that ν_{11} has an IINS intensity similar if not greater than, ν_{10}. Table 9.5 shows the assignments of Jobic et al (14)for the C_6H_6/Raney nickel system and his reassignments of the work of Lehwald et al (12) and Bertolini et al (11).

The initial Raman study on silica supported nickel found weak bands at 408 and 684cm^{-1} which were assigned to ν_{16} and ν_{11} (15). Thus, at least, C_{6v} symmetry on the surface must have existed. In another Raman study (16) all the fundamental benzene vibrations were observed below 1000cm^{-1}. They had only shifted by a small amount from those in free benzene. The biggest shift was in ν_{11} (673→776cm^{-1}). The authors postulated C_{3v} symmetry existed in the surface complex and that a band at 304cm^{-1} was indicative of a Ni-C_6H_6 stretching skeletal mode.

Table 9.5: Results and Assignments of Jobic et al for The Ni/C_6H_6 Systems (14) (cm^{-1})

Wilson No. /Vibration Description	Free Benzene (17)	Bertolini (11)	Lehwald (12)	Jobic (14)	Predicted IINS Intensity (relative) (14)
18	1035			992	93
12	1010			1003	9
1	993		940(sh)	939	9
5	991			868	87
17	969			857	143
10	849	847(ν_1)	820(ν_{11})	768	164
4	707			610	13
11	675	750	730	714	62
6	607			613	19
16	404			411	53
Ni-C				529	33
Ni-C		363		459	24
Ni-C		290	320		
Def.				92	13
Def.				89	7
Def.				43	0.01
Def.				42	0.01

Bradshaw studied the fixing of an adsorbate onto various solid surfaces (18) and the lowering of symmetry, resulting in the lifting of vibrational degeneracy, was discussed. The fixing of the molecule on the surface results in translational

and rotational degrees of freedom being lost giving rise to new vibrational bands. Using benzene as a model the vibrations of the free molecule were correlated to the adsorbed state in various configurations. The point group of the resulting surface complex was thus a sub-group. On the (111) plane three sites are available: on the 'on-top-site' C_{6v} symmetry is found, the surface complex sub-group is C_{3v} when positioned above the three-fold hollow, and when lying between two surface atoms the sub-group is C_{2v} where all degenerates are lifted. The degree of selection rule breakdown depends upon the strength of interaction with the surface. For example, on the (100) plane the on-top site is of C_{2v} symmetry but if the interaction is weak then the effective symmetry viewed by the molecules may have been determined only by lateral interactions with other molecules (band splitting can occur due to symmetric and antisymmetric combinations of vibrational wavefunctionsin a space group where there are two molecules per unit cell with each normal to the other, in other words a correlation field effect).

Richardson (19) further developed the ideas of Bradshaw. Only those vibrations with a dipole component normal to the surface were IR or EELS (specular) active where Raman active bands were due to changes in polarizability in the element α_{ZZ} (z axis $\perp^{r}$ to surface). It was felt that the intensity of new bands reflected the interaction strength responsible for the lowering of symmetry. The correlation between the point group D_{6h} and four possible sub-groups is shown in Table 9.6. Richardson discussed the work of Bertolini and Ibach (11-12), for benzene on transition metals, and saw anomalies in their analysis (eg. 3000cm^{-1} bands seen but

992cm^{-1} CC stretch not seen using EELS). This was explained as due to a stronger M-H interaction than an M-C interaction which consequently produced the non-planar 'crabbed' effect though the C_6 axis was still retained.

Table 9.6: Correlation Table for D_{6h} to C_{2v} Symmetry (41)

D_{6h} Symmetry	C_{6v}	$C_{3v}(\sigma_v)$	$C_{3v}(\sigma_d)$	C_{2v}
A_{1g}	A_1	A_1	A_1	A_1
A_{2g}	A_2	A_2	A_2	A_2
B_{1g}	B_1	A_2	A_1	B_1
B_{2g}	B_2	A_1	A_2	B_2
E_{1g}	E_1	E	E	B_1+B_2
E_{2g}	E_2	E	E	A_1+A_2
A_{1u}	A_2	A_2	A_2	A_2
A_{2u}	A_1	A_1	A_1	A_1
B_{1u}	B_2	A_1	A_2	B_2
B_{2u}	B_1	A_2	A_1	B_1
E_{1u}	E_1	E	E	B_1+B_2
E_{2u}	E_2	E	E	A_1+A_2

9.3. Experimental Details

The platinum black was cleaned as desrcibed in Chapter 3. This operation was constrained by the sintering of the material, which reduced the sample surface area, at high temperatures. The oxygen on the surface was partially removed by reduction with hydrogen at room temperature. At ~800°C all the oxygen would have been removed but sintering

would have drastically reduced the surface area. The oxide reduction produced quite high temperatures for short lengths of time. Here, most of the chemisorbed oxygen was removed. The tenacity of the more strongly held oxygen (5-10%) was dependent on the manufacturing process over which there was no control (20). Use was made of a quadrapole mass spectrometer, linked into the vacuum line, which indicated after four reduction treatments, that no further water was being produced. Probably a small quantity of strongly-held oxygen still remained.

Background subtractions were carried out as described earlier. However, platinum has a fairly high neutron adsorption cross-section compared with aluminium from which the container was made. Since the sample cans contained >80g of platinum, it would not be strictly valid to carry out a normal subtraction because it would not take into effect any absorption affect and would only remove scattering from the background sample. The absorption cross-section is energy dependent and can be related to (1/neutron velocity). The IN4 technique produces an neutron energy loss situation since high energy neutrons are used. The effect will therefore be minimal after small energy transfers but will be worse for slower neutrons. Whereas with 4H5, with a neutron energy gain situation on scattering, the greater proportion of neutrons being scattered from the sample would increase in energy. Thus the probability of absorption after scattering would be reduced. A corrective procedure may have been developed, possibly based on the work of Paalman and Pings (21), who produced a computer programme for a correction for

elastic scattering. This was not carried out and it could lead to two effects. Relative peak intensities can now only be tentatively quantified and, to a much lesser extent, the band centres could be shifted. On taking the instrument resolution into account the latter effect can be ignored since no intense bands could be generated by ignoring the absorption effect though very weak peaks and troughs may be formed.

Table 9.7 indicates the conditions in which experiments were carried out.

Table 9.7: Details of the C_6H_6/Pt Black Experiments

Figure	Frequency Range (cm^{-1})	Temperature of Study (K)	Incident Neutron Energy (cm^{-1})	Amount Benzene Adsorbed (g)	Benzene Pressure Used (torr)	Coverage (estimated)	Figure
BFDPLUTO	95-106	77	-	-	-	0	9.5
"	"	"	-	0.8-0.9	40	0.75	9.5
"	"	"	-	1.8-2.0	100	1.75	
4H5	0-400	103K	25	0.5-0.7	5	0.5	9.7,9.8
IN4	0-240	5K	264	~0.1	2	0.1	9.9
"	"	"	"	~0.7	25	0.5	
"	"	"	"	~2	100	2	

9.4 Results

Table 9.8 and 9.9 show the results gained from the experiments on the three spectrometers. Figure 9.5 shows the BFDPLUTO spectra of the platinum background sample (approximately 80g in aluminium container) run at 77K. Figure 9.6 shows the BFDPLUTO data at the two coverages of benzene. The platinum background has been subtracted to achieve the scattering due to the benzene only. Figure 9.7 shows the time-of-flight data acquired from the 4H5 experiment. Figure 9.7 (i) shows the platinum black background time-of-flight spectrum and Figure 9.7 (ii) the spectrum of the benzene adsorbed on the platinum surface and, finally, Figure 9.7 (iii) depicts the spectrum of the benzene after the platinum background had been subtracted. All the data are taken from the 90^{o} scattering angle. Figure 9.8 shows the 4H5 $P(\alpha,\beta)$ spectra at angles of 82^{o} and 90^{o} plotted against the energy in the region of interest 10-220cm^{-1}. Figure 9.9 shows the spectra of three coverages of benzene on the platinum black achieved on the IN4 instrument. The runs covered the region of acattering angles of 81 to 158^{o}. Table 9.10 indicates the average scattering angle and the number of angles in each spectrum. $P(\alpha,\beta)$ is plotted in these spectra against energy transfer.

9.5 Discussion

9.5.1 Platinum Black Only

Figures 9.5, 9.7 (i) show the IINS spectra of the platinum black only. These spectra were plotted to check the surface for hydrogeneous impurities and to observe the

Table 9.8: BFDPLUTO Vibrational Data on the C_6H_6/Pt System

Platinum Only	0.75 C_6H_6	1.75 C_6H_6
91(msh)	-	75(m)
175(s)	157(m)	168(mb)
-	215(wm)	-
269(mb)	272(s)	270(m)
381(b)	-	-
-	422(sh)	411(m)
-	471(m)	-
-	522(m)	543(wb)
-	638(s)	647(m)
-	-	686(vs)
-	810(s)	-
863(w)	-	-
-	882(w)	871(mb)

Table 9.9: Low Frequency Vibrations in the C_6H_6/Pt System

4H5		IN4		
Platinum Only	~0.5-1θ C_6H_6	~0.10θ C_6H_6	~0.5θ C_6H_6	~1.5-2.0θ C_6H_6
	443(sb)			
	213(w)	217(s)	209(ms)	211(mb)
		206(msh)		190(sh)
		175(m)	171(m)	168(msh)
165(s)	163(sb)			
			153(m)	158(s)
				127(sh)
	115(m)		121(vs)	119(s)
87(s)		90(w)		
	72(vs)		70(wb)	
	56(m)			

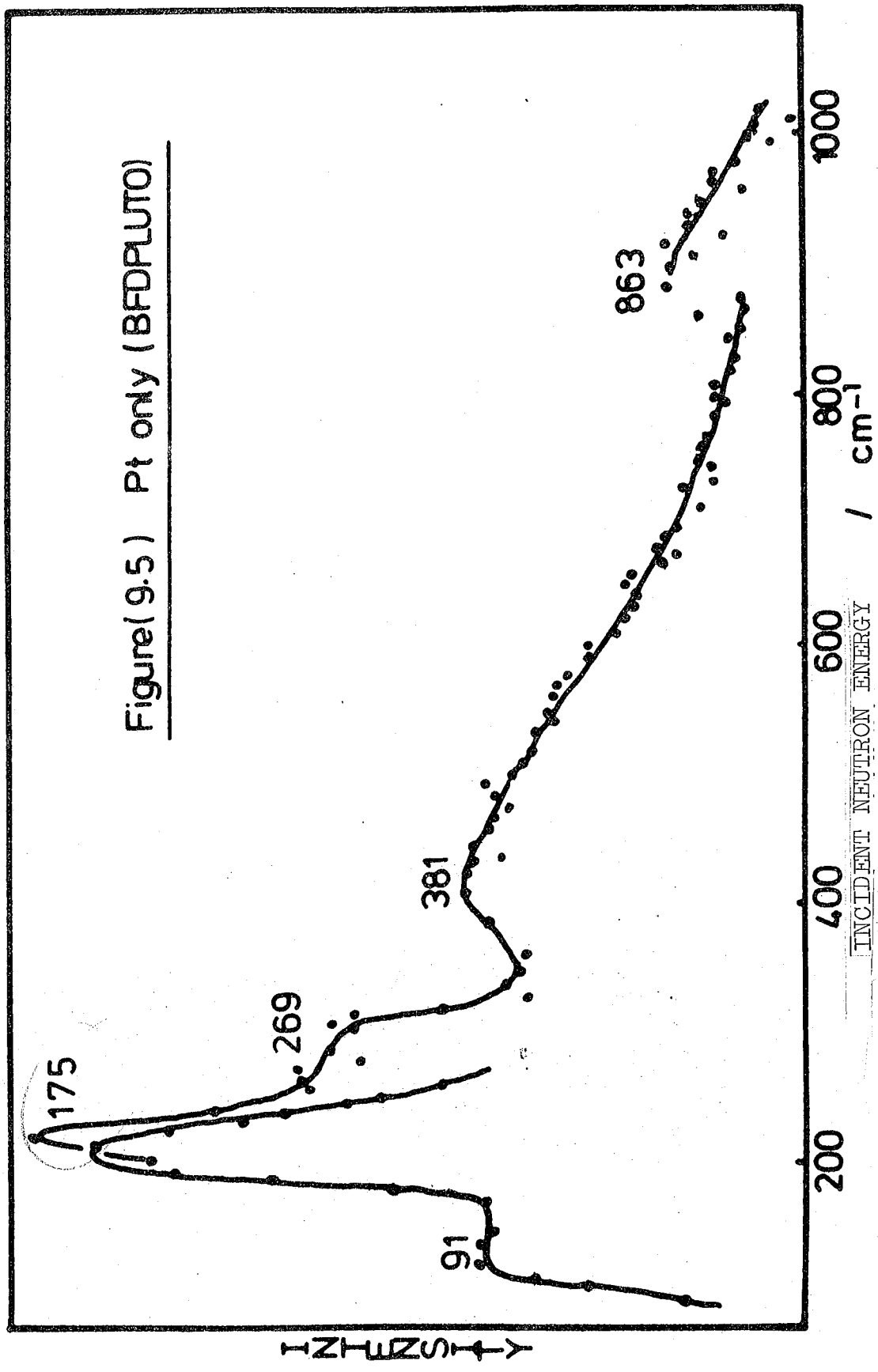
Figure(9.5) Pt only (BFDPLUTO)
175
269
381
863
91
200
400
600
800
1000
INCIDENT NEUTRON ENERGY / cm⁻¹
YIELD

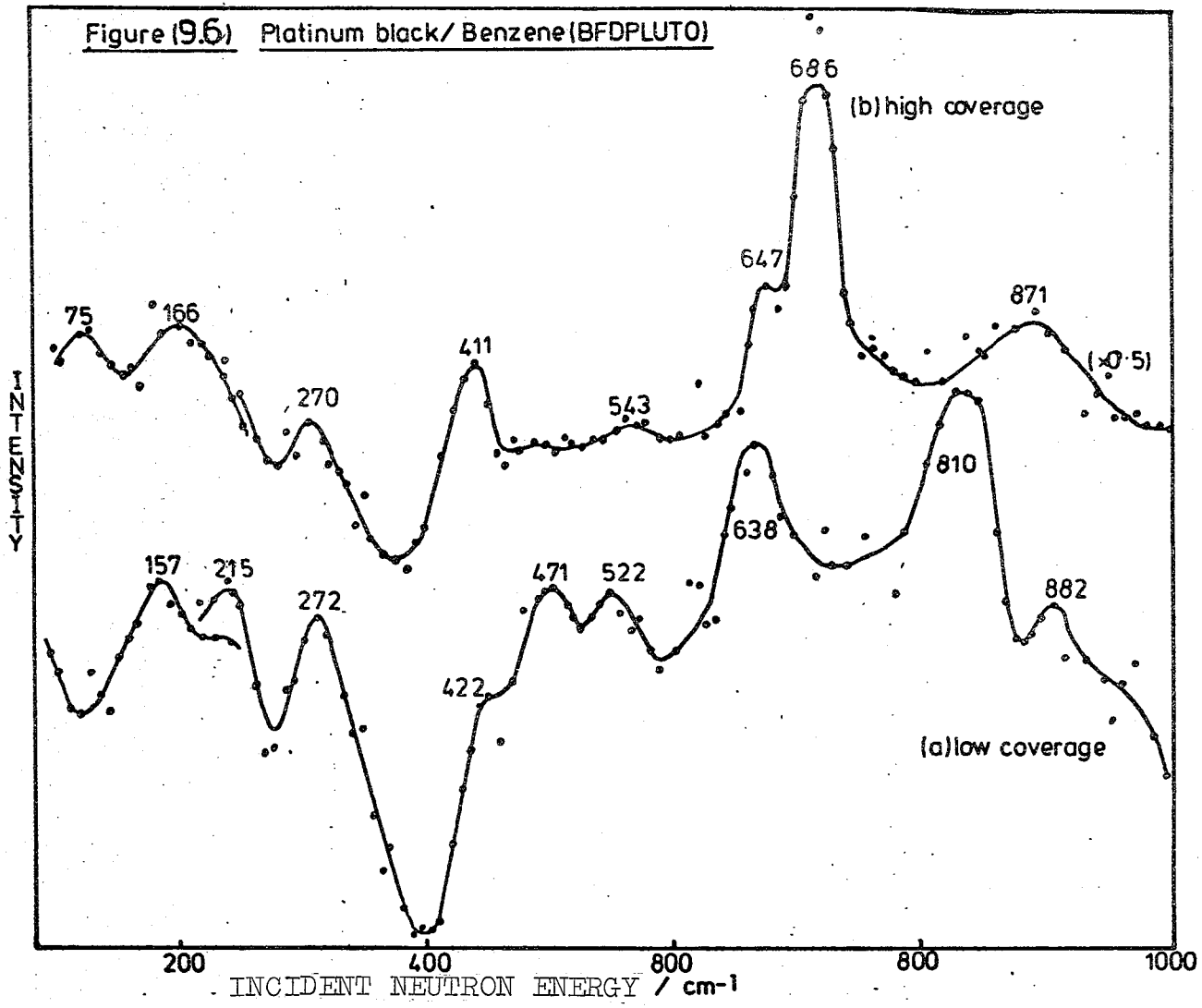
Figure (9.6) Platinum black/ Benzene (BFDPLUTO)
686
(b) high coverage
647
871
75
166
411
270
543
(×0·5)
810
638
157
215
471
522
882
272
422
(a) low coverage
INTENSITY
200
400
800
800
1000
INCIDENT NEUTRON ENERGY / cm-1

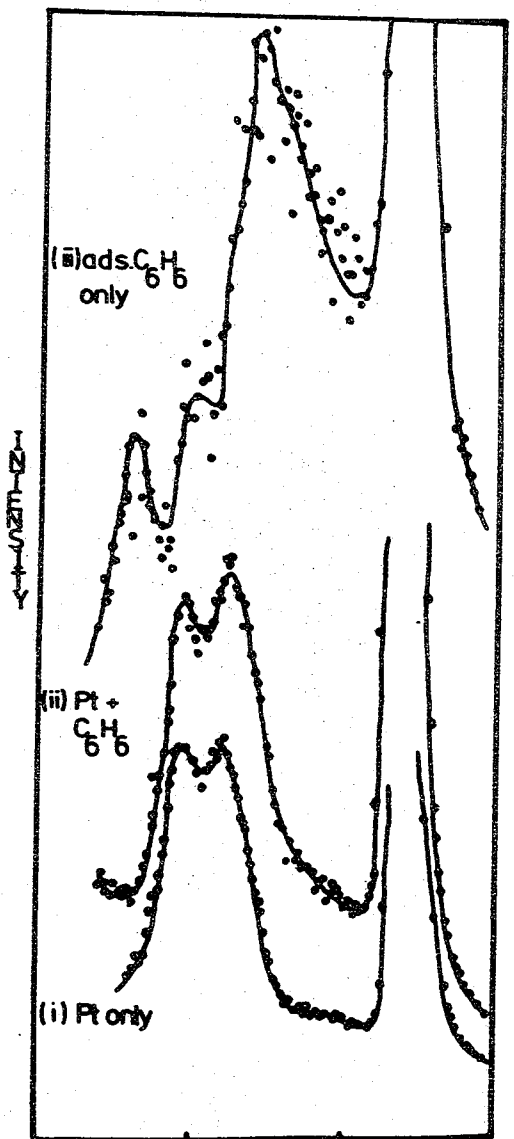

Figure (9.7) 4H5 Pt/C_6H_6 data

Figure (9.8) Pt/C_6H_6 $P(\alpha,\beta)$ data

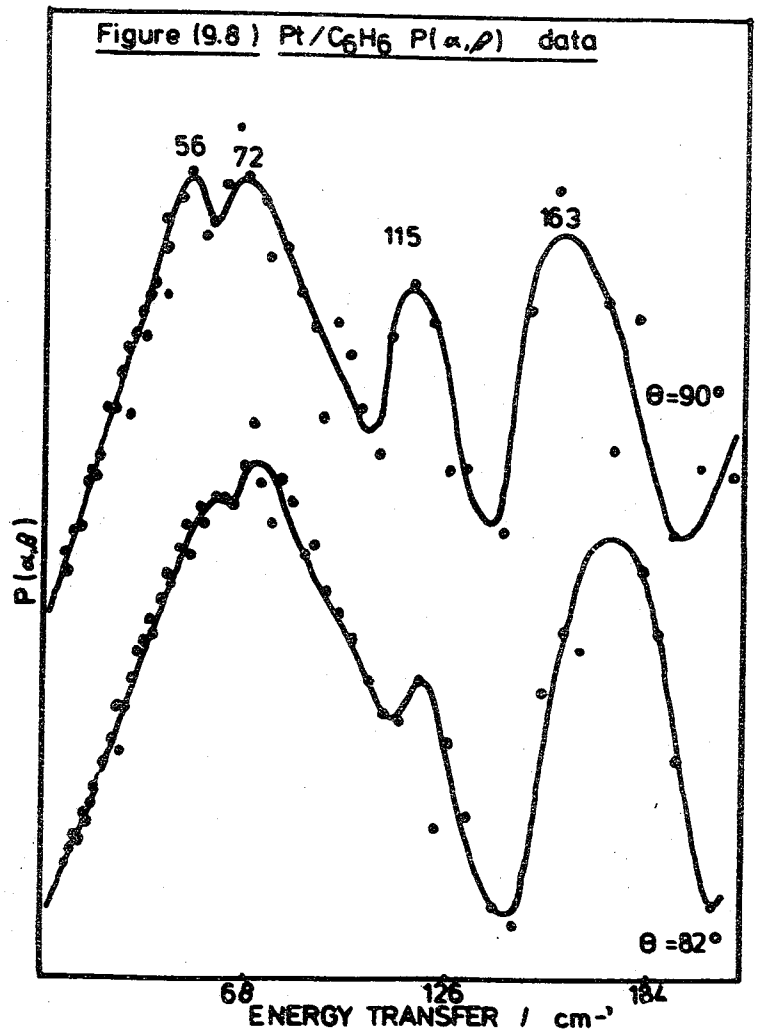

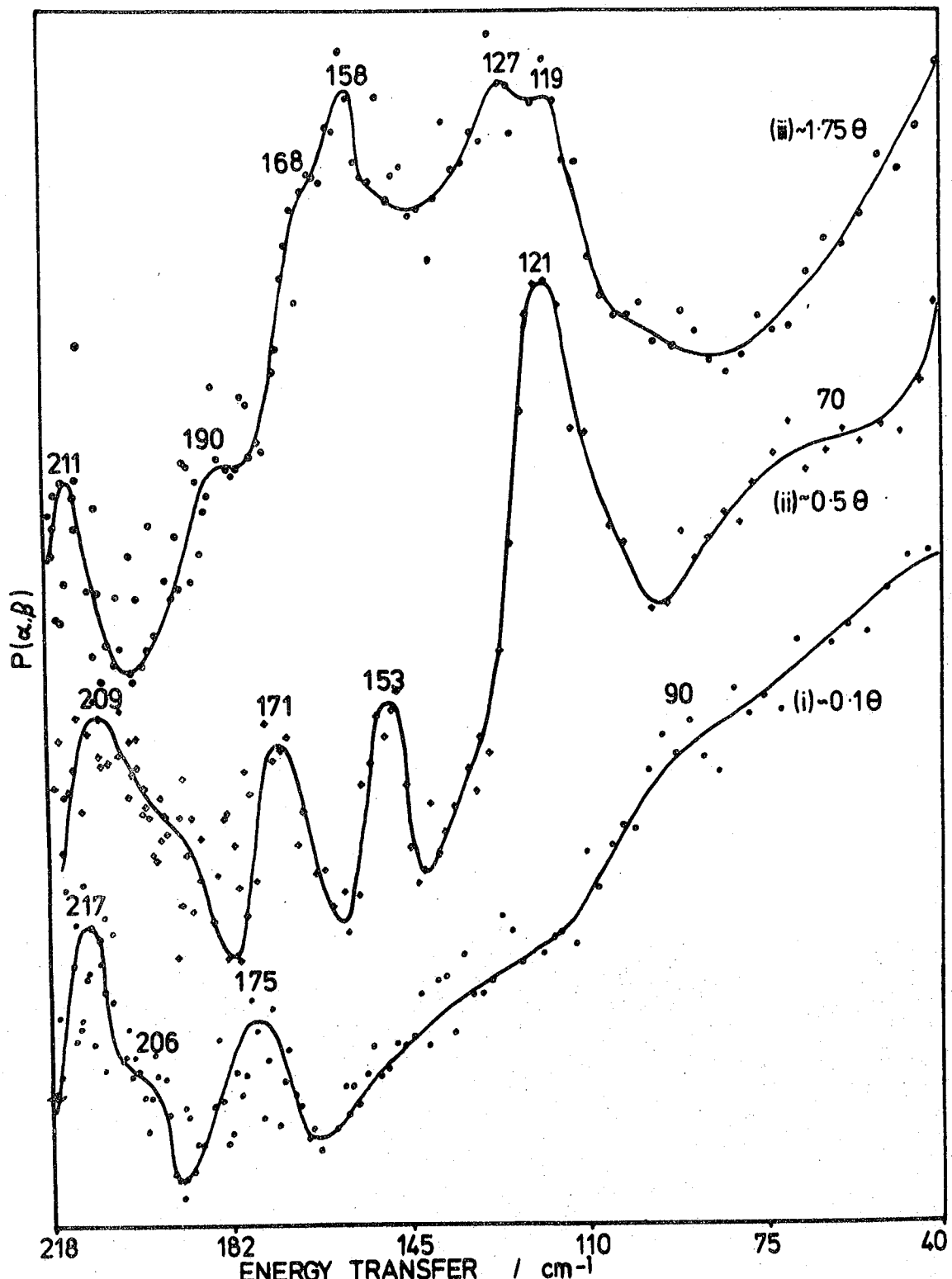

Figure (9·9) IN4 data on Pt black/ Benzene

Table 9.10: Details of Scattering Angles of IN4 Spectra

Figure Number	Coverage	Average scatt. angle	No. of angles in average	Range of scatt. angles
6.13(i)	~0.1	140.6	4	137-144
6.13(ii)	~0.5	119.3	5	115-124
6.13(iii)	~1.75	131.9	17	115-151

density of states of bulk platinum black. The latter was studied by Howard et al (22) using time-of-flight techniques.

The two lowest frequency maxima are found at 87 and 165cm^{-1} in Figure 9.7(i) of the 4H5 data and at 91 and 175cm^{-1} in Figure 9.5 of the BFDPLUTO data. This compares with the Howard data of 97 and 169cm^{-1} from an experiment carried out on 6H, another time-of-flight instrument once used at Harwell. These frequencies are very close to frequencies determined for the density of states of bulk platinum (23). There are no other features in the 4H5 spectrum but further weak bands occur in the BFDPLUTO spectrum. A shoulder is found at 269cm^{-1}, a broad band at 381cm^{-1} and an unusual feature at 863cm^{-1}. Howard found a band at 350cm^{-1} in a 6H spectrum of cleaned and degassed platinum (24). The component at 863cm^{-1} may well be due to the instrument since a sharp jump in intensity occurs between 872 and 880cm^{-1}. The raw data shows a sudden increase in counts at 880cm^{-1} for the same (approx.) length of counting time as at 872cm^{-1}. The 381cm^{-1} broad band could be the second harmonic of the

strong bulk platinum band at 175cm^{-1} though this is not favoured since 2 x 175 = 350cm^{-1}, below the observed frequency of 381cm^{-1}. Normally the overtone is observed at less than twice the fundamental frequency. The 269cm^{-1} band may be the combination of the two bulk platinum peaks at 91 and 175cm^{-1} (total = 266cm^{-1}). If these weaker bands are not explained as above then they may be indicative of a surface or even a bulk contaminant.

Possible contaminants are oxygen, hydrogen, water, carbon monoxide, sulphur, chlorine or even a hydrocarbon, which could have been deposited from the vapours of the pump system though the ion pump system used was fully trapped using liquid nitrogen.

Previous vibrational studies of these substances, adsorbed on surfaces, can be used to indicate whether they exist on or in our platinum black samples. Water adsorbed on the platinum (111) plane has been studied by Sexton very recently using EELS at 100K (25) and the OH stretch and HOH deformations were found to occur at 3400 and 1625cm^{-1} beyond of the range of this study. However, skeletal vibrations involving water and platinum at monolayer coverage were found at 700cm^{-1} (the hindered rotation) and 250cm^{-1} (the hindered translation). The 269cm^{-1} band could well be due to the latter but no vibrational band was found at all in the 700cm^{-1} region. This must be an indication that the water was removed in the cleaning operation. Howard et al also found bands at 584, 824, 1336 and 1696cm^{-1} attributed to water on platinum black at 77K, though these features lie above the region of interest (24). Sexton (25) also found a band at 550cm^{-1} attributed to a Pt-O stretch in his study of water on the

Pt(111) plane using EELS. However, no inelastic scattering would be expected from oxygen since it has a zero incoherent neutron scattering cross-section. Sulphur could be an impurity from the manufacturing process but, again, sulphur has a negligible incoherent neutron scattering cross-section. Carbon monoxide would act similar so could not be ignored as a possible impurity though the σ_{incoh} values of C and O are zero. Baro et al (26) found that CO had been an impurity in their study of hydrogen on platinum at 90K. This EELS study of hydrogen on the platinum (111) plane detected losses at 500, 1130 and 1230cm^{-1} due to adsorbed hydrogen. Howard et al (24) found vibrational bands at 500, 622 and 812cm^{-1}, using IINS at 77K, attributed to hydrogen. All of these features lie outside the range of the suspect bands. As discussed by Howard (20), chlorine has a modest incoherent scattering cross-section of 3.5 barns, compared to 79.7 barns for the hydrogen atom, which makes it a sufficiently effective scatterer of neutrons. The manufacturer had indicated that there was possibly a 0.1% sample impurity and if all this had been chlorine then appreciable scattering from chlorine would have taken place whether it was in a surface bound form or dissolved in the bulk. Pt-Cl and Pt-Cl-Pt stretches are known to occur at 315 and 350cm^{-1} respectively (27). Thus the likelihood that the 381cm^{-1} band was due to chlorine cannot be dismissed. Howard (20) thought that this reasonably could explain the similar band at 350cm^{-1} in his spectra of cleaned platinum.

From the above arguments, the following observations can be made.

(i) The 863cm^{-1} jump is due to an instrument artifact.

(ii) The 269cm^{-1} shoulder may be a combination band (91 + 175 = 266cm^{-1}).

(iii) A contaminant such as chlorine or oxygen may be present to a small degree.

(iv) The 381cm^{-1} broad band may be due to a metal-chloride stretch.

(v) There would appear to be no hydrogen, water or carbonaceous material on or in the platinum black.

(vi) Due to the actual absorption and the spectra that ensued, it would appear reasonable to assume that benzene had interacted with the platinum surface.

9.5.2. Adsorbed Benzene on Platinum Black

From the following discussion it is felt that this study of benzene adsorbed on platinum black produces two major points of interest.

(i) There are changes in the fundamental intra-molecular vibrations of benzene at low coverage that indicate that the benzene has indeed formed a surface complex on interaction with the platinum black surface.

(ii) There are possibly five new bands that cannot be explained as fundamental intra-molecular or inter-molecular benzene vibrations. The new bands are either caused by the hindered rotations and translations of the complexed benzene molecule and/or by the splitting of the doubly degenerate benzene intra-molecular fundamental vibrations. Both these give information on the exact site symmetry seen by the benzene molecule.

9.5.3. Higher Frequency Study of Benzene on Pt Black

Table 9.8, which shows the IINS features from an inspection of BFDPLUTO spectra, indicates that, with the benzene coverage approaching 2 monolayers, the similarities increase between the adsorbed benzene and solid benzene. This is reasonable because $C_6H_6\cdots\cdots C_6H_6$ interactions will increase as the molecules start to build up on top of each other. If the second layer of benzene molecules are not in direct contact with the platinum surface then they will interact through the initial monolayer with the surface as well as with the initial monolayer and the other benzene molecules in the second layer.

Table 9.11 shows the similarity between the frequencies of the intramolecular benzene vibrations in solid benzene and at a high benzene coverage on platinum black. Vibrational studies of solid benzene indicated that the out-of-plane modes were generally moved up in frequency whereas the in-plane modes increased a very small amount compared to studies of benzene vapour. The benzene molecules are 'fixed' in space in the solid so the changes found in solid benzene are to be expected to some degree on platinum since the benzene is also directionally fixed on the platinum surface. The platinum 'd' orbitals are fixed in space and the benzene-platinum interaction, if strong and if it takes place between the 'd' orbitals of the platinum and the Π^* orbitals of the benzene ring, will effectively prevent the benzene ring from freely rotating around its C_6 axis. The degree of overlap would be large because of the spatial extension of the platinum 5'd' orbitals.

Table 9.11: Frequency Variation of Benzene Intramolecular Vibrations (H.C. = High Coverage)

IR/R Gas (28)	IR/R Solid (29,30)	IINS Solid	IINS Pt+C_6H_6(H.C.)	Vibration (Wilson No.)
404	400	401	411	ν_{16}
606	607	602	-	ν_6
671	686	700	686	ν_{11}
849	856	858	871	ν_{10}

In solid benzene the spectrum Figure 7.2 , is dominated by the bands at 411, 700 and 858cm^{-1}. These bands were assigned to the out-of-plane modes ν_{16}, ν_{11} and ν_{10}. At high coverage of benzene vibrational bands exist at 411, 686 and 871cm^{-1} and these are assigned to ν_{16}, ν_{11} and ν_{10} from intensity grounds and from the comparison with the IINS spectrum of solid benzene. The only other fundamental benzene vibrations that could exist in this area are ν_4 at ~700cm^{-1}. This band obviously involves very little hydrogen motion and was not seen in the solid benzene spectrum and thus has not gained enough intensity to be seen using IINS spectroscopy. Similar studies of organometallic compounds (Chapter 7) also failed to reveal this band. Lokshin et al (31) failed to observe it from an infra-red/Raman study of $C_6H_6M(CO)_3$ complexes. ν_4 is infra-red and Raman inactive in benzene. In solid benzene, a medium intense band existed at 602cm^{-1} which was assigned to ν_6, the in-plane ring deformation. This band was not seen in the adsorbed phase.

This can be interpreted as a result of the preferential orientation of the benzene ring parallel to and lying flat above the platinum surface. In a situation where the interaction in this position is strong the amplitude of vibration parallel to the surface would be reduced somewhat and thus since no band is seen at ~600cm^{-1} this is taken as an indication that the ~2 monolayers of benzene are in such flat positions.

Above 400cm^{-1} the only other features in the spectrum lie at 543 and 647cm^{-1}. These bands exist at frequencies at which bands exist at low coverage. It is felt that these are due to benzene in the chemisorbed phase rather than second layer benzene. It is thus possible that at high coverage, the IINS data could be crudely described as that due to monolayer coverage and to the second layer coverage. Comparisons with just solid benzene will therefore be only tentative since interactions could occur that would not be found in solid benzene.

At lower coverage of benzene, approaching one monolayer the spectrum, shown in Figure 9.6, differs quite considerably from that at high coverage. The two strongest bands at 411 and 686cm^{-1} have been replaced by bands at 638 and 810cm^{-1} and a number of features in the 400-600cm^{-1} range. At this coverage it is expected that a benzene-platinum interaction is observed ie that all the benzene is chemisorbed onto the platinum black surface. IR studies of complexed benzene have been particularly useful in assigning the IR (and EELS) active, the symmetric out-of-plane CH deformation. This vibration generally moves up in frequency on complexation.

In Figure 9.6 there is only one band of any strong intensity at low coverage, at 810cm^{-1}, above 671cm^{-1} the frequency of ν_{11} in benzene vapour. Further, since ν_{11} was readily assigned at high benzene coverage, it would also be expected to exist at low coverage. The increase in frequency of 139cm^{-1} arises because an additional force constant is added to the forces within the molecule for the out-of-plane vibrations. This makes vibrations of this type much harder and therefore raises the frequencies. This added force constant in the out-of-plane direction has no affect on the force constants controlling the in-plane vibrations. It would be expected also that ν_{10} and ν_{16}, the other out-of-plane modes, would also move up in frequency in the manner of ν_{11}. The weak band at 882cm^{-1} is assigned to ν_{10} and ν_{16} could be assigned to bands at 422 or 471cm^{-1}. The justification that ν_{11}, ν_{10} and ν_{16} are observed in the IINS spectrum and the assertion that they move up in frequency arises from a study of other systems such as C_6H_6 organometallics and C_6H_6-surface studies. The following pertinent studies have been carried out on related systems.

(a) Lokshin et al carried out a comparative investigation of the vibrational spectra of arene metal tricarbonyls where M is Cr, Mo or W (31). Table 9.12 depicts the data from the region of interest.

(b) An IR study, at 77K, of MC_6H_6' species, formed from Fe, Co and Ni vapours co-condensed with C_6H_6 in an argon matrix, found evidence of π-complexing (32). The relative strengths of the M-C_6H_6 bonds were obtained from the shifts in the in-plane C=C stretching modes, which fell in frequency, and from the magnitude of the shift of ν_{11}, the CH out-of-plane

Table 9.12: Comparative Data of Lokshin et al (31)

Assignment	Solid C_6H_6	$C_6H_6Cr(CO)_3$	$C_6H_6Mo(CO)_3$	$C_6H_6W(CO)_3$
ν_{16} (E)	398	422	423	424
ν_6(E)	606	611	615	600
$\nu_{11}(A_1)$	673	786	764	775
ν_{10}(E)	846	905	892	890

deformation, to higher wavenumbers. An increase, $\Delta\nu_{11}$, of 91cm^{-1} was found in Fe(C_6H_6), 87cm^{-1} in (C_6H_6)Co and 77cm^{-1} in (C_6H_6)Ni, which compares relatively well with +90cm^{-1} for $\Delta\nu_{11}$ obtained for benzene on nickel surfaces (34). This trend from Fe to Ni was due to the ability of these metal atoms to serve as acceptors of π-electron density . In our work on platinum-benzene, ν_{11} was observed at 810cm^{-1}, an increase of 137cm^{-1}. This greater increase may well be due to the greater spatial extent of the 5'd' Pt orbitals, which act as π-electron density acceptors, whereas Fe, Co and Ni only have the less extensive 3'd' orbitals available.

(c) Lehwald et al (12) in their study of benzene on platinum (111) using EELS found a strong band, ν_{11}, which had shifted to high frequency at low coverage, 830cm^{-1} and returned to the solid benzene value at high coverage, 700cm^{-1}. The 830cm^{-1} band was assigned to benzene bonded above a single platinum atom. This is the first indication that possibly such a configuration exists on platinum black.

Lehwald et al found other bands at higher frequency, also assigned to ν_{11}, indicative of benzene bonded above a 3-fold hollow. No analogue was found in our C_6H_6/Pt black study. Thus, this may be an indication that only one species exists on Pt black. It is not surprising that these latter bands were not discovered on platinum black where only a small percentage of (111) type sites are available. There are no such 3-fold sites on the (110) or (100) planes available for benzene. So such μ_3-(C_6H_6)-Pt_3 moieties were not observed though some may still occur.

The massive increase in the frequency of ν_{11}, at low coverage, may be due to a distortion of the benzene molecule, due not only to the benzene-platinum π-interaction which would involve a rehybridization of the π-orbitals, but also to the hydrogens interacting in some way with the other platinum atoms. This would possibly produce a distorted benzene molecule. It has been postulated that the benzene hydrogen atoms reside closer to the platinum surface producing a crabbed structure (11) which has been found in organometallic complexes where ν_{11} has moved up in frequency to a high degree. A neutron diffraction study of $C_6H_6Cr(CO)_3$ (33) found that the hydrogen atoms resided closer to the chromium atom, out-of-the benzene plane. A plane-hydrogen distortion angle of 1.7° was found whereas values of $5 \pm 2^\circ$ had been estimated, by previous workers, in sandwich compounds such as dibenzene-chromium and ferrocene (34,35).

The perturbation to the benzene ring would appear to be greater on platinum rather than in the organometallic such as $C_6H_6Cr(CO)_3$ or the matrix isolated species such as C_6H_6Ni or, even from the Lehwald et al (12) study of C_6H_6/Ni

(111) if the shift in the ν_{11} frequency is a true indication of the distortion. This is only seen at low coverage of benzene.

At higher coverage, ~ 2 monolayers, the spectrum approaches that of solid benzene. Thus it is felt that the benzene-platinum interaction is changed drastically from that found at lower coverage. At ~ 2 monolayers, if the chemisorbed layer had not been changed then the IINS data would have shown characteristics indicative of the chemisorbed layer and the overlayer in the benzene intramolecular modes. This was not observed though the C_6H_6-Pt skeletal modes were possibly observed at both coverages.

The evidence for the assignment of the intramolecular benzene vibrations at low coverage is further enhanced by comparing the IINS data in Table 9.13 with a number of organometallic compounds studied in Chapter 7.

9.5.4. Symmetry of Benzene on the Surface

From the evidence presented, the majority of benzene molecules would appear to be bonded parallel to the platinum surface. This reduces the molecular symmetry (D_{6h}) when the molecule interacts with the surface. If benzene was bonded to a featureless plane, without specific surface structure, then C_{6v} symmetry would be found. This symmetry is also found when benzene is π-bonded to a point in a purely localized scheme. The structure can be made more complex and, thus, the symmetry lowered. This descent in symmetry is shown in Table 9.14 which exhibits the correlation between irreducable representations of the various group symmetries for the lowest frequency intramolecular benzene vibrations.

Table 9.13: Comparison of Some Organometallic Benzene Intramolecular Modes With the Pt/C_6H_6 System (L.C.) (L.C. = Low Coverage)

System	ν_{16}	ν_6	ν_{11}	ν_{10}
Pt + C_6H_6(L.C.)	422 471	-	810	882
($RuCl_2C_6H_6$)	439	635	878	
($RuBr_2C_6H_6$)	439	631	869	
($PdAlCl_4C_6H_6)_2$	430	615	798	
($PdAl_2Cl_7C_6H_6)_2$	439	620	782	874
$C_6H_6U(AlCl_4)_3$	414	611	790	
$CoHg_2(SCN)_6C_6H_6$	421	623	741	
$NiHg_2(SCN)_6C_6H_6$	418	635	729	
$(SbCl_3)_2C_6H_6$	416	604	721	861

If the benzene molecule interacts with a single platinum atom on a (111) type surface then there are two possible arrangements on the surface and both have C_{6v} symmetry whereas on the (100) and (110) planes, though again two possible strutures are possible, the maximum attainable symmetry is C_{2v}. These arrangements are depicted later in the chapter. Thus at least C_{2v} symmetry would appear to be held by the benzene platinum interaction on the three highest atomic-density crystal orientations, of low surface free energy, if the benzene is π-bonded to a single platinum atom. If the

Table 9.14: Correlation Between Possible Benzene Symmetry Sites

Wilson No.	cm^{-1}	D_{6h}	C_{6v}	C_{3v}	C_{2v}	C_s
ν_{16}	404	E_{2u}	E_2	E	A_1+A_2	$A'+A''$
ν_6	607	E_{2g}	E_2	E	A_1+A_2	$A'+A''$
ν_{11}	673	A_{2u}	A_1	A_1	A_1	A_1
ν_4	707	B_{2g}	B_1	A_1	A_1	A_1
ν_{10}	849	E_{1g}	E_1	E	B_1+B_2	$A'+A''$

symmetry is as low as C_{2v} then it may be possible to see splitting in the doubly degenerate intramolecular vibrations, ν_{16}, ν_6 and ν_{10}, in the region of interest. ν_6 as already discussed is not seen in the IINS spectrum. ν_{10} lies in a very poorly resolved region at $882cm^{-1}$ at low coverage, in Figure 9.6 and no splitting could be observed. In the organometallic compounds such as $C_6H_6M(CO)_3$ there is C_{3v} symmetry and thus no splitting of any E modes takes place but on the platinum surface at least C_{2v} symmetry exists on the (100) and (110) planes.

There is a band at $471cm^{-1}$ in the BFDPLUTO spectrum at low coverage of benzene on platinum black, Figure 9.6, which may be due to the second component of ν_{16}, which is a doubly degenerate deformation (D_{6h}:E_{2u} mode). Figure 7.4 shows the form of ν_{16}. The band at $471cm^{-1}$ is not found at high coverage and neither is the weaker component at $422cm^{-1}$. They are replaced by a medium strong intense band at $411cm^{-1}$.

We postulate that ν_{16} is indeed split in the low coverage spectrum into two bands at 422 and 471cm^{-1} and this is evidence that benzene can be found in at least C_{2v} symmetry.

9.5.5 Low Frequency Study of the Benzene/Platinum Black System

Three coverages of benzene were studied on the platinum black. At high coverages, in section 9.5.3., it was shown that the character of the benzene layer was approaching that of solid benzene. In this low frequency study such character is also reflected at high coverage in the appearance of bands of frequencies similar to those of the lattice vibrations of benzene. This similarity between lattice vibrational bands of solid benzene and of the higher coverage of benzene on platinum is not strictly reasonable because two monolayers does not constitute a crystalline state. One could envisage the intramolecular fundamental vibrations of adsorbed benzene would tend to appear like solid benzene but the intermolecular modes would be changed. At only two monolayers the second layer would reflect the first layer to a very great extent and would not be like the crystal form, where the molecules are not orientated in any one particular plane. Perhaps the first monolayer of benzene can be described in terms of a two dimensional lattice in the same manner as the monolayer coverages of inert gases on graphite. For example, Taub et al studied monolayer argon coverage on graphite. They could describe the argon in a two-dimensional model from its in-plane dynamical character, though the model involved an out-of-plane component due to the collective modes of the substrate

and adsorbate (36). With the second layer of benzene the character of the vibrational 'lattice' modes could be controlled by a 2-D description rather than 3-D though the out-of-plane contribution may have increased further than found in only a single layer. Thus as the coverage of benzene increases on platinum new 'lattice' vibrations will be formed, but the 'lattice' in this case would only involve two monolayers, providing the coverage was even over the platinum black surface. These intermolecular vibrations may coincide with those of crystalline benzene but they would only be coincidences.

It can be seen in Figure 9.9 that at ~0.1θ there are only two poorly resolved bands at ~175 and ~210cm^{-1}. On increasing the coverage the spectrum is dominated by the band at 121cm^{-1}. Bands also appear at 171 and 209cm^{-1} of medium intensity similar to those found at ~0.1θ. Also a weak medium intense band is formed at 153cm^{-1}. This situation is paralleled in the 4H5 spectrum which is dominated by a broad feature at 72cm^{-1} with a medium band at 115cm^{-1} and similar bands at higher frequencies. On covering the surface to a greater degree the bands found at 121 and 171cm^{-1} do not increase in relative intensity compared to the rest of the spectrum whereas the bands at 127 and 158cm^{-1} increase to a marked extent, as shown in Figure 9.9. From this it seems plausible that the 127 and 158cm^{-1} bands are indicative of intermolecular benzene vibrations or due to vibrations arising from the second layer only. Since they are only, found at high coverage whereas the bands at 121 and 171cm^{-1} appear to reach their maximum intensity at less than one monolayer coverage. These bands are probably proof of the

existence of the benzene-platinum surface complex and are C_6H_6-Pt skeletal vibrations. The changes in the band frequencies at low frequencies are shown in Table 9.15 with a possible source of the vibrations.

Table 9.15: Changes in Band Frequencies With Benzene Coverage ($<220cm^{-1}$)

IN4 ~0.1θ	IN4 ~0.5θ	4H5 ~0.5θ	IN4 ~2θ	4H5 C_6H_6 Only	Source
217(m)	209(ms)	213(w)	211(mb)	203(mb)	Difference Band
206(sh)	-	-	190(sh)	-	Unknown
175(m)	171(m)	163(sb)	178(msh)	-	Skeletal
-	153(wm)		158(s)	156(w)	Intermolecular or due to 2nd layer only
-	-	115(m)	127(sh)	-	
-	121(vs)		119(s)	-	Skeletal
-	-	-	-	109(s)	Intermolecular
90(vwb)	-	-	-	89(m)	
-	70(wb)	72(vs)	-	77(s)	
-	-	56(m)	-	68(vs)	

9.5.6. Possible New Spectral Bands

At low coverage there are possible bands indicative of the benzene-surface interaction. These arise from the rotational and translational degrees of freedom of the free benzene molecule. Figure 9.10 shows how these rotations and translations become hindered or frustrated on interaction with the surface. The rotations produce three torsions of which two are hindered to such a degree that they are

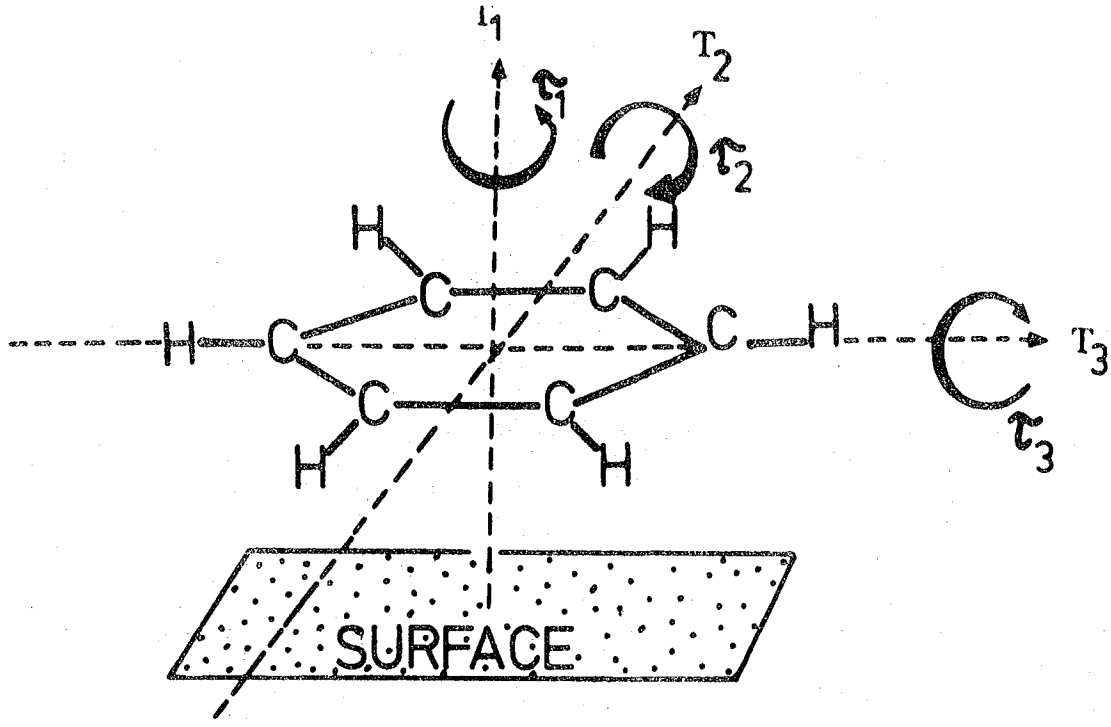

HINDERED ROTATIONS

τ_1 : Torsion one (torsion)
τ_2 : Torsion two (tilt one)
τ_3 : Torsion three (tilt two)

HINDERED TRANSLATIONS

T_1 : Stretch one (symmetric)
T_2 : Stretch two (deformation one)
T_3 : Stretch three (deformation two)

Figure (9.10) Benzene / Surface modes of Vibration

tilting motions. The translations produce a stretch perpindicular to the surface and two deformations of the adsorbate-adsorbent bond. The stretch and the torsion are thus A modes whereas the tilts and deformation are possibly both E modes. On the bonding of the benzene molecule to a point on a featureless plane the tilt and deformations are doubly-degenerate. However, the symmetry of these vibrations are derived from the symmetries, in the free molecule, of the rotations and translations. On the lowering of the symmetry to a sub-group of D_{6h} the number of former molecular modes is constant but the degeneracy may be lifted. The correlation table for the fall in symmetry of the hindered rotations and translations is shown in Table 9.16.

Table 9.16: Correlation Table for the Rotations and Translations of the Benzene Molecule

Degree of Freedom	D_{6h}	C_{6v}	(σ_v) C_{3v}	(σ_d) C_{3v}	C_{2v}	C_s
R_z	A_{2g}	A_2	A_2	A_2	A_2	A'
(R_x,R_y)	E_{1g}	E_1	E	E	$(B_1 + B_2)$	$(A' + A'')$
z	A_{2u}	A_1	A_1	A_1	A_1	A'
(x,y)	E_{1u}	E_1	E	E	$(A_1 + A_2)$	$(A' + A'')$

Whether or not the degeneracy of the tilt and deformation modes is lifted even if the benzene molecule appears to lie in a position of C_{2v} or C_s symmetry depends on the degree

of interaction with the surface. Further, even if the splitting took place whether this would be observed in an experimental IINS spectrum would be the subject of some conjecture.

On adsorption, a degree of mixing of modes is likely. Not only are the adsorbent lattice modes (if of the same symmetry) likely to mix with the molecular modes of the benzene but also the hindered degrees of freedom may mix, again if of the same symmetry. The observed vibrations could each have rotational and translational character.

The assignment of the four new bands can now be attempted. From studies of the vibrational spectra of π-complexes between metals and C_nH_n rings the torsion and deformation framework vibrations are ususally found at low frequencies ($< 200cm^{-1}$) whereas the stretch and tilt modes are generally found at higher frequencies ($> 200cm^{-1}$). Further, in IINS spectra the intensities of the E modes can be crudely related to the A and B modes by an 2:1 ratio. However, added to this latter effect, torsional modes involve large amplitude movement of the hydrogen atoms and in IINS spectra, contrary to infra-red and Raman spectra where the mode is not often seen, the torsion is the more intense of the two low frequency modes (This is generally so, though in $C_4H_4Fe(CO)_3$ the torsion is less intense than the deformation (37).)

The low coverage benzene spectrum, Figure 9.6, show bands at 522 and $638cm^{-1}$ of medium and strong intensity. These are new bands and cannot be related to fundamental benzene vibrations. Since a band at $543cm^{-1}$ at high

coverage is of weak intensity and can be assigned to the weak 540cm^{-1} band found in solid benzene, applying such an assignment to the medium intense band at 522cm^{-1} in the lower coverage case would appear to be inconsistent. Further, the very strong band at 638cm^{-1}, if it had been the ν_6 in-plane vibration of benzene, one could have expected it to have increased in intensity in the same manner as ν_{16} and ν_{11} as the coverage increased. This is not the case and it can be assigned to a framework vibration. The strong band at 638cm^{-1} is thus assigned to the doubly degenerate tilt mode. The stretch could lie at 471 or 522cm^{-1}, however, the latter band is favoured since an alternative assignment is made for the former band. Table 9.17 shows the assigned skeletal vibrations where the torsion is assigned to the strongest low frequency band at 121cm^{-1}.

Table 9.17: Assignment of New Bands in the Spectra of Benzene on Platinum Black

Frequency (cm^{-1})	Description	Symmetry
121	Torsion	A
171	Deformation	E
522	Stretch	A
638	Tilt	E

The evidence up to now indicates a strong Pt-C_6H_6 interaction compared with first row transition metals, whether in discrete organometallic form, e.g. C_6H_6Ni, or on a surface, e.g. C_6H_6/Ni(111). Thus, it is to be expected that the skeletal motions will mirror such a strong bonding situation, e.g. the barrier to the benzene rotation about its six-fold

axis would be large. Table 9.18 compares the frequencies of the tilts and stretches and $\Delta\nu_{11}$, the increase in ν_{11} from 671cm^{-1}, of the Pt black/C_6H_6 system with related surface-benzene systems and organometallic benzene complexes. There would appear to be a general trend in that as $\Delta\nu_{11}$ increases so do the frequencies of the stretches and tilts though there are anomalies e.g. the values of $\Delta\nu_{11}$ would appear to be quite small for the high frequency skeletal bands in the C_6H_6/Ni(Raney) study of Jobic et al (14) and in the 'C_6H_6M' study (C_6H_6+M in argon matrices) of Efner et al (32). From our C_6H_6/Pt black data it would appear that the benzene has changed quite drastically from the non-complexed phase compared with many other systems.

From the possible configurations that may exist on the Pt black surface, an estimate of the torsional barrier can be made using the vibrational data. This depends on the barrier multiplicity of the torsional mode which is unknown though it may be estimated. The actual geometry underwhich the benzene is found can be considered on the simplest high Miller index planes ((100), (111) and (110)) by assuming the following interatomic distances: Pt-Pt=2.78Å, C-H=1.085Å and C-C=1.397Å. These values are no doubt a gross approximation of the true picture but they can be used to fix the molecule in space above the surface. Placing the benzene molecule above a single platinum atom on the (111), (100) and (110) planes one finds that there are two positions available on each plane Figures (9.11,9.12) depict the benzene positions on the (111) and (100) planes. Positions 1 and 2 are formed by simply rotating the molecule through 30° on the (111)

Figure (9.11)
Positions C_6H_6 may hold in 'on top' sites on Pt(111)

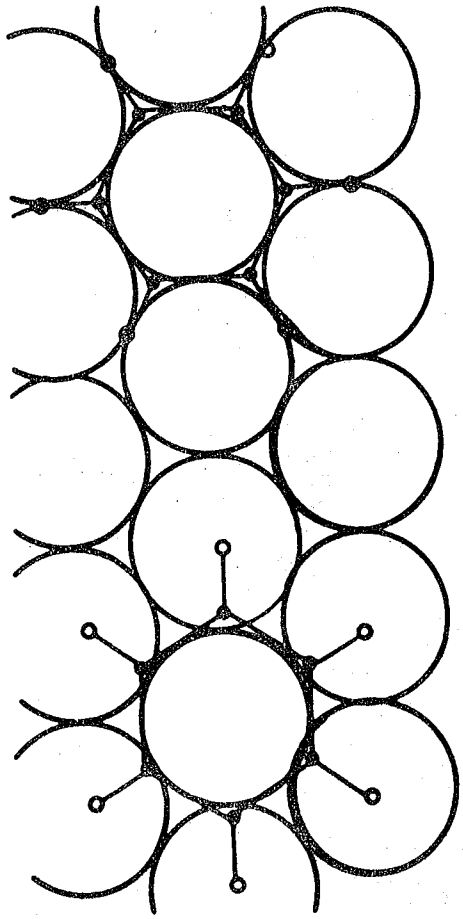

Figure (9.13)
Positions C_6H_6 may hold in Pt_2 bridging sites on Pt(111)

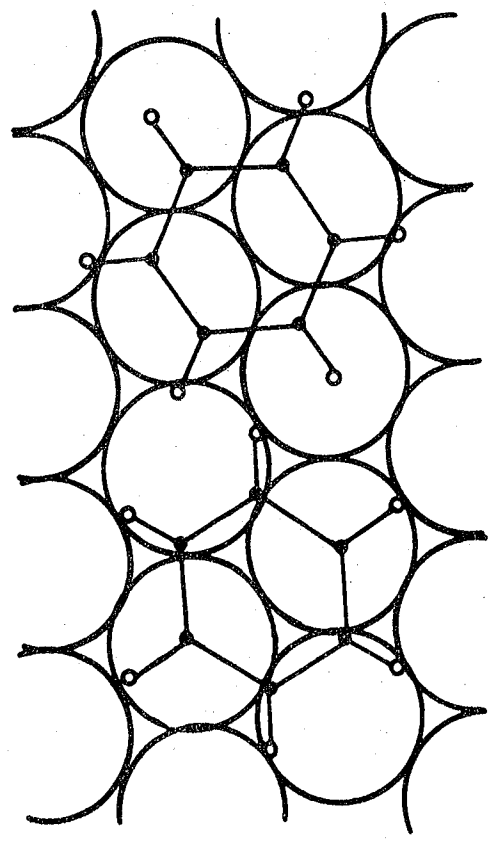

Figure (9.12)
Positions C_6H_6 may hold in 'on top' sites on Pt(100)

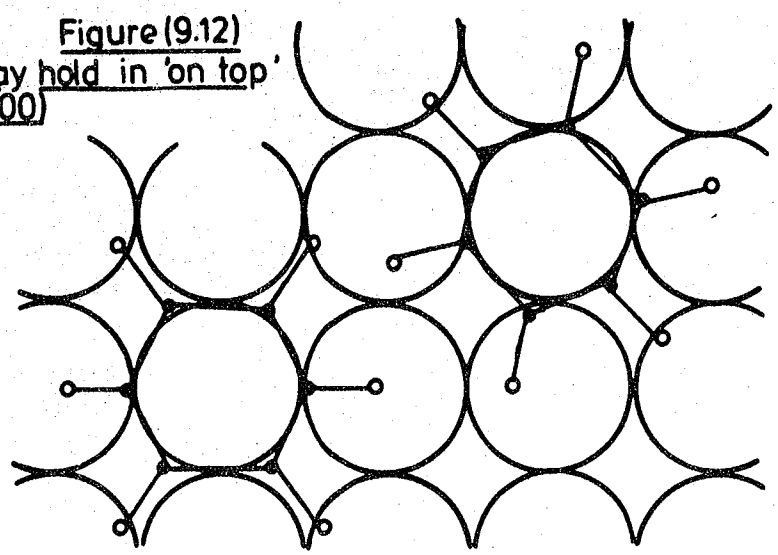

Table 9.18: Comparison of ν_{11} and Tilt and Stretch Assignments

System	$\Delta\nu_{11}$	Tilt	Stretch	Ref.
Pt black+C_6H_6	+139	638	522	Our Work
Pt(111)+C_6H_6	+159	-	350	(12)
Ni(111)+C_6H_6	+ 59	-	320	(12)
Ni(R)+C_6H_6	+ 39	529	459	(14)
'C_6H_6Fe'	+ 91	485	366	(32)
'C_6H_6Co'	+ 87	454	366	
'C_6H_6Ni'	+ 77	445	346	
$(RuCl_2C_6H_6)_2$	+207	387	278	Our Work
$(RuBr_2C_6H_6)_2$	+198	380	273	"
$(PdAlCl_4C_6H_6)_2$	+127	315	235	"
$(PdAl_2Cl_7C_6H_6)_2$	+119	303	227	"
$C_6H_6Cr(CO)_3$	+118	332	301	(31)
$C_6H_6Mo(CO)_3$	+ 93	312	264	
$C_6H_6W(CO)_3$	+104	316	267	
$CoHg_2(SCN)_6C_6H_6$	+ 70	202	282	Our Work
$Cu_4(CF_3CO_2)_4C_6H_6$	+ 62	219	269	"
$NiHg_2(SCN)_6C_6H_6$	+ 54	227	287	"
$(SbCl_3)_2C_6H_6$	+ 52	125	145	"

plane and 15^o on the other planes. (There are similar positions on the (110) plane). On the (111) plane, C_{6v} symmetry is found in both configurations whereas C_{2v} symmetry is found on the other two planes. Since the vibrational analysis indicated that the benzene lay in at

least C_{2v} symmetry, the positions found on the (110) and (100) planes appear reasonable.

For a lower symmetry position to exist on a (111) plane, the benzene would have to reside over a threefold hole giving it C_{3v} symmetry or bridging two platinum atoms, in the manner of Bertolini et al (13). There are two bridging positions available to benzene on the (111) plane C and D, and these are shown in Figure 9.13. Now this bridging position, though of C_{2v} symmetry will no doubt produce different frequency shifts in the vibrations than those found for the C_{2v} 'on-top' sites of the (111) and (100) planes. Since only one state of benzene upon the surface exists then this bridging site is dismissed. However, the benzene could reside in 'on-top' sites on all planes. This would then allow for the splitting of the intramolecular benzene E mode, ν_{16}, account for the four observed framework vibrations and account for only one single state of benzene. If there are (111) type sites available for benzene on platinum black then the site symmetry will be C_{6v} and no splitting would occur but these benzene molecules could not be differentiated from those others in C_{2v} sites in the IINS spectrum. Perhaps a high resolution Raman study would find bands due to ν_{16} (C_{6v} sites) and ν_{16a} and ν_{16b} (C_{2v} sites).

9.5.7. Calculation of the Torsional Barrier

The barrier to rotation, V_B, can be calculated using the torsional mode frequency assigned to the IINS band at $121cm^{-1}$. The reduced moment of inertia, I_r, of benzene is calculated from the co-ordinates used by Farrot et al (17). This value is 294.67×10^{-40} g.cm^2.

The effective force constant, $\frac{N^2V_B}{2}$, can be calculated if the barrier is assumed to be of the form:

$$V = \frac{V_B}{2} (1 - \cos n\theta)$$

By making the harmonic oscillator approximation the effective force constant can be calculated from:

$$\frac{N^2V_B}{2} = \frac{4\pi^2 I_r c\nu^2}{\hbar}$$

where N = Multiplicity
V_B = Barrier height
I_r = Reduced moment of inertia
c = Velocity of light
$\hbar$ = Planck's constant
ν = Torsional frequency

The effective force constant, EFC, is calculated to be 922kJmol^{-1}, using the torsional frequency of 121cm^{-1}. (A value of 1841kJmol^{-1} would be obtained if the 171cm^{-1} band had been assigned to the torsion). This value can be compared with EFC values for benzene complexes (Chapter 7) e.g. EFC is 250kJmol^{-1} in $NiHg_2(SCN)_6C_6H_6$ and 273 kJmol^{-1} in $C_6H_6Co_4(CO)_9$. Thus the EFC is ~4 times as large in the C_6H_6/Pt interaction.

The actual barrier height, V_B, can then be estimated if the multiplicity, N, is known. On the (111) plane, in an 'on-top' site, there are 12 positions in which each carbon and hydrogen can reside on a full rotation of 360°. On the (110) and (100) planes there exists 24 positions for each carbon and hydrogen atom. If these barriers were of equal height and at each position the configurations were stable then V_B would be calculated to be 12.8 and 3.2kJmol^{-1} on the two types of planes respectively.

However, in reality, this cannot be the case and many interactions would have to be taken into account to understand how the benzene and platinum surface were behaving as the arene ring executed the torsional mode about its C_6 axis. An understanding of the following would be necessary.

(i) the electronic interaction between the benzene and the platinum atom(s).

(ii) the bonding orbital symmetries of the surface 'd' orbitals and their angle with the surface plane

(iii) the degree of hybridization of the π-orbitals of the benzene ring.

(iv) the local and delocalized aspects of the surface chemical bond.

(v) the part played by the nearest neighbour platinum atoms in the surface plane and below it.

(vi) the indirect long range benzene-benzene interactions

(vii) the reconstruction of the platinum atoms, if any, and their movement during a torsional motion.

(viii) the effect on the CH bond due to changes in the hybridized π-orbitals affecting the bond electron density.

(ix) the changes in the CC, CH, CPt, HPt atom-atom distances on rotation and thus the varying heights above the Pt plane of the C and H atoms.

(x) the preference shown by the C atoms (or C_6 hexagon) for a particular surface configuration which must be balanced against any preference shown by the hydrogen atoms to reside in any specific locality.

9.6. Conclusion

This IINS study of C_6H_6 adsorbed on Pt black confirmed that C_6H_6 interacted with the Pt atoms. The interaction took the form of a π-bond parallel to the metal atom surface. Some distortion of the molecule is tentatively suggested with the hydrogen atoms residing closer to the metal surface plane than the carbon plane. The benzene would appear to be lying in a position of at least C_{2v} symmetry from the splitting of ν_{16}. This symmetry is possible on the (110) and (100)-type crystal planes if a single-Pt/C_6H_6 interaction takes place. The studies indicate that only one surface structure is found at ≤ 1 monolayer coverage. Indications of a strong C_6H_6-Pt bond are the high frequency skeletal vibrations, the large increase in ν_{11} and the large EFC of the torsional mode.

9.7 References

1. R.C. Pitkethly, A. G. Goble 2nd Int. Catal. Conf. (Paris) (1961) 1851
2. J.A. Brundege, G. Parravano J. Catal 2 (1963) 380
3. J.L. Gland, G.A. Somorjai Surface Sci. 38 (1973) 157
4. K. Baron, D.W. Blakely, G.A. Somorjai Surface Sci. 41 (1974) 45
5. P.C. Stair, G.A. Somorjai J. Chem. Phys. 67 (1977) 4361
6. L.E. Firment, G.A. Somorjai Surface Sci. 84 (1979) 275
7. J. Erkelens, S.H. Eggink-du-Burck J. Catal 15(1969) 62
8. D. Shopov, A. Palasov Comptes.Rendus. Acad. Bulg. Sci. 22 (1969) 181
9. P. Ratsanamy Chem. Age (India) 21 (1970) 889
10. G.L. Nyberg, N.V. Richardson Surface Sci. 85 (1979) 335
11. J.C. Bertollini, G. Dalmai-Imelik, J. Rousseau Surface Sci. 67 (1977) 478
12. S. Lehwald, H. Ibach, J.E. Demuth Surface Sci. 78 (1978) 577
13. J.C. Bertollini, J. Rousseau Surface Sci. 89 (1979) 467
14. H. Jobic, J. Tomkinson, J.P. Candy, P. Fouilloux, A.J. Renouprez Surface Sci. 95 (1980) 496
15. W. Krasser, A. Renouprez 'Vibrations in adsorbed layers' Julich Conf. (1978) 175
16. W. Krasser, H. Ervens, A. Fadini, A. Renouprez J. Raman Spec. 9 (1980) 80
17. J. Favrot, P. Caillet, M.T. Forel J. Chim. Phys. 71 (1974) 1337
18. A.M. Bradshaw Z. Phys. Chem. (Weisbaden) 112(1978) 33
19. N.V. Richardson Surface Sci. 87 (1979) 622
20. J. Howard Ph.D. Thesis (Durham Univ.) (1977)
21. H.H. Paalman, C.J. Pings J. Appl. Phys. 33 (1962) 2635
22. J. Howard, T.C. Waddington, C.J. Wright J. Chem. Phys. 64 (1976) 3897

23. D.K. Dutton, B.N. Brockhouse Can. J. Phys. 50 (1972) 2915

24. J. Howard, T.C. Waddington, C.J. Wright Int. Sympos. Neut. Inel. Scatt. Vienna (1977)

25. B.A. Sexton Surface Sci. 94 (1980) 435

26. A.M. Baro, H. Ibach, H.D. Bruchmann Surface Sci. 92 (1980) 384

27. D.M. Adams, P.J. Chandler, R.G. Churchill J. Chem Soc. (A) (1967) 1272

28. G. Herzberg 'IR and Raman Spectra of Polyatomic Molecules' Van Nostrand (1945)

29. R.D. Mair, D.F. Hornig J. Chem. Phys. 17 (1949) 1236

30. M. Ito, T. Shigeoka Spectrochimica Acta 22 (1966) 1029

31. B.V. Lokshin, E.B. Rusach, V.S. Kaganovich, V.V. Krivykh, A.N. Artemov, N.I. Sirotkin Zh. Strukt. Khim. (1975) 16 553

32. H.F. Efner, D.E. Tevault, W.B. Fox, R.R. Smardzewski, J. Organometal Chem. 146 (1978) 45

33. B. Rees, P. Coppens Acta. Cryst. B29 (1973) 2515

34. E. Keulen , F. Sellinek J. Organometal Chem. 5 (1966) 490

35. R.K. Bohn, A. Haaland J. Organometal Chem. 5 (1966) 470

36. H. Taub, K. Carniero, J. K. Kjems, L. Passell, J.P. M^{c}Tague Phys. Rev. (B) 16 (1977) 4551

37. J. Howard, T.C. Waddington Spectrochimica Acta 34A (1978) 445

APPENDIX

Research Colloquia, Seminars and Lectures Arranged by the Department of Chemistry between October 1977 and September 1980

19.10.77 Dr. B. Heyn (Univ. of Jena, D.D.R.), "σ-Organo-Molybdenum Complexes as Alkene Polymerisation Catalysts"

27.10.77 Prof. R.A. Filler (Illinois Institute of Technology), "Reactions of Organic Compounds with Xenon Fluorides"

2.11.77 Dr. N. Boden (Univ. of Leeds), "N.M.R. Spin-Echo Experiments for Studying Structure and Dynamical Properties of Materials Containing Interacting Spin-$\frac{1}{2}$ Pairs"

9.11.77 Dr. P.A. Madden (Univ. of Cambridge), "Raman Studies of Molecular Motions in Liquids"

14.12.77 Dr. R.O. Gould (Univ. of Edinburgh), "Crystallography to the Rescue in Ruthenium Chemistry"

25.1.78 Dr. G. Richards (Univ. of Oxford), "Quantum Pharmacology"

1.2.78 Prof. K.J. Ivin (Queens Univ., Belfast), "The Olefin Metathesis Reaction: Mechanism of Ring-Opening Polymerisation of Cycloalkenes"

3.2.78 Dr. A. Hartog (Free Univ., Amsterdam), "Some Surprising Recent Dvelopments in Organo-Magnesium Chemistry"

22.2.78 Prof. J.D. Birchall (Mond Division, I.C.I. Ltd.), "Silicon in the Biosphere"

1.3.78 Dr. A. Williams (Univ. of Kent), "Acyl Group Transfer Reactions"

3.3.78 Dr. G. van Koten (Univ. of Amsterdam), "Structure and Reactivity of Arylcopper Cluster Compounds"

15.3.78 Prof. G. Scott (Univ. of Aston), "Fashioning Plastics to Match the Environment"

22.3.78 Prof. H. Vahrenkamp (Univ. of Freiburg), "Metal-Metal Bonds in Organometallic Complexes"

19.4.78 Dr. M. Barber (U.M.I.S.T.), "Secondary Ion Mass Spectra of Surface Adsorbed Species"

15.5.78 Dr. M.I. Bruce (Univ. of Adelaide), "New Reactions of Ruthenium Compounds with Alkynes"

16.5.78 Dr. P. Ferguson (C.N.R.S., Grenoble), "Surface Plasma Waves and Adsorbed Species on Metals"

18.5.80 Prof. M. Gordon (Univ. of Essex), "Three Critical Points in Polymer Science"

22.5.78 Prof. D. Tuck (Univ. of Windsor, Ontario), "Electrochemical Synthesis of Inorganic and Organometallic Compounds"

24/25.5.78 Prof. P. von R. Schleyer (Univ. of Erlangen, Nurnberg), (i) "Planar Tetra-Coordinate Methanes, Perpendicular Ethylenes and Planar Allenes" (ii) "Aromaticity in Three Dimensions" (iii) "Non-Classical Carbocations"

21.6.78 Dr. S.K. Tyrlik (Academy of Sciences, Warsaw), "Dimethylglyoxime-Cobalt Complexes - Catalytic Black Boxes"

23.6.78 Prof. W.B. Person (Univ. of Florida), "Diode Laser Spectroscopy at 16 μm"

27.6.78 Prof. R.B. King (Univ. of Georgia, Athens, Georgia, U.S.A.), "The Use of Carbonyl Anions in the Synthesis of Organometallic Compounds"

30.6.78 Prof. G. Mateescu (Cape Western Reserve Univ.), "A Concerted Spectroscopy Approach to the Characterisation of Ions and Ion Pairs: Facts, Plans and Dreams"

15.9.78 Prof. W. Siebert (Univ. of Marburg, West Germany), "Boron Heterocycles as Ligands in Transition Metal Chemistry"

22.9.78 Prof. T. Fehlner (Univ. of Notre Dame, U.S.A.), "Ferraboranes: Syntheses and Photochemistry"

12.12.78 Prof. C.J.M. Stirling (Univ. of Bangor), "Parting is Such Sweet Sorrow - the Leaving Group in Organic Reactions"

14.2.79 Prof. B. Dunnell (Univ. of British Columbia), "The Application of N.M.R. to the Study of Motions in Molecules"

16.2.79 Dr. J. Tomkinson (Institute Laue-Langevin, Grenoble), "Studies of Adsorbed Species"

14.3.79 Dr. J.C. Walton (Univ.of St. Andrews), "Pentadienyl Radicals"

28.3.79 Dr. A. Reiser (Kodak Ltd), "Polymer Photography and the Mechanism of Cross-Link Formation in Solid Polymer Matrices"

5.4.79 Dr. S. Larsson (Univ. of Uppsala), "Some Aspects of Photoionisation Phenomena in Inorganic Systems"

25.4.79 Dr. C.R. Patrick (Univ. of Birmingham), "Chlorofluorocarbons and Stratospheric Ozone: An Appraisal of the Environmental Problem"

1.5.79 Dr. G. Wyman (European Research Office, U.S. Army), "Excited State Chemistry in Indigoid Dyes)

2.5.79 Dr. J.D. Hobson (Univ. of Birmingham), "Nitrogen-centred Reactive Intermediates"

8.5.79 Prof. A. Schmidpeter (Institute of Inorganic Chemistry, Univ. of Munich), "Five-membered Phosphorus Hetercycles Containing Dicoordinate Phosphorus"

9.5.79 Dr. A.J. Kirby (Univ. of Cambridge), "Struture and Reactivity in Intramolecular and Enzymic Catalysis"

9.5.79 Prof. G. Maier (Lahn-Giessen), "Tetra-tertbutyl-tetrahedrane

10.5.79 Prof. G. Allen, F.R.S. (Science Research Council), "Neutron Scattering Studies of Polymers"

16.5.79 Dr. J.F. Nixon (Univ. of Sussex), "Spectroscopic Studies on Phosphines and their Coordination Complexes"

23.5.79 Dr. B. Wakefield (Univ. of Salford), "Electron Transfer in Reactions of Metals and Organometallic Compounds with Polychloropyridine Derivatives"

13.6.79 Dr. G. Heath (Univ. of Edinburgh), "Putting Electrochemistry into mothballs - (Redox processes of metal porphyrins and phthalocynanines)".

14.6.79 Prof. I. Ugi (Univ. of Munich), "Synthetic Uses of Super Nucleophiles"

20.6.79 Prof. J.D. Corbett (Iowa State Univ., Ames, Iowa, U.S.A.), "Zintl Ions: Synthesis and Structure of Homopolyatomic Anions of the Post-Transition Elements"

27.6.79 Dr. H. Fuess (Univ. of Frankfurt), "Study of Electron Distribution in Crystalline Solids by X-ray and Neutron Diffraction"

21.11.79 Dr. J. Muller (Univ. of Bergen), "Photochemical Reactions of NH_3"

28.11.79 Prof. B. Cox, (Univ. of Stirling), "Macrobicyclic Cryptate Complexes: Dynamics and Selectivity".

5.12.79 Dr. G.C. Eastmand (Univ. of Liverpool), "Synthesis and Properties of Some Multi-Component Polymers"

12.12.79 Dr. C.I. Ratcliffe, "Rotor Motions in Solids"

18.12.79 Dr. K.E. Newman, (Univ. of Lausanne), "High Pressure Multinuclear n.m.r. in the Elucidation of the Mechanism of Fast, Simple Inorganic Reactions"

30.1.80 Dr. M.J. Barrow (Univ. of Edinburgh), "The Structures of Some Simple Inorganic Compounds of Silicon and Germanium - Pointers to Structural Trends in Group IV"

14.5.80 Dr. R. Hutton (Waters Associates), "Recent Developments in Multi-Milligram and Multi-Gram Scale Preparative High Performance Liquid Chromatography"

21.5.80 Dr. T.W. Bently (Univ. College of Wales, Swansea), "Medium and Structural Effects on Solvolytic Reactions"

10.7.80 Prof. P. des Marteau (Univ. of Heidelburg), "New Developments in Organonitrogen Fluorine Chemistry"